ORDERED AND DISORDERED CUBIC SYSTEMS: PYROCHLORE TO FLUORITE, NOW AND THE HORIZON

EDITED BY: Gordon James Thorogood, Sarah C. Finkeldei, Maik Kurt Lang and David Simeone

PUBLISHED IN: Frontiers in Chemistry

frontiers Research Topics

frontiers

ISSN 1664-8714
ISBN 978-2-88974-425-1
DOI 10.3389/978-2-88974-425-1

About Frontiers

Frontiers is more than just an open-access publisher of scholarly articles: it is a pioneering approach to the world of academia, radically improving the way scholarly research is managed. The grand vision of Frontiers is a world where all people have an equal opportunity to seek, share and generate knowledge. Frontiers provides immediate and permanent online open access to all its publications, but this alone is not enough to realize our grand goals.

Frontiers Journal Series

The Frontiers Journal Series is a multi-tier and interdisciplinary set of open-access, online journals, promising a paradigm shift from the current review, selection and dissemination processes in academic publishing. All Frontiers journals are driven by researchers for researchers; therefore, they constitute a service to the scholarly community. At the same time, the Frontiers Journal Series operates on a revolutionary invention, the tiered publishing system, initially addressing specific communities of scholars, and gradually climbing up to broader public understanding, thus serving the interests of the lay society, too.

Dedication to Quality

Each Frontiers article is a landmark of the highest quality, thanks to genuinely collaborative interactions between authors and review editors, who include some of the world's best academicians. Research must be certified by peers before entering a stream of knowledge that may eventually reach the public - and shape society; therefore, Frontiers only applies the most rigorous and unbiased reviews.
Frontiers revolutionizes research publishing by freely delivering the most outstanding research, evaluated with no bias from both the academic and social point of view. By applying the most advanced information technologies, Frontiers is catapulting scholarly publishing into a new generation.

What are Frontiers Research Topics?

Frontiers Research Topics are very popular trademarks of the Frontiers Journals Series: they are collections of at least ten articles, all centered on a particular subject. With their unique mix of varied contributions from Original Research to Review Articles, Frontiers Research Topics unify the most influential researchers, the latest key findings and historical advances in a hot research area! Find out more on how to host your own Frontiers Research Topic or contribute to one as an author by contacting the Frontiers Editorial Office: frontiersin.org/about/contact

ORDERED AND DISORDERED CUBIC SYSTEMS: PYROCHLORE TO FLUORITE, NOW AND THE HORIZON

Topic Editors:
Gordon James Thorogood, Australian Nuclear Science and Technology Organisation, Australia
Sarah C. Finkeldei, University of California, Irvine, United States
Maik Kurt Lang, The University of Tennessee, Knoxville, United States
David Simeone, Commissariat à l'Energie Atomique et aux Energies Alternatives (CEA), France

Citation: Thorogood, G. J., Finkeldei, S. C., Lang, M. K., Simeone, D., eds. (2022). Ordered and Disordered Cubic Systems: Pyrochlore to Fluorite, Now and the Horizon. Lausanne: Frontiers Media SA. doi: 10.3389/978-2-88974-425-1

Table of Contents

frontiers in Chemistry

EDITORIAL
published: 12 January 2022
doi: 10.3389/fchem.2021.830330

Editorial: Ordered and Disordered Cubic Systems: Pyrochlore to Fluorite, Now and the Horizon

Gordon James Thorogood[1,2]*, *Sarah C. Finkeldei*[3,4,5], *Maik Kurt Lang*[6] and *David Simeone*[7]

[1]Australian Nuclear Science and Technology Organization, Sydney, NSW, Australia, [2]Nagaoka University of Technology, Nagaoka, Japan, [3]Department of Chemistry, University of California, Irvine, Irvine, CA, United States, [4]Department of Chemical and Biomolecular Engineering, University of California, Irvine, Irvine, CA, United States, [5]Department of Materials Science and Engineering, University of California, Irvine, Irvine, CA, United States, [6]Department of Nuclear Engineering, The University of Tennessee, Knoxville, TN, United States, [7]CEA,DES,ISAS,DMN, Paris-Saclay, Gif-sur-Yvette, France

Keywords: pyrochlore, defect fluorite, disorder-compounds, density-functional theory, fluorite, mineralogy and chemistry

Editorial on the Research Topic

Ordered and Disordered Cubic Systems: Pyrochlore to Fluorite, Now and the Horizon

Any internet search for the term pyrochlore, fluorite or the derivation of the two will yield tens of thousands of results. This is clear evidence that the study of these systems, especially since the publication of the landmark review by Subramanian et al. (1983) in 1983 increases with every passing year.

The minerals fluorite and pyrochlore can be thought of as two ends of a continuum that encompass other variations such as defect fluorite. Materials with a fluorite structure are used in a wide range of applications, one reason being its ability to incorporate structural disorder. A cubic structure is the simplest in terms of symmetry and thus can accommodate certain amounts of variation in occupancy of atomic positions over a range of different crystallographic sites. It is this versatility that has seen these humble structures applied to all manner of uses ranging from fuel in a nuclear reactor (Simeone et al., 2017), fuel cell anodes (Lang et al., 2009), ion conductors (Wilde and Catlow, 1998), nuclear waste immobilization (Ewing et al., 2004), thermal barrier coatings (Wilde and Catlow, 1998), catalysts (Kim et al., 2020), and superconductors (Yonezawa et al., 2004) to name only a few. Often there is a common thread in these publications which is investigating in one form or another the order or disorder in those systems with one extreme example being high entropy pyrochlores (Oses et al., 2020).

It was our goal with this special edition to give an overview of what has traditionally been thought to be disorder in pyrochlore, how it relates to defect fluorite, to highlight the newest discoveries as well as the path forward in this research area. We included the effect of order or disorder induced by external means (irradiation, ball milling, pressure, and temperature), induced internally (changes in chemical composition and stoichiometry) and studies that advance the understanding of disorder occurring in those systems and the effect it has on the structure and properties. These studies were planned to encompass experimental, theoretical (such a density functional theory modelling) or a combination of both studies as is common in the current literature.

To place the rest of the articles into context the article by Atencio helps to summarise how definitions have changed over time, what the current nomenclature is and the reasons behind it. In the study the author concludes, and perhaps it is partly a challenge when they state that, surely there are several new pyrochlore- supergroup minerals to be described.

Edited and reviewed by:
Dmitriev Vladimir, European Synchrotron Radiation Facility, France

***Correspondence:**
Gordon James Thorogood
gjt@ansto.gov.au

Specialty section:
This article was submitted to Solid State Chemistry, a section of the journal Frontiers in Chemistry

Received: *07 December 2021*
Accepted: *14 December 2021*
Published: *12 January 2022*

Citation:
Thorogood GJ, Finkeldei SC, Lang MK and Simeone D (2022) Editorial: Ordered and Disordered Cubic Systems: Pyrochlore to Fluorite, Now and the Horizon. Front. Chem. 9:830330. doi: 10.3389/fchem.2021.830330

The work of the group from the School of Molecular Sciences and Navrotsky Eyring Center for Materials of the Universe where they examine the order-disorder of several families of cubic oxides from the point of view of how structure, composition, and thermodynamic parameters (enthalpy and entropy) determine the feasibility of different competing ordering processes and structures sets the tone for the special edition (Subramani). This enables the comparison of one structure type directly to another and so provides insight to future work and which of those studies might be most interesting and feasible.

In comparison the paper by Quinn et al. takes a theoretical approach closely aligned with Pauling's rules for ionic crystal structures and Goldschmidt's rules for ionic substitution. They propose a simple, but effective, way of determining whether a complex oxide may adopt the disordered fluorite structure and offer guidance in future synthesis.

The study by Kocevski et al. employs a slightly different theoretical approach, modelling from simple point defects to completely disordered structures, the dynamics during the disordering process, and the use of mathematical models to generate ordered solid solution configurations. The results are very similar to those of Quinn et al. and they highlight the challenges of short-range vs long range order and the definition thereof.

One advantage of disorder in pyrochlore and fluorite systems is the flexibility to incorporate elements of varying valence and ionic radius into these solid solutions. To gain further understanding into this phenonium Connor et al. employ DFT+*U* methods to examine the incorporation of U, Np, Pu, Am and Cm actinide elements into pyrochlores, activation energies for oxygen migration and radiation damage-induced structural changes in these materials. Comparison of calculated lattice parameters with experimental results are in very good agreement demonstrating the reliability of the method when applied to these systems.

Doped UO_2 is interesting being another example of a fluorite structure, that due to its flexibility can accommodate different dopants. Vinograd et al. demonstrate how linking together the thermodynamic and structural models allows the prediction of the lattice parameter as a function of z, T and the oxygen partial pressure, thus providing understanding as to the behaviour of these systems.

In an expansion of the concept of disorder in fluorite systems and how it effects ion conductivity Fossati et al. combine molecular dynamics modelling methods with computational diffraction techniques. Their results demonstrate that defects in the structure and most particularly Frenkel pairs play different roles depending on temperature. Additionally, analysis of the MD simulation boxes indicates that the additional diffraction peaks are the result of local environments with a structure close to the *Pbcn*. In these local environments, the X sublattice has HCP features.

Disorder is typically characterised via either diffraction or spectroscopy techniques. The review by Lumpkin et al. employs transmission electron diffraction to review a range of pyrochlore and defect fluorite type compounds with nominal $A_2B_2O_7$, A_2BO_5, ABC_2O_7, and other stoichiometries. Typically, the phase transformations and stability fields in these systems are mapped as a function of the ionic radii of the A and B-site cations, and they highlight situations where this is not the case and outline future investigation.

The review by Wardini et al. on probing disorder in the Transmission Electron Microscope is a must read for any student or early career researcher beginning in the field. It highlights the many methods available to study these systems, for example the section on strain analysis demonstrates how in-depth the mechanisms of disorder in these systems are. As stated in their conclusion "Going forward, as 4D-STEM is increasingly used in tandem with *in situ* and *in operando* studies, the dimensionality of these already rich, multidimensional datasets will extend into the temporal domain, as well as along the axis of the applied stimuli."

One advantage of pyrochlore being able to accommodate disorder is that cations can adopt valence states seldom reported. Kennedy et al. provide the first report of a stable valence 5 technetium oxide. Displacive disorder of the Pb cations and O(2) anions is observed, as evident from the refinements of diffraction patterns and the Raman spectroscopy. The disorder appears to allow for larger bond lengths for the Technetium thus resulting in it being in the higher valence state.

Finally, there is the work of Finkeldei et al., where the group investigates the formation of defect fluorite via the irradiation of a titanate and zirconate pyrochlore as reported in the literature. This study covers all length scales from neutron diffraction to transmission electron microscopy and somewhat controversially finds that defect fluorite does not form at low irradiation levels, which contradicts much of the literature. They state a second phase is due to the build-up of stress in the sample resulting from the localised amorphization after irradiation via He^{2+} ions. They propose a mechanism for the apparent formation of defect fluorite in X-ray diffraction patterns and it is worth comparing the results of this work with the stress characterisation of Wardini et al., it will be very interesting to see the future response to this work.

In closing, please use this special edition as one point of reference for ordered and disordered cubic systems, with the aim of clarifying the big questions in this area. This work is meant to be used as a cornerstone that may lead to new paths of discovery. Indeed, as we have already shown further development of experimental and modelling techniques have provided an improved understanding in these systems, this will continue in the future and more discoveries can be expected in these systems.

AUTHOR CONTRIBUTIONS

GT, SF, ML, and DS conceived and edited the special edition. All authors contributed to the editorial, equally.

REFERENCES

Ewing, R. C., Weber, W. J., and Lian, J. (2004). Nuclear Waste Disposal-Pyrochlore (A2B2O7): Nuclear Waste Form for the Immobilization of Plutonium and "Minor" Actinides. *J. Appl. Phys.* 95 (11 I), 5949–5971. doi:10.1063/1.1707213

Kim, M., Park, J., Kang, M., Kim, J. Y., and Lee, S. W. (2020). Toward Efficient Electrocatalytic Oxygen Evolution: Emerging Opportunities with Metallic Pyrochlore Oxides for Electrocatalysts and Conductive Supports. *ACS Cent. Sci.* 6 (6), 880–891. doi:10.1021/acscentsci.0c00479

Lang, M., Zhang, F. X., Ewing, R. C., Lian, J., Trautmann, C., and Wang, Z. (2009). Structural Modifications of Gd2Zr2-xTixO7 Pyrochlore Induced by Swift Heavy Ions: Disordering and Amorphization. *J. Mater. Res.* 24 (4), 1322–1334. doi:10.1557/jmr.2009.0151

Oses, C., Toher, C., and Curtarolo, S. (2020). High-entropy Ceramics. *Nat. Rev. Mater.* 5 (4), 295–309. doi:10.1038/s41578-019-0170-8

Simeone, D., Thorogood, G. J., Huo, D., Luneville, L., Baldinozzi, G., Petricek, V., et al. (2017). Intricate Disorder in Defect Fluorite/Pyrochlore: A concord of Chemistry and Crystallography. *Sci. Rep.* 7 (1), 3727. doi:10.1038/s41598-017-02787-w

Subramanian, M. A., Aravamudan, G., and Subba Rao, G. V. (1983). Oxide Pyrochlores - A Review. *Prog. Solid State. Chem.* 15 (2), 55–143. doi:10.1016/0079-6786(83)90001-8

Wilde, P. J., and Catlow, C. R. A. (1998). Defects and Diffusion in Pyrochlore Structured Oxides', *Solid State Ionics*. *Elsevier*. 112 (3–4), 173–183. doi:10.1016/s0167-2738(98)00190-8

Yonezawa, S., Muraoka, Y., Matsushita, Y., and Hiroi, Z. (2004). Superconductivity in a Pyrochlore-Related Oxide KOs2O6. *J. Phys. Condens. Matter.* 16 (3), L9–L12. doi:10.1088/0953-8984/16/3/L01

Conflict of Interest: The authors declare that the research was conducted in the absence of any commercial or financial relationships that could be construed as a potential conflict of interest.

Publisher's Note: All claims expressed in this article are solely those of the authors and do not necessarily represent those of their affiliated organizations, or those of the publisher, the editors, and the reviewers. Any product that may be evaluated in this article, or claim that may be made by its manufacturer, is not guaranteed or endorsed by the publisher.

frontiers in Chemistry

ORIGINAL RESEARCH
published: 01 July 2021
doi: 10.3389/fchem.2021.706269

Synthesis and Structure of Oxygen Deficient Lead-Technetium Pyrochlore, the First Example of a Valence V Technetium Oxide

*Brendan J. Kennedy[1], Timothy A. Ablott[2], Maxim Avdeev[1,3], Melody L. Carter[2], Linda Losurdo[1], Matilde Saura-Muzquiz[1], Kevin J. Thorogood[4], Jimmy Ting[1], Kia S. Wallwork[5], Zhaoming Zhang[2], Hanliang Zhu[2] and Gordon J. Thorogood[2,6]**

[1]School of Chemistry, The University of Sydney, Sydney, NSW, Australia, [2]Nuclear Fuel Cycle, Australian Nuclear Science and Technology Organisation, Kirrawee DC, NSW, Australia, [3]Australian Centre for Neutron Scattering, Australian Nuclear Science and Technology Organisation, Kirrawee DC, NSW, Australia, [4]Nuclear Materials, Australian Nuclear Science and Technology Organisation, Kirrawee DC, NSW, Australia, [5]Australian Synchrotron, Australian Nuclear Science and Technology Organisation, Clayton, VIC, Australia, [6]Department of Nuclear System Safety Engineering, Nagaoka University of Technology, Nagaoka, Japan

OPEN ACCESS

Edited by:
Vladimir Dmitriev,
European Synchrotron Radiation Facility, France

Reviewed by:
Jasper Plaisier,
Elettra Sincrotrone Trieste, Italy
Andrew Grosvenor,
University of Saskatchewan, Canada

***Correspondence:**
Gordon J. Thorogood
gjt@ansto.gov.au

Specialty section:
This article was submitted to Solid State Chemistry, a section of the journal Frontiers in Chemistry

Received: *07 May 2021*
Accepted: *08 June 2021*
Published: *01 July 2021*

Citation:
Kennedy BJ, Ablott TA, Avdeev M, Carter ML, Losurdo L, Saura-Muzquiz M, Thorogood KJ, Ting J, Wallwork KS, Zhang Z, Zhu H and Thorogood GJ (2021) Synthesis and Structure of Oxygen Deficient Lead-Technetium Pyrochlore, the First Example of a Valence V Technetium Oxide. Front. Chem. 9:706269. doi: 10.3389/fchem.2021.706269

The structure of lead-technetium pyrochlore has been refined in space group $Fd\bar{3}m$ with a = 10.36584(2) Å using a combination of synchrotron X-ray and neutron powder diffraction data and confirmed via Electron Diffraction. The oxide is found to be oxygen deficient with a stoichiometry of $Pb_2Tc_2O_{7-d}$. Displacive disorder of the Pb cations is evident from the refinements, as has been observed in $Bi_2Tc_2O_{7-d}$. X-ray absorption spectroscopic measurements at the Tc K-edge demonstrate the valence of the Tc is greater than 4.0 as anticipated from the refined oxygen stoichiometry. Raman spectroscopy confirms the presence of disorder leading us to conclude that this pyrochlore is the first example of a valence V technetium oxide.

Keywords: technetium, pyrochlore, disorder, crystallography, spectroscopy

INTRODUCTION

Technetium is unique amongst the transition metals in that no stable isotope exists. Technetium-99 is a major fission product of uranium-235 and is found in radioactive waste from nuclear fuel and, in certain jurisdictions, from the production of plutonium. Due to its long half-life ($t_{1/2} = 2.1 \times 10^5$ y) and high mobility through geological formations, the migration of ^{99}Tc is a significant challenge in nuclear waste management and it is a major contributor to the amount of radiation in the biosphere. Other isotopes of Tc are also of considerable importance, for example ^{99m}Tc is the most commonly employed isotope in nuclear medicine (Jurisson et al., 1993) and ^{95m}Tc is used as a radioisotope tracer (Conversi, 1985).

In comparison to the extensive literature on the nuclear medical applications of soluble technetium species, there is a dearth of information on the solid-state chemistry of Tc. Indeed, the work by Muller, White and Roy (Muller et al., 1964) in 1964 remains one of the most comprehensive reported studies in this area. Over the ensuring decades a small number of experimental studies have appeared including our studies of some Tc perovskites (Avdeev et al., 2011; Rodriguez et al., 2011; Thorogood et al., 2011a; Mravlje et al., 2012; Reynolds et al., 2017a), TcO_2 (Rodriguez et al., 2007; Reynolds et al., 2017b; Childs et al., 2018), inverse spinel (Thorogood et al., 2011b) and $ATcO_4$ scheelites (Kennedy et al., 2019) together with the study of some Bi-Tc oxides by Rodriguez and co-workers (Rodriguez et al., 2008) and lanthanoid pyrochlores by Hartman

et al. (2011). Theoretical studies of the lanthanoid technetate pyrochlores have also been reported (Weck et al., 2010). The extraordinary magnetic properties of $SrTcO_3$ and $CaTcO_3$ have ignited interest in Tc oxides.

Rodriguez et al. have reported the synthesis and crystal structure of the bismuth technetium pyrochlore $Bi_2Tc_2O_{7-d}$ d ~ 0.14 (Rodriguez et al., 2008). As observed for a number of other Bi pyrochlores, including $Bi_2Ru_2O_{7-d}$ (Avdeev et al., 2002), this structure is characterised by static disorder of the bismuth cations, an effect that is enhanced by the 6s (Conversi, 1985) lone pair electrons. Muller and co-workers (Muller et al., 1964) reported that the ternary lead-technetium oxide also forms a pyrochlore structure, which they suggested may be non-stoichiometric. Beyerlein and co-workers (Beyerlein et al., 1984) reported that the analogous lead-ruthenium pyrochlore is non-stoichiometric and displays oxygen vacancy ordering, the stoichiometry actually being $Pb_2Ru_2O_{6.5}$ and the resulting space group being $F\bar{4}3m$, rather than $Fd\bar{3}m$ as seen in $Bi_2Ru_2O_{7-d}$ (Beyerlein et al., 1984; Facer et al., 1993; Avdeev et al., 2002). The iridium pyrochlore $Pb_2Ir_2O_{6.5}$ (Kennedy, 1996) exhibits similar vacancy ordering and its structure is also described in $F\bar{4}3m$ however this vacancy ordered structure was not seen in $Pb_2Re_2O_{7-d}$ (Abakumov et al., 1998). It is generally believed that Re is a suitable, non-radioactive, analogue for Tc.

Given the prevalence of oxygen non-stoichiometry in pyrochlores it is probable that, as suggested by Muller et al., $Pb_2Tc_2O_{7-d}$ will be non-stoichiometric, however it is unclear if oxygen vacancy ordering will occur. The aim of the present work was to determine the structure of the lead-technetium pyrochlore, and in particular to establish the nature of any non-stoichiometry. This has been accomplished using a combination of synchrotron X-ray and neutron powder diffraction methods. As we show here the target oxide is indeed non-stoichiometric, however we find no evidence for oxygen-vacancy ordering. X-ray absorption near-edge structure (XANES) at the Tc K-edge and Raman spectroscopy measurements are also reported.

EXPERIMENTAL

Caution! ^{99}Tc is a β^- emitter (E_{max} = 0.29 MeV). Appropriate shielding was employed during the synthesis and all manipulations. The polycrystalline sample of $Pb_2Tc_2O_{7-d}$ was prepared by the addition of 2.55 g of NH_4TcO_4 to 2.34 g of $Pb(NO_3)_2$, this mixture was then dry rolled in a polyethylene vial for 2 h to ensure complete mixing, the powder was then calcined in Ar for 1 h at 650°C. The Ar used had 12 ppm of O_2, this percentage of O_2 needs to be taken into account when calcining or sintering these samples as extended exposure to even small amounts of O_2 will cause the Tc to oxidise and sample inhomogeneity will occur. The resultant calcine melted and so was ground in a mortar and pestle, wet ball milled in cyclohexane for 16 h and then tray dried. Note that milling in any other types of fluids may result in loss of Tc. Two one-gram pellets were pressed and sintered in Ar for 4 h at 800°C.

The synchrotron X-ray diffraction data were collected using the MYTHEN microstrip detector on the powder diffractometer at BL-10 of the Australian Synchrotron, Melbourne Australia (Wallwork et al., 2007). The sample (ca 1 mg) was loaded into a 0.3 mm diameter glass capillary inside a glovebox. The sealed capillary was rotated during the collection of the X-ray diffraction data. The data were recorded at room temperature in the angular range $5 < 2\theta < 85^\circ$, using X-rays of wavelength 0.82523 Å as estimated using NIST LaB_6. For high temperature measurements the sample was loaded into a 0.3 mm quartz capillary inside a glovebox and heated via a Cyberstar hot-air blower to up to 1,000°C. Neutron powder diffraction data were measured at room temperature using the high-resolution powder diffractometer Echidna at ANSTO's OPAL facility at Lucas Heights (Avdeev and Hester, 2018). These measurements were taken at λ = 1.540 Å, with the sample (~1 g) contained in a cylindrical vanadium can. The structure refinement used a combination of the synchrotron and neutron diffraction data sets using the program RIETICA (Liss et al., 2006).

X-ray absorption near-edge structure (XANES) spectra were collected from the sample as well as the $(NH_4)TcO_4$ and $SrTcO_3$ standards at the Tc K-edge on beamline BL-12 (Glover et al., 2007) at the Australian Synchrotron in transmission mode using argon-filled ionization chambers (Blanchard et al., 2014). A total of 2 mg of each Tc-containing powder sample was first mixed with an appropriate amount of BN, and the mixture was then loaded into a 3.5-mm-diameter hole at the center of a 1-mm-thick aluminum plate. The samples were sealed using Kapton tapes on both sides of the aluminum plate. The energy calibration was carried out using the Mo K-edge at 20,000 eV, steps of 0.2 eV were used across the edge. The software package Athena was used for background subtraction and normalization (Ravel and Newville, 2005).

Electron diffraction patterns and microanalyses were obtained at ANSTO using a JEOL 2000FXII TEM operated at 200 kV and equipped with a Link ISIS ultra-thin window solid-state Si(Li) detector and microanalysis system. The TEM was calibrated for electron diffraction work over a range of objective lens settings using a polycrystalline gold standard. The sample was ground and loaded onto a copper grid for analysis.

Raman spectra were obtained using a Renishaw inVia Qontor confocal Raman microscope (Renishaw plc., Wotton-under-Edge, United Kingdom) with a 532 nm continuous wave, diode-pumped solid-state laser (Renishaw plc., Wotton-under-Edge, United Kingdom). The measurements were carried out with 0.1 mW of laser power on the sample and a x50/0.5NA long working distance objective, giving rise to a focused spot of approximately 1.3 μm diameter. The scattered light was analysed in backscattering geometry using holographic notch filters, 2,400 lines/mm grating and an air-cooled CCD detector. The spectra were collected at temperatures 298 K (25°C), 273 K (0°C) and 100 K (−173°C) using a FTIR600 variable-temperature stage (Linkam Scientific Instruments Ltd, Surrey, United Kingdom). Data collection was performed over a spectral range of 89–1,348 cm^{-1} with 100 accumulations/data set of 5 s exposure time per accumulation and an equilibration time of 10 min at each temperature. To avoid potential contamination of the equipment while maximizing

temperature conductivity from the variable-temperature plate to the sample, the powder sample (ca 1 mg) was loaded into a 0.3 mm diameter quartz capillary inside a glovebox and this was sealed between two copper plates using thermal paste. An aperture in the top plate enabled the laser to reach the sample.

RESULTS AND DISCUSSION

Diffraction Studies

The structure of $Pb_2Tc_2O_{7-d}$ was initially refined as a cubic pyrochlore in space group $Fd\bar{3}m$ (Number 227) (Subramanian et al., 1983) with the Pb on the 16*d* sites, Tc on the 16*c*; O(1) on 48*f* and O(2) on 8*b*. In this structure there is only one variable fractional coordinate, for O(1) at (*x*, 1/8, 1/8) with $x \sim 0.3$. The unit cell parameter 10.36584(2) Å was determined in the Rietveld refinement using the combination of synchrotron X-ray and neutron diffraction data. This value is in excellent agreement with that reported by Muller et al. (1964) (10.361 Å). Examination of the diffraction profiles revealed weak reflections due to the presence of small amounts of an unidentified impurity phase when the *y* axis was plotted as a sqrt of counts, and they are not visible in the difference plot of counts vs. angle. These phases could not be identified because there was not a sufficient number of peaks to match with known starting elements. Upon heating these reflections disappeared and so they are assumed to be a small amount of unreacted starting material therefore such reflections were excluded from the Rietveld refinements. Refinement of the pattern collected at 1,000°C resulted in a unit cell parameter of 10.45961(5) Å with no phase change visible, the increase in unit cell parameter consistent with thermal expansion. The refinements, using X-ray or neutron diffraction data or a combination of both, gave larger than expected atomic displacement parameters [B_{iso} = 3.4(1) $Å^2$ for the O(2) atoms at (3/8 3/8 3/8)] which is indicative of vacancies. Refinement of the occupancy for this site yielded a value 0.86(4) with the displacement parameter reducing somewhat to 2.6(1) $Å^2$. There was no evidence for reflections of the type *hk*0 with $h + k = 2n$ such as the 420 or 640 reflections in the diffraction patterns indicative of a lowering of symmetry from $Fd\bar{3}m$ to $F\bar{4}3m$ as is observed for $Pb_2Ru_2O_{6.5}$ (Beyerlein et al., 1984) and $Pb_2Ir_2O_{6.5}$ (Kennedy, 1996). Evidently the structure of $Pb_2Tc_2O_{7-d}$, like that of $Pb_2Re_2O_{7-d}$ (Abakumov et al., 1998), is described by space group $Fd\bar{3}m$ and does not exhibit oxygen vacancy ordering.

Previous high resolution structural studies of pyrochlores containing Bi cations on the *A*-site including $Bi_2Tc_2O_{7-d}$ (Rodriguez et al., 2008), have revealed static disorder of the Bi cations (Vanderah et al., 2005; Somphon et al., 2006). It should be noted that this is in contrast to the study of $Ln_2Tc_2O_7$ compounds performed by Hartman and co-workers (Hartmann et al., 2011), however such disorder has also been seen in $La_2Zr_2O_7$ (Tabira et al., 2001); although it is amplified by the presence of the Bi $6s^2$ lone pair electrons (Vanderah et al., 2005). Given that Pb^{2+} is isoelectronic with Bi^{3+}, the possibility of static disorder of the Pb cations was then considered. Two models, where the Pb was displaced from the 16*d* site to either a 96*g* or 96*h* site, were explored. Both models resulted in a small improvement in the quality of the fit, however the data did not allow us to distinguish the best model between these. These two models are effectively equivalent, and we present here the results obtained with the Pb disordered on the 96*h* site. The possibility that the O(2) atom was also disordered on the 32*e* site was considered and the inclusion of such disorder resulted in a noticeable reduction in the displacement parameter for this atom to 0.71(23) $Å^2$. There is a noticeable difference in the values of the B_{iso} between the Pb and the Tc, this is due to the Biso for the 8-coordinate site in the pyrochlores being larger than that of the 6-coordinate site reflecting its more irregular environment. Interestingly the electron diffraction images of $Pb_2Re_2O_{7-d}$ published by Abakumov and co-workers (Abakumov et al., 1998) did not show any diffuse features characteristic of cation disorder suggesting there may be subtle differences between the Re and Tc oxides. Diffuse features have been observed in electron diffraction studies of numerous Bi containing pyrochlores including $Bi_2Ru_2O_7$ (Goodwin et al., 2007).

TABLE 1 | Refined atomic coordinates and atomic displacement parameters for $Pb_2Tc_2O_{7-d}$. These parameters were obtained by refinement against a combined neutron and synchrotron X-ray diffraction data set. *a* = 10.36581(2)Å R_P = 2.50 R_{WP} = 3.46% χ^2 = 12.53. A comparably good fit could be obtained if the Pb was placed on the 96*h* site.

Atom	Site	*x*	*y*	*z*	B_{iso}	N
Pb	96*h*	0	0.2523(14)	0.7477(14)	0.60(4)	2[a]
Tc	16*c*	0	0	0	0.07(2)	2
O(1)	48*f*	0.3189(1)	0.125	0.125	0.30(1)	6
O(2)	32*e*	0.3918(5)	0.3918(5)	0.3918(5)	0.71(23)	0.86(1)

[a]*N is the equivalent number of atoms present, the Pb is on the 96*h *site and shows six-fold disorder.*

The results of the refinements are summarised in **Table 1** and are illustrated in **Figure 1**.

The wide-spread prevalence of oxygen vacancies in pyrochlore oxides is rationalised by viewing the structure as based on two weakly interacting, but interpenetrating networks of formula $Pb_2O(2)$ and $Tc_2O(1)_6$ as illustrated in **Figure 2**.

The Pb cations in $Pb_2Tc_2O_{7-d}$ are in a compressed scalenohedral environment. The displacement of the Pb cations within the puckered hexagon of the PbO(1) group reduces two Pb-O(1) distances but increases the remaining four. The average Pb-O distance of 2.625(8) Å is not significantly changed from that seen in the ideal structure and is much longer than the two Pb-O(2) bonds along the $\bar{3}$ axis, 2.244(1) Å, reflecting a relatively weak interaction between the Pb and the Tc_2O_6 network. Presumably the displacement of the Pb is a response to the abnormally high bond valence that would occur if the Pb remained on the 16*d* site, viz 2.79. The BVS estimated for the Pb assuming the O(2) remains at the 8*a* site is 1.95. The Tc cations are surrounded by six O(1) atoms in a trigonal antiprism geometry with six equal Tc-O(1) distances of 1.9672(4) Å. This distance is shorter than the average Tc-O distances of 1.983 and 1.997 Å seen in $SrTcO_3$ and $CaTcO_3$ and of 2.011 Å reported for $Bi_2Tc_2O_{7-d}$, where the Tc is formally tetravalent. The BVS for Tc is estimated to be 4.48 using the R_o value of 1.859 Å reported for Tc^{5+} by Wester and Hess (2005). The Tc-O(1)-Tc angle is 137.34(6)°. This angle is appreciably larger than the 134.109(4)° found for $Bi_2Tc_2O_{7-d}$ (Rodriguez

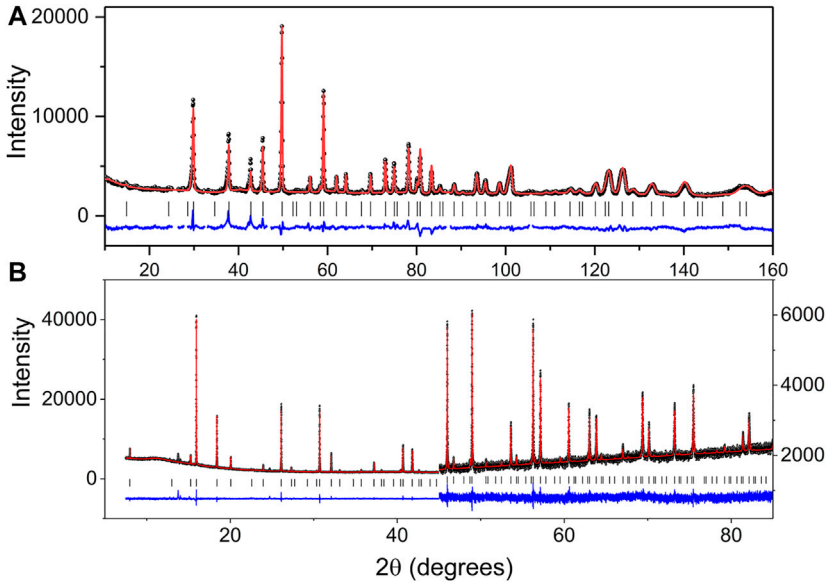

FIGURE 1 | Observed, calculated and difference **(A)** neutron and **(B)** synchrotron X-ray diffraction profiles (second half of the pattern has a scale increase of 8.3 to allow the difference and observed profiles to align) for $Pb_2Tc_2O_{7-d}$. The change in scale near $2\theta = 45^{\circ}$ in the SXRD pattern highlights both the quality of the data and fit.

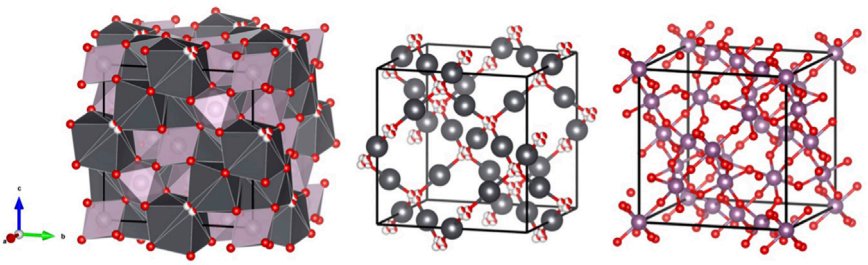

FIGURE 2 | Interconnecting network and the two separate sub lattices, Pb sites are shown in grey, Tc sites in purple, O(1) as fully coloured (red) spheres, and O(2) are red and white spheres, indicating the four-fold disorder of these.

et al., 2008). In general this bond angle is larger in the Pb pyrochlores than those seen in the corresponding Bi pyrochlores; 134.81 vs. 133.17° for $Pb_2Ru_2O_{6.5}$ (Beyerlein et al., 1984) and $Bi_2Ru_2O_7$ (Facer et al., 1993; Avdeev et al., 2002) respectively and 133.27 vs. 131.39° for the analogous Ir oxides (Kennedy, 1996). Given that these Ru and Ir pyrochlores are metallic oxides, we anticipate that $Pb_2Tc_2O_{7-d}$ will also be metallic. The magnitude of the Tc-O(1)-Tc bond angle has been associated with the presence of metallic bonding in Ru pyrochlores. The incorporation of Pb^{2+} or Bi^{3+} on the *A*-site increases this bond angle and promotes metallic bonding, however semi-conducting behavior has been observed when lanthanoid cations occupy the *A*-site (Kennedy and Vogt, 1996). Reported DFT calculations of the rare earth technetate pyrochlores suggest that these will be metallic, and although the Tc-O(1)-Tc angle in such oxides is unknown we speculate that it will be greater than that seen in the corresponding, semiconducting ruthernates.

Selected area diffraction patterns (SAD) were indexed with the SingleCrystal™ software (CrystalMaker, 2021) *via* the coordinates obtained from X-ray and neutron diffraction analysis. The experimental patterns were in good agreement with the predicted patterns as shown in **Figure 3**, the zone axis for the experimental and simulated SAD patterns is [110]. An overlay of the simulated SAD patterns on the experimental one shows crosses for the forbidden reflections that are not shown in experimental image except {002} due to double diffraction. For the space group $Fd\bar{3}m$ {002} reflections when viewed down the [110] axis are kinematically forbidden. If the TEM specimen is sufficiently thick those reflections arise due to double scattering (double diffraction) by the ±(−111) and ±(1−11) reflections (Liao, 2006).

X-ray Absorption Spectroscopy

The X-ray absorption spectrum of $Pb_2Tc_2O_{7-d}$ in the region of the Tc K-edge is dominated by a pronounced 1s - 5p dipole allowed

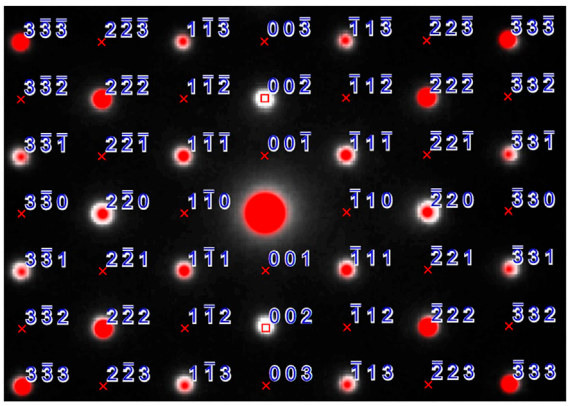

FIGURE 3 | SAD pattern with experimental data shown as white dots, red dots indicate the simulated pattern, reflections are marked, lattice absences are shown with a red cross and space group absences are shown with a red square.

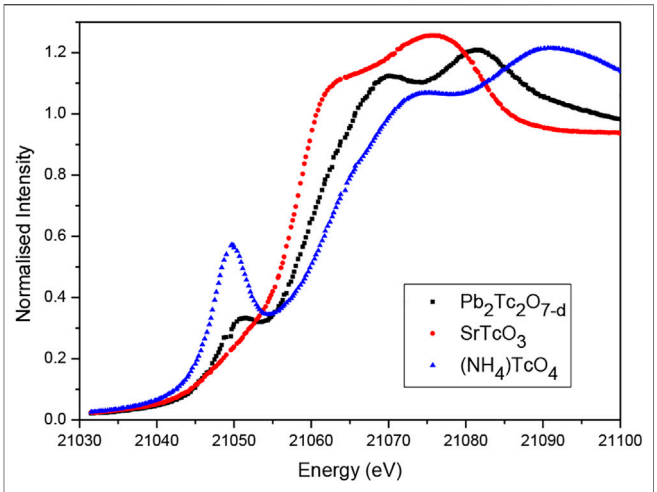

FIGURE 4 | Normalised X-ray absorption spectra of $Pb_2Tc_2O_{7-d}$, $SrTc^{4+}O_4$ and $(NH_4)Tc^{7+}O_4$. The Tc has six-fold coordination in $Pb_2Tc_2O_{7-d}$ and $SrTcO_3$ and is in a tetrahedral environment in $(NH_4)TcO_4$.

transition at about 21,058 eV. This is illustrated in **Figure 4**, together with the spectra of $SrTcO_3$ and $(NH_4)TcO_4$. It is immediately apparent from this figure that the energy of the Tc K-edge in $Pb_2Tc_2O_{7-d}$ is intermediate between that of the Tc^{4+} ($SrTcO_3$) and Tc^{7+} ($(NH_4)TcO_4$) standards. This is consistent with formal valence of Tc being greater than four as indicated by the BVS calculations. Using the stoichiometry derived from the neutron diffraction measurement, $Pb_2Tc_2O_{7-d}$, and assuming the lead remains divalent, Tc has a formal charge of +4.86.

The presence of the strong pre-edge feature in the spectrum of $Pb_2Tc_2O_{7-d}$ is somewhat unexpected. Such a feature is not apparent in the published spectra of $Bi_2Tc_2O_{7-d}$ (Rodriguez et al., 2008). The intensity of the pre-edge feature, seen in many K-edge spectra, is known to be sensitive to the site symmetry of the absorber. The transition may be assigned to a, formally dipole forbidden in centrosymmetric species, 1s → 4d transition. This transition is weakly quadrupole-allowed and gains intensity by mixing of the metal p-orbitals in a non-centrosymmetric absorber (Laplaza et al., 1996). This is clearly evident in the spectrum of tetrahedral $(NH_4)TcO_4$ where the 1s → 4d transition at 21047.7 eV is observed to be relatively intense. Studies of various Mo and Ru compounds demonstrate that well resolved pre-edge features can be observed for six-coordinate complexes where the symmetry is not strictly octahedral (Laplaza et al., 1996; Resseler et al., 2000; Sikora et al., 2007) and it is possible that this is the case here. An alternate possibility, that the sample has partially decomposed to produce a lower-symmetry material during the measurements, cannot be discounted. Irrespective of the origin of this feature in the Tc K-edge the XAS demonstrates the Tc oxidation state to be greater than 4+.

Raman Spectroscopy

Raman spectra of the $Pb_2Tc_2O_{7-\delta}$ sample were collected at 298 K (25°C), 273 K (0°C) and 100 K (−173°C). To correct for the Bose-Einstein occupation factor (Loudon, 1964), the raw data was divided by $n(\omega)+1$, where $n(\omega)$ is the Bose-Einstein distribution given by:

$$n(\omega) = \frac{1}{e^{\hbar\omega/k_B T} - 1} \quad (1)$$

Here, $\hbar$ is the reduced Plank's constant, k_B is the Boltzmann constant, T is the absolute temperature and ω is the angular frequency, which is related to the Raman shift according to **Eq. 2**:

$$\omega = 2\pi c(Raman\ shift) \quad (2)$$

where c is the speed of light.

The corrected intensities were normalized by the maximum value and fitted over the range of 100–1,000 cm^{-1} using a sum of Lorentzian functions. The obtained spectra at 298, 273, and 100 K are shown in **Figure 5**. The spectra comprise a large number of overlapping and convoluted Raman modes, and several Lorentzian peaks (>23 peaks) were needed in order to obtain a satisfactory fit of the data (see **Supplementary Material** for details of the fits). The most significant fitted bands (*i.e.,* those describing clear, "sharp" peaks in the data) are shown in blue in **Figure 5**, whereas broader peaks describing background features are shown in light grey. The same general features are observed in the spectra measured at each of the three temperatures, although the observed sharpening of the peaks at lower temperatures emphasises the doublet nature of some peaks (see grey insert of **Figure 5**).

The ideal pyrochlore structure in space group $Fd\bar{3}m$, with no cationic or anionic disorder, gives rise to six Raman-active modes, seven IR modes and one acoustic mode, according to factor group analysis (McCauley, 1973; Glerup et al., 2001). The six Raman-active modes given per set of ions and their respective crystallographic positions are:

$$A\ (16d):\ \text{none}$$
$$B\ (16c):\ \text{none}$$
$$\mathrm{O}(1)\ (48f):\ A_g + E_g + 3F_{2g}$$
$$\mathrm{O}(2)\ (8b):\ F_2g$$

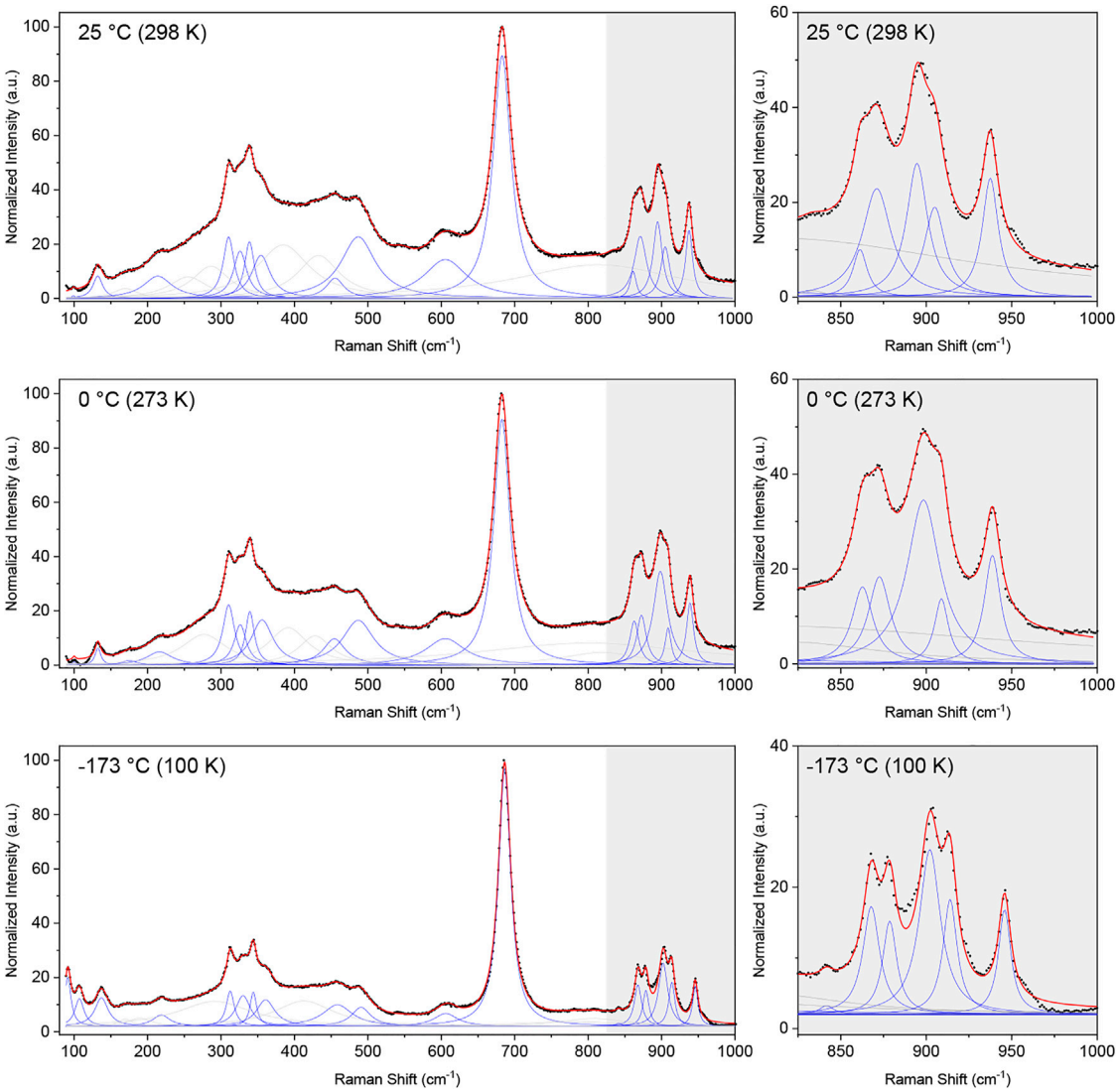

FIGURE 5 | Normalized Raman spectra corrected for the Bose-Einstein population factor (black dots) and cumulative fit (red line) of a sum of Lorentzian functions (blue and grey) to the Raman spectra collected at 298 K (25°C), 273 K (0°C) and 100 K (−173°C). The broader Lorentzian peaks, which do not describe a defined peak but contribute to the description of the background are shown in grey, whereas peaks describing clearly visible peaks are shown in blue. An enhancement of the region between 825 and 1,000 cm^{-1} is given for each temperature, emphasizing the narrower nature of the peaks at lower temperatures.

The data unequivocally shows the presence of more than the six Raman bands expected for the ideal pyrochlore structure. In disordered structures, additional bands may emerge due to a change in local symmetry or a breakdown of the selection rules leading to silent and IR-active modes to appear in the Raman spectrum (Glerup et al., 2001). In the case of the disordered $Pb_2Tc_2O_{7-d}$ studied here, with the Pb and O(2) anions occupying the 96*h* and 32*e* Wyckoff positions, respectively, group theory predicts a total of 17 Raman-active modes, given by (Kroumova et al., 2003):

$$\mathrm{Pb}\ (96h) : A_{1g} + 3E_g + 4F_{2g}$$
$$\mathrm{Tc}\ (16c) : \textit{none}$$
$$\mathrm{O(1)}\ (48f) : A_{1g} + E_g + 3F_{2g}$$
$$\mathrm{O(2)}\ (32e) : A_{1g} + E_g + 2F_{2g}$$

The number of predicted Raman-active modes agrees well with the number of significant peaks needed to obtain a satisfactory fit to the data (*i.e.*, 17 significant fitted peaks in the 100 K Raman spectrum and 16 in the other two spectra), however, given the complex nature of the spectra we cannot confidently assign the fitted peaks to correspond to the aforementioned 17 Raman-active bands predicted for a disordered pyrochlore. Nevertheless, the data clearly shows the presence of several additional modes than that of the archetypical pyrochlore structure, corroborating the displacive disorder of the

Pb and O(2) sites in $Pb_2Tc_2O_{7-d}$. A similar observation was made by Arenas et al. (2010) in their Raman study of substituted bismuth pyrochlores, where displacive disorder gave rise to additional Raman bands.

CONCLUSION

The structure of lead-technetium pyrochlore has been refined using a combined synchrotron X-ray and neutron powder diffraction data set. The oxide is found to be oxygen deficient with a stoichiometry of $Pb_2Tc_2O_{7-d}$ with disordered oxygen vacancies. In this regards the structure is similar to $Pb_2Re_2O_{7-d}$ rather than to the analogous ruthenate, which displays ordering of the oxygen vacancies. Displacive disorder of the Pb cations and O(2) anions is observed, as evident from the refinements. X-ray absorption spectroscopic measurements at the Tc K-edge demonstrate the valence of the Tc is greater than 4+. Taking into account the BVS results from diffraction analysis, the most likely conclusion is that Tc is in a 5+ oxidation sate. Raman spectroscopy confirmed a change in the local structure and coordination of the ions compared to the ideal, non-disordered pyrochlore structure, supporting the displacive disorder present in $Pb_2Tc_2O_{7-d}$.

DATA AVAILABILITY STATEMENT

The original contributions presented in the study are included in the article/**Supplementary Material**, further inquiries can be directed to the corresponding author.

AUTHOR CONTRIBUTIONS

BK, initial draft of manuscript, co conceived the research topic and performed synchrotron and neutron diffraction experiments and subsequent data analysis. TA, performed Raman data collection, manuscript production and literature review. MA, neutron diffraction and method of analyzing Technetium sample in neutron diffractometer. MC, sample synthesis. LL, data collection, manuscript production and literature review, MS, Raman data collection and analysis, manuscript production. KT, developed method for active Raman spectroscopy and literature review. JT, synchrotron data collection. KW, synchrotron data collection setup. ZZ, XANES data collection and analysis. HZ TEM data analysis. GT, project driver, final manuscript production, all scattering experiments, TEM data acquisition, Raman data collection.

ACKNOWLEDGMENTS

The authors acknowledge the financial support from the Australian Government under SIA grant SHCC000002, the use of ACNS ANSTO facilities supported by NCRIS funding as well as Mike Jovanovic with assistance in the production of the samples.

SUPPLEMENTARY MATERIAL

The Supplementary Material for this article can be found online at: https://www.frontiersin.org/articles/10.3389/fchem.2021.706269/full#supplementary-material

REFERENCES

Abakumov, A. M., Shpanchenko, R. V., Antipov, E. V., Kopnin, E. M., Capponi, J. J., Marezio, M., et al. (1998). Synthesis and Structural Study of Pb2Re2O7−xPyrochlores. *J. Solid State. Chem.* 138, 220–225. doi:10.1006/jssc.1998.7778

Arenas, D. J., Gasparov, V., Charles, H. P., and Tanner, D. B. (2010). Raman Study of Phonon Modes in Bismuth Pyrochlores. *Phys. Rev. B.* 82, 214302. doi:10.1103/physrevb.82.214302

CrystalMaker (2021). *Generated Using SingleCrystal^{TM}: A Single-crystal Diffraction Program for Mac and Windows*. Oxford, England: CrystalMaker Software Ltd.

Avdeev, M., Haas, M. K., Jorgensen, J. D., and Cava, R. J. (2002). Static Disorder from Lone-Pair Electrons in Pyrochlores. *J. Solid State. Chem.* 169, 24–34. doi:10.1016/s0022-4596(02)00007-5

Avdeev, M., Thorogood, G. J., Carter, M. L., Kennedy, B. J., Ting, J., Singh, D. J., et al. (2011). Antiferromagnetism in a Technetium Oxide. Structure of Catco3. *J. Am. Chem. Soc.* 133, 1654–1657. doi:10.1021/ja109431t

Avdeev, M., and Hester, J. R. (2018). ECHIDNA: a Decade of High-Resolution Neutron Powder Diffraction at OPAL. *J. Appl. Cryst.* 51, 1597–1604. doi:10.1107/s1600576718014048

Beyerlein, R. A., Horowitz, H. S., Longo, J. M., Leonowicz, M. E., Jorgensen, J. D., and Rotella, F. J. (1984). Neutron Diffraction Investigation of Ordered Oxygen Vacancies in the Defect Pyrochlores, Pb2Ru2O6.5 and PbT1Nb2O6.5. *J. Solid State. Chem.* 51, 253–265. doi:10.1016/0022-4596(84)90341-4

Blanchard, P. E. R., Reynolds, E., Kennedy, B. J., Ling, C. D., Zhang, Z., Thorogood, G., et al. (2014). An Unconventional Method for Measuring the TcL3-Edge of Technetium Compounds. *J. Synchrotron Radiat.* 21, 1275–1281. doi:10.1107/s1600577514014891

Childs, B. C., Lawler, K. V., Braband, H., Mast, D. S., Bigler, L., Stalder, U., et al. (2018). The Nature of the Technetium Species Formed during the Oxidation of Technetium Dioxide with Oxygen and Water. *Eur. J. Inorg. Chem.* 2018, 1137–1144. doi:10.1002/ejic.201701199

Conversi, A. (1985). Uptake and Loss of Technetium-95m in the Crab Pachygrapsus Marmoratus. *J. Environ. Radioactivity*. 2, 161–170. doi:10.1016/0265-931x(85)90005-0

Facer, G., Elcombe, M., and Kennedy, B. (1993). Bismuth Ruthenium Oxides. Neutron Diffraction and Photoelectron Spectroscopic Study of Bi2Ru2O7 and Bi3Ru3O11. *Aust. J. Chem.* 46, 1897–1907. doi:10.1071/ch9931897

Glerup, M., Nielsen, O. F., and Poulsen, F. W. (2001). The Structural Transformation from the Pyrochlore Structure, A2B2O7, to the Fluorite Structure, AO2, Studied by Raman Spectroscopy and Defect Chemistry Modeling. *J. Solid State. Chem.* 160, 25–32. doi:10.1006/jssc.2000.9142

Glover, C., McKinlay, J., Clift, M., Barg, B., and Boldeman, J. (2007). Status of the X-Ray Absorption Spectroscopy (XAS) Beamline at the Australian Synchrotron. *AIP Conf. Proc.* 882, 884–886. doi:10.1063/1.2644692

Goodwin, A. L., Withers, R. L., and Nguyen, H.-B. (2007). Real-space Refinement of Single-crystal Electron Diffuse Scattering and its Application to Bi2Ru2O7−δ. *J. Phys. Condens. Matter* 19, 335216. doi:10.1088/0953-8984/19/33/335216

Hartmann, T., Alaniz, A., Poineau, F., Weck, P. F., Valdez, J. A., Tang, M., et al. (2011). Structure Studies on Lanthanide Technetium Pyrochlores as Prospective Host Phases to Immobilize 99technetium and Fission Lanthanides from Effluents of Reprocessed Used Nuclear Fuels. *J. Nucl. Mater.* 411, 60–71. doi:10.1016/j.jnucmat.2011.01.033

Jurisson, S., Berning, D., Jia, W., and Ma, D. (1993). Coordination Compounds in Nuclear Medicine. *Chem. Rev.* 93, 1137–1156. doi:10.1021/cr00019a013

Kennedy, B. J., Injac, S., Thorogood, G. J., Brand, H. E. A., and Poineau, F. (2019). Structures and Phase Transitions in Pertechnetates. *Inorg. Chem.* 58, 10119–10128. doi:10.1021/acs.inorgchem.9b01257

Kennedy, B. J. (1996). Oxygen Vacancies in Pyrochlore Oxides: Powder Neutron Diffraction Study of Pb2Ir2O6.5and Bi2Ir2O7−y. *J. Solid State. Chem.* 123, 14–20. doi:10.1006/jssc.1996.0146

Kennedy, B. J., and Vogt, T. (1996). Structural and Bonding Trends in Ruthenium Pyrochlores. *J. Solid State. Chem.* 126, 261–270. doi:10.1006/jssc.1996.0337

Kroumova, E., Aroyo, M. I., Perez-Mato, J. M., Kirov, A., Capillas, C., Ivantchev, S., et al. (2003). Bilbao Crystallographic Server : Useful Databases and Tools for Phase-Transition Studies. *Phase Transitions*. 76, 155–170. doi:10.1080/0141159031000076110

Laplaza, C. E., Johnson, M. J. A., Peters, J. C., Odom, A. L., Kim, E., Cummins, C. C., et al. (1996). Dinitrogen Cleavage by Three-Coordinate Molybdenum(III) Complexes: Mechanistic and Structural Data1. *J. Am. Chem. Soc.* 118, 8623–8638. doi:10.1021/ja960574x

Liao, Y. (2006). *Practical Electron Microscopy and Database*. Available at https://www.globalsino.com/EM/page5001.html.

Liss, K.-D., Hunter, B., Hagen, M., Noakes, T., and Kennedy, S. (2006). Echidna-the New High-Resolution Powder Diffractometer Being Built at OPAL. *Physica B: Condensed Matter*. 385-386, 1010–1012. doi:10.1016/j.physb.2006.05.322

Loudon, R. (1964). The Raman Effect in Crystals. *Adv. Phys.* 13, 423–482. doi:10.1080/00018736400101051

McCauley, R. A. (1973). Infrared-absorption Characteristics of the Pyrochlore Structure*. *J. Opt. Soc. Am.* 63, 721–725. doi:10.1364/josa.63.000721

Mravlje, J., Aichhorn, M., and Georges, A. (2012). Origin of the High Néel Temperature in SrTc. *Phys. Rev. Lett.* 108, 197202. doi:10.1103/physrevlett.108.219903

Muller, O., White, W. B., and Roy, R. (1964). Crystal Chemistry of Some Technetium-Containing Oxides. *J. Inorg. Nucl. Chem.* 26, 2075–2086. doi:10.1016/0022-1902(64)80152-4

Ravel, B., and Newville, M. (2005). ATHENA,ARTEMIS,HEPHAESTUS: Data Analysis for X-ray Absorption Spectroscopy usingIFEFFIT. *J. Synchrotron Radiat.* 12, 537–541. doi:10.1107/s0909049505012719

Ressler, T., Timpe, O., Neisius, T., Find, J., Mestl, G., Dieterle, M., et al. (2000). Time-Resolved XAS Investigation of the Reduction/Oxidation of MoO3−x. *J. Catal.* 191, 75–85. doi:10.1006/jcat.1999.2772

Reynolds, E., Avdeev, M., Thorogood, G. J., Poineau, F., Czerwinski, K. R., Kimpton, J. A., et al. (2017). Structure and Magnetism in $\Mathrm{S}{\mathrm{r}}_{1\ensuremath{-}x}{A}_{x}\mathrm{Tc}{\Mathrm{O}}_{3}$ Perovskites: Importance of the A-site Cation. *Phys. Rev. B.* 95, 54430. doi:10.1063/1.2644692

Reynolds, E., Zhang, Z., Avdeev, M., Thorogood, G. J., Poineau, F., Czerwinski, K. R., et al. (2017). Thermal Expansion Behavior in TcO2. Toward Breaking the Tc-Tc Bond. *Inorg. Chem.* 56, 9219–9224. doi:10.1021/acs.inorgchem.7b01235

Rodriguez, E. E., Poineau, F., Llobet, A., Czerwinski, K., Seshadri, R., and Cheetham, A. K. (2008). Preparation and Crystal Structures of Bismuth Technetates: A New Metal Oxide System. *Inorg. Chem.* 47, 6281–6288. doi:10.1021/ic8003273

Rodriguez, E. E., Poineau, F., Llobet, A., Kennedy, B. J., and Avdeev, M. (2011). High Temperature Magnetic Ordering in the 4d Perovskite SrTcO3. *Phys. Rev. Lett.* 106, 67201. doi:10.1103/physrevlett.106.067201

Rodriguez, E. E., Poineau, F., Llobet, A., Sattelberger, A. P., Bhattacharjee, J., Waghmare, U. V., et al. (2007). Structural Studies of TcO2by Neutron Powder Diffraction and First-Principles Calculations. *J. Am. Chem. Soc.* 129, 10244–10248. doi:10.1021/ja0727363

Sikora, M., Oates, C. J., Szczerba, W., Kapusta, C., Zukrowski, J., Zajac, D., et al. (2007). XAS Study of Ru Doped N=1, 2 Ruddlesden-Popper Manganites. *J. Alloys Compounds*. 442, 265–267. doi:10.1016/j.jallcom.2006.06.115

Somphon, W., Ting, V., Liu, Y., Withers, R. L., Zhou, Q., and Kennedy, B. J. (2006). Local crystal Chemistry, Structured Diffuse Scattering and the Dielectric Properties of (Bi1−xYx)2(MIIINbV)O7 (M=Fe3+, In3+) Bi-pyrochlores. *J. Solid State. Chem.* 179, 2495–2505. doi:10.1016/j.jssc.2006.04.046

Subramanian, M. A., Aravamudan, G., and Subba Rao, G. V. (1983). Oxide Pyrochlores - A Review. *Prog. Solid State. Chem.* 15, 55–143. doi:10.1016/0079-6786(83)90001-8

Tabira, Y., Withers, R. L., Yamada, T., and Ishizawa, N. (2001). Annular Dynamical Disorder of the Rare Earth Ions in a La2Zr2O7 Pyrochlore via Single crystal Synchrotron X-ray Diffraction. *Z. Krist.* 216, 92–98. doi:10.1524/zkri.216.2.92.20338

Thorogood, G. J., Avdeev, M., Carter, M. L., Kennedy, B. J., Ting, J., and Wallwork, K. S. (2011). Structural Phase Transitions and Magnetic Order in SrTcO3. *Dalton Trans.* 40, 7228–7233. doi:10.1039/c1dt10445d

Thorogood, G. J., Zhang, Z., Hester, J. R., Kennedy, B. J., Ting, J., Glover, C. J., et al. (2011). Structure and Cation Ordering in Spinel-type TcCo2O4. An Example of a Trivalent Technetium Oxide. *Dalton Trans.* 40, 10924–10926. doi:10.1039/c1dt10954e

Vanderah, T. A., Levin, I., and Lufaso, M. W. (2005). An Unexpected crystal-chemical Principle for the Pyrochlore Structure. *Eur. J. Inorg. Chem.* 2005, 2895–2901. doi:10.1002/ejic.200500234

Wallwork, K. S., Kennedy, B. J., and Wang, D. (2007). The High Resolution Powder Diffraction Beamline for the Australian Synchrotron. *AIP Conf. Proc.* 879, 879–882.

Weck, P. F., Kim, E., Poineau, F., Rodriguez, E. E., Sattelberger, A. P., and Czerwinski, K. R. (2010). Structural and Electronic Trends in Rare-Earth Technetate Pyrochlores. *Dalton Trans.* 39, 7207–7210. doi:10.1039/c0dt00212g

Wester, D. W., and Hess, N. J. (2005). Bond-valence Sums for Tc-O Systems from EXAFS Data. *Inorg. Chim. Acta*. 358, 865–874. doi:10.1016/j.ica.2004.10.002

Conflict of Interest: The authors declare that the research was conducted in the absence of any commercial or financial relationships that could be construed as a potential conflict of interest.

frontiers in Chemistry

ORIGINAL RESEARCH
published: 19 August 2021
doi: 10.3389/fchem.2021.733718

Defining the Structural Stability Field of Disordered Fluorite Oxides

Eric C. O'Quinn, Devon L. Drey and Maik K. Lang*

Department of Nuclear Engineering, University of Tennessee, Knoxville, TN, United States

Fluorite-structured oxides constitute an important class of materials for energy technologies. Despite their high level of structural symmetry and simplicity, these materials can accommodate atomic disorder without losing crystallinity, making them indispensable for uses in environments with high temperature, changing chemical compositions, or intense radiation fields. In this contribution, we present a set of simple rules that predict whether a compound may adopt a disordered fluorite structure. This approach is closely aligned with Pauling's rules for ionic crystal structures and Goldschmidt's rules for ionic substitution.

Keywords: fluorite, structural stability, complex oxides, oxygen vacancy, defects, Goldschmidt, Pauling

OPEN ACCESS

Edited by:
Alexander Shtukenberg,
New York University, United States

Reviewed by:
Vladislav V. Gurzhiy,
Saint Petersburg State University, Russia
Anna Shelyug,
Institute of Solid State Chemistry, Russia

****Correspondence:***
Eric C. O'Quinn
ericoquinn@utk.edu

Specialty section:
This article was submitted to Solid State Chemistry, a section of the journal Frontiers in Chemistry

Received: *30 June 2021*
Accepted: *05 August 2021*
Published: *19 August 2021*

Citation:
O'Quinn EC, Drey DL and Lang MK (2021) Defining the Structural Stability Field of Disordered Fluorite Oxides. Front. Chem. 9:733718. doi: 10.3389/fchem.2021.733718

INTRODUCTION

Materials that are isostructural with the mineral fluorite (CaF_2) have been studied for nearly 100 years and were instrumental to Pauling (1927) and Goldschmidt (1926) in development of the first sets of atomic radii. The extraordinarily simple structure consists of a cubic array of anions, with cations filling every other cubic interstice (Navrotsky, 2010). An even simpler representation involves stacking of atomic layers in the sequence anions-cations-anions anions-cations-anions (Sickafus et al., 2005; Uberuaga and Sickafus, 2015); these layers are perfect triangular Ising nets (Wannier, 1950). While many metal cations form binary fluorite oxides (*e.g.,* CeO_2), the flexibility of the fluorite structure permits the formation of ternary or even higher-entropy (*i.e.,* more than one cation) fluorite oxides and hyper- or hypo-stoichiometric (*i.e.,* $MO_{2\pm x}$) oxygen sublattices. Based on the atomic disorder involved, these compounds have been referred to as disordered fluorites (Norberg et al., 2012; O'Quinn et al., 2020), anion-deficient fluorites (Sickafus et al., 2007; Tang et al., 2007), or defect fluorites (De Los Reyes et al., 2013). Hereafter, we describe these as "disordered fluorites," a general term encompassing fluorite structures in which structural disorder is observed on either the cation sublattice, the anion sublattice, or both. A classic example is the well-known disordered fluorite yttria-stabilized zirconia ($Y_xZr_{1-x}O_{2-0.5x}$, "cubic zirconia" or "YSZ"). In YSZ, despite the hypo-stoichiometric anion sublattice, the remaining oxygen readily forms a simple cubic framework in which the two metal cations, Y^{3+} and Zr^{4+}, distribute themselves randomly (Götsch et al., 2016). Conversely, another well-known example is the nuclear fuel uranium dioxide (UO_{2+x} + fission products). In a nuclear reactor, the fission process leads to continuous incorporation of metal cations into the fluorite lattice, oxidation of the U^{4+} cations, and a hyper-stoichiometric anion sublattice. Notwithstanding the complex chemistry of both cases, their overall structure remains remarkably simple (Navrotsky, 2010). Disordered fluorite oxides exhibit a variety of useful physical properties such as high ion conduction (van Dijk et al., 1983), low thermal conductivity (Clarke and Phillpot, 2005), and excellent radiation tolerance (Sickafus et al., 2000) which permits their use as fuel cell electrolytes (Navrotsky, 2010), thermal barrier coatings (Xu et al., 2006), and nuclear fuels (Ewing et al., 2004). Despite the prevalence and importance of this material class, there has been limited efforts to predict the structural stability field of disordered fluorite oxides.

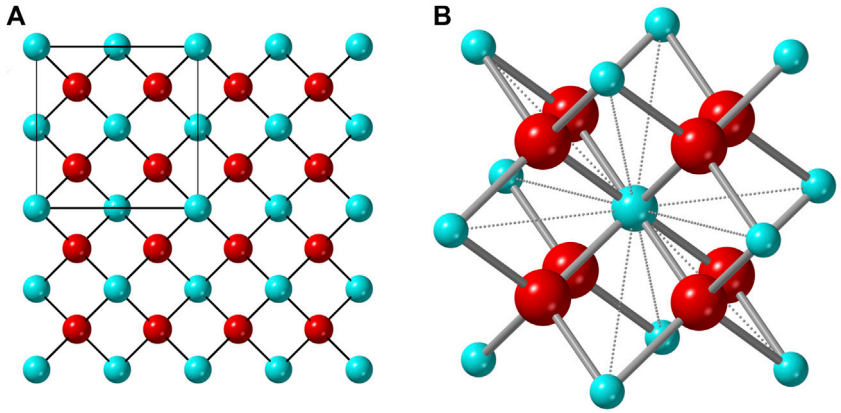

FIGURE 1 | (A) Atomistic representation of the ideal fluorite structure with the unit cell denoted by the square in the upper left corner. **(B)** The cube-octahedron represented by a polyhedron formed by twelve vertices occupied by cations (blue) and the nearest eight anions (red) to the central cation (same for any other cation).

The structural stability field of fluorite-derived structures has been previously defined only with respect to other ordered fluorite-derivative superstructures (Minervini et al., 2000; Yamamura et al., 2003). For instance, the conditions that define the boundary between pyrochlore and fluorite oxides in $A_2B_2O_7$ compounds has been the source of much investigation (Isupov and Petrov, 1958; Heremans et al., 1995; Minervini et al., 2000; Sickafus et al., 2000; Pirzada et al., 2001; Cai et al., 2011; Mouta et al., 2013; Fuentes et al., 2018). The ordered pyrochlore structure can be imagined as a $2 \times 2 \times 2$ supercell of the fluorite unit cell in which the stoichiometric oxygen vacancy is ordered at a specific location creating distinct coordination polyhedra for the two cations: an 8-fold cubic polyhedron for the larger A-cation and a smaller 6-fold octahedron for the B-cation. The commonly used rule to explain or predict the boundary of the compositionally-induced transition between disordered fluorite ordered and ordered pyrochlore is when the ionic radius ratio of the 8-coordinated A-site cation (conventionally Shannon, 1976) and the 6-coordinated B-site cation exceeds 1.46 (Subramanian et al., 1983; Minervini et al., 2000; Sickafus et al., 2000; Fuentes et al., 2018). Experimental and computational studies have shown that this ionic radius ratio is strongly correlated with the cation anti-site defect formation energy in $A_2B_2O_7$ (Minervini et al., 2000; Sickafus et al., 2000) with an increased propensity for a disordered cation sublattice and a disordered fluorite structure for lower defect energies. The ionic radius ratio is a simple way to predict if a disordered fluorite structure forms for a given $A_2B_2O_7$ composition. A similar set of guiding principles is lacking for other stoichiometries and classes of materials.

An ionic compound that exhibits a stable (or metastable) disordered structure must contain a geometric framework that permits mixing of the cation and/or anion sublattices. For the disordered fluorite structure, this is the interpenetrating face-centered-cubic cation array and simple cubic anion array (**Figure 1**); the repeat unit of the cation sublattice is twice that of the anion sublattice. Any cation in a fluorite structure is nearest neighbors with 12 other cations which form a cube-octahedral cage in which the eight nearest-neighbor anions reside. This geometry creates eight regular tetrahedra, emerging from the center cation, in which the anions reside at the circumcenter (*i.e.*, all cation-anion distances are equal). Only within the ideal fluorite structure, the anions occupy the center of these tetrahedron, and other structurally related phases (*e.g.*, pyrochlore and bixbyite) form if anions move away from their ideal positions. This process is highly correlated with the size of the cations that form the cube-octahedral cage. If some of the constitutional cations are too large (or small) compared with the cations forming the rest of the cube-octahedral cage, the enclosed anions will relax away from the center of the tetrahedron, distorting the ideal simple cubic anion array. The second characteristic of the disordered fluorite structure is the random mixing of cations on one site. The size of the two cation species must be balanced to allow for occupation of the same site but prevent both cation-anion and anion-anion repulsion, or "double repulsion." This effect can be easily conceptualized in **Figure 1**: any cation-cation distance forms a shared edge of two anion tetrahedra. If the cations are both sufficiently large, then nearest-neighbor cation-anion repulsive forces will keep the nearest-neighbor anions from close contact. If the cations are too small, however, both cation-anion and anion-anion repulsive forces (double repulsion) prevent the disordered fluorite structure from being adopted. Pauling (1960) observed that the phase boundary for MX_2 compounds between fluorite (cations in 8-fold coordination) and rutile (cations in 6-fold coordination) was explained if the ionic radii ratio of cations and anions is approximately $\sqrt{3} - 1 = 0.732$, the lower geometric limit to prevent double repulsion.

We expand this approach here and show that simple geometrical constraints aid in the formulation of simple rules to define the structural stability field of disordered fluorite. 1) For compounds with more than one cation species, the size of any cation must not be too different from the average size of all other cations; this maintains the ideal simple cubic anion array within the cube-octahedral cage. This rule can be understood as an enforcement of Goldschmidt's first rule (Goldschmidt, 1926) that free ionic mixing in an ionic crystal is limited to cases where the relative ion size is no larger than 15%. The

TABLE 1 | Summary of the different radii used in this study. The previously unreported Pauling univalent radii were calculated from Eqs 13–8 in Pauling (1960) using a value of 12 for the Born exponent (corresponding to an electron configuration), in accordance with Table 13-2 in Pauling (1960). The Pauling empirical crystal radii are from References Pauling (1929), Pauling (1960), Galasso (1970), and Rohrer (2001). Entries in bold represent previously unreported data and were calculated for this study.

Atomic number	Atom species	Charge state	Pauling empirical crystal radius (Å)	Pauling univalent radius (Å)
8	O	−2	1.40	1.76
22	Ti	+4	0.68	0.96
39	Y	+3	0.93	1.20
40	Zr	+4	0.80	1.09
41	Nb	+5	0.70	1.00
50	Sn	+4	0.71	0.96
51	Sb	+5	0.62	0.89
57	La	+3	1.15	**1.40**
58	Ce	+3	1.11	**1.36**
59	Pr	+3	1.09	**1.33**
60	Nd	+3	1.08	**1.32**
61	Pm	+3	1.06	**1.29**
62	Sm	+3	1.04	**1.27**
63	Eu	+3	1.03	**1.26**
64	Gd	+3	1.02	**1.25**
65	Tb	+3	1.00	**1.22**
66	Dy	+3	0.99	**1.21**
67	Ho	+3	0.97	**1.18**
68	Er	+3	0.96	**1.17**
69	Tm	+3	0.95	**1.16**
70	Yb	+3	0.94	**1.15**
71	Lu	+3	0.93	**1.14**
72	Hf	+4	0.81	**1.04**

potential for different cations to mix over the same site is also limited by Pauling's third and fourth rule which states that small, high-valence cations tend not to share polyhedral edges, as is done in the fluorite structure. 2) The average size of the cations in a compound must be sufficiently large that an 8-fold coordination with the anion sublattice is preferred. 3) The average size of the cations in a compound must be sufficiently small to prevent ordering to higher coordination numbers. These last two rules are an application of Pauling's first rule (Pauling, 1929) which prescribes different coordination polyhedra for cations based on their relative size to their surrounding anions. In this contribution we demonstrate how the simple rules (*I–III*) (known for nearly a century) can be used to predict the stable phase region of disordered fluorite for any given complex oxide based on their chemical composition and stoichiometry. This methodology provides an easy, accessible framework that is based on Pauling's and Goldschmidt's original rules to guidance the synthesis of novel, disordered fluorite-structured materials.

METHODOLOGY

To define the structural stability field of disordered fluorite, we identified several parameters by which chemical compounds are uniquely characterized. Given the three rules proposed in the introduction, we focused on characterizing the relative sizes of the constituent ions to one another. We used the Pauling univalent radii (Pauling, 1929), which describe the relative sizes of the outermost electron shells of a given ion (Pauling, 1960). They are referred to as "univalent" because ions are treated as though they have maintained their electron distribution but also have Coulombic interaction as though they had a charge state of ±1. Thus, this radius represents a measure of the relative spatial extensions of ions and their characteristic repulsive forces; thus, Pauling originally used the univalent radii to evaluate the second component of his first rule ("the no-rattle rule"). The Pauling univalent radius was calculated for a range of ions (**Table 1**) using the relation (Eqs 13–8 in Ref. Pauling, 1960):

$$R_z = R_1 z^{-2/(n-1)} \tag{1}$$

where R_z is the Pauling empirical crystal radius, R_1 is the Pauling univalent radius, z is the charge state of the ion, and n is the Born exponent (Table 13-2 in Ref. Pauling, 1960).

Two parameters were then calculated for various chemical compounds; first, a parameter was defined to quantify the relative size of a given cation *to all other cations, themselves*; we did this by the following relation:

$$\rho_{cation-cation} = (i)\,\frac{\langle r_{all\ cations}\rangle}{\langle r_{large\ cations}\rangle} \text{ if more cations are larger than the average}$$
$$or$$
$$(ii)\,\frac{< r_{small\ cations} >}{< r_{all\ cations} >} \text{ if more cations are smaller than the average} \tag{2}$$

where the values in angled brackets (< >) are the average radius, which is calculated either for (*i*) all cations larger or (*ii*) all cations

smaller than the average cation size. For the example of the disordered, anion-deficient fluorite Yb_3NbO_7 compound, case (*i*) applies as the majority of cations are larger (Yb) than the average cation size. Conversely, for the example of yttria-stabilized zirconia, case (*ii*) applies because the majority of cations are Zr with a smaller radius than the average cation size. For complex oxides with equal numbers of cations that are larger and smaller than the average cation size (*e.g.*, $Ho_2Zr_2O_7$), case (*i*) was applied. A second parameter was defined, $\rho_{\text{cation-anion}}$, to quantify the relative size of the cations *to the anions*:

$$\rho_{cation-anion} = \frac{\langle r_{all\ cations} \rangle}{\langle r_{all\ anions} \rangle} \tag{3}$$

This requires an average anion radius which must be determined considering any anion vacancies in the disordered fluorite structure. In an ideal fluorite structure (*i.e.*, MX_2), the average anion radius coincides with the actual anion radius because all anion positions are occupied. This changes for anion-deficient fluorite structures because the average anion radius must account for the vacant positions on the anion sublattice. For example, the average anion radius for a disordered M_4O_7 fluorite structure is $\frac{7}{8}r_O$; conceptually this means that 7 out of 8 anions have a radius equal to the oxygen radius and the 8th anion has a radius equal to 0. It should be clarified that the radius of the vacant anion is not a "vacancy radius," or radius of the resulting void space; instead, it is a "zero radius," the radius of no anion at all. Thus, **Eq. 3** may be interpreted as a generalization of Pauling's first ("no rattle") rule for more complex cases involving, for instance, anion vacancies.

A phase space was created with $\rho_{\text{cation-cation}}$ (hereafter referred to as ρ_c) on the abscissa and $\rho_{\text{cation-anion}}$ (ρ_a) on the ordinate to incorporate all possible disordered fluorite structures for different complex oxides and infer stability boundaries related to cationic and anionic radii. This procedure is illustrated for the example of the disordered, anion-deficient fluorite $Y_2Zr_2O_7$ compound. First, the average size of the two cations is determined by:

$$\frac{2r_Y + 2r_{Zr}}{4} = 1.145\text{Å}.$$

Then the parameter ρ_c is given by:

$$\frac{1.145\text{Å}}{r_Y} = 0.954.$$

Finally, the parameter ρ_a is calculated as:

$$\frac{1.145\text{Å}}{r_O * \frac{7}{8}} = 0.743,$$

with r_Y = 1.20 Å, r_Z = 1.09 Å, and r_O = 1.76 Å (**Table 1**).

RESULTS AND DISCUSSION

First, we consider the well-studied $A_2B_2O_7$ family of oxides as a model system to probe the structural stability field of disordered fluorite. Previous studies have established the phase boundary between ordered pyrochlore and disordered fluorite across a range of chemical compositions (Subramanian et al., 1983). We used Pauling's univalent radii (**Figure 2**) to re-examine these well-studied ternary oxides and to create a phase space based on the sizes of the cations relative to *one another* (ρ_c – abscissa) and with respect to the oxygen anions (ρ_a – ordinate). Experimental data show that ternary hafnate oxides ($A_2Hf_2O_7$) exhibit a disordered fluorite structure for *A* = Dy-Lu and Y (Klee and Weitz, 1969; Stanek and Grimes, 2002; Ewing et al., 2004), while ordered pyrochlore forms for A = La-Tb. In our phase space, this corresponds to a phase boundary of ρ_c = 0.928(2) (*i.e.*, 0.928 ± 0.002) which is the average value obtained by the two ρ_c values of the neighboring disordered fluorite and ordered pyrochlore compounds (**Figure 2**, red vertical lines). When the two cations become more different in size than Dy and Hf, the same coordination polyhedra simply cannot accommodate both cations and maintain the configuration of disordered fluorite, and an ordered pyrochlore structure forms. For the ternary zirconate oxides ($A_2Zr_2O_7$), the disordered fluorite structure is adopted for *A* = Tb-Lu, and Y (Roth, 1956; Klee and Weitz, 1969; Subramanian et al., 1983; Ewing et al., 2004; Reynolds et al., 2013). In **Figure 2**, the boundary between the ordered pyrochlore $Gd_2Zr_2O_7$ and the disordered fluorite $Tb_2Zr_2O_7$ corresponds to a ρ_c = 0.950(4) or an A-site

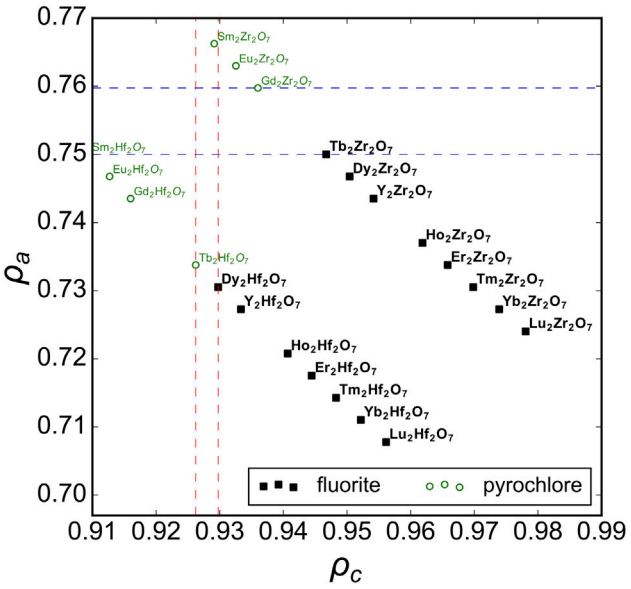

FIGURE 2 | The phase space spanned by the relative size of cations to anions, ρ_a, *versus* relative size of cations to one another, ρ_c, for $A_2B_2O_7$ oxides across a broad range of chemical compositions with experimental data compiled from Roth (1956), Klee and Weitz (1969), Subramanian et al. (1983), Minervini et al. (2000), Sickafus et al. (2000), Stanek and Grimes (2002), Ewing et al. (2004), Reynolds et al. (2013), and Drey et al. (2020). Compounds reported with a structure corresponding to disordered fluorite and ordered pyrochlore are represented by solid black squares and open green circles, respectively. The vertical dashed red lines represent the ρ_c boundaries based on ternary hafnates and the horizontal dashed blue lines the ρ_a boundaries based on ternary zirconates.

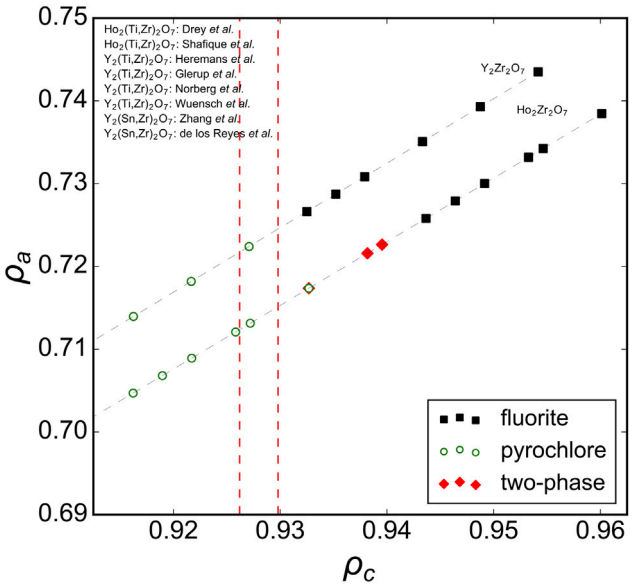

FIGURE 3 | Ternary $A_2B_2O_7$ solid solution series in the ρ_a, ρ_c phase space with ρ_c boundaries (red dashed vertical lines) established from $A_2Hf_2O_7$ compositions (**Figure 2**). Experimental data taken from Heremans et al. (1995), Kennedy et al. (1997), Wuensch et al. (2000), Glerup et al. (2001), Norberg et al. (2012), De Los Reyes et al. (2013), Zhang et al. (2013), Shafique et al. (2016), Tracy et al. (2016), and Drey et al. (2020) with reported structures that correspond to disordered fluorite (solid black squares), ordered pyrochlore (open green circles), and a mix of both (red diamonds). The dashed gray lines connect the data points and represent the trend of the solid-solution series within this phase space.

cation radius ~13% larger than that of the B-site cation. However, another way to discriminate the two compositions is based on their ρ_a values (**Figure 2**, blue horizontal lines). The phase boundary in this case is when ρ_a = 0.755(5), which means that the average cation size is ~75.5% the average anion size. If this value is exceeded, the cation sublattice will prefer a different coordination scheme that provides the larger cation of the two with more anion neighbors (*i.e.,* pyrochlore). In this way, the phase space of disordered fluorite is defined with boundaries to ordered pyrochlores based on the size of the cations with respect to the oxygen in the ternary zirconates and with the relative size among the two cations for ternary hafnates.

Analyzing previous studies on solid-solution series of ternary $A_2B_2O_7$ oxides covering the full range between ordered and disordered structures yields more insight to the compositional phase boundaries of disordered fluorite. For instance, **Figure 3** shows several solid solutions plotted in the phase space spanned by ρ_a and ρ_c with the ρ_c boundary lines overlaid from the ternary hafnates (**Figure 2**). A recent study by Drey et al. (2020) examined a solid solution between the ordered pyrochlore $Ho_2Ti_2O_7$ and disordered fluorite $Ho_2Zr_2O_7$; Ti-rich compositions adopted the pyrochlore phase, Zr-rich compositions adopted the fluorite phase, and intermediate compositions were shown to have a combination of both. The compositional boundary between ordered pyrochlore and disordered fluorite lies in a narrow ρ_c-range. Other studies have investigated compositionally similar series (*e.g.,* $Ho_2Ti_2O_7$-$Ho_2Zr_2O_7$ Shafique et al., 2016 and $Y_2Ti_2O_7$-$Y_2Zr_2O_7$ Heremans et al., 1995; Wuensch et al., 2000; Glerup et al., 2001; Norberg et al., 2012); the boundary between pyrochlore and fluorite in these series exists within the same narrow ρ_c-range. Some studies included ternary stannates ($Y_2Sn_2O_7$-$Y_2Zr_2O_7$) which have a more covalent bond character than zirconates and titanates (De Los Reyes et al., 2013; Zhang et al., 2013). It was demonstrated that the phase boundary between disordered fluorite and ordered pyrochlore is very similar to the $Y_2Ti_2O_7$-$Y_2Zr_2O_7$ and $Ho_2Ti_2O_7$-$Ho_2Zr_2O_7$ series and occurs at the same Zr-content levels. While Sn^{4+} has a larger ionic radius than Ti^{4+} (0.690 Å *versus* 0.605 Å), Sn cations have the same univalent radius as Ti cations (0.96 Å). This shows again that the univalent radius is a very useful parameter in determining the structural stability of disordered fluorite.

As mentioned above, the phase boundary of disorder fluorite with respect to the univalent radius ρ_a was determined with different $A_2Zr_2O_7$ zirconate oxides (**Figure 2** blue, dashed horizontal lines). Solid solutions involving substitution of the A-cation in $A_2Zr_2O_7$ with many intermediate compositions are useful to further probe this phase boundary (**Figure 4**). Reynolds et al. (2013) studied the long-range structure of series members between the ordered pyrochlore $Gd_2Zr_2O_7$ and disordered fluorite $Tb_2Zr_2O_7$. Fuentes et al. (2018) probed similar zirconate oxides ($A_xGd_{2-x}Zr_2O_7$) and based on the

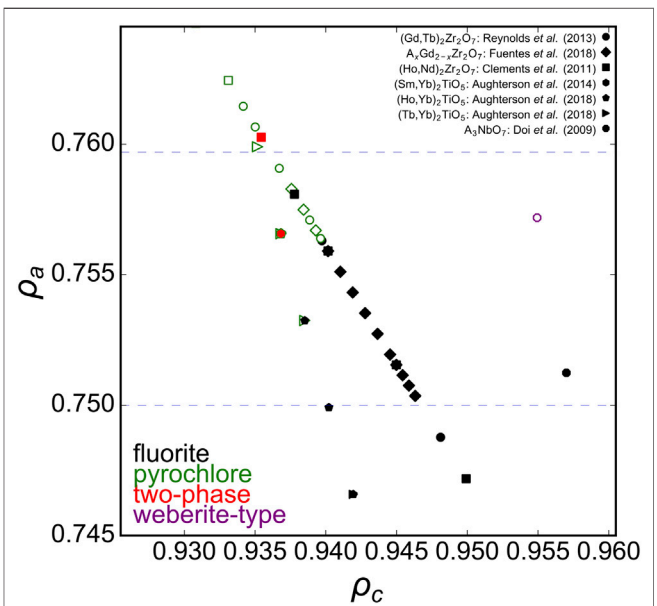

FIGURE 4 | Ternary $A_2B_2O_7$ solid solution series in the ρ_a, ρ_c phase space with ρ_a boundaries (blue dashed horizontal lines) established from $A_2Zr_2O_7$ compositions (**Figure 2**). Experimental data points represented by diamonds taken from Fuentes et al. (2018), circles from Reynolds et al. (2013), squares from Clements et al. (2011), hexagons from Aughterson et al. (2014), pentagons from Aughterson et al. (2018a), triangles from Aughterson et al. (2018b), and octagons from Doi et al. (2009). Solid black squares represent disordered fluorite, open green squares pyrochlore, and solid red squares a mix of both.

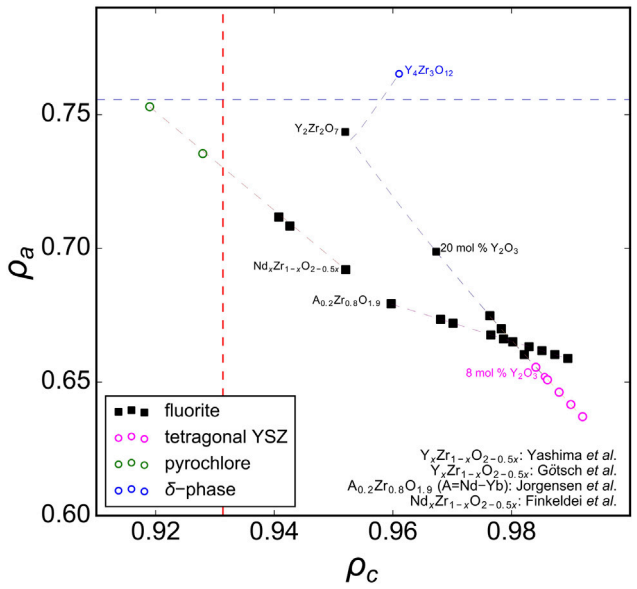

FIGURE 5 | The phase space of $A_xZr_{1-x}O_{2-0.5x}$ (stabilized zirconia with A = Ln and Y) oxides spanned by parameters ρ_a and ρ_c. Experimental data are taken from Jorgensen and Rittersh (1967), Yashima et al. (1993), Götsch et al. (2016), and Finkeldei et al. (2017) with reported structures that correspond to disordered fluorite (solid black squares), tetragonal YSZ (pink open circles), ordered pyrochlore (open green circles), and the delta phase (open blue circles). The dashed red vertical and blue horizontal lines represent refined ρ_c and ρ_a boundaries, respectively as determined in **Figures 2–4**.

experimental data of both studies, the phase boundary for the stability field of disordered fluorite occurs at $\rho_a \sim 0.756$. This agrees very well with work by Clements et al. (2011) who investigated a solid solution of ordered $Nd_2Zr_2O_7$ and disordered $Ho_2Zr_2O_7$ and reported a critical transformation from ordered pyrochlore to disordered fluorite that corresponds, in our phase space calculated with univalent radii, to $0.757 < \rho_a < 0.760$. Intriguingly, this value represents also the phase boundary of disordered fluorites that form in other families of oxides such as the ternary niobates with the general formula A_3NbO_7, for which the disordered fluorite structure is adopted for A = Dy-Lu and Y (Doi et al., 2009). This upper limit of the parameter ρ_a, (*i.e.*, on the relative size of cations with respect to the oxygen), seems to apply even to disordered fluorite oxides for which the cation:oxygen ratio is not 4:7. For example, A_2TiO_5 oxides form a disordered fluorite structure if A = Er-Lu (Aughterson et al., 2018a); together with studies on multiple $A_xYb_{1-x}TiO_5$ solid solution series by Aughterson et al. (2014), Aughterson et al. (2018a), and Aughterson et al. (2018b), this corresponds to a critical ρ_a value of 0.755–0.756, in excellent agreement with previous examples for oxides $A_2Zr_2O_7$ and A_3NbO_7 with different stoichiometries. Though the A_3TaO_7 family of oxides form disordered fluorite structures for *A* = Ho-Lu, a reliable value for Pauling's empirical crystal radius does not exist in literature; thus, no calculations on tantalate oxides were performed for this study.

Now that the upper ρ_a limit for the disordered fluorite stability field is determined, the lower limit must be found, which can be accomplished by stabilized-zirconia ($A_xZr_{1-x}O_{2-0.5x}$) compounds (**Figure 5**). Experimental data with different dopant levels of *A* = Y (Yashima et al., 1993; Götsch et al., 2016), *A* = Nd (Finkeldei et al., 2017), or different dopants at the same weight fractions (Jorgensen and Rittersh, 1967) suggest that the phase boundary between disordered fluorite and lower-symmetry ZrO_2-type structures is $\rho_a \sim 0.657$. This is just above the data point for 8 mol% yttria-stabilized zirconia (YSZ), which is generally accepted to be of a tetragonal form at room temperature (Götsch et al., 2016). Higher doping levels in YSZ produce disordered fluorite and doping beyond the upper ρ_a limit yields the delta-phase ($Y_4Zr_3O_{12}$). Neodymia-stabilized zirconia (NSZ) also follows this behavior and lies within the disordered fluorite stability field; however, samples with higher Nd doping levels form an ordered pyrochlore structure ($Nd_2Zr_2O_7$) if the ρ_c of the composition is smaller than the boundary established with ternary hafnate oxides ($A_2Hf_2O_7$) above.

When all experimental data previously discussed are presented together in one phase diagram (**Figure 6**), a distinct region of disordered fluorite is apparently constrained by critical values of ρ_c and ρ_a. The "left" boundary, $(\rho_c)_{min} = 0.931(1)$, can be interpreted as Goldschmidt's first rule for ionic mixing (the uncertainty arises from considering the phase boundaries identified by multiple studies). Compounds that have $\rho_c < (\rho_c)_{min}$ consist of cations that are too dissimilar in their size to occupy the fluorite structure's single cubic coordination polyhedron. The "upper" and "lower" boundaries, $0.657(2) \leq \rho_a \leq 0.756(2)$, are related to Pauling's first rule which defines

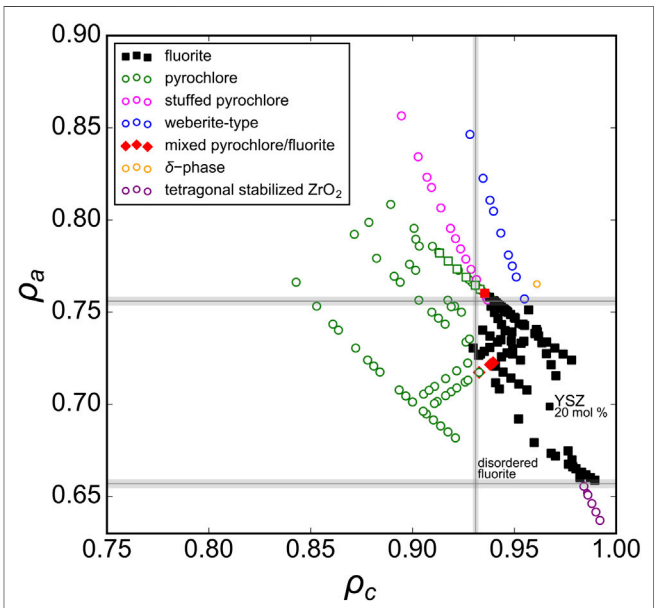

FIGURE 6 | Experimental data with a wide range of reported structures for $A_2B_2O_7$, A_2BO_5, A_3BO_7, and $A_xB_{1-x}O_{2-0.5x}$ oxides represented in the phase space created by the parameters ρ_a and ρ_c (defined by **Eqs 2**, **3**). The different symbols are defined in the legend and the gray lines denote the univalent radii boundaries that define the stability field of the disordered fluorite structure.

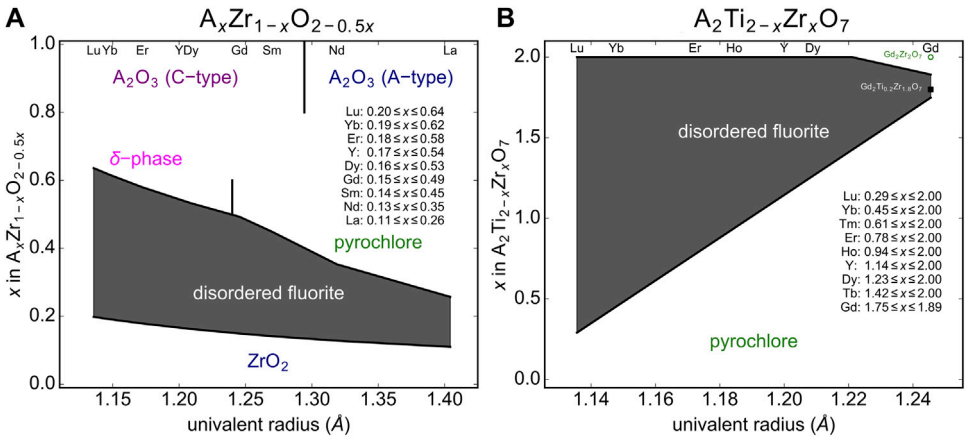

FIGURE 7 | Predicted disordered fluorite stability field (gray shaded region) for **(A)** stabilized zirconia compounds ($A_xZr_{1-x}O_{2-0.5x}$) and **(B)** $A_2Ti_{2-x}Zr_xO_7$ solid-solution series with A representing the variable cation. The phase boundaries are established by the compositional parameter *x* and the univalent radius limits based on relations given in **Eq. 4**. Neighboring phases are shown for zirconia (ZrO_2), sesquioxides (cubic "C-type" and trigonal "A-type" A_2O_3), δ-phases ($A_4Zr_3O_{12}$), and pyrochlores ($A_2B_2O_7$).

stable polyhedral configurations for cations based on their relative size to the surrounding anions. The lower boundary, $(\rho_a)_{\min}$ = 0.657(2), can be interpreted as an application of Pauling's first rule ("no rattle rule") for the lower limit of 8-fold coordination. For disordered fluorite, the average anion radius accounts for intrinsic stoichiometric vacancies which corresponds to a total cation coordination with eight oxygen positions (*e.g.,* cation coordination with seven oxygen and one vacancy is equivalent to cation coordination with eight anions with radius 7/8 r_O). Similarly, the upper boundary, $(\rho_a)_{\max}$ = 0.756(2), coincides with the upper limit of cation coordination with seven oxygen and one vacancy. For a larger cation size this coordination configuration can no longer be maintained and ordering of the anion sublattice occur away from disordered fluorite. In summary, the disordered fluorite structure forms for oxides when the following two conditions are simultaneously satisfied:

$$i = \rho_c > 0.931\,(1) \text{ and } 0.657\,(2) < \rho_a < 0.756\,(2) \qquad (4)$$

Using this structural stability field, we predict the compositional range over which disordered fluorite will form for stabilized zirconia compounds (**Figure 7A**). It is well known that for low values of *x* in $A_xZr_{1-x}O_{2-0.5x}$, a monoclinic or tetragonal ZrO_2 structure will form (Clausen and Hayes, 1999; Navrotsky, 2010; Götsch et al., 2016). Cubic, disordered fluorite forms above a critical *x* value, which is determined by the size of the *A*-cation determined; the larger the *A*-cation, the lower the *x*. Based on relation (Sickafus et al., 2005) we predict the critical compositions (*i.e.,* the minimum doping level *x*) that results in a disordered fluorite structure across the lanthanide series, and for the largest and smallest A-site cation we predict $La_{0.11}Zr_{0.89}O_{1.945}$ and $Lu_{0.19}Zr_{0.81}O_{1.905}$, respectively (**Figure 7A**). The compounds with intermediate sized *A*-site cations exhibit a minimum doping level, *x*, with a nearly linear relationship with respect to their univalent radius. There is also an upper limit for *x* above which disordered fluorite is no longer stable and we used relation (Sickafus et al., 2005) to predict the critical compositions (i.e., the maximum doping level *x*), and for the largest and smallest *A*-site cation we predict $La_{0.26}Zr_{0.74}O_{1.87}$ and $Lu_{0.64}Zr_{0.38}O_{1.68}$, respectively (**Figure 7A**). For higher doping levels across the Ln series several other phases form (e.g., pyrochlore for larger cations and -phase for smaller cations) that depend on the *A*-site cation size. The larger the *A*-site cation, the lower the critical *x*-value and the dependence on the univalent radius across the Ln series is steeper than for the lower phase boundary. This means that the phase region of disordered fluorite is wider in terms of doping level *x* for smaller *A*-site cations (e.g., Lu) as compared with larger *A*-site cations (e.g., La). The minimum predicted *x*-value for disordered fluorite stability is in a linear relation with the univalent radius; this is because all stabilized zirconia compositional series "cross" the lower boundary, $(\rho_a)_{\min}$ = 0.657(2) with only the size of the *A*-cation dopant dictating how far "horizontally" the series travels before crossing $(\rho_a)_{\min}$. The maximum predicted *x*-value, however, is determined either by the left boundary, $(\rho_c)_{\min}$ = 0.931(1), or the upper boundary, $(\rho_a)_{\max}$ = 0.756(2), depending on the A-cation; this effect is observed in **Figure 5** and explains why the maximum predicted *x*-values are not in a strictly linear relation with the univalent radius. These predictions for the compositional range over which the disordered fluorite structure is stable are largely in agreement with previous studies (Thornber et al., 1970; Bukaemskiy et al., 2021).

The second example used to predict the stability field of disordered fluorite based on relation (Sickafus et al., 2005) and the univalent radii are A_2Ti_{2-x} Zr_xO_7 solid-solution series across all lanthanide *A*-site cations (**Figure 7B**). Given the different stoichiometry, the stability field of disordered fluorite spanned by the minimum and maximum *x* value across all univalent radii has a different shape as compared to stabilized zirconia. However, the disordered fluorite structure is predicted to be stable for larger *x*-ranges for cations with smaller univalent radii (*e.g.,* Yb) as it was

the case for stabilized zirconia. This is not surprising as the smaller lanthanides are more similar in size to Zr (and Ti), and thus will have larger ρ_c values. Our model predicts, for example, that while neither $Gd_2Ti_2O_7$ nor $Gd_2Zr_2O_7$ form disordered fluorites at ambient conditions, the intermediate compositions $Gd_2Ti_{2-x}Zr_xO_7$ fall within the disordered fluorite structural stability field for $1.75 \leq x \leq 1.89$. Future experimental work should focus on this series to confirm these predictions.

CONCLUSION

A simple set of rules is proposed to define the structural stability field of disordered fluorite. Using Pauling's univalent radii, the radii associated for application in his first, "no-rattle" rule, two parameters were defined that create a two-dimensional phase space over which a range of complex oxides were evaluated. Comparison with experimental data showed that the one parameter, ρ_c, which quantifies the relative size among cations, must be above 0.931(1) for a compound to adopt the disordered fluorite structure. This is interpreted as a straightforward application of Goldschmidt's first rule for ionic mixing (ions may freely replace one another in crystals if their radii differ by less than 15%). The other parameter, ρ_a, which quantifies the relative size of the cations to the anions, must lie between 0.657(2) and 0.756(2) for a compound to adopt the disordered fluorite structure. These boundaries are correlated with the minimum and maximum limit of structural stability for cation coordination with eight oxygen positions, using an oxygen radius accounting for stoichiometric vacancies; these rules are therefore a generalization of Pauling's first "no-rattle" rule. These results offer a simple, but effective, way of determining whether a complex oxide may adopt the disordered fluorite structure and, thus, provides guidance in future synthesis endeavors for this important class of materials. The current approach considers only room temperature, equilibrium phases and does not consider far-from-equilibrium processing and synthesis which may expand the stability field of disordered fluorite.

DATA AVAILABILITY STATEMENT

The raw data supporting the conclusions of this article will be made available by the authors, without undue reservation.

AUTHOR CONTRIBUTIONS

EO and ML conceived the study. EO and DD compiled and analyzed the data. EO drafted the manuscript. EO, DD, and ML critically revised, edited, and approved the submitted version of the manuscript.

FUNDING

This work was supported by the U.S. Department of Energy (DOE), Office of Science, Basic Energy Sciences, under award DE-SC0020321. DD acknowledges support from the Integrated University Program Graduate Fellowship program.

REFERENCES

Aughterson, R. D., Lumpkin, G. R., Reyes, M. D. L., Sharma, N., Ling, C. D., Gault, B., et al. (2014). Crystal Structures of Orthorhombic, Hexagonal, and Cubic Compounds of the $Sm_{(x)}Yb_{(2-x)}TiO_5$ Series. *J. Solid State. Chem.* 213, 182–192. doi:10.1016/j.jssc.2014.02.029

Aughterson, R. D., Lumpkin, G. R., Smith, K. L., Reyes, M. d. l., Davis, J., Avdeev, M., et al. (2018). The Ion-Irradiation Tolerance of the Pyrochlore to Fluorite $Ho_{(x)}Yb_{(2-x)}TiO_5$ and Er_2TiO_5 Compounds: A TEM Comparative Study Using Both *In-Situ* and Bulk *Ex-Situ* Irradiation Approaches. *J. Nucl. Mater.* 507, 316–326. doi:10.1016/j.jnucmat.2018.05.026

Aughterson, R. D., Lumpkin, G. R., Smith, K. L., Zhang, Z., Sharma, N., and Cairney, J. M. (2018). The crystal Structures and Corresponding Ion-Irradiation Response for the $Tb_{(x)}Yb_{(2-x)}TiO_5$ Series. *Ceramics Int.* 44, 511–519. doi:10.1016/j.ceramint.2017.09.205

Bukaemskiy, A. A., Vinograd, V. L., and Kowalski, P. M. (2021). Ion Distribution Models for Defect Fluorite ZrO_2 - $AO_{1.5}$ (A = Ln, Y) Solid Solutions: I. Relationship between Lattice Parameter and Composition. *Acta Materialia* 202, 99–111. doi:10.1016/j.actamat.2020.10.045

Cai, L., Arias, A. L., and Nino, J. C. (2011). The Tolerance Factors of the Pyrochlore crystal Structure. *J. Mater. Chem.* 21, 3611–3618. doi:10.1039/c0jm03380d

Clarke, D. R., and Phillpot, S. R. (2005). Thermal Barrier Coating Materials. *Mater. Today* 8, 22–29. doi:10.1016/s1369-7021(05)70934-2

Clausen, K. N., and Hayes, W. (1999). Defect Structure of Yttria-Stabilized Zirconia and its Influence on the Ionic Conductivity at Elevated Temperatures. *Phys. Rev. B - Condens. Matter Mater. Phys.* 59, 14202–14219.

Clements, R., Hester, J. R., Kennedy, B. J., Ling, C. D., and Stampfl, A. P. J. (2011). The Fluorite-Pyrochlore Transformation of $Ho_{2-y}Nd_yZr_2O_7$. *J. Solid State. Chem.* 184, 2108–2113. doi:10.1016/j.jssc.2011.05.054

De Los Reyes, M., Whittle, K. R., Zhang, Z., Ashbrook, S. E., Mitchell, M. R., Jang, L.-Y., et al. (2013). The Pyrochlore to Defect Fluorite Phase Transition in $Y_2Sn_{2-x}Zr_xO_7$. *RSC Adv.* 3, 5090–5099. doi:10.1039/c3ra22704a

Doi, Y., Harada, Y., and Hinatsu, Y. (2009). Crystal Structures and Magnetic Properties of Fluorite-Related Oxides Ln_3NbO_7 (Ln=lanthanides). *J. Solid State. Chem.* 182, 709–715. doi:10.1016/j.jssc.2008.12.012

Drey, D. L., O'Quinn, E. C., Subramani, T., Lilova, K., Baldinozzi, G., Gussev, I. M., et al. (2020). Disorder in $Ho_2Ti_{2-x}Zr_xO_7$: Pyrochlore to Defect Fluorite Solid Solution Series. *RSC Adv.* 10, 34632–34650. doi:10.1039/d0ra07118h

Ewing, R. C., Weber, W. J., and Lian, J. (2004). Nuclear Waste Disposal-Pyrochlore ($A_2B_2O_7$): Nuclear Waste Form for the Immobilization of Plutonium and "minor" Actinides. *J. Appl. Phys.* 95, 5949–5971. doi:10.1063/1.1707213

Finkeldei, S., Kegler, P., Kowalski, P. M., Schreinemachers, C., Brandt, F., Bukaemskiy, A. A., et al. (2017). Composition Dependent Order-Disorder Transition in $Nd_xZr_{1-x}O_{2-0.5x}$ Pyrochlores: A Combined Structural, Calorimetric and Ab Initio Modeling Study. *Acta Mater.* 125, 166–176. doi:10.1016/j.actamat.2016.11.059

Fuentes, A. F., Montemayor, S. M., Maczka, M., Lang, M., Ewing, R. C., and Amador, U. (2018). A Critical Review of Existing Criteria for the Prediction of Pyrochlore Formation and Stability. *Inorg. Chem.* 57, 12093–12105. doi:10.1021/acs.inorgchem.8b01665

Galasso, F. S. (1970). "Chapter 12 - Summary of the Structure of Phases," in *Structure and Properties of Inorganic Solids: International Series of Monographs in Solid State Physics*. Editor I. S. Galasso (Oxford: Pergamon), 258–269. doi:10.1016/B978-0-08-006873-2.50015-9

Glerup, M., Nielsen, O. F., and Poulsen, F. W. (2001). The Structural Transformation from the Pyrochlore Structure, $A_2B_2O_7$, to the Fluorite Structure, AO_2, Studied by Raman Spectroscopy and Defect Chemistry Modeling. *J. Solid State. Chem.* 160, 25–32. doi:10.1006/jssc.2000.9142

Goldschmidt, V. M. (1926). Die Gesetze der Krystallochemie. *Naturwissenschaften* 14, 477–485. doi:10.1007/bf01507527

Götsch, T., Wallisch, W., Stöger-Pollach, M., Klötzer, B., and Penner, S. (2016). From Zirconia to Yttria: Sampling the YSZ Phase Diagram Using Sputter-Deposited Thin Films. *AIP Adv.* 6, 025119. doi:10.1063/1.4942818

Heremans, C., Wuensch, B. J., Stalick, J. K., and Prince, E. (1995). Fast-Ion Conducting $Y_2(Zr_xTi_{1-x})_2O_7$ Pyrochlores: Neutron Rietveld Analysis of Disorder Induced by Zr Substitution. *J. Solid State. Chem.* 117, 108–121. doi:10.1006/jssc.1995.1253

Isupov, V. A., and Petrov, N. A. (1958). Geometric Criteria of Structures of the Pyrochlore Type. *Soviet Educ.* 1, 99–100. doi:10.2753/res1060-9393010299

Jorgensen, C. K., and Rittersh, E. (1967). Powder-Diagram And Spectroscopic Studies of Mixed Oxides of Lanthanides And Quadrivalent Metals. *Mat. Meddelelser udgivet af det k. Danske vidensk. Selsk.* 35, 1.

Kennedy, B. J., Hunter, B. A., and Howard, C. J. (1997). Structural and Bonding Trends in Tin Pyrochlore Oxides. *J. Solid State. Chem.* 130, 58–65. doi:10.1006/jssc.1997.7277

Klee, W. E., and Weitz, G. (1969). Infrared Spectra of Ordered and Disordered Pyrochlore-type Compounds in the Series $RE_2Ti_2O_7$, $RE_2Zr_2O_7$ and $RE_2Hf_2O_7$. *J. Inorg. Nucl. Chem.* 31, 2367–2372. doi:10.1016/0022-1902(69)80566-x

Minervini, L., Grimes, R. W., and Sickafus, K. E. (2000). Disorder in Pyrochlore Oxides. *J. Am. Ceram. Soc.* 83, 1873–1878.

Mouta, R., Silva, R. X., and Paschoal, C. W. A. (2013). Tolerance Factor for Pyrochlores and Related Structures. *Acta Crystallogr. Sect B* 69, 439–445. doi:10.1107/s2052519213020514

Navrotsky, A. (2010). Thermodynamics of Solid Electrolytes and Related Oxide Ceramics Based on the Fluorite Structure. *J. Mater. Chem.* 20, 10577–10587. doi:10.1039/c0jm01521k

Norberg, S. T., Hull, S., Eriksson, S. G., Ahmed, I., Kinyanjui, F., and Biendicho, J. J. (2012). Pyrochlore to Fluorite Transition: The $Y_2(Ti_{1-x}Zr_x)_2O_7$ ($0.0 \leq X \leq 1.0$) System. *Chem. Mater.* 24, 4294–4300. doi:10.1021/cm301649d

O'Quinn, E. C., Sickafus, K. E., Ewing, R. C., Baldinozzi, G., Neuefeind, J. C., Tucker, M. G., et al. Predicting Short-Range Order and Correlated Phenomena in Disordered Crystalline Materials 6, eabc2758 (2020).doi:10.1126/sciadv.abc2758

Pauling, L. (1927). The Sizes of Ions and the Structure of Ionic Crystals. *J. Am. Chem. Soc.* 49, 765–790. doi:10.1021/ja01402a019

Pauling, L. (1929). The Principles Determining the Structure of Complex Ionic Crystals. *J. Am. Chem. Soc.* 51, 1010–1026. doi:10.1021/ja01379a006

Pauling, L. (1960). *The Nature of the Chemical Bond and the Structure of Molecules and Crystals: An Introduction to Modern Structural Chemistry*. 3rd Edn. Ithaca, NY: Cornell University Press, 505–562.

Pirzada, M., Grimes, R. W., Minervini, L., Maguire, J. F., and Sickafus, K. E. (2001). Oxygen Migration in $A_2B_2O_7$ Pyrochlores. *Solid State Ionics* 140, 201–208. doi:10.1016/s0167-2738(00)00836-5

Reynolds, E., Blanchard, P. E. R., Kennedy, B. J., Ling, C. D., Liu, S., Avdeev, M., et al. (2013). Anion Disorder in Lanthanoid Zirconates $Gd_{2-x}Tb_xZr_2O_7$. *Inorg. Chem.* 52, 8409–8415. doi:10.1021/ic4009703

Rohrer, G. S. (2001). *Structure and Bonding in Crystalline Materials*. Cambridge: Cambridge University Press. doi:10.1021/ic4009703

Roth, R. S. (1956). Pyrochlore-type Compounds Containing Double Oxides of Trivalent and Tetravalent Ions. *J. Res. Natl. Bur. Stand.* 56, 17. doi:10.6028/jres.056.003

Shafique, M., Kennedy, B. J., Iqbal, Y., and Ubic, R. (2016). The Effect of B-Site Substitution on Structural Transformation and Ionic Conductivity in $Ho_2(Zr_yTi_{1-y})_2O_7$. *J. Alloys Compd.* 671, 226–233. doi:10.1016/j.jallcom.2016.02.087

Shannon, R. D. (1976). Revised Effective Ionic Radii and Systematic Studies of Interatomic Distances in Halides and Chalcogenides. *Acta Cryst. Sect A.* 32, 751–767. doi:10.1107/s0567739476001551

Sickafus, K. E., Minervini, L., Grimes, R. W., Valdez, J. A., Ishimaru, M., Li, F., et al. (2000). Radiation Tolerance of Complex Oxides. *Science (80-.)* 289, 748–751. doi:10.1126/science.289.5480.748

Sickafus, K. E., Grimes, R. W., Valdez, J. A., Cleave, A., Tang, M., Ishimaru, M., et al. (2007). Radiation-induced Amorphization Resistance and Radiation Tolerance in Structurally Related Oxides. *Nat. Mater* 6, 217–223. doi:10.1038/nmat1842

Sickafus, K. E., Grimes, R. W., Corish, S. M., Cleave, A. R., Tang, M., Stanek, C. R., et al. (2005). *Layered Atom Arrangements in Complex Materials*. United States. doi:10.2172/883642

Stanek, C. R., and Grimes, R. W. (2002). Prediction of Rare-Earth $A_2Hf_2O_7$ Pyrochlore Phases. *J. Am. Ceram. Soc.* 85, 2139–2141. doi:10.1111/j.1151-2916.2002.tb00423.x

Subramanian, M. A., Aravamudan, G., and Subba Rao, G. V. (1983). Oxide Pyrochlores - A Review. *Prog. Solid State. Chem.* 15, 55–143. doi:10.1016/0079-6786(83)90001-8

Tang, M., Valdez, J. A., Sickafus, K. E., and Lu, P. (2007). Order-disorder Phase Transformation in Ion-Irradiated Rare Earth Sesquioxides. *Appl. Phys. Lett.* 90, 1–4. doi:10.1063/1.2720716

Thornber, M. R., Bevan, D. J. M., and Summerville, E. (1970). Mixed Oxides of the Type MO_2(fluorite)-M_2O_3. V. Phase Studies in the Systems ZrO_2-M_2O_3 (M = Sc, Yb, Er, Dy). *J. Solid State. Chem.* 1, 545–553. doi:10.1016/0022-4596(70)90140-4

Tracy, C. L., Shamblin, J., Park, S., Zhang, F., Trautmann, C., Lang, M., et al. (2016). Role of Composition, Bond Covalency, and Short-Range Order in the Disordering of Stannate Pyrochlores by swift Heavy Ion Irradiation. *Phys. Rev. B - Condens. Matter Mater. Phys.* 94, 1–11. doi:10.1103/physrevb.94.064102

Uberuaga, B. P., and Sickafus, K. E. (2015). Interpreting Oxygen Vacancy Migration Mechanisms in Oxides Using the Layered Structure Motif. *Comput. Mater. Sci.* 103, 216–223. doi:10.1016/j.commatsci.2014.10.013

van Dijk, M. P., de Vries, K. J., and Burggraaf, A. J. (1983). Oxygen Ion and Mixed Conductivity in Compounds with the Fluorite and Pyrochlore Structure. *Solid State Ionics* 9-10, 913–919. doi:10.1016/0167-2738(83)90110-8

Wannier, G. H. (1950). Antiferromagnetism. The Triangular Ising Net. *Phys. Rev.* 79, 357–364. doi:10.1103/physrev.79.357

Wuensch, B. J., Eberman, K. W., Heremans, C., Ku, E. M., Onnerud, P., Yeo, E. M. E., et al. (2000). Connection between Oxygen-Ion Conductivity of Pyrochlore Fuel-Cell Materials and Structural Change with Composition and Temperature. *Solid State Ionics* 129, 111–133. doi:10.1016/S0167-2738(99)00320-3

Xu, Q., Pan, W., Wang, J., Wan, C., Qi, L., Miao, H., et al. (2006). Rare-earth Zirconate Ceramics with Fluorite Structure for thermal Barrier Coatings. *J. Am. Ceram. Soc.* 89, 340–342. doi:10.1111/j.1551-2916.2005.00667.x

Yamamura, H., Nishino, H., Kakinuma, K., and Nomura, K. (2003). Crystal Phase and Electrical Conductivity in the Pyrochlore-type Composition Systems, $Ln_2Ce_2O_7$ (Ln=La, Nd, Sm, Eu, Gd, Y and Yb). *J. Ceram. Soc. Jpn.* 111, 902–906. doi:10.2109/jcersj.111.902

Yashima, M., Ohtake, K., Arashi, H., Kakihana, M., and Yoshimura, M. (1993). Determination of Cubic-tetragonal Phase Boundary in $Zr_{1-X}Y_XO_{2-X/2}$ Solid Solutions by Raman Spectroscopy. *J. Appl. Phys.* 74, 7603–7605. doi:10.1063/1.354989

Zhang, Z., Middleburgh, S. C., de los Reyes, M., Lumpkin, G. R., Kennedy, B. J., Blanchard, P. E. R., et al. (2013). Gradual Structural Evolution from Pyrochlore to Defect-Fluorite in $Y_2Sn_{2-x}Zr_xO_7$: Average vs Local Structure. *J. Phys. Chem. C* 117, 26740–26749. doi:10.1021/jp408682r

Conflict of Interest: The authors declare that the research was conducted in the absence of any commercial or financial relationships that could be construed as a potential conflict of interest.

Publisher's Note: All claims expressed in this article are solely those of the authors and do not necessarily represent those of their affiliated organizations, or those of the publisher, the editors and the reviewers. Any product that may be evaluated in this article, or claim that may be made by its manufacturer, is not guaranteed or endorsed by the publisher.

frontiers in Chemistry

REVIEW
published: 31 August 2021
doi: 10.3389/fchem.2021.712543

Modeling Disorder in Pyrochlores and Other Anion-Deficient Fluorite Structural Derivative Oxides

*V. Kocevski, G. Pilania and B. P. Uberuaga**

Materials Science and Technology Division, Los Alamos National Laboratory, Los Alamos, NM, United States

Their very flexible chemistry gives oxide materials a richness in functionality and wide technological application. A specific group of oxides that have a structure related to fluorite but with less oxygen, termed anion-deficient fluorite structural derivatives and with pyrochlores being the most notable example, has been shown to exhibit a diversity of useful properties. For example, the possibility to undergo a transition from an ordered to disordered state allows these oxides to have high radiation tolerance. Atomistic-scale calculations in the form of molecular dynamics (MD) and density functional theory (DFT) have been extensively used to understand what drives this order/disorder transition. Here we give a brief overview of how atomistic-scale calculations are utilized in modeling disorder in pyrochlores and other anion-deficient fluorite structural derivatives. We discuss the modeling process from simple point defects to completely disordered structures, the dynamics during the disordering process, and the use of mathematical models to generate ordered solid-solution configurations. We also attempt to identify the challenges in modeling short range order and discuss future directions to more comprehensive models of the disordered structures.

Keywords: fluorite, disorder–compounds, atomistic material modelling, pyrochlore, short range order (SRO)

OPEN ACCESS

Edited by:
Gordon James Thorogood, Australian Nuclear Science and Technology Organisation, Australia

Reviewed by:
Andrzej Grzechnik, RWTH Aachen University, Germany
Sabine Wurmehl, Leibniz Institute for Solid State and Materials Research Dresden (IFW Dresden), Germany

****Correspondence:***
B. P. Uberuaga
blas@lanl.gov

Specialty section:
This article was submitted to Solid State Chemistry, a section of the journal Frontiers in Chemistry

Received: *20 May 2021*
Accepted: *08 July 2021*
Published: *31 August 2021*

Citation:
Kocevski V, Pilania G and Uberuaga BP (2021) Modeling Disorder in Pyrochlores and Other Anion-Deficient Fluorite Structural Derivative Oxides. Front. Chem. 9:712543. doi: 10.3389/fchem.2021.712543

INTRODUCTION

Fluorite structural derivatives–oxides with a crystal structure related to fluorite–have attracted great interest both in fundamental research and in application. From the anion-deficient fluorite structural derivatives, pyrochlores, with a general formula $A_2B_2O_7$ ($Fd\bar{3}m$ space group), have attracted significant attention for various technological applications owing to their structural flexibility and special defect dynamics. They have been investigated as thermal barrier coatings (Lehmann et al., 2003; Cao et al., 2004; Schelling et al., 2004; Wu et al., 2004; Tryon et al., 2006; Winter and Clarke, 2007; Vaßen et al., 2010; Pan et al., 2012; Tanaka et al., 2017), solid oxide fuel cells (Heremans et al., 1995; Diazguillen et al., 2008; Kumar et al., 2008), solid oxide fuel cells (Wuensch, 2000; Pirzada, 2001; Yamamura, 2003; Shlyakhtina and Shcherbakova, 2012), quantum spin liquids (Anderson, 1973; Balents, 2010; Clark et al., 2014), high entropy oxides (Li et al., 2019; Zhao et al., 2019; Wright et al., 2021), and superconducting (Hanawa et al., 2001; Hanawa et al., 2002) and ferromagnetic/multiferroic (Greedan, 2006; Gardner et al., 2010; Wiebe and Hallas, 2015) materials. They have also attracted special interest as nuclear waste forms (Sickafus, 2000; Wang et al., 2000; Begg et al., 2001; Lian et al., 2003a; Lian et al., 2003b; Ewing et al., 2004; Helean et al., 2004; Lian et al., 2006; Lumpkin, 2006; Sickafus et al., 2007; Hartmann et al., 2011; Li et al., 2012; Sattonnay et al., 2013; Fischer et al., 2015; Raison and Haire, 2001; Lutique et al., 2003) and inert matrix fuel materials due to their high radiation tolerance. The high radiation tolerance of

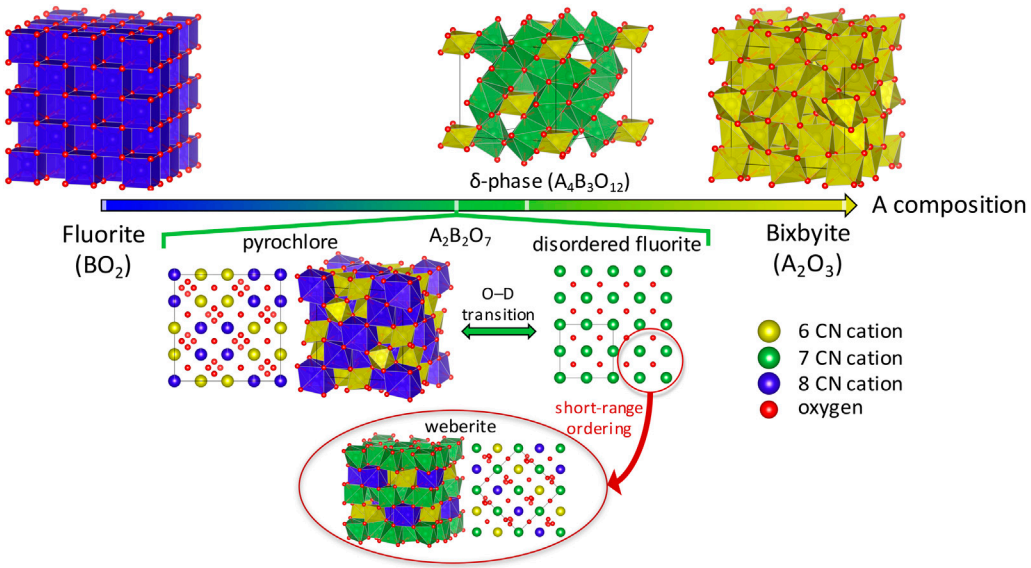

FIGURE 1 | Schematic representation of the anion-deficient fluorite structural derivative oxides, going from a fluorite (BO_2) to a bixbyite (A_2O_3) crystal structure. The cationic sites with coordination number (CN) of 6, 7 and 8 are shown as yellow, green, and blue spheres and polyhedra, respectively, while the oxygen atoms are shown as red spheres. The lower half highlights how, upon disordering, a fluorite-derivative structure such as pyrochlore can undergo an order-disorder transition to a structure resembling disordered fluorite on the long-range, but has short-range order more accurately described by a weberite-structure.

some pyrochlores is related to their ability to undergo an order-disorder transition (Subramanian et al., 1983; Lang et al., 2010; Blanchard et al., 2012; Blanchard et al., 2013; FarmerMatt et al., 2014; Popov et al., 2016; Popov et al., 2018), i.e., a low thermodynamic barrier for transition from an ordered pyrochlore to a disordered fluorite structure. In contrast, pyrochlores that have high energy cost for the order-disorder transition would amorphize under irradiation (Sickafus, 2000). Understanding the disordering process and its impact on properties is critical for a number of other applications, including ionic conductors (Kreller and Uberuaga, 2021). We note that, in contrast, spinels (AB_2O_4), which have a crystal structure related to rocksalt and have ordered cation vacancy sites, show opposite correlation between disordering energies and amorphization resistance compared to pyrochlores (Uberuaga et al., 2015), i.e., spinels that are more difficult to disorder exhibiting higher resistance to amorphization. Further, we use the term 'disorder' to mean chemical disorder in a crystalline matrix, while 'amorphization' refers to the loss of crystallinity.

The pyrochlore crystal structure can be described as an anion deficient 2 × 2 × 2 superstructure of a fluorite (BO_2), having two ordered cation sites (A in 16*d* and B in 16*c* Wykoff positions), two ordered oxygen sites (48*f* and 8*b*), and an ordered oxygen vacancy site (8*a*) (see **Figure 1**). It has been commonly accepted that the order-disorder transition is driven by the formation of cation antisite pairs and oxygen Frenkel pairs. Another anion deficient fluorite derivative termed as δ-phase (see **Figure 1**), with the general formula $A_4B_3O_{12}$, is also known to exhibit a high radiation tolerance that can be attributed to the transition from an ordered δ-phase to a disordered fluorite (Sickafus et al., 2007) structure, also promoted by the formation of cation antisites and oxygen Frenkels (Sickafus et al., 2007; Stanek et al., 2009). Generally, such a transition occurs under high energy irradiation (Sickafus, 2000; Lian et al., 2003a; Lian et al., 2003b; Helean et al., 2004) (though disorder can also be induced by temperature and synthesis conditions), and thus modeling studies of the order-disorder transition have been focused on relating the formation of these defects with radiation tolerance of pyrochlores and δ-phase. A further increase in the O vacancies gives the bixbyite structure with A_2O_3 composition, having 1/4 O vacancies in the fluorite structure. However, unlike the pyrochlore and the δ-phase, the disordered bixbyite does not have a fluorite structure, and thus we are not going to discuss it further in this review.

Studies of disordered pyrochlores suggest that the short-range structure is more ordered than is described by the random disordered fluorite structure (Liu et al., 2004; Ushakov et al., 2007; Saradhi et al., 2012; Norberg et al., 2012; Zhang et al., 2013). Recently it was shown using neutron total scattering experiments with pair distribution function (PDF) analysis that disordered pyrochlore ($Ho_2Zr_2O_7$) has the atomic arrangement of the defect fluorite on a long-range scale, but the short-range ordering is better explained by a partially ordered orthorhombic phase that is well described by a weberite-type ($C222_1$ space group) structural model (Shamblin et al., 2016). Weberite is also a superstructure of fluorite with a unit cell of $2\times\sqrt{2}\times\sqrt{2}$; it is more ordered than disordered fluorite but less ordered than pyrochlore. Unlike pyrochlore where A and B cations occupy

the 8- and 6-fold coordinated sites, respectively, in weberite the A and B cations occupy 8- and 6-fold coordinated 4*b* sites, respectively, while the 7-fold coordinated 8*c* site is equally occupied by both cations (see **Figure 1**). Note that 2-2-7 chemistries with weberite structure containing rare-earth cations have not been experimentally reported (Cai and Nino, 2009) (see **Figure 2A**), and, as far as we have found, there is only one experimental report of a 2-2-7 chemistry, $Ca_2Sb_2O_7$, that undergoes a pyrochlore-to-weberite transformation at 973 K (Brisse et al., 1972).

In the past three decades, atomic scale calculations, by means of molecular dynamics (MD) simulations with interatomic potentials and density functional theory (DFT) calculations, have been extensively used to understand the disordering process in pyrochlores by calculating the intrinsic defects formation energies (Wilde, 1998; Chartier et al., 2002; Minervini et al., 2002; Minervini et al., 2004; Panero et al., 2004; Rushton et al., 2007; Sickafus et al., 2007; Chen et al., 2008; Chen and Tian, 2010; Gunn et al., 2012; Chen et al., 2014; Uberuaga et al., 2014; Li et al., 2015; Li and Kowalski, 2018; Yang et al., 2019), looking at dynamical processes (Chartier et al., 2002; Chartier et al., 2005; Devanathan and Weber, 2005; Todorov et al., 2006; Rushton et al., 2007; Chartier et al., 2009; Devanathan et al., 2010; Xiao et al., 2010; Wang et al., 2013; Uberuaga et al., 2014) (Xiao et al., 2015; Dong et al., 2017), and using models of disordered configurations for DFT calculations (Wolff-Goodrich et al., 2015; Jiang et al., 2009; Solomon et al., 2016; Finkeldei et al., 2017; Pilania et al., 2019; Kowalski, 2020; Matsumoto et al., 2020). The simplest way to study the disorder in a material using atomistic scale calculations is to obtain the formation energies of intrinsic defects in ordered systems, which are generally accessible at a much lower computational cost than completely disordered systems. Although these dilute-limit defect energies only reflect the initial steps of disorder, they can give valuable information and qualitative agreement with experiments. In the case of pyrochlores, the basic premise would be that the formation energy of point defects, such as cation antisites, correlates with the energy to fully disorder the crystal (Uberuaga et al., 2014). A step between the study of intrinsic defects and complete disorder is analyzing dynamical processes in pyrochlores, such as threshold displacement energies, heavy ion track simulations, collision cascades, and defect accumulation. Such studies provide additional information on the energetic cost to disorder the system beyond the static intrinsic defect studies.

Performing similar simulations using ab initio MD (AIMD) is prohibitively expensive, thus a static model of the disordered fluorite is needed for DFT calculations. Such models of the disorder can be generated by arranging the A and B cations and the oxygen vacancies in a fluorite supercell, creating a special quasirandom structure (SQS) (Zunger et al., 1990) or a small set of ordered structures (Jiang and Uberuaga, 2016) such that their most relevant radial correlation functions mimic a perfectly random structure. These models provide the opportunity to compare the properties of both the ordered (pyrochlore) and

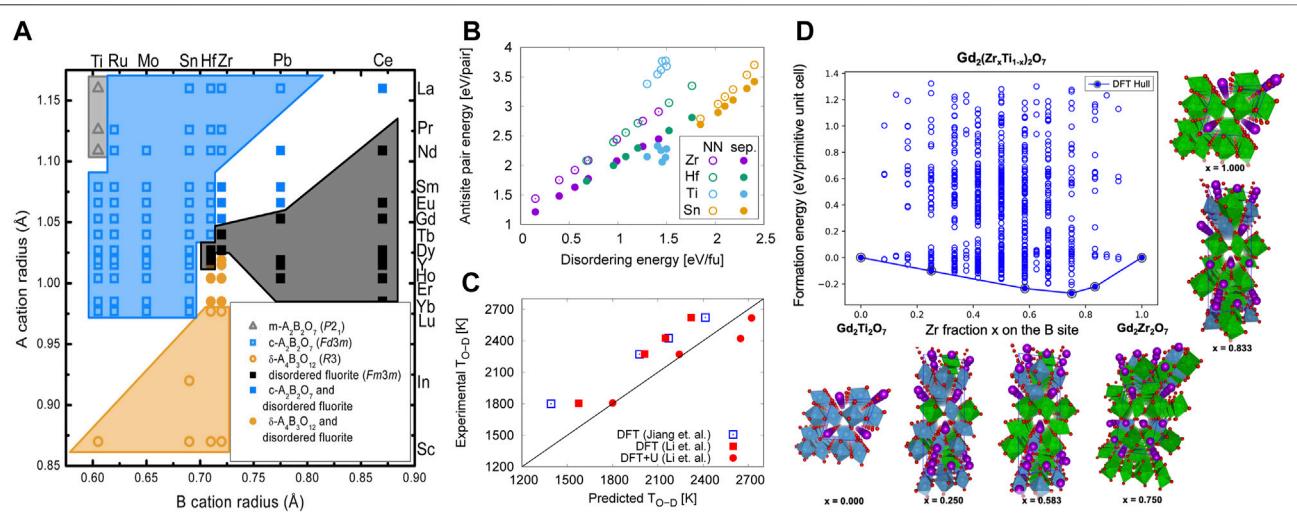

FIGURE 2 | (A) Structure map for A_3+B_4+O_4–x compounds from experimentally reported structures. Hollow gray triangles denote the monoclinic $A_2B_2O_7$ structure, hollow blue squares denote $A_2B_2O_7$ pyrochlore, and hollow orange circles denote the rhombohedral Γ-phase $A_4B_3O_{12}$. Solid black squares denote disordered fluorite. Solid symbols of the same shape as stable ordered structures denote that both the ordered structure and disordered fluorite have been observed. Reproduced from (Stanek et al., 2009). **(B)** Formation energy of cation antisite pairs in four families of rare earth (RE) pyrochlores, $RE_2B_2O_7$ (B = Zr, Hf, Ti, Sn), as a function of their disordering energies (calculated as described in (Jiang et al., 2009) and antisite separation distance. The formation energies when antisites are nearest neighbors (NN) and are separated (sep.) are shown with filled and open symbols, respectively. Adapted from (Uberuaga et al., 2014). **(C)** Comparison of the calculated order-disorder (O–D) transition temperature with experimental data (Stanek and Grimes, 2002) and (Rushton et al., 2004) for selected pyrochlores. The DFT results by (Jiang et al., 2009) and (Li et al., 2015) are shown in blue and red squares, respectively, and the DFT + U results by (Li et al., 2015) are shown in red circles. Reproduced from (Li et al., 2015). **(D)** Calculatedmixing energies per primitive unit cell for the 704 unique configurations enumerated within the $Gd_2(Zr_xTi_1–x)_2O_7$ chemistries. The DFT predicted convex hull is represented as a solid line. The atomistic configurations for the identified ground-state ordered structures on the convex hull are illustrated using purple and red spheres for Gd and O, respectively, while Ti and Zr polyhedra are depicted in blue and green colors, respectively. Reproduced from (Pilania et al., 2019).

disordered (fluorite) phases. Another approach, which can also be used to examine alternative cation arrangements and their temperature dependence via Monte Carlo, is cluster expansion (CE). Below we summarize how the above-mentioned methods are used in analyzing the order-disorder transition in anion deficient fluorite derivative phases, with a focus on pyrochlore as this system has been most extensively studied.

DEFECT FORMATION

The defect formation energies of pyrochlores were initially studied beginning more than 20 years ago using interatomic potentials (Wilde, 1998; Chartier et al., 2002; Minervini et al., 2002; Minervini et al., 2004; Rushton et al., 2007; Sickafus et al., 2007; Gunn et al., 2012), while recently more accurate DFT calculations have also been utilized (Panero et al., 2004; Chen et al., 2008; Zhang et al., 2009; Chen and Tian, 2010; Chen et al., 2014; Uberuaga et al., 2014; Li et al., 2015; Li and Kowalski, 2018; Yang et al., 2019). Despite the higher defect formation energies calculated using interatomic potentials compared to DFT, both types of studies show an apparent correlation between decreased cation antisite pair formation energies and the radiation tolerance of pyrochlores. Both also report a peak in the defect formation energies at Gd in the $A_2Ti_2O_7$ series, which agrees with the experimentally observed highest critical amorphization temperature for $Gd_2Ti_2O_7$ (Lian et al., 2003a). (Uberuaga et al. 2014) saw precisely these relationships in Ti and other pyrochlore chemistries (**Figure 2B**).

Once the oxygen Frenkel is coupled with a cation antisite pair, the formation energy of such clusters becomes lower than the isolated defects (with a few exceptions (Li et al., 2015; Li and Kowalski, 2018)). This enhanced stability of the clusters indicates that cation antisites cause local oxygen disorder, and hence, drive the formation of disordered fluorite structure. (Stanek and Grimes, 2002) and (Rushton et al., 2004) correlated the formation energies of these clusters with the experimental pyrochlore-to-disordered-fluorite transition temperatures for $A_2Hf_2O_7$ and $A_2Zr_2O_7$, respectively, showing a clear linear relation. Studies with potentials also report a threshold cluster formation energy below which disordered fluorite is preferred, demonstrating why some chemistries do not form the pyrochlore structure. (Yang et al., 2019) evaluated the defect formation energies in off-stoichiometric $A_2B_2O_7$ (A = La, Nd, Gd; B = Zr, Hf, Sn), demonstrating how the synthesis methods, i.e., excess of A_2O_3 or BO_2, can influence the radiation tolerance of pyrochlores.

The most important observations from these studies are that the energetics of cation antisites correlate with the amorphization resistance of the material and that cation and oxygen disordered are coupled. The correlation between disordering and amorphization has been explained by (Sickafus, 2000) as related to an inherent ability of the structure to create low-energy defects that do not drastically increase the stored energy in the material. On the other hand, that cation and anion disorder are linked is a consequence of the differences in preferred coordination in the A and B cations–8 and 6, respectively. As the cations are disordered, they will naturally drive rearrangement of the oxygen to best retain their preferred coordination, and these modeling results directly demonstrate this fact. However, this behavior is not universal, as we will see in our discussion of the δ-phase structure below.

DYNAMICAL PROCESSES

Threshold displacement energies (TDEs) can characterize the resistance of a given sublattice to short-range displacements in a specific crystallographic direction, by looking at the response of the crystal to a primary knock-on atom (PKA). The TDE of pyrochlores have been studied using classical MD Chartier et al., 2002; Devanathan and Weber, 2005; Dong et al., 2017) and AIMD (Xiao et al., 2010; Wang et al., 2013; Xiao et al., 2015). While both MD and AIMD give the same trend in terms of which species are easiest to displace, the calculated TDEs do not correlate with the experimental radiation tolerance of the studied $A_2Ti_2O_7$ pyrochlores.

More detailed understanding of the main mechanisms that promote the formation of disordered fluorite, and subsequently an amorphous phase, can be gained by investigating dynamical processes during collision cascades. Collision cascades in $La_2Zr_2O_7$ (Chartier et al., 2003) and $Gd_2B_2O_7$ (B = Ti, Zr, Pb) (Todorov et al., 2006; Rushton et al., 2007) display very similar behavior, with significantly higher number of O defects compared to cation defects at the end of the simulation. Despite this, the oxygen-oxygen radial distribution function of the studied pyrochlores shows no hints of amorphization. A closer look into the equilibrated structures shows that most of the displaced O atoms in the studied pyrochlores recovered to an equilibrium site (48f, 8b or 8a), except for in $Gd_2Ti_2O_7$ where the formed O defects are in interstitial sites.

Another way to study disordering processes is by simulating swift heavy ion irradiation tracks using thermal spikes. By such simulations in $Gd_2Zr_xTi_{2-x}O_7$, (Devanathan et al., 2013) showed that an amorphous area of ~2 nm forms in $Gd_2Ti_2O_7$, which shrinks with increasing Zr content, and completely disappears in $Gd_2Zr_2O_7$. The findings agree with experiments that show that $Gd_2Ti_2O_7$ becomes amorphous under swift heavy ion irradiation while $Gd_2Zr_2O_7$ forms disordered fluorite. A closer look into the disordering process in $Gd_2Ti_2O_7$ showed a formation of Gd vacancies, Ti interstitials, and Gd-on-Ti antisites that facilitate amorphization. On the other hand, only Gd and Zr antisite pairs are observed in $Gd_2Zr_2O_7$, which dissipate the excess energy.

As we discussed previously, the tendency of a pyrochlore to disorder, i.e., to form a disordered fluorite structure, is correlated with the formation energy of cation antisites and oxygen Frenkels. A more complete picture of disordering in the pyrochlore structure can be gained by introducing defects in various concentrations, and using MD to simulate the disordering process over time. Using classical MD simulations of $La_2Zr_2O_7$ pyrochlore, (Chartier et al., 2005) showed that cation antisites induce disorder on the oxygen sublattice, indicating that the transition to a disordered fluorite is driven by cation disorder.

Later (Chartier et al., 2009) extended their study to $Gd_2Zr_xTi_{2-x}O_7$ solid solutions, showing a decrease in radiation tolerance with increasing Ti content, while (Devanathan et al., 2010) compared the two end-member compositions. Both studies show that the amorphization of pyrochlores is a two-step process: initially cation antisites and oxygen Frenkels are formed, with subsequent damage increasing the concentration of cation Frenkels, especially Ti-Ti dumbbells which resist recombination, leading to amorphization. These studies reveal that simply introducing cation disorder leads to disordering of the entire structure–the anions disorder "spontaneously" in the presence of cation disorder.

Together, these dynamical simulations both reinforce the conclusions obtained from the static calculations of defects but also reveal new details of the dynamical processes underlying the formation of disorder. During irradiation, oxygen is always easier to displace, but unless cations are also displaced, that disorder oxygen structure will not persist. Cation antisites are the driver of disorder on both sublattices. However, at some defect concentration, the lattice becomes unstable and cation Frenkels start to form. The lack of dynamical recovery leads to an exceedingly high stored energy for some chemistries, which causes amorphization. Thus, the susceptibility to amorphization is a combination of both the energetic cost of the defects that are unavoidably introduced during irradiation and their inability to heal or recombine. What is still missing in the literature is a model that can actually predict the rate of amorphization for a given material as a function of temperature and dose. We suspect this is due to the shear difficulty in developing such a model for even one compound, given all of the details that must be addressed. However, such a model for even one compound would provide important insight into the most critical factors describing the kinetics of amorphization and recovery.

STRUCTURAL DISORDER

As mentioned, one can use SQS to model the disordered fluorite structure with DFT, and evaluate the energy for disordering as the energy difference between the ordered pyrochlore and the disordered SQS. (Jiang et al., 2009) used this approach to calculate the disordering energy for a set of rare-earth pyrochlores, $A_2B_2O_7$ (A = Pr, Nd, Sm, Gd, Tb, Dy, Er; B = Ti, Zr, Hf, Sn), while (Li et al., 2015) focused on a small subset of pyrochlores ($Gd_2Zr_2O_7$, $Gd_2Hf_2O_7$, $Sm_2Zr_2O_7$, $Tb_2Zr_2O_7$). Both related the disordering energy with amorphization tendencies and estimated the order-disorder temperature, T_{OD}, showing good agreement with experiments (**Figure 2c**) and highlighting the relevance of the disordered state in understanding the properties of these materials. Using the calculated T_{OD}, (Jiang et al., 2009) were also able to explain the difficulties in synthesizing of some pyrochlores. More importantly, as highlighted in **Figure 2B**, these types of calculations (Uberuaga et al., 2014) reveal a direct correlation between the energetics of cation antisite pairs and full disorder in the system.

Recently, Shamlin et al. showed experimentally that the weberite-like structure, which has a random cationic distribution on the 8*c* site (7-fold coordinated site), best represents the short-range order in the disordered structure (Shamblin et al., 2016). This has inspired DFT calculations of weberite-type disordered structures (Solomon et al., 2016; Finkeldei et al., 2017; Kowalski, 2020; Matsumoto et al., 2020), which show that disordered fluorite has higher energy than disordered weberite. It is argued that this indicates a possibility of forming weberite-type short-range ordering. However, both (Kowalski, 2020) and (Matsumoto et al., 2020) also report that some $A_2B_2O_7$ chemistries have weberite-type as a lower energy configuration, in disagreement with experiments that report either pyrochlore or δ-phase (**Figure 2A**). This is a curious result as no 2-2-7 chemistries containing +3 and +4 cations have been experimentally reported to have the weberite structure (Cai and Nino, 2009). On the other hand, calorimetry experiments indicate that the short-range order described by weberite is higher in energy than pyrochlore (Solomon et al., 2016; Finkeldei et al., 2017). The discrepancy between experiments and modeling can be explained for some chemistries, namely $A_2Zr_2O_7$ and $A_2Hf_2O_7$ (A = Ho, Er, Yb, Lu), which form δ-phase (see **Figure 2A**), suggesting δ-phase might be preferred and thus should be examined. (Matsumoto et al., 2020) also used the vibrational entropy of the $Yb_2Ti_2O_7$ pyrochlore and weberite to find the weberite-to-pyrochlore ordering transition temperature, showing that the pyrochlore ordering is preferred at temperatures above 500 K. Nevertheless, the predicted ordering transition temperature is not low enough to explain why the weberite-type structure has not been experimentally observed.

Finally, there is a possibility of even greater ordering when multiple cations are introduced into one of the sublattices. Calculations of such structures can give further insight into the drivers of ordering and the relationship between cation and anion structure. (Pilania et al., 2020) have investigated precisely this possibility in $Gd_2(Ti_{1-x}Zr_x)_2O_7$ using cluster expansion coupled with DFT calculations. As highlighted in **Figure 2D**, their calculations indicated that $Gd_2(Ti_{0.25}Zr_{0.75})_2O_7$, termed a double pyrochlore, has the lowest formation energy on the convex hull. The enhanced stability of this composition was attributed to a special configuration that allows for 7-fold coordinated Zr sites while maintaining the preferred 6-fold coordination of Ti-atoms. This kind of cation-induced change in the local oxygen coordination is what is behind the formation of weberite-like short-range order.

In our view, one of the most important results from these calculations is that the energetics of the individual cation antisites correlate very strongly with full disorder. This directly links the original calculations of isolated defects and the fully disordered structure. However, more recent experiments and calculations of disordered structures also reveal what we might call a conundrum. It is now abundantly clear that short-range order exists in the disordered and even amorphous materials. However, the calculations indicate that structures built on these short-range ordered motifs are actually more stable than pyrochlore. We will discuss this in greater depth below. Finally, the unexpected

stability of $Gd_2(Ti_{0.25}Zr_{0.75})_2O_7$, in which Zr is able to attain its preferred 7-fold coordination, suggests that, in the pyrochlore structure, Zr is frustrated. This may explain why Zr-based pyrochlores tend to be fast ion conductors, as the oxygen struggles to maintain low-energy coordination in any one configuration.

OTHER PHASES

The δ-phase was initially presented as having a higher radiation tolerance as compared to pyrochlores by (Sickafus et al., 2007), which they correlate with the lower formation energy of defect clusters. Following these findings, (Stanek et al., 2009) performed a computational study of the cation ordering in $A_4B_3O_{12}$ and calculated the disordering energy with respect to the disordered fluorite. (Interestingly, these compounds have not been experimentally observed to have cation order.) They then evaluated the T_{OD} using the same approach as (Jiang et al., 2009). The T_{OD} were found to be generally low, even lower compared to most of the pyrochlores from study, indicating that the δ-phase should disorder much more easily, and thus have high radiation tolerance, as initially indicated by static MD calculations (Sickafus et al., 2007).

Until now our discussion has focused on the specific compositions $A_2B_2O_7$ and $A_4B_3O_{12}$. However, it is possible to sample the whole phase space between BO_2 and A_2O_3 for any stable ordered fluorite structural derivative compounds. This is what (Bogicevic et al., 2001; Bogicevic and Wolverton, 2003) and (Predith et al., 2008) did using cluster expansion to find the lowest energy ordering in the ZrO_2–A_2O_3 (A = Y, Sc) and ZrO_2–Y_2O_3 phase spaces, respectively. In addition to the experimentally observed δ-phases ($Y_4Zr_3O_{12}$ and $Sc_4Zr_3O_{12}$), both report $Y_2Zr_5O_{10}$ and $Sc_2Zr_5O_{10}$ to be stable with respect to cubic ZrO_2, while (Predith et al., 2008) also report an additional $Y_2Zr_4O_{11}$ stable phase. Furthermore, Predith et al. show that only $Y_2Zr_4O_{11}$ and $Y_4Zr_3O_{12}$ phases are stable with respect to the monoclinic, lowest energy ZrO_2. None of these studies found the pyrochlore configuration to be stable, in agreement with experiments where only the stable δ-phase is observed for these compositions. In the reported stable structures, the oxygen vacancies align along the <111> direction and are always third nearest neighbors to each other, showing that cluster expansion can provide information on the short-range ordering in solid solutions. Such studies have been performed for other crystal structures, such as spinels (Jiang et al., 2012; Pilania et al., 2020), but have not been applied to fluorite derivatives as extensively because of the need to account for the coupling of disorder on the cation and anion sublattices.

These calculations both complement and contrast with the behavior we have described for pyrochlore. First, that the δ-phase structure is easy to disorder suggests it has high radiation tolerance, as has been observed (Sickafus et al., 2007). However, this structure also exhibits anion ordering despite the disordered cations, indicating that cation disorder does not always force anion disorder. Oxygen vacancy-vacancy repulsion, presumably, overcomes any coupling with the cation disorder. Further, as demonstrated by there can be a variety of other stable structures for some of these chemistries, suggesting that there is not one dominant phase and that short-range order in disordered materials may be related to these other structures as well. This has not been considered in prior research, to the best of our knowledge.

DISCUSSION AND OUTLOOK

The computational studies we have examined have provided invaluable insight into the nature of disorder in anion-deficient fluorite derivatives. It is only through atomistic modeling that the relationship between disordering and radiation tolerance has been established. However, there are a number of questions that arise from past work that can be uniquely addressed by future modeling efforts.

Classical MD simulations provide a good understanding of the processes that drive the disordering of pyrochlores to a disordered fluorite structure. However, the accuracy of MD simulations is dependent on the quality of the interatomic potential and current potentials do not capture all of the nuances of the true quantum system, such as the formation of 7-fold coordinated Zr sites predicted using DFT in $Gd_2(Ti_{0.25}Zr_{0.75})_2O_7$ (Pilania et al., 2019). Thus, new potentials could improve the understanding of the disordering processes in pyrochlores. Alternatively, AIMD using DFT forces can be performed directly to understand the disordering processes by introducing different defects in various concentrations in the simulation cells, similarly to some of the classical MD studies discussed above. Such simulations can validate classical results and provide new insight into how chemical bonding drives unique behavior. While AIMD simulations are currently computationally highly expensive, current improvements in code efficiency and computational architectures can make such simulations possible.

Using DFT calculations, SQS models of disordered fluorite provide a reasonable estimate of the T_{OD} of pyrochlores (Jiang et al., 2009; Li et al., 2015), with T_{OD} calculated with DFT + U being in very good agreement with experiments (Li et al., 2015). A more accurate estimate of T_{OD} can be obtained by accounting for vibrational entropy, as has been demonstrated in spinels (Jiang et al., 2012). Introducing the vibrational entropy to the defect formation energies can also provide more rigorous defect formation free energies, as well as a possibility to evaluate the defect concentrations at finite temperatures. A critical unknown is how equilibrium defect concentrations depend on the state of disorder–all defect calculations that have been done are for the fully ordered state and may not be representative of the disordered material.

We have discussed how cluster expansion is a powerful tool for studying the energetics of disorder, such as finding order in solid-solutions of $Gd_2(Ti_{1-x}Zr_x)_2O_7$ (Pilania et al., 2019) and the mixing between BO_2 and A_2O_3 (Predith et al., 2008). Therefore, cluster expansion can be employed to study the change from pyrochlore (ordered) to fluorite-type (disordered) structure in the studied $A_2(B_{1-x}B'_x)_2O_7$ solid solutions, accounting for mixing on the cationic sublattice between A, B and B′ cations in addition to

introducing O in the vacant 8*a* sites. While there might be challenges in developing cluster expansion models that account for the coupled order between the cation and anion sublattices, this is an integral step that must be undertaken to fully understand the nature of the short-range order in disordered pyrochlores.

Even if the disordered state is properly understood and described, this is only the beginning. To predict and ultimately design materials that leverage the disordered state, we must also know the impact on properties. As we have already noted, disordered materials have unique properties distinct from their ordered counterparts. This fact has mostly been revealed by experiments with relatively little work by modeling. There is a need, once reasonable models of the disordered state have been established, to understand the structure-property relationship of those systems. Structural properties such as short-range order and percolation networks can have dramatic effects on transport and these relationships have received scant modeling attention (Kreller and Uberuaga, 2021).

Finally, the biggest question that arises from this review is the nature of the ordering in the presumably disordered fluorite structure of these materials. Experiments indicate that short range order is present. This should be expected, as no natural material is truly random–indeed, cluster expansion studies of spinel show that short range order persists to extremely high (and unphysical) temperatures (Pilania et al., 2020). However, the random structure presents a useful conceptual limit that has been demonstrated to correlate with experimental observables such as the order-disorder transition temperature and the critical temperature for amorphization. Thus, the random structure does capture some of the physical behavior of the real materials. The key question then is when is it critical to account for the short-range order to accurately understand and predict the properties of these materials. For example, it seems clear that the nature of the short-range order is essential for understanding mass transport in these materials (Kreller and Uberuaga, 2021). However, it isn't necessary to understand chemical trends in thermodynamic behavior. Future work must elucidate not only the nature of the short-range order, but when it must be accounted for.

AUTHOR CONTRIBUTIONS

VK, GP, and BU conceived of and planned the manuscript. VK researched the literature and wrote the main body of the manuscript. All of the authors edited and contributed to the manuscript. All authors contributed to the figures.

FUNDING

This work was supported by the U.S. Department of Energy, Office of Science, Basic Energy Sciences, Materials Sciences and Engineering Division. Los Alamos National Laboratory is operated by Triad National Security, LLC, for the National Nuclear Security Administration of U.S. Department of Energy (Contract No. 89233218CNA000001).

REFERENCES

Anderson, P. W. (1973). Resonating Valence Bonds: A New Kind of Insulator? *Mater. Res. Bull.* 8 (2), 153–160. doi:10.1016/0025-5408(73)90167-0

Balents, L. (2010). Spin Liquids in Frustrated Magnets. *Nature* 464 (7286), 199–208. doi:10.1038/nature08917

Begg, B. D., Hess, N. J., McCready, D. E., Thevuthasan, S., and Weber, W. J. (2001). Heavy-Ion Irradiation Effects in $Gd_2(Ti_{2-x}Zr_x)O_7$ Pyrochlores. *J. Nucl. Mater.* 289 (1–2), 188–193. doi:10.1016/s0022-3115(00)00696-6

Blanchard, P. E. R., Clements, R., Brendan, J. K., ChrisLing, D., Emily, R., Max, A., et al. (2012). Does Local Disorder Occur in the Pyrochlore Zirconates? *Inorg. Chem.* 51 (24), 13237–13244. doi:10.1021/ic301677b

Blanchard, P. E. R., Liu, S., Brendan, J. K., Chris, D. L., Max, A., JadeAitken, B., et al. (2013). Investigating the Local Structure of Lanthanoid Hafnates $Ln_2Hf_2O_7$ via Diffraction and Spectroscopy. *The J. Phys. Chem. C* 117 (5), 2266–2273. doi:10.1021/jp311329q

Bogicevic, A., Wolverton, C., Crosbie, G. M., and Stechel, E. B. (2001). Defect Ordering in Aliovalently Doped Cubic Zirconia from First Principles. *Phys. Rev. B* 64 (1), 014106. doi:10.1103/physrevb.64.014106

Bogicevic, A., and Wolverton, C. (2003). Nature and Strength of Defect Interactions in Cubic Stabilized Zirconia. *Phys. Rev. B* 67 (2), 024106. doi:10.1103/physrevb.67.024106

Brisse, F., Stewart, D. J., Seidl, V., and Knop, O. (1972). Pyrochlores. VIII. Studies of Some 25 Pyrochlores and Related Compounds and Minerals. *Can. J. Chem.* 50 (22), 3648–3666. doi:10.1139/v72-580

Cai, L., and Nino, J. C. (2009). Complex Ceramic Structures. I. Weberites. *Acta Crystallogr. Section B Struct. Sci.* 65 (3), 269–290. doi:10.1107/s0108768109011355

Cao, X. Q., Vassen, R., and Stoever, D. (2004). Ceramic Materials for thermal Barrier Coatings. *J. Eur. Ceram. Soc.* 24 (1), 1–10. doi:10.1016/s0955-2219(03)00129-8

Chartier, A., Constantin, M., Jean-Paul, C., René Corrales, L., and Weber, W. J. (2003). Atomistic Modeling of Displacement Cascades in $La_2Zr_2O_7$ Pyrochlore. *Phys. Rev. B* 67 (17), 174102. doi:10.1103/physrevb.67.174102

Chartier, A., Constantin, M., Weber, W. J., and René Corrales, L. (2002). Theoretical Study of Disorder in Ti-Substituted $La_2Zr_2O_7$ *Phys. Rev. B* 65 (13), 134116. doi:10.1103/physrevb.65.134116

Chartier, A., Meis, C., Crocombette, J.-P., Weber, W. J., and Corrales, L. R. (2005). Molecular Dynamic Simulation of Disorder Induced Amorphization in Pyrochlore. *Phys. Rev. Lett.* 94 (2), 025505. doi:10.1103/physrevlett.94.025505

Chartier, A., Catillon, G., and Crocombette, J. P. (2009). Key Role of the Cation Interstitial Structure in the Radiation Resistance of Pyrochlores. *Phys. Rev. Lett.* 102 (15), 155503. doi:10.1103/physrevlett.102.155503

Chen, L., Su, X., and Li, Y. (2014). First-Principles Study on Cation-Antisite Defects of Stannate and Titanate Pyrochlores. *OALib* 01 (03), 1–8. doi:10.4236/oalib.1100516

Chen, Z. J., Xiao, H. Y., Zu, X. T., and Gao, F. (2008). First-Principles Calculation of Defect Formation Energies and Electronic Properties in Stannate Pyrochlores. *J. Appl. Phys.* 104 (9), 093702. doi:10.1063/1.3000558

Chen, Z. J., and Tian, D. B. (2010). First-Principles Study of Disordering Tendencies in $Gd_2B_2O_7$ (B = Ti, Sn, Zr) Compounds. *Chin. Phys. B* 19 (12), 127101. doi:10.1088/1674-1056/19/12/127101

Clark, L., Nilsen, G. J., Kermarrec, E., Ehlers, G., Knight, K. S., Harrison, A., et al. (2014). From Spin Glass to Quantum Spin Liquid Ground States in Molybdate Pyrochlores. *Phys. Rev. Lett.* 113 (11), 117201. doi:10.1103/physrevlett.113.117201

Devanathan, R., Weber, W. J., and Gale, J. D. (2010). Radiation Tolerance of Ceramicsinsights from Atomistic Simulation of Damage Accumulation in Pyrochlores. *Energ. Environ. Sci.* 3 (10), 1551. doi:10.1039/c0ee00066c

Devanathan, R., and Weber, W. J. (2005). Insights into the Radiation Response of Pyrochlores from Calculations of Threshold Displacement Events. *J. Appl. Phys.* 98 (8), 086110. doi:10.1063/1.2120889

Devanathan, R., Gao, F., and Sundgren, C. J. (2013). Role of Cation Choice in the Radiation Tolerance of Pyrochlores. *RSC Adv.* 3 (9), 2901. doi:10.1039/c2ra22745b

Diazguillen, J., Diazguillen, M., Padmasree, K., Fuentes, A., Santamaria, J., and Leon, C. (2008). High Ionic Conductivity in the Pyrochlore-type $Gd_{2-y}La_yZr_2O_7$ Solid Solution ($0 \le y \le 1$). *Solid State Ionics* 179 (38), 2160–2164. doi:10.1016/j.ssi.2008.07.015

Dong, L., Setyawan, W., Li, Y., Devanathan, R., and Gao, F. (2017). Molecular Dynamics Simulation of Low-Energy Recoil Events in Titanate Pyrochlores. *RSC Adv.* 7 (56), 35403–35410. doi:10.1039/c7ra04699e

Ewing, R. C., Weber, W. J., and Lian, J. (2004). Nuclear Waste Disposal-Pyrochlore ($A_2B_2O_7$): Nuclear Waste Form for the Immobilization of Plutonium and "Minor" Actinides. *J. Appl. Phys.* 95 (11), 5949–5971. doi:10.1063/1.1707213

Farmer, J. M., Boatner, L. A., Chakoumakos, B. C., Du, M.-H., Lance, M. J., Rawn, C. J., et al. (2014). Structural and Crystal Chemical Properties of Rare-Earth Titanate Pyrochlores. *J. Alloys Compounds* 605 (August), 63–70. doi:10.1016/j.jallcom.2014.03.153

Finkeldei, S., Kegler, P., Kowalski, P. M., Schreinemachers, C., Brandt, F., Bukaemskiy, A. A., et al. (2017). Composition Dependent Order-Disorder Transition in NdxZr1-xO2-0.5x Pyrochlores: A Combined Structural, Calorimetric and Ab Initio Modeling Study. *Acta Materialia* 125 (February), 166–176. doi:10.1016/j.actamat.2016.11.059

Fischer, C., Finkeldei, S., Brandt, F., Bosbach, D., and Luttge, A. (2015). Direct Measurement of Surface Dissolution Rates in Potential Nuclear Waste Forms: The Example of Pyrochlore. *ACS Appl. Mater. Inter.* 7 (32), 17857–17865. doi:10.1021/acsami.5b04281

Gardner, J. S., GingrasGingras, M. J. P., and Greedan, J. E. (2010). Magnetic Pyrochlore Oxides. *Rev. Mod. Phys.* 82 (1), 53–107. doi:10.1103/revmodphys.82.53

Greedan, J. E. (2006). Frustrated Rare Earth Magnetism: Spin Glasses, Spin Liquids and Spin Ices in Pyrochlore Oxides. *J. Alloys Compounds* 408–412 (February), 444–455. doi:10.1016/j.jallcom.2004.12.084

Gunn, D. S. D., Allan, N. L., Foxhall, H., Harding, J. H., Purton, J. A., Smith, W., et al. (2012). Novel Potentials for Modelling Defect Formation and Oxygen Vacancy Migration in $Gd_2Ti_2O_7$ and $Gd_2Zr_2O_7$ Pyrochlores. *J. Mater. Chem.* 22 (11), 4675. doi:10.1039/c2jm15264a

Hanawa, M., Yamaura, J., Muraoka, Y., Sakai, F., and Hiroi, Z. (2002). Structural Phase Transition in the Superconducting Pyrochlore Oxide $Cd_2Re_2O_7$. *J. Phys. Chem. Sol.* 63 (6–8), 1027–1030. doi:10.1016/s0022-3697(02)00090-2

Hanawa, M., Muraoka, Y., Tayama, T., Sakakibara, T., Yamaura, J., and Hiroi, Z. (2001). Superconductivity at 1 K in$Cd_2Re_2O_7$. *Phys. Rev. Lett.* 87 (18), 187001. doi:10.1103/physrevlett.87.187001

Hartmann, T., Alaniz, A., Poineau, F., Weck, P. F., Valdez, J. A., Tang, M., et al. (2011). Structure Studies on Lanthanide Technetium Pyrochlores as Prospective Host Phases to Immobilize 99technetium and Fission Lanthanides from Effluents of Reprocessed Used Nuclear Fuels. *J. Nucl. Mater.* 411 (1–3), 60–71. doi:10.1016/j.jnucmat.2011.01.033

Helean, K. B., Ushakov, S. V., Brown, C. E., Navrotsky, A., Lian, J., Ewing, R. C., et al. (2004). Formation Enthalpies of Rare Earth Titanate Pyrochlores. *J. Solid State. Chem.* 177 (6), 1858–1866. doi:10.1016/j.jssc.2004.01.009

Heremans, C., Wuensch, B. J., Stalick, J. K. W., and Prince, E. (1995). Fast-Ion Conducting $Y_2(Zr_xTi_{1-x})_2O_7$ Pyrochlores: Neutron Rietveld Analysis of Disorder Induced by Zr Substitution. *J. Solid State. Chem.* 117 (1), 108–121. doi:10.1006/jssc.1995.1253

Jiang, C, KurtSickafus, E., ChristopherStanek, R., SvenRudin, P., and Uberuaga, B. P. (2012). Cation Disorder in MgX_2O_4 (X= Al, Ga, in) Spinels from First Principles. *Phys. Rev. B* 86 (2), 024203. doi:10.1103/physrevb.86.024203

Jiang, C., Stanek, C. R., Sickafus, K. E., and Uberuaga, B. P. (2009). First-Principles Prediction of Disordering Tendencies in Pyrochlore Oxides. *Phys. Rev. B* 79 (10), 104203. doi:10.1103/physrevb.79.104203

Jiang, C., and Uberuaga, B. P. (2016). Efficient Ab-Initio Modeling of Random Multicomponent Alloys. *Phys. Rev. Lett.* 116 (10), 105501. doi:10.1103/physrevlett.116.105501

Kowalski, P. M. (2020). Formation Enthalpy of $Ln_2B_2O_7$-type (B = Ti, Sn, Hf, Zr) Compounds. *Scripta Materialia* 189 (December), 7–10. doi:10.1016/j.scriptamat.2020.07.048

Kreller, C. R., and Uberuaga, B. P. (2021). The Role of Cation Ordering and Disordering on Mass Transport in Complex Oxides. *Curr. Opin. Solid State. Mater. Sci.* 25 (2), 100899. doi:10.1016/j.cossms.2021.100899

Kumar, M., Raj, I. A., and Pattabiraman, R. (2008). $Y_2Zr_2O_7$ (YZ)-pyrochlore Based Oxide as an Electrolyte Material for Intermediate Temperature Solid Oxide Fuel Cells (ITSOFCs)-Influence of Mn Addition on YZ. *Mater. Chem. Phys.* 108 (1), 102–108. doi:10.1016/j.matchemphys.2007.09.010

Lang, M., Fuxiang, Z., Jiaming, Z., Jianwei, W., Jie, L., William, J. W., et al. (2010). Review of $A_2B_2O_7$ Pyrochlore Response to Irradiation and Pressure. *Nucl. Instr. Methods Phys. Res. Section B: Beam Interactions Mater. Atoms* 268 (19), 2951–2959. doi:10.1016/j.nimb.2010.05.016

Lehmann, H., Pitzer, D., Pracht, G., Vassen, R., and Stöver, D. (2003). Thermal Conductivity and Thermal Expansion Coefficients of the Lanthanum Rare-Earth-Element Zirconate System. *J. Am. Ceram. Soc.* 86 (8), 1338–1344. doi:10.1111/j.1151-2916.2003.tb03473.x

Li, Y., and Kowalski, P. M. (2018). Energetics of Defects Formation and Oxygen Migration in Pyrochlore Compounds from First Principles Calculations. *J. Nucl. Mater.* 505 (July), 255–261. doi:10.1016/j.jnucmat.2017.11.005

Li, Y., Kowalski, P. M., Beridze, G., Birnie, A. R., Finkeldei, S., and Bosbach, D. (2015). "Defect Formation Energies in A2B2O7 Pyrochlores." *Scripta Materialia* 107 (October), 18–21. doi:10.1016/j.scriptamat.2015.05.010

Li, Y. H., Uberuaga, B. P., Jiang, C., Choudhury, S., Valdez, J. A., Patel, M. K., et al. (2012). Role of Antisite Disorder on Preamorphization Swelling in Titanate Pyrochlores. *Phys. Rev. Lett.* 108(19): 195504. doi:10.1103/physrevlett.108.195504

Li, F., Zhou, L., Liu, J.-X., Liang, Y., and Zhang, G.-J. (2019). High-Entropy Pyrochlores with Low thermal Conductivity for Thermal Barrier Coating Materials. *J. Adv. Ceram.* 8 (4), 576–582. doi:10.1007/s40145-019-0342-4

Lian, J., Helean, K. B., Kennedy, B. J., Wang, L. M., Navrotsky, A., and Ewing, R. C. (2006). Effect of Structure and Thermodynamic Stability on the Response of Lanthanide Stannate Pyrochlores to Ion Beam Irradiation. *J. Phys. Chem. B* 110 (5), 2343–2350. doi:10.1021/jp055266c

Lian, J., Wang, L., Chen, J., Sun, K., Ewing, R. C., Farmer, J. M., et al. (2003). The Order-Disorder Transition in Ion-Irradiated Pyrochlore. *Acta Materialia* 51 (5), 1493–1502. doi:10.1016/s1359-6454(02)00544-x

Lian, J., Chen, J., Wang, L. M., Ewing, R. C., Farmer, J. M., Boatner, L. A., et al. (2003). Radiation-induced Amorphization of Rare-Earth Titanate Pyrochlores. *Phys. Rev. B* 68 (13), 134107. doi:10.1103/physrevb.68.134107

Liu, Y., Leslie Withers, R., and Norén, L. (2004). "The Pyrochlore to 'Defect Fluorite' Transition in the $Y_2(Zr_yTi_{1-y})_2O_7$ System and its Underlying Crystal Chemistry." *J. Solid State. Chem.* 177 (12), 4404–4412. doi:10.1016/j.jssc.2004.09.014

Lumpkin, G. R. (2006). Ceramic Waste Forms for Actinides. *Elements* 2 (6), 365–372. doi:10.2113/gselements.2.6.365

Lutique, S., Staicu, D., Konings, R. J. M., Rondinella, V. V., Somers, J., and Wiss, T. (2003). Zirconate Pyrochlore as a Transmutation Target: Thermal Behaviour and Radiation Resistance against Fission Fragment Impact. *J. Nucl. Mater.* 319 (June), 59–64. doi:10.1016/s0022-3115(03)00134-x

Matsumoto, U., Ogawa, T., Kitaoka, S., Moriwake, H., and Tanaka, I. (2020). "First-Principles Study on the Stability of Weberite-type, Pyrochlore, and Defect-Fluorite Structures of $A_2^{3+}B_2^{4+}O_7$ (A = Lu^{3+}–La^{3+}, B = Zr^{4+}, Hf^{4+}, Sn^{4+}, and Ti^{4+}). *J. Phys. Chem. C* 124 (37), 20555–20562. doi:10.1021/acs.jpcc.0c05443

Minervini, L, Grimes, R. W., and Sickafus, K. E. (2004). Disorder in Pyrochlore Oxides. *J. Am. Ceram. Soc.* 83 (8), 1873–1878. doi:10.1111/j.1151-2916.2000.tb01484.x

Minervini, L., RobinGrimes, W., Yasunori, T., Withers, R. L., and Sickafus, K. E. (2002). The Oxygen Positional Parameter in Pyrochlores and its Dependence on Disorder. *Philosophical Mag. A* 82 (1), 123–135. doi:10.1080/01418610208240001

Norberg, S. T., Hull, S., Eriksson, S. G., Ahmed, I., Kinyanjui, F., and Biendicho, J. J.. (2012). Pyrochlore to Fluorite Transition: The $Y_2(Ti_{1-x}Zr_x)_2O_7$ ($0.0 \le X \le 1.0$) System. *Chem. Mater.* 24 (22), 4294–4300. doi:10.1021/cm301649d

Pan, W., Phillpot, S. R., Wan, C., Chernatynskiy, A., and Qu, Z. (2012). Low thermal Conductivity Oxides. *MRS Bull.* 37 (10), 917–922. doi:10.1557/mrs.2012.234

Panero, W. R., Stixrude, L., and Ewing, R. C. (2004). First-Principles Calculation of Defect-Formation Energies in the $Y_2(Ti, Sn, Zr)_2O_7$ pyrochlore. *Physical Review B* 70(5): 054110. doi:10.1103/physrevb.70.054110

Pilania, G., Kocevski, V., Valdez, J. A., Kreller, C. R., and Uberuaga, B. P. (2020). "Prediction of Structure and Cation Ordering in an Ordered Normal-Inverse Double Spinel." *Commun. Mater.* 1 (1), 84. doi:10.1038/s43246-020-00082-2

Pilania, G., Puchala, B., and Uberuaga, B. P. (2019). Distortion-Stabilized Ordered Structures in A2BB'O7 Mixed Pyrochlores. *Npj Comput. Mater.* 5 (1), 7. doi:10.1038/s41524-018-0144-1

Pirzada, M. (2001). Oxygen Migration in $A_2B_2O_7$ Pyrochlores. *Solid State Ionics* 140 (3–4), 201–208. doi:10.1016/s0167-2738(00)00836-5

Popov, V. V., Menushenkov, A. P., Gaynanov, B. R., Ivanov, A. A., dAcapito, F., Puri, A., et al. (2018). Formation and Evolution of Crystal and Local Structures in Nanostructured $Ln_2Ti_2O_7$ (Ln = Gd–Dy). *J. Alloys Compounds* 746 (May), 377–390. doi:10.1016/j.jallcom.2018.02.263

Popov, V. V., Menushenkov, A. P., Yaroslavtsev, A. A., Zubavichus, Y. V., Gaynanov, B. R., Yastrebtsev, A. A., et al. (2016). Fluorite-Pyrochlore Phase Transition in Nanostructured $Ln_2Hf_2O_7$ (Ln = La–Lu). *J. Alloys Compounds* 689 (December), 669–679. doi:10.1016/j.jallcom.2016.08.019

Predith, A., Ceder, G., Wolverton, C., Persson, K., and Mueller, T. (2008). Ab Initioprediction of Ordered Ground-State Structures in ZrO_2–Y_2O_3. *Phys. Rev. B* 77 (14), 144104. doi:10.1103/physrevb.77.144104

Raison, P. E., and Haire, R. G. (2001). Zirconia-Based Materials for Transmutation of Americium and Curium: Cubic Stabilized Zirconia and Zirconium Oxide Pyrochlores. *Prog. Nucl. Energ.* 38 (3–4), 251–254. doi:10.1016/s0149-1970(00)00110-4

Rushton, M. J. D., Grimes, R. W., Stanek, C. R., and Owens, S. (2004). Predicted Pyrochlore to Fluorite Disorder Temperature for A2Zr2O7 Compositions. *J. Mater. Res.* 19 (6), 1603–1604. doi:10.1557/jmr.2004.0231

Rushton, M. J. D., Stanek, C. R., Cleave, A. R., Uberuaga, B. P., Sickafus, K. E., and Grimes, R. W. (2007). Simulation of Defects and Defect Processes in Fluorite and Fluorite Related Oxides: Implications for Radiation Tolerance. *Nucl. Instr. Methods Phys. Res. Section B: Beam Interactions Mater. Atoms* 255 (1), 151–157. doi:10.1016/j.nimb.2006.11.018

Saradhi, M. P., Ushakov, S. V., and Navrotsky, A. (2012). Fluorite-Pyrochlore Transformation in $Eu_2Zr_2O_7$ Direct Calorimetric Measurement of Phase Transition, Formation and Surface Enthalpies. *RSC Adv.* 2 (8), 3328. doi:10.1039/c2ra00727d

Sattonnay, G., Sellami, N., Thomé, L., Legros, C., Grygiel, C., Monnet, I., et al. (2013). Structural Stability of $Nd_2Zr_2O_7$ Pyrochlore Ion-Irradiated in a Broad Energy Range. *Acta Materialia* 61 (17), 6492–6505. doi:10.1016/j.actamat.2013.07.027

Schelling, P. K., Phillpot, S. R., and Grimes, R. W. (2004). Optimum Pyrochlore Compositions for Low thermal Conductivity. *Philosophical Mag. Lett.* 84 (2), 127–137. doi:10.1080/09500830310001646699

Shamblin, J., Mikhail, F., Joerg, N., CameronTracy, L., Fuxiang, Z., Sarah, F., et al. (2016). Probing Disorder in Isometric Pyrochlore and Related Complex Oxides. *Nat. Mater.* 15 (5), 507–511. doi:10.1038/nmat4581

Shlyakhtina, A. V., and Shcherbakova, L. G. (2012). New Solid Electrolytes of the Pyrochlore Family. *Russ. J. Electrochem.* 48 (1), 1–25. doi:10.1134/s1023193512010144

Sickafus, K. E., Grimes, R. W., Valdez, J. A., Cleave, A., Tang, M., Ishimaru, M., et al. (2007). Radiation-induced Amorphization Resistance and Radiation Tolerance in Structurally Related Oxides. *Nat. Mater* 6(3): 217–223. doi:10.1038/nmat1842

Sickafus, K. E. (2000). Radiation Tolerance of Complex Oxides. *Science* 289 (5480), 748–751. doi:10.1126/science.289.5480.748

Solomon, J. M., Shamblin, J., Lang, M., Navrotsky, A., and Asta, M. (2016). Chemical Ordering in Substituted Fluorite Oxides: A Computational Investigation of $Ho_2Zr_2O_7$ and $RE_2Th_2O_7$ (RE=Ho, Y, Gd, Nd, La). *Scientific Rep.* 6 (1), 38772. doi:10.1038/srep38772

Stanek, C. R., and Grimes, R. W. (2002). Prediction of Rare-Earth A2Hf2O7 Pyrochlore Phases. *J. Am. Ceram. Soc.* 85 (8), 2139–2141. doi:10.1111/j.1151-2916.2002.tb00423.x

Stanek, C. R., Jiang, C., Uberuaga, B. P., Sickafus, K. E., Cleave, A. R., and Grimes, R. W. (2009). Predicted Structure and Stability of $A_4B_3O_{12}$ δ-Phase Compositions. *Phys. Rev. B* 80 (17), 174101. doi:10.1103/physrevb.80.174101

Subramanian, M. A., Aravamudan, G., and Subba Rao, G. V. (1983). Oxide Pyrochlores a Review. *Prog. Solid State. Chem.* 15 (2), 55–143. doi:10.1016/0079-6786(83)90001-8

Tanaka, M., Kitaoka, S., Yoshida, M., Sakurada, O., Hasegawa, M., Nishioka, K., et al. (2017). Structural Stabilization of EBC with thermal Energy Reflection at High Temperatures. *J. Eur. Ceram. Soc.* 37 (13), 4155–4161. doi:10.1016/j.jeurceramsoc.2017.04.055

Todorov, I. T., Purton, J. A., Allan, N. L., and Dove, M. T. (2006). Simulation of Radiation Damage in Gadolinium Pyrochlores. *J. Phys. Condensed Matter* 18 (7), 2217–2234. doi:10.1088/0953-8984/18/7/010

Tryon, B., Feng, Q., Pollock, T. M., Wellman, R. G., Nicholls, J. R., Murphy, K. S., et al. (2006). Multilayered Ruthenium-Modified Bond coats for thermal Barrier Coatings. *Metall. Mat. Trans. A.* 37 (11), 3347–3358. doi:10.1007/bf02586169

Uberuaga, B. P., Ming, T., Chao, J., Valdez, J. A., Smith, R., et al. (2015). Opposite Correlations between Cation Disordering and Amorphization Resistance in Spinels versus Pyrochlores. *Nature Communications* 6 (1). doi:10.1038/ncomms9750

Uberuaga, B. P., Jiang, C., Stanek, C. R., Sickafus, K. E., Scott, C., and Smith, R. (2014). Prediction of Irradiation Spectrum Effects in Pyrochlores. *JOM* 66 (12), 2578–2582. doi:10.1007/s11837-014-1158-x

Ushakov, S. V., Navrotsky, A., Tangeman, J. A., and Helean, K. B. (2007). Energetics of Defect Fluorite and Pyrochlore Phases in Lanthanum and Gadolinium Hafnates. *J. Am. Ceram. Soc.* 90 (4), 1171–1176. doi:10.1111/j.1551-2916.2007.01592.x

Vaßen, R., Jarligo, M. O., Steinke, T., Mack, D. E., and Stöver, D. (2010). Overview on Advanced thermal Barrier Coatings. *Surf. Coat. Technology* 205 (4), 938–942. doi:10.1016/j.surfcoat.2010.08.151

Wang, S. X., Wang, L. M., Ewing, R. C., and Govindan Kutty, K. V. (2000). Ion Irradiation of Rare-Earth- and Yttrium-Titanate-Pyrochlores. *Nucl. Instr. Methods Phys. Res. Section B: Beam Interactions Mater. Atoms* 169 (1–4), 135–140. doi:10.1016/s0168-583x(00)00030-6

Wang, X. J., Xiao, H. Y., Zu, X. T., Zhang, Y., and Weber, W. J. (2013). Ab Initio Molecular Dynamics Simulations of Ionsolid Interactions in $Gd_2Zr_2O_7$ and $Gd_2Ti_2O_7$. *J. Mater. Chem. C* 1 (8), 1665. doi:10.1039/c2tc00192f

Wiebe, C. R., and Hallas, A. M. (2015). Frustration under Pressure: Exotic Magnetism in New Pyrochlore Oxides. *APL Mater.* 3 (4), 041519. doi:10.1063/1.4916020

Wilde, P. (1998). Defects and Diffusion in Pyrochlore Structured Oxides. *Solid State Ionics* 112 (3–4), 173–183. doi:10.1016/s0167-2738(98)00190-8

Winter, M. R., and Clarke, D. R. (2007). Oxide Materials with Low Thermal Conductivity. *J. Am. Ceram. Soc.* 90 (2), 533–540. doi:10.1111/j.1551-2916.2006.01410.x

Wright, A. J., Wang, Q., Hu, C., Yeh, Y.-T., Chen, R., and Luo, J. (2021). Single-phase Duodenary High-Entropy Fluorite/pyrochlore Oxides with an Order-Disorder Transition. *Acta Materialia* 211, 116858. doi:10.1016/j.actamat.2021.116858

Wu, J., Wei, X., Padture, N. P., Klemens, P. G., Gell, M., García, E., et al. (2004). Low-Thermal-Conductivity Rare-Earth Zirconates for Potential Thermal-Barrier-Coating Applications. *J. Am. Ceram. Soc.* 85 (12), 3031–3035. doi:10.1111/j.1151-2916.2002.tb00574.x

Wuensch, B. (2000). Connection between Oxygen-Ion Conductivity of Pyrochlore Fuel-Cell Materials and Structural Change with Composition and Temperature. *Solid State Ionics* 129 (1–4), 111–133. doi:10.1016/s0167-2738(99)00320-3

Wolff-Goodrich, S., Benjamin, E. H., Jonathan, M. S., and Asta, M.. (2015). Special Quasirandom Structure Modeling of Fluorite-Structured Oxide Solid Solutions with Aliovalent Cation Substitutions. *Modelling and Simulation in Materials Science and Engineering* 23(5): 055001. doi:10.1088/0965-0393/23/5/055001

Xiao, H. Y., Gao, F., and J Weber, W. (2010). Threshold Displacement Energies and Defect Formation Energies in $Y_2Ti_2O_7$. *J. Phys. Condensed Matter* 22 (41), 415801. doi:10.1088/0953-8984/22/41/415801

Xiao, H. Y., Weber, W. J., Zhang, Y., and Zu, X. T. (2015). Ab Initio Molecular Dynamics Simulations of Ionsolid Interactions in Zirconate Pyrochlores. *Acta Materialia* 87 (April), 273–282. doi:10.1016/j.actamat.2015.01.019

Yamamura, H. (2003). Electrical Conductivity Anomaly Around Fluoritepyrochlore Phase Boundary. *Solid State Ionics* 158 (3–4), 359–365. doi:10.1016/s0167-2738(02)00874-3

Yang, L., Wang, P., Zhang, C., Liu, Y., Cui, Y., Zhang, L., et al. (2019). Composition-Dependent Intrinsic Defect Structures in Pyroclore $RE_2B_2O_7$ (RE = La, Nd, Gd; B = Sn, Hf, Zr). *J. Am. Ceram. Soc.* 103 (1), 645–655. doi:10.1111/jace.16705

Wolff-Goodrich, S., Hanken, B. E., Solomon, J. M., and Asta, M. (2015). Special Quasirandom Structure Modeling of Fluorite-Structured Oxide Solid Solutions With Aliovalent Cation Substitution *Model. Simulat. Mater. Sci. Engin.* 23 (5), 055001. doi:10.1088/0965-0393/23/5/055001

Zhang, Z., Simon, C. M., Massey de los, R., Gregory, R. L., Brendan, J. K., Peter, E. R. B., et al. (2013). Gradual Structural Evolution from Pyrochlore to Defect-Fluorite in $Y_2Sn_{2x}Zr_xO_7$: Average vs Local Structure. *J. Phys. Chem. C* 117 (50), 26740–26749. doi:10.1021/jp408682r

Zhang, Z. L., Xiao, H. Y., Zu, X. T., Gao, F., and Weber, W. J. (2009). "First-Principles Calculation of Structural and Energetic Properties for $A_2Ti_2O_7$ (A = Lu, Er, Y, Gd, Sm, Nd, La). *J. Mater. Res.* 24 (4), 1335–1341. doi:10.1557/jmr.2009.0152

Zhao, Z., Xiang, H., Dai, F.-Z., Peng, Z., and Zhou, Y. (2019). $(La_{0.2}Ce_{0.2}Nd_{0.2}Sm_{0.2}Eu_{0.2})_2Zr_2O_7$: A Novel High-Entropy Ceramic with Low thermal Conductivity and Sluggish Grain Growth Rate. *J. Mater. Sci. Technology* 35 (11), 2647–2651. doi:10.1016/j.jmst.2019.05.054

Zunger, A., Wei, S.-H., Ferreira, L. G., and Bernard, J. E. (1990). Special Quasirandom Structures. *Phys. Rev. Lett.* 65 (3), 353–356. doi:10.1103/physrevlett.65.353

Conflict of Interest: The authors declare that the research was conducted in the absence of any commercial or financial relationships that could be construed as a potential conflict of interest.

Publisher's Note: All claims expressed in this article are solely those of the authors and do not necessarily represent those of their affiliated organizations, or those of the publisher, the editors and the reviewers. Any product that may be evaluated in this article, or claim that may be made by its manufacturer, is not guaranteed or endorsed by the publisher.

frontiers in Chemistry

ORIGINAL RESEARCH
published: 01 September 2021
doi: 10.3389/fchem.2021.719169

A Comparison of Order-Disorder in Several Families of Cubic Oxides

*T. Subramani, A. Voskanyan, K. Jayanthi, M. Abramchuk and A. Navrotsky**

School of Molecular Sciences and Navrotsky Eyring Center for Materials of the Universe, Arizona State University, Tempe, AZ, United States

Order-disorder on both cation and oxygen sites is a hallmark of fluorite-derived structures, including pyrochlores. Ordering can occur on long- and short-range scales and can result in persistent metastable states. In various cubic oxide systems, different types of disorder are seen. The purpose of this paper is to review and compare the types and energetics of order-disorder phenomena in several families of cubic oxides having pyrochlore, weberite, defect fluorite, perovskite, rocksalt, and spinel structures. The goal is to better understand how structure, composition, and thermodynamic parameters (enthalpy and entropy) determine the feasibility of different competing ordering processes and structures in these diverse systems.

Keywords: oxides, pyrochlores, fluorite, disorder, energetics

OPEN ACCESS

Edited by:
Gordon James Thorogood, Australian Nuclear Science and Technology Organisation, Australia

Reviewed by:
Andrzej Grzechnik, RWTH Aachen University, Germany
Chris Ling, The University of Sydney, Australia

****Correspondence:***
A. Navrotsky
alexnav@asu.edu

Specialty section:
This article was submitted to Solid State Chemistry, a section of the journal Frontiers in Chemistry

Received: *02 June 2021*
Accepted: *02 August 2021*
Published: *01 September 2021*

Citation:
Subramani T, Voskanyan A, Jayanthi K, Abramchuk M and Navrotsky A (2021) A Comparison of Order-Disorder in Several Families of Cubic Oxides. Front. Chem. 9:719169. doi: 10.3389/fchem.2021.719169

INTRODUCTION

Over the past two decades, there has been intense interest in defect chemistry, disorder, solid solution formation, and phase transitions in oxide pyrochlores (Glerup et al., 2001; Shlyakhtina et al., 2004; Liu et al., 2004; Knee et al., 2005; Mandal et al., 2006; Matsuhira et al., 2007; Zhang et al., 2008; Clements et al., 2011; Wang et al., 2011; de los Reyes et al., 2013; Zhang et al., 2013; Zhang et al., 2014; Popov et al., 2016; Paul et al., 2016; Rittman et al., 2017a; Rittman et al., 2017b; Simeone et al., 2017; Ponnilavan et al., 2019; Popov et al., 2020; Marlton et al., 2021; Panghal et al., 2021). Because the pyrochlore structure is a derivative of fluorite, it belongs to a large family of related structures. The interplay of short- and long-range order, especially in radiation-damaged pyrochlores, has drawn extensive attention as has amorphization and its recovery on annealing (Wang et al., 1998; Wang et al., 1999; Meldrum et al., 2001; Lian et al., 2002; Ewing et al., 2003; Lian et al., 2003a; Lian et al., 2004; Patel et al., 2008a; Patel et al., 2008b; Lang et al., 2009; Yudinsev et al., 2009; Lang et al., 2010; Xie et al., 2015; Shamblin et al., 2016a; Shamblin et al., 2016b; Kumari et al., 2016; Yang et al., 2017; Chung et al., 2018a; Chung et al., 2018b; Shamblin et al., 2018; Chung et al., 2019; Sherrod et al., 2021). Yet in a broader sense, pyrochlores are but one family of oxide materials.

Focusing on cubic structures, other families include defect fluorite ionic conductors such as yttria-stabilized zirconia (YSZ), weberites (both oxides and fluorides), rocksalt-based cation conducting oxides, perovskites, and spinels, all of which form the basis of numerous functional materials. Each of these families shows distinct and characteristic defect chemistry and order-disorder behavior.

Each simple structure (aristotype) is the parent of more complex structures showing ordering on anion and/or cation sublattices and the formation of layered structures. Modern diffraction and spectroscopy enable characterization of order on different length scales, with short-range order producing lower symmetry locally being detected increasingly often in nominally cubic structures (Radhakrishnan et al., 2011; Shamblin et al., 2016a; Shamblin et al., 2016b; Martel et al., 2017; Shamblin et al., 2018; Moran et al., 2019; Drey et al., 2020). The details of ordering are different in each structural family. Though at equilibrium at a given pressure, temperature, and composition,

defect formation and order-disorder produce, by definition, the state of lowest Gibbs free energy, this macroscopic truism begs the question of why: why, in a structural sense, is one set of defects predominant while others are not, and why, in different structure types, does one get characteristic and distinct sets of defects. Such questions can be addressed by first-principles calculations (e.g., density functional theory and molecular dynamics) or by calculations using semiempirical interatomic potential. The results, though identifying the lowest energy configurations, are hard to compare for different structures and do not immediately give physical insight, in terms of identifiable structural parameters, to the question of why (Gunn et al., 2012; Xiao et al., 2015; Perriot et al., 2016; Solomon et al., 2016; Pilania et al., 2019; O'Quinn et al., 2020). Furthermore, many of the complex structures have too many elements and too large unit cells for meaningful computations. Computational approaches to different structures (possible or nonexistent) polymorphs for a given composition have also been very limited.

For more qualitative, but also more easily transferable, insight, solid-state chemists turn to concepts like ionic radius and tolerance factor, which fundamentally derive from optimizing local cation-anion coordination in terms of geometry and bond lengths (Goldschmidt, 1926; Cai et al., 2011; Mouta et al., 2013; Song and Liu, 2020). These concepts do not easily translate into describing order on the midrange scale, other than to say that it occurs to relieve "strain" in the lattice. At the same time, midrange order is challenging to attack by *ab initio* methods because of the large number of different atoms and large unit cells needed for realistic description.

A potentially useful step in understanding the "why" is understanding the "what" across different structure types and length scales. Thus, the goal of this paper is to describe the structures, defects, and order-disorder phenomena in the several classes of oxides mentioned above, linking, whenever possible, structural and thermodynamic behavior. By comparing these groups of materials, we propose some reasons why different types of defects and ordering schemes dominate in each group and suggest some areas for future research.

Specifically, we compare the occurrence and energetics of various types of defects and disorders in two groups of cubic oxides. The first group, as well as the one we spend most time on, consists of fluorite-related structures (pyrochlore, weberite, defect fluorite, and zirconolite) and perovskite and its derivatives. Both accommodate oxygen vacancies as well as cation disorder and cation vacancies. Their structures are not close-packed and relatively flexible, accommodating large cations with high coordination numbers (7–12), and some variability in oxidation state. The second group of cubic oxides consists of rocksalt-derived phases and spinels. Both are relatively dense structures based on cubic close packing of anions and they do not easily accommodate oxygen vacancies. They maintain charge balance by cation vacancies (and occasional cation interstitials) and variation in oxidation state of transition metal (TM) ions. They typically contain smaller ions with lower cation coordination numbers (4, 5, and 6) than the first group. We describe the various structures, compositions, and types of defects and disorder and their associated energetics for both groups of materials. In comparing these structures, disorder, and thermodynamics, we then turn to the why question, why does each structure type favor certain defects and not others.

FLUORITE-DERIVED STRUCTURES

Pyrochlore

Pyrochlore oxides with idealized formula, $A_2B_2O_7$, are derivatives of the fluorite structure with ordered cations and vacancies (Subramanian et al., 1983; Chakoumakos, 1984; Ewing et al., 2004; Gardner et al., 2010). While cations with diverse valences can occupy A- and B-sites, the most common composition which has been widely studied with a focus on order-disorder phenomena is $A_2B_2O_7$ where A is a trivalent cation often rare earth and B is a tetravalent cation. The structure forms in cubic *Fd-3m* (no. 227) space group (Vanderah et al., 2005). It has five distinct Wycoff positions which are occupied by cations, anions, and vacancies. Bigger "A" cations occupy the *16d* position with eight coordinated cation coordination with oxide anions, while smaller "B" cations occupy *16c* position with six-coordinated geometry. Oxide anions go into *48f* and *8b* positions. Vacancies order in *8a* positions. Structures of defect fluorite, pyrochlore, and weberite are shown schematically in **Figure 1**.

The ordered pyrochlore structure disorders the defect fluorite structure under various conditions. The disordered defect fluorite structure of $A_2B_2O_7$ is basically the fluorite structure with cubic *Fm-3m* space group but with vacancies in O sites (Minervini et al., 2000; Wuensch and Eberman, 2000). Both A and B cations are distributed in *4a* positions and both oxygen and vacancies occupy *8c* positions, giving, as a limiting ideal case, complete disorder. All A and B cations are surrounded by seven oxide ions and a vacancy (7 + 1 coordination).

The process of disordering evolves through the formation of cation antisite pairs and Frenkel defects as discussed previously (Maram et al., 2015). The various conditions that induce disorder in pyrochlore are ionic radii of A and B cations, ball milling, temperature, pressure, and radiation damage (Subramanian et al., 1983; Heremans et al., 1995; Wuensch et al., 2000; Eberman et al., 2002; Lian et al., 2003b; Liu et al., 2004; Rushton et al., 2004; Fuentes et al., 2005; Zhang et al., 2005; Zhang and Saxena, 2005; Moreno et al., 2006a; Moreno et al., 2006b; Zhang et al., 2006; Mandal et al., 2007; Mandal and Tyagi, 2007; Zhang et al., 2007; Zhang et al., 2009; Zhang F. X. et al., 2010, Zhang et al., 2010 J; Lang et al., 2010; Sanjuán et al., 2011; Sayed et al., 2011; Shlyakhtina and Shcherbakova, 2011; Zhang et al., 2015; Rittman et al., 2017b; Turner et al., 2017; Fuentes et al., 2018; Wright et al., 2021).

Helean et al. (2004) reported enthalpies of formation for $RE_2Ti_2O_7$ systems which formed in ordered pyrochlore structure with RE = Sm - Lu. They also made similar measurements on $GdTi_{2-x}Zr_xO_7$ solid solution (Helean et al., 2000). Lian et al. (2006) published enthalpies of formation for $RE_2Sn_2O_7$ systems (RE = La, Nd, Sm, Eu, Dy, and Yb). The enthalpies of formation of $RE_2Zr_2O_7$ (RE = La, Ce, Nd, Sm, and Gd) system were also reported (Navrotsky and Ushakov, 2005; Radha et al., 2009). The enthalpies of formation became less

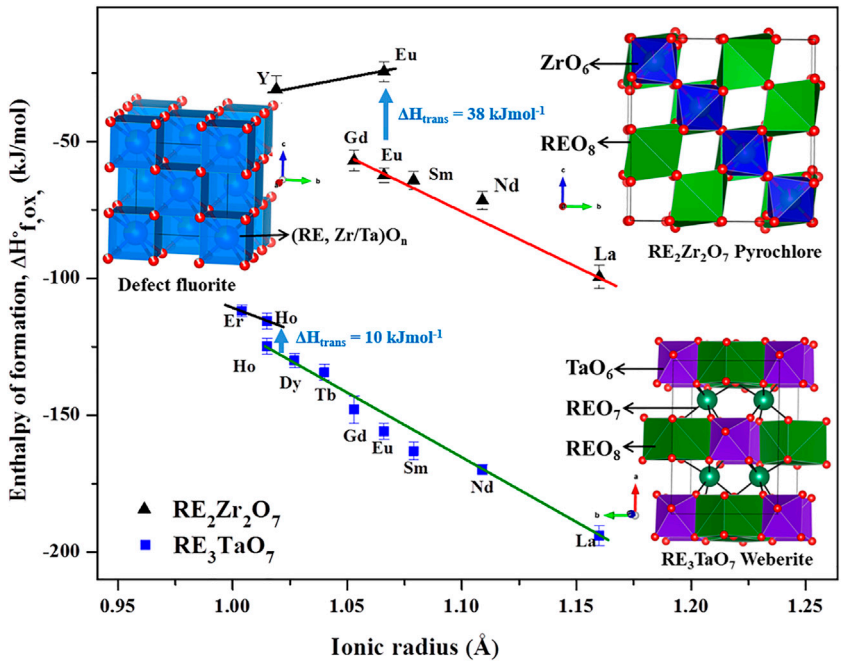

FIGURE 1 | Structure and energetics of order-disorder transitions between ordered pyrochlore, weberite, and disordered defect fluorite structures with $RE_2Zr_2O_7$ and RE_3TaO_7 systems as examples. The figure has been made based on data from the literature (Saradhi et al., 2012; Subramani and Navrotsky, 2019).

exothermic with a decrease in ionic radii from La to Lu as the structure is more prone to disorder when the tetravalent and trivalent ions are more similar in size. The measurements on the above systems were made with a focus on their behavior upon irradiation, which is important in considering them as nuclear waste forms. It was concluded that a composition more susceptible to disorder is less likely to be amorphized by radiation damage (Ewing et al., 2004).

Enthalpies of formation of hafnium pyrochlores, RE2Hf2O7 (RE = Y, La, and Gd), were reported (Lee and Navrotsky, 2004; Ushakov et al., 2007). The enthalpy of the order-disorder transition for $Hf_2Gd_2O_7$ was 23.6 ± 3.1 $kJmol^{-1}$ and entropy of transition was calculated as 12 J $K^{-1}mol^{-1}$, which was half of the maximum possible configurational entropy, indicating possible local ordering in the long-range disordered fluorite phase. Enthalpies of formation of $CaCeTi_2O_7$ and $Ca_{1.5}U_{0.65}Ti_{1.85}O_7$ were measured (Helean et al., 2002). Recently, calorimetric data were obtained for iridium-based pyrochlores, $RE_2Ir_2O_7$ (RE = La, Gd, and Y) (Nenoff et al., 2021). In most of these systems, ionic radii of A or B cations play a dominant role in inducing disorder. **Figure 1** shows formation enthalpies *vs.* ionic radii of different fluorite-related systems and enthalpy of an order-disorder transformation.

To understand the energetics of disordering, materials that disorder under different conditions must be studied. A disordered variant of $Eu_2Zr_2O_7$, which usually forms in ordered pyrochlore structure, was synthesized by soft chemical and laser melt quench methods, and the thermodynamics of the order-disorder transformation were determined (Saradhi et al., 2012). The transition enthalpy from ordered to disordered phase was 37.8 ± 3.1 $kJmol^{-1}$. *In situ* synchrotron diffraction coupled with aerodynamic levitation was performed on $Eu_2Zr_2O_7$ to study the structural progression of disorder upon increasing temperature (Maram et al., 2015). This was followed by *in situ* synchrotron diffraction on various zirconium and hafnium-based pyrochlores, $RE_2Zr_2O_7$ (RE = Sm, Eu, and Gd) and $RE_2Hf_2O_7$ (RE = La, Nd, and Sm), and modeling of the thermodynamics of disordering using configurational entropy calculations based on cation and anion site occupancies obtained from Rietveld refinement (Maram et al., 2018). This study extended early work on spinel disordering to fluorite-related systems (Navrotsky and Kleppa, 1967). The enthalpies of anion Frenkel disorder were found to be smaller than those of cation antisite disorder.

Hayun et al. (2012) investigated the energetics of highly disordered $RE_2Ti_2O_7$ (RE = Y, Gd, and Dy) formed by ball milling of their constituent binary oxides and of ordered variants formed by annealing the disordered materials at different temperatures. They found that the order-disorder transition upon annealing occurs through a two-step process.

With ionic radius, temperature, and ball milling already known to be important to induce disorder, radiation damage was then used as another "knob" to study the disorder energetics. Three different compositions in RE titanate and stannate pyrochlore systems were studied to understand the energetics of disordering induced by radiation damage (Chung et al., 2018b). Study of radiation damage, structural evolution upon annealing, and energetics of $Dy_2Ti_2O_7$ pyrochlore used a combination of nondestructive methods [pair distribution function (PDF) analysis of neutron total scattering] followed by destructive

methods (high-temperature solution calorimetry and differential scanning calorimetry). The results showed that the radiation amorphized sample had been destabilized by 243 $kJmol^{-1}$. An important observation was that, upon annealing to 1,200°C, the amorphized sample never recovered completely structurally or energetically, with enthalpy of formation closer to that of disordered $Dy_2Ti_2O_7$ produced by ball milling (Hayun et al., 2012) than to that of pristine undamaged $Dy_2Ti_2O_7$, indicating a residual destabilization in the recrystallized pyrochlore. The neutron results showed that local disordered short-range domains containing a weberite-like structure (see below for discussion of weberites), present in the amorphized sample, persisted in the annealed material. The results were consistent with weberite-type short-range ordered domains observed in disordered pyrochlores (Shamblin et al., 2016a). Chung et al. (2018a) also studied the structural evolution and energetics in another pyrochlore $Dy_2Sn_2O_7$ and found residual destabilization similar to that in $Dy_2Ti_2O_7$. They then chose $Er_2Ti_2O_7$ and induced disorder by ball milling and radiation damage to study the energetics (Chung et al., 2019). They again found similar retention of local short-range weberite structure and concluded that the residual destabilization was a general phenomenon in radiation-damaged pyrochlores.

Thermodynamics of the composition dependence of order-disorder in pyrochlore solid solutions has been studied in $Nd_xZr_{1-x}O_{2-0.5x}$ system (Finkeldei et al., 2017). They found that an order-disorder transition occurred at $0.30 < x < 0.33$. Based on calorimetric data, they showed a disordering transition enthalpy of 30 $kJmol^{-1}$and transition entropy of 16 $J\ K^{-1}mol^{-1}$, yet again far less than the configurational entropy, showing evidence for local ordering.

Though order-disorder transitions have been induced by pressure in pyrochlores, not much thermodynamic work has been carried out on them. New pyrochlores with $A_2B_2O_7$ stoichiometry have been suggested to form under high pressure (Zhou and Wiebe, 2019). It will be interesting to study the energetics of pressure-induced order-disorder transformations to explore behavior under extreme conditions.

Weberite

The weberite structure with $A_2B_2X_7$ stoichiometry is also derived from the aristotype fluorite structure, with ordering in cation and anion sublattices. The weberite structure can include different cations with different charges in A- and B-sites and fluoride or oxide ions in the anion X sites. The structural and compositional diversity has been clearly described elsewhere (Cai and Nino, 2009; Cai and Nino, 2011). The discussion in this review will be limited to weberite oxides $A_2^{3+}B_2^{4+}O_7$ and $A_3^{3+}B^{5+}O_7$, which are currently the only systems studied for the structural and energetic evolution of order-disorder.

Fluorite-derived oxides with cation ratio 1:1 and molecular formula, $A_2^{3+}B_2^{4+}O_7$, usually form in the pyrochlore rather than the weberite structure (Subramanian et al., 1983). However, $A_2^{3+}B_2^{4+}O_7$ with weberite structure was discovered by Shamblin et al. (2016a), while analyzing the local structure of $A_2B_2O_7$ pyrochlores with disorder induced by various conditions, thus realizing that the weberite structure is a metastable form for this stoichiometry. $A_3^{3+}B^{5+}O_7$ phases form in the same orthorhombic space group as weberite $A_2^{3+}B_2^{4+}O_7$ (Allpress and Rossell, 1979; Wakeshima et al., 2004; Cai and Nino, 2007; Cai and Nino, 2009; Fu and IJdo, 2009; Cai et al., 2010; Cai and Nino, 2011; Nakamura et al., 2011; King et al., 2013). There has been some confusion on which space group (*C2221* or *Ccmm*) best describes the structure. Gussev et al. (2020) recently showed that the space group *C2221* describes the weberite structure based on the short-range and long-range structure using neutron total scattering data and DFT calculations.

The weberite structure (**Figure 2**) has three distinct sites for cations, namely, *4b*, *4b*, and *8c*, and five different sites for oxide ions, *8c*, *8c*, *4a*, *4a*, and *4a*. A^{3+} cations occupy one *4b* and *8c* sites and B^{5+} cations occupy other *4b* sites in weberite-type $A_3^{3+}B^{5+}O_7$ oxides.

In $A_2^{3+}B_2^{4+}O_7$, A^{3+} and B^{4+} go into 4b sites, and 8c sites are occupied equally by both A^{3+} and B^{4+}. 4b sites form a layer of the weberite-type structure in which the A cation takes eightfold coordination forming chains of edge-shared AO_8 cuboctahedra and B cations go into sixfold coordination forming chains of edge-shared BO_6 octahedra along the c axis. Then, both AO_8 and BO_6 chains share edges in an alternating arrangement along the b axis to form AO_8-BO_6 layers. The difference between $A_3^{3+}B^{5+}O_7$ and $A_2^{3+}B_2^{4+}O_7$ comes in the other layer having 8c sites which lead to sevenfold coordination with a distorted pentagonal bipyramidal geometry. The 8c sites are occupied completely by A^{3+} cations forming edge-shared AO_7 polyhedral chains along the c axis and the chains in turn share edges along the b axis to form the AO_7 layer. AO_8-BO_6 and AO_7 layers arrange alternately to form the overall structure (Gussev et al., 2020). However, in $A_2^{3+}M_2^{4+}O_7$, 8c sites are occupied equally by both A^{3+} and B^{4+} forming $(A/B)O_7$ polyhedral layer leading to disorder (Shamblin et al., 2016a; Drey et al., 2020). So, the structure can be seen as an alternating arrangement of ordered and disordered layers in weberite-type, $A_2M_2O_7$. In other words, the structure is intermediate between ideal pyrochlore (fully ordered) and defect fluorite (fully disordered), with, presumably, intermediate configurational entropy. This partially disordered weberite structure is found in the short-range ordered domains of disordered defect fluorite materials and annealed radiation-damaged materials, suggesting that a completely ordered state is difficult to achieve in these materials and may require annealing at higher temperatures for a longer time.

The thermochemistry of two systems with A_3BO_7 (A = RE; B = Nb, and Ta) composition has been studied. Mielewczyk-Gryn and Navrotsky (2015) reported enthalpies of formation of RE_3NbO_7 (RE = Y, La, Nd, Gd-Er, and Yb) with order-disorder occurring in compounds with RE ionic radii smaller than Tb. Energetics of another system, RE_3TaO_7 (La, Nd, Sm-Yb), was reported by Subramani and Navrotsky (2019). In both systems, enthalpies of formation became less exothermic as RE ionic radii decreased, showing a trend similar to $RE_2M_2O_7$ pyrochlores. The occurrence of ordered and disordered variants for a single composition, Ho_3TaO_7, enabled the study of the energetics of the order-disorder transition. It was found that the enthalpy of transition between ordered and disordered variants was near 10 $kJmol^{-1}$ (**Figure 1**). Based on configurational

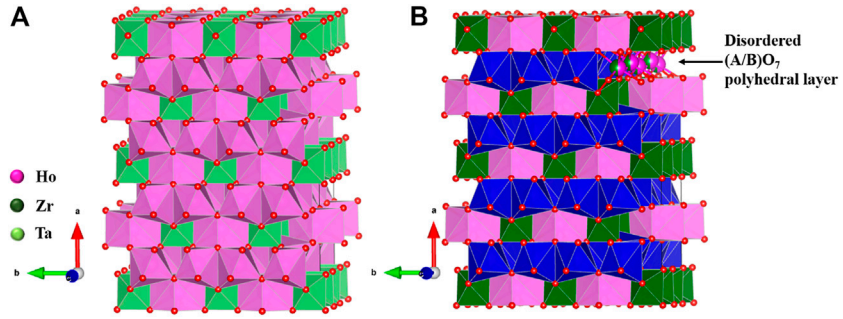

FIGURE 2 | Structure of weberite-type **(A)** Ho_3TaO_7 and **(B)** $Ho_2Zr_2O_7$, both forming in orthorhombic $C222_1$ space group. The $(A/B)O_7$ layer in which partial disorder between A and B cations is marked with blue polyhedra for clarity in **(B)**. Figure has been drawn based on the crystallographic data from the literature (Drey et al., 2020; Gussev et al., 2020). The crystal structures are drawn using the software VESTA (Momma and Izumi, 2008).

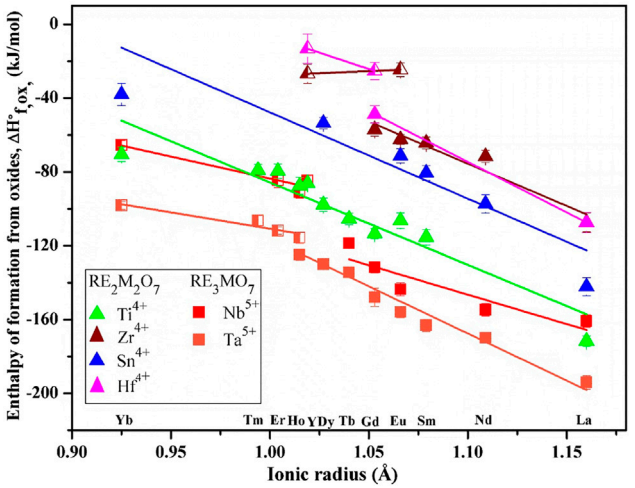

FIGURE 3 | Enthalpies of formation *vs.* ionic radius of rare earth ions. The filled squares show compounds with weberite structure. The filled triangles represent compounds with ordered pyrochlore structure. The half-filled squares and triangles indicate compounds with disordered defect fluorite structure. The data for $RE_2Ti_2O_7$ and $RE_2Sn_2O_7$ are from Helean et al. (2004) and Lian et al. (2006). The data for $RE_2Zr_2O_7$ are from Navrotsky and Ushakov (2005), Radha et al. (2009), and Saradhi et al. (2012). The data for $RE_2Hf_2O_7$ are from Navrotsky and Ushakov (2005) and Ushakov et al. (2007). The data for RE_3MO_7 (M = Nb and Ta) are from (Mielewczyk-Gryn and Navrotsky (2015) and (Subramani and Navrotsky (2019).

entropy calculations, substantial short-range ordering (SRO) in long-range disordered Ho_3TaO_7 was proposed.

Figure 3 shows enthalpies of formation *vs.* RE ionic radius. The data are based on high-temperature oxide melt solution calorimetry experiments performed by Navrotsky and coworkers over the past two decades. The plot clearly shows a trend of enthalpies of formation becoming less exothermic as RE ionic radii decrease for various fluorite-related systems. It is noteworthy that few systems have a single composition that exhibits both ordered and disordered polymorphs. A linear fit was used separately on enthalpies of formation of compositions with ordered and disordered structures in each system. The slopes show some scatter for ordered structures but are similar for ordered structures and are much less steep for disordered ones. In the future, one may be able to estimate enthalpies of formation for a whole series of rare earth by measuring the enthalpy of formation of a single composition in the system and applying the average slope.

Thermochemistry of pure weberite $A_2B_2O_7$ materials cannot be measured directly because such phases generally do not exist. The radiation-damaged and annealed samples that Chung et al. (2018a) measured contained weberite-like short-range ordered local domains, but the exact amount of such domains is hard to estimate. The thermochemical measurements made by Hayun et al. (2012) on disordered $A_2B_2O_7$ samples produced by ball milling might have had similar short-range ordered weberite domains, but there are no samples left for further studies. Drey et al. (2020a) described disordering in an unirradiated $Ho_2(Ti_{1-x}Zr_x)_2O_7$ solid solution in which one of the end members, $Ho_2Ti_2O_7$, had the ordered pyrochlore structure and other, $Ho_2Zr_2O_7$, formed in the disordered defect fluorite structure. They investigated the long-range and short-range ordering using Rietveld refinement and PDF analysis of neutron scattering data. They found that an order-disorder transition occurred abruptly at the long-range crystallographic scale around x = 0.6, while order-disorder occurred gradually with increasing x on the short-range (nano)scale. The measured heats of mixing suggested that the solid solution could be considered a mixture of two phases at the nanoscale, agreeing with local structure studies. The structure of $Ho_2Zr_2O_7$ was reported to be completely weberite *C2221* at the short-range scale by neutron PDF analysis. Thermochemical data for another related solid solution between pyrochlore $Y_2Ti_2O_7$ and defect fluorite Y_3NbO_7 were reported recently (Winiarz et al., 2020). Though niobium-rich members formed in a disordered structure based on XRD analysis, there were additional reflections indicating possible superstructure. More structural analysis is needed to delineate these order-disorder phenomena.

Understanding the energetics of order-disorder transitions induced by other parameters like temperature, radiation damage and pressure in weberite materials are open fields for future studies. Recently, a new oxide of composition $MgTiSi_2O_7$

with weberite structure in the MgO-SiO_2-TiO_2 system has been discovered under high pressure and high-temperature conditions similar to the ones found in the Earth's transition zone and lower mantle (Bindi et al., 2017; Matrosova et al., 2020). $MgTiSi_2O_7$ weberite has cation occupancy disordering with Mg and Ti ions sharing the A cation sites and Si and Ti occupying the B cation sites (Bindi et al., 2017). This may lead to some "entropy stabilization." The work suggests the possibility of finding various new compositions with fluorite-related structure in planetary interiors. Thus, thermochemistry of pressure-induced order-disorder transitions will be interesting for pyrochlores in view of understanding their formation, existence, and role in planetary interiors.

Other Fluorite-Related Structures

Y_2O_3 ($YO_{1.5}$) doping in zirconia (ZrO_2) introduces oxygen vacancies and leads to stabilization of zirconia in disordered cubic defect fluorite structure. These materials are called cubic yttria-stabilized zirconia (c-YSZ). The enthalpies of formation of disordered c-YSZ materials in the $YO_{1.5}$-ZrO_2 solid solution have been measured (Lee et al., 2003). They found that the enthalpy of mixing was negative with a very negative interaction parameter suggesting substantial SRO. Annealing produced an ordered δ-phase ($Y_4Zr_3O_{12}$) and enabled the study of the energetics of order-disorder. There is no difference in the enthalpy of solution of the δ-phase and the disordered c-YSZ solid solution. This suggests strong short-range order in the nominally disordered c-YSZ. The appearance of the δ-phase superstructure in XRD patterns may indicate growth of domain size in ordered regions rather than the onset of ordering. Lee and Navrotsky (2004) reported even more negative interaction parameters for $YO_{1.5}$-HfO_2 solid solution than for $YO_{1.5}$-ZrO_2 and suggested even stronger SRO. Simoncic and Navrotsky (2007a) studied different $REO_{1.5}$-HfO_2 solid solutions which formed in nominally disordered structure and again found strong negative interaction parameters indicating SRO (Simoncic and Navrotsky, 2007a). Simoncic and Navrotsky (2007b) found similar negative interaction parameter for other RE_2O_3($REO_{1.5}$)-ZrO_2 and RE_2O_3($REO_{1.5}$)-HfO_2 solid solutions, confirming and generalizing short-range order in these long-range disordered materials as well.

The enthalpies of formation of CeO_2 doped with La_2O_3, Gd_2O_3, and Y_2O_3, are positive (Chen and Navrotsky, 2006) in contrast to $YO_{1.5}$-ZrO_2 and $YO_{1.5}$-HfO_2 systems The reason for such behavior was attributed to the larger ionic radius of Ce^{4+} than that of Zr^{4+} and Hf^{4+} ions, making 7-fold coordination less favorable for the larger tetravalent ion and limiting the favorable energetics associated with oxide ion transfer (Chen et al., 2005). La_2O_3 and Y_2O_3-doped ThO_2 were studied by Aizenshtein et al. (2010). The energetics of these two systems were balanced by competition between a destabilizing factor due to cation size mismatch and a stabilizing factor due to defect clustering. The compositions with maximum endothermic enthalpies of formation in both La and Y doped ceria and thoria systems exhibited maximum ionic conductivity. As clustering became more pronounced at higher doping levels, ionic conductivity stayed constant or decreased while the mixing energetics became more favorable. Buyukkilic et al. (2012) and Buyukkilic et al. (2014) carried out a systematic study on the energetics of singly and doubly doped CeO_2 with Nd_2O_3 and Sm_2O_3. The doubly doped system had less average size mismatch, and the maxima in conductivity and heat of mixing were both shifted to higher doping levels, with heat of mixing smaller in magnitude. Enthalpies of defect association of the doubly doped (Nd.Sm) in a 1:1 ratio system were less exothermic than those of singly doped (Nd or Sm) systems. These studies show that ionic conductivity, defect association, and heats of mixing are closely related.

Zirconolites [$CaMTi_2O_7$ (M = Zr and Hf)] are another set of pyrochlore-related compounds derived from fluorite with defects but with lower symmetry and higher ordering for cations (Grey et al., 2003; Salamat et al., 2013; McCaugherty and Grosvenor, 2019). They are studied for the possible application as nuclear waste materials to host actinides in high-level waste (Vance et al., 1994; Ewing et al., 2004). Various types of disorder have been induced in the zirconolite structure using chemical substitution and high pressure (Whittle et al., 2012; Salamat et al., 2013). The enthalpies of formation of undoped $CaMTi_2O_7$ (M = Zr and Hf) and uranium doped $CaZrTi_2O_7$ have been reported (Putnam et al., 1999a; Putnam et al., 1999b; Subramani et al., 2020). However, energetics of disordering in zirconolites have not been explored in depth. Such studies would be very useful to understand the process of disordering in such highly ordered systems.

PEROVSKITE AND RELATED STRUCTURES

Structure and Occurrence

Perovskites derived from the ideal cubic aristotype structure are among the most, if not the most, rigorously investigated class of materials. Perovskite *sensu stricto* is a $CaTiO_3$ mineral and compounds with the isotypical crystal structures and ABX_3 (where A is an alkali, alkali earth, or lanthanide metal, B is a TM, and X is an oxygen or halogen atom) general formula are classified as inorganic perovskites. The perovskite structure is based on a corner-sharing array of octahedra which creates a large central site with room for a larger cation. This structure has flexibility in terms of rotation and distortion of the octahedra. The ideal cubic ABX_3 perovskite (space group *Pm3m*) has a large A cation at a twelve-coordinated site (A-site) by the X anions and a medium-size B cation at a six-coordinated site (B-site). The B-site cations are strongly bonded with the X anion, while A-site cations have weaker interactions. It forms a three-dimensional network of the corner-sharing BX_6 octahedra where A cations occupy empty cuboctahedral cavities (**Figure 4A**). If one removes all A cations from the twelve-coordinated sites, the simple ReO_3 structure is generated (**Figure 4B**).

In perovskite oxides, the A-site cation can have +1, +2, or +3 oxidation states, whereas the B-site cation can have a +3, +4, or +5 oxidation state to realize the charge neutrality of ionic structure. The presence of oxygen excess or deficiency in the lattice can cause the departure of stoichiometry from the ideal ABO_3. The

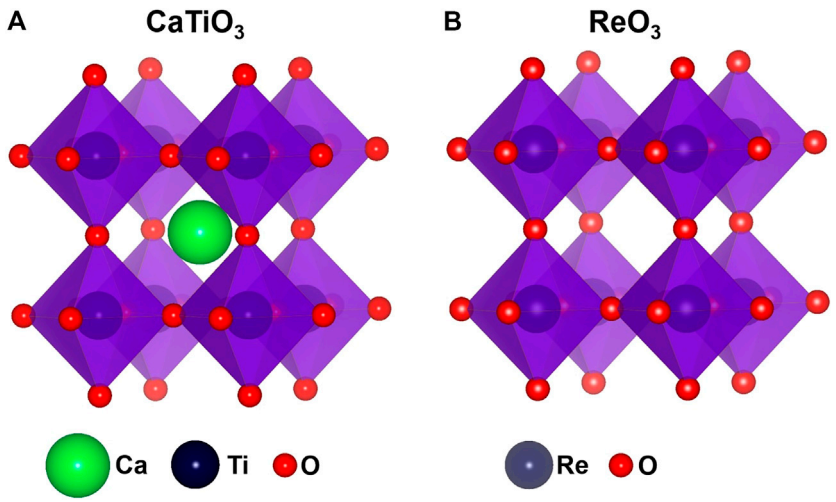

FIGURE 4 | (A) $CaTiO_3$ perovskite structure and **(B)** ReO_3 structure with empty cuboctahedral A-site.

strongly bonded framework of octahedra allows changing the elemental composition of A- and B-sites or partial substitution of cations without structural collapse. The presence of empty space in the perovskite structure can accommodate various octahedral tilts and distortions, reflecting the flexibility of the framework of octahedra. As a result, countless new perovskites with fascinating physical and chemical properties have been synthesized and have found applications in almost all areas of modern technology. Furthermore, the significance of perovskites extends to and beyond the Earth, since silicate perovskites based on $MgSiO_3$ are thermodynamically stable in the mantle of planets larger than Mars (Szuromi and Grocholski, 2017).

Reflecting the large flexibility of its crystal structure and its ability to show different properties depending upon the environment, perovskite can be well described as an "inorganic chameleon" (Stølen et al., 2006). The perovskite oxides commonly crystallize in a cubic structure, but, depending on the ionic radii and electronegativity of the corresponding cations, tilting or expansion/contraction of the octahedra occurs, leading to the formation of lower symmetry structures. The empirical prediction of whether the ABX_3 compound can form a stable cubic structure can be derived from a dimensionless number called the Goldschmidt tolerance factor *t*:

$$t = \frac{(r_a + r_b)}{\sqrt{2}(r_b + r_x)}$$

where r_a, r_b, and r_x are the ionic radii of A, B, and X ions, respectively (Goldschmidt, 1926). The closer this factor is to unity, the better the normal metal-oxygen bond lengths of both cations can be satisfied without distortions of the ideal structure. The tolerance factor possesses acceptable predictive power for oxide and fluoride structures. The ideal cubic perovskite $SrTiO_3$ has t = 1, and the closer the t value to unity, the greater the energetic stability of the structure (Navrotsky and Donald, 1989;

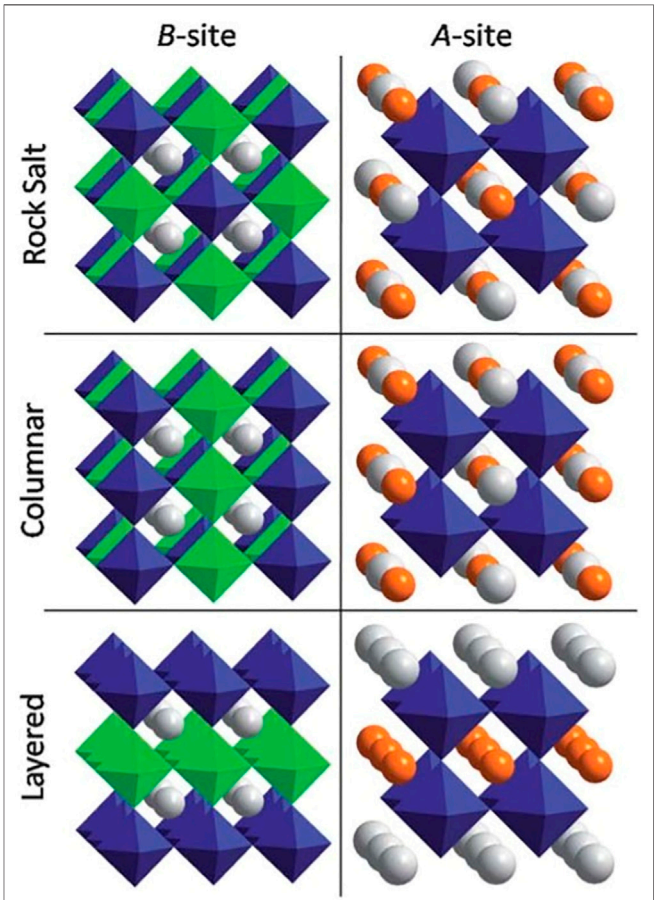

FIGURE 5 | Cation ordering possibilities in perovskites for B-site ordering in $A_2BB'X_6$ and for A-site ordering in $AA'B_2X_6$ perovskites. Reproduced with permission from King and Woodward (2010), Copyright Royal Society of Chemistry.

Navrotsky, 1994). If t is between 0.9 and 1.0, predominantly cubic structures form, while below and above that limit significant distortions of the structure take place. When B is large and A is small, t < 1, the structure lowers its symmetry to fill the space, whereas if t > 1, hexagonal perovskite forms with face-sharing octahedra. The thermodynamic stability of various perovskites within a large compositional range has been extensively studied by high-temperature melt solution calorimetry in Navrotsky's laboratory (Linton et al., 1998; Laberty et al., 1999; Xu et al., 2003; Cheng et al., 2005; Cheng and Navrotsky, 2005; Xu et al., 2005).

Perovskite properties can be tuned to a great degree by partial cation substitution. It can take place at either the A- or the B-site resulting in the double perovskites with $A_2BB'X_6$ or $AA'B_2X_6$ formula, respectively. The A/A' and B/B' cations may remain disordered at their corresponding sites, or they can order forming A-site or B-site ordered perovskites (Smyth, 1985; Anderson et al., 1993; Davies et al., 2008; King and Woodward, 2010; Vasala and Karppinen, 2015; Tilley, 2016). Three ordering patterns can be realized for either the A- or B-site cations. The most symmetric and most frequently encountered group is called rock salt or 1:1 ordering because the pattern of two different cations is equivalent to the anion and cation positions in the NaCl-type structure with Fm3m symmetry. This superstructure is also known as the elpasolite (K_2NaAlF_6) structure. Besides rocksalt ordering, cations can order into columns, or layers as shown in **Figure 5** (King and Woodward, 2010).

These types of ordering are less common than the rocksalt-type ordering. The NaCl-type arrangement is 0D since two compositionally similar octahedra are alternating and separated from each other. The 1D and 2D ordering patterns result from columnar or layered ordering since it allows connectivity of the $B'X_6$ octahedra in one or two dimensions, respectively. The energetic stability of cation order is mainly driven by the charge and size difference of B/B' or A/A' cations. Among all three ordering patterns, the rocksalt-type ordering is usually thermodynamically most favorable because it increases the separation between highly charged B' cations and hence decreases the Coulombic repulsive interactions. Then, it comes columnar configuration and 2D ordering is the least favorable due to the presence of four B' cations neighboring with another B' cation. Depending on the stoichiometric ratio of B:B', the 1:2 and 1:3-layer ordering of cations can take place, which is the closest analog to the NaCl-type ordering (Davies et al., 2008). A-site ordering in perovskites is much less common compared to the B-site ordering. One way of achieving A-site ordering is by octahedral tilting which creates different size voids within the interconnected BX_3 network. The $a^+a^+a^+$ tilting stabilization is the most commonly occurring type among the Glazer tilt systems (King and Woodward, 2010). The perovskites with this type of tilting usually contain larger cations such as an alkali, alkaline earth, or rare earth at the A-site, with much smaller cation at the A'-site. Cubic perovskites with $AA_3'B_4O_{12}$ general formula accommodate this type of cation ordering and compounds with this structure can form a metastable high pressure ζ-Mn_2O_3 phase (Ovsyannikov et al., 2013; Tilley, 2016). However, the number of reported A-site ordered perovskites is significantly smaller than the B-site ordered ones, and therefore the interesting question is why B-site ordering is more common than A-site ordering. This can be due to the small charge or size mismatch between A and A' cations, while the difference of cation sizes and charges between B and B' atoms can be larger. Generally, a large difference in valence, size, and coordination between two cations located at the same crystallographic site leads to the stabilization of a more ordered structure.

Oxygen Vacancy Formation

Another uniqueness of perovskite relative to many other crystal structures is its ability to accommodate a large concentration of oxygen vacancies ($ABO_{3-\delta}$) without structural decomposition. The most oxygen deficiency is achieved close to $\delta = 0.5$, although even nonstoichiometry higher than $\delta = 0.8$ has been reported for $Ba_{1-x}Sr_xCo_{1-y}Fe_yO_{3-\delta}$ composition (Kubicek et al., 2017).

The ordering of oxygen vacancies along the (110) direction relative to the perovskite structure at $\delta = 0.5$ often results in a new family of compounds known as brownmillerite (Ca_2AlFeO_5) with a layering of differently coordinated B and B' cations (Smyth, 1985; King and Woodward, 2010; Tilley, 2016). The oxygen-deficient octahedra then transform into tetrahedra forming alternate layers of BO_6 octahedra and BO_4 tetrahedra in the ... OTOT ... sequence. The room temperature stable ordered brownmillerite transforms into perovskite with disordered oxygen vacancies at elevated temperatures (>800°C) (Shin et al., 1978). The transformation is gradual involving the coexistence of intermediate ordered and disordered phases or it may appear first order (Prasanna and Navrotsky, 1994). Disordering occurs through the formation of defect clusters which are statistically distributed in the cubic perovskite framework. Like in perovskites, B-site ordering is quite common for B-site substituted brownmillerites (King and Woodward, 2010). Also, the concentration of defects can be significantly altered through doping with different cations, often resulting in disordered cubic phases (Patrakeev et al., 2006). Another important parameter that affects the composition and phase formation is the oxygen partial pressure during the synthesis. If variable valence cations such as iron are present, low oxygen partial pressures brownmillerite and disordered perovskite phases can coexist, while at elevated temperatures transformation into disordered or ordered cubic structure takes place (Prado et al., 2004). The addition of oxygen to a brownmillerite structure can convert some of the tetrahedral layers into octahedral on forming intermediate intergrowth phases ($A_nB_nO_{3n-1}$) between pure perovskite and brownmillerite. For example, at $n = 3$, Grenier compounds with ... OOTOOT ... stacking can be generated. The whole range of oxygen-deficient intermediate compounds $0 < \delta < 0.5$ may be thermodynamically metastable relative to the stable perovskite and brownmillerite end members. Indeed, it has been shown that $Ca_3Fe_2TiO_8$ and $Ca_4Fe_2Ti_2O_{11}$ intermediate phases are energetically metastable relative to their parent $CaTiO_3$ and $Ca_2Fe_2O_5$ (Prasanna and Navrotsky, 1994).

Square pyramidal BO_5 coordination polyhedra can form if the oxygen vacancies are ordered in single octahedral sites rather than in two sites as in brownmillerite. These types of compounds

include manganites (e.g., $Sr_2Mn_2O_5$), cobaltites (e.g., $LaBaCo_2O_{5.5}$), and ferrites (e.g., $SrFeO_{2.5+\delta}$) (Tofield et al., 1975; Caignaert et al., 1985; Rautama et al., 2009). Another interesting family of oxygen-deficient perovskite is cuprates $ACuO_{3-\delta}$ in which copper atoms have square pyramidal and square planar coordination (Murphy et al., 1987; Rao and Raveu, 1989). Due to such unique structural geometry, these materials (e.g., $YBa_2Cu_3O_x$) exhibit high-temperature superconducting properties (Murphy et al., 1987).

Creating A-site deficiency, while retaining the corner-shared octahedral framework, can be realized in the so-called perovskite tungsten bronzes A_xWO_3, which undergo multiple structural changes upon increasing the concentration of A cations. For example, orthorhombic $Ca_{0.01}WO_3$ transforms into tetragonal phase at $Ca_{0.03}WO_3$ and eventually into cubic at $Ca_{0.12}WO_3$ (Tilley, 2016). Titanates, tantalates, and niobates are also capable of withstanding partially occupied A-sites if the charge neutrality is preserved (e.g., $Ce_{0.33}NbO_3$).

If the A-sites are completely empty in the perovskite structure and B cation has +6 oxidation state, cubic ReO_3 structure forms (**Figure 4B**). The slight reduction of anion content in some oxides with ReO_3 structure generates randomly distributed point defects, which undergo ordering and subsequent annihilation at high concentration of anion vacancies forming planar 2D defects known as crystallographic shear (CS) planes (Magneli, 1956; Wadsley, 1958; Voskanyan and Navrotsky, 2021). This suggests that the ordering of defects is thermodynamically favorable. Recently, Voskanyan and Navrotsky showed that TiO_2-Nb_2O_5 Wadsley-Roth CS phases are energetically metastable and stabilized *via* configurational entropy arising from the cation disorder at elevated temperatures (Voskanyan et al., 2020). In many oxides, defect clustering at the short-range scale is energetically more favorable and long-range ordering of vacancies does not take place. The reason for this is still not well understood and needs further theoretical and experimental investigations. In particular, the distribution and optimization of cluster size need further study.

Although some of the ReO_3 based compounds form CS phases, perovskites with occupied A-sites generally do not. This clearly indicates that the presence of filled A-sites hinders the formation of shear planes and at oxygen-deficient conditions, generation of BO_4 or BO_5 coordination polyhedra is more favorable in stabilizing the structure. From a kinetic viewpoint, shear plane formation involves cooperative migration of defects, which may be hampered in the presence of A cations.

Besides their high tolerance to oxygen deficiency, perovskites can also accommodate extra oxygen in their structure resulting in homologous series with $A_nB_nO_{3n+2}$ general formula (Nanot et al., 1974; Smyth, 1985). For example, with the addition of extra oxygen, $SrTaO_3$ perovskite can be converted into $Sr_2Ta_2O_7$ (n = 4) compound which belongs to the orthorhombic crystal system with space group Cmcm (Fu and Skrabalak, 2017). It consists of perovskite-type slabs four TaO_6 octahedra thick and two Sr sites, one within the slabs and the other between the slabs. The excess oxygen terminates one of the separated corners of the octahedra. Compared with perovskites, these compounds are likely to be also energetically metastable, and it will be of great interest to calculate the energetic penalty to form these structures from perovskites and how their energetics is compared with those of perovskite to brownmillerite transition.

ROCKSALT STRUCTURES

Structures and Occurrence

Lithium TM oxides (LTMO) with rocksalt structure are formed when lithium and TM occupy the cation site and oxide ion occupy anion sites of structures derived from the simple rocksalt (NaCl) aristotype. The unique feature of this rocksalt structure is that both cation and anions occupy regular octahedral coordination. Close-packed oxygen atoms occupy sites of face-centered cubic (FCC) lattices; the lithium and TM occupy the FCC sublattice of octahedral interstices. The typical cation arrangement in LTMO structures was reviewed and later explained using atomistic modeling (Hewston and Chamberland, 1987; Wu et al., 1998). The arrangement of Li and TM in these LTMO structures may vary as shown in **Figure 6** (Urban et al., 2014). Disordered rocksalt oxides (DRO) exhibit a random arrangement of Li and TM (at least at the long-range scale), leading to the α-$LiFeO_2$ structure shown in **Figure 6A**, while layered compounds exhibit an ordered arrangement of Li and TM in alternating planes along the (*111*) direction, leading to the α-$NaFeO_2$ structure shown in **Figure 6B**. The spinel-like low-temperature structure of $LiCoO_2$ and the γ-$LiFeO_2$ structure are two other cation-ordered variants of the rocksalt structure shown in **Figures 6C,D** (Clément et al., 2020).

DRS compounds can be composed of a wide variety of TM species, Ti, Cr, Mn Fe, Nb, and Mo with a large range of compositions in this structure space, whereas the layered LTMO appear to be restricted to Ni, Co, and Mn. However, there are extensive studies on the layered structure and its stability, which is attributed to its ability to independently relax the oxygen octahedra around each type of cation (Wu et al., 1998).

The electronic, optical, and magnetic properties exhibited by LTMO are governed by the type of Li-TM bond formed which in turn are dependent on the electronic configuration and size of the trivalent cation. Hewston and Chamberland (1987) investigated first-row TM (M) LMTO and showed that partially filled t_{2g} orbitals and t_{2g}-t_{2g} orbital overlap result in d electron delocalization in $LiTiO_2$ and Li_xVO_2 resulting in paramagnetic behavior of the former and semiconducting to metallic behavior of the latter. $LiScO_2$ with no d valence electrons is insulating, whereas the TM to the right of vanadium are characterized by contracted t_{2g} orbitals, prohibiting direct t_{2g}-t_{2g} orbital interactions and hence exhibiting localized *d* orbitals and semiconducting behavior.

Layered rocksalt structures form when the M^{3+} cation is significantly smaller than Li^+, as observed in $LiVO_2$, $LiCrO_2$, (Rudorff and Becker, 1954), $LiNiO_2$, (Dyer et al., 1954), and $LiCoO_2$ (Orman and Wiseman, 1984); the structure is further stabilized by independent relaxation of bond length in LiO_6 and TMO_6 octahedra (Wu et al., 1998). However, in $LiScO_2$ (Wu et al., 1998), cations are of similar size, the relaxation effect is less

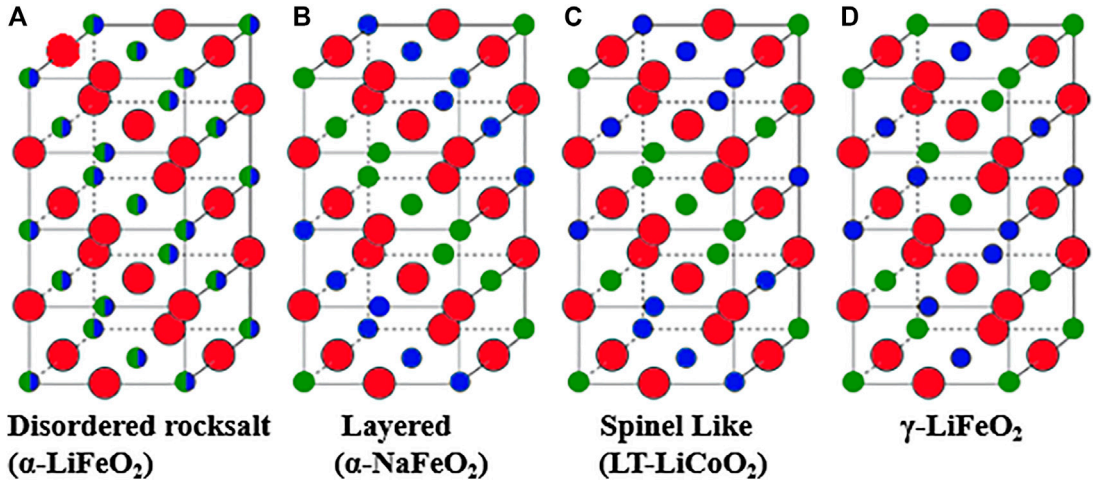

FIGURE 6 | Rocksalt lithium transition metal oxides: **(A)** disordered rocksalt structure with equivalent cation sites, **(B)** layered structure with α-$NaFeO_2$ structure, **(C)** low-temperature spinel-like $LiCoO_2$ structure, and **(D)** γ-$LiFeO_2$ structure. Oxygen is indicated by red circles and Li and TM are indicated by small green and blue circles. Adapted with permission from Urban et al. (2014), Copyright Wiley-VCH.

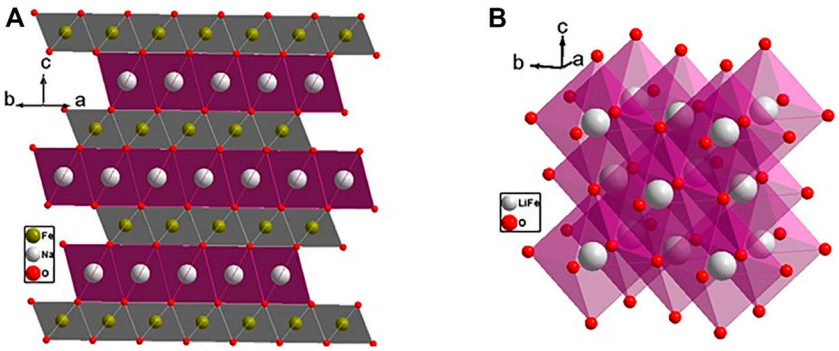

FIGURE 7 | (A) Layered cation-ordered lithium transition metal oxide (*R*-3*m* space group); **(B)** cation disordered rocksalt structure (*Fm*-3*m* space group).

significant, and the structure is dictated by electrostatic interactions resulting in γ- $LiFeO_2$ structure (**Figure 6D**). $LiMnO_2$ crystallizes in a low-temperature orthorhombic form with ordered Li^+ and Mn^{3+} ions, unique among the other LTMO, and attributed this structure to the presence of Jahn-Teller distorted Mn^{3+} ion. However, at high temperature, the cation-ordered rocksalt structure forms (Dunitz and Orgel, 1957; Goodenough, 1959; Hoppe et al., 1975). $LiCoO_2$ adopts a spinel structure with cations in 16*c* and 16*d* octahedral sites when made by low-temperature synthesis routes (Gummow and Thackeray, 1992; Rossen et al., 1993; Lee et al., 2016). Although various combinations of TM can form the layered structure, only a few will remain layered when a significant amount of Li^+ is removed from the structure. Only those TM which not only possess very high octahedral site preference but also retain such preference on oxidation as in Ni^{3+}/Ni^{4+} (d^7 to d^6) and Co^{3+}/Co^{4+} (d^6 to d^5) will have high enough thermodynamic and kinetic barriers to prevent disordering of the layered structure (Clément et al., 2020).

The cation disordered structure is the high-temperature and high-entropy form of the other structure types. Disorder in rocksalt structures can also be achieved, probably metastable, by ball milling (Dachille and Roy, 1964; Gutman, 1994).

First-principles computational studies are crucial in screening the compositional space for likely disordered structure and to shed light on the origin of cation disorder (Urban et al., 2017). For metallic alloys, Hume-Rothery and Powell (1935) rules predict that alloys are formed when species have similar electronegativities and difference in atomic radii is no more than 15%, and this rule is a possible guideline for ionic materials like oxides. Disorder in LMTO occurs with TM having larger ionic radius and charge differences, while current understanding would predict increasing disorder with smaller differences. The ability of the disordered structures to accommodate distortions in their octahedra may be a stabilizing factor.

Urban et al. (2017) suggested that the ability of the structure to accommodate disorder depends on the d- orbital occupancy in

the TM. When cations are randomly distributed in the rocksalt structure, differences in ionic radii and charges create distortion in the O_h sites; these distortions must be shared by the neighboring octahedra. Thus, the energy benefit of distorting the octahedra to better fit various cations may determine the ability of the structure to accommodate cation disorder (Clément et al., 2020). Urban et al. (2017) have investigated the octahedral distortion modes in LTMO and concluded that the TM with d^0 electrons accommodates octahedral distortion at the lowest energy. The band energy of d^0 TM depends on the lower-lying oxygen-dominated orbitals that are always occupied and are insensitive to site distortions (Clément et al., 2020). Disorder in the rocksalt structures is best stabilized by TM having no valence d electron even when the ionic radius and charge differences are relatively large (Urban et al., 2017). These electronic structure studies show that the redox-inactive d^0 metals (Ti^{4+}, V^{5+}, Nb^{5+}, and Mo^{6+}) in LTMO occupy the distorted O_h site, leaving the less distorted cation site for the other redox-active TM, thus stabilizing the disordered rocksalt structure. In other words, not only does the d^0 cation have a low-energy penalty in distorted sites, but also their flexibility to distort allows the other TM cations with d electrons to optimize their distortions. Nevertheless, some DRO with no d^0 TM have been synthesized (Freire et al., 2017; Freire et al., 2018; House et al., 2018). Li_2MnO_2F possesses a disordered rocksalt structure with cation vacancies (House et al., 2018), and Li_2MnO_3-disordered rocksalt with vacancies enhances the electrochemical properties of cathode materials (Freire et al., 2017; Freire et al., 2018).

Murphy et al. (1982) studied Li insertion in various close-packed titanate framework. $LiTiO_2$ spinel transforms to $Li_2Ti_2O_4$ on lithiation, which is accompanied by displacement of Li from Td sites to the O_h sites which are vacant in the spinel structure (*Fd-3m* space group) resulting in rocksalt structure (*Fm-3m*). Metastable $Li_2Ti_2O_4$ irreversibly transforms into the disordered rocksalt structure above 600°C (Murphy et al., 1982). The stable high-temperature form for $LiTiO_2$ is a disordered rocksalt structure. Hua et al. (2019) had investigated structural insights in the formation of Li- and Mn-rich layered oxides; *in situ* high-temperature synchrotron radiation diffraction reveals the transformation of the lithium-rich layered phase (*R-3m*) to a lithium poor spinel phase (*Fd-3m*) *via* an intermediate lithium-containing rocksalt phase (*Fm-3m*) which is accompanied by the release of oxygen and lithium.

Consequences of Cation Disorder

Ordered and disordered LMTO are cathode materials and changes in their chemical composition and structure affect the stability, capacity, energy density, and performance. Disordering results in radically different properties compared to the ordered rocksalt structure. Having excess lithium in the structure, diffusion processes are altered, easier anion redox, smaller and isotropic lattice expansion, and possible fluorine substitution, all leading to enhancement of electrochemical performance in lithium-ion battery applications.

LMTO cathode materials function by reversible extraction and insertion of Li^+. To support continuous ion migration, the cathode material has to meet the following requirements: 1) the material must have facile ion diffusion *via* low-barrier channels and 2) the diffusion channels need to form a percolating network. The diffusion mechanism involves Li^+ ions moving from the octahedral site to an adjacent edge-shared octahedral site through the empty face-shared tetrahedral site, referred to as o-t-o diffusion. The size of the T_d site and electrostatic interaction between Li^+ in the activated T_d site and the four cations in the face-sharing octahedra forming a tetrahedral cluster has a major impact on the Li^+ diffusion barrier. There are five types of tetrahedral cluster formed when the Li^+ and TM species occupy the cation lattice: 0-TM, 1-TM, 2-TM, 3-TM, and 4-TM (Kang and Ceder, 2006; Kang et al., 2006). Li diffusion pathway requires at least two O_h Li connected *via* an activated T_d site; thus, 3-TM and 4-TM environments are excluded. In layered LTMO, every T_d site is coordinated by either 3 Li and 1-TM or 1 Li and 3 TM, out of which only 1 TM sustains Li migration. The size of the T_d site is dependent on the layers' spacing of the Li slab (Kang and Ceder, 2006; Kang et al., 2006). In layered LMTO which has a separate Li layer and TM layer (**Figure 7A**), the ionic radius of Li is larger than that of TM, and the layer spacing of the Li slab lies in the range of 2.6–2.7 Å (Urban et al., 2014). All the Li sites are equivalent in layered LMTO and hence all are interconnected by 1-TM and form a 2D percolating network inside the Li slab. A migration barrier is associated with 1-TM diffusion during charging because of the increasing electrostatic repulsion when the TM is oxidized to higher valence and also due to a change in the slab distance. The electrostatic attraction between the Li and the oxygen atom decreases during charging. At the end of the charge when almost all the Li would be extracted and the Li slab collapses, the lithium mobility decreases.

In cation disordered rocksalt structures, there are no separate layers for Li and TM and no defined slab distance (**Figure 7B**). Instead, there is a significant reduction in the slab spacing to 2.3–2.4 Å and the size of the T_d site due to cation mixing. The 2-TM channel is inactive and the 1-TM channel can support Li migration in cation disordered structures or if only 0-TM channels are available. In 0-TM, the absence of TM in face-sharing octahedra reduces electrostatic repulsion in the activated Li site, and the diffusion barrier is independent of the T_d height and the TM composition (Urban et al., 2014).

Long-range lithium diffusion depends on both the low-energy diffusion barrier and the percolating network formed by interconnecting the diffusion channel. In layered LMTO, all the Li ions are connected *via* 1-TM forming a 2D percolating network for Li conduction in Li slabs. Urban et al. (2014) have done Monte Carlo simulations to study the impact of cation disorder and Li content on Li percolation *via* the 0-TM channel. Though the amount of lithium is greater in the cation disordered structure, the percolation network of the 0-TM channel still forms at a critical Li concentration.

SRO in Defect Rocksalt Oxides

Nominally disordered rocksalt structures do exhibit some degree of SRO. SRO is known to control local transport (Ji et al., 2019). The SRO has previously been studied by a combination of experimental (electron diffraction, solid-state nuclear magnetic resonance, and 2D and 3D nanoscale X-ray spectro-microscopy), as well as by theoretical methods (DFT and MD simulations)

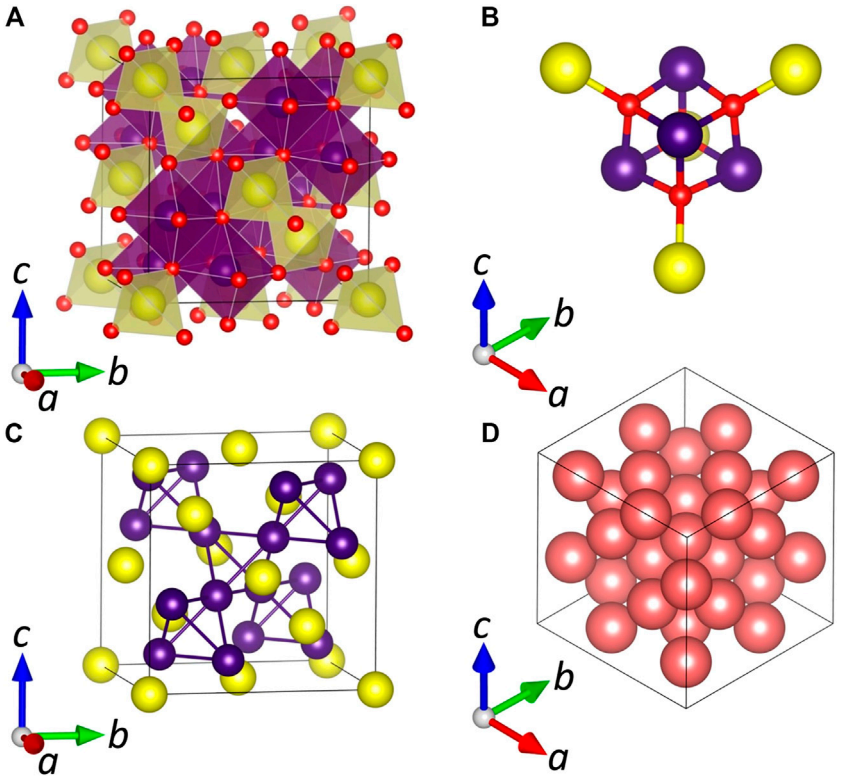

FIGURE 8 | (A) A general view of the normal spinel unit cell ($Fd\bar{3}m$) with an origin on the A-site cation (Wyckoff site 8*a*). **(B)** A fragment of the crystal structure illustrating coordination surroundings of the X anion. **(C)** The metal sublattice AB_2 forming a framework of the Laves phase. **(D)** A cubic close-packed array of anions in the X sublattice. A, B, and X sites are shown as yellow, purple, and red spheres, respectively.

(Clément et al., 2018; Kan et al., 2018; Ji et al., 2019; Jones et al., 2019).

Kan et al. (2018) proposed that local cation ordering redirects Li movement through nonequilibrium pathways, which results in the chemical heterogeneity evidenced by 2D and 3D maps of manganese valence state in $Li_xNb_{0.3}Mn_{04}O_2$. Ji et al. (2019) showed that SRO controls the Li transport by altering the distribution of 0-TM, 1-TM, and 2-TM channels as well as connectivity between them. Ji et al. (2019) explained the difference in the performance of $Li_{1.2}Mn_{0.4}Ti_{0.4}O_2$ and $Li_{1.2}Mn_{0.4}Zr_{0.4}O_2$ based on differences in SRO. Ji et al. (2019) had modeled SRO in a variety of $Li_{1.2}M'_aM''_bO_2$ structures ($M'_a = V^{3+}$, Mn^{2+}, Mn^{3+}, Co^{2+}, and Ni^{2+} and $M''_b = Ti^{4+}$, Zr^{4+}, Nb^{5+}, and Mo^{6+}) using DFT and rationalized SRO based on charge and size effects.

SPINELS

Structure and Cation Distribution

The term "spinel" originates from the name of the naturally occurring mineral $MgAl_2O_4$, which is also well-known as a gemstone because of its variable color characteristics owing to the TM impurities (Malíčková et al., 2021). The spinel structural family consists of numerous materials with the basic formula AB_2X_4 where cation A can be either an alkali, alkaline earth, or a TM and cation B can be almost any TM or aluminum, gallium, and indium. The anion X is represented by O^{2-}, S^{2-}, Se^{2-}, Te^{2-}, F^-, or CN^- species (Zhao et al., 2017). Fortunate conjunction of mixed valence, site preference, a remarkable variety of chemical compositions, and synthetic flexibility in spinels give rise to a wide range of useful functions such as magnetism (Gorter, 1950; Song and Zhang, 2004), catalytic activity (Dong et al., 2019; Kim et al., 2020), and superconductivity (Hagino et al., 1995; Moshopoulou, 2004) as well as electronic, optical, and electrochemical performance (Verwey et al., 1947; Ferg et al., 1994; Aizawa et al., 2002; Jouini et al., 2007; Kim et al., 2014).

The rich story of spinel structural chemistry began in 1915 when the crystal structure was determined for the first time in two independent works by Bragg and Nishikawa (Bragg, 1915; Nishikawa, 1915). At first glance, the structure is represented by a three-dimensional ensemble made of vertice/edge-sharing AX_4 tetrahedra and BX_6 octahedra (**Figure 8A**). A FCC unit cell ($Fd\bar{3}m$) accommodates 8 A, 16 B, and 32 X atoms resulting in eight formula units ($Z = 8$). Each anion X is tetrahedrally coordinated by one cation A situated in the tetrahedral cage and three cations B situated in octahedral cages (**Figure 8B**). A closer look at the unit cell reveals other important structural features. Specifically, the A sublattice possesses a diamond-like structure with a periodicity equal to the unit cell parameter. At the same time, both A and B sublattices together form a structure reminiscent of that in the Laves phase $MgCu_2$ (Stein et al., 2004). Thus, the overall spinel lattice can be imagined as a Laves phase

structured AB_2 atomic array (**Figure 8C**) embedded into a matrix of a cubic close-packed (ccp) arrangement of X anions (**Figure 8D**). The ccp arrangement contains 96 available interstices in total (64 tetrahedral + 32 octahedral); however, only a fraction of them is populated by cations in the spinel structure. However, the ccp packing is imperfect, and the corresponding X layers are corrugated due to minor deviations of anion coordinates from the ideal position. From the crystallography viewpoint, these distortions originate from the flexibility of the Wyckoff site *32e*; hence an additional parameter is required to describe atomic coordinates. It is denoted as the anion position parameter u (also known as the oxygen parameter in oxide spinels). Depending on the choice of origin, an ideal value of u for the perfect ccp arrangement can be either 0.250 or 0.375 for the origin at an octahedral vacancy ($\bar{3}m$) or an A-site cation ($\bar{4}3m$, such as in **Figure 8**), respectively. From geometric considerations, the anion position parameter is connected to both the cubic unit cell parameter a and cation-ligand distances in the tetrahedral ($R_{A\text{-}X}$) and octahedral ($R_{B\text{-}X}$) cages according to $R_{A-X} = \sqrt{3}a(u - \frac{1}{4})$ and $R_{B-X} = a\sqrt{2(u - \frac{3}{8})^2 + (\frac{5}{8} - u)^2}$, or $R_{A-X} = \sqrt{3}a(u - \frac{1}{8})$ and $R_{B-X} = a\sqrt{2(u - \frac{1}{4})^2 + (\frac{1}{2} - u)^2}$ for the $\bar{4}3m$ and $\bar{3}m$ origin settings, respectively. Therefore, distortions in the ccp arrangement of X result in corresponding changes in AX_4 and BX_6 polyhedra as the tetrahedra expand while the octahedra contract with increasing u. This optimization of tetrahedral and octahedral bond lengths to best fit the cations in the structure is the physical reason for the deviation from ideal cubic close packing.

Figure 8 illustrates an ideal (normal) scenario in which distinct A and B cations are entirely separated in the tetrahedral and octahedral interstices; hence the chemical formula can be written as $A(B)_2X_4$ where brackets denote the octahedral site. However, as was initially shown in 1935 by Barth and Posnjak (1932), spinels may possess an inverse atomic layout in which the tetrahedral sites are fully occupied by B cations, while half of the octahedral sites are occupied by A cations and half by B cations so that the chemical formula is $B(AB)X_4$. Later, the terms "normal" and "inverse" spinel were proposed by Verwey and Heilmann (1947) to denote these two limiting scenarios. In some materials, the cation distribution is very close to the normal or inverse limits. For example, the naturally occurring mineral spinel, $MgAl_2O_4$ (which gives its name to the structure), is a nearly perfect normal spinel, while $Fe(NiFe)O_4$ is an example of the inverse structure (Zhao et al., 2017). The terms "normal" and "inverse" are also applicable to binary phases, in which the same TM cations with different oxidation states tend to occupy distinct crystallographic sites. As such, the mineral hausmannite (Mn_3O_4) has a normal spinel structure where Mn^{2+} cations occupy tetrahedral interstices, and Mn^{3+} cations occupy octahedral interstices; therefore, an accurate formula is $Mn^{2+}(Mn^{3+})_2O_4$ (Garcês Gonçalves Jr. et al., 2018). In contrast, the minerals magnetite (Fe_3O_4) and greigite (Fe_3S_4) possess an inverse structure $Fe^{3+}(Fe^{3+}Fe^{2+})X_4$ (Chang et al., 2008).

In many spinel materials, the cation distribution falls between the normal and inverse limits, so different cation species are disordered and present in both types of sites. Taking such disorder into account, the general formula of spinel has to be written as $A_{1-i}(B_{2-i}A_i)X_4$, where i is a degree of inversion (the inversion parameter). Although it is clear that the normal spinel ($i = 0$) corresponds to the most ordered state, the inverse and intermediate distributions possess configurational entropy. If one assumes that the cations on each sublattice are randomly distributed, the composition of maximum entropy occurs at i = 0.667, and this may be thought of as the limiting case for disordering, with both initially normal and initially inverse spinels tending toward this random distribution at high temperature.

This assumption of randomness on each sublattice permits the construction of relatively simple thermodynamic models of cation disordering and the calculation of cation interchange energies and site preference energies. Understanding the long-range cation disorder in spinels is crucial because it substantially impacts physical properties. For example, Zhu et al. (2018) performed synthesis at variable temperatures to control the crystallinity and cation distribution in the photoanode $ZnFe_2O_4$, which can be used in the water-splitting reaction. $ZnFe_2O_4$ nanorods with a higher degree of disorder have enhanced charge carrier transport and higher photogenerated charge separation efficiency. Ndione et al. (2014) established a relation between cation disorder and conductivity in the $ZnCo_2O_4$ (normal) and $NiCo_2O_4$ (inverse) spinels, where increasing disorder leads to ZnO_h antisite defects and increase of the p-type conductivity for $i < 0.5$ in the former and a metal-insulator transition for $0.5 < i < 1.0$ in the latter. The long-range cation disorder also influences principal magnetic properties in spinels, such as magnetic transition temperature, saturation magnetization, and magnetic exchange interactions (Willard et al., 1999).

Short-Range Order

The above considerations appear adequate for order/disorder which can be detected by commonly used techniques such as X-ray diffraction. However, there are also scenarios of the local (short-range) cation ordering that can be observed in the spinel structure. Ivanov et al. (2010) performed a study of $NiFe_2O_4$ single crystals *via* polarization Raman measurements in conjunction with lattice dynamics calculations. The number of observed Raman modes is significantly larger than one expected from the inverse spinel structure $Fe(NiFe)O_4$ in which Ni^{2+} and Fe^{3+} cations are mixed statistically in the octahedral site B. The obtained data were explained by the formation of local lower symmetry domains of α- ($P4_122/P4_322$) or β-type (*Imma*) having a size of ≤50 lattice constants. The domains can be organized in a twinned motif with the I, II, III, IV, V, or VI orientation for the α- and β-type, respectively. While the α-type is fully supported by the observed number of Raman bands and polarization rules, the β-type satisfies only a fraction of the obtained bands; however, it cannot be completely ruled out due to good agreement between calculated and observed bands at specific frequencies.

Furthermore, the possible existence of both types of domains in superposition together with twinning complicates data interpretation. O'Quinn et al. (2020) proposed the Pauling rule as a base to understand the SRO phenomena in spinel, weberite, and pyrochlore structures. According to Pauling's second rule, the sum of the bond strengths (a charge divided by coordination number) of the cations should be equal to the charge of the anion. In the normal spinel structure, each anion X is surrounded by three octahedrally coordinated cations B and one tetrahedrally coordinated cation A (**Figure 8B**). In the oxide spinel $MgAl_2O_4$, such arrangement leads to the sum of bond strengths 2.0, which is in excellent agreement with Pauling's second rule. When inversion occurs, the number of possible anion coordinations extends to eight (**Figure 8B**). However, in $MgAl_2O_4$, only two of these configurations (with bond strength 2.083 and 1.917) are close to satisfying Pauling's second rule and suggesting preference for these local clusters with such ion arrangement in the disordered $MgAl_2O_4$ samples (O'Quinn et al., 2020).

DISCUSSION: WHY DO DIFFERENT STRUCTURES HAVE DIFFERENT MODES OF DISORDER?

It is clear that, for any significant disorder to exist, the structure has to be flexible enough to accommodate it without exorbitant energetic penalty. In general, defects and disorder raise energy and entropy, and the balance of these terms determines the equilibrium extent of disorder at a given composition, temperature, and pressure. In largely ionic oxide systems, cation size and charge are major factors determining both structure and defect chemistry. In comparing the four groups of structures discussed here, one can draw the following inferences. The fluorite-derived structures are the most tolerant of disorder on both cation and anion sublattices. Its aristotype structure consists of alternating occupied and unoccupied cubes of anions (Subramanian et al., 1983; Chakoumakos, 1984; Ewing et al., 2004; Gardner et al., 2010). This means that a change in coordination or bonding in one filled cube has relatively little influence on the next filled cube because they do not directly share anion vertices. This structural feature may explain the easy formation of oxygen vacancies and the wide homogeneity ranges in AO_2-$BO_{1.5}$ systems like YSZ, but it does not readily explain the wealth of different ordered phases and the overwhelming evidence for clustering at various length scales. Such clustering and/or ordering involves cooperative interactions involving the lattice dynamics (and in some cases electron delocalization) at length scales of nanometers to micrometers, not just those involving nearest and next nearest-neighbor interactions. The wealth of structural phase transitions involving changes in symmetry but having very small thermodynamic consequence (enthalpies of transformation less than 5 kJ/mol in magnitude) in both fluorite and perovskite structures speaks to the closely balanced energetics and lattice dynamics of these structures.

The thermodynamic favorability of disordering has been associated with a decrease in the cation radii ratio (r_A/r_B) for most of the fluorite-related systems. However, this trend is not observed in rare earth titanate and stannate pyrochlore systems, $RE_2M_2O_7$ (M = Ti and Sn), in which only the ordered structure has been observed for all compositions all the way to RE = Yb, the smallest rare earth ion (Kennedy, 1996; Baroudi et al., 2015). One reason for such preference for the ordered structure might be the coordination geometry around Ti and Sn cations. They tend to prefer octahedral coordination as found in their natural binary oxide minerals TiO_2 and SnO_2 which crystallize in the rutile structure (Burdett et al., 1987; Bolzan et al., 1997). The ordered structure offers six-coordinated geometry for Ti and Sn cations, whereas seven-coordinated geometry is found for all cations in the disordered structure. The stronger covalency associated with tin may also be a factor favoring the ordered state.

For the idealized structures, configurational entropy increases in the order pyrochlore, weberite, and defect fluorite as disorder increases. The existence of short-range weberite domains within both amorphized and defect fluorite structures and their persistence into recrystallized pyrochlore is still somewhat a mystery and may represent a combination of thermodynamic and kinetic effects. The thermodynamic driver may be a compromise between energy and entropy, but the size distribution of the domains and interactions at their interfaces with the host structure (amorphous, defect fluorite, or pyrochlore) are still poorly known.

From the structural point of view, though the fully disordered structure has common seven coordination geometry for A and B cations and randomness for vacancies, the bigger A and smaller B cations prefer higher and lower coordination, respectively, leading to ordering of vacancies and consequently to locally ordered structure in nanoscale domains (Shamblin et al., 2016a). The occurrence of weberite nanodomains, which do not grow to macroscopic size and which represent a structure not seen in the equilibrium phase diagram, appears to be a unique feature of pyrochlore systems. From the kinetic point of view, annealing of such domains still needs study. Nor is it clear why certain $A_2B_2O_7$ materials crystallize as pyrochlore, others were weberite, though in both cases, as the cations become more similar, the defect fluorite structure becomes more favorable and may occur as a high-temperature equilibrium phase. The preference of $A_2B_2O_7$ and A_3BO_7 for pyrochlore and weberite structures, respectively, may reflect the different cationic charge and resulting differences in electrostatic energies, but these factors have not been explored quantitatively. In terms of coordination geometry and distortions, the weberite structure appears to be more flexible than the pyrochlore structure by accepting cations in different coordination geometries (six to eight) and being more tolerant of polyhedral distortions (Cai and Nino, 2009; Cai and Nino, 2011). This flexibility may be more important when the cation charge difference is greater.

Furthermore, the fluorite-based materials do not readily form layered or two-dimensional superstructures, and the oxygen vacancies are not coalesced into shear planes or ordered CS structures. Why are such structures unfavorable? One of the reasons may be that the vacancies tend to be separated from each other to reduce the destabilization due to electrostatic repulsion as the fluorite structure is compact without an open framework.

Also, when the vacancies in fluorite-related systems are increased to stoichiometry $A_2B_2O_6$, the bixbyite structure with ordered vacancies forms (King et al., 2013). The bixbyite structure may "outcompete" other arrangements, including shear structures, in energy. Thus, the lack of the latter may reflect the existence of an even better structural arrangement rather than any intrinsic instability of shear. A computational approach to the stability and defect chemistry of these different hypothetical polymorphs is likely to be informative.

Perovskites are also tolerant of oxygen vacancies, but these often aggregate into specific ordered and layered structures or are essentially eliminated in CS structures. Within the perovskites, the framework of corner-linked octahedra is strongly bound yet flexible. The oxygen sublattice is far from being close-packed. In terms of distortions, both tilting of octahedra and off-centering of cations within them are mechanisms to adjust bond lengths. Much of this behavior is captured by the geometric arguments embedded in the Goldschmidt tolerance factor. Phase transitions involving these distortions are generally small in energy and entropy, and the more symmetrical structures occur with increasing temperature. If the volume of the perovskite increases with increasing symmetry, as is often the case, then the pressure will extend the temperature stability field of the more disordered structures.

From the thermodynamic point of view, the annihilation of oxygen vacancies should be an energetically favorable process since vacancy formation is energetically expensive. Following this argumentation, shear plane formation, involving vacancy elimination, should be a more prevalent type of defect accommodation in different crystal structures. However, it is not common, and one should also consider that the metal-metal distances become shorter in shear planes compared with their original positions. Therefore, to form shear planes, the exothermic energy released from annihilation of oxygen vacancies should be larger than the endothermic energy of cation repulsions in shear planes. So far, only a few oxides based on ReO_3 and rutile structures have been reported to form ordered shear structures. Based on this knowledge, it appears that the flexibility of the framework, some structural openness rather than close packing, high polarizability of atoms, octahedral coordination of metal atoms, and presence of corner-shared oxygen appear to all be essential for the formation of shear structures.

The clustering of vacancies into shear planes and their ordering into periodic structures diminishes the configurational entropy initially present on the anion sublattice. Presumably ordering is associated with a stabilizing energy (enthalpy) contribution and the formation of the shear phase reflects a balance between ΔH and $T\Delta S$. However, phases with ordered shear planes often appear to need another source of configurational entropy to stabilize them. This may arise from cation disorder in regions between the shear planes (Voskanyan and Navrotsky, 2021). This necessary and delicate balance of energetics within and between the shear planes may contribute to the relative rarity of shear structures.

The rocksalt and spinel structures contain (almost) cubic close-packed anion sublattices. Oxygen vacancies do not occur at appreciable levels but cation vacancies (and in some cases interstitials) are relatively easily accommodated. Charge balance occurs largely through variation in TM oxidation state. The cations are generally more similar in size than those occupying A- and B-sites in fluorite derivatives and perovskites. Though to a first approximation the ions on each sublattice are randomly mixed, there is increasing evidence of short-range order. Such local ordering, only beginning to be studied in detail, may suggest possible complexities in rocksalt and spinel structures analogous to those first discovered in pyrochlores and perovskites.

The discussion above reminds us how little we still know about short and midrange ordering, which appears to be a very general phenomenon in oxides. Cation radius and coordination number, as well as the openness and flexibility of the framework, appear to be the major factors influencing defect chemistry. To complement empirical trends and observations, rigorous first-principles calculations comparing different structures at the same composition would provide insight into the stability and defect chemistry in different, heretofore unsynthesized, polymorphs.

CONCLUSION

Fluorite-derived phases include a number of different structures, with high oxygen vacancy concentrations and varying degrees of cation disorder. SRO leading to cluster formation and nanoscopic weberite domains are common themes. The energetics of these phases and their solid solutions are complex because these materials are often neither completely ordered nor completely disordered, with the equilibrium degree of ordering depending on temperature, pressure, and composition. Nonequilibrium disorder can be produced by different means and its annealing appears to require long-term heating at temperatures above 1,200°C. The size, nature, and energetics of clusters and nanoscopic domains deserve additional systematic study.

Perovskites are very flexible in composition, cation ordering schemes, distortions, and the incorporation of oxygen vacancies. In addition to order-disorder on both A and B cation sites, the formation of clusters involving oxygen vacancies is possible. A unique way of ordering and eliminating oxygen vacancies, not seen in fluorite structures, is the development of shear planes and their ordering into various families of CS structures, not seen in the other structure types discussed here but observed in lower symmetry structures, such as those derived from rutile. Thermodynamically, ordering into shear planes decreases the entropy associated with oxygen vacancies, but disorder in other parts of the structure may add a stabilizing configurational entropy term, perovskite structures.

Both ordered and disordered rocksalt structures form a variety of systems. It is important to realize that the relation between ordered and disordered structures definitely is not a true order-disorder transition at the same chemical composition. Rather, ordered and disordered lithium TM oxides form having an entirely different composition. It is clear that a number of factors related to cation size and the nature of the TM affect the structure formed at a given composition. In contrast to fluorite and perovskite structures, oxygen vacancies do not play a significant role in either ordered or disordered rocksalt oxides. However, distortion of polyhedra and short-range order are important in nominally DRO. Much work remains to be done

to understand these changes on an atomistic level and to optimize structures and compositions for battery operation.

Order-disorder in spinels is dominated by the exchange (disordering) of cations between octahedral and tetrahedral sites. Though interstitial cations may sometimes exist, oxygen vacancies are generally not incorporated. It is interesting that spinels, long considered to be "simple" in the sense of random cation arrangements on each sublattice, may in fact harbor ordering on different length scales analogous to that seen in fluorite, perovskite, and rocksalt phases.

DATA AVAILABILITY STATEMENT

The original contributions presented in the study are included in the article/supplementary files; further inquiries can be directed to the corresponding author.

AUTHOR CONTRIBUTIONS

AN conceptualized and designed the study. TS, AV, KJ, and MA wrote sections of the paper based on their prior published experimental work. All authors contributed to editing and coordinating the sections into a final manuscript but the major part of that work was done by AN.

FUNDING

The authors acknowledge the Department of Energy and the National Science Foundation for support over many years that allowed the thermodynamic and structural studies summarized here. The preparation of this review was supported by the Department of Energy, Office of Basic Energy Sciences, Grant DE-FG02-03ER46053.

REFERENCES

Aizawa, H., Ohishi, N., Ogawa, S., Watanabe, E., Katsumata, T., Komuro, S., et al. (2002). Characteristics of Chromium Doped Spinel Crystals for a Fiber-Optic Thermometer Application. *Rev. Scientific Instr.* 73 (8), 3089–3092. doi:10.1063/1.1491998

Aizenshtein, M., Shvareva, T. Y., and Navrotsky, A. (2010). Thermochemistry of Lanthana- and Yttria-Doped Thoria. *J. Am. Ceram. Soc.* 93, 4142–4147. doi:10.1111/j.1551-2916.2010.04001.x

Allpress, J. G., and Rossell, H. J. (1979). Fluorite-related Phases Ln3MO7, Ln = Rare Earth, Y, or Sc, M = Nb, Sb, or Ta. I. Crystal Chemistry. *J. Solid State. Chem.* 27, 105–114. doi:10.1016/0022-4596(79)90149-X10.1016/0022-4596(79)90149-x

Anderson, M. T., Vaughey, J. T., and Poeppelmeier, K. R. (1993). Structural Similarities Among Oxygen-Deficient Perovskites. *Chem. Mater.* 5, 151–165. doi:10.1021/cm00026a003

Baroudi, K., Gaulin, B. D., Lapidus, S. H., Gaudet, J., and Cava, R. J. (2015). Symmetry and Light Stuffing ofHo2Ti2O7, Er2Ti2O7, andYb2Ti2O7characterized by Synchrotron X-ray Diffraction. *Phys. Rev. B* 92, 24110. doi:10.1103/PhysRevB.92.024110

Barth, T. F. W., and Posnjak, E. (1932). Spinel Structures: with and without Variate Atom Equipoints. *Z. Kristallogr. Cryst. Mater.* 82 (1-6), 325–341. doi:10.1524/zkri.1932.82.1.325

Bindi, L., Sirotkina, E. A., Bobrov, A. V., Pushcharovsky, D., and Irifune, T. (2017). Discovery of MgTiSi2O7: a New High-Pressure Silicate with the Weberite Structure Synthesized at Transition-Zone Conditions. *Phys. Chem. Minerals* 44, 419–424. doi:10.1007/s00269-016-0868-8

Bolzan, A. A., Fong, C., Kennedy, B. J., and Howard, C. J. (1997). Structural Studies of Rutile-type Metal Dioxides. *Acta Crystallogr. Sect. B* 53, 373–380. doi:10.1107/S0108768197001468

Bragg, W. H. (1915). The Structure of the Spinel Group of Crystals. *Lond. Edinb. Dublin Phil. Mag. J. Sci.* 30, 305–315. doi:10.1080/14786440808635400

Burdett, J. K., Hughbanks, T., Miller, G. J., Richardson, J. W., and Smith, J. V. (1987). Structural-electronic Relationships in Inorganic Solids: Powder Neutron Diffraction Studies of the Rutile and Anatase Polymorphs of Titanium Dioxide at 15 and 295 K. *J. Am. Chem. Soc.* 109, 3639–3646. doi:10.1021/ja00246a021

Buyukkilic, S., Kim, S., and Navrotsky, A. (2014). Defect Chemistry of Singly and Doubly Doped Ceria: Correlation between Ion Transport and Energetics. *Angew. Chem. Int. Ed.* 53, 9517–9521. doi:10.1002/anie.201404618

Buyukkilic, S., Shvareva, T., and Navrotsky, A. (2012). Enthalpies of Formation and Insights into Defect Association in Ceria Singly and Doubly Doped with Neodymia and Samaria. *Solid State Ionics* 227, 17–22. doi:10.1016/j.ssi.2012.08.017

Cai, L., Arias, A. L., and Nino, J. C. (2011). The Tolerance Factors of the Pyrochlore crystal Structure. *J. Mater. Chem.* 21, 3611–3618. doi:10.1039/C0JM03380D

Cai, L., Denev, S., Gopalan, V., and Nino, J. C. (2010). Phase Transition in Weberite-type Gd3NbO7. *J. Am. Ceram. Soc.* 93, 875–880. doi:10.1111/j.1551-2916.2009.03494.x

Cai, L., and Nino, J. C. (2009). Complex Ceramic Structures. I. Weberites. *Acta Crystallogr. Sect. B Struct. Sci.* 65, 269–290. doi:10.1107/S0108768109011355

Cai, L., and Nino, J. C. (2007). Structure and Dielectric Properties of Ln3NbO7 (Ln=Nd, Gd, Dy, Er, Yb and Y). *J. Eur. Ceram. Soc.* 27, 3971–3976. doi:10.1016/j.jeurceramsoc.2007.02.077

Cai, L., and Nino, J. C. (2011). Synchrotron and Neutron Powder Diffraction Study of Phase Transition in Weberite-type Nd3NbO7 and La3NbO7. *J. Solid State. Chem.* 184, 2263–2271. doi:10.1016/j.jssc.2011.06.017

Caignaert, V., Nguyen, N., Hervieu, M., and Raveau, B. (1985). Sr2Mn2O5, an Oxygen-Defect Perovskite with Mn(III) in Square Pyramidal Coordination. *Mater. Res. Bull.* 20, 479–484. doi:10.1016/0025-5408(85)90101-110.1016/0025-5408(85)90101-1

Chakoumakos, B. C. (1984). Systematics of the Pyrochlore Structure Type, Ideal A2B2X6Y. *J. Solid State. Chem.* 53, 120–129. doi:10.1016/0022-4596(84)90234-2

Chang, L., Roberts, A. P., Tang, Y., Rainford, B. D., Muxworthy, A. R., and Chen, Q. (2008). Fundamental Magnetic Parameters from Pure Synthetic Greigite (Fe3S4). *J. Geophys. Res.* 113 (B6), 104. doi:10.1029/2007JB005502

Chen, W., Lee, T. A., and Navrotsky, A. (2005). Enthalpy of Formation of Yttria-Doped Ceria. *J. Mater. Res.* 20, 144–150. doi:10.1557/JMR.2005.0017

Chen, W., and Navrotsky, A. (2006). Thermochemical Study of Trivalent-Doped Ceria Systems: CeO2– MO1.5 (M = La, Gd, and Y). *J. Mater. Res.* 21, 3242–3251. doi:10.1557/jmr.2006.0400

Cheng, J., and Navrotsky, A. (2005). Energetics of La1−xAxCrO3−δ Perovskites (A=Ca or Sr). *J. Solid State. Chem.* 178, 234–244. doi:10.1016/j.jssc.2004.11.028

Cheng, J., Navrotsky, A., Zhou, X. D., and Anderson, H. U. (2005). Thermochemistry of La1-xSrxFeO3-δ Solid Solutions ($0.0 \leq X \leq 1.0$, $0.0 \leq \delta \leq 0.5$). *Chem. Mater.* 17, 2197–2207. doi:10.1021/cm048613o

Chung, C.-K., Lang, M., Xu, H., and Navrotsky, A. (2018a). Thermodynamics of Radiation Induced Amorphization and thermal Annealing of Dy2Sn2O7 Pyrochlore. *Acta Materialia* 155, 386–392. doi:10.1016/j.actamat.2018.06.003

Chung, C.-K., O'Quinn, E. C., Neuefeind, J. C., Fuentes, A. F., Xu, H., Lang, M., et al. (2019). Thermodynamic and Structural Evolution of Mechanically Milled and swift Heavy Ion Irradiated Er2Ti2O7 Pyrochlore. *Acta Mater.* 181, 309–317. doi:10.1016/j.actamat.2019.09.022

Chung, C.-K., Shamblin, J., O'Quinn, E. C., Shelyug, A., Gussev, I., Lang, M., et al. (2018b). Thermodynamic and Structural Evolution of Dy2Ti2O7 Pyrochlore after swift Heavy Ion Irradiation. *Acta Materialia* 145, 227–234. doi:10.1016/j.actamat.2017.12.044

Clément, R. J., Kitchaev, D., Lee, J., and Gerbrand Ceder, G. (2018). Short-range Order and Unusual Modes of Nickel Redox in a Fluorine-Substituted Disordered Rocksalt Oxide Lithium-Ion Cathode. *Chem. Mater.* 30, 6945–6956. doi:10.1021/acs.chemmater.8b03794

Clément, R. J., Lun, Z., and Ceder, G. (2020). Cation-disordered Rocksalt Transition Metal Oxides and Oxyfluorides for High Energy Lithium-Ion Cathodes. *Energy Environ. Sci.* 13, 345–373. doi:10.1039/C9EE02803J

Clements, R., Hester, J. R., Kennedy, B. J., Ling, C. D., and Stampfl, A. P. J. (2011). The Fluorite-Pyrochlore Transformation of Ho2−yNdyZr2O7. *J. Solid State. Chem.* 184, 2108–2113. doi:10.1016/j.jssc.2011.05.054

Dachille, F., and Roy, R. (1964). Effectiveness of Shearing Stresses in Accelerating Solid Phase Reactions at Low Temperatures and High Pressures. *J. Geology.* 72, 243–247. doi:10.1086/626979

Davies, P. K., Wu, H., Borisevich, A. Y., Molodetsky, I. E., and Farber, L. (2008). Crystal Chemistry of Complex Perovskites: New Cation-Ordered Dielectric Oxides. *Annu. Rev. Mater. Res.* 38, 369–401. doi:10.1146/annurev.matsci.37.052506.084356

de los Reyes, M., Whittle, K. R., Zhang, Z., Ashbrook, S. E., Mitchell, M. R., Jang, L.-Y., et al. (2013). The Pyrochlore to Defect Fluorite Phase Transition in Y2Sn2−xZrxO7. *RSC Adv.* 3, 5090–5099. doi:10.1039/C3RA22704A

DongQu, C. Z., Qu, Z., Qin, Y., Fu, Q., Sun, H., and Duan, X. (2019). Revealing the Highly Catalytic Performance of Spinel CoMn2O4 for Toluene Oxidation: Involvement and Replenishment of Oxygen Species Using *In Situ* Designed-TP Techniques. *ACS Catal.* 9, 6698–6710. doi:10.1021/acscatal.9b01324

Drey, D. L., O'Quinn, E. C., Subramani, T., Lilova, K., Baldinozzi, G., Gussev, I. M., et al. (2020a). Disorder in Ho2Ti2−xZrxO7: Pyrochlore to Defect Fluorite Solid Solution Series. *RSC Adv.* 10, 34632–34650. doi:10.1039/D0RA07118H

Dunitz, J. D., and Orgel, L. E. (1957). Electronic Properties of Transition-Metal Oxides-II. *J. Phys. Chem. Sol.* 3, 318–323. doi:10.1016/0022-3697(57)90035-5

Dyer, L. D., Borie, B. S., Jr., and Smith, G. P. (1954). Alkali Metal-Nickel Oxides of the Type MNiO2. *J. Am. Chem. Soc.* 76, 1499–1503. doi:10.1021/ja01635a012

Eberman, K., Wuensch, B. J., and Jorgensen, J. D. (2002). Order-disorder Transformations Induced by Composition and Temperature Change in (SczYb1−z)2Ti2O7 Pyrochlores, Prospective Fuel Cell Materials. *Solid State Ionics* 148, 521–526. doi:10.1016/S0167-2738(02)00099-1

Ewing, R. C., Lian, J., and Wang, L. M. (2003). Ion Beam-Induced Amorphization of the Pyrochlore Structure-type: a Review. *MRS Proc.* 792, 190–201. doi:10.1557/PROC-792-R2.1

Ewing, R. C., Weber, W. J., and Lian, J. (2004). Nuclear Waste Disposal-Pyrochlore (A2B2O7): Nuclear Waste Form for the Immobilization of Plutonium and "minor" Actinides. *J. Appl. Phys.* 95, 5949–5971. doi:10.1063/1.1707213

Ferg, E., Gummow, R. J., de Kock, A., and Thackeray, M. M. (1994). Spinel Anodes for Lithium-ion Batteries. *J. Electrochem. Soc.* 141, 11–L147. doi:10.1149/1.2059324

Finkeldei, S., Kegler, P., Kowalski, P. M., Schreinemachers, C., Brandt, F., Bukaemskiy, A. A., et al. (2017). Composition Dependent Order-Disorder Transition in Nd Zr1−O2−0.5 Pyrochlores: A Combined Structural, Calorimetric and Ab Initio Modeling Study. *Acta Materialia* 125, 166–176. doi:10.1016/j.actamat.2016.11.059

Freire, M., Diaz-Lopez, M., Bordet, P., Colin, C. V., Lebedev, O. I., Kosova, N. V., et al. (2018). Investigation of the Exceptional Charge Performance of the 0.93Li4−xMn2O5-0.07Li2O Composite Cathode for Li-Ion Batteries. *J. Mater. Chem. A.* 6, 5156–5165. doi:10.1039/C8TA00234G

Freire, M., Lebedev, O. I., Maignan, A., Jordy, C., and Pralong, V. (2017). Nanostructured Li2MnO3: a Disordered Rock Salt Type Structure for High Energy Density Li Ion Batteries. *J. Mater. Chem. A.* 5, 21898–21902. doi:10.1039/C7TA07476J

Fu, J., and Skrabalak, S. E. (2017). Enhanced Photoactivity from Single-Crystalline SrTaO 2 N Nanoplates Synthesized by Topotactic Nitridation. *Angew. Chem. Int. Ed.* 56 (45), 14169–14173. doi:10.1002/anie.201708645

Fu, W. T., and IJdo, D. J. W. (2009). On the crystal Structures of Ln3MO7 (Ln=Nd, Sm, Y and M=Sb, Ta)-Rietveld Refinement Using X-ray Powder Diffraction Data. *J. Solid State. Chem.* 182, 2451–2455. doi:10.1016/j.jssc.2009.06.028

Fuentes, A. F., Boulahya, K., Maczka, M., Hanuza, J., and Amador, U. (2005). Synthesis of Disordered Pyrochlores, Ti2O7 (, Gd and Dy), by Mechanical Milling of Constituent Oxides. *Solid State. Sci.* 7, 343–353. doi:10.1016/j.solidstatesciences.2005.01.002

Fuentes, A. F., Montemayor, S. M., Maczka, M., Lang, M., Ewing, R. C., and Amador, U. (2018). A Critical Review of Existing Criteria for the Prediction of Pyrochlore Formation and Stability. *Inorg. Chem.* 57, 12093–12105. doi:10.1021/acs.inorgchem.8b01665

Garcês Gonçalves, P. R., Jr., De Abreu, H. A., and Duarte, H. A. (2018). Stability, Structural, and Electronic Properties of Hausmannite (Mn3O4) Surfaces and Their Interaction with Water. *J. Phys. Chem. C* 122 (36), 20841–20849. doi:10.1021/acs.jpcc.8b06201

Gardner, J. S., Gingras, M. J. P., and Greedan, J. E. (2010). Magnetic Pyrochlore Oxides. *Rev. Mod. Phys.* 82, 53–107. doi:10.1103/RevModPhys.82.53

Glerup, M., Nielsen, O. F., and Poulsen, F. W. (2001). The Structural Transformation from the Pyrochlore Structure, A2B2O7, to the Fluorite Structure, AO2, Studied by Raman Spectroscopy and Defect Chemistry Modeling. *J. Solid State. Chem.* 160, 25–32. doi:10.1006/jssc.2000.9142

Goldschmidt, V. M. (1926). Die Gesetze der Krystallochemie. *Naturwissenschaften* 14, 477–485. doi:10.1007/bf01507527

Goodenough, J. B. (1959). On the Influence of 3d4 Ions on the Magnetic and Crystallographic Properties of Magnetic Oxides. *J. Phys. Radium* 20, 155–159. doi:10.1051/jphysrad:01959002002-3015500

Gorter, E. W. (1950). Magnetization in Ferrites: Saturation Magnetization of Ferrites with Spinel Structure. *Nature* 165, 798–800. doi:10.1038/165798a0

Grey, I. E., Mumme, W. G., Ness, T. J., Roth, R. S., and Smith, K. L. (2003). Structural Relations between Weberite and Zirconolite Polytypes-Refinements of Doped 3T and 4M Ca2Ta2O7 and 3T CaZrTi2O7. *J. Solid State. Chem.* 174, 285–295. doi:10.1016/S0022-4596(03)00222-6

Gummow, R., and Thackeray, M. M. (1992). Lithium-cobalt-nickel-oxide Cathode Materials Prepared at 400$deg;C for Rechargeable Lithium Batteries. *Solid State Ionics* 53-56, 681–687. doi:10.1016/0167-2738(92)90447-W

Gunn, D. S. D., Allan, N. L., Foxhall, H., Harding, J. H., Purton, J. A., Smith, W., et al. (2012). Novel Potentials for Modelling Defect Formation and Oxygen Vacancy Migration in Gd2Ti2O7 and Gd2Zr2O7 Pyrochlores. *J. Mater. Chem.* 22, 4675–4680. doi:10.1039/C2JM15264A

Gussev, I. M., O'Quinn, E. C., Baldinozzi, G., Neuefeind, J., Ewing, R. C., Zhang, F., et al. (2020). Local Order of Orthorhombic Weberite-type Y3TaO7 as Determined by Neutron Total Scattering and Density Functional Theory Calculations☆. *Acta Materialia* 196, 704–709. doi:10.1016/j.actamat.2020.07.005

Gutman, E. M. (1994). *Mechanochemistry of Solid Surfaces*. Singapore: World Scientific Publishing Co Inc. doi:10.1142/2373

Hagino, T., Seki, Y., Wada, N., Tsuji, S., Shirane, T., Kumagai, K.-i., et al. (1995). Superconductivity in Spinel-type compoundsCuRh2S4andCuRh2Se4. *Phys. Rev. B* 51, 12673–12684. doi:10.1103/PhysRevB.51.1267318

Hayun, S., Tran, T. B., Lian, J., Fuentes, A. F., and Navrotsky, A. (2012). Energetics of Stepwise Disordering Transformation in Pyrochlores, RE2Ti2O7 (RE=Y, Gd and Dy). *Acta Materialia* 60, 4303–4310. doi:10.1016/j.actamat.2012.04.007

Helean, K. B., Begg, B. D., Navrotsky, A., Ebbinghaus, B., Weber, W. J., and Ewing, R. C. (2000). Enthalpies of Formation of Gd2(Ti2-xZrx)O7 Pyrochlores. *MRS Proc.* 663, 691. doi:10.1557/PROC-663-691

Helean, K. B., Navrotsky, A., Vance, E. R., Carter, M. L., Ebbinghaus, B., Krikorian, O., et al. (2002). Enthalpies of Formation of Ce-Pyrochlore, Ca0.93Ce1.00Ti2.035O7.00, U-Pyrochlore, Ca1.46U4+0.23U6+0.46Ti1.85O7.00 and Gd-Pyrochlore, Gd2Ti2O7: Three Materials Relevant to the Proposed Waste Form for Excess Weapons Plutonium. *J. Nucl. Mater.* 303, 226–239. doi:10.1016/s0022-3115(02)00795-x

Helean, K. B., Ushakov, S. V., Brown, C. E., Navrotsky, A., Lian, J., Ewing, R. C., et al. (2004). Formation Enthalpies of Rare Earth Titanate Pyrochlores. *J. Solid State. Chem.* 177, 1858–1866. doi:10.1016/j.jssc.2004.01.009

Heremans, C., Wuensch, B. J., Stalick, J. K., and Prince, E. (1995). Fast-Ion Conducting Y2(Zr Ti1-)2O7 Pyrochlores: Neutron Rietveld Analysis of Disorder Induced by Zr Substitution. *J. Solid State. Chem.* 117, 108–121. doi:10.1006/jssc.1995.1253

Hewston, T. A., and Chamberland, B. L. (1987). A Survey of First-Row Ternary Oxides LiMO2 (M = Sc-Cu). *J. Phys. Chem. Sol.* 48, 97–108. doi:10.1016/0022-3697(87)90076-X

Hoppe, R., Brachtel, G., and Jansen, M. (1975). Zur Kenntnis der Oxomanganate(III):, Uber LiMnO2 und B NaMnO2. *J. Anorg. Allg. Chem.* 417, 1–10. doi:10.1002/zaac.19754170102

House, R. A., Jin, L., Maitra, U., Tsuruta, K., Somerville, J. W., Förstermann, D. P., et al. (2018). Lithium Manganese Oxyfluoride as a New Cathode Material Exhibiting Oxygen Redox. *Energ. Environ. Sci.* 11, 926–932. doi:10.1039/C7EE03195E

Hua, W., Wang, S., Knapp, M., Leake, S. J., Senyshyn, A., Richter, C., et al. (2019). Structural Insights into the Formation and Voltage Degradation of Lithium- and Manganese-Rich Layered Oxides. *Nat. Commun.* 10, 5365. doi:10.1038/s41467-019-13240-z

Hume-Rothery, W., and Powell, H. M. (1935). On the Theory of Super-lattice Structures in Alloys. *Z. Kristallogr.* 91, 23–47. doi:10.1524/zkri.1935.91.1.23

Ivanov, V. G., Abrashev, M. V., Iliev, M. N., Gospodinov, M. M., Meen, J., and Aroyo, M. I. (2010). Short-range B-site Ordering in the Inverse Spinel ferrite NiFe2O4. *Phys. Rev. B* 82, 024104. doi:10.1103/PhysRevB.82.024104

Ji, H., Urban, A., Kitchaev, D. A., Kwon, D.-H., Artrith, N., Ophus, C., et al. (2019). Hidden Structural and Chemical Order Controls Lithium Transport in Cation-Disordered Oxides for Rechargeable Batteries. *Nat. Commun.* 10, 592. doi:10.1038/s41467-019-08490-w

Jones, M. A., Reeves, P. J., Seymour, I. D., Cliffe, M. J., Dutton, S. E., and Grey, C. P. (2019). Short-range Ordering in a Battery Electrode, the 'cation-Disordered' Rocksalt Li1.25Nb0.25Mn0.5O2. *Chem. Commun.* 55, 9027–9030. doi:10.1039/C9CC04250D

Jouini, A., Yoshikawa, A., Brenier, A., Fukuda, T., and Boulon, G. (2007). Optical Properties of Transition Metal Ion-Doped MgAl2O4 Spinel for Laser Application. *Phys. Stat. Sol. (C)* 4 (3), 1380–1383. doi:10.1002/pssc.200673872

Kan, W. H., Deng, B., Xu, Y., Shukla, A. K., Bo, T., Zhang, S., et al. (2018). Understanding the Effect of Local Short-Range Ordering on Lithium Diffusion in Li1.3Nb0.3Mn0.4O2 Single-Crystal Cathode. *Chem* 4 (9), 2108–2123. doi:10.1016/j.chempr.2018.05.008

Kang, K., and Ceder, G. (2006). Factors that Affect Li Mobility in Layered Lithium Transition Metal Oxides. *Phys. Rev. B: Condens. Matter Mater. Phys.* 74, 094105. doi:10.1103/PhysRevB.74.094105

Kang, K., Meng, Y. S., Bréger, J., Grey, C. P., and Ceder, G. (2006). Electrodes with High Power and High Capacity for Rechargeable Lithium Batteries. *Science* 311, 977–980. doi:10.1126/science.1122152

Kennedy, B. J. (1996). Structural Trends in Pyrochlore Oxides. *Msf* 228-231, 753–758. doi:10.4028/www.scientific.net/msf.228-231.753

Kim, J., Pieczonka, N. P. W., and Yang, L. (2014). Challenges and Approaches for Hhgh-voltage Spinel Lithium-ion Batteries. *ChemPhysChem* 15 (10), 1940–1954. doi:10.1002/cphc.201400052

Kim, Y., Kwon, S., Song, Y., and Na, K. (2020). Catalytic CO2 Hydrogenation Using Mesoporous Bimetallic Spinel Oxides as Active Heterogeneous Base Catalysts with Long Lifetime. *J. CO2 Utilization* 36, 145–152. doi:10.1016/j.jcou.2019.11.005

King, G., Thompson, C. M., Greedan, J. E., and Llobet, A. (2013). Local Structure of the Vacancy Disordered Fluorite Yb3TaO7 from Neutron Total Scattering. *J. Mater. Chem. A.* 1, 10487–10494. doi:10.1039/C3TA12100C

King, G., and Woodward, P. M. (2010). Cation Ordering in Perovskites. *J. Mater. Chem.* 20, 5785–5796. doi:10.1039/B926757C

Knee, C. S., Holmlund, J., Andreasson, J., Käll, M., Eriksson, S. G., and Börjesson, L. (2005). Order-disorder-order Phase Transitions in the Pyrochlore superconductorCd2Re2O7. *Phys. Rev. B* 71, 214518. doi:10.1103/PhysRevB.71.214518

Kubicek, M., Bork, A. H., and Rupp, J. L. M. (2017). Perovskite Oxides - a Review on a Versatile Material Class for Solar-To-Fuel Conversion Processes. *J. Mater. Chem. A.* 5, 11983–12000. doi:10.1039/C7TA00987A

Kumari, R., Kulriya, P. K., Grover, V., Shukla, R., Saravanan, K., Mohapatra, S., et al. (2016). Radiation Stability of Gd2Zr2O7: Effect of Stoichiometry and Structure. *Ceram. Int.* 42, 103–109. doi:10.1016/j.Ceram.Int.2015.08.007

Laberty, C., Navrotsky, A., Rao, C. N. R., and Alphonse, P. (1999). Energetics of Rare Earth Manganese Perovskites A1−xA′xMnO3 (A=La, Nd, Y and A′=Sr, La) Systems. *J. Solid State. Chem.* 145, 77–87. doi:10.1006/jssc.1999.8220

Lang, M., Zhang, F. X., Ewing, R. C., Lian, J., Trautmann, C., and Wang, Z. (2009). Structural Modifications of Gd2Zr2-xTixO7 Pyrochlore Induced by swift Heavy Ions: Disordering and Amorphization. *J. Mater. Res.* 24, 1322–1334. doi:10.1557/jmr.2009.0151

Lang, M., Zhang, F., Zhang, J., Wang, J., Lian, J., Weber, W. J., et al. (2010). Review of A2B2O7 Pyrochlore Response to Irradiation and Pressure. *Nucl. Instr. Methods Phys. Res. Section B: Beam Interactions Mater. Atoms* 268, 2951–2959. doi:10.1016/j.nimb.2010.05.016

Lee, E., Blauwkamp, J., Castro, F. C., Wu, J., Dravid, V. P., Yan, P., et al. (2016). Exploring Lithium-Cobalt-Nickel Oxide Spinel Electrodes for ≥3.5 V Li-Ion Cells. *ACS Appl. Mater. Inter.* 8, 27720–27729. doi:10.1021/acsami.6b09073

Lee, T. A., and Navrotsky, A. (2004). Enthalpy of Formation of Cubic Yttria-Stabilized Hafnia. *J. Mater. Res.* 19, 1855–1861. doi:10.1557/JMR.2004.0234

Lee, T. A., Navrotsky, A., and Molodetsky, I. (2003). Enthalpy of Formation of Cubic Yttria-Stabilized Zirconia. *J. Mater. Res.* 18, 908–918. doi:10.1557/JMR.2003.0125

Lian, J., Chen, J., Wang, L. M., Ewing, R. C., Farmer, J. M., Boatner, L. A., et al. (2003a). Radiation-induced Amorphization of Rare-Earth Titanate Pyrochlores. *Phys. Rev. B* 68, 134107. doi:10.1103/PhysRevB.68.134107

Lian, J., Helean, K. B., Kennedy, B. J., Wang, L. M., Navrotsky, A., and Ewing, R. C. (2006). Effect of Structure and Thermodynamic Stability on the Response of Lanthanide Stannate Pyrochlores to Ion Beam Irradiation. *J. Phys. Chem. B* 110, 2343–2350. doi:10.1021/jp055266c

Lian, J., Wang, L., Chen, J., Sun, K., Ewing, R. C., Matt Farmer, J., et al. (2003b). The Order-Disorder Transition in Ion-Irradiated Pyrochlore. *Acta Materialia* 51, 1493–1502. doi:10.1016/S1359-6454(02)00544-X10.1016/s1359-6454(02)00544-x

Lian, J., Wang, L. M., Haire, R. G., Helean, K. B., and Ewing, R. C. (2004). Ion Beam Irradiation in La2Zr2O7-Ce2Zr2O7 Pyrochlore. *Nucl. Instr. Methods Phys. Res. Section B: Beam Interactions Mater. Atoms* 218, 236–243. doi:10.1016/j.nimb.2004.01.007

Lian, J., Zu, X. T., Kutty, K. V. G., Chen, J., Wang, L. M., and Ewing, R. C. (2002). Ion-irradiation-induced Amorphization ofLa2Zr2O7pyrochlore. *Phys. Rev. B* 66, 54108. doi:10.1103/PhysRevB.66.054108

Linton, J., Navrotsky, A., and Fei, Y. (1998). The Thermodynamics of Ordered Perovskites on the CaTiO3- FeTiO3 Join. *Phys. Chem. Min.* 25, 591–596. doi:10.1007/s002690050152

Liu, Y., Withers, R. L., and Norén, L. (2004). The Pyrochlore to 'defect Fluorite' Transition in the Y2(ZryTi1−y)2O7 System and its Underlying crystal Chemistry. *J. Solid State. Chem.* 177, 4404–4412. doi:10.1016/j.jssc.2004.09.014

Magneli, A. (1956). Some Aspects of the crystal Chemistry of Oxygen Compounds of Molybdenum and Tungsten Containing Structural Elements of ReO3 or Perovskite Type. *J. Inorg. Nucl. Chem.* 2, 330–339. doi:10.1016/0022-1902(56)80086-9

Malíčková, I., Bačík, P., Fridrichová, J., Hanus, R., Illášová, L., Štubňa, J., et al. (2021). Optical and Luminescence Spectroscopy of Varicolored Gem Spinel from Mogok, Myanmar and Lục Yên. *Vietnam. Minerals.* 11 (2), 169. doi:10.3390/min11020169

Mandal, B. P., Banerji, A., Sathe, V., Deb, S. K., and Tyagi, A. K. (2007). Order-disorder Transition in Nd2−yGdyZr2O7 Pyrochlore Solid Solution: An X-ray Diffraction and Raman Spectroscopic Study. *J. Solid State. Chem.* 180, 2643–2648. doi:10.1016/j.jssc.2007.07.007

Mandal, B. P., Garg, N., Sharma, S. M., and Tyagi, A. K. (2006). Preparation, XRD and Raman Spectroscopic Studies on New Compounds RE2Hf2O7 (RE=Dy, Ho, Er, Tm, Lu, Y): Pyrochlores or Defect-Fluorite? *J. Solid State. Chem.* 179, 1990–1994. doi:10.1016/j.jssc.2006.03.036

Mandal, B. P., and Tyagi, A. K. (2007). Preparation and High Temperature-XRD Studies on a Pyrochlore Series with the General Composition Gd2−xNdxZr2O7. *J. Alloys Comp.* 437, 260–263. doi:10.1016/j.jallcom.2006.07.093

Maram, P. S., Ushakov, S. V., Weber, R. J. K., Benmore, C. J., and Navrotsky, A. (2015). *In Situ* diffraction from Levitated Solids under Extreme Conditions - Structure and thermal Expansion in the Eu2O3 - ZrO2 System. *J. Am. Ceram. Soc.* 98, 1292–1299. doi:10.1111/jace.13422

Maram, P. S., Ushakov, S. V., Weber, R. J. K., Benmore, C. J., and Navrotsky, A. (2018). Probing Disorder in Pyrochlore Oxides Using *In Situ* Synchrotron Diffraction from Levitated Solids-A Thermodynamic Perspective. *Sci. Rep.* 8. doi:10.1038/s41598-018-28877-x

Marlton, F. P., Zhang, Z., Zhang, Y., Proffen, T. E., Ling, C. D., and Kennedy, B. J. (2021). Lattice Disorder and Oxygen Migration Pathways in Pyrochlore and Defect-Fluorite Oxides. *Chem. Mater.* 33, 1407–1415. doi:10.1021/acs.chemmater.0c04515

Martel, L., Naji, M., Popa, K., Vigier, J.-F., and Somers, J. (2017). Fingerprint of Local Disorder in Long Range Ordered Isometric Pyrochlores. *Sci. Rep.* 7, 12269. doi:10.1038/s41598-017-12544-8

Matrosova, E. A., Bobrov, A. V., Bindi, L., Pushcharovsky, D. Y., and Irifune, T. (2020). Titanium-rich Phases in the Earth's Transition Zone and Lower Mantle: Evidence from Experiments in the System MgO - SiO2 -TiO2(±Al2O3) at 10-24 GPa and 1600 °C. *Lithos* 366–367, 105539. doi:10.1016/j.lithos.2020.105539

Matsuhira, K., Wakeshima, M., Nakanishi, R., Yamada, T., Nakamura, A., Kawano, W., et al. (2007). Metal-Insulator Transition in Pyrochlore Iridates Ln2Ir2O7 (Ln = Nd, Sm, and Eu). *J. Phys. Soc. Jpn.* 76, 043706–043727. doi:10.1143/JPSJ.76.043706

McCaugherty, S., and Grosvenor, A. P. (2019). Low-temperature Synthesis of CaZrTi2O7 Zirconolite-type Materials Using Ceramic, Coprecipitation, and Sol-Gel Methods. *J. Mater. Chem. C* 7, 177–187. doi:10.1039/c8tc04560g

Meldrum, A., White, C. W., Keppens, V., Boatner, L. A., and Ewing, R. C. (2001). Irradiation-induced Amorphization ofCd2Nb2O7pyrochlore. *Phys. Rev. B* 63, 104109. doi:10.1103/PhysRevB.63.104109

Mielcewczyk-Gryn, A., and Navrotsky, A. (2015). Enthalpies of Formation of Rare Earth Niobates. *Re3nbo7. Am. Mineral.* 100, 1578–1583. doi:10.2138/am-2015-5210

Minervini, L., Grimes, R. W., and Sickafus, K. E. (2000). Disorder in Pyrochlore Oxides. *J. Am. Ceram. Soc.* 83, 1873–1878. doi:10.1111/j.1151-2916.2000.tb01484.x

Momma, K., and Izumi, F. (2008). VESTA: A Three-Dimensional Visualization System for Electronic and Structural Analysis. *J. Appl. Crystallogr.* 41, 653–658. doi:10.1107/S0021889808012016

Moran, R. F., McKay, D., Tornstrom, P. C., Aziz, A., Fernandes, A., Grau-Crespo, R., et al. (2019). Ensemble-Based Modeling of the NMR Spectra of Solid Solutions: Cation Disorder in Y2(Sn,Ti)2O7. *J. Am. Chem. Soc.* 141, 17838–17846. doi:10.1021/jacs.9b09036

Moreno, K. J., Fuentes, A. F., Maczka, M., Hanuza, J., and Amador, U. (2006a). Structural Manipulation of Pyrochlores: Thermal Evolution of Metastable Gd2(Ti1−yZry)2O7 Powders Prepared by Mechanical Milling. *J. Solid State. Chem.* 179, 3805–3813. doi:10.1016/j.jssc.2006.08.023

Moreno, K. J., Guevara-Liceaga, M. A., Fuentes, A. F., García-Barriocanal, J., León, C., and Santamaría, J. (2006). Room-temperature Synthesis and Conductivity of the Pyrochlore Type Dy2(Ti1−yZry)2O7 ($0 \leqslant y \leqslant 1$) Solid Solution. *J. Solid State. Chem.* 179, 928–934. doi:10.1016/j.jssc.2005.12.015

Moshopoulou, E. G. (2004). Superconductivity in the Spinel Compound LiTi2O4. *J. Am. Ceram. Soc.* 82 (12), 3317–3320. doi:10.1111/j.1151-2916.1999.tb02245.x

Mouta, R., Silva, R. X., and Paschoal, C. W. A. (2013). Tolerance Factor for Pyrochlores and Related Structures. *Acta Crystallogr. Sect. B* 69, 439–445. doi:10.1107/S2052519213020514

Murphy, D. W., Greenblatt, M., Zahurak, S. M., Cava, R. J., Waszczak, J. V., Hull, G. W., et al. (1982). Lithium Insertion in Anatase: a New Route to the Spinel LiTi2O4. *Rev. Chim. Minor.* 19, 441.

Murphy, D. W., Sunshine, S., van Dover, R. B., Cava, R. J., Batlogg, B., Zahurak, S. M., et al. (1987). New Superconducting Cuprate Perovskites. *Phys. Rev. Lett.* 58, 1888–1890. doi:10.1103/PhysRevLett.58.1888

Nakamura, A., Doi, Y., and Hinatsu, Y. (2011). Magnetic Properties of Barium Uranate Ba2U2O7. *J. Solid State. Chem.* 184, 531–535. doi:10.1016/j.jssc.2010.12.023

Nanot, M., Queyroux, F., Gilles, J.-C., Carpy, A., and Galy, J. (1974). Phases multiples dans les systèmes Ca2Nb2O7-NaNbO3 et La2Ti2O7CaTiO3: Les séries homologues de formule AnBnO3n+2. *J. Solid State. Chem.* 11, 272–284. doi:10.1016/S0022-4596(74)80032-0

Navrostky, A., and Kleppa, O. J. (1967). The Thermodynamics of Cation Distributions in Simple Spinels. *J. Inorg. Nucl. Chem.* 29 (11), 2701–2714. doi:10.1016/0022-1902(67)80008-3

Navrotsky, A. (1994). *Physics and Chemistry of Earth Materials*. Cambridge University Press. doi:10.1017/cbo9781139173650

Navrotsky, A., and Ushakov, S. V. (2005). "Thermodynamics of Oxide Systems Relevant to Alternative Gate Dielectrics," in *Materials Fundamentals of Gate Dielectrics,"*. Editors A. A. Demkov and A. Navrotsky (Dordrecht: Springer Netherlands), 57–108.

Navrotsky, A., and Weidner, D. J. (1989). 45. American Geophysical Union, 146.Perovskite: A Structure of Great Interest to Geophysics and Materials Science*Geophys. Monogr. Ser.*

Ndione, P. F., Shi, Y., Stevanovic, V., Lany, S., Zakutayev, A., Parilla, P. A., et al. (2014). Control of the Electrical Properties in Spinel Oxides by Manipulating the Cation Disorder. *Adv. Funct. Mater.* 24 (5), 610–618. doi:10.1002/adfm.201302535

Nenoff, T. M., Rademacher, D. X., Rodriguez, M. A., Garino, T. J., Subramani, T., and Navrotsky, A. (2021). Structure-property and Thermodynamic Relationships in Rare Earth (Y, Eu, Pr) Iridate Pyrochlores. *J. Solid State. Chem.* 299, 122163. doi:10.1016/j.jssc.2021.122163

Nishikawa, S. (1915). Structure of Some Crystals of the Apinel Group. *Proc. Math. Phys. Soc. Jpn.* 8, 199–209. doi:10.11429/ptmps1907.8.7_199

O'Quinn, E. C., Sickafus, K. E., Ewing, R. C., Baldinozzi, G., Neuefeind, J. C., Tucker, M. G., et al. (2020). Predicting Short-Range Order and Correlated Phenomena in Disordered Crystalline Materials. *Sci. Adv.* 6, eabc2758. doi:10.1126/sciadv.abc2758

Orman, H. J., and Wiseman, P. J. (1984). Cobalt(III) Lithium Oxide, CoLiO2: Structure Refinement by Powder Neutron Diffraction. *Acta Crystallogr. C* 40, 12–14. doi:10.1107/S0108270184002833

Ovsyannikov, S. V., Abakumov, A. M., Tsirlin, A. A., Schnelle, W., Egoavil, R., Verbeeck, J., et al. (2013). Perovskite-like Mn2O3: A Path to New Manganites. *Angew. Chem. Int. Ed.* 52, 1494–1498. doi:10.1002/anie.201208553

Panghal, A., Kumar, Y., Kulriya, P. K., Shirage, P. M., and Singh, N. L. (2021). Atomic Order-Disorder Engineering in the La2Zr2O7 Pyrochlore under Low Energy Ion Irradiation. *Ceramics Int.* 47, 20248–20259. doi:10.1016/j.ceramint.2021.04.032

Patel, M. K., Vijayakumar, V., Avasthi, D. K., Kailas, S., Pivin, J. C., Grover, V., et al. (2008a). Effect of swift Heavy Ion Irradiation in Pyrochlores. *Nucl. Instr. Methods Phys. Res. Section B: Beam Interactions Mater. Atoms* 266, 2898–2901. doi:10.1016/j.nimb.2008.03.135

Patel, M. K., Vijayakumar, V., Kailas, S., Avasthi, D. K., Pivin, J. C., and Tyagi, A. K. (2008b). Structural Modifications in Pyrochlores Caused by Ions in the Electronic Stopping Regime. *J. Nucl. Mater.* 380, 93–98. doi:10.1016/j.jnucmat.2008.07.007

Patrakeev, M. V., Kharton, V. V., Bakhteeva, Y. A., Shaula, A. L., Leonidov, I. A., Kozhevnikov, V. L., et al. (2006). Oxygen Nonstoichiometry and Mixed Conductivity of SrFe1−xO3−δ (M=Al, Ga): Effects of B-Site Doping. *Solid State. Sci.* 8, 476–487. doi:10.1016/j.solidstatesciences.2006.01.006

Paul, B., Singh, K., Jaroń, T., Roy, A., and Chowdhury, A. (2016). Structural Properties and the Fluorite-Pyrochlore Phase Transition in La 2 Zr 2 O 7 : The Role of Oxygen to Induce Local Disordered States. *J. Alloys Comp.* 686, 130–136. doi:10.1016/j.jallcom.2016.05.347

Perriot, R., Dholabhai, P. P., and Uberuaga, B. P. (2016). The Role of Surfaces, Chemical Interfaces, and Disorder on Plutonium Incorporation in Pyrochlores. *Phys. Chem. Chem. Phys.* 18, 22852–22863. doi:10.1039/C6CP03543D

Pilania, G., Puchala, B., and Uberuaga, B. P. (2019). Distortion-stabilized Ordered Structures in A2BB'O7 Mixed Pyrochlores. *Npj Comput. Mater.* 5, 7. doi:10.1038/s41524-018-0144-1

Ponnilavan, V., Venkatesan, K., Nandha Kumar, P., and Kannan, S. (2019). Discrete Crystallization of Fluorite and Subsequent Pyrochlore Phase Transitions in Dy2Zr2O7 Facilitated by Ti4+ Additions. *Mater. Chem. Phys.* 236, 121788. doi:10.1016/j.matchemphys.2019.121788

Popov, V. V., Menushenkov, A. P., Ivanov, A. A., Yastrebtsev, A. A., Gaynanov, B. R., d'Acapito, F., et al. (2020). A XAFS Investigation of Amorphous-To-Crystalline and Fluorite-To-Pyrochlore Phase Transitions in Ln2M2O7 (Ln = Gd, Tb, Dy; M = Ti, Zr). *Radiat. Phys. Chem.* 175, 108469. doi:10.1016/j.radphyschem.2019.108469

Popov, V. V., Menushenkov, A. P., Yaroslavtsev, A. A., Zubavichus, Y. V., Gaynanov, B. R., Yastrebtsev, A. A., et al. (2016). Fluorite-pyrochlore Phase Transition in Nanostructured Ln2Hf2O7 (Ln = La-Lu). *J. Alloys Comp.* 689, 669–679. doi:10.1016/j.jallcom.2016.08.019

Prado, F., Grunbaum, N., Caneiro, A., and Manthiram, A. (2004). Effect of La3+ Doping on the Perovskite-To-Brownmillerite Transformation in Sr1−xLaxCo0.8Fe0.2O3−δ ($0 \leq x \leq 0.4$). *Solid State Ionics* 167, 147–154. doi:10.1016/j.ssi.2003.12.006

Prasanna, T. R. S., and Navrotsky, A. (1994). Energetics in the Brownmillerite-Perovskite Pseudobinary Ca2Fe2O5-CaTiO3. *J. Mater. Res.* 12, 3121–3124. doi:10.1557/JMR.1994.3121

Putnam, R. L., Navrotsky, A., Woodfield, B. F., Boerio-Goates, J., and Shapiro, J. L. (1999a). Thermodynamics of Formation for Zirconolite (CaZrTi2O7) fromT=298.15 K toT=1500 K. *The J. Chem. Thermodynamics* 31, 229–243. doi:10.1006/jcht.1998.0445

Putnam, R. L., Navrotsky, A., Woodfield, B. F., Shapiro, J. L., Stevens, R., and Boerio-Goates, J. (1999b). Thermochemistry of Hf-Zirconolite, CaHf Ti2O7. *MRS Proc.* 556, 11. doi:10.1557/PROC-556-11

Radha, A. V., Ushakov, S. V., and Navrotsky, A. (2009). Thermochemistry of Lanthanum Zirconate Pyrochlore. *J. Mater. Res.* 24, 3350–3357. doi:10.1557/jmr.2009.0401

Radhakrishnan, A. N., Rao, P. P., Linsa, K. S. M., Deepa, M., and Koshy, P. (2011). Influence of Disorder-To- Order Transition on Lattice thermal Expansion and Oxide Ion Conductivity in (CaxGd1−x)2(Zr1−xMx)2O7 Pyrochlore Solid Solutions. *Dalt. Trans.* 40, 3839–3848. doi:10.1039/C0DT01688H

Rao, C. N. R., and Raveau, B. (1989). Structural Aspects of High-Temperature Cuprate Superconductors. *Acc. Chem. Res.* 22, 106–113.

Rautama, E.-L., Caignaert, V., Boullay, P., Kundu, A. K., Pralong, V., Karppinen, M., et al. (2009). New Member of the "112" Family, LaBaCo2O5.5: Synthesis, Structure, and Magnetism. *Chem. Mater.* 21 (1), 102–109. doi:10.1021/cm8021775

Rittman, D. R., Turner, K. M., Park, S., Fuentes, A. F., Park, C., Ewing, R. C., et al. (2017a). Strain Engineered Pyrochlore at High Pressure. *Sci. Rep.* 7, 1–10. doi:10.1038/s41598-017-02637-9

Rittman, D. R., Turner, K. M., Park, S., Fuentes, A. F., Yan, J., Ewing, R. C., et al. (2017b). High-pressure Behavior of A2B2O7 Pyrochlore (A=Eu, Dy; B=Ti, Zr). *J. Appl. Phys.* 121, 045902. doi:10.1063/1.4974871

Rossen, E., Reimers, J. N., and Dahn, J. R. (1993). Synthesis and Electrochemistry of Spinel LT-LiCoO2. *Solid State Ionics* 62, 53–60. doi:10.1016/0167-2738(93)90251-W

Rüdorff, W., and Becker, H. (1954). Notizen: Die Strukturen von LiVO2, NaVO2, LiCrO2 und NaCrO2. *Z. Naturforsch. B.* 9, 614–615. doi:10.1515/znb-1954-0911

Rushton, M. J. D., Grimes, R. W., Stanek, C. R., and Owens, S. (2004). Predicted Pyrochlore to Fluorite Disorder Temperature for A2Zr2O7 Compositions. *J. Mater. Res.* 19, 1603–1604. doi:10.1557/JMR.2004.0231

Salamat, A., McMillan, P. F., Woodhead, K., Hector, A. L., Garbarino, G., et al. (2013). Structural Transformations and Disordering in Zirconolite (CaZrTi2O7) at High Pressure. *Inorg. Chem.* 52, 1550–1558. doi:10.1021/ic302346g

Sanjuán, M. L., Guglieri, C., Díaz-Moreno, S., Aquilanti, G., Fuentes, A. F., Olivi, L., et al. (2011). Raman and X-ray Absorption Spectroscopy Study of the Phase Evolution Induced by Mechanical Milling and thermal Treatments inR2Ti2O7pyrochlores. *Phys. Rev. B* 84, 104207. doi:10.1103/PhysRevB.84.104207

Saradhi, M. P., Ushakov, S. V., and Navrotsky, A. (2012). Fluorite-pyrochlore Transformation in Eu2Zr2O7-Direct Calorimetric Measurement of Phase Transition, Formation and Surface Enthalpies. *RSC Adv.* 2, 3328–3334. doi:10.1039/C2RA00727D

Sayed, F. N., Grover, V., Bhattacharyya, K., Jain, D., Arya, A., Pillai, C. G. S., et al. (2011). Sm2−xDyxZr2O7Pyrochlores: Probing Order−Disorder Dynamics and Multifunctionality. *Inorg. Chem.* 50, 2354–2365. doi:10.1021/ic200108u

Shamblin, J., Feygenson, M., Neuefeind, J., Tracy, C. L., Zhang, F., Finkeldei, S., et al. (2016a). Probing Disorder in Isometric Pyrochlore and Related Complex Oxides. *Nat. Mater* 15, 507–511. doi:10.1038/nmat4581

Shamblin, J., Tracy, C. L., Ewing, R. C., Zhang, F., Li, W., Trautmann, C., et al. (2016b). Structural Response of Titanate Pyrochlores to swift Heavy Ion Irradiation. *Acta Materialia* 117, 207–215. doi:10.1016/j.actamat.2016.07.017

Shamblin, J., Tracy, C. L., Palomares, R. I., O'Quinn, E. C., Ewing, R. C., Neuefeind, J., et al. (2018). Similar Local Order in Disordered Fluorite and Aperiodic Pyrochlore Structures. *Acta Materialia* 144, 60–67. doi:10.1016/j.actamat.2017.10.044

Sherrod, R., O'Quinn, E. C., Gussev, I. M., Overstreet, C., Neuefeind, J., and Lang, M. K. (2021). Comparison of Short-Range Order in Irradiated Dysprosium Titanates. *Npj Mater. Degrad.* 5, 19. doi:10.1038/s41529-021-00165-6

Shin, S., Yonemura, M., and Ikawa, H. (1978). Order-disorder Transition of Sr2Fe2O5 from Brownmillerite to Perovskite Structure at an Elevated Temperature. *Mater. Res. Bull.* 13, 1017–1021. doi:10.1016/0025-5408(78)90166-610.1016/0025-5408(78)90166-6

Shlyakhtina, A. V., Shcherbakova, L. G., Knotko, A. V., and Steblevskii, A. V. (2004). Study of the Fluorite?pyrochlore?fluorite Phase Transitions in Ln2Ti2O7 (Ln=Lu, Yb, Tm). *J. Solid State. Electrochem.* 8, 661–667. doi:10.1007/s10008-003-0491-8

Shlyakhtina, A. V., and Shcherbakova, L. G. (2011). Polymorphism and High-Temperature Conductivity of Ln2M2O7 (Ln=Sm–Lu; M=Ti, Zr, Hf) Pyrochlores. *Solid State Ionics* 192, 200–204. doi:10.1016/j.ssi.2010.07.013

Simeone, D., Thorogood, G. J., Huo, D., Luneville, L., Baldinozzi, G., Petricek, V., et al. (2017). Intricate Disorder in Defect Fluorite/pyrochlore: A concord of Chemistry and Crystallography. *Sci. Rep.* 7, 1–7. doi:10.1038/s41598-017-02787-w

Simoncic, P., and Navrotsky, A. (2007a). Energetics of Rare-Earth-Doped Hafnia. *J. Mater. Res.* 22, 876–885. doi:10.1557/jmr.2007.0133

Simoncic, P., and Navrotsky, A. (2007b). Systematics of Phase Transition and Mixing Energetics in Rare Earth, Yttrium, and Scandium Stabilized Zirconia and Hafnia. *J. Am. Ceram. Soc.* 90, 2143–2150. doi:10.1111/j.1551-2916.2007.01678.x

Smyth, D. M. (1985). Defects and Order in Perovskite-Related Oxides. *Annu. Rev. Mater. Sci.* 15, 329–357. doi:10.1146/annurev.ms.15.080185.001553

Solomon, J. M., Asta, M., Shamblin, J., Lang, M., Shamblin, J., and Navrotsky, A. (2016). Chemical Ordering in Substituted Fluorite Oxides: a Computational Investigation of Ho2Zr2O7 and RE2Th2O7 (RE=Ho, Y, Gd, Nd, La). *Sci. Rep.* 6, 38772. doi:10.1038/srep38772

Song, Q., and Zhang, Z. J. (2004). Shape Control and Associated Magnetic Properties of Spinel Cobalt Ferrite Nanocrystals. *J. Am. Chem. Soc.* 126, 6164–6168. doi:10.1021/ja049931r

Song, Z., and Liu, Q. (2020). Tolerance Factor, Phase Stability and Order–Disorder of the Pyrochlore Structure. *Inorg. Chem. Front.* 7, 1583–1590. doi:10.1039/D0QI00016G

Stein, F., Palm, M., and Sauthoff, G. (2004). Structure and Stability of Laves Phases. Part I. Critical Assessment of Factors Controlling Laves Phase Stability. *Intermetallics* 12 (7-9), 713–720. doi:10.1016/j.intermet.2004.02.010

Stølen, S., Bakken, E., and Mohn, C. E. (2006). Oxygen-deficient Perovskites: Linking Structure, Energetics and Ion Transport. *Phys. Chem. Chem. Phys.* 8, 429–447. doi:10.1039/B512271F

Subramani, T., Baker, J., Xu, H., and Navrotsky, A. (2020). Synthesis, Characterization, and Enthalpies of Formation of Uranium Substituted Zirconolites. *ACS Earth Space Chem.* 4, 1878–1887. doi:10.1021/acsearthspacechem.0c00182

Subramani, T., and Navrotsky, A. (2019). Energetics of Formation and Disordering in Rare Earth Weberite RE3TaO7 Materials. *Inorg. Chem.* 58, 16126–16133. doi:10.1021/acs.inorgchem.9b02675

Subramanian, M. A., Aravamudan, G., and Rao, G. V. S. (1983). Oxide Pyrochlores: a Review. *Chemistry* 2, 55–143. doi:10.1016/0079-6786(83)90001-8

Szuromi, P., and Grocholski, B. (2017). Natural and Engineered Perovskites. *Science* 358, 732–733. doi:10.1126/science.358.6364.732

Tilley, R. J. D. (2016). *Perovskites: Structure-Property Relationships*. Chichester: John Wiley & Sons.

Tofield, B. C., Greaves, C., and Fender, B. E. F. (1975). The SrFeO2.5/SrFeO3.0 System. Evidence of a New Phase Sr4Fe4O11 (SrFeO2.75). *Mater. Res. Bull.* 10, 737–745. doi:10.1016/0025-5408(75)90059-8

Turner, K. M., Rittman, D. R., Heymach, R. A., Tracy, C. L., Turner, M. L., Fuentes, A. F., et al. (2017). Pressure-induced Structural Modifications of Rare-Earth Hafnate Pyrochlore. *J. Phys. Condens. Matter* 29, 255401. doi:10.1088/1361-648X/aa7148

Urban, A., Abdellahi, A., Dacek, S., Artrith, N., and Ceder, G. (2017). Electronic-structure Origin of Cation Disorder in Transition-Metal Oxides. *Phys. Rev. Lett.* 119, 176402. doi:10.1103/PhysRevLett.119.176402

Urban, A., Lee, J., and Ceder, G. (2014). The Configurational Space of Rocksalt-type Oxides for High-Capacity Lithium Battery Electrodes. *Adv. Energ. Mater.* 4, 1400478. doi:10.1002/aenm.201400478

Ushakov, S. V., Navrotsky, A., Tangeman, J. A., and Helean, K. B. (2007). Energetics of Defect Fluorite and Pyrochlore Phases in Lanthanum and Gadolinium Hafnates. *J. Am. Ceram. Soc.* 90, 1171–1176. doi:10.1111/j.1551-2916.2007.01592.x

Vance, E. R., Begg, B. D., Day, R. A., and Ball, C. J. (1994). Zirconolite-rich Ceramics for Actinide Wastes. *MRS Proc.* 353, 767. doi:10.1557/PROC-353-767

Vanderah, T. A., Levin, I., and Lufaso, M. W. (2005). An Unexpected crystal-chemical Principle for the Pyrochlore Structure. *Eur. J. Inorg. Chem.* 2005, 2895–2901. doi:10.1002/ejic.200500234

Vasala, S., and Karppinen, M. (2015). A2B′B″O6 Perovskites: A Review. *Prog. Solid State. Chem.* 43, 1–36. doi:10.1016/j.progsolidstchem.2014.08.001

Verwey, E. J., Haayman, P. W., and Romeijn, F. C. (1947). Physical Properties and Cation Arrangement of Oxides with Spinel Structures II. Electronic Conductivity. *J. Chem. Phys.* 15, 181–187. doi:10.1063/1.174646410.1063/1.1746466174

Verwey, E. J. W., and Heilmann, E. L. (1947). Physical Properties and Cation Arrangement of Oxides with Spinel Structures I. Cation Arrangement in Spinels. *J. Chem. Phys.* 15, 174–180. doi:10.1063/1.1746464

Voskanyan, A. A., Abramchuk, M., and Navrotsky, A. (2020). Entropy Stabilization of TiO2-Nb2O5 Wadsley-Roth Shear Phases and Their Prospects for Lithium-Ion Battery Anode Materials. *Chem. Mater.* 32, 5301–5308. doi:10.1021/acs.chemmater.0c01553

Voskanyan, A. A., and Navrotsky, A. (2021). Shear Pleasure: the Structure, Formation, and Thermodynamics of Crystallographic Shear Phases. *Annu. Rev. Mater. Res.* 51, 521–540. doi:10.1146/annurev-matsci-070720-013445

Wadsley, A. D. (1958). "Modern Structural Inorganic chemistry." Liversidge Research Lecture. *J. Proc. Roy. Soc. N.S.W.* 92, 25–35.

Wakeshima, M., Nishimine, H., and Hinatsu, Y. (2004). Crystal Structures and Magnetic Properties of Rare Earth Tantalates RE3TaO7(RE = Rare Earths). *J. Phys. Condens. Matter* 16, 4103–4120. doi:10.1088/0953-8984/16/23/025

Wang, J., Zhang, F., Lian, J., Ewing, R. C., and Becker, U. (2011). Energetics and Concentration of Defects in Gd2Ti2O7 and Gd2Zr2O7 Pyrochlore at High Pressure. *Acta Materialia* 59, 1607–1618. doi:10.1016/j.actamat.2010.11.025

Wang, S. X., Wang, L. M., Ewing, R. C., and Govindan Kutty, K. V. (1998). Ion Irradiation Effects for Two Pyrochlore Compositions: Gd2Ti2O7 and Gd2Zr207. *MRS Proc.* 540, 355. doi:10.1557/PROC-540-355

Wang, S. X., Wang, L. M., Ewing, R. C., Was, G. S., and Lumpkin, G. R. (1999). Ion Irradiation-Induced Phase Transformation of Pyrochlore and Zirconolite. *Nucl. Instr. Methods Phys. Res. Section B: Beam Interactions Mater. Atoms* 148, 704–709. doi:10.1016/S0168-583X(98)00847-7

Whittle, K. R., Hyatt, N. C., Smith, K. L., Margiolaki, I., Berry, F. J., Knight, K. S., et al. (2012). Combined Neutron and X-ray Diffraction Determination of Disorder in Doped zirconolite-2M. *Am. Mineral.* 97, 291–298. doi:10.2138/am.2012.3848

Willard, M. A., Nakamura, Y., Laughlin, D. E., and McHenry, M. E. (1999). Magnetic Properties of Ordered and Disordered Spinel-phase Ferrimagnets. *J. Am. Ceram. Soc.* 82 (12), 3342–3346. doi:10.1111/j.1151-2916.1999.tb02249.x

Winiarz, P., Mielewczyk-Gryń, A., Lilova, K., Wachowski, S., Subramani, T., Abramchuk, M., et al. (2020). Conductivity, Structure, and Thermodynamics of Y2Ti2O7-Y3NbO7 Solid Solutions. *Dalton Trans.* 49, 10839–10850. doi:10.1039/d0dt02156c

Wright, A. J., Wang, Q., Hu, C., Yeh, Y.-T., Chen, R., and Luo, J. (2021). Single-phase Duodenary High-Entropy Fluorite/pyrochlore Oxides with an Order-Disorder Transition. *Acta Materialia* 211, 116858. doi:10.1016/j.actamat.2021.116858

Wu, E. J., Tepesch, P. D., and Ceder, G. (1998). Size and Charge Effects on the Structural Stability of LiMO2 (M = Transition Metal) Compounds. *Philosophical Mag. B* 77, 1039–1047. doi:10.1080/13642819808206403

Wuensch, B., Eberman, K. W., Heremans, C., Ku, E. M., Onnerud, P., Yeo, E. M. E., et al. (2000). Connection between Oxygen-Ion Conductivity of Pyrochlore Fuel-Cell Materials and Structural Change with Composition and Temperature. *Solid State Ionics* 129, 111–133. doi:10.1016/S0167-2738(99)00320-310.1016/s0167-2738(99)00320-3

Wuensch, B. J., and Eberman, K. W. (2000). Order-disorder Phenomena in A2B2O7 Pyrochlore Oxides. *JOM* 52, 19–21. doi:10.1007/s11837-000-0155-4

Xiao, H. Y., Weber, W. J., Zhang, Y., Zu, X. T., and Li, S. (2015). Electronic Excitation Induced Amorphization in Titanate Pyrochlores: an Ab Initio Molecular Dynamics Study. *Sci. Rep.* 5, 8265. doi:10.1038/srep08265

Xie, Q.-R., Zhang, J., Yin, D.-M., Guo, Q.-X., and Li, N. (2015). Krypton Ion Irradiation-Induced Amorphization and Nano-crystal Formation in Pyrochlore Lu 2 Ti 2 O 7 at Room Temperature. *Chin. Phys. B* 24, 126103. doi:10.1088/1674-1056/24/12/126103

Xu, H., Navrotsky, A., Su, Y., and Balmer, M. L. (2005). Perovskite Solid Solutions along the NaNbO3–SrTiO3Join: Phase Transitions, Formation Enthalpies, and Implications for General Perovskite Energetics. *Chem. Mater.* 17, 1880–1886. doi:10.1021/cm047785i

Xu, H., Su, Y., Balmer, M. L., and Navrotsky, A. (2003). A New Series of Oxygen-Deficient Perovskites in the NaTixNb1-xO3-0.5x System: Synthesis, Crystal Chemistry, and Energetics. *Chem. Mater.* 15, 1872–1878. doi:10.1021/cm020963s

Yang, D., Xia, Y., Wen, J., Liang, J., Mu, P., Wang, Z., et al. (2017). Role of Ion Species in Radiation Effects of Lu2Ti2O7 Pyrochlore. *J. Alloys Comp.* 693, 565–572. doi:10.1016/j.jallcom.2016.09.227

Yudinsev, S. V., Lukinykh, A. N., Tomilin, S. V., Lizin, A. A., and Stefanovsky, S. V. (2009). Alpha-decay Induced Amorphization of Cm-Doped Gd2TiZrO7. *J. Nucl. Mater.* 385, 200–203. doi:10.1016/j.jnucmat.2008.09.036

Zhang, F. X., Lang, M., and Ewing, R. C. (2015). Atomic Disorder in Gd2Zr2O7 Pyrochlore. *Appl. Phys. Lett.* 106, 191902. doi:10.1063/1.4921268

Zhang, F. X., Lang, M., Liu, Z., and Ewing, R. C. (2010a). Pressure-Induced Disordering and Anomalous Lattice Expansion inLa2Zr2O7Pyrochlore. *Phys. Rev. Lett.* 105, 15503. doi:10.1103/PhysRevLett.105.015503

Zhang, F. X., Lang, M., Tracy, C., Ewing, R. C., Gregg, D. J., and Lumpkin, G. R. (2014). Incorporation of Uranium in Pyrochlore Oxides and Pressure-Induced Phase Transitions. *J. Solid State. Chem.* 219, 49–54. doi:10.1016/j.jssc.2014.07.011

Zhang, F. X., Lian, J., Becker, U., Wang, L. M., Hu, J., Saxena, S., et al. (2007). Structural Distortions and Phase Transformations in Sm2Zr2O7 Pyrochlore at High Pressures. *Chem. Phys. Lett.* 441, 216–220. doi:10.1016/j.cplett.2007.05.018

Zhang, F. X., Manoun, B., and Saxena, S. K. (2006). Pressure-induced Order-Disorder Transitions in Pyrochlore RE2Ti2O7 (RE=Y, Gd). *Mater. Lett.* 60, 2773–2776. doi:10.1016/j.matlet.2006.01.095

Zhang, F. X., Manoun, B., Saxena, S. K., and Zha, C. S. (2005). Structure Change of Pyrochlore Sm2Ti2O7 at High Pressures. *Appl. Phys. Lett.* 86, 181906. doi:10.1063/1.1925307

Zhang, F. X., and Saxena, S. K. (2005). Structural Changes and Pressure-Induced Amorphization in Rare Earth Titanates RE2Ti2O7 (RE: Gd, Sm) with Pyrochlore Structure. *Chem. Phys. Lett.* 413, 248–251. doi:10.1016/j.cplett.2005.07.094

Zhang, F. X., Wang, J. W., Lian, J., Lang, M. K., Becker, U., and Ewing, R. C. (2008). Phase Stability and Pressure Dependence of Defect Formation inGd2Ti2O7andGd2Zr2O7Pyrochlores. *Phys. Rev. Lett.* 100, 2–5. doi:10.1103/PhysRevLett.100.045503

Zhang, J., Lian, J., Fuentes, A. F., Zhang, F., Lang, M., Lu, F., et al. (2009). Enhanced Radiation Resistance of Nanocrystalline Pyrochlore Gd2(Ti0.65Zr0.35)2O7. *Appl. Phys. Lett.* 94, 243110. doi:10.1063/1.3155855

Zhang, J., Lian, J., Zhang, F., Wang, J., Fuentes, A. F., and Ewing, R. C. (2010b). Intrinsic Structural Disorder and Radiation Response of Nanocrystalline Gd2(Ti0.65Zr0.35)2O7 Pyrochlore. *J. Phys. Chem. C* 114, 11810–11815. doi:10.1021/jp103371j

Zhang, Z., Middleburgh, S. C., de los Reyes, M., Lumpkin, G. R., Kennedy, B. J., Blanchard, P. E. R., et al. (2013). Gradual Structural Evolution from Pyrochlore to Defect-Fluorite in Y2Sn2-xZrxO7: Average vs Local Structure. *J. Phys. Chem. C* 117, 26740–26749. doi:10.1021/jp408682r

Zhao, Q., Yan, Z., Chen, C., and Chen, J. (2017). Spinels: Controlled Preparation, Oxygenreduction/evolution Reaction Application, and beyond, *Chem. Rev.* 117, 10121–10211. doi:10.1021/acs.chemrev.7b00051

Zhou, H., and Wiebe, C. R. (2019). High-pressure Routes to New Pyrochlores and Novel Magnetism. *Inorganics* 7. doi:10.3390/inorganics7040049

Zhu, X., Guijarro, N., Liu, Y., Schouwink, P., Wells, R. A., Le Formal, F., et al. (2018). Spinel Structural Disorder Influences Solar-Water-Splitting Performance of ZnFe2 O4 Nanorod Photoanodes. *Adv. Mater.* 30, 1801612. doi:10.1002/adma.201801612

Conflict of Interest: The authors declare that the research was conducted in the absence of any commercial or financial relationships that could be construed as a potential conflict of interest.

Publisher's Note: All claims expressed in this article are solely those of the authors and do not necessarily represent those of their affiliated organizations, or those of the publisher, the editors, and the reviewers. Any product that may be evaluated in this article, or claim that may be made by its manufacturer, is not guaranteed or endorsed by the publisher.

frontiers in Chemistry

ORIGINAL RESEARCH
published: 06 September 2021
doi: 10.3389/fchem.2021.713368

Pyrochlore-Supergroup Minerals Nomenclature: An Update

Daniel Atencio *

Instituto de Geociências – Universidade de São Paulo, São Paulo, Brazil

The general formula of the pyrochlore-supergroup minerals is $A_2B_2X_6Y$. The mineral names are composed of two prefixes and one root name (identical to the name of the group). The first prefix refers to the dominant anion (or cation or H_2O or vacancy) of the dominant valence at the *Y*-site. The second prefix refers to the dominant cation of the dominant valence [or H_2O or vacancy] at the *A*-site. Thirty-one pyrochlore-supergroup mineral species are currently distributed into four groups [pyrochlore (*B* = Nb, *X* = O), microlite (*B* = Ta, *X* = O), roméite (*B* = Sb^{5+}, *X* = O), and elsmoreite (*B* = W, *X* = O)] and two unassigned members [hydrokenoralstonite (*B* = Al, *X* = F) and fluornatrocoulsellite (*B* = Mg, *X* = F)]. However, when the new nomenclature system of this supergroup was introduced (2010) only seven mineral species, namely, oxycalciopyrochlore, hydropyrochlore, hydroxykenomicrolite, oxystannomicrolite, oxystibiomicrolite, hydroxycalcioroméite, and hydrokenoelsmoreite, were valid. The seven species belong to the cubic crystal system and space group $Fd\bar{3}m$ and O is predominant in the *X* structural site. The 24 new mineral species described between 2010 and 2021 are cesiokenopyrochlore, fluorcalciopyrochlore, fluornatropyrochlore, hydrokenopyrochlore, hydroxycalciopyrochlore, hydroxynatropyrochlore, hydroxykenopyrochlore, hydroxymanganopyrochlore, hydroxyplumbopyrochlore, fluorcalciomicrolite, fluornatromicrolite, hydrokenomicrolite, hydroxycalciomicrolite, kenoplumbomicrolite, oxynatromicrolite, oxycalciomicrolite, oxybismutomicrolite, fluorcalcioroméite, hydroxyferroroméite, oxycalcioroméite, oxyplumboroméite, fluornatrocoulsellite, hydrokenoralstonite, and hydroxykenoelsmoreite. Among the new species, hydroxycalciomicrolite belongs to a different space group of the cubic system, i.e., $P4_232$. There are also some mineral species that crystallize in the trigonal system. Hydrokenoelsmoreite occurs as 3*C* ($Fd\bar{3}m$) and 6*R* ($R\bar{3}$) polytypes. Hydrokenomicrolite occurs as 3*C* ($Fd\bar{3}m$) and 3*R* ($R\bar{3}m$) polytypes, of which the latter corresponds to the discredited "parabariomicrolite." Fluornatrocoulsellite crystallizes as 3*R* ($R\bar{3}m$) polytype. Surely there are several new pyrochlore-supergroup minerals to be described.

Keywords: pyrochlore supergroup, nomenclature, pyrochlore group, microlite group, elsmoreite group, roméite group

OPEN ACCESS

Edited by:
Sarah C. Finkeldei, University of California, Irvine, United States

Reviewed by:
Xiaolong Zhu, Merck, United States
Brendan Kennedy, The University of Sydney, Australia

***Correspondence:**
Daniel Atencio
datencio@usp.br

Specialty section:
This article was submitted to Solid State Chemistry, a section of the journal Frontiers in Chemistry

Received: *22 May 2021*
Accepted: *06 August 2021*
Published: *06 September 2021*

Citation:
Atencio D (2021) Pyrochlore-Supergroup Minerals Nomenclature: An Update. Front. Chem. 9:713368. doi: 10.3389/fchem.2021.713368

INTRODUCTION

The nomenclature system currently valid for the pyrochlore supergroup was introduced by Atencio et al. (2010) to replace the one authored by Hogarth (1977). Subsequently, clarifications (Christy and Atencio, 2013), remarks (Hogarth, 2013), a response to the remarks (Atencio, 2013), and a paper on the incorporation of two minerals already known to the supergroup (Atencio et al., 2017) were published. When the new nomenclature system of this supergroup was introduced (Atencio et al., 2010), only seven mineral species, namely, oxycalciopyrochlore, hydropyrochlore, hydroxykenomicrolite, oxystannomicrolite, oxystibiomicrolite, hydroxycalcioroméite, and hydrokenoelsmoreite, were valid. Between 2010 and 2021, 24 new mineral species were described. The following text describes the nomenclature of pyrochlore-supergroup minerals. The nomenclature system has been updated to include the pyrochlore-supergroup minerals discovered in recent years, whose available information might be difficult for an interested reader to find. The representative minerals from each group are discussed in detail. All known minerals of the supergroup are listed in one place, so this text can be regarded as a kind of a digest of all natural species. There are two aims in compiling this data. The first is to enable a reader to identify both the chemical composition and source of a given mineral and the second is to enable the reader to identify the primary data associated with the mineral.

CRYSTALLOGRAPHY, CHEMISTRY, AND THE NOMENCLATURE SCHEME

The general formula of the pyrochlore-supergroup minerals is $A_2B_2X_6Y$. In this formula, *A* typically is a large [8]-coordinated cation with a radius of ~1.0 Å or a vacancy (□) but can also be H_2O. For structural reasons, *A* can be subdivided into constituents without lone-pair electrons (*e.g.*, Na, Ca), which occupy 16 d in $Fd\bar{3}m$, and stereoactive cations (e.g., Sb^{3+}), which occupy less symmetrical positions displaced slightly from 16d, e.g., 96 g. For the purpose of this nomenclature, no subdivision is made. The *A*-site therefore may host Na, Ca, Ag, Mn, Sr, Ba, Fe^{2+}, Pb^{2+}, Sn^{2+}, Sb^{3+}, Bi^{3+}, Y, Ce (and other *REE*), Sc, U, Th, □, or H_2O. *B* is a [6]-coordinated cation (site 16c), typically of high field-strength. This site thus may contain Ta, Nb, Ti^{4+}, Sb^{5+}, W, but also V^{5+}, Sn^{4+}, Zr, Hf, Fe^{3+}, Mg, Al, and Si. *X* typically is O but can include subordinate OH and F (site 48f). *Y* typically is an anion but can also be a vacancy, H_2O, or a very large (>>1.0 Å) monovalent cation (site 8b). Examples are OH^-, F, O, □, H_2O, K, Cs, and Rb. Displacements to 96g, 32e, and 192i positions were also located. See the basis for formula calculation in Atencio et al. (2010). Synthetic pyrochlores have a much more variable chemical composition than natural examples (Subramanian et al., 1983).

The mineral names are composed of two prefixes and one root name (identical to the name of the group). The first prefix refers to the dominant anion (or cation or H_2O or □) of the dominant valence at the *Y*-site. The second prefix refers to the dominant cation of the dominant valence [or H_2O or □] at the *A*-site. Where the first and second prefixes are equal, then only one prefix is applied ("hydropyrochlore," not "hydrohydropyrochlore"). The mineral groups are given in **Table 1**.

As a mineral group consists of two or more minerals (Mills et al., 2009), ralstonite and coulsellite cannot really be considered, for now, as mineral groups. Hydrokenoralstonite and fluornatrocoulsellite should be designated as unassigned members of the pyrochlore supergroup, because there is no other member to allow a group to be established.

Currently, there is no valid betafite-group mineral.

The seven species valid in 2010 belong to the cubic crystal system and space group $Fd\bar{3}m$. Among the new species, hydroxycalciomicrolite belongs to a different space group of the cubic system, i.e., $P4_232$. There are also some mineral species that crystallize in the trigonal system. Hydrokenoelsmoreite occurs as 3*C* ($Fd\bar{3}m$) and 6*R* ($R\bar{3}$) polytypes. Hydrokenomicrolite occurs as 3*C* ($Fd\bar{3}m$) and 3*R* ($R\bar{3}m$) polytypes, of which the latter corresponds to the discredited "parabariomicrolite." Fluornatrocoulsellite crystallizes as 3*R* ($R\bar{3}m$) polytype. The symmetry is lowered due to ordering on either A sites or B sites (Ercit et al., 1986; Rouse et al., 1998; Atencio, 2016; Mills et al., 2016; Andrade et al., 2017; Mills et al., 2017). The pyrochlore structure (**Figure 1**) is an essential building block for other minerals and mineral groups, such as alunite (Goreaud and Raveau, 1980) or pittongite (Grey et al., 2006).

TABLE 1 | Mineral groups of the pyrochlore supergroup.

Group	*B*	*X*
Elsmoreite	W^{6+}	O^{2-}
Pyrochlore	Nb^{5+}	O^{2-}
Microlite	Ta^{5+}	O^{2-}
Roméite	Sb^{5+}	O^{2-}
Betafite	Ti^{4+}	O^{2-}
Ralstonite	Al^{3+}	F^{1-}
Coulsellite	Mg^{2+}	F^{1-}

B: *the dominant cation of the dominant valence at the* B*-site.*
X: *the dominant anion of the dominant valence at the* X*-site.*

THE GROUPS AND SPECIES

Table 2 shows the species of the pyrochlore supergroup, except hydrokenoralstonite and fluornatrocoulsellite.

Following that, simplified formulae are given for the pyrochlore species. Note that subordinate components at the *A*, *B*, *X*, or *Y* sites have no nomenclatural significance and any of these could be replaced by "#", indicating an unspecified heterovalent species required for charge balance.

PYROCHLORE GROUP

Oxycalciopyrochlore (Atencio et al., 2010), $Ca_2Nb_2O_6O$, $Fd\bar{3}m$, *a* 10.356(2) Å, *V* 1110.6 (7) $Å^3$, first described by Černý et al. (1979)

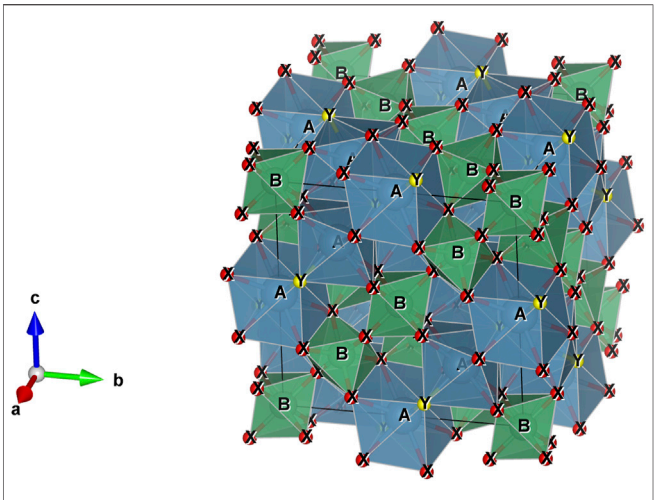

FIGURE 1 | Pyrochlore crystal structure drawn using VESTA 3 (Momma and Izumi, 2011).

TABLE 2 | Mineral species of the pyrochlore (P), microlite (M), roméite (R), elsmoreite (E), and betafite (B) groups. Blue: already valid in 2010; red: expected in 2010 and described later; brown: expected in 2010 but not yet described; green: not foreseen in 2010 but described later.

***A*↓ *Y*→**	**O**	**OH**	**F**	**□**	**H_2O**	**Cs**
□		P M E	P		P M E	P
H_2O					P M	
Na	M P	P	P M R			
Ca	P M R B	P M R	P M R			
Sr			P			
Fe^{2+}		R				
Mn^{2+}		P				
Sn^{2+}	M					
Pb	P R	P		P M		
Sb^{3+}	M					
Bi	M					
Y	P					
U	B					

as "stibiobetafite." The IMA number was not quoted in the original description of "stibiobetafite." Type locality: Věžná I pegmatite, Věžná, Žďár nad Sázavou District, Vysočina Region, Czech Republic.

Hydropyrochlore (Atencio et al., 2010), (H_2O, #)$_2Nb_2O_6(H_2O)$, *Fd*$\bar{3}$*m, a* 10.580 Å, *V* 1184.29 Å^3, first described by van Wambeke (1978) as "kalipyrochlore." The IMA number was not quoted in the original description of "kalipyrochlore." Type locality: Lueshe Mine, Bwito, Rutshuru Territory, North Kivu, DR Congo.

Cesiokenopyrochlore (Agakhanov et al., 2021), (□, #)$_2Nb_2O_6Cs$, *Fd*$\bar{3}$*m, a* 10.444(1) Å, *V* 1139.5(2) Å^3. IMA number: 2016-104. Type locality: Tetezantsio pegmatites, Tetezantsio-Andoabatokely Pegmatite Field, Andrembesoa, Betafo, Vakinankaratra, Madagascar.

Fluorcalciopyrochlore (Li et al., 2016), (Ca, #)$_2Nb_2O_6F$, *Fd*$\bar{3}$*m, a* 10.4164(9) Å, *V* 1130.19 Å^3. IMA number: 2013-055. Type locality: Bayan Obo deposit (Bayun-Obo deposit; Baiyunebo deposit), Bayan Obo, Bayan Obo mining district, Baotou City (Baotou Prefecture), Inner Mongolia, China.

Fluornatropyrochlore (Jingwu et al., 2015), (Na, #)$_2Nb_2O_6F$, *Fd*$\bar{3}$*m, a* 10. 5,053(10) Å, *V* 1159.4 Å^3. IMA number: 2013-056. Type locality: Boziguoer intrusion, Baicheng Co. (Bay Co.), Akesu Prefecture (Aksu Prefecture; Aqsu Prefecture), Xinjiang, China.

Hydrokenopyrochlore (Biagioni et al., 2018), (□, #)$_2Nb_2O_6(H_2O)$, *Fd*$\bar{3}$*m, a* 10.4887(8) Å, *V* 1153.9 Å^3. IMA number: 2017-005. Type locality: Antandrokomby pegmatite, Manandona Valley, Sahatsiho Ambohimanjaka, Ambositra, Amoron'i Mania, Madagascar.

Hydroxycalciopyrochlore (Yang et al., 2014), (Ca, #)$_2Nb_2O_6(OH)$, *Fd*$\bar{3}$*m, a* 10.381(4) Å, *V* 1118.7 Å^3. IMA number: 2011-026. Type locality: Maoniuping Mine, Mianning County, Liangshan Yi, Sichuan, China.

Hydroxynatropyrochlore (Ivanyuk et al., 2019), (Na, #)$_2Nb_2O_6(OH)$, *Fd*$\bar{3}$*m, a* 10.3276(5) Å, *V* 1101.5 Å^3. IMA number: 2017-074. Type locality: Phoscorite-carbonatite pipe, Kovdor Massif, Murmansk Oblast, Russia.

Hydroxykenopyrochlore (Miyawaki et al., 2017, pending publication), (□, #)$_2Nb_2O_6$ (OH), *Fd*$\bar{3}$*m, a* 10.590(5) Å, *V* 1187.65 Å^3. IMA number: 2017-030a. Type locality: Araxá mine, Araxá complex, Barreiro, Araxá, Minas Gerais, Brazil.

Hydroxymanganopyrochlore (Chukanov et al., 2013), (Mn^{2+}, #)$_2Nb_2O_6$ (OH), *Fd*$\bar{3}$*m, a* 10.2523(2) Å, *V* 1077.62 Å^3. IMA number: 2012-005. Type locality: In den Dellen quarries, Mendig, Mendig, Mayen-Koblenz District, Rhineland-Palatinate, Germany.

Hydroxyplumbopyrochlore (Li et al., 2020), (Pb, #)$_2Nb_2O_6$ (OH), *Fd*$\bar{3}$*m, a* 10.558 (2) Å, *V* 1176.91 Å^3. IMA number: 2018-145. Type locality: Jabal Sayid mine (Jabal Sayid Cu-Zn deposit), Medina Region, Saudi Arabia.

"Fluorstrontiopyrochlore" (Atencio et al., 2010), (Sr, #)$_2Nb_2O_6F$, a possible new species, analysis published (Franchini et al., 2005). Occurrence: Jasimampa prospect, Ojo de Agua Department, Santiago del Estero Province, Argentina.

"Fluorkenopyrochlore" (Atencio et al., 2010), (□, #)$_2Nb_2O_6F$, a possible new species, analyses published (Kartashov et al., 1998; Schmitt et al., 2002). Occurrences: Khaldzan Buragtag massif, Myangad District, Khovd Province, Mongolia; Amis Complex, Brandberg Complex, Brandberg Area, Dâures Constituency, Erongo Region, Greenland.

"Oxynatropyrochlore" (Atencio et al., 2010), (Na, #)$_2Nb_2O_6O$, a possible new species, analyses published (Hogarth and Horne 1989; Knudsen 1989; Chukanov et al., 1999). Occurrences: Locality 2, Ndale Area, Fort Portal, Kabarole, Western Region, Uganda; Qaqqaarsuk, Maniitsoq, Maniitsoq Island, Qeqqata, Greenland; Mika pegmatite, Rangkul' Highlands, Gorno-Badakhshan, Tajikistan.

"Oxyplumbopyrochlore" (Atencio et al., 2010), $Pb_2Nb_2O_6O$, a possible new species, analysis published (Voloshin and Pakhomovskiy, 1986). Occurrence: Kola Peninsula, Murmansk Oblast, Russia.

"Oxyyttropyrochlore-(Y)" (Atencio et al., 2010), (Y, #)$_2Nb_2O_6O$, a possible new species, analysis published (Tindle and Breaks, 1998). Occurrence: Separation Rapids Lithium Project (Separation Lake area), Kenora District, Ontario, Canada.

"Kenoplumbopyrochlore" (Atencio et al., 2010), (Pb, #)$_2$ Nb_2O_6□, a possible new species, analysis published (Voloshin and Pakhomovskiy, 1986). Occurrence: Ploskaya Mt, Western Keivy Massif, Keivy Mountains, Lovozersky District, Murmansk Oblast, Russia.

MICROLITE GROUP

Hydroxykenomicrolite (Atencio et al., 2010), (□, #)$_2$$Ta_2O_6$ (OH), *Fd*$\bar{3}$*m, a* 10.526 (5) Å, *V* 1166.244 Å^3, first described by Voloshin et al. (1981) as "cesstibtantite." The IMA number was not quoted in the original description of "cesstibtantite." Type locality: Vasin-Myl'k Mt, Voron'i Tundry, Murmansk Oblast, Russia.

Oxystannomicrolite (Atencio et al., 2010), $Sn_2Ta_2O_6O$, *Fd*$\bar{3}$*m, a* 10.470 Å, *V* 1147.73 Å^3, first described by Vorma and Siivola (1967) as "sukulaite." The IMA number was not quoted in the original description of "sukulaite." Type locality: Sukula Pegmatites, Tammela, Tavastia Proper, Finland.

Oxystibiomicrolite (Atencio et al., 2010), (Sb^{3+}, #)$_2$$Ta_2O_6O$, *Fd*$\bar{3}$*m, a* 10.455(2) Å, *V* 1142.80 Å^3, first described by Groat et al. (1987) as "stibiomicrolite." The IMA number was not quoted in the original description of "stibiomicrolite." Type locality: Varuträsk, Skellefteå, Västerbotten County, Sweden.

Fluorcalciomicrolite (Andrade et al., 2013a), (Ca^{2+}, #)$_2$ Ta_2O_6F, *Fd*$\bar{3}$*m, a* 10.4191 (6) Å, *V* 1131.07 Å^3. IMA number: 2012-036. Type locality: Volta Grande mine (Mibra mine), Nazareno, Minas Gerais, Brazil.

Fluornatromicrolite (Witzke et al., 2011), (Na, #)$_2$ Ta_2O_6F, *Fd*$\bar{3}$*m, a* 10.4451 (2) Å, *V* 1139.56 Å^3. IMA number: 1998-018. Type locality: Quixaba pegmatite, Quixaba, Frei Martinho, Paraíba, Brazil.

Hydrokenomicrolite (Andrade et al., 2013b; Atencio, 2016), (□, #)$_2$$Ta_2O_6$ (H_2O). Hydrokenomicrolite-3*C* polytype: Cubic, *Fd*$\bar{3}$*m, a* 10.454(1) Å. *V* 1142.5 (2) Å^3. Hydrokenomicrolite-3*R* polytype: Trigonal, *R*$\bar{3}$*m, a* 7.4290(6), *c* 18.505 (2) Å, *V* 884.5 (1) Å^3. IMA Numbers: hydrokenomicrolite (hydrokenomicrolite-3*C*) 2011-103; "parabariomicrolite" (hydrokenomicrolite-3*R*): 84-3. Type localities: Hydrokenomicrolite-3*C* (described as hydrokenomicrolite by Andrade et al., 2013b), Volta Grande pegmatite, Nazareno, Minas Gerais, Brazil. Hydrokenomicrolite-3*R* (formerly described as "parabariomicrolite" by Ercit et al., 1986), Alto do Giz pegmatite, Equador Co., Rio Grande do Norte, Brazil.

Hydroxycalciomicrolite (Andrade et al., 2017), (Ca^{2+}, #)$_2$ Ta_2O_6(OH), $P4_232$, *a* 10.4205(8) Å *V* 1131.53 Å^3. The first pyrochlore-supergroup mineral with long range ordering of Ca and □ on the *A* sites, that invokes reduction of symmetry. IMA number: 2013-073. Type locality: Volta Grande mine (Mibra mine), Nazareno, Minas Gerais, Brazil.

Kenoplumbomicrolite (Atencio et al., 2018)**,** (Pb, #)$_2$ Ta_2O_6□, $P4_232$, *a* 10.575 (5) Å *V* 1182.6 Å^3. IMA number: 2015-007-a. Type locality: Ploskaya Mt, Western Keivy Massif, Keivy Mountains, Lovozersky District, Murmansk Oblast, Russia.

Oxynatromicrolite (Fan et al., 2016), (Na, #)$_2$ Ta_2O_6O, *Fd*$\bar{3}$*m, a* 10.420(6) Å, *V* 1131.4 Å^3. IMA number: 2013-063. Type locality: Pegmatite vein no. 309, Guanpo pegmatite field, Guanpo, Lushi County, Sanmenxia, Henan, China.

Oxycalciomicrolite (Menezes da Silva et al., 2020), $Ca_2Ta_2O_6O$, *Fd*$\bar{3}$*m, a* 10.4325 (4) Å, *V* 1135.46(14) Å^3. IMA number: 2019-110. Type locality: Fumal pegmatite, Nazareno, Minas Gerais, Brazil.

Oxybismutomicrolite (Kasatkin et al., 2020), (Bi, #)$_2$ Ta_2O_6O, *Fd*$\bar{3}$*m, a* 10.475 (1) Å, *V* 1149.38 Å^3. IMA number: 2019-047. Type locality: Solnechnaya pegmatite, Malkhan pegmatite field (Malchan; "Malechansk"), Krasnyi Chikoy, Zabaykalsky Krai, Russia.

"Hydromicrolite" (Atencio et al., 2010), (H_2O, #)$_2$ Nb_2O_6(H_2O), a possible new species, analysis published (Andrade, 2007). Occurrence: Volta Grande mine (Mibra mine), Nazareno, Minas Gerais, Brazil.

ROMÉITE GROUP

Hydroxycalciorоméite (Atencio et al., 2010), (Ca, #)$_2$$Sb_2^{5+}O_6$(OH), *Fd*$\bar{3}$*m, a* 10.264 Å, *V* 1081.31 Å^3, first described by Hussak and Prior (1895) as "lewisite." IMA number: a pre-IMA mineral. Type locality: Tripuí (Tripuhy), Ouro Preto, Minas Gerais, Brazil.

Fluorcalciorоméite (Atencio et al., 2013), (Ca, #)$_2$ $Sb_2^{5+}O_6F$, *Fd*$\bar{3}$*m, a* 10.2987 (8) Å, *V* 1092.31 Å^3. IMA number: 2012-093. Type locality: Starlera Mine, Starlera Valley, Ferrera, Viamala Region, Grisons, Switzerland.

Hydroxyferroroméite (Mills et al., 2017a), (Fe^{2+}, #)$_2$$Sb_2^{5+}O_6$(OH), *Fd*$\bar{3}$*m, a* 10.25 (3) Å, *V* 1077 Å^3. IMA number: 2016-006. Type locality: Correc d'en Llinassos (Ravin d'en Llinassous), Oms, Céret, Pyrénées-Orientales, Occitanie, France.

Oxycalciorоméite (Biagioni et al., 2013), $Ca_2Sb_2^{5+}O_6O$, *Fd*$\bar{3}$*m, a* 10.3042 (7) Å, *V* 1094.06 Å^3. IMA number: 2012-022. Type locality: Buca della Vena Mine, Ponte Stazzemese, Stazzema, Lucca Province, Tuscany, Italy.

Oxyplumboroméite (Hålenius and Bosi, 2013), $Pb_2Sb_2^{5+}O_6O$, *Fd*$\bar{3}$*m, a* 10.3783 (6) Å, *V* 1117.84 Å^3. IMA number: 2013-042. Type locality: Harstigen Mine, Pajsberg, Persberg ore district, Filipstad, Värmland County, Sweden.

"Fluornatroroméite" (Atencio et al., 2010), (Na, #)$_2$ $Sb_2^{5+}O_6F$, a possible new species, crystal structure determined (Matsubara et al., 1996). Occurrence: Gozaisho mine, Iwaki, Japan.

ELSMOREITE GROUP

Hydrokenoelsmoreite (Atencio et al., 2010), □$_2$$W_2O_6$ (H_2O), first described by Williams et al. (2005) as "elsmoreite". Hydrokenoelsmoreite-3*C* polytype: Cubic, *Fd*$\bar{3}$*m, a* 10.3065(3) Å. *V* 1094.80 Å^3. Hydrokenoelsmoreite-6*R* polytype: Trigonal, *R*$\bar{3}$, *a* 7.2882(2), *c* 35.7056(14) Å, *V* 1642.51 Å^3. IMA Numbers: "elsmoreite" (hydrokenoelsmoreite-3*C*) 2003-059. Type localities: Hydrokenoelsmoreite-3*C* (described as elsmoreite by Williams et al., 2005): Elsmore Tin Mine (Elsmore Tin lodes), Elsmore, Gough Co., New South Wales, Australia;

hydrokenoelsmoreite-3*C* and hydrokenoelsmoreite-6*R* (formerly "ferritungstite") from Hemerdon mine (now Drakelands mine) in Devon, United Kingdom (Mills et al., 2016).

Hydroxykenoelsmoreite (Mills et al., 2017b), $(□, \#)_2 W_2O_6(OH)$, Trigonal, $R\bar{3}$, *a* 7.313(2), *c* 17.863(7) Å, *V* 827(1) Å^3. IMA number: 2016-056. Type locality: Masaka gold mine, Muyinga Province, Burundi.

UNASSIGNED MEMBERS

Fluornatrocoulsellite (Atencio et al., 2017), $(Na, \#)_2 Mg_2F_6F$, $R\bar{3}m$, *a* 7.1620(1), *c* 17.5972(3) Å, *V* 781.7049 Å^3, first described by Birch et al. (2009) as "cousellite." IMA number: 2009-046 (coulsellite). Type locality: Mt Cleveland Mine, Luina, Heazlewood district, Waratah-Wynyard municipality, Tasmania, Australia.

Hydrokenoralstonite (Atencio et al., 2017), $□_2Al_2F_6(H_2O)$, $Fd\bar{3}m$, *a* 9.91(4) Å. *V* 973.24 Å^3, first described by Brush (1871) as "ralstonite." IMA number: pre-IMA mineral. Type locality: Ivigtut Mine, Arsuk Fjord, Sermersooq, Greenland.

BETAFITE GROUP

"Oxycalciobetafite" (Atencio et al., 2010), $(Ca,\#)_2Ti_2O_6O$, a possible new species, analysis published (Meyer and Yang, 1988). Occurrence: Fra Mauro Base (Apollo 14 landing site), Fra Mauro Highlands, The Moon.

"Oxyuranobetafite" (Atencio et al., 2010), $(U, \#)_2 Ti_2O_6O$, a possible new species, analysis published (Mokhov et al., 2008). Occurrence: Luna 24 landing site, Mare Crisium, The Moon.

DATA AVAILABILITY STATEMENT

The original contributions presented in the study are included in the article/supplementary material; further inquiries can be directed to the corresponding author.

AUTHOR CONTRIBUTIONS

The author confirms being the sole contributor of this work and has approved it for publication.

ACKNOWLEDGMENTS

The author acknowledges FAPESP (Fundação de Amparo à Pesquisa do Estado de São Paulo) for financial support (process 2019/23498-0) and CNPq for research productivity scholarship (process 303431/2019-9).

REFERENCES

Agakhanov, A. A., Kasatkin, A. V., Britvin, S. N., Siidra, O. I., Pautov, L. A., Pekov, I. V., et al. (2021). Cesiokenopyrochlore, the First Natural Niobate with an Inverse Pyrochlore Structure. *Can. Mineral.* 59, 149–157. doi:10.3749/canmin.2000056

Andrade, M. B., Atencio, D., Chukanov, N. V., and Ellena, J. (2013b). Hydrokenomicrolite, $(□,H_2O)_2Ta_2(O,OH)_6(H_2O)$, a New Microlite-Group mineral from Volta Grande Pegmatite, Nazareno, Minas Gerais, Brazil. *Am. Mineral.* 98, 292–296. doi:10.2138/am.2013.4186

Andrade, M. B., Atencio, D., Persiano, A. I. C., and Ellena, J. (2013a). Fluorcalciomicrolite, $(Ca,Na,□)_2Ta_2O_6F$, a New Microlite-Group mineral from Volta Grande Pegmatite, Nazareno, Minas Gerais, Brazil. *Mineral. Mag.* 77 (7), 2989–2996. doi:10.1180/minmag.2013.077.7.08

Andrade, M. B. (2007). "Estudo cristaloquímico de minerais do grupo do pirocloro no Brasil,". Tese de Doutorado (São Paulo: Instituto de Geociências), 207. doi:10.11606/T.44.2007.tde-30072007-165039

Andrade, M. B., Yang, H., Atencio, D., Downs, R. T., Chukanov, N. V., Lemée-Cailleau, M. H., et al. (2017). Hydroxycalciomicrolite, $Ca_{1.5}Ta_2O_6(OH)$, a New Member of the Microlite Group from Volta Grande Pegmatite, Nazareno, Minas Gerais, Brazil. *Mineral. Mag.* 81, 555–564. doi:10.1180/minmag.2016.080.116

Atencio, D., Andrade, M. B., Bastos Neto, A. C., and Pereira, V. P. (2017). Ralstonite Renamed Hydrokenoralstonite, Coulsellite Renamed Fluornatrocoulsellite, and Their Incorporation into the Pyrochlore Supergroup. *Can. Mineral.* 55 (1), 115–120. doi:10.3749/canmin.1600056

Atencio, D., Andrade, M. B., Bindi, L., Bonazzi, P., Zoppi, M., Stanley, C. J., et al. (2018). Kenoplumbomicrolite, $(Pb,□)_2Ta_2O_6[□,(OH),O]$, a New mineral from Ploskaya, Kola Peninsula, Russia. *Mineral. Mag.* 82, 1049–1055. doi:10.1180/minmag.2017.081.082

Atencio, D., Andrade, M. B., Christy, A. G., Gieré, R., and Kartashov, P. M. (2010). The Pyrochlore Supergroup of Minerals: Nomenclature. *Can. Mineral.* 48, 673–698. doi:10.3749/canmin.48.3.673

Atencio, D., Ciriotti, M. E., and Andrade, M. B. (2013). Fluorcalcioroméite, $(Ca,Na)_2Sb_2^{5+}(O,OH)_6F$, a New Roméite-Group mineral from Starlera Mine, Ferrera, Grischun, Switzerland: Description and crystal Structure. *Mineral. Mag.* 77, 467–473. doi:10.1180/minmag.2013.077.4.06

Atencio, D. (2016). Parabariomicrolite Discredited as Identical to hydrokenomicrolite-3*R*. *Mineral. Mag.* 80, 923–924. doi:10.1180/minmag.2016.080.129

Atencio, D. (2013). The Pyrochlore Supergroup: Remarks on Nomenclature - Response. *Can. Mineral.* 51 (5), 803–804. doi:10.3749/canmin.51.5.803

Biagioni, C., Meisser, N., Nestola, F., Pasero, M., Robyr, M., Roth, P., et al. (2018). Hydrokenopyrochlore, $(□,\#)_2Nb_2O_6{\cdot}H_2O$, a New Species of the Pyrochlore Supergroup from the Sahatany Pegmatite Field, Antananarivo Province, Madagascar. *ejm* 30, 869–876. doi:10.1127/ejm/2018/0030-2761

Biagioni, C., Orlandi, P., Nestola, F., and Bianchin, S. (2013). Oxycalcioroméite, Ca2Sb2O6O, from Buca Della Vena Mine, Apuan Alps, Tuscany, Italy: a New Member of the Pyrochlore Supergroup. *Mineral. Mag.* 77, 3027–3037. doi:10.1180/minmag.2013.077.7.12

Birch, W. D., Grey, I. E., Mumme, W. G., and Pring, A. (2009). Coulsellite, a New mineral from the Cleveland Mine, Luina, Tasmania. *Aust. J. Mineralogy* 15, 21–24.

Brush, G. J. (1871). On Ralstonite, a New Fluoride from Arksut Fiord [Greenland]. *Am. J. Sci.* s3-2, 30–31. doi:10.2475/ajs.s3-2.7.30

Černý, P., Hawthorne, F. C., Laflamme, J. H. G., and Hinthorne, J. R. (1979). Stibiobetafite, a New Member of the Pyrochlore Group from Vežná, Czechoslovakia. *Can. Mineral.* 17, 583–588.

Christy, A. G., and Atencio, D. (2013). Clarification of Status of Species in the Pyrochlore Supergroup. *Mineral. Mag.* 77 (1), 13–20. doi:10.1180/minmag.2013.077.1.02

Chukanov, N. V., Blass, G., Zubkova, N. V., Pekov, I. V., Pushcharovskii, D. Y., and Prinz, H. (2013). Hydroxymanganopyrochlore: A New mineral from the Eifel Volcanic Region, Germany. *Dokl. Earth Sc.* 449 (1), 342–345. doi:10.1134/s1028334x13030100

Chukanov, N. V., Skrigitil, A. M., Kuzmina, O. V., and Zadov, A. E. (1999). Bismutopyrochlore (Bi, U, Ca, Pb)$_{1+x}$(Nb,Ta)$_2$O$_6$(OH)·*n*H$_2$O – a New mineral from the Mika Pegmatite Vein (Eastern Pamirs). *Zapiski Vsesoyuznoye Mineralogichestogo Obshchestvo* 128 (4), 36–41.

Ercit, T. S., Hawthorne, F. C., and Černy, P. (1986). Parabariomicrolite, a New Species and its Structural Relationship to the Pyrochlore Group. *Can. Mineral.* 24, 655–663.

Fan, G., Ge, X., Li, G., Yu, A., and Shen, G. (2016). Oxynatromicrolite, $(Na,Ca,U)_2Ta_2O_6(O,F)$, a New Member of the Pyrochlore Supergroup from Guanpo, Henan Province, China. *Mineralogical Mag.* 81 (4), 743–751.

Franchini, M., Lira, R., Meinert, L., Ríos, F. J., Poklepovic, M. F., Impiccini, A., et al. (2005). Na-Fe-Ca Alteration and LREE (Th-Nb) Mineralization in marble and granitoids of Sierra de Sumampa, Santiago del Estero, Argentina. *Econ. Geology* 100, 733–764. doi:10.2113/100.4.733

Goreaud, M., and Raveau, B. (1980). Alunite and Crandallite: a Structure Derived from that of Pyrochlore. *Am. Mineral.* 65, 953–956.

Grey, I. E., Birch, W. D., Bougerol, C., and Mills, S. J. (2006). Unit-cell Intergrowth of Pyrochlore and Hexagonal Tungsten Bronze Structures in Secondary Tungsten Minerals. *J. Solid State. Chem.* 179, 3860–3869. doi:10.1016/j.jssc.2006.08.030

Groat, L. A., ČErný, P., and Ercit, T. S. (1987). Reinstatement of Stibiomicrolite as a Valid Species. *Geologiska Föreningen i Stockholm Förhandlingar* 109, 105–109. doi:10.1080/11035898709453757

Hålenius, U., and Bosi, F. (2013). Oxyplumboroméite, Pb2Sb2O7, a New mineral Species of the Pyrochlore Supergroup from Harstigen Mine, Värmland, Sweden. *Mineral. Mag.* 77, 2931–2939. doi:10.1180/minmag.2013.077.7.04

Hogarth, D. D. (1977). Classification and Nomenclature of the Pyrochlore Group. *Am. Mineral.* 62, 403–410.

Hogarth, D. D., and Horne, J. E. T. (1989). Non-metamict Uranoan Pyrochlore and Uranpyrochlore from Tuff Near Ndale, Fort Portal Area, Uganda. *Mineral. Mag.* 53, 257–262. doi:10.1180/minmag.1989.053.370.14

Hogarth, D. D. (2013). The Pyrochlore Group: Remarks on Nomenclature. *Can. Mineral.* 51 (5), 801. doi:10.3749/canmin.51.5.801

Hussak, E., and Prior, G. T. (1895). Lewisite and Zirkelite, Two New Brazilian Minerals. *Mineral. Mag. J. Mineral. Soc.* 11, 80–88. doi:10.1180/minmag.1895.011.50.05

Ivanyuk, G. Y., Yakovenchuk, V. N., Panikorovskii, T. L., Konoplyova, N., Pakhomovsky, Y. A., Bazai, A. V., et al. (2019). Hydroxynatropyrochlore, $(Na,Ca,Ce)_2Nb_2O_6(OH)$, a New Member of the Pyrochlore Group from the Kovdor Phoscorite-Carbonatite Pipe, Kola Peninsula, Russia. *MinMag.* 83 (1), 107–113. doi:10.1180/minmag.2017.081.102

Jingwu, Y., Li, G., Guangming, Y., Ge, X., Xu, H., and Wang, J. (2015). Fluornatropyrochlore, a New Pyrochlore Supergroup mineral from the Boziguoer Rare Earth Element deposit, Baicheng County, Akesu, Xinjiang, China. *Can. Mineral.* 53, 455–460.

Kartashov, P. M., Mokhov, A. V., and Kovalenko, V. I. (1998). Rare Earth Sr-Pyrochlore from Western Mongolia: The First Find in Association with Alkalic Granites. *Doklady Earth Sci.* 359, 510–513.

Kasatkin, A. V., Britvin, S. N., Peretyazhko, I. S., Chukanov, N. V., Škoda, R., and Agakhanov, A. A. (2020). Oxybismutomicrolite, a New Pyrochlore-Supergroup mineral from the Malkhan Pegmatite Field, Central Transbaikalia, Russia. *MinMag.* 84, 444–454. doi:10.1180/mgm.2020.25

Knudsen, C. (1989). "Pyrochlore Group Minerals from the Qaqarssuk Carbonatite Complex," in *Lanthanides, Tantalum and Niobium*. Editors P. Möller, P. Černý, and F. Saupe (Berlin: Springer-Verlag). doi:10.1007/978-3-642-87262-4_3

Li, G., Yang, G., Lu, F., Xiong, M., Ge, X., Pan, B., et al. (2016). Fluorcalciopyrochlore, a New mineral Species from Bayan Obo, Inner Mongolia, P.R. China. *Can. Mineral.* 54, 1285–1291.

Li, T., Li, Z., Fan, G., Fan, H., Zhong, J., Jahdali, N. S., et al. (2020). Hydroxyplumbopyrochlore, $(Pb1.5,□0.5)Nb_2O_6(OH)$, a New Member of the Pyrochlore Group from Jabal Sayid, Saudi Arabia. *MinMag.* 84 (5), 785–790. doi:10.1180/mgm.2020.69

Matsubara, S., Kato, A., Shimizu, M., Sekiuchi, K., and Suzuki, Y. (1996). Romeite from the Gozaisho Mine, Iwaki, Japan. *Mineralogical J.* 18 (4), 155–160. doi:10.2465/minerj.18.155

Menezes da Silva, V. H. R., Ávila, C. A., Neumann, R., Faulstich, F. R. L., Alves, F. E. A., Almeida, F. B., Cidade, T. P., and Sousa, S. S. C. G. (2020). Oxycalciomicrolite, $(Ca,Na)_2(Ta,Nb,Ti)_2O_6(O,F)$, a new member of the microlite group (pyrochlore supergroup) from the Paleoproterozoic São João del Rei Pegmatite Province, Minas Gerais state, Brazil. *MinMag.* 84, 854–858. doi:10.1180/mgm.2020.74

Meyer, C., and Yang, S. V. (1988). Tungsten-bearing Yttrobetafite in Lunar Granophyre. *Am. Mineral.* 73, 1420–1425.

Mills, S. J., Christy, A. G., Kampf, A. R., Birch, W. D., and Kasatkin, A. (2017b). Hydroxykenoelsmoreite, the First New mineral from the Republic of Burundi. *ejm* 29, 491–497. doi:10.1127/ejm/2017/0029-2618

Mills, S. J., Christy, A. G., Rumsey, M. S., Spratt, J., Bittarello, E., Favreau, G., et al. (2017a). Hydroxyferroroméite, a New Secondary Weathering mineral from Oms, France. *ejm* 29, 307–314. doi:10.1127/ejm/2017/0029-2594

Mills, S. J., Christy, A. G., Rumsey, M. S., and Spratt, J. (2016). The crystal Chemistry of Elsmoreite from the Hemerdon (Drakelands) Mine, UK: hydrokenoelsmoreite-3*C* and hydrokenoelsmoreite-6*R*. *Mineral. Mag.* 80, 1195–1203. doi:10.1180/minmag.2016.080.058

Mills, S. J., Hatert, F., Nickel, E. H., and Ferraris, G. (2009). The Standardisation of mineral Group Hierarchies: Application to Recent Nomenclature Proposals. *ejm* 21, 1073–1080. doi:10.1127/0935-1221/2009/0021-1994

Miyawaki, R., Momma, K., Matsubara, S., Sano, T., Shigeoka, M., and Horiuchi, H. (2017). Hydroxykenopyrochlore, IMA 2017-030a, CNMNC Newsletter No. 39. *Mineralogical Mag.* 81, 1279–1286. October 2017, page 1285.

Mokhov, A. V., Kartashov, P. M., Bogatikov, O. A., Ashikhmina, N. A., Magazina, L. O., and Koporulina, E. V. (2008). Fluorite, Hatchettolite, Calcium Sulfate, and bastnasite-(Ce) in the Lunar Regolith from Mare Crisium. *Dokl. Earth Sc.* 422 (1), 1178–1180. doi:10.1134/s1028334x08070416

Momma, K., and Izumi, F. (2011). VESTA 3for Three-Dimensional Visualization of crystal, Volumetric and Morphology Data. *J. Appl. Cryst.* 44, 1272–1276. doi:10.1107/s0021889811038970

Rouse, R. C., Dunn, P. J., Peacor, D. R., and Wang, L. (1998). Structural Studies of the Natural Antimonian Pyrochlores. *J. Solid State. Chem.* 141, 562–569. doi:10.1006/jssc.1998.8019

Schmitt, A. K., Trumbull, R. B., Dulski, P., and Emmermann, R. (2002). Zr-Nb-REE Mineralization in Peralkaline Granites from the Amis Complex, Brandberg (Namibia): Evidence for Magmatic Pre-enrichment from Melt Inclusions. *Econ. Geology* 97, 399–413. doi:10.2113/gsecongeo.97.2.399

Subramanian, M. A., Aravamudan, G., and Subba Rao, G. V. (1983). Oxide Pyrochlores - A Review. *Prog. Solid State. Chem.* 15, 55–143. doi:10.1016/0079-6786(83)90001-8

Tindle, A. G., and Breaks, F. W. (1998). Oxide Minerals of the Separation Rapids Rare-Element Granitic Pegmatite Group, Northwestern Ontario. *Can. Mineral.* 36, 609–635. doi:10.1119/1.879923

van Wambeke, L. (1978). Kalipyrochlore, a New mineral of the Pyrochlore Group. *Am. Mineral.* 63, 528–530.

Voloshin, A. V., Men'shikov, Yu. P., Pakhomovskiy, Ya. A., and Polezhaeva, L. I. (1981). Cesstibtantite, $(Cs,Na)SbTa_4O_{12}$ – a New mineral from Granitic Pegmatites. *Zapiski Vsesoyuznoye Mineralogichestogo Obshchestvo* 116, 345–351.

Voloshin, A. V., and Pakhomovskiy, Ya. A. (1986). *Minerals and mineral Formation Evolution in Amazonite Pegmatites of Kola peninsula*. Leningrad: Nauka, 168.

Vorma, A., and Siivola, J. (1967). Sukulaite – $Ta_2Sn_2O_7$ – and Wodginite as Inclusions in Cassiterite in the Granite Pegmatite in Sukula, Tammela, in SW Finland. *Bull. de la Comm. géologique de Finlande* 229, 173–187.

Williams, P. A., Leverett, P., Sharpe, J. L., Colchester, D. M., and Rankin, J. (2005). Elsmoreite, Cubic $WO_{3-0}.5H_2O$, a New mineral Species from Elsmore, New South Wales, Australia. *Can. Mineral.* 43, 1061–1064. doi:10.2113/gscanmin.43.3.1061

Witzke, T., Steins, M., Doering, T., Schuckmann, W., Wegner, R., and Pöllmann, H. (2011). Fluornatromicrolite, $(Na, Ca, Bi)_2Ta_2O_6F$, A New Mineral Species from Quixaba, Paraiba, Brazil. *Can. Mineral.* 49, 1105–1110. doi:10.3749/canmin.49.4.1105

Yang, G., Li, G., Xiong, M., Pan, B., and Yan, C. (2014). Hydroxycalciopyrochlore, a New mineral Species from Sichuan, China. *Acta Geologica Sinica - English Edition* 88, 748–753. doi:10.1111/1755-6724.12235

Conflict of Interest: The author declares that the research was conducted in the absence of any commercial or financial relationships that could be construed as a potential conflict of interest.

Publisher's Note: All claims expressed in this article are solely those of the authors and do not necessarily represent those of their affiliated organizations, or those of the publisher, the editors and the reviewers. Any product that may be evaluated in this article, or claim that may be made by its manufacturer, is not guaranteed or endorsed by the publisher.

frontiers in Chemistry

ORIGINAL RESEARCH
published: 18 October 2021
doi: 10.3389/fchem.2021.723507

Structural Aspects of the Superionic Transition in AX_2 Compounds With the Fluorite Structure

Paul C. M. Fossati[1]*, *Alain Chartier*[1] and *Alexandre Boulle*[2]

[1]DES–Service de Corrosion et du Comportement des Matériaux dans leur Environnement (SCCME), CEA Saclay, Université Paris Saclay, Gif-sur-Yvette, France, [2]Institut de Recherche sur les Céramiques (IRCer), CNRS UMR 7315, Université de Limoges, Centre Européen de la Céramique, Limoges, France

Some AX_2 binary compounds with the fluorite structure (space group $Fm\bar{3}m$) are well-known examples of materials exhibiting transitions to ionic superconducting phases at high temperatures below their melting points. Such superionic states have been described as either highly defective crystals or part-crystal, part-liquid states where the *A* ions retain their crystalline order whilst the *X* ions undergo partial melting. However, no detailed description of the structure of these phases exists. We present here the results of our investigation of the structural changes that occur during these transitions and the structural characteristics of the resulting superionic materials. This work is based on atomic-scale molecular dynamics modelling methods as well as computational diffraction techniques. We employed a set of empirical potentials representing several compounds with the fluorite structure to investigate any potential-dependent effect. We show the importance of small-scale structure changes, with some local environments showing a hexagonal symmetry similar to what is seen in the scrutinyite structure that has been documented for example in UO_2.

Keywords: molecular dynamics, fluorite, superionic, atomic-scale simulation, computational diffraction, XRD

OPEN ACCESS

Edited by:
Gordon James Thorogood, Australian Nuclear Science and Technology Organisation, Australia

Reviewed by:
Ranjan Mittal, Bhabha Atomic Research Centre (BARC), India
Jacob Eapen, North Carolina State University, United States
Samrath Lal Chaplot, Bhabha Atomic Research Centre (BARC), India

***Correspondence:**
Paul C. M. Fossati
paul.fossati@cea.fr

Specialty section:
This article was submitted to Solid State Chemistry, a section of the journal Frontiers in Chemistry

Received: *10 June 2021*
Accepted: *30 August 2021*
Published: *18 October 2021*

Citation:
Fossati PCM, Chartier A and Boulle A (2021) Structural Aspects of the Superionic Transition in AX_2 Compounds With the Fluorite Structure. Front. Chem. 9:723507. doi: 10.3389/fchem.2021.723507

1 INTRODUCTION

Superionic conductors are ionic solids that exhibit a very high ionic conductivity, close to that of their melt or comparable to that of a liquid electrolyte (Rice and Roth, 1972; Boyce and Huberman, 1979). The first materials undergoing a transition to a superionic state were documented in the 19th century (Faraday, 1849). Such a transition is now known in several compounds with the fluorite structure (Derrington et al., 1975). In the literature, this is referred to as the Faraday transition, Bredig transition, or diffuse transition because the change occurs over a finite temperature range instead of a single temperature. It corresponds to a second-order or class III superionic transition (O'Keeffe, 1976; Hull, 2004). Common examples are fluorides such as CaF_2, SrF_2, BaF_2, or β-PbF_2 (Lidiard, 1980), but also chlorides such as $SrCl_2$ (Carr et al., 1978; Dixon, 1980; Gillan and Dixon, 1980; Fomin, 2021) or β-$BaCl_2$ (Hull et al., 2011), or oxides such as Li_2O (Fracchia et al., 1998; Goel et al., 2004), CeO_2 (Klarbring et al., 2018), or UO_2 (Hiernaut et al., 1993). It has also been demonstrated by simulations in more complex compounds such as actinides mixed oxides $(U,Pu)O_2$ (Cooper et al., 2015; Takoukam-Takoundjou et al., 2020; Bathellier et al., 2021) $(U,Th)O_2$ (Cooper et al., 2014a), or $(Pu,Th)O_2$ (Galvin et al., 2016).

Besides the increased ionic conductivity, a known feature of the superionic transition is a peak in the constant-volume heat capacity $C_P(T)$ with a characteristic Λ shape (Goff et al., 1991). The cause

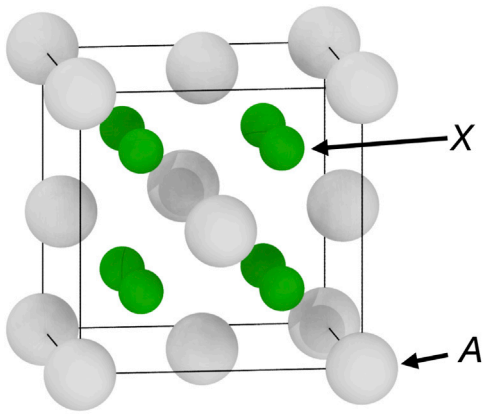

FIGURE 1 | The fluorite structure (space group $Fm\bar{3}m$) for AX_2 compounds, showing both *A* and *X* sublattices.

for this is an increase in the enthalpy $H(T)$ beyond what would be expected from the trend measured from the same materials at low temperatures (Naylor, 1945; Dworkin and Bredig (1963, 1968)). This has been commonly referred to as anomalous heat (Dworkin and Bredig, 1968; Szwarc, 1969). Coincidently, an anomalous increase in the lattice parameter of the materials can also be measured, or equivalently a Λ peak in the linear thermal expansion coefficient $\alpha(T)$ (Goff et al., 1991). Both peaks have their highest point at the same temperature for any given compound, which is conventionally taken as the superionic transition temperature T_S.

The fluorite structure (space group $Fm\bar{3}m$) is common for many compounds with the AX_2 form (Hayes (1974)). In the classic fluorite structure, following the prototype CaF_2, *A* is a cation—such as Ca^{2+}, Sr^{2+}, U^{4+} — whereas *X* is an anion—commonly F^-, Cl^-, or O^{2-}. This structure can be viewed as the combination of a face-centred cubic (FCC) sublattice containing the *A* chemical species and a simple cubic (SC) sublattice with the *X* species, as shown in **Figure 1**. The anti-fluorite structure is very closely related, the only difference being that in this case *A* is an anion, and *X* is a cation. Both Na_2O and Li_2O are common examples of the anti-fluorite structure. However, this difference in ionic character does not change the geometry of the crystals. In the rest of the article, both structures will be referred to as either *fluorite* or $Fm\bar{3}m$, but the conclusions apply equally to anti-fluorites.

Compounds with the fluorite structure have been very well studied for industrial applications (*e.g.* UO_2, CeO_2, yttria–stabilised zirconia), or because they are a simple model for ionic conductors (Hayes, 1974). Their tendency to behave as superionic conductors at high temperatures has been a particular area of interest since the 1970s. The nature of the high-temperature superionic phase in AX_2 compounds with the fluorite structure is not fully explained yet, and conflicting interpretations exist. One of them is that high conductivity is the result of the availability of many crystalline sites for diffusion resulting from extensive Frenkel disorder and defects clustering on the *X* sublattice (Hutchings et al., 1984; Hull et al., 2011). Another view is that the superionic phase is the combination of a melted *X* sublattice and an *A* sublattice that retains its crystalline character, and thus the integrity of the material (Boyce et al., 1977; Castiglione and Madden, 2001). Recent works on the dynamical behaviour of the superionic phase of UO_2 and Li_2O seem to validate this description, showing string-like collective diffusion mechanisms otherwise common in supercooled liquids (Gray-Weale and Madden, 2004; Annamareddy and Eapen, 2017; Zhang et al., 2019). This interpretation is also strengthened by measurements of entropy changes during superionic transitions, which produced results consistent with some partial melting (O'Keeffe, 1976; Boyce et al., 1977).

In this work, we set out to investigate the structural aspects of the superionic transition in compounds with the fluorite structure. We aim to provide some insight on key structure changes happening at that transition and on the structural characteristics of the superionic phase. Molecular dynamics (MD) techniques have been recognised as a powerful tool for a very long time for the study of ionic conducting oxides (Catlow et al., 1978). It is particularly well-suited for this type of investigations that bridge thermodynamical properties and structural features. Indeed, its atomic-scale resolution makes accessible structure details such as point defects, local environments, or structure changes. This has resulted in a large collection of empirical potential that can be used to simulate a variety of compounds. Instead of focusing on one specific material, we considered a list of them for which successful potentials have been published. This way, we intend to describe phenomena that are characteristic of ionic compounds in the $Fm\bar{3}m$ structure rather than specific to one composition or one potential.

Structures from MD simulations of superionic phases can be very difficult to analyse because of temperature-induced effects. This includes not only structural defects that form normally at high temperatures, such as Frenkel pairs, Schottky trios, or larger clusters, but also the resulting strain fields that distort the structure, and large thermal vibrations. All of this obscures the underlying structure of the materials and makes any structural analysis challenging. To overcome this, we employed computational diffraction techniques to generate virtual X-ray diffraction (XRD) patterns. These provide another way of characterising structural features that are difficult to describe otherwise, by showing structures in the reciprocal space that are not subject to the same perturbations as the atomic positions at high temperatures.

2 METHODS

2.1 Empirical Potentials

We selected a broad range of empirical potentials that have been designed to simulate crystals with the fluorite structure. Thanks to the sustained interest for AX_2 materials with the $Fm\bar{3}m$ structure, a large number of such potentials are available and can be used for our purposes. The final set of compounds that can be simulated using the selected potentials included seven different chemical compositions, with some fluorides, oxides and one chloride. Most

TABLE 1 | Empirical potentials used in this study.

Compound	Potential	Charges	Interactions
BaF2	Catlow and Norgett (1973)[a]	Formal	Buck. + ZBL
	Cazorla et al. (2018)	Formal	Buckingham
	Sayle et al. (2003)	Formal	Buckingham
CaF_2	Bingham et al. (1989)	Formal	Buckingham
	Catlow and Norgett (1973)[a]	Formal	Buck. + ZBL
	Evangelakis and Pontikis (1989)	Formal	Buck. + ZBL
	Sayle et al. (2003)	Formal	Buckingham
Li_2O	Asahi et al. (2014)	Partial	Buckingham
	Oda et al. (2007)	Partial	Buckingham
	Pedone et al. (2006)	Partial	Morse + repulsion
β-PbF_2	Catlow et al. (1978)[a]	Formal	Buckingham
$SrCl_2$	Bendall and Catlow (1980)[a]	Formal	Buckingham
	Gillan and Dixon (1980)	Formal	Buckingham
SrF_2	Bingham et al. (1989)	Formal	Buckingham
	Catlow and Norgett (1973)[a]	Formal	Buck. + ZBL
	Cazorla et al. (2018)	Formal	Buckingham
UO_2	Cooper et al. (2014b)[a]	Partial	Buck. + EAM
	Morelon et al. (2003)	Partial	4-terms Buck

[a]*The Catlow and Bendall potentials originally had polarisable shells, which were ignored in this study.*

of these compositions were represented by several different potentials listed in **Table 1** with their main characteristics.

The seven selected compounds include some variety in the properties of both *A* and *X* ions. The *X* ions were Li, F, Cl, or O, having electric charges of respectively +1, −1,−1, and−2. The ions on the *A* sublattice were O, Ca, Sr, Ba, Pb, or U with masses ranging from 16 u to 238 u, and with $\frac{A}{X}$ mass ratio from 2.31 (Li_2O) to 14.88 (UO_2). The potentials we used take different analytical forms. Most of the potentials, particularly older ones, use simple Buckingham interactions. However, they are not identical to each other and differ in the numerical values of their parameters and their fitting procedure. Indeed, they have been initially fitted to reproduce different properties such as defect energies at room temperatures, which are not necessarily related to the superionic transition. In some more recent potentials, the electric charges of the different species are a parameter that was adjusted during the potentials fitting in the same way as the parameters of the non-electrostatic pair interactions. This reflects the imperfect ionic nature of these materials. Amongst the potentials used in this study, it is the case for the potentials representing Li_2O and UO_2. Some potentials use analytical forms other than Buckingham, such as Morse (Pedone potential for Li_2O), 4-terms Buckingham (Morelon potential for UO_2), or additional embedded atom model (EAM) many-body contributions (CRG potential for UO_2). The Pedone potential was not even designed to simulate the $Fm\bar{3}m$ structure, but instead complex minerals and glasses. The analytical form of the electrostatic interactions was the Wolf summation (Wolf et al., 1999).

In some instances, several potentials were proposed in the original references. This is the case for the Catlow potential for BaF_2, CaF_2, and SrF_2, and the Oda potential for Li_2O. For the Catlow potential, we chose the first model of the three proposed. The difference between the first and second model is only a different set of parameter for the core-shell interactions, and the third model showed less accurate lattice parameters at higher temperatures in preliminary simulations. For the Oda potential for Li_2O, we selected the FIT-GGA parameters, which offered the most accurate thermal expansion and melting point.

All the potentials we used predicted the $Fm\bar{3}m$ structure as the ground state at room pressure, and showed reasonable thermodynamical properties. However, no assessment regarding the quality of the potentials, or their ability to reproduce quantitatively given materials properties, was made otherwise.

Some of the potentials were designed with polarisable core-shell models to improve dielectric properties and elastic constants. However, the shell models tested tended to show instabilities and large fluctuations of the thermodynamical properties at high temperatures. We therefore ignored core-shell interactions when using these potentials, and considered only rigid ions. This should not affect the structure at low temperatures because of the way the interactions were fitted. In fact, the first step in the potential design process was to adjust the pair interactions to reproduce the structure correctly (Catlow and Norgett, 1973). Adjusting the parameters for the shell models was done in a following step, to improve dielectric constants. In any case, these potentials were not intended to reproduce very disordered structures or melts, therefore they should not be less accurate in principle than other, rigid-ions only potentials at high temperatures.

In addition, the Catlow potentials for BaF_2, CaF_2, and SrF_2, as well as the Evangelakis potential for CaF_2 showed some instability at high temperatures, due to the relatively low energy barrier in their F–F Buckingham interactions. To avoid issues during the simulations with ions falling in the Buckingham singularity at short separation distances, a Ziegler-Biersack-Littmark (ZBL) contribution was added (Ziegler et al., 1985). We used the switching scheme implemented in LAMMPS with an outer radius of 2.0 Å and inner radii of 1.5 Å and 1.6 Å for the Catlow and Evangelakis potentials respectively. The Catlow potential for α-PbF_2 was derived independently and did not suffer from the same issue, and was therefore not modified.

Considering this diversity of compounds and potentials, it is expected to see some variance in the properties and structures of each specific material depending on the potential used. However, this diversity is also expected to limit any bias in our results by separating effects shown with only some of the potentials from common features independent of potentials details. Our intent was to identify features and qualitative behaviour universal in crystals with the $Fm\bar{3}m$ structure, rather than finding the absolute most accurate potentials. For this reason, we privileged a larger number of potentials rather than a more limited selection. This means that our results should be interpreted in general in terms of trends across compounds and potentials, and not quantitative predictions of materials properties. We will point out when a given potential deviates significantly from experimental results, or from the behaviour of other potentials.

2.2 Molecular Dynamics Simulations

The input structures for the MD simulations were 10 × 10 × 10 supercells of the conventional $Fm\bar{3}m$ unit cell. This resulted in cubic simulation boxes with 12 ,000 atoms and sides around 50 Å long, depending on potential and temperature. With all the potentials, electrostatic interactions were calculated using the Wolf sum with a damping parameter of 0.3 $Å^{-1}$ (Wolf et al., 1999). All pair interactions, including electrostatics, were truncated and shifted using a cutoff radius of 11 Å.

Equilibrium MD calculations were carried out from room temperature to the temperature at which only liquid phases were observed. This upper bound for the temperature range depends on both composition and potential. To sample these ranges similarly for each potentials, 50 evenly-spaced temperatures were selected in each case. The code used was LAMMPS (Plimpton, 1995), with both temperature and pressure controlled by the time-reversible Tuckerman integrator (Tuckerman et al., 2006) based on the Nosé-Hoover (Nosé, 1984) method and the Parrinello-Rahman strain energy (Parrinello and Rahman, 1981). When structure optimisation was useful, it was done by minimising the potential energy of the structure whilst keeping the simulation box fixed, using the implementation of the Broyden—Fletcher—Goldfarb—Shanno (BFGS) algorithm from the L-BFGS library (Byrd et al., 1995).

Each simulation consisted of a several successive relaxation steps. The first one was a constant-temperature, fixed-volume (*NVT*) equilibration for 10 ps in order to thermalise the simulation box. This was followed by a fixed-temperature and room-pressure (*NPT*) equilibration for 240 ps, during which the average box lengths were calculated. Both cell size and shape were allowed to fluctuate during this step in order to avoid constraining the relaxation process. Although the box shape could change during this step, it remained very close to cubic on average except in simulations of liquids. Then, the box shape was fixed to match the average shape calculated during the *NPT* step. Following this, each supercell underwent a last *NVT* relaxation for 10 ps. Finally, data was accumulated over a 20 ps simulation at constant volume and energy (*NVE*). The time step for all these simulations was 1 fs, and the damping time for the thermostat and barostat were 0.01 and 0.5 ps respectively. The enthalpy $H(T)$ was determined for each temperature T in K by taking its average over the *NVE* runs. The constant-pressure heat capacity $C_P(T)$ was then determined by differentiating the enthalpy

$$C_P(T) = \frac{\partial H}{\partial T} \ . \tag{1}$$

This was done numerically using a second-order centred finite difference scheme. The lattice parameter $a(T)$ was calculated by taking the average of the box size along the x, y, and z axes and dividing it by 10, the number of conventional cells along each direction. The linear thermal expansion coefficient

$$\alpha(T) = \frac{\partial \ln(a)}{\partial T} \tag{2}$$

was calculated using the measured lattice parameter, with the same numerical scheme employed to calculate $C_P(T)$. **Eq. 2** was used instead of the equivalent and more common expression $\alpha = \frac{1}{a}\frac{\partial a}{\partial T}$ for the increased numerical precision of its finite differences discrete form. Statistical sampling of the phase space is important, particularly when considering highly disordered structures. For this reason, all simulations were run three times independently, with identical initial atomic positions but different initial velocities. The figures presented here are averages over these three simulations, but figures showing the complete data are available in the **Supplementary Material** for this article.

Diffusion being an important aspect of the superionic transition, we also calculated diffusion coefficients from the MD simulations. This was done by using the Einstein relation

$$D = \frac{1}{6} \lim_{t\to\infty} \frac{d}{dt} \langle |\mathbf{u}(t)|^2 \rangle, \tag{3}$$

where t is the simulation time, and $\mathbf{u}$ is the atomic displacement. The mean squared displacements $\langle |\mathbf{u}(t)|^2 \rangle$ were calculated for both A and X species separately, to produce specific diffusion coefficients.

Point defects are an important structural feature at high temperatures. Since they play an important role in diffusion and have been linked to the onset of the superionic transition (Hiernaut et al., 1993), it is useful to be able to determine how common they are. Given that the structure considered here are stoichiometric to ensure electric charge neutrality and that the number of atoms is fixed and does not change over the course of a simulation, the only possible defects are Frenkel pairs, where an ion leaves its initial lattice site to form an interstitial elsewhere in the crystal. Counting the number of Frenkel pairs requires counting either the number of vacancies or the number of interstitials. We did so by mapping each ion in structures of interest taken from MD simulations to a reference crystal, which was a $Fm\bar{3}m$ structure with the same composition and lattice parameter. Thus, there are three possibilities for each lattice site. It can be: (i) empty, indicating the presence of a vacancy; (ii) occupied by one ion; or (iii) occupied by two ions, which indicates the presence of an interstitial. This analysis has been performed separately for the A (FCC) and X (SC) sublattices. It can result in principle in under-counting defects compared to experimental methods, if some ions are displaced enough to leave their site but not enough to be mapped onto another one. We also did not consider the interstitial octahedral site as a separate site for the purpose of the defects analysis.

We performed additional structure analysis using the polyhedral template matching (PTM) (Larsen et al., 2016) technique implemented in Ovito (Stukowski, 2010). This method assigns a kind of symmetry environment to each atom by comparing the relative positions of its neighbours to reference polyhedra for prototype structures such as simple cubic, hexagonal close packed, body-centred cubic, or face-centred cubic. This was used to show the structural disorder across the superionic transition. The RMSD cutoff for the PTM analysis was set to 0.5 for all structures.

TABLE 2 | Thermophysical properties at room temperature for the different potentials, compared to experimental references: (1) Wicks and Block (1963); (2) Roberts and White (1986); (3) Dworkin and Bredig (1968); (4) Johnston and Bauer (1951); (5) Hull et al. (1988); (6) Popov et al. (2017); (7) Schröter and Nölting (1980); (8) Smith et al. (1963); (9) Pavlov et al. (2017); (10) Martin (1988).

Compound	Potential	$C_P/10^{-4}$ eV/(atom K)		$\alpha/10^{-5}$ K^{-1}	
		This work	Exp	This work	Exp
BaF_2	Catlow and Norgett (1973)	2.69	2.44[1]	1.82	1.96[2]
	Cazorla et al. (2018)	2.71		2.93	
	Sayle et al. (2003)	2.71		2.92	
CaF_2	Bingham et al. (1989)	2.72	2.66[3]	2.49	1.90[2]
	Catlow and Norgett (1973)	2.70		1.71	
	Evangelakis and Pontikis (1989)	2.71		1.96	
	Sayle et al. (2003)	2.70		2.34	
Li_2O	Asahi et al. (2014)	2.69	1.80[4]	2.82	2.78[5]
	Oda et al. (2007)	2.70		2.34	
	Pedone et al. (2006)	2.78		3.25	
β-PbF_2	Catlow et al. (1978)	2.71	2.56[1]	2.29	2.85[6]
$SrCl_2$	Bendall and Catlow (1980)	2.69	2.67[7]	2.82	2.50[2]
	Gillan and Dixon (1980)	2.81		3.57	
SrF_2	Bingham et al. (1989)	2.70	2.43[8]	2.57	1.97[2]
	Catlow and Norgett (1973)	2.68		1.72	
	Cazorla et al. (2018)	2.67		2.09	
UO_2	Cooper et al. (2014b)	2.56	2.14[9]	0.97	0.976[10]
	Morelon et al. (2003)	2.60		1.13	

2.3 Diffraction Patterns

Powder diffraction patterns were generated using the Debyer code, which implements the Debye scattering equations (Farrow and Billinge, 2009; Wojdyr, (https://github.com/wojdyr/debyer)). We use the copper $K\alpha_1$ wavelength λ = 1.54056 Å for these calculations. In order to increase the signal-to-noise ratio, the 12 ,000-atom fluorite cells were first duplicated 7 times in all three directions, resulting in 4,116 000-atoms supercells. To investigate separately the structures of the A and X sublattices, additional supercells were set up by copying the full supercells and then removing either the cations or the anions. Thus, for each simulation we calculated a full pattern accounting for all the atoms, plus partial patterns representing respectively the structures of the A and X sublattices. A sinc damping function was applied to the radial distribution functions. This, in combination with the supercells, is helpful to limit artefacts from the Fourier transform, which would otherwise be large if the 12 ,000-atoms boxes had been used instead. We set the cutoffs for the Fourier transforms to less than one half of the lengths of the supercells. The intensity was finally plotted in powder XRD patterns as a function of the scattering angle 2θ.

Two-dimensional single crystal diffraction patterns were generated using the approach described in (Jin et al., 2020). So called reciprocal space maps (RSMs) were computed in the HHL planes, where H and L are non-integer multiples of the reciprocal lattice unit cell of a given fluorite structure $1/a_{AX_2}(T)$, where $a_{AX_2}(T)$ is the lattice parameter of the AX_2 crystal at the considered temperature T. In order to increase the signal-to-noise ratio the HHL planes have a "thickness" of $\frac{1}{4}$ reciprocal lattice unit cell over which the intensity was integrated. The RSMs were computed with the 12 ,000–atoms cells which results in a visible broadening of the reciprocal lattice points, and the presence of finite box size interference fringes, especially visible at low disorders.

In order to quantify the intensities of the different reflections observed in the RSMs, line scans (with a 0.2 width in HKL units) were first extracted from the 2D data. These scans were further modelled with pseudo -Voigt functions— *i.e.* a linear superposition of a Gaussian and a Lorentzian function—to represent the Bragg peaks, an asymmetrical Gaussian function to represent the isotropic diffuse scattering and an additional linear background. The intensities were obtained after a conventional least-square fitting of the model to the 1D scans.

3 RESULTS AND DISCUSSION

3.1 Thermodynamical Properties

As a first step, the general behaviour of the potentials was assessed by calculating their thermodynamical properties as a function of temperature: enthalpy H, constant-volume heat capacity C_P, and thermal expansion coefficient α. These were used to verify that all potentials predicted a superionic transition for their compound, and to estimate the transition temperature T_S.

Some room-temperature properties calculated using the empirical potentials are shown in **table 2**. The constant-pressure heat capacities are very similar across the potentials, and close to the value expected from the Dulong–Petit law of

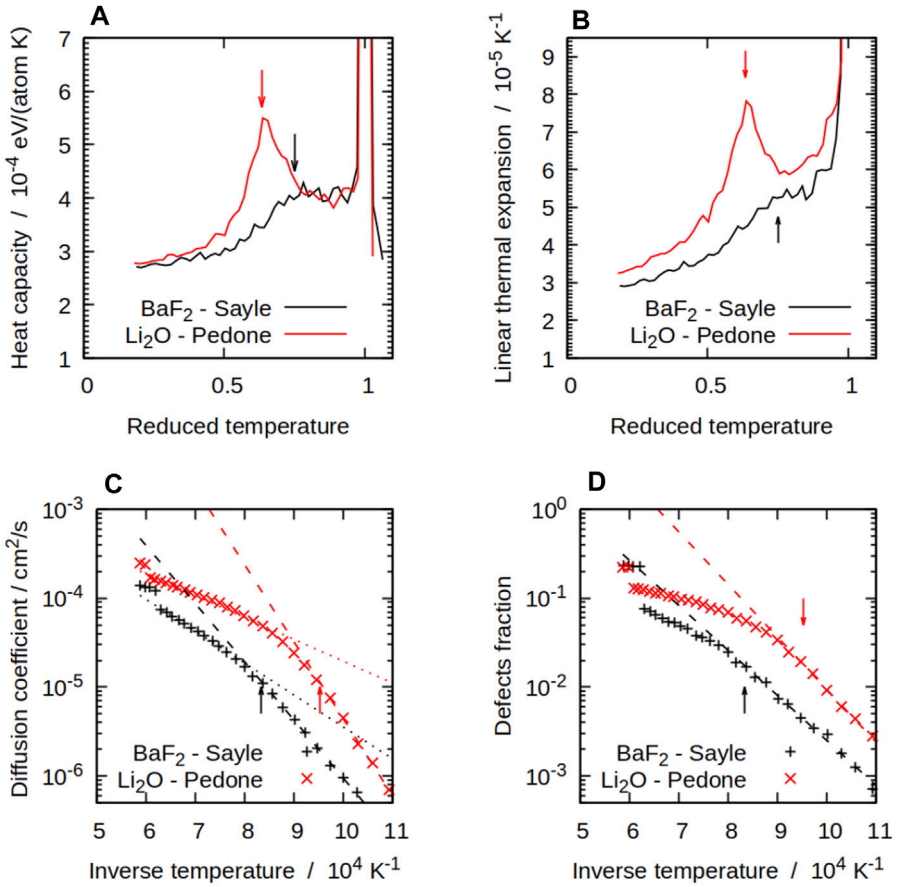

FIGURE 2 | Some thermodynamical and structural properties of compounds with the $Fm\bar{3}m$ structure, BaF_2 with the Sayle potential (Sayle et al., 2003) and Li_2O with the Pedone potential (Pedone et al., 2006): **(A)** constant-pressure heat capacity; **(B)** linear thermal expansion coefficient; **(C)** diffusion coefficient; **(D)** numbers of defects. Reduced temperatures in **(A)** and **(B)** are $\frac{T}{T_M}$, where T_M is the mechanical melting temperature of each compound. The arrows indicate the superionic transition temperatures T_S.

$2.59 \cdot 10^{-4}$ eV/(atom K). This indicates a strong harmonic behaviour from all the potentials, consistently with experimental observations. The main discrepancy with experiments is with Li_2O, which has a significantly smaller heat capacity. The linear thermal expansion coefficient is more potential-dependent than the heat capacity. In general, the models tend to over-estimate α, sometimes significantly. For example, the Cazorla and Sayle potentials for BaF_2, as well as the Bingham and Sayle potentials for CaF_2, the Gillan potential for $SrCl_2$, and the Bingham potential for SrF_2 have errors between 40 and 50%. This is not surprising, considering that α is very sensitive to the details of the potentials, and that the parameters are almost never fitted to it. Overall, the values for both C_P and α show that all the potentials behave well at room temperature, even though some are more accurate than others for these properties.

The simulation were performed in a temperature range from 300 K to the temperature T_M at which the initial crystal turned into a liquid. This transition does not correspond to the experimental melting point T_m, and is in general higher as shown in **Table 2**. By definition, the melting point measured experimentally is the temperature at which the liquid becomes thermodynamically more favourable than the crystal. However, this does not mean that the crystal is strictly unstable: it can be metastable instead and require climbing a non-negligible energy barrier to melt. The small length-scale and short times considered in our simulations inhibits nucleation of a liquid phase, which is the first step of a usual melting transition, by preventing the structure from climbing that energy barrier. The solid to liquid transition we observe is more analogous to a mechanical melting mechanism, and indicate the temperature at which the crystal becomes unstable rather than metastable (Wang et al., 1997). Other methods, such as the so-called moving interface technique (Morris et al., 1994), would be required to measure the thermodynamical melting points T_m accurately. For this reason and to avoid confusion, the thermodynamical (experimental) and mechanical melting points will be noted T_m and T_M respectively throughout this article.

The most visible manifestation of the superionic transition from an experimental point of view is the Λ-shaped peak in C_P, or equivalently the inflection point in the enthalpy $H(T)$. Such peaks have been reported for several fluoride (Hull, 2004), chloride (Schröter and Nölting, 1980; Hull et al., 2011), and oxide (Ralph,

TABLE 3 | Superionic transition temperatures T_S for the different potentials, compared to experimental references. Superionic transition temperatures were calculated from $C_P(T)$ curves, except for those marked.

Compound	Potential	T_S/K		T_m/K	T_M/K
		This work	Ref	Ref	This work
BaF_2	Catlow and Norgett (1973)	1,550	1,135[b(1)]	1,350[b(1)]	2,290
	Cazorla et al. (2018)	1,200[a]	1,275[(2)]	1,628[(2)]	1,630
	Sayle et al. (2003)	1,200[a]	1,300[(3)]	1,555[(3)]	1,600
CaF_2	Bingham et al. (1989)	1,300[a]	-	1,660[b(1)]	1,910
	Catlow and Norgett (1973)	1,650	1,400[b(1)]		2,670
	Evangelakis and Pontikis (1989)	1,400	1,430[(5)]	1,696[(2)]	2,430
	Sayle et al. (2003)	1,300[a]		1,633[(4)]	1980
Li_2O	Asahi et al. (2014)	1,275	1,350[(6)]	1,703[(7)]	1,910
	Oda et al. (2007)	1,300			1,950
	Pedone et al. (2006)	1,050			1,650
β-PbF_2	Catlow et al. (1978)	1,400[a]	711[(8)]	1,128[(2)]	1,950
$SrCl_2$	Bendall and Catlow (1980)	1,200[a]	1,001[(5)]	1,148[(2)]	1,510
	Gillan and Dixon (1980)	920[a]		1,146[(4)]	1,290
SrF_2	Bingham et al. (1989)	1,200[a]	1,150[b(1)]	1,430[b(1)]	1,810
	Catlow and Norgett (1973)	1,630	1,370[(3)]	1,746[(2)]	2,530
	Cazorla et al. (2018)	1,500[a]	1,400[(2)]	1,723[(4)]	2,080
UO_2	Cooper et al. (2014b)	2,550	2,670[(9)]	3,126[(10)]	3,440
	Morelon et al. (2003)	2,600[a]			4,100

[a]*which were estimated from D(T) curves. The reference values are from experiments, except for those marked.*
[b]*which come from DFT calculations. The T_M temperatures are the mechanical melting points from our simulations. Whilst they are not directly comparable, we also provide experimental melting points T_m for context. Experimental references are: (1) Cazorla et al. (2018); (2) Lidiard (1980); (3) Thomas (1976); (4) Catlow et al. (1978); (5) Dworkin and Bredig (1968); (6) Hull et al. (1988); (7) Kurasawa (1982); (8) Dickens et al. (1982); (9) Hiernaut et al. (1993); (10) Böhler et al. (2014).*

1987) compounds with the $Fm\bar{3}m$ structure. Amongst the potentials considered here, some, such as the Pedone potential for Li_2O shown in **Figure 2**, showed a well-defined, sharp peak as generally expected. It was not as clear for other potentials such as the Gillan potential for $SrCl_2$, the Cazorla potential for BaF_2, or the Sayle potential for BaF_2, which is also shown in **Figure 2**. These potentials actually showed a plateau instead of a peak, and the superionic transition is not very visible when looking at thermodynamical properties for such potentials. The other potentials show intermediate behaviours, with C_P peaks with various degrees of sharpness. Two potentials for the same compound can have different C_P characteristics. An example of this is BaF_2, where the Catlow potential has a very sharp peak, whilst no peak is visible with the Cazorla potential. Figures equivalent to **Figure 2** for the other potentials can be found in the **Supplementary Material** for this article. A similar behaviour, also with a sharp Λ-shaped peak, was observed in the linear thermal expansion coefficient $\alpha(T)$. Interestingly, the potentials showing a strong C_P peak similarly tend to show a clear α peak at the same temperature. From the $C_P(T)$ and $\alpha(T)$ curves, we can define four qualitatively different temperature ranges:

i) a low-temperature regime, in which the heat capacity varies slowly as a polynomial;
ii) an exponential increase leading to the top of the Λ peak and the superionic transition, attributed to the formation of Frenkel defects (Szwarc, 1969);
iii) a decrease forming the right-side of the Λ peak;
iv) a high-temperature regime in which C_p varies slowly, leading to T_M.

Some potentials show only some of these features. For instance, regime (i) can be very short for potentials with a low superionic transition temperature. The potential in which the C_P peak is not visible would not have a clear stage (iii), instead going directly from (ii) to (iv). For the potentials that show all four stages, the C_P peak is the simplest way of measuring the superionic transition temperature T_S, which is by convention the temperature corresponding to the top of the peak. This is naturally more difficult to measure for potentials that show a plateau or no peak at all.

The potentials show significant variation in their predictions for T_S, with differences of ~300 K between the lowest and highest values for each compound. This highlights the variety of purposes for which the potentials were designed. More recent potentials tend to be more accurate, presumably thanks to more sophisticated potentials fitting techniques. Potentials that were intended to reproduce the superionic transition, such as Oda for Li_2O, are unsurprisingly the most accurate. Overall, the trend across materials is reproduced, with $SrCl_2$ and UO_2 having respectively a lower and a higher T_S on average compared to the other materials. The main outlier is the Catlow potential for β-PbF_2, which overestimates T_S by 700 K. However, few other potentials are available for this compound, which makes the discussion of any potential-dependent effect difficult. It should also be noted that Pb^{2+} ions in PbF_2 are quite polarisable, which

TABLE 4 | Formation enthalpies for *X* Frenkel pairs in the fluorite structures (H_f). Experimental references are: (1) Lorger et al. (2019); (2) Bollmann (1980); (3) Lidiard (1974); (4) Farley et al. (1991); (5) Chadwick et al. (1988); (6) Samara (1979); (7) Boyce et al. (1977); (8) Bollmann et al. (1970); (9) Matzke (1987).

Compound	Potential	H_f/eV	
		This work	Exp
BaF_2	Catlow and Norgett (1973)	3.67	1.6[1], 1.81[2], 1.9[3]
	Cazorla et al. (2018)	2.07	
	Sayle et al. (2003)	2.01	
CaF_2	Bingham et al. (1989)	2.58	2.2–2.8[3], 2.43[2]
	Catlow and Norgett (1973)	2.99	
	Evangelakis and Pontikis (1989)	1.69	
	Sayle et al. (2003)	1.26	
Li_2O	Asahi et al. (2014)	2.98	1.8[1], 2.1[4], 2.53[5]
	Oda et al. (2007)	2.30	
	Pedone et al. (2006)	1.17	
β-PbF_2	Catlow and Norgett (1973)	2.93	0.89[6], 1.06[7]
$SrCl_2$	Bendall and Catlow (1980)	2.64	1.6–1.8[3], 1.26–5.0[2]
	Gillan and Dixon (1980)	1.64	
SrF_2	Bingham et al. (1989)	2.37	1.74[8], 2.05[2], 1.7–2.3[3]
	Catlow and Norgett (1973)	3.65	
	Cazorla et al. (2018)	3.87	
UO_2	Cooper et al. (2014b)	8.58	2.6–4.2[2], 5.6[9]
	Morelon et al. (2003)	4.18	

could point to a limitation of the rigid ions models to simulate this material. This point has been made in the literature (Castiglione and Madden, 2001), where calculations were done using shell models, with results closer to experimental references. The mechanical melting temperatures T_M are not available experimentally, therefore those obtained from our simulations cannot be compared directly with references. We could still verify that they were greater than the reported melting temperatures T_m for each compound.

The transition temperature T_S has been linked to the melting point T_m. The values for both T_S and T_M from our simulations are summarised in **Table 3** and compared with experimental values. There is some variation across potentials, but overall there is a qualitative agreement for T_S, *i.e.* compounds with a high transition temperature experimentally also tend to have higher values using empirical potentials. It has been reported that the $\frac{T_S}{T_m}$ ratio is generally around 0.8 (Hiernaut et al., 1993). However, this is not very accurate, as experimental references summarised in **Table 3** show $\frac{T_S}{T_m}$ ratios between 0.63 (for β-PbF_2) and 0.85 (for SrF_2 and CaF_2). Whilst we did not measure the thermodynamical melting points T_m that would be directly comparable with experiments, we did measure the mechanical melting points T_M. The $\frac{T_S}{T_M}$ ratios from our simulations are similarly scattered. They are potential-dependent, and range from 0.57 (for CaF_2 with the Evangelakis potential) to 0.79 (for $SrCl_2$ with the Bendall potential).

3.2 Point Defects and Diffusion

We calculated the fraction of point defects as a function of temperature for each potential. In general, we found as expected that the fraction of *A* defects was negligible in most of the considered temperature ranges (Catlow and Norgett (1973)). In all cases, the number of *A* Frenkel pairs just below T_M was still two orders of magnitude smaller than that of *X* defects. No defect at all could be seen on the *A* sublattice for temperatures lower than about 100 K below T_S, therefore they will be ignored and the following discussion is focused on the *X* defects.

Populations of *X* defects were significant at higher temperatures with all the potentials we considered. **Figure 2D** shows this for both BaF_2 and Li_2O with the Sayle and Pedone potentials respectively. The simulations showed a pattern with a transition from a low-temperature Arrhenius regime, in which the *X* defect fractions takes the form

$$N_{def}(T) = N_0\ e^{-H_f/2k_BT}\ , \tag{4}$$

where H_f is the formation enthalpy of an *X* Frenkel pair, to a high-temperature regime in which the number of defects grows with a smaller effective formation energy. The effective formation enthalpy below the superionic transition H_f is shown for all potentials in **Table 4**. The difference between both regimes and the inflection point can be seen in **Figure 2D**. The T_S temperature marks the start of the deviation of the number of defects calculated from MD form its low-temperature fit. This links the change in defect properties to the onset of the superionic transition. The same pattern was observed for all potentials, with some variation in the magnitude of the transition. In general, potentials showing a sharp C_P peak also had a large difference between the low-temperature and high-temperature behaviours. On the other hand, in cases such as $SrCl_2$ with the Gillan

TABLE 5 | Activation energies for the *X* diffusion process in both the perfect fluorite phase (E_a^c) and the superionic states (E_a^s). The reference values are from experiments, except for those marked.

Compound	Potential	E_a^c/eV		E_a^s/eV	
		This work	Exp	This work	Ref
BaF_2	Catlow and Norgett (1973)	2.90	1.6[(1)], 2.52[(2)]	0.61	0.48[(2)]
	Cazorla et al. (2018)	1.32		0.95	
	Sayle et al. (2003)	1.30		0.73	
CaF_2	Bingham et al. (1989)	1.52	1.92[(3)], 2.02[(1)], 3.34[(2)]	0.86	0.74[(2)]
	Catlow and Norgett (1973)	2.89		0.65	
	Evangelakis and Pontikis (1989)	2.19		0.61	
	Sayle et al. (2003)	1.63		0.82	
Li_2O	Asahi et al. (2014)	2.02	1.6[(4)], 2.52[(5)]	0.63	0.98[a(6)]
	Oda et al. (2007)	1.68		0.67	
	Pedone et al. (2006)	1.50		0.48	
β-PbF_2	Catlow and Norgett (1973)	1.95	1.04[(7)]	0.81	-
$SrCl_2$	Bendall and Catlow (1980)	1.89	4.43[(2)]	0.83	0.42[(2)]
	Gillan and Dixon (1980)	1.07		0.86	
SrF_2	Bingham et al. (1989)	1.80	1.81[(3)]	0.79	0.55[(2)]
	Catlow and Norgett (1973)	2.76		0.63	
	Cazorla et al. (2018)	2.04		0.95	
UO_2	Cooper et al. (2014b)	5.35	2.46–2.57[(8)]	1.43	
	Morelon et al. (2003)	2.74		1.40	

[a]*which come from DFT calculations. References are: (1) Ando et al. (1980); (2) Voronin and Volkov (2001); (3) Bollmann et al. (1970); (4) Lorger et al. (2019); (5) Oishi et al. (1979); (6) Gupta et al. (2019); (7) Samara (1979); (8) Ando and Oishi (1983).*

potential, the transition is not very noticeable and there is not a large difference between both regimes. At low temperatures, **Equation 4** can be fitted to data from the MD simulations to estimate the formation energy of *X* Frenkel pairs. Formation enthalpies for *X* Frenkel pairs for all the considered potential are summarised in **Table 4**. In general, the empirical potentials are in qualitative agreement with available references and their formation enthalpies fall within the range of experimental values. Notable outliers are the Catlow and Cooper potentials for BaF_2 and UO_2, which significantly over-estimate H_f, and Pedone for Li_2O, which under-estimate it. Beyond the superionic transition, the *X* sublattice is expected to be highly disordered. However, defects are detected using the $Fm\bar{3}m$ structure as a reference, which may be inadequate in presence of large distortions and possible extended defects. For this reason, the number of defects is much less reliable in the superionic phase, and no attempt was made at obtaining a quantitative measurement of the number of point defects in this case.

Crystals in the $Fm\bar{3}m$ structure are known to exhibit three different diffusion behaviours (Voronin and Volkov, 2001). The diffusion is extrinsic when it is limited by the availability of extrinsic defects to provide diffusion pathways. It becomes intrinsic, with a higher activation energy, when the temperature is high enough to provide a significant population of Frenkel pairs. Diffusion is then mediated by point defects hopping, and depends on the availability of *X* Frenkel pairs. Finally, in the superionic phase, diffusion is faster and is thought to involve collective displacements (Annamareddy and Eapen, 2017), with a lower activation energy than the intrinsic Frenkel pair mechanism (Voronin, 1995; Voronin and Volkov, 2001). Whilst our simulations could not reproduce extrinsic diffusion mechanisms because of the lack of extrinsic defects, we found intrinsic and superionic behaviours consistent with what could be expected from the literature. Both behaviours are visible in **Figure 2C**. We fitted exponential functions of the form $D(T) = D_0\ e^{-E_a/k_B T}$ to the calculated diffusion coefficients on both sides of the superionic transition to obtain diffusion activation energies E_a^c and E_a^s for the perfect crystal and the superionic phase respectively. The resulting activation energies are shown in **Table 5**. All the potentials considered here showed an activation energy change during the superionic transition, with $E_a^c > E_a^s$, albeit to different degrees. The crossover between the low- and high-temperature behaviours does not occur at T_S for the potentials for which T_S could be calculated from the Λ peak in the $C_P(T)$ curves. Instead, as was the case for the number of defects, T_S marks the point at which the diffusion coefficients from MD start deviating from the low-temperature fit. The switch to the high-temperature behaviour itself occurs over a temperature range of a few hundred Kelvins. The upper bound of this range corresponds to the transition between regimes (iii) and (iv) as described in **Section 3.1**, *i.e.,* to the high-temperature end of the Λ peak. For potentials that do not show a clear peak in $C_P(T)$, the change in diffusion coefficients can be used to estimate T_S. This method is less accurate, however, because the deviation of $D(T)$ to the fit is more difficult to characterise than a clear peak of C_P. All the transitions temperatures are summarised in **Table 3**.

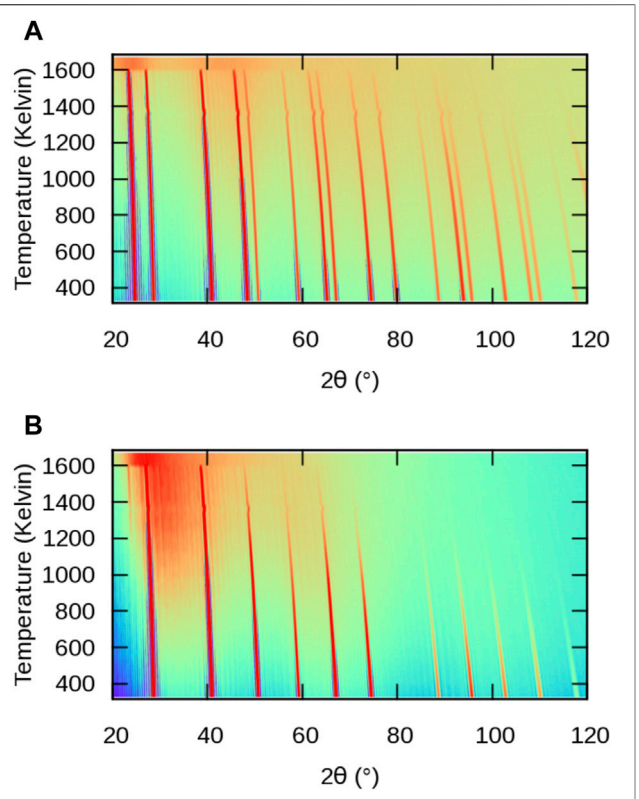

FIGURE 3 | Simulated powder XRD patterns from MD simulations of BaF_2 using the Sayle potential (Sayle et al., 2003) as a function of temperature: **(A)** full structure; **(B)** F sublattice only.

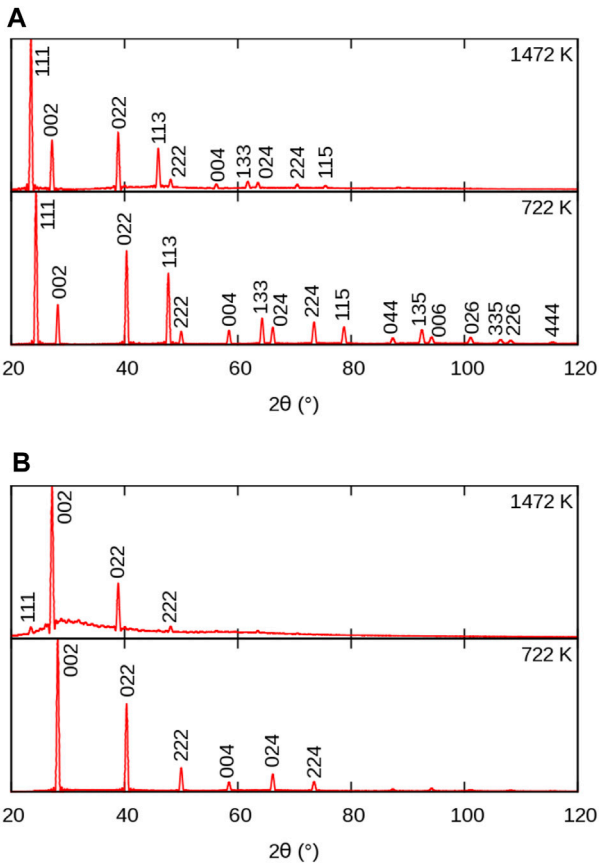

FIGURE 4 | Simulated powder XRD patterns from MD simulations of BaF_2 using the Sayle potential (Sayle et al., 2003), at temperatures below and above the superionic transition: **(A)** full crystal; **(B)** F sublattice only. Peak indices refer to the full $Fm\bar{3}m$ structure. The superionic transition temperature for this potential is 1,300 K.

The activation energies in the $Fm\bar{3}m$ phases E_a^c from the MD simulation agree with the experimental references in general.

The fact that all potentials showed two different regimes for diffusion of the X chemical species regardless of the presence of a peak in C_P and α confirms that the superionic transition can hapen without resulting in Λ peaks. This means that it is not inconceivable that such a transition could also happen without Λ peak in real materials. In fact, there are reports of this in $SrCl_2$ (Dent et al., 2004).

3.3 Simulated Powder XRD Patterns

As mentioned previously, the analysis of the structural evolution of AX_2 fluorites with temperature by a direct analysis of the MD simulations proved very challenging, particularly in the superionic phases. An approach to avoid this issue is to visualise the information contained in MD cells in a more compact representation. This is for instance the case when considering the radial distribution functions (RDFs). In the present study we choose to compute powder XRD patterns, *i.e.*, Fourier transforms of RDFs. They are more sensitive to long-range atomic order and its alteration (Debelle et al., 2014), and are therefore a very useful complement to real-space structure analysis. We illustrate our findings with the example of BaF_2 with the Sayle empirical potential, bearing in mind that all conclusions drawn below are qualitatively valid for all the other potentials. This particular case was selected firstly because it exhibits XRD features common to all the composition–potential combinations investigated, with clearly visible temperature-dependent evolutions. It also has a plateau in C_P and α instead of a Λ peak. It is hence both a representative example of all configurations investigated in this work, and a demonstration of a superionic transition without a Λ peak.

The evolution of powder XRD patterns as a function of temperature is illustrated in **Figure 3** (2θ–T figure), considering all atoms in the MD cell (**Figure 3A**) and only the X sublattice (**Figure 3B**). We will refer to them as full-crystal XRD and X-only XRD patterns, respectively. Additionally, we report selected full XRD and X-only XRD patterns at two temperatures on **Figure 4**.

Let us first consider the full XRD patterns shown in **Figures 3**, **4 A**. At 300 K, the characteristic peaks of the fluorite unit cell are clearly visible and can be indexed within the $Fm\bar{3}m$ symmetry group. Unsurprisingly, these peaks gradually shift towards smaller angles with increasing temperature, following the thermal expansion of the material. This is more pronounced at higher angles in agreement with the derivative of Bragg's law

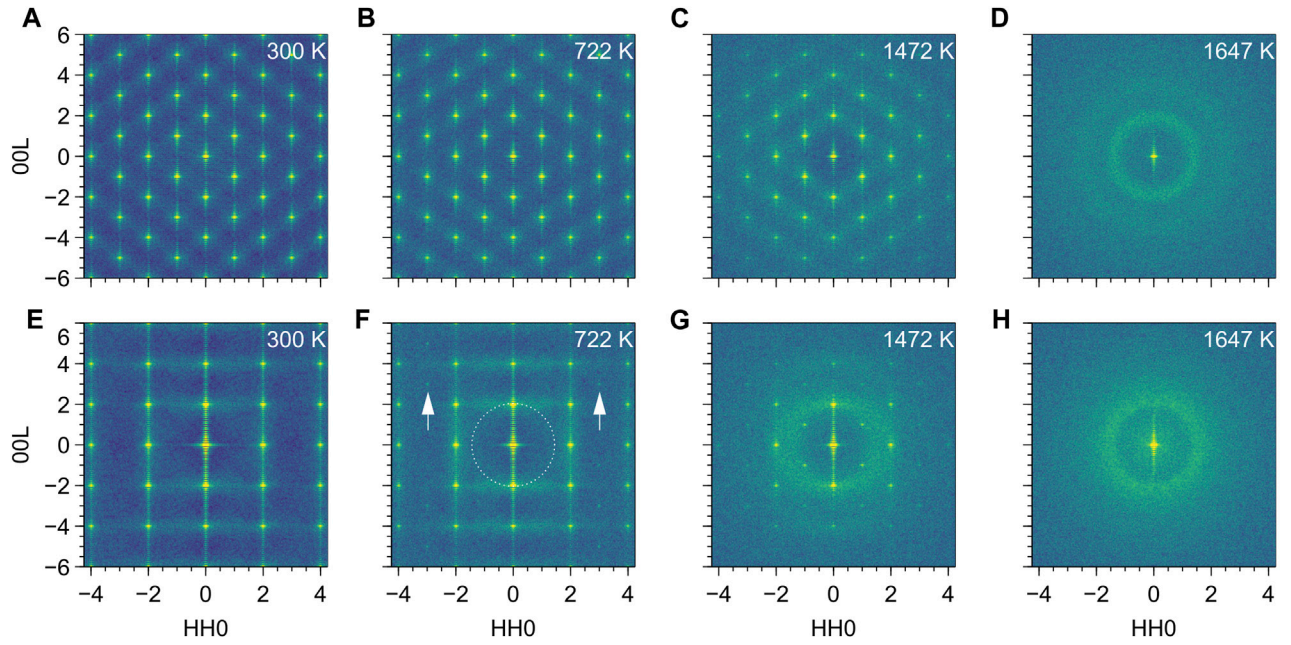

FIGURE 5 | Simulated reciprocal space maps from MD simulations of BaF_2 using the Sayle potential (Sayle et al., 2003): **(A–D)** Ba sublattice; **(E–H)** F sublattice. In **(F)** the arrows indicate the $\overline{1}13$ and 113 superstructure peaks, and the dotted line highlights the diffuse halo. The intensity is plotted on a logarithmic scale to enhance low-intensity details.

$$\Delta 2\theta = -2\alpha \Delta T \tan\theta \,, \tag{5}$$

ΔT being the temperature change.

The intensity of the peaks also decreases with increasing temperature, as a result of increasing local disorder, *i.e.* increasing thermal motion. The decrease in intensity is quantified by the Debye-Waller factor (Trueblood et al., 1996), which, in the case of harmonic and isotropic vibrations, is expressed by the simple expression

$$T(\theta) = \exp\left[-8\pi^2 \langle u^2 \rangle \sin^2\theta/\lambda^2\right] \tag{6}$$

where u is the displacement of the atom from its regular lattice site. The effect of intensity damping is more pronounced at higher angles, as was the case for the peak shift.

Finally, it can be noticed that a background of diffuse scattering develops around the most intense peaks. The intensity of this background increases up to the melting point where only diffuse scattering remains, but with a significantly redistributed intensity. The origin of this diffuse scattering background lies in the presence of thermal motion also responsible for the above-mentioned intensity damping, but it can also reveal the presence of structural defects.

In all the cases we investigated, the *A*-specific pattern was virtually identical to the full-crystal pattern. For this reason, the *A* patterns will not be discussed here, but $2\theta - T$ maps can be found int the **Supplementary Material**. The similarity between full-crystal and *A*-only patterns can be simply understood by considering the difference in atomic numbers *Z* between light elements constituting the *X* sublattice (F, Cl, O), as compared to the heavier elements occupying the *A* sublattice (Ca, Ba, Pb, U). The latter dominate the overall XRD signal the intensity of which is proportional to Z^2, thus making the contribution from lighter elements fainter.

Let us now consider the *X*-only XRD patterns shown in **Figures 3**, **4 B**. Besides the similar general features related to thermal expansion (peak shift) and thermal motion (decrease in intensity) there are two noticeable differences with the full-crystal patterns. The first difference is the positions and intensities of the peaks. This is easily explained by the fact that the *X* sublattice has a SC symmetry, as opposed to the FCC symmetry of the full fluorite structure. The lattice parameter of the SC sublattice is half of that of the overall $Fm\overline{3}m$ structure. To avoid any ambiguity, we index the peaks of the *X*-only patterns using the same Miller indices as the full fluorite structure. This means that, for instance, the peak labeled 200 would correspond to the 100 peak of a SC unit cell of the *X* sublattice.

The second difference between *X* and full-crystal powder XRD patterns is the diffuse scattering background. Its intensity relative to the Bragg peaks is much higher, which indicates a much higher level of disorder on the *X* sublattice than on the *A* sublattice. The diffuse scattering is also more broadly distributed across the 2θ range, roughly centred around the 200 peak. This is a sign of the presence of amorphous or highly disordered local environments with a first neighbour distance approximately given by the *X*–*X* distance in the corresponding sublattice.

An additional 111 peak (or $\frac{1}{2}\frac{1}{2}\frac{1}{2}$ in a base SC cell) emerges at temperatures around T_S in the *X*-only patterns. This peak could not be detected in the full XRD pattern because its position exactly coincides with the 111 peak of the fluorite structure. The appearance of a superstructure peak with halved Miller indices

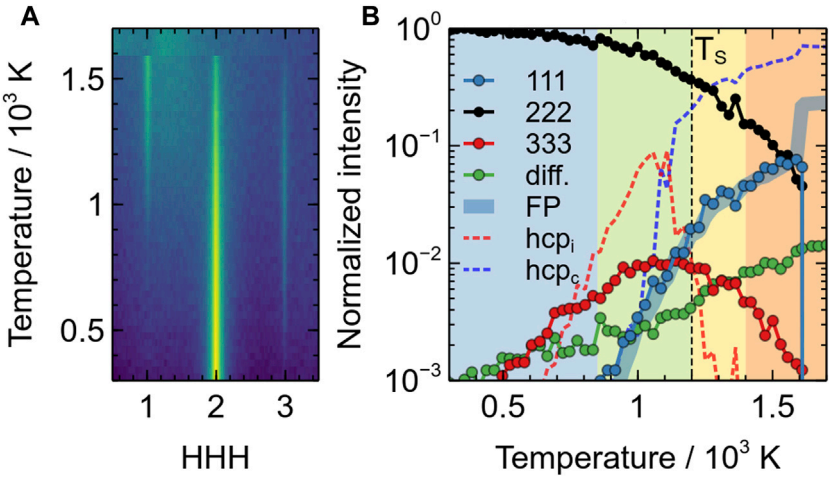

FIGURE 6 | Evolution of the intensity of the additional single-crystal XRD peaks in the superionic phase of BaF_2 using the Sayle potential: **(A)** evolution of the [111] intensity distribution as a function of temperature; **(B)** evolution of the 111 (blue circles), 222 (black circles), 333 (red circles) and diffuse scattering (green circles) peaks as a function of temperature. All intensities are on a logarithmic scale and normalised with respect to the room temperature of the 222 peak. Lines represent the evolutions of FP (thick blue), isolated HCP environments (red dotted) and clustered HCP environments (dotted blue). The different coloured areas correspond to the different regimes (i)–(iv) mentioned in the text.

points to a doubling of the periodicity of the unit cell of the *X* sublattice, which becomes equal to that of the overall $Fm\bar{3}m$ crystal. However, the lack of other superstructure peaks such as 113 and the weak intensity of the 111 peak makes it difficult to draw firm conclusions from those XRD patterns. For this reason, we now consider single-crystal diffraction.

3.4 Simulated Single-Crystal XRD Patterns

Single-crystal XRD provides another way of understanding the structural changes related to the superionic transition. Similarly to powder XRD, because it operates in the reciprocal space, it can reveal long-range features that are difficult to observe directly in simulation boxes due to thermal noise and increasing disorder at high temperatures. However, in contrast with powder XRD, there is no orientation averaging involved in the calculation. Hence, it is possible to precisely select definite regions of the reciprocal space to analyse. In order to be able to detect the appearance of superstructure peaks of the type 111, 113, etc., we computed the intensity distribution in (*HHL*) reciprocal lattice planes (that is, with a $[1\bar{1}0]$ zone axis). As for the powder diffraction study, we focus on BaF_2 with the Sayle potential and we use Miller indices relative to the $Fm\bar{3}m$ structure even when discussing the *X* sublattice. Data showing the evolution of the RSMs of all investigated cases are available in the **Supplementary Material**.

We first briefly discuss the RSMs obtained from the *A* sublattice shown in **Figures 5A–D**. From room temperature up to T_S, besides diffuse scattering concentrated around the Bragg peaks, no significant changes were observed. The peak coordinates have here been corrected for thermal expansion to allow for an easier comparison between different temperatures. At T_M, a diffuse scattering halo characteristic of an amorphous structure is observed pointing to the melting of the material (**Figure 5D**). These observations lead to two important conclusions. Firstly, apart from the observed thermal diffuse scattering, the fact that the signal from the *A* sublattice remains constant throughout the process - with no visible peak shift, peak broadening or splitting, or additional diffuse scattering—seems to indicate that the *A* sublattice is free of structural defects. This is in stark contrast with the *X* sublattice, which we will discuss shortly. We also know from direct analysis of the MD simulations shown in **Section 3.2** that these defects are rare up until T_M. Secondly, the thermal diffuse scattering forms streaks along the main ⟨111⟩ directions, indicating that atomic displacements are more pronounced in the close-packed {111} planes. This is also consistent with the weak and inhomogeneous diffuse scattering observed in the powder XRD data.

As far as thermal diffuse scattering is concerned, similar conclusions can be drawn for the *X* sublattice shown in **Figures 5E–H**. Diffuse scattering streaks appear along the {001} and {110} planes of the SC structure, pointing to enhanced thermal motion in the corresponding lattice planes. However, as soon as the temperature increases, major changes are observed on the *X* sublattice. The first difference is the appearance of weak intensity high-order 33*L* superstructure peaks (for instance at 722 K, indicated by the arrows on **Figure 5F**). The second noticeable difference is the increase of the diffuse scattering connecting the Bragg peaks, together with the appearance of a weak diffuse scattering halo with [002] radius, indicated on the figure by a dotted circle. The halo is barely visible in the RSM in this case, but it can be definitely detected by analysing line scans performed along the [111] direction (see also **Figure 6**). The RSMs of all cases investigated are given in the **Supplementary Material**. All of them exhibit the diffuse halo appearing almost concomitantly with the 33*L* peaks with varying intensity. In the superionic phase (**Figure 5G**, representing a

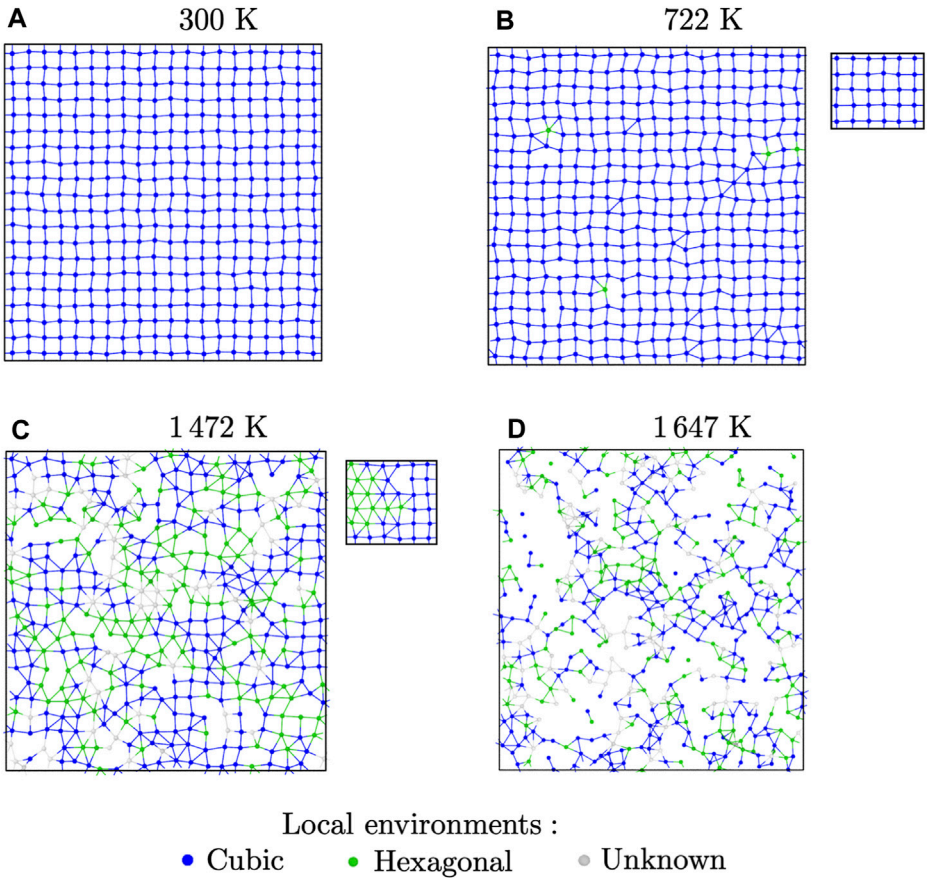

FIGURE 7 | Slices showing (100) F atomic planes from MD relaxation of BaF_2 with the Sayle potential at different temperatures, with Ba ions hidden for clarity: **(A)** room-temperature perfect crystal; **(B)** crystal with Frenkel defects; **(C)** superionic structure; **(D)** liquid. The colour code indicates the type of local environment according to the Polyhedral Template Matching analysis. The insets show the same slices after energy minimisation.

structure at 1,472 K), additional 11*L* superstructure peaks are formed and the diffuse halo is now clearly visible. It should be noted that the apparent ellipsoidal shape of the halo is due to the partial superposition of the halo with the diffuse streaks along [110] and [001]. The 33*L* peaks are still visible, but their intensity decreases because thermal motion starts affecting high angle reflections. Finally, all Bragg peaks disappear at T_M. Only the diffuse halo remains then, characteristic of an amorphous structure, in this case of the molten phase. All the potentials showed both the additional peaks and the diffuse halo. However, the relative intensity of these features is potential- or material-dependent. For instance, all the potential for Li_2O showed a particularly intense diffuse halo, which is explained by the fact that the light element Li is significantly affected by thermal motion. Some potentials also produced fainter 33*L* and 11*L* peaks than others. All these features are visible in the animations, which can be found in the **Supplementary Material**.

This evolution is summarised in **Figure 6**, which depicts the changes of the [111] line scans and the different intensities with temperature. There, it can be clearly observed that the diffuse halo starts to appear at a temperature slightly higher than room temperature (~400–500 K, green circles), hence pointing to thermal vibrations. It then steadily increases with temperature. The 333 peak appears almost concomitantly (~500 K, red circles) and reaches a maximum close to T_S. Around 850 K, the 111 peak starts to increase significantly (blue circles). This corresponds to the end of stage (i) and the beginning of stage (ii). The end of stage (ii), marking the superionic transition correspond to a temperature where the intensity of the 111 peak exhibit a change in slope and where the intensity of the 333 peak starts decreasing. Finally at T_M, all intensities drop to 0 except the diffuse scattering, which remains constant.

This evolution is consistent with the powder XRD data, in particular the appearance of a 111 peak at T_S and a broad diffuse scattering background in *X*-only patterns. However, because of the orientation averaging inherent in powder XRD and the consecutive peak overlap, it is not possible to detect low intensity details as those discussed here. Finally, the fact that the diffuse scattering steadily increases until the melting temperature without any discontinuity, reinforces the description of the *X* substructure as a liquid made in the literature. In the next section, we discuss the origin of the superstructure peaks.

3.5 Structure of the Superionic Phase

Visual examination of the structures during MD simulations at different temperatures reveals some structural changes. To highlight them, we extracted slices from supercells from MD simulations of BaF_2 using the Sayle potential. The slices are 3 Å thick and centred on {100} atomic planes containing only F ions. At room temperature, the potential predicts a perfect $Fm\overline{3}m$ crystal. The slice at 300 K (**Figure 7A**) indeed shows a square structure, corresponding to the {100} faces of the cubes forming the *X* sublattice.

At intermediate temperatures, such as 722 K as in **Figure 7B**, some local distortions are visible, showing isolated triangular features. Visualisation of these features is helped by the use of the polyhedral template matching technique, which provides a characterisation of the local environment around each particle. At this temperature, almost all of the F ions are still in their ideal (SC) local environment. The closest matching structure for the ions with non-cubic local environments is HCP. The apparition of HCP local environments has been verified for all the potentials. With most of them, it coincides with the end of regime i and beginning of regime (ii). Most of the time, it also seemed to happen before Frenkel pairs were detected. However, this should be treated with caution. Indeed, the methods we used to count Frenkel pairs, though qualitatively accurate, can result in an under-estimation of the number of defects. On the other hand, the PTM analysis could also be too sensitive, resulting in false positives.

This changes around the superionic transition temperature T_S. Indeed, in the superionic phase of regimes (iii) and (iv), we could see some clustering of the atoms with HCP environments, which were much more likely to be first neighbours. This is shown in **Figure 7C**, where we can see clusters of HCP environments mixed with cubic regions. This pattern holds until the mechanical melting point T_M, after which the structure becomes liquid (**Figure 7D**).

The ions with unknown local environments are cases where the PTM algorithm could not decide how to categorise the particle. There are very few of them below T_S. For example, in the case of BaF_2 with the Sayle potential, they represent 5% of all F ions at the superionic transition. They are more prevalent in the superionic phase, but still amount to 13% at the mechanical melting point. They are much more present in the liquid phase, where the structure is not well-suited to the PTM analysis. These ions with disordered local environments are expected to contribute to the diffuse scattering observed in both powder and single-crystal diffraction patterns. The MD simulation boxes in the superionic phases also show that there can be a high degree of misorientation between the different types of local environments. This also contributes to the diffuse scattering.

This evolution of the number of ions with HCP local environments is plotted in **Figure 6**, together with the XRD data. This figure clearly confirms the findings described previously. Isolated HCP environments appear at relatively low temperatures ($\sim$ 600 K), well before Frenkel pairs. The concentration of those isolated HCP environments, noted hcp_i, are neatly correlated with the apparition of the 33*L* superstructure peaks, which indicate that these defects reduce the unit-cell symmetry to a period of $\sim\frac{1}{3}$ of the (111) fluorite lattice spacing.

In terms of temperature range, the fraction of clustered HCP environments, noted hcp_c, is almost perfectly correlated both with the fraction of Frenkel pairs, and the intensity of the 111 peak. This indicates that the Frenkel pairs are at the origin of (i) the clustering of HCP environments, and (ii) the formation of ordered local environments on the *X* sublattice, with a periodicity equal to that of a fluorite unit-cell.

The PTM analysis in itself does not give a complete picture of the local environments it detects. For example, the actual local environments also depend on the position of neighbours on the *A* sublattice. Those were completely ignored in our PTM analysis, which was done separately for each sublattice. Determination of the local environments directly from MD simulations proved all but impossible due to distortions and large thermal fluctuations in the superionic phases. To work around this, we performed constant-volume geometry optimisations from the final structure of the MD simulations for each potential and temperature. During this operation, the ions were moved towards more energetically favorable positions, thus removing thermal noise from vibrations and unstable defects. The results were structures that were easier to interpret and characterise. It should be noted, however, that the energy-minimised and high-temperature structures are not the same. Indeed, some temperature-activated phenomena disappear during geometry optimisation. Thus, the energy-minimised structure can only provide some clues as to how to interpret high-temperature MD simulations.

The structures optimised from high-temperature simulations showed both cubic and non-cubic local environments after PTM analysis. The trend was also similar to what was observed in high-temperature simulations. In regime i, all potentials produced a perfect $Fm\overline{3}m$ crystal after optimisation. This changed in regime (ii), where we could observe some isolated ions with non-cubic environments, as well as some trapped Frenkel pairs, which could not recombine during energy minimisation. Above the superionic transition temperature, most potentials showed a separation into two phases, which contained the cubic and non-cubic environments respectively. Visual examination of the non-cubic phase showed the same triangular pattern observed in MD simulations, except that the pattern covered extensive regions of the simulation box instead of small, elongated clusters. This is visible in the inset in **Figure 7C**. In addition, because all thermal noise was removed, we could isolate the non-cubic environment for a more thorough characterisation. We found that the structure we isolated had the symmetry elements of the *Pbcn* space group. This space group corresponds to the scrutinyite structure (α-PbO_2), and is well-known in some compounds of the AX_2 form. In particular, there are some instances of such compounds undergoing a pressure-induced phase transition to distorted fluorite structures Léger and Haines (1997); López-Moreno et al. (2016). A transition from $Fm\overline{3}m$ to *Pbcn* hasn't been documented in materials with the fluorite structure, however, except for UO_2, where it was seen during fracture (Zhang et al. (2012)) or under tensile mechanical loading (Fossati et al. (2013)). Even in that case, the *Pbcn* phase was not thermodynamically stable.

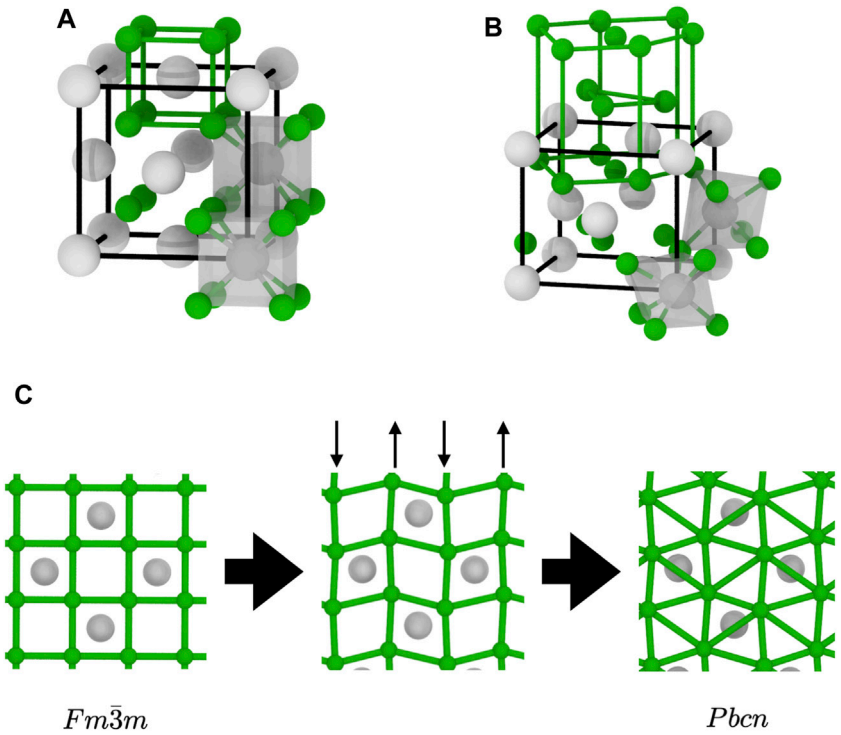

FIGURE 8 | Structural transition between the two AX_2 structures relevant to this study: **(A)** $Fm\bar{3}m$; **(B)** *Pbcn*; and **(C)** deformation of a [100] atomic plane during the transition, with the vertical arrows indicating the displacement of the columns of *C* ions. The bonds emphasise the structure of the *X* sublattice: simple cubic in $Fm\bar{3}m$ and distorted hexagonal close packed (HCP) in *Pbcn*. The polyhedra show the coordination environments of the *A* ions: cubic in $Fm\bar{3}m$ and octahedral in *Pbcn*. Subfigures on the bottom show the changes in a [010] plane during the transition and the appearance of the triangular patterns in the basal planes of the HCP substructure.

In the *Pbcn* structure, the *X* sublattice has a distorted HCP structure, whilst the *A* sublattice remains close to FCC, as shown in **Figure 8B**. The pattern shown in the (0001) basal plane of the *X* sublattice in that structure, shown in **Figure 8**, is the triangular pattern visible in both MD simulations and energy-minimised structures. Thus, we can conclude that the non-cubic local environments detected by the PTM analysis are actually *X* ions which have a local environment consistent with that of the *Pbcn* structure. The overall structure of the superionic phase, however, is quite different from what was observed during the $Fm\bar{3}m \rightarrow Pbcn$ transition (Fossati et al., 2013). Indeed, it does not consist in a clear separation between a $Fm\bar{3}m$ and *Pbcn* phases. It is formed instead of a mixture of local environments with different structures, along with some ions with a disordered environment. Moreover, we can see on **Figure 7C** that there can be a large degree of disorientation between different local environments.

We can now propose a mechanism for the superionic transition in materials with the fluorite structure. Upon heating, the *X* sublattice is subject to thermal vibrations compatible the with symmetry of the crystal. This gives rise to the diffuse scattering in the {001} planes observed in the RSMs of the *X* sublattice. There is a known vibration mode that fits this description. It is the B_{1u} mode with a $[0\,0\,\frac{1}{2}]$ wavevector, which has been linked to the superionic transition in CeO_2 (Klarbring et al., 2018). The polarisation vector of this mode corresponds exactly to the displacement of the *X* ions at the beginning of the $Fm\bar{3}m \rightarrow Pbcn$ transition shown in **Figure 8C**. These distortions result in the appearance of local environments with HCP symmetry elements, initially isolated and distributed in the $Fm\bar{3}m$ structure. Upon further heating, the crystal starts forming *X* Frenkel pairs. This coincides with the clustering of isolated HCP local environments, with symmetry elements characteristic of the *Pbcn* structure, throughout the crystal. These local environments are responsible for the anomalous enthalpy, and the exponential increase in the heat capacity leading to the Λ peak. The structure change could also be the reason of the different diffusion mechanism in the superionic phase. In contrast, the volume fraction of the disordered (liquid- or amorphous-like structure), responsible for the diffuse scattering halo, steadily increases from room temperature up to melting without any noticeable change. It is hence unlikely to be involved in the drastic changes observed in the thermodynamic properties.

4 CONCLUSION

We used a wide selection of empirical potentials to simulate several different compounds with the fluorite structure and investigate structural changes between the low-temperature perfect structure and that of the superionic phase.

Although a full validation of each potential was not done here, we verified that the properties they predict are realistic by comparing them to available experimental values. In particular, the superionic transition temperatures, the enthalpies of formation for the *X* Frenkel pairs, and the activation energies for *X* diffusion in both the $Fm\overline{3}m$ and superionic phases were found to be adequate. Therefore, whilst the potentials are quantitatively imperfect when taken separately, we are confident that the qualitative trends they show are not potential dependent.

From a thermodynamical point of view, not all the potentials reproduced the characteristic C_P and α peaks usually associated with the superionic transition, despite showing other aspects such as structural disorder and a change in the diffusion properties. This demonstrates that the transition could occur without a clearly-visible peak. Different potentials for the same compound could also exhibit different behaviour. For example, in BaF_2, the Catlow potential showed a sharp Λ peak in its $C_P(T)$ curve, whereas the Sayle potentials showed a broad plateau, and the transition was almost invisible from the thermodynamical properties of the Cazorla potential.

All potentials are characterised by a 2-regime diffusion behaviour, with a change in the apparent activation energy at the superionic transition consistent with available experimental data. Moreover, populations of *X* Frenkel pairs showed a similar trend, with a low-temperature Arrhenius regime followed by a progressive transition towards a lower apparent formation energy in the superionic phases. This is consistent with a transition from a diffusion process mediated by isolated point defects in low-temperature crystals to a collective process involving clusters in the superionic phases.

Powder and single-crystal XRD patterns were calculated from the MD simulation boxes for investigate structural changes from the reciprocal space. Whilst the *A* sublattices did not change from room temperature to the melting point, additional Bragg peaks on the *X* sublattices showed the emergence of new structural features distinct from the simple partially molten structure sometimes assumed. This observation could not be made using experiments, which could not have separated signals from both sublattices. Subsequent analysis of the MD simulation boxes could determine that the additional peaks are the result from a the presence of local environments with a structure close to the *Pbcn* structure. In these local environments, the *X* sublattice has HCP features. This work is a demonstration of the power of combined MD and computational diffraction techniques to described structures associated with widespread disorder.

Following our observations, we can describe the evolution with temperature of the structure of the fluorite compounds, following the four stages defined from thermodynamical properties and outlined in **Section 3.1**. Only the *X* sublattice is discussed in the following: the *A* sublattice remains FCC from room temperature to T_M, with some distortions at high temperatures.

Stage (i)

This is the low-temperature regime, in which the heat capacity varies slowly as a polynomial. Near the end of this temperature range, isolated hexagonal local environments are formed in an otherwise perfect $Fm\overline{3}m$ matrix. This stage is the extrinsic diffusion regime. No diffusion could be measured from the MD simulations because for their short time scale and lack of extrinsic defects.

Stage (ii)

In this regime, $C_P(T)$ follows an exponential increase leading to the top of the Λ peak, or the left-hand edge of the plateau depending on the potential. The end of this stage is T_S and the onset of the superionic transition. The structure is characterised by the accumulation of Frenkel pairs and hexagonal environments becoming more present. The number of isolated HCP environments peaks near the end of this stage. This corresponds to the intrinsic diffusion regime, limited by Frenkel pairs, where diffusion coefficients follow an Arrhenius law.

Stage (iii)

In this transition stage, the $C_P(T)$ curve decreases sharply, forming the high-temperature side of the Λ peak. The number of isolated hexagonal environments also decreases, to become negligible by the end of this stage, at which point all the hexagonal local environments are part of clusters. The beginning of this stage is associated with a change in slope of the Frenkel pair concentration, diffusion coefficient, and the concentration of clustered hexagonal local environments, which all increase at a reduced rate. The diffusion coefficients progressively change from the stage (ii) to the stage iv Arrhenius regimes. This stage might not be visible if the potential does not predict a C_P peak.

Stage (iv)

The growth of the $C_P(T)$ curve resumes slowly, leading to the mechanical melting at T_M. The structure is characterised by a mixture of regions with hexagonal local environments, and regions that retain the cubic local environment of the perfect fluorite structure. The *X* diffusion coefficient follows another Arrhenius law, with an activation energy smaller than that of stage (ii), underlying the collective diffusion mechanism underlines elsewhere (Annamareddy et al., 2014).

DATA AVAILABILITY STATEMENT

The raw data supporting the conclusions of this article will be made available by the authors, without undue reservation.

AUTHOR CONTRIBUTIONS

All authors listed have made a substantial, direct and intellectual contribution to the work, and approved it for publication.

FUNDING

This work was granted access to the HPC resources of the TGCC computing centre, under the DARI allocation A0100911528.

SUPPLEMENTARY MATERIAL

The Supplementary Material for this article can be found online at: https://www.frontiersin.org/articles/10.3389/fchem.2021.723507/full#supplementary-material

REFERENCES

Ando, K., Akiyama, M., and Oishi, Y. (1980). Lattice Diffusion Coefficient of Oxygen in Lithium Oxide. *J. Nucl. Mater.* 95, 259–264. doi:10.1016/0022-3115(80)90367-0

Ando, K., and Oishi, Y. (1983). Diffusion Characteristics of Actinide Oxides. *J. Nucl. Sci. Tech.* 20, 973–982. doi:10.1080/18811248.1983.9733499

Annamareddy, A., and Eapen, J. (2017). Low Dimensional String-like Relaxation Underpins Superionic Conduction in Fluorites and Related Structures. *Sci. Rep.* 7, 44149. doi:10.1038/srep44149

Annamareddy, V. A., Nandi, P. K., Mei, X., and Eapen, J. (2014). Waxing and Waning of Dynamical Heterogeneity in the Superionic State. *Phys. Rev. E* 89, 010301. doi:10.1103/physreve.89.010301

Asahi, R., Freeman, C. M., Saxe, P., and Wimmer, E. (2014). Thermal Expansion, Diffusion and Melting of Li_2O Using a Compact Forcefield Derived From ab Initio Molecular Dynamics. *Model. Simul. Mater. Sci. Eng.* 22, 075009. doi:10.1088/0965-0393/22/7/075009

Bathellier, D., Lainet, M., Freyss, M., Olsson, P., and Bourasseau, E. (2021). A New Heat Capacity Law for UO_2, PuO_2 and $(U,Pu)O_2$ Derived from Molecular Dynamics Simulations and Useable in Fuel Performance Codes. *J. Nucl. Mater.* 549, 152877. doi:10.1016/j.jnucmat.2021.152877

Bendall, P. J., and Catlow, C. R. A. (1980). Calculations of Point Defect Properties. Disorder in Pure and Doped Strontium Chloride. *J. Phys. Colloques* 41, C6–C61. doi:10.1051/jphyscol:1980616

Bingham, D., Cormack, A. N., and Catlow, C. R. A. (1989). Rigid-ion Potentials for SrF_2, CaF_2 and GdF_3. *J. Phys. Condens. Matter* 1, 1205–1212. doi:10.1088/0953-8984/1/7/004

Böhler, R., Welland, M. J., Prieur, D., Cakir, P., Vitova, T., Pruessmann, T., et al. (2014). Recent Advances in the Study of the UO_2-PuO_2 Phase Diagram at High Temperatures. *J. Nucl. Mater.* 448, 330–339. doi:10.1016/j.jnucmat.2014.02.029

Bollmann, W. (1980). Formation Enthalpy of Schottky Defects in Alkali Halide Crystals and of Anti-frenkel Defects in CaF_2-type Crystals. *Phys. Stat. Sol. (A)* 61, 395–410. doi:10.1002/pssa.2210610210

Bollmann, W., Görlich, P., Hauk, W., and Mothes, H. (1970). Ionic Conduction of Pure and Doped CaF_2 and SrF_2 Crystals. *Phys. Stat. Sol. (A)* 2, 157–170. doi:10.1002/pssa.19700020120

Boyce, J. B., and Huberman, B. A. (1979). Superionic Conductors: Transitions, Structures, Dynamics. *Phys. Rep.* 51, 189–265. doi:10.1016/0370-1573(79)90067-X

Boyce, J. B., Mikkelsen, J. C., Jr, and O'Keeffe, M. (1977). Ion Dynamics and Sublattice Melting in the Superionic Conductor PbF_2. *Solid State. Commun.* 21, 955–958. doi:10.1016/0038-1098(77)90898-5

Byrd, R. H., Lu, P., Nocedal, J., Zhu, C., and Zhu, C. (1995). A Limited Memory Algorithm for Bound Constrained Optimization. *SIAM J. Sci. Comput.* 16, 1190–1208. doi:10.1137/0916069

Carr, V. M., Chadwick, A. V., and Saghafian, R. (1978). The Electrical Conductivity of PbF_2 and $SrCl_2$ crystals at High Temperatures. *J. Phys. C: Solid State. Phys.* 11, L637–L641. doi:10.1088/0022-3719/11/15/006

Castiglione, M. J., and Madden, P. A. (2001). Fluoride Ion Disorder and Clustering in Superionic PbF_2. *J. Phys. Condens. Matter* 13, 9963–9983. doi:10.1088/0953-8984/13/44/311

Catlow, C. R. A., Comins, J. D., Germano, F. A., Harley, R. T., and Hayes, W. (1978). Brillouin Scattering and Theoretical Studies of High-Temperature Disorder in Fluorite Crystals. *J. Phys. C: Solid State. Phys.* 11, 3197–3212. doi:10.1088/0022-3719/11/15/019

Catlow, C. R. A., and Norgett, M. J. (1973). Shell Model Calculations of the Energies of Formation of point Defects in Alkaline Earth Fluorides. *J. Phys. C: Solid State. Phys.* 6, 1325–1339. doi:10.1088/0022-3719/6/8/002

Cazorla, C., Sagotra, A. K., King, M., and Errandonea, D. (2018). High-pressure Phase Diagram and Superionicity of Alkaline Earth Metal Difluorides. *J. Phys. Chem. C* 122, 1267–1279. doi:10.1021/acs.jpcc.7b10975

Chadwick, A. V., Flack, K. W., Strange, J. H., and Harding, J. (1988). Defect Structures and Ionic Transport in Lithium Oxide. *Solid State Ionics* 28-30, 185–188. doi:10.1016/s0167-2738(88)80030-4

Cooper, M. W. D., Murphy, S. T., Fossati, P. C. M., Rushton, M. J. D., and Grimes, R. W. (2014a). Thermophysical and Anion Diffusion Properties of $(U_x,Th_{1-x})O_2$. *Proc. R. Soc. A.* 470, 20140427. doi:10.1098/rspa.2014.0427

Cooper, M. W. D., Murphy, S. T., Rushton, M. J. D., and Grimes, R. W. (2015). Thermophysical Properties and Oxygen Transport in the $(U_x,Pu_{1-x})O_2$ Lattice. *J. Nucl. Mater.* 461, 206–214. doi:10.1016/j.jnucmat.2015.03.024

Cooper, M. W. D., Rushton, M. J. D., and Grimes, R. W. (2014b). A many-body Potential Approach to Modelling the Thermomechanical Properties of Actinide Oxides. *J. Phys. Condens. Matter* 26, 105401. doi:10.1088/0953-8984/26/10/105401

Debelle, A., Boulle, A., Chartier, A., Gao, F., and Weber, W. J. (2014). Interplay between Atomic Disorder, Lattice Swelling, and Defect Energy in Ion-Irradiation-Induced Amorphization of SiC. *Phys. Rev. B* 90, 174112. doi:10.1103/physrevb.90.174112

Dent, A., Madden, P. A., and Wilson, M. (2004). Simulation of CaF_2 in the Superionic State: Comparison of an Empirical and Realistic Potential. *Solid State Ionics* 167, 73–81. doi:10.1016/j.ssi.2004.01.002

Derrington, C. E., Lindner, A., and O'Keeffe, M. (1975). Ionic Conductivity of Some Alkaline Earth Halides. *J. Solid State. Chem.* 15, 171–174. doi:10.1016/0022-4596(75)90241-8

Dickens, M. H., Hayes, W., Hutchings, M. T., and Smith, C. (1982). Investigation of Anion Disorder in PbF_2 at High Temperatures by Neutron Diffraction. *J. Phys. C: Solid State. Phys.* 15, 4043–4060. doi:10.1088/0022-3719/15/19/006

Dixon, M. (1980). Molecular Dynamics Simulation of Fast-Ion Conduction in $SrCl_2$. II. Distribution of Ions and Specific Heat Anomaly. *J. Phys. C: Solid State. Phys.* 13, 1919–1929. doi:10.1088/0022-3719/13/10/011

Dworkin, A. S., and Bredig, M. A. (1968). Diffuse Transition and Melting in Fluorite and Antifluorite Type of Compounds. Heat Content of Potassium Sulfide from 298 to 1260. Degree.K. *J. Phys. Chem.* 72, 1277–1281. doi:10.1021/j100850a035

Dworkin, A. S., and Bredig, M. A. (1963). The Heats of Fusion and Transition of Alkaline Earth and Rare Earth Metal Halides. *J. Phys. Chem.* 67, 697–698. doi:10.1021/j100797a038

Evangelakis, G. A., and Pontikis, V. (1989). Direct Computation of the Superionic Conductivity in CaF_2 by Constant-Temperature Equilibrium and Nonequilibrium Molecular Dynamics. *Europhys. Lett.* 8, 599–604. doi:10.1209/0295-5075/8/7/003

Faraday, M. (1849). *Experimental Researches in Electricity*. London: R. and J. E. Taylor.

Farley, T. W. D., Hayes, W., Hull, S., Hutchings, M. T., and Vrtis, M. (1991). Investigation of Thermally Induced Li^+ Ion Disorder in Li_2O Using Neutron Diffraction. *J. Phys. Condens. Matter* 3, 4761–4781. doi:10.1088/0953-8984/3/26/001

Farrow, C. L., and Billinge, S. J. L. (2009). Relationship between the Atomic Pair Distribution Function and Small-Angle Scattering: Implications for Modeling of Nanoparticles. *Acta Cryst. Sect A.* 65, 232–239. doi:10.1107/S0108767309009714

Fomin, Y. D. (2021). Melting Line and Thermodynamic Properties of a Superionic Compound $SrCl_2$ by Molecular Dynamics Simulation. *Phys. Chem. Liquids* 1, 1–9. doi:10.1080/00319104.2021.1916934

Fossati, P. C. M., Van Brutzel, L., Chartier, A., and Crocombette, J.-P. (2013). Simulation of Uranium Dioxide Polymorphs and Their Phase Transitions. *Phys. Rev. B* 88, 214112. doi:10.1103/PhysRevB.88.214112

Fracchia, R. M., Barrera, G. D., Allan, N. L., Barron, T. H. K., and Mackrodt, W. C. (1998). Lithium Oxide and Superionic Behaviour-A Study Using Potentials from Periodic Ab Initio Calculations. *J. Phys. Chem. Sol.* 59, 435–445. doi:10.1016/S0022-3697(97)00208-4

Galvin, C. O. T., Cooper, M. W. D., Rushton, M. J. D., and Grimes, R. W. (2016). Thermophysical Properties and Oxygen Transport in $(Th_x,Pu_{1-x})O_2$. *Sci. Rep.* 6, 36024. doi:10.1038/srep36024

Gillan, M. J., and Dixon, M. (1980). Quasi-elastic Scattering in Fast-Ion Conducting $SrCl_2$: a Molecular Dynamics Study. *J. Phys. C: Solid State. Phys.* 13, L835–L839. doi:10.1088/0022-3719/13/30/003

Goel, P., Choudhury, N., and Chaplot, S. L. (2004). Superionic Behavior of Lithium Oxide Li_2O: A Lattice Dynamics and Molecular Dynamics Study. *Phys. Rev. B* 70. doi:10.1103/physrevb.70.174307

Goff, J. P., Hayes, W., Hull, S., and Hutchings, M. T. (1991). Neutron Powder Diffusion Study of the Fast-Ion Transition and Specific Heat Anomaly in Beta -lead Fluoride. *J. Phys. Condens. Matter* 3, 3677–3687. doi:10.1088/0953-8984/3/21/001

Gray-Weale, A., and Madden, P. A. (2004). Dynamical Arrest in Superionic Crystals and Supercooled Liquids. *J. Phys. Chem. B* 108, 6624–6633. doi:10.1021/jp037706a

Gupta, M. K., Singh, B., Goel, P., Mittal, R., Rols, S., and Chaplot, S. L. (2019). Lithium Diffusion in Li_2X (X=O , S, and Se): Ab Initio Simulations and Inelastic Neutron Scattering Measurements. *Phys. Rev. B* 99, 224304. doi:10.1103/physrevb.99.224304

Hayes, W. (1974). *Crystals with the Fluorite Structure — Electronic, Vibrational, and Defect Properties*. Oxford: Clarendon Press.

Hiernaut, J. P., Hyland, G. J., and Ronchi, C. (1993). Premelting Transition in Uranium Dioxide. *Int. J. Thermophys.* 14, 259–283. doi:10.1007/BF00507813

Hull, S., Farley, T. W. D., Hayes, W., and Hutchings, M. T. (1988). The Elastic Properties of Lithium Oxide and Their Variation with Temperature. *J. Nucl. Mater.* 160, 125–134. doi:10.1016/0022-3115(88)90039-6

Hull, S., Norberg, S. T., Ahmed, I., Eriksson, S. G., and Mohn, C. E. (2011). High Temperature crystal Structures and Superionic Properties of $SrCl_2$, $SrBr_2$, $BaCl_2$ and $BaBr_2$. *J. Solid State. Chem.* 184, 2925–2935. doi:10.1016/j.jssc.2011.09.004

Hull, S. (2004). Superionics: crystal Structures and Conduction Processes. *Rep. Prog. Phys.* 67, 1233–1314. doi:10.1088/0034-4885/67/7/r05

Hutchings, M. T., Clausen, K., Dickens, M. H., Hayes, W., Kjems, J. K., Schnabel, P. G., et al. (1984). Investigation of Thermally Induced Anion Disorder in Fluorites Using Neutron Scattering Techniques. *J. Phys. C: Solid State. Phys.* 17, 3903–3940. doi:10.1088/0022-3719/17/22/011

Jin, X., Boulle, A., Chartier, A., Crocombette, J.-P., and Debelle, A. (2020). Analysis of Strain and Disordering Kinetics Based on Combined RBS-Channeling and X-ray Diffraction Atomic-Scale Modelling. *Acta Materialia* 201, 63–71. doi:10.1016/j.actamat.2020.09.076

Johnston, H. L., and Bauer, T. W. (1951). Low Temperature Heat Capacities of Inorganic Solids. VII. Heat Capacity and Thermodynamic Functions of Li_2O. Thermodynamics of the Li_2O-H_2o System1. *J. Am. Chem. Soc.* 73, 1119–1122. doi:10.1021/ja01147a070

Klarbring, J., Skorodumova, N. V., and Simak, S. I. (2018). Finite-temperature Lattice Dynamics and Superionic Transition in Ceria from First Principles. *Phys. Rev. B* 97, 104309. doi:10.1103/physrevb.97.104309

Kurasawa, T., Takahashi, T., Noda, K., Takeshita, H., Nasu, S., and Watanabe, H. (1982). Thermal Expansion of Lithium Oxide. *J. Nucl. Mater.* 107, 334–336. doi:10.1016/0022-3115(82)90434-2

Larsen, P. M., Schmidt, S., and Schiøtz, J. (2016). Robust Structural Identification via Polyhedral Template Matching. *Model. Simul. Mater. Sci. Eng.* 24, 055007. doi:10.1088/0965-0393/24/5/055007

Léger, J.-M., and Haines, J. (1997). Crystal Chemistry of the AX_2 Compounds under Pressure. *Eur. J. Solid State. Inorg. Chem.* 34, 785–796.

Lidiard, A. B. (1974). in *Crystals with the Fluorite Structure*. Editor W. Hayes (Oxford: Clarendon Press).

Lidiard, A. B. (1980). "Lattice Defects in Crystals with the Fluorite Structure,". (AERE report T. P. 841).

López-Moreno, S., Romero, A. H., Mejía-López, J., and Muñoz, A. (2016). First-principles Study of Pressure-Induced Structural Phase Transitions in MnF_2. *Phys. Chem. Chem. Phys.* 18, 33250–33263. doi:10.1039/c6cp05467f

Lorger, S., Usiskin, R., and Maier, J. (2019). Transport and Charge Carrier Chemistry in Lithium Oxide. *J. Electrochem. Soc.* 166, A2215–A2220. doi:10.1149/2.1121910jes

Martin, D. G. (1988). The thermal Expansion of Solid UO_2 and (U, Pu) Mixed Oxides - a Review and Recommendations. *J. Nucl. Mater.* 152, 94–101. doi:10.1016/0022-3115(88)90315-7

Matzke, H. (1987). Atomic Transport Properties in UO_2 and Mixed Oxides $(U, Pu)O_2$. *J. Chem. Soc. Faraday Trans. 2* 83, 1121–1142. doi:10.1039/F29878301121

Morelon, N.-D., Ghaleb, D., Delaye, J.-M., and Van Brutzel, L. (2003). A New Empirical Potential for Simulating the Formation of Defects and Their Mobility in Uranium Dioxide. *Phil. Mag.* 83, 1533–1555. doi:10.1080/1478643031000091454

Morris, J. R., Wang, C. Z., Ho, K. M., and Chan, C. T. (1994). Melting Line of Aluminum from Simulations of Coexisting Phases. *Phys. Rev. B* 49, 3109–3115. doi:10.1103/physrevb.49.3109

Naylor, B. F. (1945). Heat Contents at High Temperatures of Magnesium and Calcium Fluorides1. *J. Am. Chem. Soc.* 67, 150–152. doi:10.1021/ja01217a052

Nosé, S. (1984). A Unified Formulation of the Constant Temperature Molecular Dynamics Methods. *J. Chem. Phys.* 81, 511–519. doi:10.1063/1.447334

Oda, T., Oya, Y., Tanaka, S., and Weber, W. J. (2007). Validation of Potential Models for Li_2O in Classical Molecular Dynamics Simulation. *J. Nucl. Mater.* 367-370, 263–268. doi:10.1016/j.jnucmat.2007.03.139

Oishi, Y., Kamei, Y., Akiyama, M., and Yanagi, T. (1979). Self-diffusion Coefficient of Lithium in Lithium Oxide. *J. Nucl. Mater.* 87, 341–344. doi:10.1016/0022-3115(79)90570-1

O'Keeffe, M. (1976). "Phase Transitions and Translational freedom in Solid Electrolytes," in *Superionic Conductors*. Editors G. D. Mahan and W. L. Roth (New York: Plenum Press).

Parrinello, M., and Rahman, A. (1981). Polymorphic Transitions in Single Crystals: A New Molecular Dynamics Method. *J. Appl. Phys.* 52, 7182–7190. doi:10.1063/1.328693

Pavlov, T. R., Wenman, M. R., Vlahovic, L., Robba, D., Konings, R. J. M., Van Uffelen, P., et al. (2017). Measurement and Interpretation of the Thermo-Physical Properties of UO_2 at High Temperatures: The Viral Effect of Oxygen Defects. *Acta Materialia* 139, 138–154. doi:10.1016/j.actamat.2017.07.060

Pedone, A., Malavasi, G., Menziani, M. C., Cormack, A. N., and Segre, U. (2006). A New Self-Consistent Empirical Interatomic Potential Model for Oxides, Silicates, and Silica-Based Glasses. *J. Phys. Chem. B* 110, 11780–11795. doi:10.1021/jp0611018

Plimpton, S. (1995). Fast Parallel Algorithms for Short-Range Molecular Dynamics. *J. Comput. Phys.* 117, 1–19. doi:10.1006/jcph.1995.1039

Popov, P. A., Sidorov, A. A., Kul'chenkov, E. A., Anishchenko, A. M., Avetissov, I. C., Sorokin, N. I., et al. (2017). Thermal Conductivity and Expansion of PbF_2 Single Crystals. *Ionics* 23, 233–239. doi:10.1007/s11581-016-1802-2

Ralph, J. (1987). Specific Heat of UO_2, ThO_2, PuO_2 and the Mixed Oxides $(Th_x U_{1-x})O_2$ and $(Pu_{0.2} U_{0.8}) O_{1.97}$ by Enthalpy Data Analysis. *J. Chem. Soc. Faraday Trans. 2* 83, 1253–1262. doi:10.1039/F29878301253

Rice, M. J., and Roth, W. L. (1972). Ionic Transport in Super Ionic Conductors: a Theoretical Model. *J. Solid State. Chem.* 4, 294–310. doi:10.1016/0022-4596(72)90121-1

Roberts, R. B., and White, G. K. (1986). Thermal Expansion of Fluorites at High Temperatures. *J. Phys. C: Solid State. Phys.* 19, 7167–7172. doi:10.1088/0022-3719/19/36/008

Samara, G. A. (1979). Pressure and Temperature Dependences of the Ionic Conductivities of Cubic and Orthorhombic lead Fluoride (PbF_2). *J. Phys. Chem. Sol.* 40, 509–522. doi:10.1016/0022-3697(79)90079-9

Sayle, D. C., Doig, J. A., Parker, S. C., and Watson, G. W. (2003). Synthesis, Structure and Ionic Conductivity in Nanopolycrystalline BaF_2/CaF_2. *Chem. Commun.* 15, 1804–1806. doi:10.1039/b305393h

Schröter, W., and Nölting, J. (1980). Specific Heats of Crystals with the Fluorite Structure. *J. Phys. Colloques* 41, C6–C20. doi:10.1051/jphyscol:1980605

Smith, D. F., Gardner, T., Letson, B., and Taylor, A. R. (1963). *Thermodynamic Properties of Strontium Chloride and Strontium Fluoride from 0° to 300°K, Rep no. 6316*. Washington: (US Department of the Interior, Bureau of Mines).

Stukowski, A. (2010). Visualization and Analysis of Atomistic Simulation Data with OVITO-The Open Visualization Tool. *Model. Simul. Mater. Sci. Eng.* 18, 015012. doi:10.1088/0965-0393/18/1/015012

Szwarc, R. (1969). The Defect Contribution to the Excess Enthalpy of Uranium Dioxide-Calculation of the Frenkel Energy. *J. Phys. Chem. Sol.* 30, 705–711. doi:10.1016/0022-3697(69)90024-9

Takoukam-Takoundjou, C., Bourasseau, E., and Lachet, V. (2020). Study of Thermodynamic Properties of U1-yPuyO_2 MOX Fuel Using Classical Molecular Monte Carlo Simulations. *J. Nucl. Mater.* 534, 152125. doi:10.1016/j.jnucmat.2020.152125

Thomas, M. W. (1976). Neutron Diffraction Evidence for Anion Sublattice Disordering in Alkali Earth Fluorides at High Temperatures. *Chem. Phys. Lett.* 40, 111–115. doi:10.1016/0009-2614(76)80131-5

Trueblood, K. N., Bürgi, H. B., Burzlaff, H., Dunitz, J. D., Gramaccioli, C. M., Schulz, H. H., et al. (1996). Atomic Dispacement Parameter Nomenclature. Report of a Subcommittee on Atomic Displacement Parameter Nomenclature. *Acta Cryst. Sect A.* 52, 770–781. doi:10.1107/S0108767396005697

Tuckerman, M. E., Alejandre, J., López-Rendón, R., Jochim, A. L., and Martyna, G. J. (2006). A Liouville-Operator Derived Measure-Preserving Integrator for Molecular Dynamics Simulations in the Isothermal-Isobaric Ensemble. *J. Phys. A: Math. Gen.* 39, 5629–5651. doi:10.1088/0305-4470/39/19/S18

Voronin, B. M. (1995). Some Simple Thermodynamic Approaches to Superionic Disorder in Fluorite-type Crystals: Application to $SrCl_2$ and K_2S. *J. Phys. Chem. Sol.* 56, 839–847. doi:10.1016/0022-3697(94)00276-2

Voronin, B. M., and Volkov, S. V. (2001). Ionic Conductivity of Fluorite Type Crystals CaF_2, SrF_2, BaF_2, and $SrCl_2$ at High Temperatures. *J. Phys. Chem. Sol.* 62, 1349–1358. doi:10.1016/s0022-3697(01)00036-1

Wang, J., Li, J., Yip, S., Wolf, D., and Phillpot, S. (1997). Unifying Two Criteria of Born: Elastic Instability and Melting of Homogeneous Crystals. *Physica A: Stat. Mech. its Appl.* 240, 396–403. doi:10.1016/S0378-4371(97)00161-1

Wicks, C. E., and Block, F. E. (1963). *Thermodynamic Properties of 65 Elements: Their Oxides, Halides, Carbides and Nitrides, Rep no. 605*. Washington: (US Government Printing Office).

Wojdyr, M. Debye's Scattering Equation & Other Analysis of Atomistic Models, Available at: https://github.com/wojdyr/debyer (Accessed 6 september 2021)

Wolf, D., Keblinski, P., Phillpot, S. R., and Eggebrecht, J. (1999). Exact Method for the Simulation of Coulombic Systems by Spherically Truncated, Pairwise R^{-1} Summation. *J. Chem. Phys.* 110, 8254–8282. doi:10.1063/1.478738

Zhang, H., Wang, X., Chremos, A., and Douglas, J. F. (2019). Superionic UO_2: A Model Anharmonic Crystalline Material. *J. Chem. Phys.* 150, 174506. doi:10.1063/1.5091042

Zhang, Y., Liu, X.-Y., Millett, P. C., Tonks, M., Andersson, D. A., and Biner, B. (2012). Crack Tip Plasticity in Single crystal UO_2: Atomistic Simulations. *J. Nucl. Mater.* 430, 96–105. doi:10.1016/j.jnucmat.2012.06.044

Ziegler, J. F., Biersack, J. P., and Littmark, U. (1985). *The Stopping and Range of Ions in Matter, Vol. 1*. Oxford: Pergamon Press.

Conflict of Interest: The authors declare that the research was conducted in the absence of any commercial or financial relationships that could be construed as a potential conflict of interest.

Publisher's Note: All claims expressed in this article are solely those of the authors and do not necessarily represent those of their affiliated organizations, or those of the publisher, the editors and the reviewers. Any product that may be evaluated in this article, or claim that may be made by its manufacturer, is not guaranteed or endorsed by the publisher.

frontiers in Chemistry

ORIGINAL RESEARCH
published: 03 November 2021
doi: 10.3389/fchem.2021.733321

Pyrochlore Compounds From Atomistic Simulations

*Timothy Connor[1], Oskar Cheong[2,3,4], Thomas Bornhake[2,3,4], Alison C. Shad[5], Rebekka Tesch[2,3,4], Mengli Sun[3,6], Zhengda He[2,3], Andrey Bukayemsky[7], Victor L. Vinograd[7], Sarah C. Finkeldei[1,2] and Piotr M. Kowalski[2,3]**

[1]Department of Chemistry, Chemical and Biomolecular Engineering, and Materials Science and Engineering, University of California, Irvine, Irvine, CA, United States, [2]Forschungszentrum Jülich GmbH, Institute of Energy and Climate Research - IEK-13, Theory and Computation of Energy Materials, Jülich, Germany, [3]Jülich Aachen Research Alliance, JARA Energy & Center for Simulation and Data Science (CSD), Jülich, Germany, [4]Chair of Theory and Computation of Energy Materials, Faculty of Georesources and Materials Engineering, RWTH Aachen University, Aachen, Germany, [5]Walter Scott Jr. College of Engineering, Colorado State University, Fort Collins, CO, United States, [6]School of Nuclear Science and Technology, Lanzhou University, Lanzhou, China, [7]Forschungszentrum Jülich GmbH, Institute of Energy and Climate Research - IEK-6, Nuclear Waste Management and Reactor Safety, Jülich, Germany*

Pyrochlore compounds ($A_2B_2O_7$) have a large applicability in various branches of science and technology. These materials are considered for use as effective ionic conductors for solid state batteries or as matrices for immobilization of actinide elements, amongst many other applications. In this contribution we discuss the simulation-based effort made in the Institute of Energy and Climate Research at Forschungszentrum Jülich and partner institutions regarding reliable computation of properties of pyrochlore and defect fluorite compounds. In the scope of this contribution, we focus on the investigation of dopant incorporation, defect formation and anion migration, as well as understanding of order-disorder transitions in these compounds. We present new, accurate simulated data on incorporation of U, Np, Pu, Am and Cm actinide elements into pyrochlores, activation energies for oxygen migration and radiation damage-induced structural changes in these materials. All the discussed simulation results are combined with available experimental data to provide a reliable description of properties of investigated materials. We demonstrate that a synergy of computed and experimental data leads to a superior characterization of pyrochlores, which could not be easily achieved by either of these methods when applied separately.

Keywords: pyrochlores, atomistic simulations, energy storage materials, ceramics, solid solutions, solid state electrolyte, radiation damage

OPEN ACCESS

Edited by:
Franziska Luise Emmerling, Federal Institute for Materials Research and Testing (BAM), Germany

Reviewed by:
Xiaolong Zhu, Merck, United States
Fatemeh Moosavi, Ferdowsi University of Mashhad, Iran

****Correspondence:***
Piotr M. Kowalski
p.kowalski@fz-juelich.de

Specialty section:
This article was submitted to Solid State Chemistry, a section of the journal Frontiers in Chemistry

Received: *30 June 2021*
Accepted: *13 October 2021*
Published: *03 November 2021*

Citation:
Connor T, Cheong O, Bornhake T, Shad AC, Tesch R, Sun M, He Z, Bukayemsky A, Vinograd VL, Finkeldei SC and Kowalski PM (2021) Pyrochlore Compounds From Atomistic Simulations. Front. Chem. 9:733321. doi: 10.3389/fchem.2021.733321

1 INTRODUCTION

Pyrochlore-type ceramics are functional materials with a wide range of applications, including ionic conductors (Wuensch, 2000; Diazguillen et al., 2008; Kumar et al., 2008; Mandal et al., 2008; Shlyakhtina and Shcherbakova, 2012; Anithakumari et al., 2016), coatings (Feng et al., 2013), luminescent materials (Park et al., 2001; Öztürk et al., 2020) or matrices for immobilization of nuclear waste (Ringwood et al., 1979; Wang et al., 1999; Ewing et al., 2004; Bosbach et al., 2020). Significant research effort has been devoted to the complex characterization of these materials in order to understand their physical and chemical properties that make them multi-functional compounds (e.g., Sickafus et al., 2000; Ewing et al., 2004; Ushakov et al., 2007; Li et al., 2015; Uberuaga et al., 2015; Chung et al., 2018a; Maram et al., 2018; Drey et al., 2020). On many occasions,

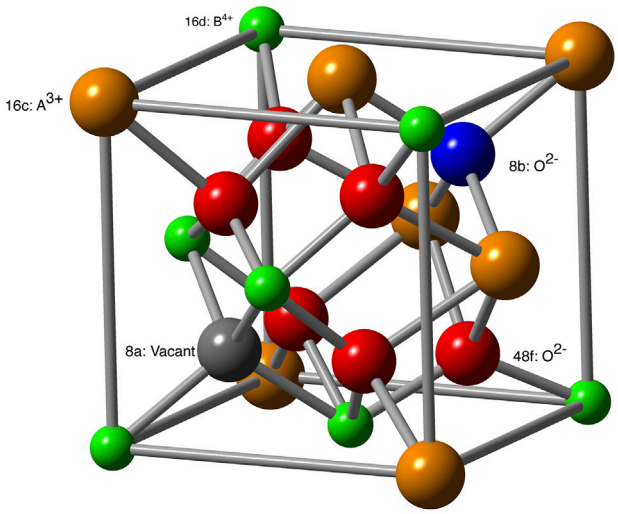

FIGURE 1 | Structure of $A_2B_2O_7$ pyrochlore. Different crystallographic positions are labeled. For anion sublattice these are also indicated by different colors: 48*f* (red), 8*a* (gray, vacant site in stoichiometric pyrochlore) and 8*b* (blue).

atomistic simulations have supported the interpretation of experimentally seen phenomena and a joint experimental and simulation-based research effort has led to an enhanced understanding of the experimental data (e.g., Finkeldei et al. (2017); Kowalski (2020)). There is a vast amount of past research on pyrochlore-type ceramics that involve various experimental, theoretical and computer-aided research techniques. Here we focus on discussing and reporting results of atomistic simulation efforts with which we have contributed to enhanced, although still far from being complete, understanding of various aspects of these materials.

Pyrochlores are crystalline solids ($A_2B_2O_7$) with the Fd-3m space group (227) and represent a superstructure of the fluorite structure (Ewing et al., 2004). In these compounds the *A* cation is typically a trivalent rare earth metal, and the *B* cation is typically a tetravalent transition metal element. The structure of one eighth of a stoichiometric pyrochlore unit cell is given in **Figure 1**. The *A*-site is 8-fold coordinated on the 16*c* Wyckoff position, and the *B*-site is 6-fold coordinated at the 16*d* position. The oxygen anions occupy the 48*f* and 8*b* positions. *A*-site cations are coordinated to six 48*f* and two 8*b* oxygens, with the *A*-48*f* bond lengths slightly longer than the *A* − 8*b* bonds. The *B*-site cations are coordinated to six 48*f* oxygens, and are adjacent to the vacant 8*a* sites.

In the last two decades, atomistic modeling became a widely used research technique in various research fields, including pyrochlores (Sickafus et al., 2000; Chroneos et al., 2013; Jahn and Kowalski, 2014; Li et al., 2015; Uberuaga et al., 2015; Wu et al., 2019). We used it intensively over the past decade for computation of various physical and chemical properties of pyrochlore-type ceramics. In particular, the computer-aided simulations have been applied to understand defect formation (Li et al., 2015; Kowalski et al., 2016; Li et al., 2016; Li and Kowalski, 2018), disordering behavior (Finkeldei et al., 2017; Kowalski, 2020), ionic conductivity (Li and Kowalski, 2018; Bukaemskiy et al., 2021) and structural incorporation of actinide elements (Finkeldei et al., 2020) in this class of materials. Besides our efforts, many other computational studies have substantially contributed to understanding different properties of these materials. In one of the first application of atomistic modeling to pyrochlores, van Dijk et al. (1985) found two distinct vacancy defect configurations, which is helpful in understanding the ability of these materials to conduct oxygen ions (e.g., Pirzada et al. (2001); Li and Kowalski (2018)). In a series of papers, Sickafus et al., 2000; Sickafus et al., 2007; Minervini et al., 2002; Minervini et al., 2000 applied force-field-based simulations to understand defect formation and disordering tendencies in pyrochlores. This effort was later followed by related *ab initio* simulations (e.g., Panero et al., 2004; Jiang et al., 2009; Vanpoucke et al., 2011; Li et al., 2015). Structural transformations under irradiation have been investigated by classical and *ab initio* molecular dynamics methods (Chartier et al., 2003; Chartier et al., 2005; Chartier et al., 2009; Crocombette and Chartier, 2007; Xiao et al., 2015). These are just a few examples of successful applications of atomistic modeling techniques to the research on pyrochlore-type ceramics.

The tendency of pyrochlores to disorder, and the ordering of the state they eventually reach, is an important, widely investigated aspect that impacts, for instance, radiation damage resistance (where the ability to form a disordered phase can prevent total amorphization) or ionic conductivity. Until recently, many studies assumed that pyrochlore disorders to an ideal defect fluorite, a crystalline solid in which cations and oxygen/oxygen vacancy distributions are completely random (e.g., Jiang et al. (2009); Li et al. (2015)). This concept has been successfully applied by Jiang et al. (2009) to derive the disordering transition temperature for a series of pyrochlore hafnates and zirconates using the concept of Special Quasi-random Structure (SQS) (Zunger et al., 1990) to model the disordered pyrochlore as perfectly disordered defect fluorite phase. The Density Functional Theory (DFT)-based simulations give a reasonably good agreement with measured values, although with an offset of ~ 300 K. This has been corrected by application of the DFT + *U* method, with the self-consistently derived Hubbard *U* parameter values, that better accounts for the electronic correlations (Li et al., 2015). It has been demonstrated by calorimetric measurements (Ushakov et al., 2007; Saradhi et al., 2012; Finkeldei et al., 2017) as well as by neutron total scattering experiments (Shamblin et al., 2016) that disordered pyrochlore compounds retain a significant amount of local order, called short range ordering (SRO). The later studies found that such SRO can be well described with long-range ordered weberite model. This has been supported by the atomistic simulations of Kowalski (2020), who has shown that fully disordered compounds would be thermodynamically unstable against mixture of relevant oxides, and that the weberite-type structural representation of disordered pyrochlore results in computed formation enthalpies that match the existing measurements reasonably well.

Several pyrochlore-type compounds are considered as fast ionic conductors (Mandal et al., 2008; Diazguillen et al., 2008; Anithakumari et al., 2016; Moon and Tuller, 1988). In general, zirconia-based compounds are known to show high ionic conductivity. Among these, yttria-stabilized zirconia is considered as one of the fastest ionic conductors (Ahamer et al., 2017; Kowalski et al., 2021). In pyrochlore-type compounds, the ionic conduction happens through hopping between 48*f* sites. In an ideal pyrochlore these sites are fully occupied (**Figure 1**). In order to allow conduction, vacancies must be formed on the 48*f* sites (van Dijk et al., 1985; Pirzada et al., 2001; Li and Kowalski, 2018). Typically, this occurs via transfer of an oxygen atom to the vacant 8*a*-site and formation of an anion Frenkel pair defect. For pyrochlores containing heavier lanthanides, the oxygen diffusion path involves formation of a split vacancy state (van Dijk et al., 1985; Li and Kowalski, 2018). Li and Kowalski (2018) have shown that this state stabilizes the vacancy and leads to a significant increase of the activation barrier for diffusion and decrease of the ionic conductivity. This is consistent with the experimental measurements of ionic conductivity in zirconate-pyrochlores (Yamamura, 2003). Bukaemskiy et al. (2021) constructed a model for oxygen diffusion in zirconia doped with trivalent elements, in which the oxygen conductivity was assumed proportional to the probability of a vacancy jump between clusters in a certain typical configuration occurring more frequently due to SRO. Such a model has been successfully applied together with atomistic simulations to derive the ionic conductivity in yttria-stabilized zirconia materials (Kowalski et al., 2021). Here, with simulations of energies of defects formation on anion sublattice and activation barriers for oxygen diffusion we will discuss the mechanisms of ionic conductivity in a series of zirconate pyrochlores.

Another important aspect of pyrochlores is their ability to effectively immobilize radionuclide elements such as Pu and minor actinides (Np, Am, Cm) (Ewing et al., 2004; Bosbach et al., 2020). A matrix of pyrochlore-type is thus considered as a durable nuclear waste form to increase safety of radioactive materials permanently disposed in a deep geological repository. An important aspect of such a strategy is non-proliferation, by immobilizing large stockpiles of weapons grade Pu in a form of durable material (Ewing et al., 2004). Understanding the mechanism of structural incorporation of actinides into pyrochlore ceramics is of utmost importance in assessing the performance of pyrochlores as nuclear waste forms. In that respect, Nästren et al. (2009) measured the lattice parameter and Extended X-ray Absorption Fine Structure (EXAFS) spectra of various $Nd_2Zr_2O_7$ pyrochlores doped with different actinide elements (Th, U, Np, Pu, Am) in various oxidation states, and concluded that these actinides were incorporated on the *A* (Nd) site. With the aid of atomistic simulations Ji (2018) demonstrated that the lattice parameter change upon doping with actinide elements resembles the experimental data only when assuming doping on *A* cation site (Nd), regardless of the actinide valence state. Here we applied more accurate computational methodology to confirm this hypothesis. More recently, applying a combination of EXAFS and atomistic simulations Finkeldei et al. (2020) demonstrated that Pu incorporates in the same way as Pu(IV) species, although EXAFS measurements could possibly also indicate distribution of Pu between Nd and Zr cation sites. Another aspect of using pyrochlores as nuclear waste form is their resistance to radiation damage (e.g., $Gd_2Zr_2O_7$, Ewing et al. (2004)). This behavior is associated with a thermodynamic easiness of an order/disorder transformation and transformation to defect fluorite phase (disordered pyrochlore), aspects which, as aforementioned, have been in focus of series of atomistic modeling studies as well as irradiation experiments (e.g., Lian et al. (2006b); Chung et al. (2018a); Crocombette et al. (2006); Chartier et al. (2009)).

In this contribution we provide an overview of recent atomistic modeling activities on the pyrochlore-type ceramics, focusing on information that has been delivered by activities at Forschungszentrum Jülich, and that allowed on many occasions for better characterization of these materials, including structural data, thermodynamic stability and disordering tendencies. As a novelty we present computational results on: structural parameters of pyrochlores doped with actinides, activation barriers for ionic conduction in this class of materials and behavior of pyrochlores under irradiation. We highlight a cross-linking, interdisciplinary character of the research on pyrochlores, from which the general science community could highly benefit.

2 COMPUTATIONAL APPROACH

The here reported *ab initio*[1] calculations were performed with the DFT-based Quantum-ESPRESSO package (Giannozzi et al., 2009). It consists of an integrated suite of computer codes capable of nanoscale materials modeling, including electronic structure calculations. Most importantly for the studies on pyrochlores, it allows for the state-of-the-art application of DFT + *U* approach to improve description of correlation effects among *f* electrons. We applied the PBE and PBEsol exchange-correlation functionals (Perdew et al., 1996; Perdew et al., 2008). The energies were computed with the PBE functional, while the PBEsol functional has been applied in the structural investigation. This is because by correctly reproducing the slowly varying electron density limit, when compared with the PBE approximation, PBEsol results in much better description of structural parameters of solids (Perdew et al., 2008), although at the cost of a lower accuracy of the computed energies. Application of PBEsol exchange-correlation functional is especially important for consideration of structural incorporation of elements into the pyrochlore phases. The core electrons of atoms have been represented by the ultrasoft pseudopotentials (Vanderbilt, 1990), with the relevant plane-wave energy cutoff of 50 Ryd. Following our broad experience on computation of lanthanide orthophosphates and zirconates,

[1]In this contribution we call DFT methods an *ab initio* approach as the exchange-correlation functionals applied in our studies, PBE and PBEsol, were designed based on pure-theoretical considerations.

and uranium-oxides (e.g., Beridze and Kowalski, 2014; Blanca-Romero et al., 2014; Li et al., 2015; Beridze et al., 2016; Kowalski et al., 2021) here we applied a parameter free DFT + *U* approach. In this method, the Hubbard *U* parameter values are computed from first principles using the linear response method of Cococcioni and de Gironcoli (2005). This computational setup has been extensively tested by us in several studies and, among others, proved to give very accurate results for *Ln*-O bond lengths (Blanca-Romero et al., 2014; Beridze et al., 2016). For the simulations of oxygen migration and defect formation energies we applied the *"f in the core"* approach, in which *f* electrons are not computed explicitly, but their presence is simulated by pseudopotentials. These simulations are more stable and give results that are comparable to these obtained with the outlined DFT + *U* approach for materials properties that do not directly involve *f* elements (see discussions in Blanca-Romero et al. (2014) and Beridze et al. (2016)).

The activation barriers were computed using the Nudged Elastic Band (NEB) method as implemented in Quantum-ESPRESSO package. The climbing image method and a set of five images were applied to compute the transition state and relevant activation barriers.

The simulations of radiation damage were performed with the aid of force-field-based molecular dynamics simulations using the LAMMPS code (Plimpton, 1995), using the random cation displacement procedure applied by us recently to simulations of irradiated borosilicate glasses (Sun et al., 2021). Similar procedure has been applied in previous atomistic simulation studies of pyrochlores (Chartier et al., 2005; Ji, 2018). Here, we simulated systems containing 2376 atoms (216 formula units) and the interatomic interactions were described by the simple Buckingham-type interaction potential of Minervini et al. (2000) and Stanek et al. (2002). The damage accumulation molecular dynamics simulations were performed in an iterative loop, with intervals between single cation defect formation of 2 ps. Within this short time, the NPT (constant pressure-temperature) simulations were performed assuming ambient condition. These were followed by a displacement of a randomly selected cation in random direction and distance, so that the displacement distance was at least 6 Å (to assure formation of a permanent defect).

3 RESULTS AND DISCUSSION

3.1 Structural Data

3.1.1 Stoichiometric Pyrochlores

Correct prediction of structural parameters by a simulation method is a key factor for atomistic modeling-based characterization of materials. The force fields used in classical molecular dynamics simulations are often parameterized to reproduce structural parameters of investigated materials, and this has been also the case in the research on pyrochlores (e.g. Minervini et al., 2000). In similar way, the *ab initio* and, in principle, DFT simulations, are also expected to provide a good description of the structures of solids. However, different applied approximations (e.g., exchange-correlation functionals) result in different quality of the computed structural data (Perdew et al., 2008; Blanca-Romero et al., 2014). In a series of papers on orthophosphates we demonstrated that a very good match to the structural parameters, especially the *Ln*-O bond lengths, can be obtained with the PBEsol exchange-correlation functional (Perdew et al., 2008) and the DFT + *U* method with the Hubbard *U* parameter derived from first principles (Blanca-Romero et al., 2014; Beridze et al., 2016; Kowalski et al., 2021). Finkeldei et al. (2017) have shown that PBEsol functional can predict accurate value of the lattice parameter of the $Nd_2Zr_2O_7$ pyrochlore. We note that those calculations were performed with the *f in the core* approach (see **Section 2**). With the PBEsol exchange-correlation functional and the outlined parameter-free DFT + *U* method Blanca-Romero et al. (2014) got excellent results for the *Ln*–O bond-lengths in and volumes of $LnPO_4$ compounds. Here we test if such a method could predict good lattice parameters and *Ln*–O bond-lengths for series of zirconate-pyrochlores. In **Table 1** we provide a set of the Hubbard *U* parameters computed for different lanthanide cations. The values are consistent with the previous simulations of Li et al. (2015) for pyrochlores and the aforementioned results of Blanca-Romero et al. (2014) for lanthanide phosphates. There is a clear trend that reflects strength of the electronic correlations for different *Ln* cations. The Hubbard *U* parameter increases along lanthanide series, reaching maximum for Eu and then becomes smaller for Gd. This is an effect of completely filled half *f*-shell of Gd^{3+}.

An important test of a computational method is its ability to reproduce the measured lattice parameters of computed crystalline solids. Although some studies report excellent match of the computed lattice parameters of pyrochlores to the measured values (Feng et al., 2011), our previous studies have shown that the structural parameters of lanthanide-orthophosphates are very sensitive to the applied computational method, especially to the exchange-correlation functional (Blanca-Romero et al., 2014). A correct computation of strongly correlated 4*f* electrons also plays an important role in those cases. The lattice parameters of considered stoichiometric pyrochlores have been measured at ambient conditions by different studies (Sasaki et al., 2004; Harvey et al., 2005; Mandal et al., 2007; Nästren et al., 2009; Hagiwara et al., 2013; Koohpayeh et al., 2014; Vaisakhan Thampi et al., 2017). These are collected in **Figure 2** and compared to the computed data. With our computational setup, applying the PBEsol exchange-correlations functional, we got excellent match to the measured lattice parameters of all the considered stoichiometric zirconate pyrochlores, with a difference within ~ 0.04 Å. We note that thermal expansion contributes to this difference at the level of ~ 0.01 Å (see **Section 3.1.3**). Such a good result is very important when, for instance, analyzing the structural change upon doping pyrochlores with actinide elements (**Section 3.1.3**). On the other hand, it is clear that the PBE exchange-correlation functional overestimates the lattice parameter by ~ 0.12 Å.

TABLE 1 | The computed Hubbard *U* parameter values and *Ln* – O bond lengths *d* (computed with the DFT *"f in the core"* and DFT + *U* methods), reported as differences from the measured bond-lengths (last column, data from Harvey et al. (2005); Koohpayeh et al. (2014); Vaisakhan Thampi et al. (2017); Hagiwara et al. (2013); Mandal et al. (2007); Nästren et al. (2009); Sasaki et al. (2004)), for *Ln* cations in $Ln_2Zr_2O_7$ pyrochlores. The lengths of short/long bonds are reported, with the average error (AE) provided in the last row.

Compound	*U* Parameter (eV)	Δd_{Ln-O}^{DFT+U} (Å)	Δd_{Ln-O}^{DFT} (Å)	d_{Ln-O}^{exp} (Å)
La	2.8	–0.006/–0.002	0.000/–0.002	2.339/2.642
Ce	3.7	–0.003/–0.003	–0.002/–0.003	2.327/2.614
Pr	4.3	–0.006/–0.009	–0.005/–0.010	2.317/2.596
Nd	5.0	–0.006/–0.005	–0.009/–0.016	2.311/2.583
Pm	5.1			
Sm	6.3	0.008/–0.085	–0.005/–0.099	2.290/2.631
Eu	7.6	0.016/0.014	–0.007/–0.007	2.285/2.524
Gd	3.9	–0.001/0.040	–0.011/0.018	2.282/2.485
AE		0.003/0.028	0.006/0.022	

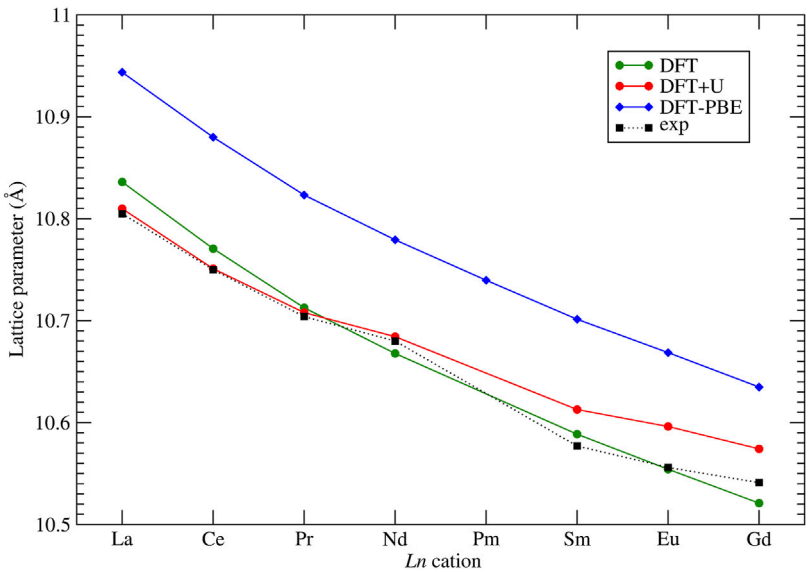

FIGURE 2 | Computed with the DFT *"f in the core"* and DFT + *U* methods, and measured at ambient conditions lattice parameters of series of $Ln_2Zr_2O_7$ pyrochlores. Experimental data come from Harvey et al. (2005); Koohpayeh et al. (2014); Vaisakhan Thampi et al. (2017); Hagiwara et al. (2013); Mandal et al. (2007); Nästren et al. (2009); Sasaki et al. (2004). The lines connecting the data points are plotted as eye guidance to show the trends.

3.1.2 Non-Stoichiometric Compositions: $Nd_xZr_{1-x}O_{2-x/2}$

The lattice parameter of non-stoichiometric fluorite and pyrochlore compounds can be predicted with an ion-close-packing approach by taking into account charges and coordination numbers of *A* and *B* cations and the presence of oxygen vacancies (Ohmichi et al., 1981; Hong and Virkar, 1995; Marrocchelli et al., 2012, 2013; Bukaemskiy et al., 2021). The fluorite lattice parameter, *a*, can be expressed as a function of the average radii of cations and anions as follows

$$a = \frac{4}{\sqrt{3}}(R_c + R_a), \quad (1)$$

where R_c and R_a are additive sums of contributions from all types of cations and anions. The pyrochlore lattice parameter is twice the fluorite lattice parameter. It has been recognized that a vacancy can be viewed as an anion species with a certain effective radius. Models, which apply this approach to fluorite compounds are divided into two groups. In the first group, the vacancy radius is found to be significantly smaller than the radius of an oxygen anion (Hong and Virkar, 1995; Marrocchelli et al., 2012; Marrocchelli et al., 2013), in the second group the vacancy is significantly larger than the oxygen anion (Ohmichi et al., 1981; Bukaemskiy et al., 2021). As discussed recently by Bukaemskiy et al. (2021), the distinction is due to taking or not taking into an account a change in the average cation coordination due to the insertion of vacancies. If the average cation coordination is counted properly as $8 - 2x$, then the vacancy radius is predicted to be about 11% larger than the ionic radius of O^{2-}. The later approach is shown to be consistent with the results of *ab initio* simulations (Stapper et al., 1999; Bukaemskiy et al., 2021). The loss of the negative charge of an oxygen anion (due to a

vacancy formation) pushes the four cations that form tetrahedron encapsulating the 8*a* vacancy (**Figure 1**) away by ~ 0.18 Å, indicating the vacancy size to be larger than O^{2-}. On the other hand, the six nearest oxygen atoms move towards the vacancy (and to the four cations nearest to the vacancy) by ~ 0.24 Å. In the first group of models, both the extension and the contraction effects are mapped onto the vacancy size thus making its radius smaller than that of O^{2-}. In the second group of models, the latter contraction effect is taken into account via a change in the cation radii. The coordination numbers of the four cations are decreased due to the vacancy formation, consequently their cation radii decrease. The average cation coordination number in the stoichiometric pyrochlore is thus 7 ($8 - 2x$ for $x = 0.5$), while it is eight in the ideal fluorite ($x = 0$). Models that take into account the change in cation coordination allow a more accurate description of the lattice parameter variation in fluorite and pyrochlore compounds, because they are sensitive not only to changes in the average composition, but also to short- and long-range order effects. For example, due to the long-range order in pyrochlore, the coordination numbers of *A* and *B* cations appear to be significantly different from the average value of 7. The *B* cation is 6-fold coordinated, while the *A* cation is 8-fold coordinated. As shown by Bukaemskiy et al. (2021), the tendency of *B* cations to lower their coordination number, i.e. to attract vacancies, can be deduced to exist at non-stoichiometric compositions as well. For example, the lattice parameter variation in $A_xB_{1-x}O_{2-0.5x}$ systems ($A = Ln$, Y; $B = Zr$) within the interval of $0 < x < 1/3$ can be explained under the assumption that all vacancies are fully surrounded by *B* cations and all *A* cations keep their coordination equal to 8. It is further shown that this strategy breaks down at $x > 1/3$, when the amount of Zr is insufficient for building up the surrounding of isolated vacancies. Within the interval of $1/3 < x < 0.5$ two different models of SRO develop, one of which is consistent with the type of order in pyrochlore. The tendency of a (large) vacancy to reside close to a *B* cation is valid only in systems in which a *B* cation is significantly smaller than an *A* cation. When the radii of *A* and *B* cations are approximately equal, the electrostatic tendency of a vacancy association to an *A* (III) cation becomes more important. This is confirmed by the *ab initio* simulations (Bogicevic et al., 2001; Bogicevic and Wolverton, 2003; Solomon et al., 2016).

Finkeldei et al. (2017) investigated the series of $Nd_xZr_{1-x}O_{2-x/2}$ compositions by applying XRD and calorimetric measurements, and *ab initio* modeling methods. The XRD data show gradual, linear decrease in the lattice parameter upon lowering of Nd content with *x*, showing slightly different slopes within fluorite ($0.23 < x < 0.30$) and pyrochlore ($0.33 < x < 0.53$) domains. The observed trend for pyrochlore compounds has been well reproduced by the computed data, applying a structural model in which with gradual decreasing of Nd content, the oxygen vacancies are randomly filled with oxygen atoms.

3.1.3 $Nd_2Zr_2O_7$ Pyrochlore Doped With Actinides

When stoichiometric pyrochlore is doped with actinide elements, the main questions are the incorporation site (*A* or *B* cation) and the oxidation state of the dopant. The experimental data on $Nd_2Zr_2O_7$ pyrochlore of Nästren et al. (2009) and Finkeldei et al. (2020) indicate doping at the *A* cation site (Nd), even when the oxidation state of *An* cation is larger than 3+ . In order to shed light on this phenomenon we performed calculations of the lattice parameter of a series of $Nd_2Zr_2O_7$ pyrochlores doped with different actinide elements (*An* = U, Np, Pu, Am, Cm). In the first step we computed the Hubbard *U* parameters for actinides incorporated into the Nd-pyrochlore at different cation sites and in different oxidation states. The values are listed in **Table 2**. The computed values are consistent with the results of our previous studies (e.g., Beridze and Kowalski (2014); Beridze et al. (2016); Kvashnina et al. (2018); Sun et al. (2021)). There is an increase in the Hubbard *U* parameter with the oxidation state of *An* cation, and a general increase along actinide series, which is similar to the trend obtained for the *Ln* series (**Table 1**). This has an impact on the lattice parameters of *An*-doped pyrochlores.

TABLE 2 | The computed Hubbard *U* parameters for *An* dopants, in different oxidation state on Nd site and as tetravalent species on Zr site, in $Nd_2Zr_2O_7$ pyrochlore. Values are in eV.

Actinide	*An* (III)	*An* (IV)	*An* (IV) on Zr	*An*(V)
U	-	1.7	2.3	2.2
Np	-	2.1	2.0	2.6
Pu	2.4	2.6	2.6	
Am	2.6	3.3	3.1	-
Cm	1.7	3.8	3.3	-

Figure 3 shows the computed and measured (Nästren et al., 2009) lattice parameters of $Nd_2Zr_2O_7$ pyrochlore doped with different actinides. In order to be consistent with the measurements of Nästren et al. (2009), all the computed values were re-scaled to actinide stoichiometries of 0.2 per $A_2B_2O_7$ formula unit and were corrected for thermal expansion using the linear thermal expansion coefficient (TEC) and assuming ambient temperature of 298 K. There is some disagreement in the literature about the low temperature (from 0 K up to 300 K) TEC of neodymium zirconate pyrochlores (Kutty et al., 1994; Shimamura et al., 2007; Liu et al., 2010; Feng et al., 2012; Guo et al., 2015) (range from $5 \cdot 10^{-6}\,K^{-1}$ to $12 \cdot 10^{-6}\,K^{-1}$). Here we applied the representative value of $9.11\ 10^{-5}\,K^{-1}$ determined by Kutty et al. (1994). We note, however, that due to the uncertainty in the TEC, the lattice parameters values computed here could have an additional error of ~ 0.01 Å. Nevertheless, with the selected TEC we perfectly reproduce the measured lattice parameter of stoichiometric $Nd_2Zr_2O_7$ pyrochlore, which is essential when predicting the change in the lattice parameter upon incorporation of actinide elements.

The measurements of Nästren et al. (2009) show a clear linear-like relationship between the lattice parameter of *An*-doped $Nd_2Zr_2O_7$ and the ionic radius of the *An* cation. **Figure 3** shows that when the *f* electrons are not computed explicitly, this trend is captured only on the qualitative level. In contrast, the lattice parameters computed with the parameter-free DFT + *U* method used here, with the Hubbard correction applied to *An* and *Ln* elements, successfully reproduce the linear relationship identified by Nästren et al. (2009). This shows the importance of electronic correlations on reliable and accurate computation of

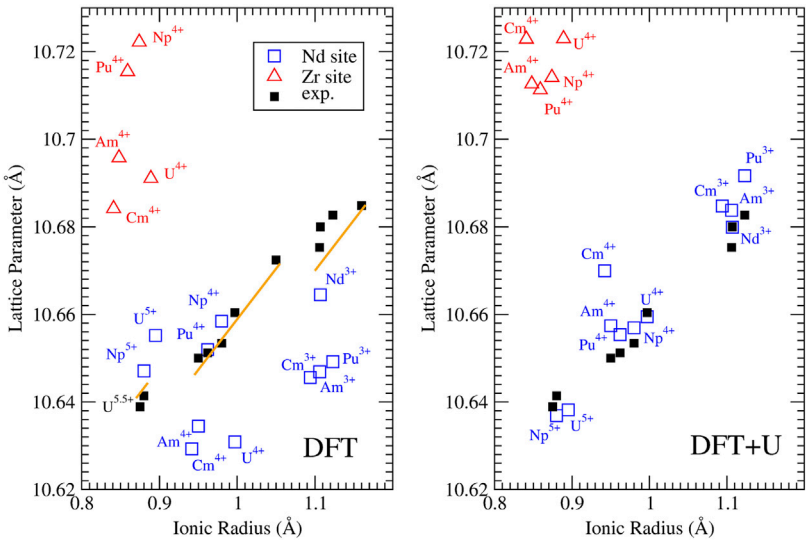

FIGURE 3 | Computed with the DFT *"f in the core"* (left panel) and DFT + *U* (right panel) methods, and measured lattice parameters for $Nd_2Zr_2O_7$ doped with various actinides on Nd (blue squares) and Zr (red triangles) sites. The experimental data collected at ambient conditions (black filled squares) are those of Nästren et al. (2009). The orange solid lines represent prediction of ion-close-packing model of Bukaemskiy et al. (2021). The model predicts three different linear dependencies that correspond to the cases of +3, +4 and +5 *An* cations substituting on the Nd site.

lattice parameters of *f* elements containing oxides. The calculations show that tetravalent and pentavalent actinides, when doped on the Nd^{3+} sites, cause a significant lattice contraction, while tetravalent actinides when doped on the Zr^{4+} site lead to significant lattice expansion. The later effect occurs because 6-fold coordinated Zr^{4+} has the ionic radius of only 0.72 Å (Shannon, 1976), which is significantly smaller than that of the considered *An* cations. As the measurements of Nästren et al. (2009) show a lattice contraction for all tetra and pentavalent actinides, the excellent match between the values computed here and the experimental data supports their interpretation that the actinides cations are incorporated on the Nd-site.

On the computational side, the DFT + *U* method improves accuracy of the predicted lattice parameters, reducing the average error from 0.017 Å (obtained with the simple DFT-PBEsol approach (*f in the core*) to just 0.005 Å (i.e. less than 0.1%), which is an unprecedented accuracy having in mind that 4*f* and 5*f* elements are computationally challenging. Pu^{3+} is also correctly predicted to expand the lattice. Furthermore, the prediction of the lattice parameters of pristine material (Nd^{3+}) and that of Pu^{3+} doped systems have relative errors of only 0.001 and 0.09%, respectively. Even considering the uncertainty in the TEC, these are excellent results showing that the parameter free DFT + *U* method is a highly reliable tool for predicting lattice parameters in the actinide-pyrochlore system.

An interesting observation is that doping with Cm^{4+} produces a significantly greater lattice parameter than with Am^{4+}, breaking the linear relationship followed by the other *An* cations' cases. This is not expected as Cm^{4+} has smaller ionic radius than Am^{4+}. We note, however, that such a subtle differences have been observed due to so-called tetrad effect associated with the number of electrons in *f* shells (e.g., Wilden et al. (2019)). On the computational side, the reason for this is a significantly larger Hubbard *U* parameter value derived for Cm^{4+} than that for Am^{4+} or Cm^{3+} (**Table 2**). This resembles the case of Eu^{3+} and Gd^{3+} (**Table 1**) and results from the strongest electronic correlation effects for cations with nearly complete *f* half-shell (i.e., with 6 *f* electrons). Unfortunately, we do not have experimental data for Cm doped $Nd_2Zr_2O_7$ in the data set of Nästren et al. (2009) to confirm our claim. Confirmation of such effect would be a direct demonstration of impact of electronic correlation effects on the structural arrangements in *f* elements oxides.

Empirical models can be applied to predict the change in lattice parameters of doped materials. The ion-close-packing model of Bukaemskiy et al. (2021) provides information on the structural effects occurring in a doped compound purely due to charges in coordination numbers of the constituent cations. **Figure 3** shows the variation of lattice parameters of actinide-bearing Nd-pyrochlore computed with the ion-packing model, utilizing the Shannon's cation radii (Shannon, 1976). The model provides values that are in good agreement with the experimental lattice parameter data and the *ab initio* calculations discussed above (although it can not capture the discussed, subtle effects resulting from the electronic correlations). This is yet another confirmation of the *A* cation site doping scenario irrespectively of the valence state of *An* cations. On the other hand, the empirical model suggests that the linear relationship observed by Nästren et al. (2009) between the lattice parameter and the radius of *An* cation is split into three linear trends corresponding to +3, +4 and +5 cations.

TABLE 3 | The T_{O-D} in K computed with different methods: modeling disordered phase by defect fluorite (PY-DF), weberite (PY-WB) and defect fluorite/weberite mixture by the two state model of Finkeldei et al. (2017) (PY-WB/DF), and measured for selected pyrochlore compounds. In parentheses we provide the estimated configurational entropy of disordered phase in J/K/mol.

Compound	$Nd_2Zr_2O_7$	$Gd_2Hf_2O_7$
PY-DF	2,310 (48.1)	2,252 (48.1)
PY-WB	3,452 (11.5)	2039 (11.5)
PY-WB/DF	2,405 (38.1)	2,327 (26.3)
exp	2,573	2,723

3.2 Formation Enthalpies

3.2.1 Stoichiometric Pyrochlore: Order-Disorder Transition

The formation enthalpies from oxides for series of stoichiometric pyrochlore-type compounds were measured by Helean et al. (2004) ($Ln_2Ti_2O_7$), Lian et al. (2006a) ($Ln_2Sn_2O_7$), Ushakov et al. (2007) ($Ln_2Hf_2O_7$) and Radha et al. (2009); Saradhi et al. (2012) ($Ln_2Zr_2O_7$). Kowalski (2020) derived these values with the DFT-based atomistic modeling methods. He was able to reproduce the experimentally seen trends in the behavior of formation enthalpies along the lanthanide series with the derived values within 20 kJ/mol. Accurate computation of formation enthalpies is crucial for predicting other important parameters, such as for instance, the order-disorder transition temperature (Jiang et al., 2009; Li et al., 2015) and the extend of ordering in disordered pyrochlore compounds.

Atomistic modeling studies have been applied to predict the order-disorder transition temperature (T_{O-D}) of series of stoichiometric pyrochlore compounds. This parameters is usually computed assuming simple relationship between the enthalpy ΔH and entropy ΔS of disordering process:

$$T_{O-D} = \frac{\Delta H}{\Delta S}, \tag{2}$$

and an estimate of the disordering entropy assuming a complete disordering of the disordered phase (e.g., Jiang et al. (2009)). Earlier atomistic modeling studies derived this parameter by applying simple force-fields to describe interatomic interactions (Minervini et al., 2000; Sickafus et al., 2000). Jiang et al. (2009) applied DFT to derive T_{O-D} and obtained values that are smaller by ~300 K from the measured values, but the experimentally observed trend in decrease of transition temperature along lanthanide series has been well captured. The main reason for this offset is the application of the standard DFT method with the *f* electrons included into the pseudopotential core and not computed explicitly. Li et al. (2015) have shown that the prediction of T_{O-D} is significantly improved when *f* electrons are computed explicitly and the electronic correlations computed with the DFT + *U* method with the Hubbard *U* parameter derived from first principles using the linear response method (Cococcioni and de Gironcoli, 2005). They got a nearly perfect agreement with the measured T_{O-D} for $Sm_2Zr_2O_7$, $Gd_2Zr_2O_7$, $Gd_2Hf_2O_7$ and $Tb_2Hf_2O_7$ compounds.

The aforementioned computed results may be seen surprising in view of the more recent finding of significant SRO in this class of compounds (Shamblin et al., 2016). We notice however, that a SRO is accompanied by a simultaneous decrease in the disordering enthalpy and entropy, as demonstrated by Kowalski (2020). This results in preservation of constancy of the ratio given in **Eq. 2**. Furthermore, as shown by Finkeldei et al. (2017) for $Nd_2Zr_2O_7$, the correct prediction of T_{O-D} may require application of more complex model of disordered phase. In that study a simple two-state statistical model has been applied. Results of applying such a model to selected pyrochlore compounds is given in **Table 3**. We note that the prediction could be improved with: 1) a better computational setup (explicit computation of *f* electrons, Li et al. (2015)) and 2) with a better structural model of disordered pyrochlore, and disordering entropy in such a system. The later would require more advanced thermodynamic modeling approach.

The extend of SRO in stoichiometric defect fluorite compositions has been demonstrated experimentally with calorimetric measurements (Ushakov et al., 2007; Saradhi et al., 2012; Finkeldei et al., 2017) and neutron scattering data (Shamblin et al., 2016). The later data are best fitted with a weberite-type structural representation, in which SRO is emulated via a long-range ordered phase that includes both ordered and disordered sublattices. This finding has been supported by atomistic simulations of Kowalski (2020) who has shown that formation enthalpies computed with the weberite-type structural model are in good agreement with the aforementioned calorimetric measurements and that fully disordered defect fluorite structure is thermodynamically unfeasible. The fact that weberite-type structural model fits nicely the data, however, is not a direct proof that this model gives the best possible characterization of cation and anion distribution in the disordered pyrochlore. Theoretical considerations lead to other possible structural arrangements (Bukaemskiy et al., 2021; Vinograd and Bukaemskiy, 2021). The weberite model may not be the best solution for the configurational entropy of the disordered phase, as the nominal entropy effect of a pyrochlore/weberite transformation (11.52 J/K/mol) seems too small to fit the calorimetric data for $Eu_2Zr_2O_7$ (18 J/K/mol, Saradhi et al. (2012); Finkeldei et al. (2017)). Nevertheless, the data for $Gd_2Hf_2O_7$ (12 J/K/mol, Ushakov et al. (2007)) seem to be consistent with the weberite scenario. The recent simulation study of Vinograd and Bukaemskiy (2021) provided a thermodynamic model for the disordered fluorite, which counts the configurational entropy contributions only from *A* and *B* cations occurring in the same coordination. The model assumes that the disordered fluorite is characterized by an ordered distribution of vacancies and a random distribution of *A* and *B* cations that all occur in the 7-fold coordination. The resulting nominal entropy of 23.04 J/K/mol is larger than the aforementioned experimental data, but such a model can not be easily rejected considering the likely presence of a degree of disorder in measured pyrochlore samples, which would lead to underestimation of disordering entropy by the calorimetry studies. Nevertheless, the model of Vinograd and Bukaemskiy

(2021) provides a semi-quantitative description of the solution calorimetry data at non-stoichiometric compositions of $A_xB_{1-x}O_{2-0.5x}$ systems with A = Sm, Gd, Dy and Y. It predicted the stabilization of various types of short and long-range order, depending on the temperature and the composition.

3.2.2 Non-Stoichiometric Pyrochlore: $Nd_xZr_{1-x}O_{2-x/2}$

Finkeldei et al. (2017) studied the composition-induced disordering in $Nd_xZr_{1-x}O_{2-x/2}$ pyrochlore by applying XRD, calorimetric and atomistic modeling methods. On experimental side they were able to detect the formation of a disordered fluorite phase at x = 0.31 (corresponding to Zr/Nd ratio of 2). This has been clearly indicated by a small change in the lattice parameter vs. x slope, within a narrow transition region in which the two phases with slightly different lattice parameters coexist, and by a significant increase in the measured formation enthalpy of ~30 kJ/mol, which corresponds to the disordering entropy of ~16 J/K/mol. The later value is significantly smaller than the value expected for the fully disordered defect fluorite phase of ~24 J/K/mol and clearly indicates the presence of a significant SRO. Finkeldei et al. (2017) introduced a disordering model in which, upon decrease of Nd content, vacant sites are gradually and randomly occupied by oxygen atoms (coming from excess of ZrO_2). They were able to reproduce well the change in the lattice parameter and formation enthalpy of pyrochlore phase, but significantly overestimated the formation enthalpy of defect fluorite compounds series. Following experimental finding of weberite-type SRO by Shamblin et al. (2016), Finkeldei et al. (2017) modelled the disordered phase as a statistical mixture of weberite and ideally disordered defect fluorite. With this approach, the measured data could be reproduced reasonably well, which shows yet another evidence for significant SRO in this class of compounds and demonstrates that weberite is a reasonable model for this phenomenon. On the other hand, these simulations have shown that weberite model, providing a good structural description of local ordering in defect fluorite, may not be a perfect model for predicting configurational entropies, implying the need for an additional (more disordered) structural component.

3.3 Defect Formation Energies

Besides formation enthalpies, several atomistic modeling studies focused on understanding the formation of defects in pyrochlore compounds (Minervini et al., 2000; Sickafus et al., 2000; Li et al., 2015; Li and Kowalski, 2018). The ability of a material to accumulate defects is considered as a descriptor of radiation damage resistance (Sickafus et al., 2000; Sickafus et al., 2007). Two main defects have been considered, cation-antisite (flipping positions of cations A and B) and anion Frenkel pair (moving an 48*f* oxygen to an 8*a* vacant site). In order to understand the tendency of a material to accumulate defects, Sickafus et al. (2000) computed cation antisite defect formation energies using force-field-based description of interactions. They showed that compounds that are prone to transition to defect fluorite have cations A and B of similar sizes, and resulting lower cation antisite defect formation energy. In more accurate DFT-based simulations, Li et al. (2015) have found a good correlation between the anion-Frenkel pair defect formation energy and formation of defect fluorite. For the compounds that form disordered phase, or transfer to it at temperature, the anion Frenkel pair defect formation energy is small or negative, which is indicated in **Figure 4**. The follow up experimental studies of Maram et al. (2018) confirmed this prediction. Li and Kowalski (2018) demonstrated that a combination of cation antisite and anion Frenkel pair defects results in lowering of the resulting defect formation energy and barrier for oxygen migration. This strongly indicates that mobility on the oxygen sublattice is responsible for the disordering and enhanced radiation damage resistance of selected pyrochlores (e.g., $Gd_2Zr_2O_7$).

3.4 Ionic Conductivity

Zirconia-based materials, including pyrochlore, are considered as prospective ionic conductors for solid state electrolytes (Wuensch, 2000; Diazguillen et al., 2008; Kumar et al., 2008; Mandal et al., 2008; Shlyakhtina and Shcherbakova, 2012; Anithakumari et al., 2016). One of the striking examples is yttria-stabilized zirconia - one of the fastest solid state ionic conductors known (Kowalski et al., 2021). The oxygen conduction in a stoichiometric pyrochlore occurs due to jumps of oxygens, or oxygen vacancies, between the neighboring 48*f* sites. In stoichiometric pyrochlore these sites are fully occupied. In order thus to allow for oxygen diffusion, a vacancy must be formed on a 48*f* site. This occurs via transfer of an oxygen atom to a 8*a* vacant site (Pirzada et al., 2001; Li and Kowalski, 2018). When such a vacancy configuration forms, it can migrate through the 48*f* lattice. van Dijk et al. (1985) realized that in addition to a simple vacancy on 48*f* site, a split vacancy state could be more stable for pyrochlores with heavier lanthanides. In such a state, a 48*f* oxygen ion adjacent to the 48*f* vacancy moves to an interstitial location displaced symmetrically between the two vacant 48*f* sites and the adjacent 8*a* site (Pirzada et al., 2001). The energy difference between the two vacancy configurations computed here is illustrated in the right panel of **Figure 4**. The results indicate stabilization of split vacancy state for Sm and heavier lanthanides. However, the result depends significantly on the computational setup, for instance on the exchange-correlation functional. The difference between energies computed with the PBE and PBEsol functionals is ~ 0.4 eV. We note that there is a correlation between the energy of formation of anion Frenkel pair and the energy difference between the two vacancy configurations, $\Delta E_{split-single} \sim 1.8E_{AFP} + 0.3$ eV. Maram et al. (2018) measured the energy of formation of anion Frenkel pair defect of ~0.1–0.3 eV for $Sm_2Zr_2O_7$, $Eu_2Zr_2O_7$ and $Gd_2Zr_2O_7$. These data, although measured indirectly and at high temperatures, and thus also highly uncertain, would indicate that the computed values shown in left panel of **Figure 4** are underestimated by as much as ~ 0.4 – 0.9 eV. If so, the computed energy difference between the two vacancy states could be also underestimated by as much as ~ 0.7–1.6 eV, which would indicate formation of split vacancy state for lanthanides heavier than Sm, e.g. after Eu, as illustrated in **Figure 4**.

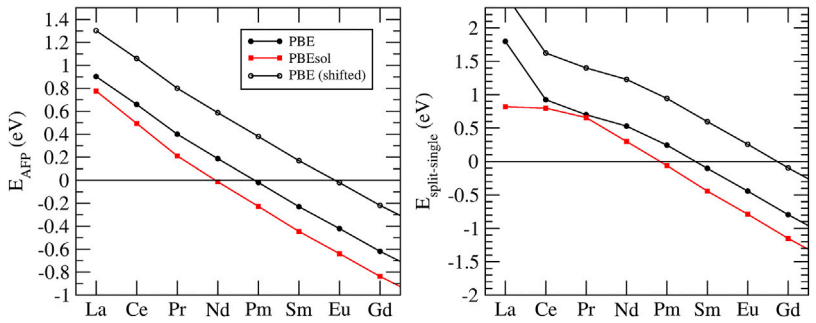

FIGURE 4 | Anion Frenkel pair defect formation energy (E_{AFP}, left panel) and the difference in the energy between split and single vacancy configurations ($E_{split-single}$, right panel) in a series of $Ln_2Zr_2O_7$ pyrochlores. The values were computed with the PBE (black filled circles) and PBEsol (red filled squares) exchange-correlation functionals. The black open circles show the predictions with E_{AFP} adjusted by 0.4 eV to match the measurements of Maram et al. (2018), as discussed in **Section 3.4**.

TABLE 4 | The activation energy (simulated, $E_{a,sim}$; measured $E_{a,\,exp}$, Yamamura (2003)) and energy barriers (E_b) for oxygen migrations in series of $Ln_2Zr_2O_7$ pyrochlores. The energy barriers for 48*f*-48*f* diffusion path for single ($E_{b,single}$) and split ($E_{b,split}$) vacancy states, as well as barrier for oxygen migration from 48*f* to 8*a* site ($E_{b,8a}$) are reported. The second set of experimental values represent the results of our fits to the data of Yamamura (2003). Values are in eV.

Compound	$E_{a,sim}$	$E_{a,\,exp}$	$E_{b,single}$	$E_{b,split}$	$E_{b,8a}$
La	-	0.56/0.63	0.74	-	-
Ce	1.39	-	0.74	-	0.69
Pr	1.13	-	0.73	-	0.49
Nd	0.91	0.68/0.61	0.73	-	0.38
Pm	0.69	-	0.71	1.17	0.31
Sm	0.46	0.56/0.71	0.69	1.21	0.24
Eu	0.28	0.58/0.61	-	1.23	0.19
Gd	0.58	0.88/0.94	-	1.21	0.14

Simulations of Li and Kowalski (2018) show good match of the computed activation energy to the values measured by various studies. Li and Kowalski (2018) and present studies have shown that the split vacancy state forms for zirconate pyrochlores with heavier lanthanides. This splitting state substantially increases the activation barrier for ionic conductivity (Li and Kowalski, 2018). Series of calculations of zirconate pyrochlores with different *Ln* cations performed here show that the barrier for oxygen migrations is ~ 0.7 eV and ~ 1.2 eV for single and split vacancy configurations, respectively (**Table 4**). The computed activation barriers, taken as a sum of the barrier for oxygen diffusion and the anion Frenkel pair defect formation energy (Li and Kowalski, 2018), are reported in **Table 4**. The decrease in the ionic conductivity and the related increase in the activation energy in $Gd_2Zr_2O_7$ (by ~ 0.3 eV with respect to $Eu_2Zr_2O_7$) as reported by Yamamura (2003) is thus a direct manifestation of the split-vacancy state formation. The difference in the computed activation energy between $Gd_2Zr_2O_7$ and $Eu_2Zr_2O_7$ of ~ 0.3 eV is well consistent with the experimental results.

3.5 Radiation Damage

Radiation damage resistance of pyrochlore compound is an important property for application of these materials as immobilization matrices for radionuclides. For pyrochlores, this property is associated with the tendency of a compound to disorder. The pyrochlore compounds like $Gd_2Zr_2O_7$ show enhanced resistance to radiation, forming disordered solid phase (defect fluorite) under irradiation, while other compounds, such as $Gd_2Ti_2O_7$ amorphize (Ewing et al., 2004). There have been a few atomistic modeling studies aiming at understanding of this disordering-induced radiation damage resistance process (e.g., Crocombette and Chartier (2007); Chartier et al. (2003); Crocombette et al. (2006); Chartier et al. (2009); Chartier et al. (2002)). These aimed at delivering parameters such as critical amorphization dose (irradiation dose at which amorphous phase

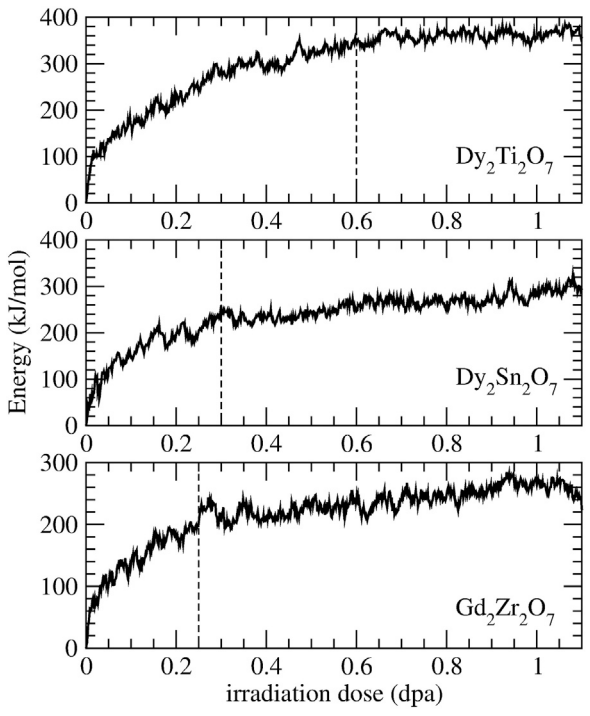

FIGURE 5 | Simulated radiation damage effect on the internal energy for $Dy_2Ti_2O_7$, $Dy_2Sn_2O_7$ and $Gd_2Zr_2O_7$ pyrochlores. The vertical dashed lines indicate the simulated critical amorphization doses.

TABLE 5 | The simulated (H_{sim}) and measured (H_{exp}, Chung et al. (2018a) and Chung et al. (2018b)) amorphization enthalpy and critical amorphization dose (AD) (Ewing et al., 2004) in selected pyrochlores. The values of enthalpies are in kJ/mol. The Anion Frenkel Pair defect formation energy computed with the force fields ($E_{AFP,1}$, Minervini et al. (2000)) and DFT simulations ($E_{AFP,2}$, Li et al. (2015)) are given in eV.

Compound	H_{sim}	H_{exp}	AD_{sim} (dpa)	AD_{exp} (dpa)	$E_{AFP,1}$	$E_{AFP,2}$
$Dy_2Ti_2O_7$	364	243 ± 6	0.6	0.25	10.0	1.0
$Dy_2Sn_2O_7$	282	284 ± 6	0.3	-	6.4	1.5
$Gd_2Zr_2O_7$	257	-	0.25	-	4.8	-0.6

is reached), critical temperature (above which irradiation-induced amorphization does not happen due to self-healing behavior), and at understanding of structural changes upon irradiation.

Recently, using classical molecular dynamics simulations Sun et al. (2021) successfully simulated radiation damage effects in a series of borosilicate glasses. With a defect accumulation procedure they were able to deliver information on critical irradiation dose, Young's modulus and stored internal energy that are consistent with the measured data. Here we applied a similar procedure to derive the critical amorphization dose and amorphization energy of the $Gd_2Zr_2O_7$, $Dy_2Sn_2O_7$ and $Dy_2Ti_2O_7$ pyrochlores, the last two measured by Chung et al. (2018a,b). The results are given in **Figure 5** and **Table 5**. The reported change in energy with irradiation dose is consistent with previous simulations of $La_2Zr_2O_7$ (Crocombette et al., 2006), with similar values for the amorphization energy (~ 170–240 kJ/mol, Crocombette et al. (2006)) and critical irradiation dose (~ 0.25 dpa, Crocombette et al. (2006)). We were able to reproduce well the measured critical amorphization dose of ~ 0.3 dpa in the case of $Dy_2Sn_2O_7$ (Ewing et al., 2004). The computed amorphization energy for this compound is also consistent with the measured value of 284 ± 6 kJ/mol (Chung et al., 2018a). On the other hand, in the case of $Dy_2Ti_2O_7$, the simulations overestimate the critical dose (~ 0.6 dpa vs. ~ 0.25 dpa, Lian et al. (2003)) and the amorphization energy. For $Gd_2Zr_2O_7$ we also obtained amorphization at ~ 0.25 dpa, while this compound in reality transfers to disordered crystalline phase. The reason for such a discrepancy is the applied simplified description of the interatomic interactions in the performed simulations. The radiation damage tendencies in pyrochlores are correlated to the energy cost of defects formation in their crystalline lattice. In **Table 5** we list the anion Frenkel pair defect formation energy as predicted with the applied here empirical force field parameterization of Minervini et al. (2000); Stanek et al. (2002). These energies are significantly larger than these predicted with the *ab initio* calculations (Li et al., 2015) or measurements of Maram et al. (2018). It is thus not surprising that with the applied force fields we are able to amorphize all the considered compounds. On the other hand, the trend in the anion Frenkel pair defect formation energies reflects the order of measured amorphization energies. The negative or small value for $Gd_2Zr_2O_7$ would also indicate transition to disordered phase and high resistance to radiation-induced amorphization. The importance of applying correct force fields in simulations of radiation damage is discussed in Sun et al. (2021). Our results strongly suggest that for reliable simulations of radiation damage effects in pyrochlores, the applied force-fields must be reparameterized. We also note that it is difficult to directly compare the simulated and experimental data on irradiated pyrochlores. This is because of significantly different irradiation doses in simulations, experiments and these expected under nuclear waste storage conditions, as well as due to simplistic, ballistic description of the radiation damage by the applied atomistic simulations (Chartier et al., 2009; Sun et al., 2021).

4 CONCLUSIONS

In this contribution we have presented an overview of our decade-long atomistic modeling research on pyrochlore-type ceramics. We discussed the molecular-level, atomistic simulations-based investigation of structural, thermodynamic, diffusion and radiation-induced properties that are of importance for applications of these materials in energy storage devices or as matrices for immobilization of actinides. We elucidate the importance of correct computation of strongly correlated *f* electrons. This is demonstrated by very accurate prediction of the lattice parameters of series of zirconate-pyrochlores doped with actinides, achieved with the parameter-free DFT + U method in which the Hubbard U parameter is derived from first principles. The comparison of the computed lattice parameter of $Nd_2Zr_2O_7$ pyrochlore doped with different actinide elements to the measured data allows for a confident conclusion regarding the *An* doping site. Such an analysis clearly indicates that actinides are incorporated on Nd site, independently of their oxidation state (+3, +4 or +5). We discussed the role of atomistic modeling in understanding the formation of ordering in disordered pyrochlore phases. By computing the defect formation energies and migration barriers for oxygen atoms, we delivered insights into ionic diffusion in pyrochlore compounds. We explain the drop in the measured ionic conductivity for lanthanides heavier than Eu by the formation of the split vacancy states, which significantly increase the activation barrier for oxygen diffusion. Last but not least, with the classical molecular dynamics simulations, we derived the amorphization energy of selected, irradiated pyrochlore compounds and obtained a good qualitative match to the measured values of disordering enthalpies. The predicted critical amorphization doses are also reasonably well consistent with experiment. However, we highlight some essential differences between the simulated and measured data that are related to inaccuracies in the applied computational methods, including DFT approximations that are based on different types of exchange-correlation functionals, and to simplistic description of interatomic interactions by Buckingham-type interaction potentials that have been intensively used in the research on pyrochlores, especially in the investigation of irradiation effects. In-depth analysis of the measured data with the simulated results allows, on the one hand, for revealing the atomic-scale mechanism governing the investigated phenomena and on the other hand understanding the limitations of the applied computational methods. This should

allow for further improvement of the predictive power of the atomistic simulation methods.

DATA AVAILABILITY STATEMENT

The raw data supporting the conclusions of this article will be made available by the authors, without undue reservation.

AUTHOR CONTRIBUTIONS

PK performed collective analysis of the data, supplementary calculations and overall structuring and editing of the manuscript. TC and AS computed structural parameters of pyrochlores. TC, AS and RT derived the Hubbard *U* parameters, ZH, PK, OC and TB computed defect formation energies and activation barriers for oxygen diffusion, MS and PK performed simulations of radiation damage, AB and VV provided assessment of structural and thermodynamic properties based on empirical models, SF provided expertise on experimental investigation of pyrochlores. All Authors contributed to the analysis of data and writing of the text on parts relevant to their individual contributions.

ACKNOWLEDGMENTS

The authors gratefully acknowledge the computing time granted by the JARA Vergabegremium and provided on the JARA Partition part of the supercomputers JURECA at Forschungszentrum Jülich and CLAIX at RWTH Aachen University.

REFERENCES

Ahamer, C., Opitz, A. K., Rupp, G. M., and Fleig, J. (2017). Revisiting the Temperature Dependent Ionic Conductivity of Yttria Stabilized Zirconia (YSZ). *J. Electrochem. Soc.* 164, F790–F803. doi:10.1149/2.0641707jes

Anithakumari, P., Grover, V., Nandi, C., Bhattacharyya, K., and Tyagi, A. K. (2016). Utilizing Non-stoichiometry in $Nd_2Zr_2O_7$pyrochlore: Exploring superior Ionic Conductors. *RSC Adv.* 6, 97566–97579. doi:10.1039/c6ra08722a

Beridze, G., and Kowalski, P. M. (2014). Benchmarking the DFT+U Method for Thermochemical Calculations of Uranium Molecular Compounds and Solids. *J. Phys. Chem. A.* 118, 11797–11810. doi:10.1021/jp5101126

Beridze, G., Birnie, A., Koniski, S., Ji, Y., and Kowalski, P. M. (2016). DFT + U as a Reliable Method for Efficient Ab Initio Calculations of Nuclear Materials. *Prog. Nucl. Energ.* 92, 142–146. doi:10.1016/j.pnucene.2016.07.012

Blanca Romero, A., Kowalski, P. M., Beridze, G., Schlenz, H., and Bosbach, D. (2014). Performance of DFT+U Method for Prediction of Structural and Thermodynamic Parameters of Monazite-type Ceramics. *J. Comput. Chem.* 35, 1339–1346. doi:10.1002/jcc.23618

Bogicevic, A., and Wolverton, C. (2003). Nature and Strength of Defect Interactions in Cubic Stabilized Zirconia. *Phys. Rev. B* 67, 024106. doi:10.1103/physrevb.67.024106

Bogicevic, A., Wolverton, C., Crosbie, G. M., and Stechel, E. B. (2001). Defect Ordering in Aliovalently Doped Cubic Zirconia from First Principles. *Phys. Rev. B* 64, 014106. doi:10.1103/physrevb.64.014106

Bosbach, D., Brandt, F., Bukaemskiy, A., Deissmann, G., Kegler, P., Klinkenberg, M., et al. (2020). Research for the Safe Management of Nuclear Waste at Forschungszentrum Jülich: Materials Chemistry and Solid Solution Aspects. *Adv. Eng. Mater.* 22, 1901417. doi:10.1002/adem.201901417

Bukaemskiy, A. A., Vinograd, V. L., and Kowalski, P. M. (2021). Ion Distribution Models for Defect Fluorite ZrO_2 - $AO_{1.5}$ (A = L*n*, Y) Solid Solutions: I. Relationship between Lattice Parameter and Composition. *Acta Mater.* 202, 99–111. doi:10.1016/j.actamat.2020.10.045

Chartier, A., Meis, C., Weber, W. J., and Corrales, L. R. (2002). Theoretical Study of Disorder in Ti-substitute$dLa_2Zr_2O_7$. *Phys. Rev. B* 65, 134116. doi:10.1103/physrevb.65.134116

Chartier, A., Meis, C., Crocombette, J.-P., Corrales, L. R., and Weber, W. J. (2003). Atomistic Modeling of Displacement Cascades in$La_2Zr_2O_7$pyrochlore. *Phys. Rev. B* 67, 174102. doi:10.1103/physrevb.67.174102

Chartier, A., Meis, C., Crocombette, J. P., Weber, W. J., and Corrales, L. R. (2005). Molecular Dynamic Simulation of Disorder Induced Amorphization in Pyrochlore. *Phys. Rev. Lett.* 94, 025505. doi:10.1103/PhysRevLett.94.025505

Chartier, A., Catillon, G., and Crocombette, J.-P. (2009). Key Role of the Cation Interstitial Structure in the Radiation Resistance of Pyrochlores. *Phys. Rev. Lett.* 102, 155503. doi:10.1103/physrevlett.102.155503

Chroneos, A., Rushton, M. J. D., Jiang, C., and Tsoukalas, L. H. (2013). Nuclear Wasteform Materials: Atomistic Simulation Case Studies. *J. Nucl. Mater.* 441, 29–39. doi:10.1016/j.jnucmat.2013.05.012

Chung, C.-K., Lang, M., Xu, H., and Navrotsky, A. (2018a). Thermodynamics of Radiation Induced Amorphization and thermal Annealing of $Dy_2Sn_2O_7$ Pyrochlore. *Acta Mater.* 155, 386–392. doi:10.1016/j.actamat.2018.06.003

Chung, C.-K., Shamblin, J., O'Quinn, E. C., Shelyug, A., Gussev, I., Lang, M., et al. (2018b). Thermodynamic and Structural Evolution of $Dy_2Ti_2O_7$ Pyrochlore after swift Heavy Ion Irradiation. *Acta Mater.* 145, 227–234. doi:10.1016/j.actamat.2017.12.044

Cococcioni, M., and de Gironcoli, S. (2005). Linear Response Approach to the Calculation of the Effective Interaction Parameters in the LDA+U Method. *Phys. Rev. B* 71, 035105–035120. doi:10.1103/physrevb.71.035105

Crocombette, J.-P., and Chartier, A. (2007). Molecular Dynamics Studies of Radiation Induced Phase Transitions in $La_2Zr_2O_7$ Pyrochlore. *Nucl. Instr. Methods Phys. Res. Section B: Beam Interact. Mater. Atoms* 255, 158–165. Computer Simulation of Radiation Effects in Solids. doi:10.1016/j.nimb.2006.11.019

Crocombette, J.-P., Chartier, A., and Weber, W. J. (2006). Atomistic Simulation of Amorphization Thermokinetics in Lanthanum Pyrozirconate. *Appl. Phys. Lett.* 88, 051912. doi:10.1063/1.2171651

Diazguillen, J., Diazguillen, M., Padmasree, K., Fuentes, A., Santamaria, J., and Leon, C. (2008). High Ionic Conductivity in the Pyrochlore-type $Gd_{2-y}La_yZr_2O_7$ Solid Solution (0≤y≤1). *Solid State Ionics* 179, 2160–2164. doi:10.1016/j.ssi.2008.07.015

Drey, D. L., O'Quinn, E. C., Subramani, T., Lilova, K., Baldinozzi, G., Gussev, I. M., et al. (2020). Disorder in $Ho_2Ti_{2-x}Zr_xO_7$: Pyrochlore to Defect Fluorite Solid Solution Series. *RSC Adv.* 10, 34632–34650. doi:10.1039/d0ra07118h

Ewing, R. C., Weber, W. J., and Lian, J. (2004). Nuclear Waste Disposal-Pyrochlore ($A_2B_2O_7$): Nuclear Waste Form for the Immobilization of Plutonium and "minor" Actinides. *J. Appl. Phys.* 95, 5949–5971. doi:10.1063/1.1707213

Feng, J., Xiao, B., Wan, C. L., Qu, Z. X., Huang, Z. C., Chen, J. C., et al. (2011). Electronic Structure, Mechanical Properties and thermal Conductivity of $Ln_2Zr_2O_7$ (L*n*=La, Pr, Nd, Sm, Eu and Gd) Pyrochlore. *Acta Mater.* 59, 1742–1760. doi:10.1016/j.actamat.2010.11.041

Feng, J., Xiao, B., Zhou, R., and Pan, W. (2012). Thermal Expansions of $Ln_2Zr_2O_7$ (L*n* = La, Nd, Sm, and Gd) Pyrochlore. *J. Appl. Phys.* 111, 103535. doi:10.1063/1.4722174

Feng, J., Xiao, B., Zhou, R., and Pan, W. (2013). Thermal Conductivity of Rare Earth Zirconate Pyrochlore from First Principles. *Scripta Mater.* 68, 727–730. doi:10.1016/j.scriptamat.2013.01.010

Finkeldei, S., Kegler, P., Kowalski, P. M., Schreinemachers, C., Brandt, F., Bukaemskiy, A. A., et al. (2017). Composition Dependent Order-Disorder Transition in Nd_xZr_{1-x}–$O_{2-0.5x}$ Pyrochlores: A Combined Structural, Calorimetric and Ab Initio Modeling Study. *Acta Mater.* 125, 166–176. doi:10.1016/j.actamat.2016.11.059

Finkeldei, S., Stennett, M. C., Kowalski, P. M., Ji, Y., de Visser-Týnová, E., Hyatt, N. C., et al. (2020). Insights into the Fabrication and Structure of Plutonium Pyrochlores. *J. Mater. Chem. A.* 8, 2387–2403. doi:10.1039/c9ta05795a

Giannozzi, P., Baroni, S., Bonini, N., Calandra, M., Car, R., Cavazzoni, C., et al. (2009). Quantum Espresso: a Modular and Open-Source Software Project for Quantum Simulations of Materials. *J. Phys. Condens. Matter* 21, 395502. doi:10.1088/0953-8984/21/39/395502

Guo, L., Zhang, Y., Wang, C., Zhao, X., and Ye, F. (2015). Phase Structure Evolution and thermal Expansion Variation of Sc_2O_3 Doped $Nd_2Zr_2O_7$ Ceramics. *Mater. Des.* 82, 114–118. doi:10.1016/j.matdes.2015.05.056

Hagiwara, T., Yamamura, H., Nomura, K., and Igawa, M. (2013). Relationship between crystal Structure and Oxide-Ion Conduction in $Ln_2Zr_2O_7$ (Ln = Eu, Nd and La) System Deduced by Neutron and X-ray Diffraction. *J. Ceram. Soc. Jpn.* 121, 205–210. doi:10.2109/jcersj2.121.205

Harvey, E. J., Whittle, K. R., Lumpkin, G. R., Smith, R. I., and Redfern, S. A. T. (2005). Solid Solubilities of (La Nd,)$_2$(Zr,Ti)$_2O_7$ Phases Deduced by Neutron Diffraction. *J. Solid State. Chem.* 178, 800–810. doi:10.1016/j.jssc.2004.12.030

Helean, K. B., Ushakov, S. V., Brown, C. E., Navrotsky, A., Lian, J., Ewing, R. C., et al. (2004). Formation Enthalpies of Rare Earth Titanate Pyrochlores. *J. Solid State. Chem.* 177, 1858–1866. doi:10.1016/j.jssc.2004.01.009

Hong, S. J., and Virkar, A. V. (1995). Lattice Parameters and Densities of Rare-Earth Oxide Doped Ceria Electrolytes. *J. Am. Ceram. Soc.* 78, 433–439. doi:10.1111/j.1151-2916.1995.tb08820.x

Jahn, S., and Kowalski, P. M. (2014). Theoretical Approaches to Structure and Spectroscopy of Earth Materials. *Rev. Mineralogy Geochem.* 78, 691–743. doi:10.2138/rmg.2014.78.17

Ji, Y. (2018). *Atomistic Modeling of Nuclear Waste Materials : Cases of Ceramic Waste Forms and Nuclear Graphite*. Veröffentlicht auf dem Publikationsserver der RWTH Aachen University. Aachen: Rheinisch-Westfälische Technische Hochschule Aachen. Dissertation. doi:10.18154/RWTH-2018-230012

Jiang, C., Stanek, C. R., Sickafus, K. E., and Uberuaga, B. P. (2009). First-principles Prediction of Disordering Tendencies in Pyrochlore Oxides. *Phys. Rev. B* 79, 104203–104207. doi:10.1103/physrevb.79.104203

Koohpayeh, S. M., Wen, J.-J., Trump, B. A., Broholm, C. L., and McQueen, T. M. (2014). Synthesis, Floating Zone crystal Growth and Characterization of the Quantum Spin Ice $Pr_2Zr_2O_7$ Pyrochlore. *J. Cryst. Growth* 402, 291–298. doi:10.1016/j.jcrysgro.2014.06.037

Kowalski, P. M., Beridze, G., Li, Y., Ji, Y., Friedrich, C., Şaşioğlu, E., et al. (2016). Feasible and ReliableAB InitioApproach to Computation of Materials Relevant for Nuclear Waste Management. *Ceram. Trans.* 258, 205–217. doi:10.1002/9781119236016.ch21

Kowalski, P. M., He, Z., and Cheong, O. (2021). Electrode and Electrolyte Materials from Atomistic Simulations: Properties of Li_xFePO_4 Electrode and Zircon-Based Ionic Conductors. *Front. Energ. Res.* 9, 107. doi:10.3389/fenrg.2021.653542

Kowalski, P. M. (2020). Formation Enthalpy of $Ln_2B_2O_7$-type (B=Ti,Sn,Hf,Zr) Compounds. *Scripta Mater.* 189, 7–10. doi:10.1016/j.scriptamat.2020.07.048

Kumar, M., Raj, I. A., and Pattabiraman, R. (2008). $Y_2Zr_2O_7$ (YZ)-pyrochlore Based Oxide as an Electrolyte Material for Intermediate Temperature Solid Oxide Fuel Cells (ITSOFCs)-Influence of Mn Addition on YZ. *Mater. Chem. Phys.* 108, 102–108. doi:10.1016/j.matchemphys.2007.09.010

Kutty, K. V. G., Rajagopalan, S., Mathews, C. K., and Varadaraju, U. V. (1994). Thermal Expansion Behaviour of Some Rare Earth Oxide Pyrochlores. *Mater. Res. Bull.* 29, 759–766. doi:10.1016/0025-5408(94)90201-1

Kvashnina, K. O., Kowalski, P. M., Butorin, S. M., Leinders, G., Pakarinen, J., Bès, R., et al. (2018). Trends in the Valence Band Electronic Structures of Mixed Uranium Oxides. *Chem. Commun.* 54, 9757–9760. doi:10.1039/c8cc05464a

Li, Y., and Kowalski, P. M. (2018). Energetics of Defects Formation and Oxygen Migration in Pyrochlore Compounds from First Principles Calculations. *J. Nucl. Mater.* 505, 255–261. doi:10.1016/j.jnucmat.2017.11.005

Li, Y., Kowalski, P. M., Beridze, G., Birnie, A. R., Finkeldei, S., and Bosbach, D. (2015). Defect Formation Energies in $A_2B_2O_7$ Pyrochlores. *Scripta Mater.* 107, 18–21. doi:10.1016/j.scriptamat.2015.05.010

Li, Y., Kowalski, P. M., Beridze, G., Blanca-Romero, A., Ji, Y., Vinograd, V. L., et al. (2016). Atomistic Simulations of Ceramic Materials Relevant for Nuclear Waste Management: Cases of Monazlte and Pyrochlore. *Ceram. Trans.* 255, 165–175. doi:10.1002/9781119234531.ch15

Lian, J., Chen, J., Wang, L. M., Ewing, R. C., Farmer, J. M., Boatner, L. A., et al. (2003). Radiation-induced Amorphization of Rare-Earth Titanate Pyrochlores. *Phys. Rev. B* 68, 134107. doi:10.1103/physrevb.68.134107

Lian, J., Helean, K. B., Kennedy, B. J., Wang, L. M., Navrotsky, A., and Ewing, R. C. (2006a). Effect of Structure and Thermodynamic Stability on the Response of Lanthanide Stannate Pyrochlores to Ion Beam Irradiation. *J. Phys. Chem. B* 110, 2343–2350. doi:10.1021/jp055266c

Lian, J., Weber, W. J., Jiang, W., Wang, L. M., Boatner, L. A., and Ewing, R. C. (2006b). Radiation-induced Effects in Pyrochlores and Nanoscale Materials Engineering. *Nucl. Instr. Methods Phys. Res. Section B: Beam Interact. Mater. Atoms* 250, 128–136. doi:10.1016/j.nimb.2006.04.157

Liu, Z.-G., Ouyang, J.-H., Zhou, Y., and Xia, X.-L. (2010). Electrical Conductivity and thermal Expansion of Neodymium-Ytterbium Zirconate Ceramics. *J. Power Sourc.* 195, 3261–3265. doi:10.1016/j.jpowsour.2009.11.135

Mandal, B. P., Banerji, A., Sathe, V., Deb, S. K., and Tyagi, A. K. (2007). Order-disorder Transition in $Nd_{2-y}Gd_yZr_2O_7$ Pyrochlore Solid Solution: An X-ray Diffraction and Raman Spectroscopic Study. *J. Solid State. Chem.* 180, 2643–2648. doi:10.1016/j.jssc.2007.07.007

Mandal, B. P., Deshpande, S. K., and Tyagi, A. K. (2008). Ionic Conductivity Enhancement in $Gd_2Zr_2O_7$ Pyrochlore by Nd Doping. *J. Mater. Res.* 23, 911–916. doi:10.1557/jmr.2008.0112

Maram, P. S., Ushakov, S. V., Weber, R. J. K., Benmore, C. J., and Navrotsky, A. (2018). Probing Disorder in Pyrochlore Oxides Using *In Situ* Synchrotron Diffraction from Levitated Solids-A Thermodynamic Perspective. *Sci. Rep.* 8, 10658. doi:10.1038/s41598-018-28877-x

Marrocchelli, D., Bishop, S. R., Tuller, H. L., and Yildiz, B. (2012). Understanding Chemical Expansion in Non-stoichiometric Oxides: Ceria and Zirconia Case Studies. *Adv. Funct. Mater.* 22, 1958–1965. doi:10.1002/adfm.201102648

Marrocchelli, D., Bishop, S. R., and Kilner, J. (2013). Chemical Expansion and its Dependence on the Host Cation Radius. *J. Mater. Chem. A.* 1, 7673–7680. doi:10.1039/c3ta11020f

Minervini, L., Grimes, R. W., and Sickafus, K. E. (2000). Disorder in Pyrochlore Oxides. *J. Am. Ceram. Soc.* 83, 1873–1878. doi:10.1111/j.1151-2916.2000.tb01484.x

Minervini, L., Grimes, R. W., Tabira, Y., Withers, R. L., and Sickafus, K. E. (2002). The Oxygen Positional Parameter in Pyrochlores and its Dependence on Disorder. *Philos. Mag. A* 82, 123–135. doi:10.1080/01418610208240001

Moon, P., and Tuller, H. (1988). Intrinsic Fast Oxygen Ionic Conductivity in the $Gd_2Zr_2O_7$, and $Y_2Zr_2O_7$, Pyrochlore Systems. In *Symposium M Solid State Ionics I*. 135 of *MRS Proceedings*. doi:10.1557/PROC-135-149

Nästren, C., Jardin, R., Somers, J., Walter, M., and Brendebach, B. (2009). Actinide Incorporation in a Zirconia Based Pyrochlore $(Nd_{1.8}An_{0.2})Zr_2O_{7+x}$ (*An*=Th, U, Np, Pu, Am). *J. Solid State. Chem.* 182, 1–7. doi:10.1016/j.jssc.2008.09.017

Ohmichi, T., Fukushima, S., Maeda, A., and Watanabe, H. (1981). On the Relation between Lattice Parameter and O/m Ratio for Uranium Dioxide-Trivalent Rare Earth Oxide Solid Solution. *J. Nucl. Mater.* 102, 40–46. doi:10.1016/0022-3115(81)90544-4

Öztürk, E., Karacaoglu, E., and Kalem, V. (2020). Photoluminescence and Piezoelectric Behaviour of $Y_2Zr_2O_7$ Pyrochlore-based Multifunctional Materials and the Influence of Eu 3^+ and Sm 3^+. *Luminescence* 35, 406–411. doi:10.1002/bio.3741

Panero, W., Stixrude, L., and Ewing, R. (2004). First-principles Calculation of Defect-Formation Energies in the Y_2(Ti,Sn,Zr)$_2O_7$ Pyrochlore. *Phys. Rev. B* 70, 054110. doi:10.1103/physrevb.70.054110

Park, J. K., Kim, C. H., Choi, K. J., Park, H. D., and Choi, S. Y. (2001). Photoluminescence Behavior of Al^{3+}, Pr^{3+} Doped Perovskite $La_{2/3}TiO_3$ and Pyrochlore $La_2Ti_2O_7$. *J. Mater. Res.* 16, 2568–2571. doi:10.1557/jmr.2001.0352

Perdew, J. P., Burke, K., and Ernzerhof, M. (1996). Generalized Gradient Approximation Made Simple. *Phys. Rev. Lett.* 77, 3865–3868. doi:10.1103/physrevlett.77.3865

Perdew, J. P., Ruzsinszky, A., Csonka, G. I., Vydrov, O. A., Scuseria, G. E., Constantin, L. A., et al. (2008). Restoring the Density-Gradient Expansion for Exchange in Solids and Surfaces. *Phys. Rev. Lett.* 100, 136406. doi:10.1103/physrevlett.100.136406

Pirzada, M., Grimes, R. W., Minervini, L., Maguire, J. F., and Sickafus, K. E. (2001). Oxygen Migration in $A_2B_2O_7$ Pyrochlores. *Solid State Ionics* 140, 201–208. doi:10.1016/s0167-2738(00)00836-5

Plimpton, S. (1995). Fast Parallel Algorithms for Short-Range Molecular Dynamics. *J. Comput. Phys.* 117, 1–19. doi:10.1006/jcph.1995.1039

Radha, A. V., Ushakov, S. V., and Navrotsky, A. (2009). Thermochemistry of Lanthanum Zirconate Pyrochlore. *J. Mater. Res.* 24, 3350–3357. doi:10.1557/jmr.2009.0401

Ringwood, A. E., Kesson, S. E., Ware, N. G., Hibberson, W., and Major, A. (1979). Immobilisation of High Level Nuclear Reactor Wastes in SYNROC. *Nature* 278, 219–223. doi:10.1038/278219a0

Saradhi, M. P., Ushakov, S. V., and Navrotsky, A. (2012). Fluorite-pyrochlore Transformation in $Eu_2Zr_2O_7$-Direct Calorimetric Measurement of Phase Transition, Formation and Surface Enthalpies. *RSC Adv.* 2, 3328–3334. doi:10.1039/c2ra00727d

Sasaki, T., Ukyo, Y., Kuroda, K., Arai, S., Muto, S., and Saka, H. (2004). Crystal Structure of $Ce_2Zr_2O_7$ and .BETA.-$Ce_2Zr_2O_{7.5}$. *J. Ceram. Soc. Jpn.* 112, 440–444. doi:10.2109/jcersj.112.440

Shamblin, J., Feygenson, M., Neuefeind, J., Tracy, C. L., Zhang, F., Finkeldei, S., et al. (2016). Probing Disorder in Isometric Pyrochlore and Related Complex Oxides. *Nat. Mater.* 15, 507–511. doi:10.1038/nmat4581

Shannon, R. D. (1976). Revised Effective Ionic Radii and Systematic Studies of Interatomic Distances in Halides and Chalcogenides. *Acta Cryst. Sect A.* 32, 751–767. doi:10.1107/s0567739476001551

Shimamura, K., Arima, T., Idemitsu, K., and Inagaki, Y. (2007). Thermophysical Properties of Rare-Earth-Stabilized Zirconia and Zirconate Pyrochlores as Surrogates for Actinide-Doped Zirconia. *Int. J. Thermophys.* 28, 1074–1084. doi:10.1007/s10765-007-0232-9

Shlyakhtina, A. V., and Shcherbakova, L. G. (2012). New Solid Electrolytes of the Pyrochlore Family. *Russ. J. Electrochem.* 48, 1–25. doi:10.1134/s1023193512010144

Sickafus, K. E., Minervini, L., Grimes, R. W., Valdez, J. A., Ishimaru, M., Li, F., et al. (2000). Radiation Tolerance of Complex Oxides. *Science* 289, 748–751. doi:10.1126/science.289.5480.748

Sickafus, K. E., Grimes, R. W., Valdez, J. A., Cleave, A., Tang, M., Ishimaru, M., et al. (2007). Radiation-induced Amorphization Resistance and Radiation Tolerance in Structurally Related Oxides. *Nat. Mater* 6, 217–223. doi:10.1038/nmat1842

Solomon, J. M., Shamblin, J., Lang, M., Navrotsky, A., and Asta, M. (2016). Chemical Ordering in Substituted Fluorite Oxides: a Computational Investigation of $Ho_2Zr_2O_7$ and $RE_2Th_2O_7$ (RE=Ho, Y, Gd, Nd, La). *Sci. Rep.* 6, 38772. doi:10.1038/srep38772

Stanek, C. R., Minervini, L., and Grimes, R. W. (2002). Nonstoichiometry in $A_2B_2O_7$ Pyrochlores. *J. Am. Ceram. Soc.* 85, 2792–2798. doi:10.1111/j.1151-2916.2002.tb00423.x

Stapper, G., Bernasconi, M., Nicoloso, N., and Parrinello, M. (1999). Ab Initiostudy of Structural and Electronic Properties of Yttria-Stabilized Cubic Zirconia. *Phys. Rev. B* 59, 797–810. doi:10.1103/physrevb.59.797

Sun, M., Jahn, S., Peng, H., Zhang, X., Wang, T., and Kowalski, P. M. (2021). Properties of Irradiated Sodium Borosilicate Glasses from experiment and Atomistic Simulations. *J. Am. Ceram. Soc.* 104, 4479–4491. doi:10.1111/jace.17830

Uberuaga, B. P., Tang, M., Jiang, C., Valdez, J. A., Smith, R., Wang, Y., et al. (2015). Opposite Correlations between Cation Disordering and Amorphization Resistance in Spinels versus Pyrochlores. *Nat. Commun.* 6, 8750. doi:10.1038/ncomms9750

Ushakov, S. V., Navrotsky, A., Tangeman, J. A., and Helean, K. B. (2007). Energetics of Defect Fluorite and Pyrochlore Phases in Lanthanum and Gadolinium Hafnates. *J. Am. Ceram. Soc.* 90, 1171–1176. doi:10.1111/j.1551-2916.2007.01592.x

Vaisakhan Thampi, D. S., Prabhakar Rao, P., and Renju, U. A. (2017). Studies on Order - Disorder Transition, Lattice Expansion and Ionic Conductivity in Aliovalent Cation Substituted Sm2Zr2O7 System. *J. Solid State. Chem.* 255, 121–128. doi:10.1016/j.jssc.2017.08.011

Vandijk, M., Burggraaf, A., Cormack, A., and Catlow, C. (1985). Defect Structures and Migration Mechanisms in Oxide Pyrochlores. *Solid State Ionics* 17, 159–167. doi:10.1016/0167-2738(85)90067-0

Vanderbilt, D. (1990). Soft Self-Consistent Pseudopotentials in a Generalized Eigenvalue Formalism. *Phys. Rev. B* 41, 7892–7895. doi:10.1103/physrevb.41.7892

Vanpoucke, D. E. P., Bultinck, P., Cottenier, S., Van Speybroeck, V., and Van Driessche, I. (2011). Density Functional Theory Study of $La_2Ce_2O_7$: Disordered Fluorite versus Pyrochlore Structure. *Phys. Rev. B* 84, 054110. doi:10.1103/physrevb.84.054110

Vinograd, V. L., and Bukaemskiy, A. A. (2021). Ion Distribution Models for Defect Fluorite ZrO_2 - $AO_{1.5}$ (A = Ln, Y) Solid Solutions: II. Thermodynamics of Mixing and Ordering. *Acta Mater.* 202, 55–67. doi:10.1016/j.actamat.2020.10.046

Wang, S. X., Begg, B. D., Wang, L. M., Ewing, R. C., Weber, W. J., and Kutty, K. V. G. (1999). Radiation Stability of Gadolinium Zirconate: A Waste Form for Plutonium Disposition. *J. Mater. Res.* 14, 4470–4473. doi:10.1557/jmr.1999.0606

Wilden, A., Kowalski, P., Klaß, L., Kraus, B., Kreft, F., Modolo, G., et al. (2019). Unprecedented Inversion of Selectivity and Extraordinary Difference in the Complexation of Trivalent F Elements by Diastereomers of a Methylated Diglycolamide. *Chemistry* 25, 5507–5513. Wiley deal. doi:10.1002/chem.201806161

Wu, X., Kang, F., Duan, W., and Li, J. (2019). Density Functional Theory Calculations: A Powerful Tool to Simulate and Design High-Performance Energy Storage and Conversion Materials. *Prog. Nat. Sci. Mater. Int.* 29, 247–255. doi:10.1016/j.pnsc.2019.04.003

Wuensch, B. (2000). Connection between Oxygen-Ion Conductivity of Pyrochlore Fuel-Cell Materials and Structural Change with Composition and Temperature. *Solid State Ion* 129, 111–133. doi:10.1016/s0167-2738(99)00320-3

Xiao, H. Y., Weber, W. J., Zhang, Y., Zu, X. T., and Li, S. (2015). Electronic Excitation Induced Amorphization in Titanate Pyrochlores: an Ab Initio Molecular Dynamics Study. *Sci. Rep.* 5, 8265. doi:10.1038/srep08265

Yamamura, H. (2003). Electrical Conductivity Anomaly Around Fluorite-Pyrochlore Phase Boundary. *Solid State Ionics* 158, 359–365. doi:10.1016/s0167-2738(02)00874-3

Zunger, A., Wei, S.-H., Ferreira, L. G., and Bernard, J. E. (1990). Special Quasirandom Structures. *Phys. Rev. Lett.* 65, 353–356. doi:10.1103/physrevlett.65.353

Conflict of Interest: The authors declare that the research was conducted in the absence of any commercial or financial relationships that could be construed as a potential conflict of interest.

Publisher's Note: All claims expressed in this article are solely those of the authors and do not necessarily represent those of their affiliated organizations, or those of the publisher, the editors and the reviewers. Any product that may be evaluated in this article, or claim that may be made by its manufacturer, is not guaranteed or endorsed by the publisher.

frontiers in Chemistry

ORIGINAL RESEARCH
published: 08 November 2021
doi: 10.3389/fchem.2021.706736

Insight Into Disorder, Stress and Strain of Radiation Damaged Pyrochlores: A Possible Mechanism for the Appearance of Defect Fluorite

Sarah C. Finkeldei[1,2,3], Shirley Chang[1], Mihail Ionescu[4], Daniel Oldfield[4], Joel Davis[4], Gregory R. Lumpkin[4], David Simeone[5], Max Avdeev[4], Felix Brandt[6], Dirk Bosbach[6], Martina Klinkenberg[6] and Gordon J. Thorogood[4,7]**

[1]Department of Chemistry, University of California, Irvine, Irvine, CA, United States, [2]Department of Chemical and Biomolecular Engineering, University of California, Irvine, Irvine, CA, United States, [3]Department of Materials Science and Engineering, University of California, Irvine, Irvine, CA, United States, [4]Australian Nuclear Science and Technology Organisation, Lucas Heights, NSW, Australia, [5]CEA/DEN/DMN/SRMA/LA2M-LRC CARMEN, CEA, Université Paris-Saclay, Gif-sur-Yvette, France, [6]Forschungszentrum Juelich GmbH, Institute of Energy and Climate Research, IEK-6: Nuclear Waste Management and Reactor Safety, Juelich, Germany, [7]Department of Nuclear System Safety Engineering, Nagaoka University of Technology, Nagaoka, Japan

OPEN ACCESS

Edited by:
Vladimir Dmitriev, European Synchrotron Radiation Facility, France

Reviewed by:
Marco Milanesio, Università del Piemonte Orientale, Italy
Richard Beanland, University of Warwick, United Kingdom

***Correspondence:**
Sarah C. Finkeldei
sfinkeld@uci.edu
Gordon J. Thorogood
gjt@ansto.gov.au

Specialty section:
This article was submitted to Solid State Chemistry, a section of the journal Frontiers in Chemistry

Received: *07 May 2021*
Accepted: *01 October 2021*
Published: *08 November 2021*

Citation:
Finkeldei SC, Chang S, Ionescu M, Oldfield D, Davis J, Lumpkin GR, Simeone D, Avdeev M, Brandt F, Bosbach D, Klinkenberg M and Thorogood GJ (2021) Insight Into Disorder, Stress and Strain of Radiation Damaged Pyrochlores: A Possible Mechanism for the Appearance of Defect Fluorite. Front. Chem. 9:706736. doi: 10.3389/fchem.2021.706736

We have examined the irradiation response of a titanate and zirconate pyrochlore—both of which are well studied in the literature individually—in an attempt to define the appearance of defect fluorite in zirconate pyrochlores. To our knowledge this study is unique in that it attempts to discover the mechanism of formation by a comparison of the different systems exposed to the same conditions and then examined *via* a range of techniques that cover a wide length scale. The conditions of approximately 1 displacement per atom *via* He^{2+} ions were used to simulate long term waste storage conditions as outlined by previous results from Ewing in a large enough sample volume to allow for neutron diffraction, as not attempted previously. The titanate sample, used as a baseline comparison since it readily becomes amorphous under these conditions behaved as expected. In contrast, the zirconate sample accumulates tensile stress in the absence of detectable strain. We propose this is analogous to the lanthanide zirconate pyrochlores examined by Simeone et al. where they reported the appearance of defect fluorite diffraction patterns due to a reduction in grain size. Radiation damage and stress results in the grains breaking into even smaller crystallites, thus creating even smaller coherent diffraction domains. An $(ErNd)_2(ZrTi)_2O_7$ pyrochlore was synthesized to examine which mechanism might dominate, amorphization or stress/strain build up. Although strain was detected in the pristine sample *via* Synchrotron X-ray diffraction it was not of sufficient quality to perform a full analysis on.

Keywords: nuclear waste form materials, radiation damage and others irradiation effects, order/disorder phase transition, pyrochlore, stress, neutron diffraction, transmission electron microscopy

INTRODUCTION

Pyrochlores cover a large variation of compositions (Subramanian et al., 1983) and there have been numerous publications that endeavor to understand the tolerance pyrochlores have to radiation damage (Lian et al., 2002; Sattonnay et al., 2008; Pilania et al., 2017; Holesinger et al., 2019). The reason for this goes well beyond the application to immobilize nuclear waste (Lumpkin and Ewing, 1985; Ewing et al., 2004) and the subsequent amorphization (Lang et al., 2009). Due to properties

such as colossal magnetoresistance (Subramanian et al., 1996), ion conduction (Subramanian et al., 1985; Heremans et al., 1995; Pirzada et al., 2001), and superconductivity (Yonezawa et al., 2004) pyrochlores and their variations have many applications such as thermal barrier coatings (Lehmann et al., 2003), fuel cells (Bae and Steele, 1999), and thermo-electrics (Rao et al., 1986). All of these applications and properties are related in some way to the disorder within the system being either engineered or making use of the materials resistance to it (Simeone et al., 2017). To study pyrochlores as potential nuclear waste forms, accelerated radiation damage to simulate the effects caused by either fission fragments or the interactions with neutrons (Nordlund et al., 2015) is achieved by ion irradiation of a pyrochlore's near surface. Characterization of the material is typically performed *ex situ* since ions are generally produced by an accelerator. One of the issues with using ions is that they have a very small interaction volume when compared with the bulk of the material and so typically produce a very thin layer and thus small amount of damaged material to be examined, utilizing techniques such as Glancing Incidence X-Ray Diffraction (GIXRD) (Li et al., 2012) or Transmission Electron Microscopy (TEM) (Lian et al., 2002). More recently there have been attempts to combine other techniques such as spectroscopy with GIXRD and TEM (Lenz, 2019). In an attempt to better understand the order/disorder process up to the amorphization of the structure and how that may also be related to the stress and strain imparted, we have irradiated two well studied pyrochlores $Er_2Ti_2O_7$ (routinely reported as transforming to amorphous material under irradiation) (Sickafus KE. et al., 2000; Li et al., 2012) and $Nd_2Zr_2O_7$ (routinely reported as transforming to a defect fluorite under irradiation) (Lutique et al., 2003). He^{2+} ions were used to capitalize on the wealth of data already in the literature (Zhang et al., 2015; Hu et al., 2018). The reasoning behind the choice of the two pyrochlores was guided by the fact that as R_A/R_B decreases, the pyrochlore structure becomes less stable (Helean et al., 2004). Helean et al. performed a comprehensive study where they examined the relationship between R_B and ΔH_{f-ox} for titanates at 298 K and found that it is non-linear and approximately parallels the increasing "resistance" to ion-beam-induced amorphization as R_A/R_B decreases. For example, Lumpkin et al. (2009) when irradiating $Nd_2Zr_2O_7$ with 1.0 MeV Kr ions reported a *Tc* of 135 K as compared to the *Tc* value of 804 K for $Er_2Ti_2O_7$ as reported by Helean et al. (2004) indicating that $Nd_2Zr_2O_7$ has a higher resistance to amorphization as compared to $Er_2Ti_2O_7$. Combined characterization *via* neutron diffraction commonly used for bulk materials (in this study applied to approximately one quarter of a 100 micron thin sample as noted by EBSD), electron backscatter diffraction (EBSD) as used in surface examination and TEM, typically a high-resolution technique, enabled mechanistic insights into how the disorder process proceeds. Fabrication of a solid solution $(ErNd)_2(TiZr)_2O_7$ sample was predicted to provide additional information on the dominating behavior within a solid solution. However, due to the presence of a second phase only preliminary studies were performed on the solid solution sample. There are two main advantages to using He^{2+} ions for radiation damage, the first being that the accelerating voltage of the ion can be varied to allow for damage over a range of depths thus achieving what would be considered bulk damage in a very thin section of the material. Second, the use of He^{2+} ions for irradiation is a simulant for alpha particles, a common fission fragment found in nuclear waste forms and nuclear fuel. Current literature related to radiation damage lists the amount of damage as displacements per atom (dpa). In this study we aimed for damage of approximately 1 dpa to examine the onset of disorder. Being able to vary the range of irradiation depths on a thin pellet allowed us to obtain a "bulk" amount or significant proportion of radiation-damaged material to perform high-resolution neutron diffraction as well as analysis of subsequent subsamples for EBSD and TEM. This approach mimics typical radiation damage e.g. caused by alpha particles, which occurs throughout the waste form or fuel rather than solely at the surface. The effects of damage due to alpha particles in a bulk pyrochlore has not been studied due to the above stated challenges. Typically to understand this type of damage solid solutions are used with simulants to impart disorder and then conclusions are drawn as to what types of phase changes may occur. Here, neutron diffraction data obtained from the damaged samples was analyzed to determine the difference in disorder and the behavior of the cations vs. the anions as well as to compare the degree of stress and strain in the damaged material with the undamaged material.

In reviewing the literature there are different ways that the effect of He^{2+} ions being accelerated at a ceramic can be envisaged. If we consider each interaction of the He^{2+} ions as ballistic phenomena as per Scapin (Martina Scapin, 2013) where the interaction is considered a high strain rate case they have stated that the material is in a hydrostatic state, in which the three normal components of stress are all equal to the pressure (opposite in sign). This also implies that the three normal components of strain are equal. This leads to the assumption that the pressure is proportional to the volumetric strain, and the scale factor is represented by the bulk modulus. The hydrostatic component of stress is associated to the pressure in the material, which is equal to the trace of the complete stress tensor. Ceramics are characterized by having a small plastic deformation and nearly flat fracture surfaces, which originates from a single crack propagation. Scapin (Martina Scapin, 2013) also envisioned the He^{2+} ions as a pressure wave incident on the sample the pressure can be used as failure parameter defining a failure model (i.e., accelerating voltage of the ions). The spalling defines the failure of a material in the case of high hydrostatic tensile loads, which usually characterize all the phenomena in which a high compressive wave is reflected into a tensile one by a free surface. The part of the component behind the impacted area (i.e., below the SRIM calculated depth) could be subjected to considerable values of tensile hydrostatic stresses, in accordance with the propagation of cylindrical pressure shock-waves (Martina Scapin, 2013).

Researchers at CERN have taken a similar approach in their study of beam-induced damage mechanisms and their calculation (Bertarelli, 2014), where they have made the assumption of purely hydrostatic (fluid-like) behavior of the impacted solids (each ion

interaction can be imagined a cone shaped shock wave moving forward), which is typically acceptable when the achieved stresses greatly exceed the flow strength of the material and the stress tensor can be approximately reduced to its hydrostatic component only; nowadays, the deviatoric component, responsible for material strength. This internal strain energy can be partitioned into one part associated with volume change (caused by hydrostatic stress, $\sigma_{avg} = (\sigma 1 + \sigma 2 + \sigma 3)/3$ and another part associated with distortion of the shape of the material element by the remaining portion of the principal stresses, corresponding to the deviatoric components of the stress tensor.

The determination of hydrostatic stress *via* diffraction has been applied to several material types such as ceramics; Bartolomé et al. (2008), Sattonnay et al. (2007), as well as irradiated polymers; Mallick et al. (2006). Also in some alloys, an analogous behavior is observed as per Rösler et al. (2007). The stainless steel X5CrNi18-10, which is austenitic (face-centred cubic) at room temperature, is only metastable. Thus, the ferritic phase is thermodynamically stable, but the transformation does not occur because the driving force is too small. Under mechanical load, for instance during forming, a martensitic transformation can take place in parts of the component. Due to this characteristic Parikin et al. (2011), Maimaitiyili et al. (2019) have also calculated the hydrostatic stress. As per Sattonnay et al. (2007) if the material is elastically isotropic, only two elastic constants, the Young modulus and the Poisson ratio, are required to describe the elastic behavior of the material in any state of stress. According to Bartolomé et al. (2008) in their study "neutron diffraction residual stress analysis of zirconia toughened alumina (ZTA) composites", they stated that when the composite is cooled from the sintering temperature, the reinforcement contracts more than the matrix. This resulted in tensile stress in the particles and compressive stress in the matrix. Since the particles were nearly spherical in form the mean field stress is generally hydrostatic. Bartolomé et al. (2008) highlighted the work of Wang et al. (1994), Alexander et al. (1995) where they studied the internal stresses and transformations of Al_2O_3/Ce-TZP as function of zirconia volume fraction. In their study they used a powder diffractometer and consequently measured the average strain and hence assumed the stress to be hydrostatic.

In this study to compare the strain measurements derived from the neutron data, synchrotron data was obtained from the pristine pellets, the strain values were determined and subsequently compared with the undamaged data from the neutron diffraction. Cross sections of the undamaged and damaged material were then prepared for EBSD in an attempt to understand how the damage may have affected the grains in the bulk as compared to the damage mechanisms outlined by Martina Scapin (2013) and Bertarelli (2014). TEM specimens of these affected grains were prepared *via* Focused Ion Beam (FIB) to determine if any of the common characteristics such as black spot damage could be detected.

MATERIALS AND METHODS

Synthesis

The $Nd_2Zr_2O_7$ pyrochlore samples were fabricated by a wet chemical synthesis approach. 0.1 molar aqueous solutions of $Nd(NO_3)_3$ and $ZrOCl_2$ were prepared, mixed and the hydroxides were co-precipitated in 25% liquid NH_4OH. A detailed description can be found elsewhere (Finkeldei et al., 2014). The dried and ground precipitate was calcined at 600°C for 2 h in air. The calcined powder was ground with a pestle and mortar and pellets were cold pressed with 40 kN in a 10 mm die for 7 s. Sintering of the pellets took place for 15 h at 1,600°C in air with a heating and cooling rate of 5.3°C/min. Since there were no similar starting materials available for titanium at the time the $Er_2Ti_2O_7$ pellets were fabricated *via* a solid-state reaction procedure. Therefore, Er_2O_3 and TiO_2 were mixed in the appropriate amounts for an equimolar ratio of Er and Ti. The powders were ground and mixed for 2 × 30 min at 550 rpm with a planetary ball mill in a ZrO_2 mixing bowl with ZrO_2 grinding media. A short-wet milling step in acetone was applied at 400 rpm for 3 min and the grinding media were separated from the milled powder *via* sieving. The same pressing procedure as for the $Nd_2Zr_2O_7$ pellets was applied. A first sintering took place in air for 15 h at 1,600°C with a second grinding step following the above-described procedure applied, and the dried powder repressed into pellets. A second sintering step at the same conditions as before was applied.

$(NdEr)_2(ZrTi)_2O_7$ pellets were synthesized from Er_2O_3, TiO_2, Nd_2O_3 and ZrO_2 starting powders. Equimolar amounts of Nd, Er, Zr and Ti were mixed in a mortar, homogenized and milled as described for the $Er_2Ti_2O_7$ pellet fabrication. A calcination step took place at 900°C for 2 h with a fast heating and cooling rate. After grinding the calcined powder was pressed into pellets and sintered as described above. Post sintering the pellets had stuck to the aluminum sintering plate on the bottom of the pellets. For each composition eight pellets were prepared that were approximately 4 mm in thickness.

Density Determination and Microstructural Characterization

The microstructure and chemical composition of the pellets were analyzed with a Quanta 200F from FEI and an EDS system from EDAX. The pellet microstructures were determined prior to the irradiation experiments.

The sintered density was determined geometrically for all fabricated pellets. For one pellet of each composition the density was also determined by the Archimedes method, for full data see supplementary information.

Sample Irradiation

Slices of approximately 150 microns were cut to provide enough material for the surfaces to be ground to be parallel from the topside of the pellets. Sequential polishing using 15, 3, and 1/10 μm diamond slurry on hard, nap-less polishing cloths was then performed to obtain samples of approximately 100–130 microns

in thickness whilst removing any damage produced due the cutting process. It was difficult to produce a set of samples that were consistently 100 microns in thickness due to the fragility of the samples. The samples were then irradiated with He^{2+} ions perpendicular to the surface, at multiple single energies (2, 3, 4, 5, and 6 MeV) at a fluence of 1×10^{16} ions/cm^2, in a vacuum of 10^{-5} Pa, on the ANSTO STAR tandem accelerator, at the Centre for Accelerator Science (CAS). Considering the uncertainty of penetration depth due to channeling, void production and other processes this is equivalent to a total depth of approximately 20–25 microns and is discussed in detail in the SRIM calculation section. The average He^{2+} particle current on the sample surface was around 500 nA, and it was continuously monitored by integrating the sample charge, and periodically monitored by Faraday cup measurements. The samples were mounted on a large heat sink (Al) as compared to the sample size, using thermal-conductive paste, and based on previous calibration experiments we concluded that the irradiation was carried out at approximately room temperature. From previous calibration runs, it was estimated that the temperature of the samples increased rapidly in the first minutes of irradiation and stabilized after that for the rest of the irradiation, well below 60°C for the entire length of the runs.

SRIM Simulations

Displacements per atom were calculated with SRIM/TRIM 2013 (Ziegler et al., 2010) by using the *Detailed Calculation with full Damage Cascades* mode for the $Er_2Ti_2O_7$ and $Nd_2Zr_2O_7$ pyrochlores. This mode of the Transport of Ions in Matter (TRIM) program calculates all collisional damage of the He^{2+} ions within the target material. The densities used in calculations were determined by the Archimedes method for a single pellet for each chemical composition and slices from multiple pellets were used for the He^{2+} irradiation experiment. The density variation for the remaining pellets, was determined by dividing the weight by the volume of the pellet ($V = \pi r^2 h$) and below 0.9%.

The displacement energy E_d values that were provided within the TRIM program for $Er_2Ti_2O_7$ and $Nd_2Zr_2O_7$ were 25 eV, for the A and B site cations, and 28 eV for the oxygen anions for both compositions. Many of these displacement energies are only assumptions and as experiments or simulations are performed the values are updated in the package. To further complicate matters the experimental stopping powers for heavy ions contain far more scatter than for light ions, hence there are larger errors for heavy ions, Be–U. This is the reason why it important to source more recent values and according to the literature (Sickafus et al., 2000b; Li et al., 2015) it is highly unlikely that the E_d value for oxygen is larger than for the cations within a pyrochlore. Therefore, these values were replaced with E_d values resulting from molecular dynamic (MD) simulations by Dong et al. (2017) for the $Er_2Ti_2O_7$. Dong et al. report average E_d values for each sublattice in an $Er_2Ti_2O_7$ sample to be 85 eV for Er^{3+}, 197 eV for Ti^{4+}, and 75 eV for O^{2-}. For $Nd_2Zr_2O_7$ the TRIM auto-populate E_d values were replaced with average values for the three crystallographic directions [100], [110], and [111] from Xiao et al. (2015) which resulted in E_d energies of 28.5 eV for Nd^{3+}, 32.2 eV for Zr^{4+}, and 11.6 eV for O^{2-}. These threshold displacement energies were determined *via ab initio* MD by Xiao et al. (2015). The higher E_d values for the titanate pyrochlore compared to the zirconate pyrochlore can be explained by their calculation *via* MD simulation, whereas the E_d values for the zirconate pyrochlore were calculated *via* ab-initio MD simulations.

One example of inconstancies in modeling radiation damage *via* SRIM is the study of Wittmaack et al. entitled "Reliability of a popular simulation code for predicting sputtering yields of solids and ranges of low-energy ions" (Wittmaack, 2004) where low energy is considered to be anything below an accelerating voltage of 5 keV. They report that there were several discrepancies between modeling *via* SRIM and experimental data and that the low-energy electronic stopping powers of SRIM-2003 were found to be much too low. They also reported that there were variations between SRIM-2000 and SRIM-2003 due to the changes in the software to address some of these issues, thus the latest version of the software should always be used. However, with each iteration, comparisons still need to be performed to determine the reliability of the software to predict both dpa and damage depth.

Other publications have investigated the discrepancy between modeling and damage depth (Simeone et al., 2015) with the majority finding that damage occurred deeper into the sample than predicted by SRIM, again being attributed to issues with electronic stopping.

Considering all the assumptions and issues the reader should bear in mind that these simulations then are only used as a guide with regards to dpa and penetration depth and the variation and reliability of SRIM have long been discussed in the literature, however as it is freely available and used widely in the community it has become the standard.

Synchrotron and Neutron Diffraction Data Collection

Synchrotron X-ray powder diffraction (SXRD) was performed at room temperature on the powder diffractometer at beamline BL-10 of the Australian Synchrotron (Wallwork et al., 2007). Data were collected over the angular range $4 < 2\theta < 84.5°$, using X-rays of wavelength 0.72797 Å, as determined by structural refinement of NIST SRM660b LaB_6 standard diluted with diamond powder. Samples (~0.1 mg) were housed in a 0.3-mm-diameter glass capillary, which were then rotated during the measurements. Data was obtained using a bank of 16 Mythen detectors, each of which covers 5° and collected for 3 min at each of the two detector positions, to avoid gaps in the data from the individual modules.

Neutron powder diffraction (NPD) experiments were performed at the high-resolution powder diffractometer Echidna (Avdeev and Hester, 2018) at ANSTO's Australian Centre for Neutron Scattering (ACNS) facility at Lucas Heights on both the irradiated and unirradiated samples of $Er_2Ti_2O_7$ and $Nd_2Zr_2O_7$ under the same conditions as a previous examination of LaB_6 standard that had been manufactured with enriched ^{11}B. Diffraction patterns were acquired at room temperature over an angular range of

$14.876^{\circ} < 2\theta < 162.00^{\circ}$, at intervals of 0.125°, using neutrons of wavelength 1.622 Å, Supplementary Figure S1. The $Er_2Ti_2O_7$ sample broke apart due to exposure to the He^{2+} ion beam and had to be held together wrapped in Al foil to ensure the geometry was as close as possible to the undamaged sample.

The SXRD and NPD data were analysed by the Rietveld method using the TOPAS refinement program (Coelho, 2018). The instrumental function was determined with the strain/stress-free NIST LaB_6 standard reference material SRM660b (Black et al., 2020). Once the pseudo-Voigt functions were determined they were used for all subsequent data analysis to ensure that all effects on the spectra were due to the sample.

EBSD Method

The Pyrochlore samples were prepared for EBSD analysis by mounting them in cross section to allow examination of the damaged through to the undamaged region. Sequential polishing using 15, 3 and 1 μm diamond slurry on hard, nap-less polishing cloths, was followed by a final polish using colloidal silica on a neoprene type polishing cloth. Both polished sample surfaces were then coated with approximately 1.5 nm of platinum *via* an ion sputter coater to prevent charging. The samples were then mapped using a Zeiss Ultra Plus SEM coupled with an Oxford Instruments HKL Nordlys EBSD detector system at an accelerating voltage of 20 kV. The EBSD maps were generated using the HKL Channel 5 software. The entire thickness of the samples was mapped with a step size of 0.106 and 0.129 μm for the Zr and Ti samples respectively and determined. A further map of the Zr sample was then performed on select grains of interest at higher magnification to locate an area for TEM sample preparation using the FIB.

FIB Method

The instrument used for the TEM sample preparation was a Zeiss Auriga 60 focused ion beam microscope. A 20 × 2 μm rectangular layer of protective platinum was first deposited above the area of the desired cross section to protect the surface from the ion beam.

To ensure that neither damage was introduced or recovered/reduced the following method was used to prepare the TEM specimens. Coarse milling of a trapezoidal shaped trench was performed on both sides of this platinum layer using Ga^+ ions for milling, the trench was first milled at 30 kV 8 nA and then a rectangular shaped cut was done 1.5 degrees off axis using 30 kV 2 nA to form the final lamella shape with parallel sides before lifting out. A "u" cut was then made at a shallow tilt angle in order to free the bottom and sides of the lamella. The lamella was then lifted out *in situ* using the OmniProbe 200 nanomanipulator system and attached onto a TEM copper grid *via* platinum deposition for further thinning and polishing inside the FIB. The polishing process involved positioning the lamella 0.5 degrees off the axis of the ion beam on each side starting with a 30 kV 600 nA ion probe, followed by a 30 kV 120 pA ion probe. The off-axis position accounts for the ion beam shape to keep the sides of the lamella parallel whilst polishing.

Further thinning was then carried out with a 15 kV 80 pA ion probe at 3 degrees off axis to remove the damage created by the 30 kV gallium ions. A final polishing step was applied with a 5 kV 20 pA ion probe at 3° then a long polish in deposition mode at 2 kV 20 pA at six degrees off milling access to remove any further damage created by the higher energy gallium ions in the previous steps. For comparison Engelmann et al. (2003) studied single crystalline Si, which is very sensitive to sputter amorphization. In their paper they state the following "The thickness of the amorphization layer could not be reduced significantly by decreasing the Ga^+ ion energy down to 10 keV, reducing the probe current to the lowest possible value of 1 pA or varying the sputter angle. A reduction of the amorphization depth down to 7 nm was only possible with a 5 keV Ga^+ ion beam (the lowest ion energy attainable in the used FIB tool) and tilting the lamella to ±7°, subsequent ion milling of the FIB-cut TEM lamella with 3.5 keV Ar^+ ions at a tilt angle of 15° resulted in a near-surface amorphization depth of 5–6 nm. This value is close to the near-surface amorphization of 4 nm that was measured on a classically prepared TEM sample with final 3.5 keV Ar^+ ion milling. Using 1.5 keV Ar^+ ions and tilting the sample by ± 20° the near-surface amorphization is between 2 and 3 nm Further to this point in their study of Si etched *via* Ga ions Mayer et al. (2007) found the following "Reduction of the amorphous layer thickness in a sidewall of Si as a function of Ga energy. The cross sections of FIB lamellae show that FIB milling at 88° incident angle and 30, 5, and 2 ion energy results in amorphous layers of ~22, 2.5, and 0.5–1.5 nm thickness, respectively", "The reduction of sidewall damage in Si at 2 keV polishing can produce TEM specimens which reveal sub-Ångström information", "The advantage to using the FIB itself is that the beam may be focused, and hence the specimen can be imaged for exact placement of the final polishing window. Similar low energy FIB techniques have been used to prepare specimens for atom probe analysis, where results show that no deleterious ion mixing occurs". To ensure that the damage layer was either small or not visible on either the edge or covering the whole lamella, high resolution EBSD was performed on the $Nd_2Zr_2O_7$ sample, **Supplementary Figure S2**. The image clearly shows essentially crystalline material and an absence of an amorphous layer or a recrystallized layer covering the lamella of a single orientation. In addition there was the absence of an oriented alteration layer as shown can occur by Mayer et al. (2007). We therefore have assumed that any damage observed in the TEM is due to irradiation by the He^{2+} ions and not due to sample preparation.

The atomic structure of the irradiated samples was studied using transmission electron microscopy (TEM) on the FIB lamellae. TEM was performed on a JEOL 2200FS microscope, operated at an accelerating voltage of 200 keV. The TEM was equipped with a Gatan UltraScan1000, and Orius camera. Atomic lattice images and diffraction patterns were collected in bright field, imaging in dark field mode did not yield further details about the samples such as the evidence of bend contours.

RESULTS

Microstructural Characterization

The SEM images **Supplementary Figure S3** reveal the microstructure of the $Nd_2Zr_2O_7$, $Er_2Ti_2O_7$ and

$(NdEr)_2(ZrTi)_2O_7$ sintered pellets prior to irradiation. The $Nd_2Zr_2O_7$ sample shows a heterogeneous surface with high and low density areas. The $Er_2Ti_2O_7$ sample showed a dense microstructure with a homogeneous porosity. The $(NdEr)_2(ZrTi)_2O_7$ revealed the presence of a second phase that was identified *via* EDS to consist mainly of aluminum and neodymium and most likely evolved during sintering *via* contamination of the pellet with the sintering crucible. Therefore, the solid solution sample was not utilized in the irradiation experiments as the presence of a second phase may have had unforeseen effects on the strain and stress in the sample after irradiation.

Irradiation Calculations

Supplementary Figure S4 in the supplementary information shows the TRIM calculations for the overall dpa/depth values for the $Nd_2Zr_2O_7$ and $Er_2Ti_2O_7$ samples respectively. The dpa plots refer to the summation of the subsequent He^{2+} irradiations with 2, 3, 4, 5, and 6 MeV with a fluence of 1×10^{16} ions/cm^2.

Synchrotron XRD

The instrument was characterized with a standard composed of diamond and LaB_6 (SRM 660b—Line Position and Line Shape Standard for Powder Diffraction) to provide instrumental parameters for Rietveld refinement, the background was estimated using a 16-term shifted Chebyschev function. The reasoning behind the use of LaB_6 is that the material is produced to be strain free and so once instrumental parameters have been set any subsequent change in these parameters is due to the sample and not a variation of the instrument. Diamond has been added to the LaB_6 to dilute the sample and thus reduce the issue of absorption from the Lanthanum in the sample which in this geometry may result in variation of intensity or position of the diffracted peaks. Scale factor, detector zero-point, lattice parameters, atomic coordinates and atomic displacement parameters were refined together with the peak profile parameters. Reasonable fits were obtained with the following values of R_{wp} 4.64%, R_p 3.32%, GOF 2.73. The peaks were fitted with pseudo-Voigt (PV_TCHZ) peak type (Thompson et al., 1987) with the following parameters, U = 0.000189(9), V = −0.000201(12), W = 0.000031(5), Z = 0, X = 0.0002(14), Y = 0 these were then used for the refinements of the $Er_2Ti_2O_7$, $Nd_2Zr_2O_7$ and $(ErNd)_2(TiZr)_2O_7$ samples. Parameters of note were as follows; LaB_6 a = 4.1533842(19) Å, and ε = 0.000076(2), wt% = 7.817(18); Diamond a = 3.5642611(17) Å, ε = 0.0000980(8), wt% = 92.183(18) %. For comparison the quoted lattice parameter is a = 4.156826 (8) Å in the NIST certificate a difference of 0.0034418 Å. These measurements confirmed the applied analysis since the NIST LaB_6 standard is manufactured to have no strain. Results of the refinements are given in **Table 1**. Note all values are quoted in accordance with the IUCR recommendations for statistical descriptors in crystallography.

Parameters for $Er_2Ti_2O_7$, $Nd_2Zr_2O_7$ are consistent with those found in the literature (Farmer et al., 2014; Xu et al., 2015) and both refinements yielded strain results that are of the same order of magnitude as that of the LaB_6 sample, therefore it can be assumed that the initial strain for both of these samples is zero.

TABLE 1 | Refined parameters for samples $Er_2Ti_2O_7$, $Nd_2Zr_2O_7$ and $(ErNd)_2(TiZr)_2O_7$ from S-XRD data. Where *a* is the lattice parameter, *x* (O) is the value of the *48f* site, B*A* is the overall isotropic displacement parameter of the *A* cation, B*B* is the overall isotropic displacement parameter of the *B* cation, B (O1) is the overall isotropic displacement parameter of the oxygen at the O1 position, B(O2) is the overall isotropic displacement parameter of the oxygen at the O2 position, *A*-O(1) is the distance between the A cation and the oxygen at the O1 position, *A*-O(2) is the distance between the A cation and the oxygen at the O2 position, *B*-O(1) is the distance between the B cation and the oxygen at the O1 position, ε0 is the calculated strain, R_p is the R-pattern (background corrected), R_{wp} is the R-weighted pattern (background corrected), and GOF is the goodness of fit.

Sample	$Er_2Ti_2O_7$	$Nd_2Zr_2O_7$	$(ErNd)_2(TiZr)_2O_7$
a, Å	10.07834(5)	10.68052(2)	10.325528(11)
x (O)	0.3316(2)	0.3339 (19)	0.3274(2)
B *A*, Å^2	0.469(3)	0.599(3)	Nd + 3 0.11(4) Er + 3 0.89(4)
B *B*, Å^2	0.255(8)	0.456(5)	Zr + 4 0.730(13) Ti + 4 0.270(13)
B (O1), Å^2	0.71(5)	1.15(4)	0.45(9)
B(O2), Å^2	0.66(8)	0.81(7)	0.10(12)
A-O(1), Å	2.18201	2.3124	2.23554
A-O(2), Å	2.4609(14)	2.5905(11)	2.5509(18)
B-O(1), Å	1.9620(9)	2.0901(7)	1.9927(11)
ε0	0.000094(5)	0.0000938(10)	0.000232(3)
R_p, %	2.87	3.46	2.57
R_{wp}, %	4.3	4.76	4.57
GOF	1.95	2.54	2.95

Refinement of the A and B site occupancy of the $(ErNd)_2(TiZr)_2O_7$ solid solution sample indicates that the majority cation on the A site is Er and the majority on the B site is Zr with a stoichiometry of $(Er_{0.89}Nd_{0.11})_2(Zr_{0.73}Ti_{0.27})_2O_7$. The diffraction pattern showed evidence of a second phase as shown in **Figure 1**, after matching of the six peaks present and based on the composition a compatible cif file was identified and it is most likely a cubic phase of space group $Pm\bar{3}m$ with a lattice parameter of 3.75670(3) Å. This cif file was used in the subsequent refinement and semiquantitative analysis. A structural analysis of the second phase was attempted but due to the scarcity of peaks and their low intensity a suitable refinement could not be obtained.

Semi-quantitative analysis resulted in values of 94.93(3)% for $(Er_{0.89}Nd_{0.11})_2(Zr_{0.73}Ti_{0.27})_2O_7$ and 5.07(3)% for the unknown cubic phase. The $(Er_{0.89}Nd_{0.11})_2(Zr_{0.73}Ti_{0.27})_2O_7$ lattice parameter lay between the $Er_2Ti_2O_7$ and $Nd_2Zr_2O_7$ samples at a value of 10.325528(11) Å. Moreover, contrary to the pure endmembers the solid solution sample contained strain at a value of 0.000232(3). Given the sample did contain inherent strain it would have been valuable to see the effect of radiation damage, however due to the presence of a second phase which may affect the results this sample was not included in the irradiation experiments.

Neutron Diffraction

Defect fluorite as defined by Heremans et al. (1995) in their neutron diffraction study of $Y_2(Zr_yTi_{1-y})_2O_7$ and often cited for example by Ewing et al. (2004), is described as follows, "Pyrochlore is an unusual oxide in that the order–disorder

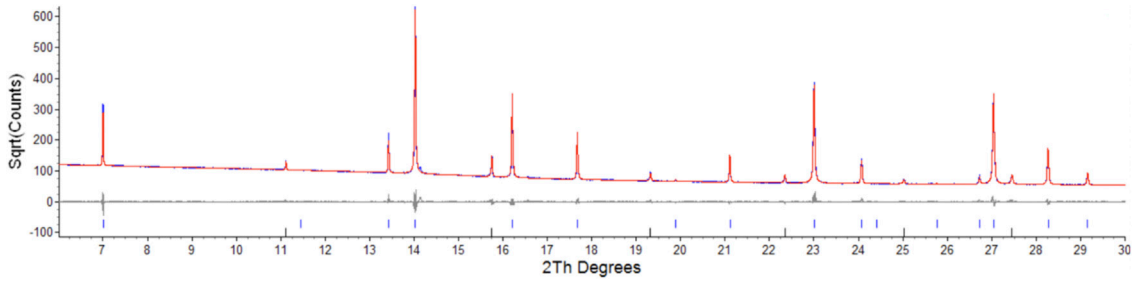

FIGURE 1 | Low angle section of rietveld plot for the $(ErNd)_2(TiZr)_2O_7$ sample, the red line is data, blue is calculated, grey is the difference plot, blue markers are the main phase and black markers are the unknown phase. Y axis is square root of counts to highlight the second phase, barely visible in a plot of counts vs. angle.

transformation occurs simultaneously on both the cation, as well as the anion lattice among three anion sites: 48f, 8a, and 8b. However, the cation and anion disordering may occur to different degrees and at different temperatures." As stated by Ewing et al. (2004), Heremans et al. (1995) investigated the chemically induced order–disorder transition in the $Y_2(Zr_yTi_{1-y})_2O_7$ system by analyzing the fractional occupancy of the interstitial 8a site and the effective scattering length for the A- and B-site cations, a measure of the extent of cation antisite disorder. With the increasing concentrations of Zr at the B-site, the structure of the $Y_2(Zr_yTi_{1-y})_2O_7$ solid solution progressively changes to a defect-fluorite structure at y = 0.9. The anion disorder precedes the disordering of the cation lattice. The interstitial 8a site was filled immediately with the oxygen ions displaced from the nearest-neighbor anion site, the 48f oxygen, upon the addition of the larger Zr-cation. The occupancy of the interstitial 8a site increases linearly with Zr-content over the entire range of the solid solution. The onset of cation disorder occurred at $y > 0.45$ and was coupled with disordering of anions at the 8b site. Complete mixing of all three cation species occurs abruptly in the compositional range of $0.6 < y \leq 0.9$. The positional parameter for 48f oxygen has been found to increase sharply to 0.375 for the ideal fluorite structure due to the occupancy of oxygen at the interstitial 8a site and the decreasing average ionic radius difference at the A- and B-sites as the extent of cation mixing increases. In greater detail Heremans et al. (1995) report that for y = 0.3, 0.45, 0.6 and 0.9, the value of x for O(1) placed at 48f progressively reduced in the following sequence, 0.4173(2), 0.4110(2), 0.4022(3) and finally 0.375 with a corresponding increase in lattice parameter for y = 0.3, 0.45, 0.6 with a(Å) increasing from 10.1906(2), 10.2447(2) to 10.2890(5). We therefore have a set of common parameters to define if the irradiated pyrochlores are transforming to defect fluorite *via* examination of the O(1) position and a lattice parameter change, all of which can be provided by neutron diffraction.

The methodology used for the neutron diffraction data reduction was the same as that used for the synchrotron data to enable calculation of strain in the damaged samples.

The fit obtained for the LaB_6 (SRM 660b—Line Position and Line Shape Standard for Powder Diffraction) had the following values of R_{wp} 9.22, R_p 6.98, GOF 1.41. The peaks were fitted with a pseudo-Voigt (PV_TCHZ) peak type of the following parameters, U = −0.03(8), V = −0.06(3), W = 0.24(3), Z = 0, X = 0, Y = 0 these were then used for the refinements of the $Er_2Ti_2O_7$, $Nd_2Zr_2O_7$ samples. The lattice parameter was a = 4.15644(7) Å as compared to 4.156826 (8) Å as quoted in the NIST certificate (a difference of 0.000379 Å) and the strain was effectively zero with a value of ε = 0.000(9). Results of the refinements are given in **Table 2**. Since there is a direct correlation between the occupancy of the sites and the overall isotropic displacement parameter the occupancy was not refined and set at a value of 1. If the occupancy was refined, a slight variation in this value may have resulted in an apparent variation in the overall isotropic displacement parameter and so give an indication of disorder, when there was none. The plot of the refined $Nd_2Zr_2O_7$ sample demonstrating the quality of fit for the undamaged neutron data is given in supplementary **Supplementary Figure S5**.

Considering the conditions listed above to classify a pyrochlore transformation to a defect fluorite we can see from **Table 2** the values for the $Er_2Ti_2O_7$ sample do not vary greatly between the unirradiated and irradiated sample with regards to lattice parameter and the value of x at the 48f site. The $Nd_2Zr_2O_7$ sample showed significant changes post irradiation with the neutron diffraction pattern showing evidence of two phases being present in the ratio of 57(4) % for phase 1 (p1) and 43(4) % for phase two (p2) when refined as two separate pyrochlore phases. The diffraction pattern showing two phases, difference plot and inset of the high angle peaks is given in **Figure 2**. The values are higher than expected for the irradiated volume and we will discuss this further on.

Attempts were made to refine one phase as a defect fluorite as outlined by Heremans et al. (1995). This resulted in values of Rwp: 3.86, Rp: 3.04, for the pyrochlore phase and Rwp: 27.54, Rp: 38.37 for the defect fluorite phase, this was primarily due to the absences of peaks in model that result from scattering of the anions as outlined by Heremans et al. where for hkl $h \neq 4n$, $k \neq 4n$, and $l \neq 4n$, $h + k + l = 4n$ (Heremans et al., 1995) as shown in **Figure 3**. Attempts to refine the second phase with the reported defect fluorite structure for $Nd_2Zr_2O_7$ with a lattice parameter of 5.1485Å and space group $Fm\bar{3}m$ (Loong et al., 1995) resulted in very high R factors (Rwp: 31.47, Rp: 40.86) and no further attempts were made with regards to this strategy.

Table 2 shows that both phases differ from the unirradiated sample, in that they have different overall isotropic displacement parameters in comparison to the unirradiated sample. Of interest is the fact that one of the phases has varied from the original

TABLE 2 | Refined parameters for neutron data. Where *a* is the lattice parameter, *x* (O) is the value of the *48f* site, B*A* is the overall isotropic displacement parameter of the *A* cation, B*B* is the overall isotropic displacement parameter of the *B* cation, B (O1) is the overall isotropic displacement parameter of the oxygen at the O1 position, B(O2) is the overall isotropic displacement parameter of the oxygen at the O2 position, *A*-O(1) is the distance between the A cation and the oxygen at the O1 position, *A*-O(2) is the distance between the A cation and the oxygen at the O2 position, *B*-O(1) is the distance between the B cation and the oxygen at the O1 position, ε0 is the calculated strain, R_p is the R-pattern (background corrected), R_{wp} is the R-weighted pattern (background corrected), and GOF is the goodness of fit. For the zirconate sample two pyrochlore phases were identified as consequence of irradiation which are both provided here.

Sample	$Er_2Ti_2O_7$	$Er_2Ti_2O_7$ (ir)	$Nd_2Zr_2O_7$	$Nd_2Zr_2O_7$ p1	$Nd_2Zr_2O_7$ p2
a, Å	10.0878(18)	10.0906 (23)	10.6471 (18)	10.6780(3)	10.6443(4)
x (O)	0.4205(3)	0.4216(4)	0.3374(3)	0.3323(8)	0.3408(10)
B *A*, $Å^2$	1.14(10)	0.96(17)	0.63(8)	1.0(3)	0.5(3)
B *B*, $Å^2$	1.42(15)	1.6(2)	0.90(8)	1.3(3)	0.9(4)
B (O1), $Å^2$	1.03(9)	0.80(15)	1.37(8)	1.8(3)	1.1(3)
B(O2), $Å^2$	0.43(12)	0.30(19)	0.67(16)	0.1(3)	2.4(8)
A-O(1), Å	2.1841	2.1847	2.3052	2.3118	2.3046
A-O(2), Å	2.4777(18)	2.485(2)	2.557(2)	2.597(5)	2.531(6)
B-O(1), Å	1.9553(11)	1.9519(15)	2.0997(14)	2.085(3)	2.116(5)
R_p, %	2.98	2.97	2.54	2.81	2.81
R_{wp}, %	3.75	4.1	3.25	3.53	3.53
GOF	0.8	1.7	1.27	0.79	0.79

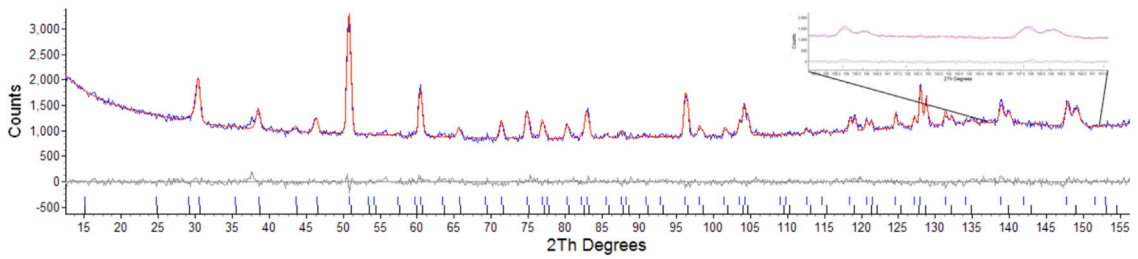

FIGURE 2 | Rietveld refinement of radiation damaged $Nd_2Zr_2O_7$ showing difference plot and assignment of both phases, insert highlights the two sets of peaks corresponding to the two pyrochlore phases.

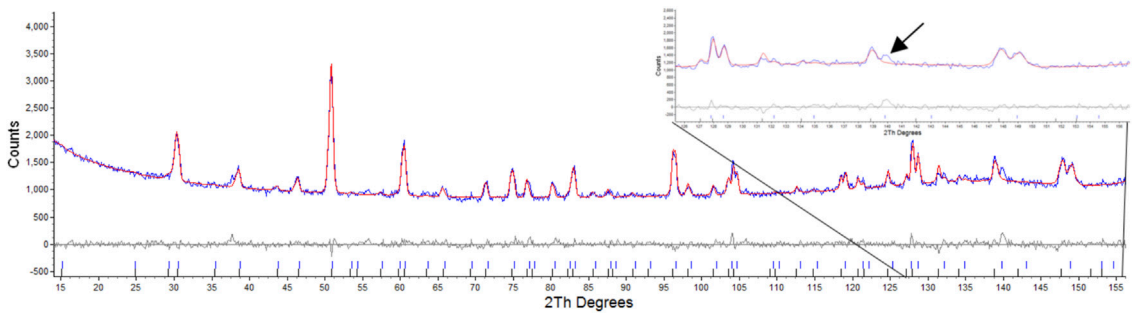

FIGURE 3 | Rietveld refinement of radiation damaged $Nd_2Zr_2O_7$ showing difference plot and assignment of defect fluorite and pyrochlore, insert highlights the absence of the equivalent reflections for the (10 6 4) and (12 2 2) that result only due to scattering from Oxygens as per Heremans et al.

lattice parameters by only 0.03% whereas the other varies by 0.3%, a difference of one order of magnitude in variation and like that reported by Heremans et al. however, both phases were refined to be pyrochlore. This is contrary to most reports in relation to irradiation of this phase that report the disappearance of the pyrochlore superstructure peaks indicating the transition to a defect fluorite, though most of these studies have been performed with X-ray diffraction which is less sensitive to Oxygen positions. To determine if the irradiation had resulted in positional disorder of either the cations, anions or both as outlined by Heremans et al. the refinements were repeated (**Table 3**) to determine the anisotropic displacement parameters for indications of initial movement of either cations or anions towards a fluorite like phase.

TABLE 3 | Refined parameters where *A* U (1,1) and *A* U (1,2) are the anisotropic displacement parameters of the *A* cation, *B* U (1,1) and *B* U (1,2) are the anisotropic displacement parameters of the *B* cation, O1 U (1,1) and O1 U (1,2) are the anisotropic displacement parameters of the oxygen at the O1 position, O2 U (1,1) is the anisotropic displacement parameter of the oxygen at the O2 position, *A*-BVS is the bond valence sum of the A cation, *B*-BVS is the bond valence sum of the B cation, ε0 is the calculated strain, R_p is the R-pattern (background corrected), R_{wp} is the R-weighted pattern (background corrected), and GOF is the goodness of fit for the unirradiated and irradiated $Er_2Ti_2O_7$ and $Nd_2Zr_2O_7$ samples.

Sample	$Er_2Ti_2O_7$	$Er_2Ti_2O_7$ (ir)	$Nd_2Zr_2O_7$	$Nd_2Zr_2O_7$ p1	$Nd_2Zr_2O_7$ p2
A U (1,1), Å^2	0.0157(13)	0.0158(15)	0.0083(11)	0.015(3)	0.002(4)
A U (1,2), Å^2	−0.0041(12)	−0.0040(13)	0.0011(11)	0.002(2)	0.010(4)
B U (1,1), Å^2	0.018(2)	0.020(2)	0.0126(11)	0.019(4)	0.013(5)
B U (1,2), Å^2	−0.006(3)	−0.006(3)	0.0077(17)	0.010(4)	−0.001(5)
O1 U (1,1), Å^2	0.0123(11)	0.0125(12)	0.0214(13)	0.028(4)	0.017(4)
O1 U (1,2), Å^2	0, 0, 0.0038(17)	0, 0, −0.0019(19)	0, 0, −0.0003(15)	0, 0, 0.009(4)	0, 0, −0.011(4)
O2 U (1,1), Å^2	0.0075(19)	0.006(2)	0.001(2)	0.001(4)	0.021(10)
A-BVS	2.957(16)	2.950(16)	3.010(16)	2.821(38)	3.087(47)
B-BVS	4.087(13)	4.087(14)	3.893(17)	4.022(33)	3.800(41)
ε0	0.00(8)	0.000(3)	0.00(8)	0.0(3)	0.000(5)
R_p, %	2.98	2.97	2.54	2.81	2.81
R_{wp}, %	3.75	4.1	3.25	3.53	3.53
GOF	0.8	1.7	1.27	0.79	0.79

As before there is little difference between the irradiated and unirradiated $Er_2Ti_2O_7$ sample with BVS values indicating that there is insignificant displacement of the cations or anions from their original ideal positions. It is highly likely that the irradiated region in the material has become amorphous and a comparison of diffraction patterns before and after irradiation on similar amounts of material shows evidence of an increase in background which can most likely be attributed to the scattering from the amorphous material. To determine the amorphous content, the neutron diffraction data from the irradiated sample was used to replace the data in the fit of the unirradiated sample and the background was not refined. A peaks phase was then inserted with several fundamental parameter peaks throughout the pattern and this phase refined to account for the additional incoherent scattering in the pattern. By inserting a peak phase, the chemical composition remained the same resulting in the same neutron scattering factors. The amount of amorphous material was then simply a percentage comparison of areas which were 17479 for the crystalline compared to 41488 for the amorphous, equivalent to approximately a 30% crystalline volume. If we consider the SRIM calculations indicated a minimum penetration of 20 microns into a 100–130 micron thick sample equating to 20–15% which is approximately an error of 1/3 and the potential errors in the penetration depth listed above they do not account for the variability. As stated previously the $Er_2Ti_2O_7$ sample broke apart due to exposure to the He^{2+} ion beam and had to be held together wrapped in Al foil to ensure the geometry was as close as possible to the undamaged sample. However, if this was not the case and the sample was not in the center of the diffractometer due to this arrangement it is possible that this contributed to incoherent scattering, which was not accounted for in the method, i.e. the increase in background was attributed to amorphous material and not the incoherent scatter and so giving rise to a larger than expected value for amorphous content. Conversely, since thin Al foil was bent and wrapped around the sample the assumption was that it may exhibit strain which could be evaluated. Not only could the Al structure be refined but calculating strain by the same peak shape analysis method resulted in a value of 0.0004(14). This supports the applied methodology given a value of strain could not be determined for the ceramic component of the diffraction pattern due to a change in peak shape. Comparison of refined data for the $Nd_2Zr_2O_7$ sample indicates that both phases 1 and 2 are different to the unirradiated sample. Variations can be seen in the displacement parameters for both the cations and the anions as compared to the undamaged sample. The calculated BVS indicated that there is over bonding and under bonding in each of the phases compared to the unirradiated specimen, however this is minimal. If A and B site mixing were occurring in phase 1 the BVS sums would not match so closely to the original sample, as compared to the work of Simeone et al. (2017) where they demonstrated an equivalent BVS of approximately 4.2 for La^{3+} and 3 for Zr ^{4}+ for defect fluorite. If we consider that Heremans et al. reported approximately a 0.5% change in lattice parameter and given the irradiated phase exhibited a change of 0.3% one might expect a corresponding change in the x value of the 48f position in the oxygen. For this change in lattice parameter Heremans et al. reported a corresponding reduction of 1.5% in the value for 48f towards 0.375, our study also observed a 1.5% reduction from a value of 0.3374(3), thus moving the oxygen further from the ideal value of 0.375 not towards it. It is difficult to directly compare displacement parameters to the study of Heremans et al. because they have chosen to refine both the occupancy of the site with the overall isotropic displacement parameters whereas we have fixed ours at occupancy 1. There is an increase in disorder of the A and B cation and to highlight the possible difference in phases for the irradiated zirconate sample **Supplementary Figure S6** shows the difference in the ellipsoids due to the anisotropic displacement parameters. Compared to the unirradiated sample, phase 1 shows evidence of the Nd and Zr cations

increasing in disorder parallel with the 111 plane while the O1 oxygens have moved slightly in a direction perpendicular to the 111 plane. In comparison phase 2 indicates a reduction in disorder of the cations while the O1 anions are now being stretched out parallel with the 111 plane. It was anticipated that analysis of the neutron diffraction data would indicate a migration of cations and anions towards an equivalent fluorite structure as reported but a comparison from previous indicates that this is not the case if we remember the statement "The anion disorder precedes the disordering of the cation lattice. The interstitial 8a site was filled immediately with the oxygen ions displaced from the nearest-neighbor anion site, the 48f oxygen, upon the addition of the larger Zr-cation". In the same paragraph Ewing et al. (2004), made the contradictory statement "Pyrochlore is an unusual oxide in that the order–disorder transformation occurs simultaneously on both the cation, as well as the anion lattice among three anion sites: 48f, 8a, and 8b. However, the cation and anion disordering may occur to different degrees and at different temperatures." This can be interpreted as a contradiction given the statements; the anion disorder first occurs, that cation disorder can occur simultaneously and that it can occur to different degrees at different temperatures. The standard definition often seen in the literature for the presence of defect fluorite is the loss of superlattice reflections in a powder diffraction pattern; in our analysis thus far, we have shown that the superlattice reflections are maintained, the oxygen at position (O1) does not move towards a value of 0.375 and that there is very little if any evidence of A and B site mixing due to bond valence sum calculations and yet there is a significant lattice parameter shift. Please note we have provided the raw neutron diffraction data as excel files in the supplementary information for the reader to examine.

Given that the Rietveld analysis did not indicate the presence of strain in either of the two pyrochlore phases that evolved from the irradiation of the zirconate sample and yet phase 1 accounted for approximately 50% of the coherent scattering pattern (much larger than that predicted by SRIM) as determined by quantitative phase analysis, one possible explanation for the appearance of the second phase is that a significant portion of the sample is in a stressed state. One could argue that the second phase is due to internal gas pressure however if we consider the work of Agarwal (2015) who demonstrated that He^{2+} is essentially insoluble in pyrochlore it is unlikely that we can attribute the total effect due to He^{2+}. Drawing upon the work of Martina Scapin (2013), Bertarelli (2014), Oden (1992) who studied residual stress in ceramics where they demonstrated that for the case of Cu irradiation of Al_2O_3 as the penetration depth increases the surface effect will have a limited influence and a hydrostatic stress state is expected, we will assume the second phase to be a region of hydrostatic stress where all three strains are equal. If we consider that the $Er_2Ti_2O_7$ broke apart due to expose to the He^{2+} it is highly likely that are large degree of swelling has occurred withing the interaction region and it has failed due to hydrostatic stress. To investigate further the role hydrostatic stress could play, we have assumed the amount of stress in the damaged sample where the average lattice strain in any given direction [*hkl*] can be defined by:

$$\varepsilon_{hkl} = \frac{d - d_0}{d_0}$$

Where d is the stressed lattice spacing and d_0 is the stress-free lattice spacing along the respective [*hkl*]. Given that no peak broadening could be determined which would be indicative of strain, it is possible that the values were too small, a condition commonly associated with hydrostatic or volumetric stress. Examination of the differences in d-spacing between the non-irradiated and irradiated samples showed a uniform change, that is the value of d-d_0 was consistent for each reflection as can been seen in the spreadsheets provided in the supplementary information. If this value did vary it could be an indicator that stacking faults were present. For example, in a cubic system where say the value of d-d_0 for the 220 reflection ($h \pm k \pm l \neq 3n$) as compared to say the 111 and 222 reflections is different this can indicate the presence of a stacking fault and reveal its orientation (Dupraz et al., 2015). As per Bartolomé et al. (2008) where they found that the average strains in zirconia toughened alumina were essentially equal leading them to conclude that the stress was hydrostatic and that the stress normal to the surface may be approaching zero due to the apparent depth as per Debelle and Declémy (2010) and Oden (1992). The deviatoric stress and strain based on Hooke's Law can be represented as follows per (Noyan and Cohen, 1987), where ϵ_{ij} is the strain tensor, E is Young's modulus, ν is Poisson's ratio, σ_{ij} is the stress tensor, δ_{ij} is the Kronecker delta, and σ_{kk} is the average stress:

$$\epsilon_{ij} = \frac{1}{E}\left[(1+\upsilon)\sigma_{ij} - \upsilon\delta_{ij}\sigma_{kk}\right]$$

If we multiply both sides of the above equation by δ_{ij} the net result is:

$$\epsilon_{kk} = \frac{(1-2\upsilon)}{E}\sigma_{kk}$$

where ϵ_{kk} is the hydrostatic strain. The hydrostatic strain is simply the average of the three normal strains of any strain tensor. It should also be noted that one confusing aspect of hydrostatic strain is that it can be nonzero in incompressible materials such as ceramics. It is the determinant of the deformation gradient that is the true measure of volume change, and hydrostatic strain is only a convenient approximation of that when the strains are small. This is the case for our example where the observed strain for the (111) is approximately 0.00289; where the definition of small strain refers to the situation where we assume that changes after a displacement are so small that the total geometry is virtually unchanged.

If we now consider the above equation as follows, where the hydrostatic strains are now represented as $\bar{\varepsilon}$ (the average strain) and the hydrostatic stress σ:

$$\sigma = \frac{E}{1-2\nu}\bar{\varepsilon}$$

The above equation allows us to determine the value and nature of the hydrostatic stress for the two phases seen in the radiation damaged pyrochlore by the use of the published parameters for Young's modulus and Poisson's ratio by Feng et al. (2011) which are 219 GPa and 0.222 respectively, yielding values of 1.141 MPa for phase 1 and -0.105 MPa for phase 2. These values indicate that phase 1 is under tensile stress and that phase 2 is under a very small amount of compressive stress.

To examine this concept further recounting as per Sattonnay et al. (2007) if the material is elastically isotropic, only two elastic constants, the Young modulus and the Poisson ratio, are required to describe the elastic behavior of the material in any state of stress. We can take advantage of the reported elastic coefficients of $Nd_2Zr_2O_7$ (Feng et al., 2011), which are C_{11} = 243 GPa, C_{12} = 69 GPa, and C_{44} = 47 GPa. For a cubic system the values for elastic compliance can be obtained from the coefficients *via* the following formulae.

$$S_{11} = \frac{C_{11} + C_{12}}{(C_{11} - C_{12})(C_{11} + 2C_{12})}$$
$$S_{12} = \frac{-C_{12}}{(C_{11} - C_{12})(C_{11} + 2C_{12})}$$
$$S_{44} = \frac{1}{C_{44}}$$

We therefore obtain compliance values of S_{11} = 0.00471 GPa, S_{12} = -0.00104 GPa and S_{44} = 0.02128 GPa for $Nd_2Zr_2O_7$.

By employing the Voight-Reuss approximation (K. D. Verma and D. Nag, 1965) where the Voight bulk modulus (B_v) and shear modulus (G_v) are given by the following:

$$B_v = \frac{(C_{11} + 2C_{12})}{3}$$
$$G_v = \frac{(C_{11} - C_{12} + 3C_{44})}{5}$$

and the Reuss bulk modulus (B_r) and Reuss shear modulus (G_r) are

$$B_r = \frac{1}{3S_{11} + 6S_{12}}$$
$$G_r = \frac{15}{4S_{11} - 4S_{12} + 3S_{44}}$$

For the coefficients of $Nd_2Zr_2O_7$ we obtain Voight values of B_v = 127 GPa and G_v = 63 GPa which are consistent with the values of Feng et al., and Reuss values of B_r = 127 GPa and Gr = 172.77 GPa. The Voight and Reuss values represent the upper and lower limits of polycrystalline constraints, and the estimate of the bulk and shear moduli can be taken as the mean of the extremes. The elastic anisotropy can be described by the universal anisotropic index A^U (K. D. Verma and D. Nag, 1965) and the indexes of compression and shear are denoted by A_B (Rice, 1971) and A_G (Ravindran et al., 1998) all of which can be calculated as follows:

$$A^U = 5\frac{G_V}{G_R} + \frac{B_V}{B_R} - 6$$

TABLE 4 | Young's modulus in the normal direction of the three low index planes (100), (110), (111) and Poisson's ratio can be calculated for the three lower index planes in directions (*hkl*) in orthogonal directions.

	Direction	E_{hkl} GPa	$\upsilon(\mathbf{hkl}, \theta)$	Stress p1 MPa	Stress p2 MPa
Plane (100)	[010]	212.4808	0.2211	1.1039	−0.1020
	[00$\bar{1}$]	212.4808	0.2211	1.1039	−0.1020
Plane (110)	[$\bar{1}$10]	139.8231	0.1455	0.5715	−0.0528
	[00$\bar{1}$]	139.8231	0.4875	16.1793	−1.4947
Plane (111)	[$\bar{1}$10]	125.5164	0.3353	1.1039	−0.1020
	[11$\bar{2}$]	125.5164	0.3353	1.1039	−0.1020

$$A_B = \frac{B_V - B_R}{B_V + B_R}$$
$$A_G = \frac{G_V - G_R}{G_V + G_R}$$

For these three a value of zero indicates elastic isotropy and the variation from zero indicates anisotropic elastic properties. Our calculation resulted in values of A^U = −3.177 indicating anisotropic behaviour; A_B = 0 indicating isotropic compression and A_G = −0.4656 indicating the sample will exhibit shear anisotropy. To examine the effect of this we can calculate Young's modulus in the normal direction of the three low index planes (100), (110), (111) (Zhang et al., 2007).

$$\frac{1}{E_{hkl}} = S_{11} - 2S_0\frac{(hk)^2 + (hl)^2 + (lk)^2}{(h^2 + k^2 + l^2)^2}$$

Where,

$$S_0 = S_{11} - S_{12} - \frac{1}{2}S_{44}$$

And Poisson's ratio can be calculated for the three lower index planes in directions (*hkl*) in orthogonal directions (Zhang et al., 2007);

$$\upsilon(hkl, \theta) = \left\{S_{12} + \frac{S_0}{(h^2 + k^2 + l^2)}\left[\left(\frac{h^2 l}{\sqrt{h^2 + k^2}\sqrt{h^2 + k^2 + l^2}}\cos\theta - \frac{hk}{\sqrt{h^2 + k^2}}\sin\theta\right)^2 + \left(\frac{k^2 l}{\sqrt{h^2 + k^2}\sqrt{h^2 + k^2 + l^2}}\cos\theta + \frac{hk}{\sqrt{h^2 + k^2}}\sin\theta\right)^2 + \left(\frac{l\sqrt{h^2 + k^2}}{\sqrt{h^2 + k^2 + l^2}}\cos\theta\right)^2\right]\right\} \Big/ \left[-S_{11} + 2S_0\frac{(hk)^2 + (hl)^2 + (lk)^2}{(h^2 + k^2 + l^2)^2}\right]$$

the calculated values for Young's modulus and Poisson's ratio are given in **Table 4**.

There is no anisotropy in Bulk modulus with only a slight anisotropy in the Young's modulus which is still comparable to the value of the Bulk modulus. Variations in Poisson's ratio in two of the planes (100) and (111) does not occur however there are obvious anisotropic behaviour in the (110) plane as related to the shear anisotropy noted in the value of A_G. This may appear large but if we compare these values to the system Ni_3Al (Luan et al., 2018) which is an alloy but nonetheless can serve as an example of a material that does exhibit anisotropic behaviour and so will be subject to higher shear stresses, the values for Young's modulus

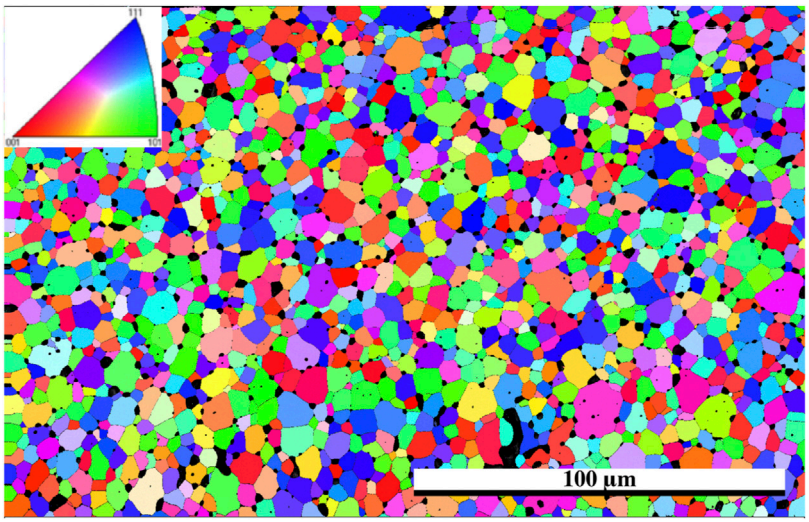

FIGURE 4 | EBSD grain orientation map of $Er_2Ti_2O_7$ utilizing cif generated from neutron diffraction of the unirradiated specimen, direction of He^{2+} ions are from the bottom of the image, inset shows pole figure orientation.

were 112.094, 212.973, and 304.241 Gpa for the (100), (110) and (111) planes, respectively and Poisson's ratio in the (110) for the same directions were -0.14 and 0.76 respectively. The equivalent calculated values of stress for all directions except for the (110) plane in the $[00\bar{1}]$ are all very similar to the values obtained for the bulk which leads us to assume that the behaviour of $Nd_2Zr_2O_7$ will be relatively uniform. This result reinforces the concept that for $Nd_2Zr_2O_7$ the material is essentially elastically isotropic and only two elastic constants, the Young modulus and the Poisson ratio, are required to describe the elastic behavior of the material in any state of stress.

Therefore, the most likely explanation for the appearance of two phases post irradiation is that the sample has stress in the irradiated region and the variation in lattice parameters is due to hydrostatic tensile (p1) and compressive (p2) stress. To gain further insight into the irradiated regions and the concept that the incident ions had imparted a hydrostatic stress front past the predicted depth by SRIM the samples were then examined *via* EBSD and TEM.

EBSD

The EBSD map of the $Er_2Ti_2O_7$ sample was generated based on the cif file of the unirradiated specimen obtained from neutron diffraction analysis. The purpose of performing EBSD was to determine if any gross changes had occurred from the damaged to the undamaged region and if there was a change in grain size and orientation as reported by Wen et al. (2016). As can be seen in the orientation map (**Figure 4**) there is no observable change from the damaged region at the bottom of the image to the undamaged region at the top. Given that the refinement of patterns indicated that only one phase was present in the sample that had been irradiated along with amorphous material, it is conceivable that in the damaged areas there is still sufficient coherence to generate a pattern for the EBSD to detect, giving the appearance of a still fully crystalline material. Considering that this study was at <1 dpa, the crystalline appearance of the only slightly damaged material in the EBSD pattern is understandable.

For comparison the $Nd_2Zr_2O_7$ sample was mapped in the same way as the $Er_2Ti_2O_7$ sample to determine if there was variation between the damaged and undamaged regions. For consistency the cif file that was assigned to the undamaged unstressed region was used for mapping. As can be seen in **Figure 5** there is an overall greater variation in grain size which is inherent to the sample. However, there is a slight indication in the damaged region that some of the grains had broken up.

The sample was then mapped with the two neutron diffraction generated cif files: one associated with the undamaged region and the other from the damaged region associated with the residual stress (phase 1). The resultant map indicated a larger proportion of phase 1 in the damaged region and so a higher resolution map was taken of that area. It should also be noted with closer examination that there appears to be damaged grains deeper than the stated penetration by SRIM calculations which is consistent with a hydrostatic stress field penetrating beyond the predicted layer (Martina Scapin, 2013; Bertarelli, 2014) with some appearing as deep as 30 microns into the sample, however the center region of the sample appears to be damage free. The results from the high-resolution EBSD phase map **Figure 6** reveal some grains that show very little of phase 1 while others appeared to contain a uniform distribution of phase 1 throughout the grain. It is possible that as the sample accumulates damaged regions, a buildup of residual stress will lead to grain refinement as seen in alloys thus causing the larger grain to break up into smaller grains. The fact that some grains are more damaged than others may also be an artifact of orientation and the damage occurring is related to the anisotropy as outlined in the diffraction results.

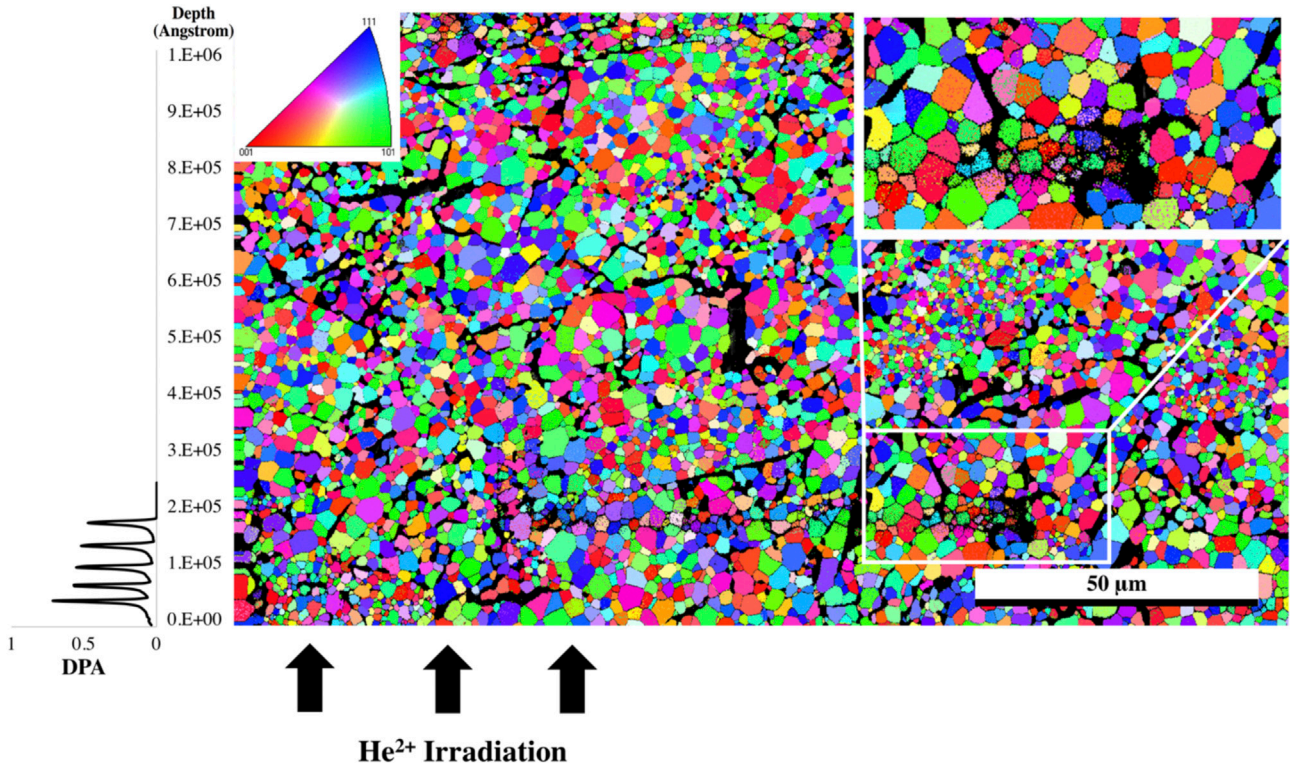

FIGURE 5 | EBSD grain orientation map of the irradiated $Nd_2Zr_2O_7$ sample utilizing the cif generated from neutron diffraction assigned to the undamaged part of the sample, direction of He^{2+} ions are from the bottom of the image. The white rectangle indicates the area where the high-resolution EBSD was taken in **Figure 6**, and the top left inset shows pole figure orientation. The plot to the left is the SRIM simulation and is provided as a comparison for penetration depth of the He^{2+} ions.

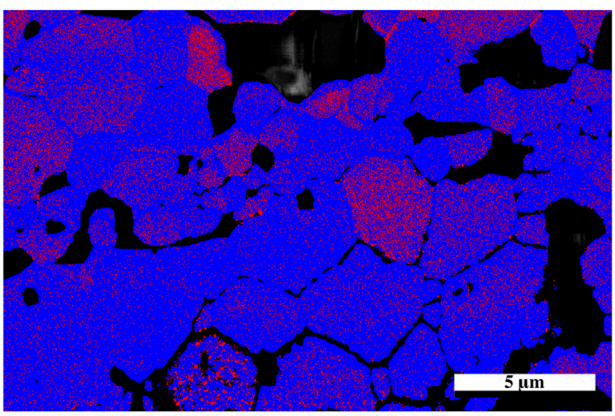

FIGURE 6 | High resolution EBSD phase map of irradiated $Nd_2Zr_2O_7$ utilizing cifs generated from neutron diffraction assigned to the undamaged and damaged parts of the sample, direction of He^{2+} ions are from the bottom of the image. Red areas indicate phase 1.

TEM Analysis of the Irradiated Pyrochlore Specimens

$Er_2Ti_2O_7$

A lower magnification bright field image of the TEM sample prepared by FIB methods is shown in **Figure 7**. Bend contours in this image indicate that the material is predominantly crystalline; however, this does not preclude the presence of disorder due to radiation damage. A high-resolution TEM image was recorded from a location within the circled area of **Figure 7** and is shown in **Figure 8**.

By reference to the scale bars, the image shown in **Figure 8** is much smaller than the circled area shown in **Figure 7** and therefore may sit mostly within a band of lighter grey contrast within the circled area. Note that even though there are bend contours in **Figure 7**, the lighter bands are not necessarily tilted completely out of a diffracting condition due to distortion of the sample. Furthermore, the high-resolution image clearly shows the presence of lattice fringes that are consistent with the two strongest diffracted beams in the FFT, which is shown in the inset of **Figure 8**. This diffraction pattern is close to, but not precisely aligned on a [110] zone axis of pyrochlore, such that one of the two <111> systematic rows is excited more strongly than the other. The stronger row exhibits a pair of (444) beams, a pair of stronger (222) beams sitting on a diffuse ring, and a pair of very weak (111) beams inside of the diffuse ring. The measured spacing between the lattice fringes is approximately 0.3 nm, which is close to the spacing of the (222) lattice planes of $Er_2Ti_2O_7$. The lattice image also shows some local areas wherein the fringes are less distinct or absent altogether and this is consistent with the diffuse scattering shown in the diffraction pattern. Similar electron diffraction patterns and

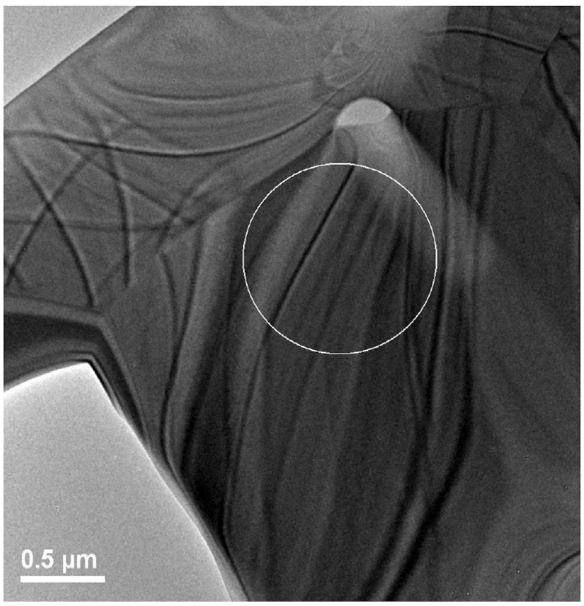

FIGURE 7 | Image showing region where high resolution TEM was performed on irradiated $Er_2Ti_2O_7$ sample. Grain boundaries can easily be seen in the image as well as bend contours.

images have been observed previously in pyrochlore and interpreted in terms of strain and domain size during the crystalline to amorphous transformation in pyrochlore (e.g., Lumpkin and Ewing, 1988).

To further investigate the arrangement of disordered and ordered material in the irradiated region an image at a higher magnification but at the same orientation as **Figure 8** was taken of the previous image, (**Figure 9**). There are clear regions of disorder and order, with some of the disorder existing within the areas where lattice fringes are visible and areas outside of the lattice fringes. As with **Figure 8** this appearance is like former crystalline to amorphous transformation in pyrochlore studies (Lumpkin and Ewing, 1988; Lian et al., 2009).

$Nd_2Zr_2O_7$

To investigate the possible cause of the dual phases visible in the high-resolution EBSD image (**Figure 6**) a TEM sample from the area highlighted in **Figure 5** was prepared *via* FIB for high resolution TEM examination. Two regions were examined and are circled in the image to provide a reference to indicate where the presented images originate from, it should be noted that these areas were representative of the entire grains and the TEM image was recorded from a location within the circled area.

Firstly, there are areas that appear to be very faint bend contours like those seen in the $Er_2Ti_2O_7$ sample, therefore the sample was imaged in dark field mode and is given in **Supplementary Figure S7**. Imaging in objective aperture dark field mode highlights the presence of bend contours. However, the image was acquired in STEM mode with an annular dark field detector and the contrast mechanism is different, even so, if the crystal was bent to any degree, it should be visible and as can be seen in the supplementary figure there was no evidence of high contrast areas, an indication that the sample is bent. The area at the top of the sample that corresponded to a low abundance of secondary phase will be discussed first. As can be seen in the high-resolution image **Figure 10**, the area displays a very high degree of order (crystallinity), and lattice fringes are visible throughout most of the sample. A FFT of the image was performed (inset of

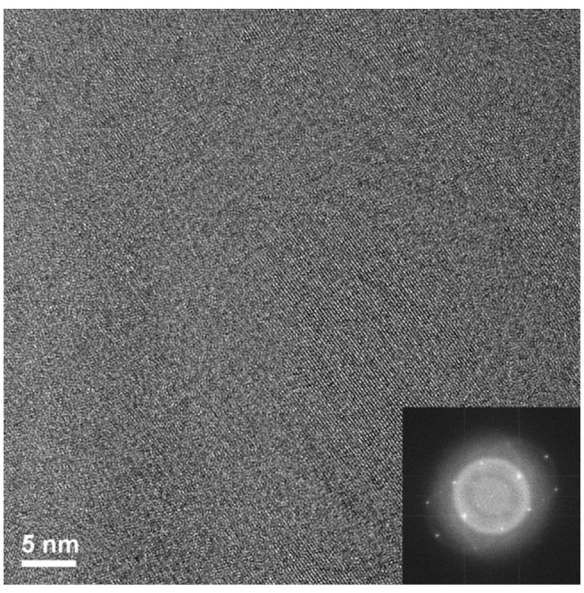

FIGURE 8 | High resolution TEM image of circled area of irradiated $Er_2Ti_2O_7$ from **Figure 5** and the FFT of high-resolution image (inset).

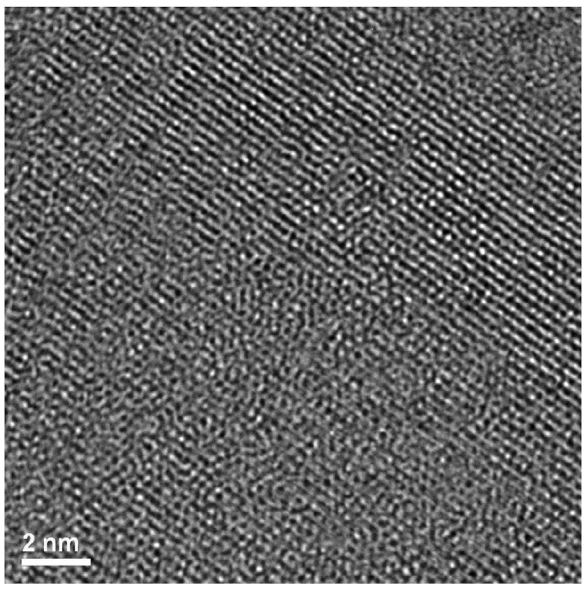

FIGURE 9 | Magnified area of high-resolution region of irradiated $Er_2Ti_2O_7$ showing ordered and disordered regions.

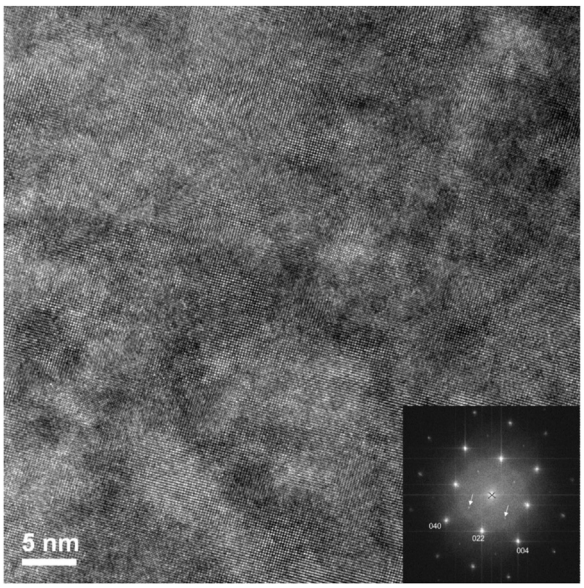

FIGURE 10 | High magnification image of irradiated $Nd_2Zr_2O_7$ area at the top of the lift out of **Figure 12** showing no evidence of disorder.

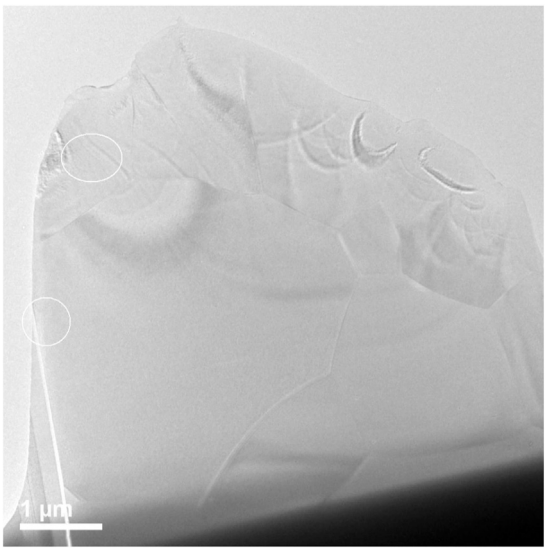

FIGURE 12 | Top of lift out area in Figure, showing highly ordered lattice fringes. The FFT inset of the high-resolution image is viewed down the [1 0 0] and shows a very small amount of diffuse scattering, possibly from amorphous material. Superlattice reflections are indicated by the arrows.

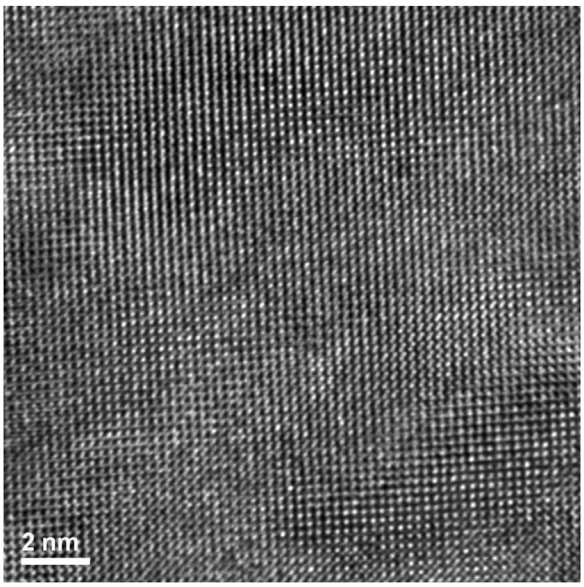

FIGURE 11 | Lift out area of the irradiated $Nd_2Zr_2O_7$ sample prepared *via* FIB. The two chosen areas contain a high and low amount of second phase of the altered pyrochlore phase after irradiation, respectively.

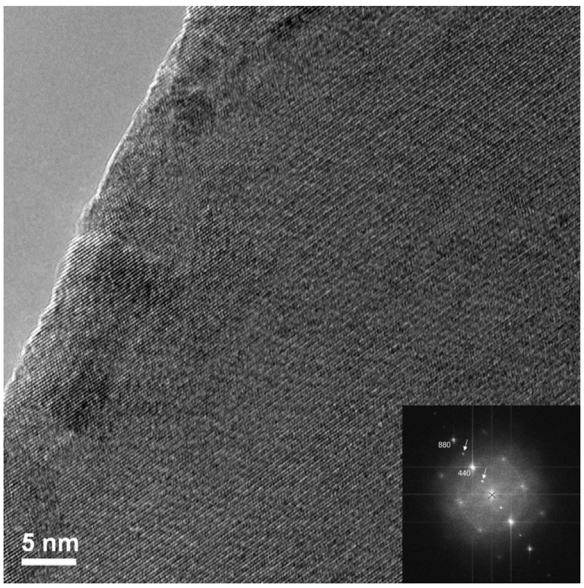

FIGURE 13 | High resolution image of lower circled FIB lift out area of irradiated $Nd_2Zr_2O_7$ (**Figure 12**) showing intertwined regions of disorder. The FFT inset of the high-resolution image is viewed down the [−1 −1 1], the diffuse scattering is indicative of the areas of disorder that can be seen in the image. Superlattice reflections are indicated by the arrows.

Figure 10) and there was very little evidence of disorder, which was more pronounced for the $Er_2Ti_2O_7$ sample, **Figure 7**.

To determine if disorder was present within the lattice fringes as in the $Er_2Ti_2O_7$ sample an image (**Figure 11**) was acquired at higher magnification at the center of **Figure 10**. It is apparent that the area examined is devoid of disorder with regular lattice fringes clearly visible.

The region corresponding to a high proportion of the second phase (from a location within the circled area in **Figure 12**) was subsequently examined *via* high resolution TEM, **Figure 13**. This diffraction pattern is close to, but not precisely aligned on a [−1−11] zone axis of pyrochlore. There are obvious areas of

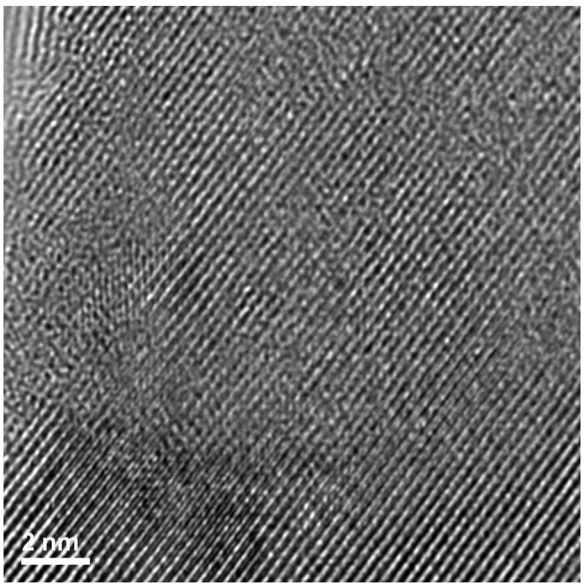

FIGURE 14 | High magnification image showing how the disorder exists for irradiated $Nd_2Zr_2O_7$ within the region where lattice fringes are visible.

disorder, however what is of interest is that they appear to be intertwined within the lattice fringes. This observation/behavior is very different to the $Er_2Ti_2O_7$ sample where large areas of disorder were visible and may be mainly due to the difference in radiation tolerance as discussed in the introduction.

To confirm that these regions were in fact disordered or areas of amorphous material a FFT was performed on the image (inset). The FFT clearly exhibits characteristics associated with disorder evidenced *via* the diffuse scattering visible in the inset in **Figure 13**, With the diffuse ring sitting on the (440). A region of amorphous material as described by Mayer et al. (2007) was visible along some sections of the lamella as shown in **Supplementary Figure S8**.

A high magnification image (center of **Figures 13**, **14**) shows how the disorder is intertwined throughout the sample. The change from order to disorder could be described as a continuum whereas the $Er_2Ti_2O_7$ sample had regions that were either ordered or disordered, indicating a different radiation response mechanism for the titanate and zirconate pyrochlore samples. One issue with the thickness of the TEM lamellae is the effect of being able to resolve the high-resolution image to some depth, z, into the crystal which may also be causing distortion of the lattice fringes. The variation adjacent to the areas of damage may have some domains, possibly point defects and clusters that are a result of the adjacent damage. However these areas of damage are very similar to those seen in previous studies of Lumpkin and Ewing (1988) and Lian et al. (2009).

DISCUSSION

The aim of the study was to detect the early onset of phase transformation in relation to stress and strain of different pyrochlores, one prone to amorphization, one reported to undergo a transformation to defect fluorite and one a solid solution. With regards to the solid solution of the Zirconate and Titanate pyrochlore, the synthesis method employed was not sufficient to achieve a 50:50 ratio of A and B cations according to the diffraction results. However, the fact that the as fabricated sample contained strain is an indicator that if the sample could be synthesized to have a 50:50 ratio analysis of the irradiation response would be insightful regarding whether the titanate or zirconate behavior would be dominating.

First let us discuss the $Er_2Ti_2O_7$ sample and its response to irradiation. Initial characterization showed the pristine sample to be very typical of those synthesized by others, it was highly crystalline with some porosity and an average grain size of approximately 2 microns according to the EBSD images. Analysis of both the synchrotron and neutron diffraction patterns yielded results that were consistent with those reported in the literature with no inherent strain and therefore it can be considered an archetypal pristine example. Irradiation *via* He^{2+} ions resulted in the sample breaking into smaller pieces once it was removed from the mount, this could be due to many reasons that include internal hydrostatic stresses that built up because of the thin nature of the sample, He^{2+} migrating to grain boundaries during irradiation due to insolubility of He^{2+} in pyrochlore, swelling of the irradiated side due to amorphization, volume change due to the formation of helium bubbles or all of the above. Rietveld quantitative phase analysis of the irradiated sample indicated that approximately 30% of the sample had become amorphous which is reasonable given the depth to which it was irradiated and the target dpa and the errors mentioned in the analysis technique. It is also highly likely that the hydrostatic stress field that extended below the predicted depth (Bertarelli, 2014) may have contributed to the amorphization process. Examination *via* EBSD to compare predicted damage depth with degradation in EBSD pattern was not conclusive since the irradiated grains still contained enough coherent areas to produce kikuchi lines that could be indexed *via* the cif generated from neutron diffraction analysis of the pristine sample. This assumption was confirmed *via* TEM, on a sample lifted out from the middle of the predicted damage region. Examination *via* high resolution TEM (**Figure 8**) indicated that there are regions that are intermixed with disorder and lattice fringes. When a FFT was performed on this region (**Figure 8**) diffraction spots could be seen in conjunction with a diffuse halo. An image taken at higher magnification (**Figure 9**) shows these intermixed regions of disorder that are reminiscent of the maze-like patterns in bulk metallic glasses which may lead to the formation of nano crystals resulting from annealing as reported in bulk metallic glasses by Sarac et al. (2016). This result agrees with the neutron diffraction analysis in that there are areas that have become amorphous while others are essentially no different from the starting material. This is therefore a possible explanation as to why no strain or stress was detected in the irradiated sample since any part that might exhibit those properties has become amorphous and any residual stress has been relieved through the fracturing of the sample. It is also of interest that the mosaic pattern produced by the irradiation is very similar to that predicted for the damage of

alloys by Simeone et al. (2019). While the material has become amorphous with respect to normal scattering methods there still exists a pattern to the arrangement of the atoms.

The SEM-EBSD results for $Nd_2Zr_2O_7$ were like those of the $Er_2Ti_2O_7$ sample in that it was highly crystalline with some porosity. However, there was a larger grain size distribution, most likely because Zr pyrochlores are harder to sinter due to their refractory nature. Prior to irradiation, the synchrotron and neutron diffraction patterns yielded results that were consistent with those reported in the literature with no inherent strain and therefore it can also be considered an archetypal example. In comparison to the $Er_2Ti_2O_7$ sample upon irradiation the $Nd_2Zr_2O_7$ sample did not break apart when removed from the sample mount which intuitively suggests that there was a mechanism at play allowing it to accommodate the radiation damage. Rietveld analysis of the neutron diffraction data proved clear evidence of the co-existence of two pyrochlore phases, not a pyrochlore and defect fluorite phase as might be suggested when considering the multiple glancing incidence XRD studies. One of the phases appeared to be very similar to the undamaged material while the other had a lattice parameter that was increased as might be expected in a diffraction pattern exhibiting residual stress. While neutron diffraction data revealed no evidence of strain in either of the phases there is evidence of an increase in disorder of both the cations and anions as shown in **Table 2** and **Supplementary Figure S6**. The method to determine hydrostatic stress as outlined yielded values of hydrostatic residual stress; 1.141 MPa for phase 1 and −0.105 MPa for phase 2, indicating that phase 1 is under tensile stress and that phase 2 is under a very small amount of compressive stress and still fairly like the pristine pyrochlore sample. Considering the studies mentioned previously this is indicative of a ballistic hydrostatic stress field moving deeper into the sample. For comparison it is a well known phenomena that H^+ migrates deeper into zirconium alloys under the effects of hydrostatic stress (Motta et al., 2019).

Examination *via* EBSD to compare this damaged and undamaged area in $Nd_2Zr_2O_7$ at first showed very little difference as seen in **Figure 5**. However, when high resolution EBSD in **Figure 6** was performed utilizing both cif files derived from neutron diffraction it was apparent that some grains were composed of high proportions of both phases on a very fine scale. The area highlighted in **Figure 5** was prepared for TEM examination *via* FIB to obtain a better understanding of the nature of this region. First the upper area which would be considered to not have any residual stress due to the presence of only phase 2 was examined. This area proved to be highly crystalline with very little disorder as can be seen in **Figure 10**. In contrast the grain assumed to have a large amount of residual stress due to the presence of both phases exhibited discrete islands of disorder as shown in **Figure 13** and **Figure 14**. FFT of this area resulted in a pattern composed of sharp spots in an area of diffuse scattering with the absence of a halo as seen in the $Er_2Ti_2O_7$ sample. A higher magnification image reveals that very disordered islands exist in an otherwise highly ordered lattice. There are no regions exhibiting the maze-like pattern as seen in the $Er_2Ti_2O_7$ sample. It is possible that the highly disordered region would not be able to contribute to the coherent scattering and most likely is imparting stress to the surrounding lattice resulting in reduction in the lattice parameter as damage accumulates. If we consider the events of each ion interaction as a localised heating event there is a parallel with this process and the thermal cycling of thermal barrier coatings and the buildup of residual thermal stresses accumulated during thermal cycling as reported by Guo et al. (2016) for $La_2Zr_2O_7$. Given that this sample has undergone only a small amount of radiation damage as compared to many of the studies reported in the literature it is conceivable that as more damage occurs the residual stress would continue to build up until the point where the grain fractures due to the pressure front as described earlier. Conversely it could be similar to the process outlined by L M Wang et al. (2000) in their *ex-situ* irradiation study of $Ca_2La_8(SiO_4)_6O_2$. They reported nanostructure formation with a random orientation induced in ceramics by ion beam irradiation at temperatures near the critical amorphization temperature, below the normal crystallization temperature of corresponding amorphous materials. The nanostructure formation is a competition between amorphization and thermally activated recrystallization. In a $Ca_2La_8(SiO_4)_6O_2$, nanocrystals were induced by 1.5 MeV Kr^+ irradiation at a fluence of 1×10^{14} ions/cm^2 at 673 K, slightly below the critical amorphization temperature. The nanocrystals had the same crystal structure as the original phase as confirmed by electron diffraction. This process has not been viewed in the $Nd_2Zr_2O_7$ sample however accumulation of amorphous (spherical) regions that may be partly recrystallized would then lead to the scenario where smaller diffraction domains are formed as the grain slowly breaks up due to internal stresses. This process is then analogous to the study of Simeone et al. (2019) where small domains are formed due to grain subdivision with the appearance of a transformation to defect fluorite. A similar process where there is a reduction in *Tc* due to grain size has been reported by Wen et al. (2016) for titanate ceramics. It is therefore possible that with further damage to the zirconate sample the same effect as reported by Simeone et al. would be seen as the damaged grains become progressively divided into smaller coherent scattering domains, thus providing a potential mechanism for the reported transformation of zirconate pyrochlores from pyrochlore to defect fluorite when examined *via* conventional diffraction methods, given x-rays only interact with the upper 2 microns of the sample. Since the titanate based pyrochlore becomes amorphous and does not appear to be able to accommodate more damage and stress, this might be the underlying reason for titanate pyrochlores to transform immediately to the disordered, amorphous state, rather than to the defect fluorite structure when also considered in the context of the study conducted by Wen et al. To extend the argument further this transformation is often simulated through cation substitution in what can be considered type 2 internal strain due to lattice misfit on the atomic length scale. As stated previously our solid solution sample exhibited signs of strain, and thus it is possible that the inherent strain could cause the disruption of the coherent diffraction domains to produce the apparent pyrochlore to defect fluorite transformation. The process could be driven by what is colloquially referred to as compositional strain in solid state chemistry. There are already indications of this mechanism in the literature in various publications that place the defect fluorite transformation boundary at different values of B cation substitution. It is merely a function of how well the samples have

been produced to achieve a solid solution to either mitigate or enhance the lattice misfit on the atomic length scale which then results in either their ability to inhibit or enable stress relief.

CONCLUSION

We have shown that for both the $Er_2Ti_2O_7$ and $Nd_2Zr_2O_7$ pyrochlores strain can't be detected by peak shape analysis and is most likely regular in nature and that they didn't undergo a phase transformation to defect fluorite when they are irradiated at levels of approximately 1 dpa *via* He^{2+} ion irradiation at room temperature. The neutron diffraction results indicate an increase in disorder for the irradiated sections of the sample and they still exhibited coherent scattering. There was evidence of hydrostatic stress in the $Nd_2Zr_2O_7$ sample that was quantified while approximately 30% of the $Er_2Ti_2O_7$ sample became amorphous. EBSD results confirmed the presence of stress *via* mapping of the two pyrochlore phases throughout certain $Nd_2Zr_2O_7$ grains to varying degrees. The bulk of both samples remained crystalline to the point of being able to generate kikuchi patterns that could be indexed to the parent phases and so provide orientation information. TEM confirmed the results of the neutron scattering and EBSD while at the same time providing insight into the recovery and radiation response mechanisms of both compositions to irradiation *via* He^{2+} ions. We conclude in a similar fashion as Simeone et al. (2019) that in this study defect fluorite $Nd_2Zr_2O_7$ did not form and it is indeed possible that it does not form for examples of irradiated zirconate pyrochlores if they behave in a similar fashion. This leads to future experimentational studies: the repetition of our irradiated titanate and zirconate samples to examine the grains that appear to have the highest regions of stress *via* nano Raman spectroscopy to determine if the domains do indeed break down and in-depth stress experiments to confirm if the bulk of the stress is similar in nature to the examples cited. Then subsequently if those sub domains still produce a pattern consistent with pyrochlore as seen by Simeone et al. (2019) with nano-grains of $La_2Zr_2O_7$ as this will provide additional insights about the here proposed radiation response mechanism for zirconate and titanate pyrochlores. Future work will also focus on the synthesis of a range of pyrochlore solid solutions with mixed B cations to perform similar irradiation experiments coupled with grain size effects.

DATA AVAILABILITY STATEMENT

The original contributions presented in the study are included in the article/**Supplementary Material**, further inquiries can be directed to the corresponding authors.

AUTHOR CONTRIBUTIONS

SF, conceptualization and concept driver, sample preparation and analysis, writing—original draft. SC, analysis of TEM diffraction patterns, literature review, figure preparation and writing—original draft. MI, performed sample irradiations. DO, TEM examination and analysis. JD, EBSD sample preparation and examination and data analysis. GL, TEM interpretation. DS conceptualization and writing—review and editing. MA neutron diffraction and analysis. FB, writing—review and editing. DB, writing—review and editing. MK, SEM imaging, writing—review and editing. GT, conceptualization and concept driver, writing—original draft, all diffraction results analysis, microscopy data interpretation and stress analysis.

FUNDING

The authors acknowledge the financial support from the Australian Government under SIA grant SHCC000002. We also acknowledge the use of CAS and ACNS ANSTO facilities supported by NCRIS funding.

ACKNOWLEDGMENTS

We would like to thank Mr. Tim Palmer for EBSD sample preparation and sample sectioning, and Mr. David Carr for fruitful discussions in relation to hydrostatic residual stress.

SUPPLEMENTARY MATERIAL

The Supplementary Material for this article can be found online at: https://www.frontiersin.org/articles/10.3389/fchem.2021.706736/full#supplementary-material

REFERENCES

Agarwal, S. (2015). *Helium Mobility in Advanced Nuclear Ceramics. Materials Science [cond-mat.mtrl-sci]*. Paris, France: Université Paris Sud.

Alexander, K. B., Becher, P. F., Wang, X.-L., and Hsueh, C.-H. (1995). Internal Stresses and the Martensite Start Temperature in Alumina-Zirconia Composites: Effects of Composition and Microstructure. *J. Am. Ceram. Soc.* 78 (2), 291–296. doi:10.1111/j.1151-2916.1995.tb08799.x

Avdeev, M., and Hester, J. R. (2018). ECHIDNA: A Decade of High-Resolution Neutron Powder Diffraction at OPAL. *J. Appl. Cryst.* 51 (6), 1597–1604. doi:10.1107/S1600576718014048

Bae, J.-M., and Steele, B. C. H. (1999). Properties of Pyrochlore Ruthenate Cathodes for Intermediate Temperature Solid Oxide Fuel Cells. *J. Electroceramics* 3 (1), 37–46. doi:10.1023/A:1009962831952

Bartolomé, J. F., Bruno, G., and DeAza, A. H. (2008). Neutron Diffraction Residual Stress Analysis of Zirconia Toughened Alumina (ZTA) Composites. *J. Eur. Ceram. Soc.* 28 (9), 1809–1814. doi:10.1016/j.jeurceramsoc.2007.12.037

Bertarelli, A. (2014). Beam-Induced Damage Mechanisms and Their Calculation. *2014 Jt. Int. Accelerator Sch. Beam Loss Accelerator Prot. Proc.* 002 (November), 159–227. doi:10.5170/CERN-2016-002.159

Black, D. R., Mendenhall, M. H., Brown, C. M., Henins, A., Filliben, J., and Cline, J. P. (2020). Certification of Standard Reference Material 660c for Powder Diffraction. *Powder Diffraction* 35 (1), 17–22. doi:10.1017/S0885715620000068

Coelho, A. A. (2018). TOPAS and TOPAS-Academic: an Optimization Program Integrating Computer Algebra and Crystallographic Objects Written in C++. *J. Appl. Cryst.* 51, 210–218. doi:10.1107/S1600576718000183

Debelle, A., and Declémy, A. (2010). XRD Investigation of the Strain/Stress State of Ion-Irradiated Crystals. *Nucl. Instr. Methods Phys. Res. Section B: Beam Interactions Mater. Atoms* 268 (9), 1460–1465. doi:10.1016/j.nimb.2010.01.009

Dong, L., Setyawan, W., Li, Y., Devanathan, R., and Gao, F. (2017). Molecular Dynamics Simulation of Low-Energy Recoil Events in Titanate Pyrochlores. *RSC Adv.* 7 (56), 35403–35410. doi:10.1039/c7ra04699e

Dupraz, M., Beutier, G., Rodney, D., Mordehai, D., and Verdier, M. (2015). Signature of Dislocations and Stacking Faults of Face-Centred Cubic Nanocrystals in Coherent X-Ray Diffraction Patterns: A Numerical Study. *J. Appl. Cryst.* 48 (Pt 3), 621–644. doi:10.1107/S1600576715005324

Engelmann, H. J., Volkmann, B., Ritz, Y., Saage, H., Stegmann, H., Robiliard, Q. D., et al. (2003). TEM Sample Preparation Using Focused Ion Beam - Capabilities and Limits. *Microsc. Today* 11 (2), 22–25. doi:10.1017/S1551929500052457

Ewing, R. C., Weber, W. J., and Lian, J. (2004). Nuclear Waste Disposal-Pyrochlore (A2B2O7): Nuclear Waste Form for the Immobilization of Plutonium and "minor" Actinides. *J. Appl. Phys.* 95 (11 I), 5949–5971. doi:10.1063/1.1707213

Farmer, J. M., Boatner, L. A., Chakoumakos, B. C., Du, M.-H., Lance, M. J., Rawn, C. J., et al. (2014). Structural and Crystal Chemical Properties of Rare-Earth Titanate Pyrochlores. *J. Alloys Compd.* 605, 63–70. doi:10.1016/j.jallcom.2014.03.153

Feng, J., Xiao, B., Wan, C. L., Qu, Z. X., Huang, Z. C., Chen, J. C., et al. (2011). Electronic Structure, Mechanical Properties and thermal Conductivity of $Ln_2Zr_2O_7$ (Ln=La, Pr, Nd, Sm, Eu and Gd) Pyrochlore. *Acta Materialia* 59 (4), 1742–1760. doi:10.1016/j.actamat.2010.11.041

Finkeldei, S., Brandt, F., Rozov, K., Bukaemskiy, A. A., Neumeier, S., and Bosbach, D. (2014). Dissolution of ZrO2 Based Pyrochlores in the Acid PH Range: A Macroscopic and Electron Microscopy Study. *Appl. Geochem.* 49, 31–41. doi:10.1016/j.apgeochem.2014.06.014

Guo, X., Lu, Z., Jung, Y.-G., Li, L., Knapp, J., and Zhang, J. (2016). "Thermomechanical Properties of Bilayer La2Zr2O7 Thermal Barrier Coatings," in Energy Technology 2016: Carbon Dioxide Management and Other Technologies, 155–160. doi:10.1007/978-3-319-48182-1_18

Helean, K. B., Ushakov, S. V., Brown, C. E., Navrotsky, A., Lian, J., Ewing, R. C., et al. (2004). Formation Enthalpies of Rare Earth Titanate Pyrochlores. *J. Solid State. Chem.* 177 (6), 1858–1866. doi:10.1016/j.jssc.2004.01.009

Heremans, C., Wuensch, B. J., Stalick, J. K., and Prince, E. (1995). Fast-Ion Conducting Y2(Zr Ti1-)2O7 Pyrochlores: Neutron Rietveld Analysis of Disorder Induced by Zr Substitution. *J. Solid State. Chem.* 117 (1), 108–121. doi:10.1006/jssc.1995.1253

Holesinger, T. G., Valdez, J. A., Janish, M. T., Wang, Y., and Uberuaga, B. P. (2019). Potential Benefit of Amorphization in the Retention of Gaseous Species in Irradiated Pyrochlores. *Acta Materialia* 164, 250–260. doi:10.1016/j.actamat.2018.10.049

Hu, Q., Zeng, J., Wang, L., Shu, X., Shao, D., Zhang, H., et al. (2018). Helium Ion Irradiation Effects on Neodymium and Cerium Co-doped Gd 2 Zr 2 O 7 Pyrochlore Ceramic. *J. Rare Earths* 36 (4), 398–403. doi:10.1016/j.jre.2017.11.005

K. D. Verma, J., and D. Nag, B. (1965). On the Elastic Moduli of a Crystal and Voigt and Reuss Relations. *J. Phys. Soc. Jpn.* 20 (4), 635–636. doi:10.1143/JPSJ.20.635

Lang, M., Zhang, F. X., Ewing, R. C., Lian, J., Trautmann, C., and Wang, Z. (2009). Structural Modifications of Gd2Zr2-xTixO7 Pyrochlore Induced by swift Heavy Ions: Disordering and Amorphization. *J. Mater. Res.* 24 (4), 1322–1334. doi:10.1557/jmr.2009.0151

Lehmann, H., Pitzer, D., Pracht, G., Vassen, R., and Stöver, D. (2003). Thermal Conductivity and Thermal Expansion Coefficients of the Lanthanum Rare-Earth-Element Zirconate System. *J. Am. Ceram. Soc.* 86 (8), 1338–1344. doi:10.1111/j.1151-2916.2003.tb03473.x

Lenz, C. (2019). *Quantification of Structural Radiation Damage in Ceramic Waste-form Materials Using M-Luminescence Spectroscopy of REE 3 +.*

Li, Y. H., Wang, Y. Q., Xu, C. P., Valdez, J. A., Tang, M., and Sickafus, K. E. (2012). Microstructural Evolution of the Pyrochlore Compound Er2Ti2O7 Induced by Light Ion Irradiations. *Nucl. Instr. Methods Phys. Res. Section B: Beam Interactions Mater. Atoms* 286, 218–222. doi:10.1016/j.nimb.2011.12.034

Li, Y., Kowalski, P. M. P. M., Beridze, G., Birnie, A. R., Finkeldei, S., and Bosbach, D. (2015). Defect Formation Energies in A2B2O7 Pyrochlores. *Scripta Materialia* 107, 18–21. doi:10.1016/j.scriptamat.2015.05.010

Lian, J., Wang, L. M., Chen, J., Ewing, R. C., and Kutty, K. V. G. (2002). Heavy Ion Irradiation of Zirconate Pyrochlores. *Mater. Res. Soc. Symp. - Proc.* 713, 507–512. doi:10.1557/proc-713-jj11.35

Lian, J., Wang, L. M., Sun, K., and Ewing, R. C. (2009). *In Situ* TEM of Radiation Effects in Complex Ceramics. *Microsc. Res. Tech.* 72 (3), 165–181. doi:10.1002/jemt.20669

Loong, C. K., Richardson, J. W., and Ozawa, M. (1995). Crystal Phases, Defects, and Dynamics of Adsorbed Hydroxyl Groups and Water in Pure and Lanthanide-Modified Zirconia: A Neutron-Scattering Study. *J. Catal.* 157 (2), 636–644. doi:10.1006/jcat.1995.1329

Luan, X., Qin, H., Liu, F., Dai, Z., Yi, Y., and Li, Q. (2018). The Mechanical Properties and Elastic Anisotropies of Cubic Ni3Al from First Principles Calculations. *Crystals* 8 (8), 307. doi:10.3390/cryst8080307

Lumpkin, G., and Ewing, R. (1988). Alpha-Decay Damage in Minerals of the Pyrochlore Group. *Phys. Chem. Minerals* 16 (1), 2–20. doi:10.1007/BF00201325

Lumpkin, G. R., and Ewing, R. C. (1985). Natural Pyrochlores: Analogues for Actinide Host Phases in Radioactive Waste Forms. *Mater. Res. Soc. Symposia Proc.* 44, 647–654. doi:10.1557/PROC-44-647

Lumpkin, G. R., Smith, K. L., Blackford, M. G., Whittle, K. R., Harvey, E. J., Redfern, S. A. T., et al. (2009). Ion Irradiation of Ternary Pyrochlore Oxides. *Chem. Mater.* 21 (13), 2746–2754. doi:10.1021/cm9003917

Lutique, S., Staicu, D., Konings, R. J. M., Rondinella, V. V., Somers, J., and Wiss, T. (2003). Zirconate Pyrochlore as a Transmutation Target: Thermal Behaviour and Radiation Resistance against Fission Fragment Impact. *J. Nucl. Mater.* 319, 59. doi:10.1016/s0022-3115(03)00134-x

Maimaitiyili, T., Woracek, R., Neikter, M., Boin, M., Wimpory, R., Pederson, R., et al. (2019). Residual Lattice Strain and Phase Distribution in Ti-6Al-4V Produced by Electron Beam Melting. *Materials* 12 (4), 667. doi:10.3390/ma12040667

Mallick, B., Patel, T., Behera, R. C., Sarangi, S. N., Sahu, S. N., and Choudhury, R. K. (2006). Microstrain Analysis of Proton Irradiated PET Microfiber. *Nucl. Instr. Methods Phys. Res. Section B: Beam Interactions Mater. Atoms* 248 (2), 305–310. doi:10.1016/j.nimb.2006.04.153

Martina Scapin (2013). *Shock-Wave and High Strain-Rate Phenomena in Matter-Modeling and Applications, No. March*. Turin, Italy: Politecnico Di Torino, 183. Available at: http://porto.polito.it/2507944/1/PhD_thesis_SCAPIN_def.pdf.

Mayer, J., Giannuzzi, L. A., Kamino, T., and Michael, J. (2007). TEM Sample Preparation and FIB-Induced Damage. *MRS Bull.* 32 (5), 400–407. doi:10.1557/mrs2007.63

Motta, A. T., Capolungo, L., Chen, L.-Q., Cinbiz, M. N., Daymond, M. R., Koss, D. A., et al. (2019). Hydrogen in Zirconium Alloys: A Review. *J. Nucl. Mater.* 518, 440–460. doi:10.1016/j.jnucmat.2019.02.042

Nordlund, K., Sand, A. E., Granberg, F., Zinkle, S. J., Stoller, R., Averback, R. S., et al. (2015). *Primary Radiation Damage in Materials, OCDE/Nuclear Science*. Paris, France: Nuclear Science NEA/NSC.

Noyan, I. C., and Cohen, J. B. (1987). *Residual Stress Measurement by Diffraction and Interpretation*. New York: Springer-Verlaag.

Oden, M. (1992). Residual Stress in Ceramics and Ceramic Composites. Available at: https://inis.iaea.org/search/download.aspx?RN=24022074&redURL=http://www.iaea.org/inis/collection/NCLCollectionStore/_Public/24/022/24022074.pdf.

Parikin, P., Killen, P., and Rafterry, A. (2011). Measurements of Residual Stresses in Cold-Rolled 304 Stainless Steel Plates Using X-Ray Diffraction with Rietveld Refinement Method. *Atom Indo.* 35 (1), 19–36. doi:10.17146/aij.2009.45

Pilania, G., Whittle, K. R., Jiang, C., Grimes, R. W., Stanek, C. R., Sickafus, K. E., et al. (2017). Using Machine Learning to Identify Factors that Govern Amorphization of Irradiated Pyrochlores. *Chem. Mater.* 29, 2574–2583. doi:10.1021/acs.chemmater.6b04666

Pirzada, M., Grimes, R. W., Minervini, L., Maguire, J. F., and Sickafus, K. E. (2001). Oxygen Migration in A2B2O7 Pyrochlores. *Solid State Ionics* 140 (3–4), 201–208. doi:10.1016/S0167-2738(00)00836-5

Rao, V. V., Rangarajan, G., and Srinivasan, R. (1986). Thermoelectric Power of RE2Mo2O7 Pyrochlores. *J. Phys. Chem. Sol.* 47 (4), 395–400. doi:10.1016/0022-3697(86)90030-2

Ravindran, P., Fast, L., Korzhavyi, P. A., Johansson, B., Wills, J., and Eriksson, O. (1998). Density Functional Theory for Calculation of Elastic Properties of Orthorhombic Crystals: Application to TiSi2. *J. Appl. Phys.* 84 (9), 4891–4904. doi:10.1063/1.368733

Rice, R. W. (1971). *The Compressive Strength of Ceramics BT - Ceramics in Severe Environments*. Boston, MA: Springer US, 195–229.

Rösler, J., Bäker, M., and Harders, H. (2007). Mechanical Behaviour of Ceramics, *Mechanical Behaviour of Engineering Materials*. Berlin: Springer, 227–255. doi:10.1007/978-3-540-73448-2_7

Sarac, B., Zhang, L., Kosiba, K., Pauly, S., Stoica, M., and Eckert, J. (2016). Towards the Better: Intrinsic Property Amelioration in Bulk Metallic Glasses. *Sci. Rep.* 6 (June). doi:10.1038/srep27271

Sattonnay, G., Lahrichi, M., Herbst-Ghysel, M., Garrido, F., and Thomé, L. (2007). Stress Field Induced by Swift Heavy Ion Irradiation in Cubic Yttria Stabilized Zirconia. *J. Appl. Phys.* 101 (10), 103516–6. doi:10.1063/1.2733745

Sattonnay, G., Moll, S., Thomé, L., Legros, C., Herbst-Ghysel, M., Garrido, F., et al. (2008). Heavy-Ion Irradiation of Pyrochlore Oxides: Comparison between Low and High Energy Regimes. *Nucl. Instr. Methods Phys. Res. Section B: Beam Interactions Mater. Atoms* 266 (12–13), 3043–3047. doi:10.1016/j.nimb.2008.03.161

Sickafus, K. E., Minervini, L., Grimes, R. W., Valdez, J. A., and Hartmann, T. (2000a). A Comparison between Radiation Damage Accumulation in Oxides with Pyrochlore and Fluorite Structures. *Radiat. Effects Defects Sol.* 155 (1–4). doi:10.1080/10420150108214104

Sickafus, K. E., Minervini, L., Grimes, R. W., Valdez, J. A., Ishimaru, M., Li, F., et al. (2000b). Radiation Tolerance of Complex Oxides. *Science* 289 (5480), 748–751. doi:10.1126/science.289.5480.748

Simeone, D., Costantini, J. M., Luneville, L., Desgranges, L., Trocellier, P., and Garcia, P. (2015). Characterization of Radiation Damage in Ceramics: Old Challenge New Issues? *J. Mater. Res.* 30 (9), 1495–1515. doi:10.1557/jmr.2015.77

Simeone, D., Thorogood, G. J., Huo, D., Luneville, L., Baldinozzi, G., Petricek, V., et al. (2017). Intricate Disorder in Defect Fluorite/Pyrochlore: A Concord of Chemistry and Crystallography. *Sci. Rep.* 7 (1), 3727. doi:10.1038/s41598-017-02787-w

Simeone, D., Thorogood, G. J., Murphy, G. L., Forestier, A., Garcia, P., and Luneville, L. (2019). Radiation-Induced Micro-structures as Ground States of a Swift-Hohenberg Energy Functional. *J. Appl. Phys.* 125 (6), 065103. doi:10.1063/1.5072798

Subramanian, M. A., Aravamudan, G., and Subba Rao, G. V. (1983). Oxide Pyrochlores - A Review. *Prog. Solid State. Chem.* 15 (2), 55–143. doi:10.1016/0079-6786(83)90001-8

Subramanian, M. A., Toby, B. H., Ramirez, A. P., Marshall, W. J., Sleight, A. W., and Kwei, G. H. (1996). Colossal Magnetoresistance without Mn3+/Mn4+ Double Exchange in the Stoichiometric Pyrochlore Tl2Mn2O7. *Science* 273 (5271), 81–84. doi:10.1126/science.273.5271.81

Subramanian, M., Subramanian, R., and Clearfield, A. (1985). Fast Ion Conduction in the Defect Pyrochlore System KBxW2−xO6(B = Al, Ti and Ta). *Solid State Ionics* 15 (1), 15–19. doi:10.1016/0167-2738(85)90101-8

Thompson, P., Cox, D. E., and Hastings, J. B. (1987). Rietveld Refinement of Debye-Scherrer Synchrotron X-Ray Data from Al2O3. *J. Appl. Cryst.* 20 (2), 79–83. doi:10.1107/S0021889887087090

Wallwork, K. S., Kennedy, B. J., and Wang, D. (2007). The High Resolution Powder Diffraction Beamline for the Australian Synchrotron. *AIP Conf. Proc.* 879, 879. doi:10.1063/1.2436201

Wang, L. M., Wang, S. X., Ewing, R. C., Meldrum, A., Birtcher, R. C., Newcomer Provencio, P., et al. (2000). Irradiation-Induced Nanostructures. *Mater. Sci. Eng. A* 286 (1), 72–80. doi:10.1016/S0921-5093(00)00677-8

Wang, X.-L., Hubbard, C. R., Alexander, K. B., Becher, P. F., Fernandez-Baca, J. A., and Spooner, S. (1994). Neutron Diffraction Measurements of the Residual Stresses in Al2O3-ZrO2 (CeO2) Ceramic Composites. *J. Am. Ceram. Soc.* 77, 1569–1575. doi:10.1111/j.1151-2916.1994.tb09758.x

Wen, J., Sun, C., Dholabhai, P. P., Xia, Y., Tang, M., Chen, D., et al. (2016). Temperature Dependence of the Radiation Tolerance of Nanocrystalline Pyrochlores A2Ti2O7 (A = Gd, Ho and Lu). *Acta Materialia* 110, 175–184. doi:10.1016/j.actamat.2016.03.025

Wittmaack, K. (2004). Reliability of a Popular Simulation Code for Predicting Sputtering Yields of Solids and Ranges of Low-Energy Ions. *J. Appl. Phys.* 96 (5), 2632–2637. doi:10.1063/1.1776318

Xiao, H. Y., Weber, W. J., Zhang, Y., and Zu, X. T. (2015). Ab Initio Molecular Dynamics Simulations of Ion-Solid Interactions in Zirconate Pyrochlores. *Acta Materialia* 87, 273–282. doi:10.1016/j.actamat.2015.01.019

Xu, J., Anand, V. K., Bera, A. K., Frontzek, M., Abernathy, D. L., Casati, N., et al. (2015). Magnetic Structure and crystal-field States of the Pyrochlore antiferromagnetNd2Zr2O7. *Phys. Rev. B* 92 (22), 224430. doi:10.1103/PhysRevB.92.224430

Yonezawa, S., Muraoka, Y., Matsushita, Y., and Hiroi, Z. (2004). Superconductivity in a Pyrochlore-Related Oxide KOs2O6. *J. Phys. Condens. Matter* 16 (3), L9–L12. doi:10.1088/0953-8984/16/3/L01

Zhang, J.-M., Zhang, Y., Xu, K.-W., and Ji, V. (2007). Young's Modulus Surface and Poisson's Ratio Curve for Cubic Metals. *J. Phys. Chem. Sol.* 68 (4), 503–510. doi:10.1016/j.jpcs.2007.01.025

Zhang, J., Wang, Y. Q., Tang, M., Sun, C., Yin, D. M., and Li, N. (2015). Helium Irradiation Induced Micro-swelling and Phase Separation in Pyrochlore Lu2Ti2O7. *Nucl. Instr. Methods Phys. Res. Section B: Beam Interactions Mater. Atoms* 342, 179–183. doi:10.1016/j.nimb.2014.09.036

Ziegler, J. F., Ziegler, M. D., and Biersack, J. P. (2010). SRIM - The Stopping and Range of Ions in Matter (2010). *Nucl. Instrum. Methods Phys. Res. B.* 268 (11–12), 1818–1823. doi:10.1016/j.nimb.2010.02.091

Conflict of Interest: The authors declare that the research was conducted in the absence of any commercial or financial relationships that could be construed as a potential conflict of interest.

Publisher's Note: All claims expressed in this article are solely those of the authors and do not necessarily represent those of their affiliated organizations, or those of the publisher, the editors and the reviewers. Any product that may be evaluated in this article, or claim that may be made by its manufacturer, is not guaranteed or endorsed by the publisher.

frontiers in Chemistry

ORIGINAL RESEARCH
published: 08 November 2021
doi: 10.3389/fchem.2021.705024

Thermodynamic and Structural Modelling of Non-Stoichiometric *Ln*-Doped UO_2 Solid Solutions, *Ln* = {La, Pr, Nd, Gd}

Victor L. Vinograd, Andrey A. Bukaemskiy, Giuseppe Modolo, Guido Deissmann and Dirk Bosbach*

Institute of Energy and Climate Research IEK 6, Nuclear Waste Management and Reactor Safety, Forschungszentrum Jülich, Jülich, Germany

Available data on the dependence of the equilibrium chemical potential of oxygen on degrees of doping, z, and non-stoichiometry, x, y, in $U_{1-z}Ln_zO_{2+0.5(x-y)}$ fluorite solid solutions and data on the dependence of the lattice parameter, a, on the same variables are combined within a unified structural-thermodynamic model. The thermodynamic model fits experimental isotherms of the oxygen potential under the assumptions of a non-ideal mixing of the endmembers, UO_2, $UO_{2.5}$, $UO_{1.5}$, $LnO_{1.5}$, and $Ln_{0.5}U_{0.5}O_2$, and of a significant reduction in the configurational entropy arising from short-range ordering (SRO) within cation-anion distributions. The structural model further investigates the SRO in terms of constraints on admissible values of cation coordination numbers and, building on these constraints, fits the lattice parameter as a function of z, y, and x. Linking together the thermodynamic and structural models allows predicting the lattice parameter as a function of z, T and the oxygen partial pressure. The model elucidates contrasting structural and thermodynamic changes due to the doping with $LaO_{1.5}$, on the one hand, and with $NdO_{1.5}$ and $GdO_{1.5}$, on the other hand. An increased oxidation resistance in the case of Gd and Nd is attributed to strain effects caused by the lattice contraction due to the doping and to an increased thermodynamic cost of a further contraction required by the oxidation.

Keywords: UO_2 fluorite, non-stoichiometry, oxidation resistance, lattice parameter, thermodynamic modelling

OPEN ACCESS

Edited by:
Maik Kurt Lang,
The University of Tennessee, United States

Reviewed by:
Xiaolong Zhu,
Merck (United States), United States
Anna Shelyug,
Institute of Solid State Chemistry, Russia

****Correspondence:***
V. L. Vinograd
v.vinograd@fz-juelich.de

Specialty section:
This article was submitted to Solid State Chemistry, a section of the journal Frontiers in Chemistry

Received: *04 May 2021*
Accepted: *22 September 2021*
Published: *08 November 2021*

Citation:
Vinograd VL, Bukaemskiy AA, Modolo G, Deissmann G and Bosbach D (2021) Thermodynamic and Structural Modelling of Non-Stoichiometric Ln*-Doped UO_2 Solid Solutions,* Ln *= {La, Pr, Nd, Gd}. Front. Chem. 9:705024. doi: 10.3389/fchem.2021.705024*

1 INTRODUCTION

One important aspect of a safety case for a geological repository for the high-level nuclear waste (e.g., UO_2-based spent nuclear fuel, SNF) is to characterize the corrosion behaviour of and the consequent radionuclide release from the disposed wastes, after waste containers will be eventually breached due to corrosion. After unloading from a reactor (e.g., a light water reactor), the SNF still contains ~95 wt% of uranium and ~5 wt% of fission products and transuranium elements (TRU), Pu, Am, and Cm. Fission and activation products formed during irradiation of oxide fuels (e.g., UO_2) could be classified into three categories, namely: 1) those forming metallic inclusions (e.g., Mo, Tc, Ru, Rh, and Pd), 2) those forming oxide precipitates (e.g., Rb, Cs, Ba, Zr, Nb, and Mo), and 3) those remaining as components of a solid solution with UO_2 (e.g., Sr, Zr, Nb, lanthanides (Ln), and TRU) (Kleykamp, 1988; Bruno and Ewing, 2006; Carbol et al., 2012; Ewing, 2015).

In the repository system groundwater is the principal medium for the transport of radionuclides from the waste to the environment including corrosion of the waste. The unique chemical conditions are characterized by 1) generally reducing conditions due to a significant amount of hydrogen produced due to the anoxic corrosion of metallic waste containers, 2) the presence of locally formed oxidizing conditions caused by radiolytic products such as H_2O_2, and 3) complex groundwater chemistry. The radiolytic oxidants evoke locally oxidizing effects at the spent fuel surface leading to an oxidative dissolution of the waste, due to the oxidation of poorly soluble U(IV) to easily soluble U(VI) (Shoesmith, 2000; Eriksen et al., 2012; Shoesmith et al., 2013; Bosbach et al., 2020; Hansson et al., 2021).

During the last decades, a number of studies addressed the corrosion behaviour of SNF, leading to a good phenomenological understanding of the instant release of radionuclides and long-term corrosion rates (Kleykamp, 1985; Fanghänel et al., 2013; Ewing, 2015; Lemmens et al., 2017; Curti and Kulik, 2020). Here we focus on the question how the doping of uranium dioxide by a variety of fission and activation products affects the corrosion rate under repository conditions.

As fission yields of lanthanides, such as La, Ce, Pr, and Nd, due to the fission of ^{235}U and ^{239}Pu are high (Kleykamp, 1985), leading to significant amount of lanthanides dissolved in the UO_2 matrix (up to 2–4 at%), UO_2–$LnO_{1.5}$ systems may serve as analogues of spent fuels illustrating certain aspects of burn-up on chemical stability (Ferry et al., 2005; Bruno and Ewing, 2006; Carbol et al., 2012). Effects of oxidative dissolution have been recently measured in aqueous (typically with H_2O_2 added) and in electrochemical systems both at corrosive (rest) potentials and at potentials promoting the conversion of U^{+4} to higher oxidation states. Such experiments applied to Gd-, Dy-, and Y-bearing samples have shown that the doping reduces dissolution yields and oxidative (anodic) currents relative to those measured for pure UO_2 (Trummer et al., 2010; Razdan and Shoesmith, 2013; Casella et al., 2016; Kim et al., 2017; Liu et al., 2017; Barreiro Fidalgo and Jonsson, 2019). Similar reductions of oxidation rates have been measured for simulated fuels (SIMFUELs) that in addition to lanthanides contain a variety of other dopants (He et al., 2007; Nilsson and Jonsson, 2011; Razdan and Shoesmith, 2013; Liu et al., 2017).

Despite this effort, mechanisms of resistance to oxidation in *Ln*- or Y-doped systems and in chemically more complex simulated fuels remain unclear. In several studies the stabilizing effect was linked to the formation of *Ln*-V_O clusters (V_O denotes an oxygen vacancy), which are thought to reduce the number of vacant sites that could host oxygen anions (Razdan and Shoesmith, 2013; Kim et al., 2017; Liu et al., 2017). The formation of these clusters has been discussed in the frame of a point-defect model of *Ln*-doped UO_2 by Park and Olander (Park and Olander, 1992). However, the fraction of such clusters in hyper-stoichiometric (oxidized) samples is predicted to be very small. Casella et al. (Casella et al., 2016) suggested that the stabilizing effect of Ln^{3+} could be related to its effectively negative charge that repels O-interstitials, O_i, and thus limits the fraction of interstitial sites able to accommodate an excess oxygen. Kim et al. (Kim et al., 2001) proposed that the decreased rates of oxidation in air measured on Gd-doped samples were due to a decreased fraction of U^{+4} (the fraction of cations able to be oxidized) caused by the ingrowth of Gd^{+3} and U^{+5}. Furthermore, as most of the experiments have been done with dopants that promoted lattice contraction, a proposition was made that the stabilizing effect could be caused by a reduced rate of diffusion of oxygen anions into the interstitial sites promoted by the contraction (Kim et al., 2017). The study of Kim et al. (Kim et al., 2017) further proposed that variations in electrochemical reactivity of Gd-doped samples characterized by different types of non-stoichiometry could be related to different degrees of lattice contraction observed on Gd-doping in hypo-, hyper- and strictly-stochiometric samples. The largest effect of Gd on the oxidative anodic currents was noted in hyper-stoichiometric samples, those characterised by the strongest decrease in the lattice parameter with doping (Kim et al., 2017).

The similarity of stabilizing effects due to the doping observed in electrochemical oxidation (He et al., 2007; Razdan and Shoesmith, 2013; Kim et al., 2017; Liu et al., 2017), in oxidative dissolution (Trummer et al., 2010; Casella et al., 2016; Barreiro Fidalgo and Jonsson, 2019) and in air oxidation experiments (Kim et al., 2001) suggests that all these phenomena might be linked to a common thermodynamic factor.

The resistance of the $UO_{2\pm\delta}$ solid solution to oxidation in air, where δ denotes deviation from stoichiometry, can be equated to the thermodynamic force (free energy) required for an insertion of an extra oxygen anion into its structure. This force at the thermodynamic equilibrium is proportional to the chemical potential of oxygen gas that is required for attaining a certain degree of hypo- or hyper-stoichiometry. Indeed, a large experimental effort has been invested in studying effects of *Ln*-doping on the chemical potential of oxygen in equilibrium with a given degree of hypo- or hyper-stoichiometry at a fixed temperature (Hagemark and Broli, 1967; Tetenbaum and Hunt, 1968; Javed, 1972; Saito, 1974; Une and Oguma, 1983a; Nakamura and Fujino, 1987; Lindemer and Sutton, 1988; Yoshida et al., 2011; Lee et al., 2016a; McMurray and Silva, 2016). These experiments invariably show that the larger the doping, the higher is the chemical potential, or, equivalently, the partial pressure of oxygen, at which a given degree of non-stoichiometry can be attained. Studies based on point-defect theory (Park and Olander, 1992), CALPHAD methodology (Saunders and Miodownik, 1998; Hillert, 2001) and on dual solution Gibbs energy minimization method (Karpov et al., 2001; Kulik et al., 2013) provided thermodynamically sound models able to predict the equilibrium partial pressure of oxygen at a given degree of doping and/or non-stoichiometry (Guéneau et al., 2011; McMurray et al., 2013; Degueldre et al., 2014; McMurray et al., 2015; Lee et al., 2016a; McMurray and Silva, 2016; Curti and Kulik, 2020). However, little effort has been so far invested in correlating these models with lattice parameter data. We argue here that a further understanding of mechanisms of oxidation resistance could be gained from a model that provides an accurate thermodynamic description of data on the dependence of the oxidation potential on the dopant type, on the degree of doping and non-stoichiometry, and

simultaneously evaluates the dependence of the lattice parameter of UO_2 on the same set of parameters. Previous research has shown that the lattice parameter, *a*, of fluorite solid solution changes markedly as a function of the type and degree of doping and the extent of non-stoichiometry (Ohmichi et al., 1981; Fukushima et al., 1983; Schreinemachers et al., 2014; Lee et al., 2016b; Schreinemachers et al., 2020). Combining this abundant structural information with thermodynamic data may provide means for understanding the role of the structure in the oxidation resistance of doped UO_2.

Here we develop structural-thermodynamic models for $U_{1-z}Ln_zO_{2+0.5(x-y)}$ solid solutions (*Ln* = {La, Pr, Nd, Gd}), in which the non-stoichiometry, $0.5(x-y)$, originates due to the presence of a fraction *x* of $UO_{2.5}$ ($U = U^{+5}$) and/or a fraction *y* of $AO_{1.5}$ ($A = Ln^{+3}, U^{+3}$) components. The aim is to predict the non-stoichiometry, the equilibrium cation species fractions and the lattice parameter, *a*, as functions of the composition, *z*, the temperature *T*, and the partial pressure of oxygen, P_{O_2}, that is measured relative to the standard pressure, P^0 (P^0 = 101325 Pa). The parameters *x* and *y* thus define the degrees of hyper- and hypo-stoichiometry reflecting the presence of oxygen interstitials or oxygen vacancies, respectively. The term "cation species", in contract to simply a "cation", includes the information on both the chemical type of a cation and its coordination number in the fluorite solid solution. For example, $U^{4,7}$ denotes U^{+4} in the 7-fold coordination. The coordination numbers are important as they determine the cation sizes and, thus, the lattice parameter. The systems of *Ln* = {La, Pr, Nd, Gd} are particularly convenient for such a study as they cover contrasting cases of the lattice response to $LnO_{1.5}$ doping: the extension, i.e. a positive d*a*/d*x* slope (La), a close to zero slope (Pr) and a negative slope (Nd, Gd). The thermodynamic part is worked out via a fit to $\log(P_{O_2}/P^0)$ data vs. non-stoichiometry data at a fixed value of *T*. The structural part is based on fitting the lattice parameter data via an ion-close-packing concept (Ohmichi et al., 1981; Lee et al., 2016b; Bukaemskiy et al., 2021). This concept includes the dependence of average cation radii on average cation coordination numbers that vary as functions of composition and non-stoichiometry and assigns a certain fixed radius to the oxygen vacancy (Bukaemskiy et al., 2021; Vinograd and Bukaemskiy, 2021). The cation radii are either taken from Shannon (Shannon, 1976) or fitted to available *a* vs. *z*, and *a* vs. O/M data. The relationship between the thermodynamic and structural description is set via common assumptions on cation and anion distribution and ordering. These assumptions, on the one hand, constrain equations for the entropy/enthalpy of mixing and, on the other hand, limit allowed values of cation coordination numbers imposing constrains on the average cation radius and, thus, on the lattice parameter.

An important practical aspect of the present study is the development of a model that relates the equilibrium lattice parameter, *a*, to *z*, *x*, and *y* and simultaneously to *T* and P_{O_2}. The model can, thus, be used to calculate P_{O_2} or *T* at synthesis conditions from *a* vs. *z* plots and to predict P_{O_2} and *T* that are required for synthesising samples with a desired degree on non-stoichiometry and a desired derivative d*a*/d*x*. The model consistently reproduces the relationship that the higher the level of doping, the higher is the oxidation potential that is required to equilibrate a sample of a given degree of hyper-stoichiometry at a given temperature, while this dependence is enhanced within the row of La < Pr < Nd < Gd.

2 METHODS AND MODELS

2.1 Thermodynamic Model

The thermodynamic model assumes a system of a constant chemical composition at a given temperature. The composition of the solid phase is defined by the fractions *z* and 1–*z* of the chemical endmembers with the compositions of $LnO_{1.5}$ and UO_2, respectively. We also assume that a system includes a large fixed amount of O_2 gas with its partial pressure maintained at a given value. The endmember UO_2 is assumed to exist in three different structural forms, namely, the stoichiometric UO_2, the hypo-stoichiometric $UO_{1.5}$ associated with ¼ moles of O_2 gas and the hyper-stoichiometric $UO_{2.5}$ associated with a negative amount of ¼ moles of O_2. The negative sign implies that when excess O is inserted into UO_2, an equivalent quantity (in moles) of O_2 gas annihilates in the system. The equal sum of the endmembers $LnO_{1.5}$ and UO_2 reacts producing the fifth endmember, $Ln_{0.5}U_{0.5}O_2$–1/8 O_2 (**Figure 1**), which is also associated with a negative amount of O_2 gas. When not explicitly indicated, the list of the endmembers will be associated with low case indices in the order 1- $UO_{1.5}$, 2- UO_2, 3- $UO_{2.5}$, 4- $LnO_{1.5}$, and 5- $Ln_{0.5}U_{0.5}O_2$. This set of endmembers is sufficient to describe variations in stoichiometry of fluorite solid solutions at not too large fractions of $LnO_{1.5}$. Fractions larger than $z = 0.5$ may require the consideration of the $U_{1/3}Ln_{2/3}O_2$ endmember to describe stoichiometric states and the UO_3 endmember to describe hyper-stoichiometry. Both these endmembers contain U^{+6}. As the final aim of this study is to characterize the oxidation resistance of SNF, in which the content of $LnO_{1.5}$ does not exceed few atomic percent, we have chosen to limit the set of U species to U^{+3}, U^{+4}, and U^{+5}. Thus, the present model should be applied with caution when $z > 0.5$. The gas phase component associated with an endmember will be often omitted for brevity. For example, the endmember $UO_{2.5}$ means a $UO_{2.5}$ coexisting with a negative amount of ¼ moles of O_2 gas. This recognition is important in the following definition of the standard Gibbs free energies of the endmembers. The free energy of each endmember is composed of two contributions, one arising from a solid-state transformation (insertion/deletion of 0.5 mole of O into/from the UO_2 structure) and one arising from a creation (or an annihilation) of an equivalent amount of O_2 gas. The latter contribution is proportional to the chemical potential of O_2. The sum of these contributions is modelled relative to an equivalent combination of the free energies of $LnO_{1.5}$ and stoichiometric UO_2. The free energies of the latter endmembers are set equal zero. As the standard free energies of the other endmembers explicitly depend on the chemical potential, a change in the chemical potential, or a change in the partial pressure of O_2, induces a change in endmember fractions. When the pressure is low (the chemical potential of O_2 is strongly negative), $UO_{1.5}$ + ¼ O_2

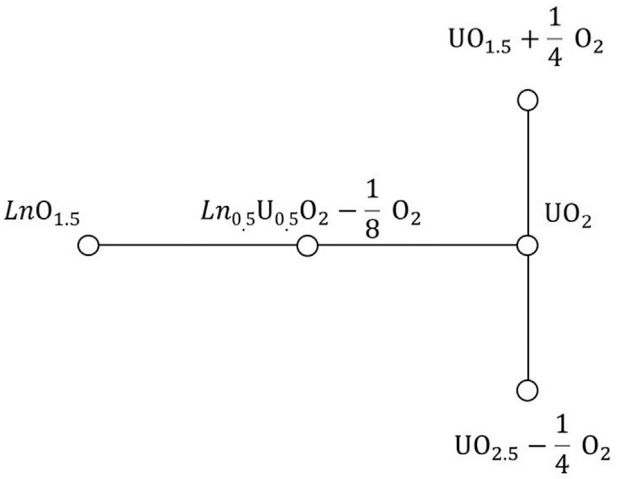

FIGURE 1 | Relationship between endmembers of the thermodynamic model. Note, that all Ln-free endmembers have the same chemical composition of UO_2.

endmember is stabilised over UO_2. When the chemical potential is close to zero, $UO_{2.5}$ – ¼ O_2 is stabilised over UO_2, consistently with the thermodynamic instability of UO_2 in air. A shift of the endmember fractions towards the formation of the $UO_{2.5}$ and $Ln_{0.5}U_{0.5}O_2$ implies an oxidation of a fraction of U^{+4} to U^{+5}, while a relative increase in the fraction of $UO_{1.5}$ implies a reduction of a fraction of U^{+4} to U^{+3}. The equilibrium endmember fractions are obtained via the minimization of the Gibbs free energy, which includes an additive sum of endmember contributions, a non-ideal term arising from the interactions between the endmembers and an entropic term. The equilibrium calculations are done here using a specially written FORTRAN code.

2.1.1 A Model of $UO_{2+0.5(x-y)}$

Pure UO_2 fluorite is described here as a combination of two binary solid solution models spanning between the endmembers UO_2 and $UO_{1.5}$, in the first case, and UO_2 and $UO_{2.5}$, in the second case. U^{+6} states, i.e. the UO_3 endmember, are not included within the present effort. The free energy of stoichiometric UO_2 is set equal to zero, while the free energies of $UO_{2.5}$ – ¼ O_2 and $UO_{1.5}$ + ¼ O_2 endmembers are set equal to the effects of the reactions

$$UO_2 = UO_{2.5} - \frac{1}{4}O_2 \tag{1}$$

and

$$UO_2 = UO_{1.5} + \frac{1}{4}O_2 \tag{2}$$

For example, the effect of **Eq. 1** splits into the effect of addition of 0.5 mole of O into the solid and the effect of annihilation of ¼ moles of O_2 gas prepared at a given temperature T with a given partial pressure

$$G_{UO2.5} = \Delta G^0_{UO2.5} - (T - T^0)\Delta S^0_{UO2.5} - \frac{1}{4}\mu^{T,P^0}_{O_2} \tag{3}$$

Similarly, the effect of **Eq. 2** splits into the effect of removing of 0.5 mole of O from the solid and the effect of creating of ¼ moles of O_2 gas

$$G_{UO1.5} = \Delta G^0_{UO1.5} - (T - T^0)\Delta S^0_{UO1.5} + \frac{1}{4}\mu^{T,P^0}_{O_2} \tag{4}$$

The parameters ΔG^0_i and ΔS^0_i are determined by fitting. The chemical potential of O_2 gas is computed as

$$\mu^{T,P^0}_{O_2} = -S^0_{O_2}(T - T^0) + C_{p^0_{O_2}}\left(T - T^0 - Tln\left(\frac{T}{T^0}\right)\right) + RT\ln\left(P_{O_2}/P^0\right) \tag{5}$$

where $S^0_{O_2}$ = 205.1373 J/K/mol and $C_{p^0_{O_2}}$ = 29.355 J/K/mol and where P^0 = 101,325 Pa, $T^0 = 298.15k$ (Finnis et al., 2005).

The reference Gibbs free energies for hypo-stoichiometric, $UO_{2\text{-}0.5y}$, and hyper-stoichiometric solutions, $UO_{2+0.5x}$, are written as follows

$$G_{hypo} = yG_{UO1.5} + (1 - y)G_{UO2} \tag{6}$$

and

$$G_{hyper} = xG_{UO2.5} + (1 - x)G_{UO2} \tag{7}$$

respectively, where y and x are the mole fractions of the components $UO_{1.5}$ and $UO_{2.5}$. Naturally, only the solid part of an endmember contributes to the structural formula, however, an equivalent positive or negative mole fraction of O_2 gas is always associated with it. Thus, the quantities in **Eqs. 6**, **7** depend on the chemical potential of O_2. The excess free energies are given as follows

$$G^{exess}_{hypo} = y(1 - y)\left(W^h_{13} - TW^s_{13}\right) \tag{8}$$

and

$$G^{exess}_{hyper} = x(1 - x)\left(W^h_{23} - TW^s_{23}\right) \tag{9}$$

where W^h_{13} and W^s_{13} refer to the interaction between solid $UO_{1.5}$ and UO_2 and W^h_{23} and W^s_{23} refer the interaction between solid UO_2 and $UO_{2.5}$. The upper indices "h" and "s" denote enthalpic and entropic parts of the interaction parameters. All these parameters are determined by fitting.

Modelling the configurational entropy of anions requires consideration of effects of local order. Following (Bukaemskiy et al., 2021; Vinograd and Bukaemskiy, 2021) we assume a type of a short-range ordering in which two vacancies cannot approach each other closer than the fourth nearest anion-anion distance. Such a distribution can be emulated by restricting the location of vacancies to a simple cubic sublattice of the anion lattice in which the nearest distance is equal to the fourth nearest distance of the original anion lattice. This model implies that the mixing of vacancies and oxygen anions occurs on 1/8-th of available anion sites, while the concentration of vacancies within the sublattice is 8 times larger than the average concentration of vacancies of $0.25y$. These assumptions lead to the equation

$$S^{conf}_{O/V} = -0.25R\left(2y\ln(2y) + (1-2y)\ln(1-2y)\right) \quad (10)$$

which is valid for $0 < y < 0.5$. A more detailed derivation of **Eq. 10** and of other entropy equations that appear further in the text is given in the Supplementary Materials.

The hyper-stoichiometric solution is characterized by the presence of oxygen interstitials, which are assumed to occupy octahedral sites. One of recent simulation studies provided arguments in favour of a model containing mono- and di-interstitials, with the proportion of di-interstitials increased at larger values of x (Palomares et al., 2019). Two types of di-interstitial cluster, the Willis cluster (Willis, 1978) and the split di-interstitial (Andersson et al., 2009) have been proposed based on neutron diffraction experiments and ab initio calculations. On the other hand, structural studies of compositions close to U_4O_9 stoichiometry ($x = 0.5$) suggested the presence of cubooctahedral clusters composed of interstitials and lattice anions shifted from their ideal positions (Bevan et al., 1986). We assume here that the appearance of cubooctahedral clusters signifies a transition from a defect fluorite type solid solution to a solid solution based of a U_4O_9-type structure and do not make an attempt of modelling the latter. We assume that the distribution of interstitials in hyper-stoichiometric defect fluorite could be simulated assuming the presence of mono- and di-interstitials only. To emulate the presence of just two types of clusters (i.e., the absence of higher-order clusters) we assume the existence of a sublattice within the ideal FCC lattice of interstitials, which is composed of an ordered arrangement of isolated (non-overlapping) pairs of initially vacant interstitial sites. Such an arrangement implies that only ¼ of totally available vacant sites can be occupied by O-interstitials. The concentration of interstitials within such a sublattice increases in four times from the value of $0.5x$ to the value of $2x$. We further assume that the occupation of pairs of vacant sites within the sublattice occurs randomly. These assumptions lead to the following equation for the entropy of mixing

$$S^{conf}_{Oi/Vi} = -0.25R\left(2x\ln(2x) + (1-2x)\ln(1-2x)\right) \quad (11)$$

which is valid in hyper-stoichiometric domain of $0 < x < 0.5$. Accidentally, this equation is similar to **Eq. 10**. This circumstance appears important as the thermodynamic data on $UO_{2+0.5(x-y)}$ show a nearly symmetric relationship between hypo- and hyper-stoichiometric branches of $\log\left(P_{O_2}/P^0\right)$ data vs. non-stoichiometry.

The splitting of the model into the independent "hypo" and "hyper" domains is based on the assumptions that the reactions

$$O = O_i + V \quad (12)$$

and

$$2U^{+4} = U^{+3} + U^{+5} \quad (13)$$

do not occur separately from each other and that both are strongly shifted to the left. Practically, we assume that oxygen vacancies and oxygen interstitials annihilate each other, and the same assumption is made for U^{+3} and U^{+5} cations. These assumptions are reasonable at not too high temperatures considering large enthalpy effects of ~4 and ~1.5 eV computed for these reactions ab initio (Nerikar et al., 2009; Cooper et al., 2018). The present model is thus not intended for modelling of UO_2 at very high temperatures (~2000 K and above), where these assumptions become invalid. A consequence of these assumptions is that the chemical potential of O_2 in equilibrium with pure UO_2 cannot be defined, i.e. pure UO_2 coexists with a range of $\log(P_{O_2}/P^0)$ values. A further simplification made here is that the entropy effects associated with U^{+4}/U^{+5} and U^{+4}/U^{+3} mixing cannot be separated out from the effects of O_i/V_i and O/V mixing. Thus, we count only the entropy effects associated with the anions. A possible physical interpretation behind ignoring the entropy effects due to U^{+4}/U^{+5} and U^{+4}/U^{+3} mixing is that the electron distribution that distinguishes U^{+5}/U^{+3} from U^{+4} adjusts itself spontaneously to a given arrangement of oxygen vacancies or oxygen interstitials.

2.1.2 *Ln*-Doped UO_2-Based Solid Solutions

Ln^{+3} can be charge balanced in the fluorite solid solution according to two different schemes

$$U^{+4} + \frac{1}{2}O^{-2} = Ln^{+3} + \frac{1}{2}V \quad (14)$$

and

$$2U^{+4} = Ln^{+3} + U^{+5} \quad (15)$$

The first scheme implies the creation of oxygen vacancies. The second scheme requires an oxidation of one U^{+4} cation per one Ln^{+3}. These schemes are put into the correspondence with $LnO_{1.5}$ and $Ln_{0.5}U_{0.5}O_2$ endmembers, respectively, where the latter implies the simultaneous addition of equal fractions of Ln^{+3} and U^{+5}. The free energy of $Ln_{0.5}U_{0.5}O_2$ endmember is defined here via the reaction

$$\frac{1}{2}UO_2 + \frac{1}{2}LnO_{1.5} = Ln_{0.5}U_{0.5}O_2 - \frac{1}{8}O_2 \quad (16)$$

as follows

$$G_{Ln0.5U0.5O2} = \Delta G^0_{Ln0.5U0.5O2} - \left(T - T^0\right)\Delta S^0_{Ln0.5U0.5O2} - \frac{1}{8}\mu^{T,P^0}_{O_2} \quad (17)$$

According to the previously made assumption, U^{+5} cannot occur together with U^{+3}, as these cations annihilate each other via inverse reaction (**Eq. 13**). Thus, the $Ln_{0.5}U_{0.5}O_2$ and $UO_{1.5}$ endmembers cannot occur together. Due to this circumstance, doped hypo-stoichiometric solid solutions at a given fraction z of $LnO_{1.5}$ could be conveniently split into two types, I and II, defined by the inequalities $0.5 > y > z$ and $z > y > 0$, respectively. The relationship of $0.5 > y > z$ implies that the fraction of vacancies is larger than this occurring due to the sole presence of the $LnO_{1.5}$ endmember. Thus, $UO_{1.5}$ endmember must necessarily be present creating an

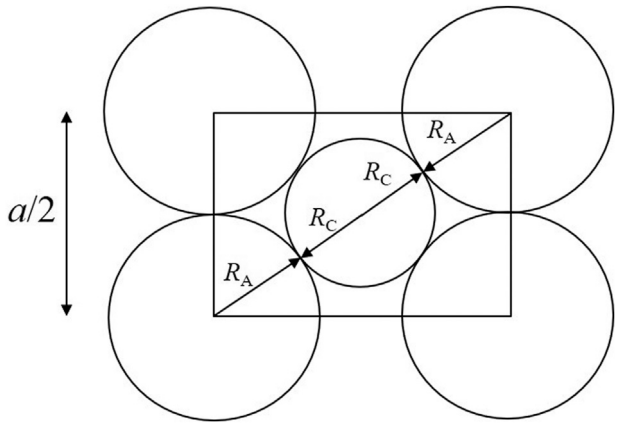

FIGURE 2 | Geometric relationship used in the ion-packing model. The rectangle corresponds to the cross section of a cube composed of eight anions along its face diagonal. The spheres representing cations and anions are constrained to touch along the body diagonal. An additional condition (not used in the ion-packing model) could be set by requiring the spheres of anions to touch themselves along [100].

additional fraction of vacancies. This also implies that in such a solid solution Ln occurs only as $LnO_{1.5}$. On the other hand, the relationship of $z > y > 0$ implies that the fraction of vacancies is smaller than this occurring due to the sole presence of $LnO_{1.5}$, thus, a certain fraction of $LnO_{1.5}$ is to be converted into $Ln_{0.5}U_{0.5}O_2$. This second case is further split into the sub-cases IIa and IIb depending on $z < 0.5$ and $z > 0.5$. First, we consider the case I of $0.5 > y > z$.

2.1.3 Hypo-Stoichiometric Solid Solution, $z < y < 0.5$, Type I

The reference free energy is spanned by the three endmembers UO_2, $UO_{1.5}$, and $LnO_{1.5}$ according to the following equation

$$G^{\mathrm{ref}}_{\mathrm{hypo,I}} = \sum\nolimits_i X_i G_i \tag{18}$$

The excess free energy is given by

$$G^{\mathrm{exess}}_{\mathrm{hypo,I}} = \sum\nolimits_{j\neq i} X_i X_j \left(W^{\mathrm{h}}_{ij} - TW^{\mathrm{s}}_{ij}\right) \tag{19}$$

where $X_{\mathrm{UO2}} = 1 - y$, $X_{\mathrm{UO1.5}} = y - z$, $X_{Ln\mathrm{O1.5}} = z$

The configurational entropy of this solid solution has two contributions. The already familiar contribution due to the mixing of vacancies and lattice O^{2-} anions is given by **Eq. 10**. The contribution due to the mixing of Ln^{+3} with U^{+4}, and U^{+3} requires a special consideration. In a solid solution, in which the radii of III- and IV-valent cations have similar sizes, the III-valent cations are expected to be associated with vacancies (Solomon et al., 2014). This association is modelled here by requesting the coordination number of III-valent cations to be 7. The consequence is that Ln^{+3} can mix only with 7-fold U cations, the restriction that directly affects the configurational entropy. One can further note that the total fraction of 7-fold cations in such a solid solution is $2y$. The structural formula becomes $U^{4,8}_{1-2y}U^{4,7}_{y}Ln^{3,7}_{z}U^{3,7}_{y-z}O_{2-0.5y}$. This formula, in turn, implies that Ln^{+3} can mix with U cations only over $2y$ sites. The configurational entropy is thus given by the following equation

$$S^{\mathrm{conf}}_{\mathrm{hypo,I}} = -R\left(z\ln\left(\frac{z}{2y}\right) + (2y - z)\ln\left(\frac{2y - z}{2y}\right)\right) \tag{20}$$

A more detailed derivation of this equation is given in Supplementary Materials.

The total Gibbs free energy of the model is then given as

$$G_{\mathrm{hypo,I}} = G^{\mathrm{ref}}_{\mathrm{hypo,I}} + G^{\mathrm{exess}}_{\mathrm{hypo,I}} - T\left(S^{\mathrm{conf}}_{\mathrm{OV}} + S^{\mathrm{conf}}_{\mathrm{hypo,I}}\right) \tag{21}$$

which is a function of z, T, P_{O_2}, and y. The equilibrium relationship between all these parameters is obtained via the minimization of **Eq. 21** with respect to y.

2.1.4 Hypo-Stoichiometric Solid Solution, $0 < y < z$, $z < 0.5$, Type IIa

In this case the endmember $UO_{1.5}$ is absent, thus U^{+5} formation is allowed, and, thus, two *Ln*-bearing endmembers can co-exist. The reference and the excess free energies are given by the equations

$$G^{\mathrm{ref}}_{\mathrm{hypo,IIa}} = \sum\nolimits_i X_i G_i \tag{22}$$

and

$$G^{\mathrm{exess}}_{\mathrm{hypo,IIa}} = \sum\nolimits_{j\neq i} X_i X_j \left(W^{\mathrm{h}}_{ij} - TW^{\mathrm{s}}_{ij}\right) \tag{23}$$

where $X_{\mathrm{UO2}} = 1 - y - 2(z - y)$, $X_{Ln0.5U0.5O2} = 2(z - y)$, $X_{Ln\mathrm{O1.5}} = y$.

As in the case I, we assume that III-valent cations, i.e. Ln^{+3}, are associated to vacancies. However, a part of *Ln* cations is involved in building the $Ln_{0.5}U_{0.5}O_2$ endmember, which is intrinsically stoichiometric. Thus, it is natural to expect that a fraction $z–y$ of *Ln* cations remains in 8-fold coordination. As the total fraction of 7-fold cations is $2y$, a fraction of y U^{+4} cations need to be

TABLE 1 | Structural formulas of the solid solution models and the expressions to calculate average cation radii.

	Structural formula	R_C
I	$U^{4,8}_{1-2y}U^{4,7}_{y}Ln^{3,7}_{z}U^{3,7}_{y-z}O_{2-0.5y}$	$(1-2y)R^{4,8}_{U} + yR^{3,7}_{U} + zR^{3,7}_{Ln} + (y-z)R^{3,7}_{U}$
IIa	$U^{4,8}_{1-2z}Ln^{3,8}_{z-y}U^{5,8}_{z-y}Ln^{3,7}_{y}U^{4,7}_{y}O_{2-0.5y}$	$(1-2z)R^{4,8}_{U} + y(R^{4,7}_{U} + R^{3,7}_{Ln}) + (z-y)(R^{3,8}_{U} + R^{5,8}_{U})$
IIb	$U^{4,7}_{1-2z+y}Ln^{3,7}_{y+z-0.5}U^{5,7}_{z-0.5}Ln^{3,8}_{0.5-y}U^{5,8}_{0.5-y}O_{2-0.5y}$	$(1-2z+y)R^{4,7}_{U} + (y+z-0.5)R^{3,7}_{Ln} + (z-0.5)R^{5,7}_{U} + (0.5-y)(R^{3,8}_{Ln} + R^{5,8}_{U})$
III	$U^{4,8}_{1-2z-x}Ln^{3,8}_{z}U^{5,8}_{z}U^{5,9}_{x}O_{2+0.5x}$	$(1-2z-x)R^{4,8}_{U} + z(R^{3,8}_{Ln} + R^{5,8}_{U}) + xR^{5,9}_{U}$

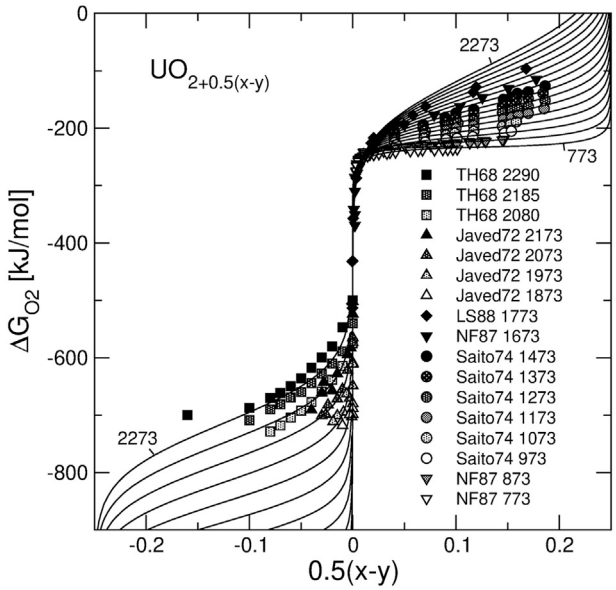

FIGURE 3 | Oxygen chemical potential plotted vs. non-stoichiometry parameter of $UO_{2+0.5(x-y)}$. Solid lines are the isotherms predicted with the model. The temperature range is from 773 to 2273 K. The experimental data are from Tetenbaum and Hunt (Tetenbaum and Hunt, 1968), Javed (Javed, 1972), Lindemer and Sutton (Lindemer and Sutton, 1988), Nakamura and Fujino (Nakamura and Fujino, 1987) and Saito (Saito, 1974).

transferred into the 7-fold coordination. The structural formula takes the form $U^{4,8}_{1-2z}Ln^{3,8}_{z-y}U^{5,8}_{z-y}Ln^{3,7}_{y}U^{4,7}_{y}O_{2-0.5y}$. The configurational entropy of cations has two contributions, one from cations in the 7-fold coordination and one from cations in the 8-fold coordination, which occur with the total fractions of $2y$ and $1–2y$, respectively. Both contributions are combined below in one equation as follows

$$S^{\mathrm{conf}}_{\mathrm{hypo,IIa}} = 2Ry\ln 2 - R\left((1-y-z)\ln\left(\frac{1-y-z)}{1-2y}\right) + (z-y)\ln\left(\frac{z-y}{1-2y}\right)\right) \quad (24)$$

The total Gibbs free energy of the model is then given as

$$G_{\mathrm{hypo,IIa}} = G^{\mathrm{ref}}_{\mathrm{hypo,IIa}} + G^{\mathrm{exess}}_{\mathrm{hypo,IIa}} - T\left(S^{\mathrm{conf}}_{\mathrm{O/V}} + S^{\mathrm{conf}}_{\mathrm{hypo,IIa}}\right) \quad (25)$$

This model is valid for $z < 0.5$. When $z = 0.5$, all $U^{4,8}$cations become exhausted. The next model overcomes this constraint by transferring a fraction of $Ln^{3,8}$ and $U^{5,8}$cations into the 7-fold coordination.

2.1.5 Hypo-Stoichiometric Solid Solution, $2z - 1 < y < 0.5$, $0.5 < z < 0.75$, Type IIb

When $z > 0.5$, the fraction of $Ln^{3,8}$ and the same fraction of $U^{5,8}$ can be written as $z - y = (0.5–y) + (z - 0.5)$. If $z > 0.5$ this arrangement would violate the requirement that the total fraction of 8-fold cations is $1 - 2y$. We assume that the fractions $z - 0.5$ of $Ln^{3,8}$ and $z - 0.5$ of $U^{5,8}$cations are transferred to the 7-fold coordination. The structural formula takes the form $U^{4,7}_{1-2z+y}Ln^{3,7}_{y+z-0.5}U^{5,7}_{z-0.5}Ln^{3,8}_{0.5-y}U^{5,8}_{0.5-y}O_{2-0.5y}$ and the configurational entropy is given as:

$$S^{\mathrm{conf}}_{\mathrm{hypo,IIb}} = -2R(0.5-y)\ln\frac{0.5-y}{1-2y} - R\left((y+z-0.5)\ln\left(\frac{y+z-0.5}{2y}\right) + (y-z+0.5)\ln\left(\frac{y-z+0.5}{2y}\right)\right) \quad (26)$$

Other equations remain same as in the case IIa.

2.1.6 Hyper-Stoichiometric Solution, Type III

Assuming that vacancies are absent at hyper-stoichiometric compositions, Ln^{+3} can occur only as $Ln_{0.5}U_{0.5}O_2$. Consequently, there are two fractions of U^{+5}, a fraction of U^{+5}, that is needed to balance Ln^{+3}, and a fraction of U^{+5} that is needed to balance O-interstitials. The reference Gibbs free energy and the excess Gibbs free energy are given as follows

$$G^{\mathrm{ref}}_{\mathrm{hyper}} = \sum_i X_i G_i \quad (27)$$

$$G^{\mathrm{exess}}_{\mathrm{hyper}} = \sum_{j\neq i} X_i X_j\left(W^{\mathrm{h}}_{ij} - TW^{\mathrm{s}}_{ij}\right) \quad (28)$$

where $X_{\mathrm{UO2}} = 1 - 2z - x$, $X_{\mathrm{Ln0.5U0.5O2}} = 2z$, $X_{\mathrm{UO2.5}} = x$.

Considering that $Ln_{0.5}U_{0.5}O_2$ is intrinsically stoichiometric, all Ln^{+3} cations and the equivalent fraction of U^{+5} cations are assumed to be in 8-fold coordination. The other U^{+5} cations that balance the interstitials may formally be prescribed coordination numbers larger than 8, because O-interstitials are expected to be in a close association to these cations due to the attraction of

TABLE 2 | Fitted standard state parameters defining the thermodynamic properties of the endmembers.

	i	ΔG_i^0(kJ/mol)	ΔS_i^0 (J/K/mol)
UO_2	2	0	0
$LnO_{1.5}$	4	0	0
$UO_{1.5}$	1	336.9	16.7
$UO_{2.5}$	3	−75.0	30.6
$Gd_{0.5}U_{0.5}O_2$	5	−64.65	6.0
$Nd_{0.5}U_{0.5}O_2$	5	−63.3	12.0
$Pr_{0.5}U_{0.5}O_2$	5	−60.4	16.0
$La_{0.5}U_{0.5}O_2$	5	−56.25	10.0

TABLE 3 | Margules interaction parameters in kJ/mol determined via a model fit to the thermodynamic data.

	i	*j*	W_{ij}^h	W_{ij}^s
UO_2—$UO_{2.5}$	2	3	24.37	18.75
UO_2—$UO_{1.5}$	2	1	17.30	11.9
$Gd_{0.5}U_{0.5}O_2$—$UO_{2.5}$	5	3	40.0	0
$Nd_{0.5}U_{0.5}O_2$—$UO_{2.5}$	5	3	35.0	0
$Pr_{0.5}U_{0.5}O_2$—$UO_{2.5}$	5	3	30.0	0
$La_{0.5}U_{0.5}O_2$—$UO_{2.5}$	5	3	15.0	0
$GdO_{1.5}$—UO_2	4	2	60.0	0
$NdO_{1.5}$—UO_2	4	2	40.0	0
$PrO_{1.5}$—UO_2	4	2	60.0	0
$LaO_{1.5}$—UO_2	4	2	70.0	0
$Ln_{0.5}U_{0.5}O_2$—UO_2	5	2	0	0
$LnO_{1.5}$—$UO_{1.5}$	4	1	0	0
$Ln_{0.5}U_{0.5}O_2$—$LnO_{1.5}$	5	4	0	0

differently charged species. For simplicity we assign to all these atoms the 9-fold coordination. The structural formula of doped hyper-stoichiometric solid solution is $U^{4,8}_{1-x-2z}Ln^{3,8}_z U^{5,8}_z U^{5,9}_x O_{2+0.5x}$.

As Ln^{+3} cations are assumed to preserve the coordination of 8, they can be mixed with U atoms only over the fraction 1 − x of 8-fold coordinated sites, thus the configurational entropy of cations is given by the equation

$$S^{\text{conf}}_{\text{hyper}} = -R\left((1-x-z)\ln\left(\frac{1-x-z}{1-x}\right) + z\ln\left(\frac{z}{1-x}\right)\right) \quad (29)$$

The total Gibbs free energy of the model is then given as

$$G_{\text{hyper}} = G^{\text{ref}}_{\text{hyper}} + G^{\text{exess}}_{\text{hyper}} - T\left(S^{\text{conf}}_{\text{Oi/Vi}} + S^{\text{conf}}_{\text{hyper}}\right) \quad (30)$$

which is a function of z, T, P_{O_2}, and x. An equilibrium relationship between all these parameters is obtained via the minimization of **Eq. 30** with respect to x.

2.2 Structural Model

Previous research has shown that the lattice parameter of UO_2 solid solutions varies as a function of the composition and non-stoichiometry, and that these variations could be predicted based on an ionic packing model (Ohmichi et al., 1981; Fukushima et al., 1983; Lee et al., 2016b; Bukaemskiy et al., 2021). This model utilizes a geometrical relationship between the lattice parameter, a, and the sum of the averaged radii of cations, R_C, and anions, R_A

$$a = \frac{4}{\sqrt{3}}\left(\langle R_C\rangle + \langle R_A\rangle\right), \quad (31)$$

which is determined by **Figure 2**.

The radii of cation/anions are further evaluated as sums all of cation/anion radii weighted by the cation/anion fractions that contribute to the structural formula, where the anions include the lattice oxygen O^{2-} and the oxygen vacancy

$$\langle R_A\rangle = (1-0.25y)R_O + 0.25yR_V \quad (32)$$

$$\langle R_C\rangle = \sum_C\sum_K\sum_i X_C^{i,K}R_C^{i,K} \quad (33)$$

where $R_C^{i,K}$ and $X_C^{i,K}$ are the radius and the fraction of a C cation in i oxidation state and K-fold coordination and where R_O and R_V are the effective radii of the lattice oxygen anion and of the oxygen vacancy. The upper-case indices are used to characterize both the charge and the coordination number of a cation.

Following the study of Bukaemskiy et al. (Bukaemskiy et al., 2021) we assume that a vacancy has a defined radius that is larger than the ionic radius of oxygen. Such a model is consistent with the requirement that the average cation coordination number in hypo-stochiometric samples, K, is smaller than eight. An alternative description (Hong and Virkar, 1995; Marrocchelli et al., 2012; Marrocchelli et al., 2013) maintains the vacancy to be smaller than the radius of O^{2-}, while keeping the coordination number of all cations equal to eight. We emphasize that in our approach the cation coordination numbers are made consistent not only with the condition of $K = 8 - 2y$, but also with assumptions of short-range anion ordering. Interstitials do not contribute to **Eq. 32**. Thus, the average anion radius in the case of

TABLE 4 | Cation radii (in Å) accepted in the study.

C^i	$R_C^{i,7}$	$R_C^{i,8}$	$R_C^{i,9}$
Gd^3	1.0012	1.0537	
Nd^3	1.0476	1.0994	
Pr^3	1.0680	1.1190	
La^3	1.1014	1.1665	
U^3	1.0995	1.1547	
U^4	0.9400	0.9952	
U^5	0.8400	0.8635	0.9760

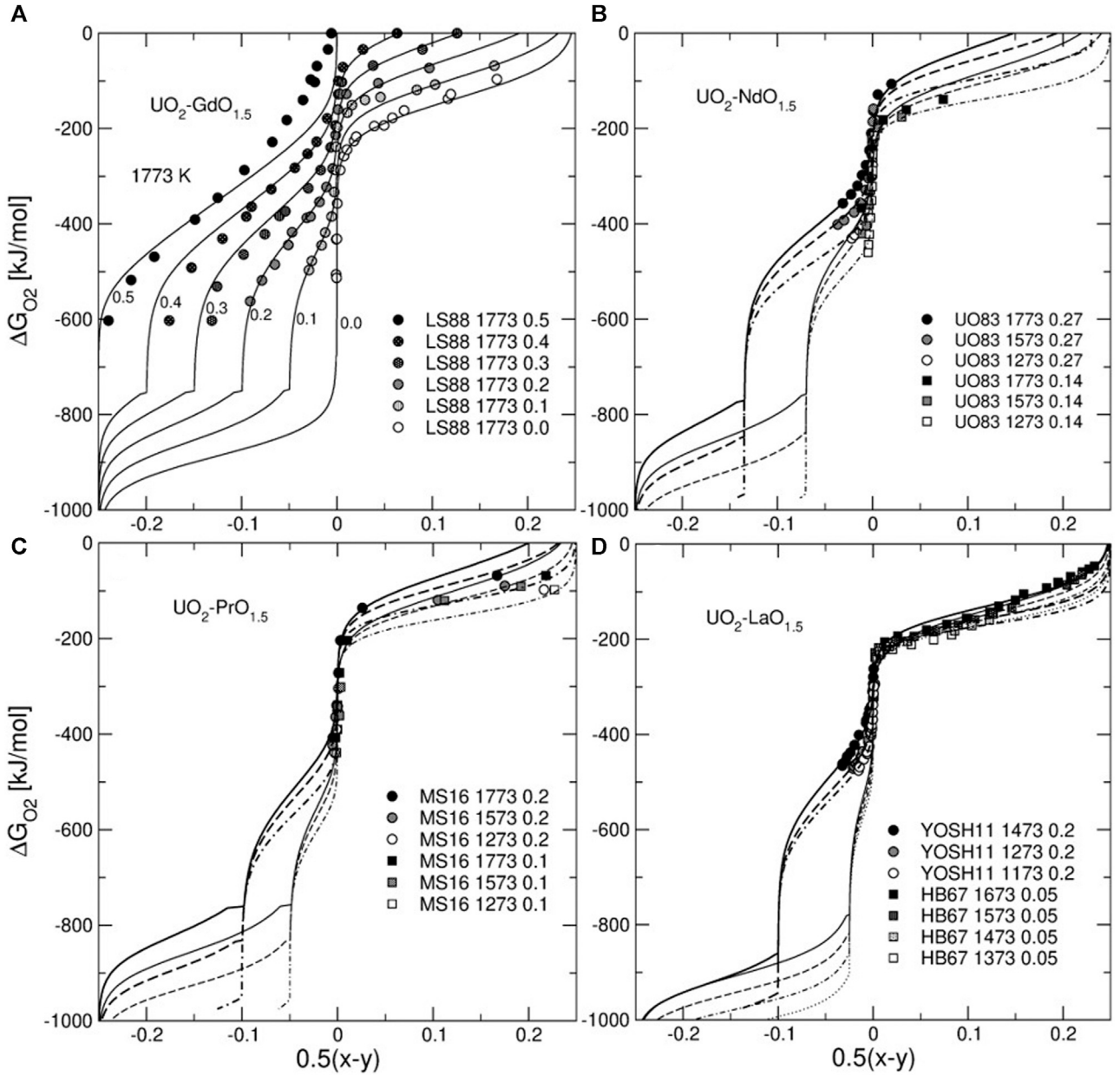

FIGURE 4 | Oxygen chemical potential plotted vs. non-stoichiometry parameter of $U_{1-z}Ln_zO_{2+0.5(x-y)}$. Lines are the isotherms predicted with the model. The temperature ranges in (b), (c), and (d) span the synthesis temperature interval given in the legend (the solid and the dotted lines correspond to the highest and lowest temperatures, respectively). The experimental data are from Lindemer and Sutton (Lindemer and Sutton, 1988), Une and Oguma (Une and Oguma, 1983a), McMurray and Silva (McMurray and Silva, 2016), Yoshida et al. (Yoshida et al., 2011) and Hagemark and Broli (Hagemark and Broli, 1967). Note an increase in the magnitude of the composition effect on the chemical potential of O_2 in the direction from La to Gd.

model III, where the vacancies are absent, is simply equal R_O. The size effect of an interstitial is included into the effective radii of cations that occur in a close contact with the interstitial, i.e. into the effective radii of $U^{5,9}$.

The radii of *Ln*, of O^{2-} and of a vacancy are adopted from our previous study on ZrO_2—$LnO_{1.5}$ systems (Bukaemskiy et al., 2021). (Some radii in this set were slightly varied reflecting specific properties of UO_2-based systems). The average radii can be trivially computed from the structural formulas corresponding to the models introduced above provided that the parameters *x*, *y*, and *z* are known. The relevant structural formulas and the equations to calculate average cation radii are given in **Table 1**.

The thermodynamic model predicts the equilibrium *x* and *y* parameters as functions of *z*, *T*, and P_{O_2}. Consequently, the lattice parameter is also a function of *z*, *T*, and P_{O_2}. Conveniently, for the relevant systems of *Ln* = {La, Pr, Nd, Gd} the data cover a range of synthesis conditions, while it is usually possible to distinguish

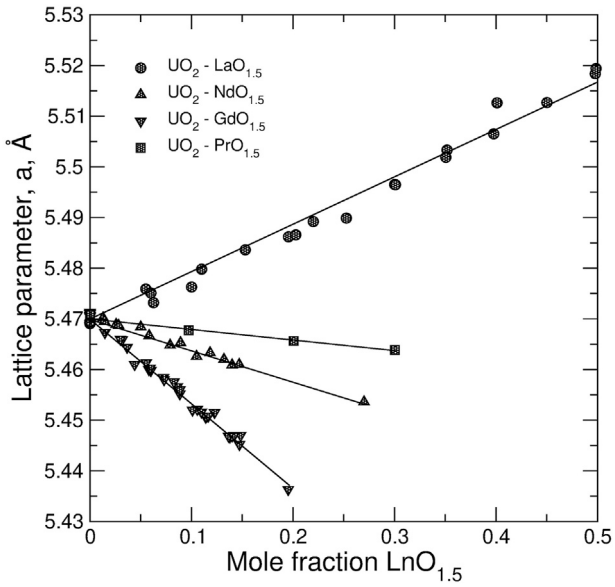

FIGURE 5 | The dependence of the lattice parameter in stoichiometric UO_2–$LnO_{1.5}$ systems on the composition. The data are fitted to linear equations to determine the radii of $U^{4,8}$, $Ln^{3,8}$, and $U^{5,8}$,. The experimental data are from (La) Hill (Hill, 1962), Stadlbauer et al. (Stadlbauer et al., 1974), Preiur et al. (Prieur et al., 2018); (Pr) Yamashita et al. (Yamashita et al., 1985); (Nd) Une and Oguma (Une and Oguma, 1983a), Ohmichi et al. (Ohmichi et al., 1981), Fukushima et al. (Fukushima et al., 1983); (Gd) Baena et al. (Baena et al., 2015), Ohmichi et al. (Ohmichi et al., 1981), Cardinaels et al. (Cardinaels et al., 2012), Leyva et al. (Leyva et al., 2002), Fukushima et al. (Fukushima et al., 1982), Hirai and Ishimoto (Hirai and Ishimoto, 1991), Soldati et al. (Soldati et al., 2016).

limiting states with well-defined stoichiometric relations, such as the strictly stoichiometric case ($y = x = 0$, the fractions of Ln^{+3} and U^{+5} are equal) and the fully reduced hypo-stoichiometric case (U^{+5} is absent, $y = z$). The available data were used to fit either the radius of U^{+5} or refine the radius of a vacancy. The cation radii of a fraction of U atoms in hyper-stoichiometric systems are affected by an unknown effect of addition of O-interstitials. Here we introduced a hypothetic U^{+5} cation in 9-fold coordination to reflect the effect of these extra oxygen atoms on the lattice parameter. The radius of $U^{5,9}$ has been determined via a fit to available data on the dependence of the lattice parameter of pure $UO_{2+0.5x}$ on x for $x < 0.30$.

3 RESULTS AND DISCUSSION

3.1 Thermodynamic Model

Figure 3 shows the results of the model fit to $\Delta G_{O_2} = RT\log\left(P_{O_2}/P^0\right)$ vs. non-stoichiometry data for pure $UO_{2+0.5(x-y)}$. Importantly, good fits to both hypo- and hyper-stoichiometric samples were achieved with a minimum set of adjustable parameters. An important observation is that for a given temperature in hyper-stoichiometric domain the oxygen chemical potential increases at high degrees of non-stoichiometry. Thus, the higher the x value, the more stable is UO_2 against a further oxidation. This effect is reflected in the positive values of W_{23}^{h} and W_{23}^{s} parameters that describe the interaction between UO_2 and $UO_{2.5}$. The values of all fitted parameters are given in **Tables 2**, **3**, **4**. Although our model does not explicitly include disproportionation (**Eqs. 12**, **13**), the

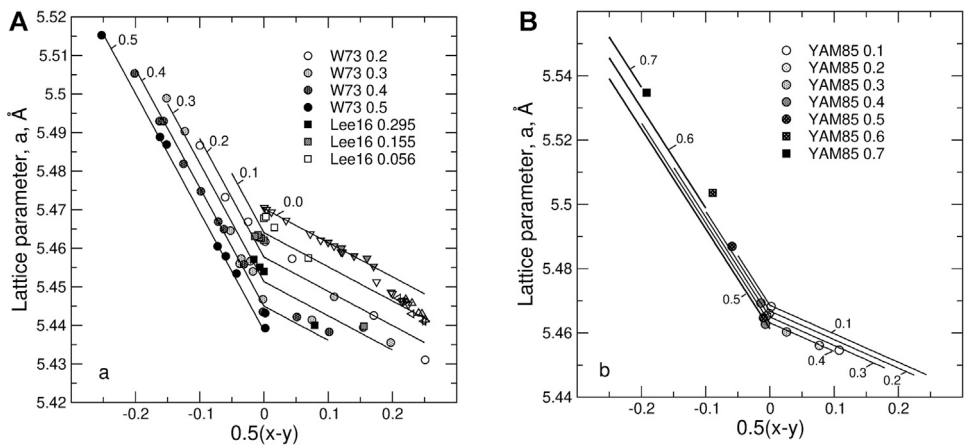

FIGURE 6 | The dependence of the lattice parameter on non-stoichiometry, $0.5(x-y)$, and z in **(A)** $U_{1-z}Nd_zO_{2+0.5(x-y)}$ and **(B)** $U_{1-z}Pr_zO_{2+0.5(x-y)}$ systems. Solid lines are compositional isopleths predicted with the model. The experimental data (circles and squares) are from Wadier (Wadier, 1973) (circles), Lee et al. (Lee et al., 2016b) (squares), Yamashita et al. (Yamashita et al., 1985) (circles and squares are the samples synthesized at 1623 K), Lynds et al. (Lynds et al., 1963) (open down triangles), Belbeoch (Belbeoch et al., 1964) (shaded down triangles), Matsui and Naito (Matsui and Naito, 1975) (open up triangles), Schaner (Schaner, 1960) (left triangles), Grønvold (Grønvold, 1955) (shaded up triangles). The data on pure UO_2 obviously fall on two trends. The first trend that extends from the stoichiometric UO_2 up to $x \sim 0.30$ is assumed to represent the fluorite-type solid solution. The trend extending to larger x values is assumed to represent U_4O_9-type structure. Thus, only the data from the first trend were used in the fit.

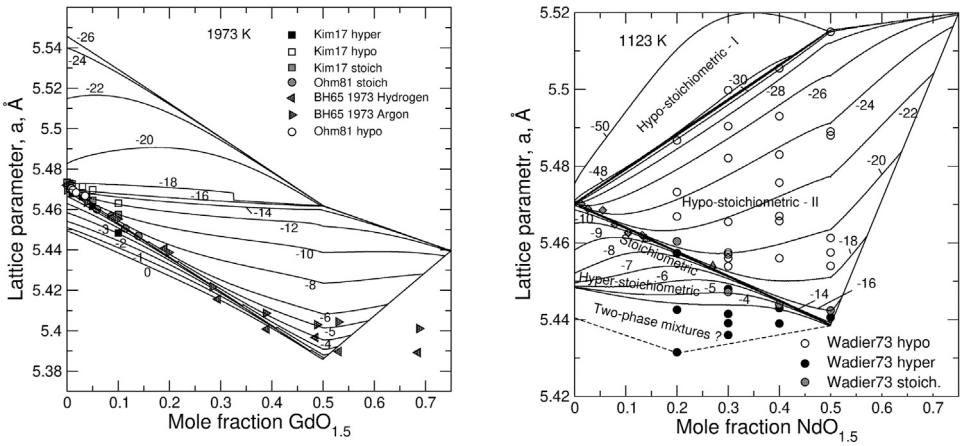

FIGURE 7 | Relationship between the lattice parameter and the degree of doping, z, in $GdO_{1.5}$—UO_2 **(left)** and $NdO_{1.5}$–UO_2 **(right)** systems. Solid lines are calculated with the model isopleths of constant $\log(P_{O_2}/P^0)$. Dashed lines schematically outline the two-phase field, where fluorite solid solution likely coexists with U_4O_9-type solid solution. The fluorite phase is subdivided into three fields which correspond to hypostoichiometric I, hypo-stoichiometric II and hyper-stoichiometric solid solutions for which different models are implemented. The hypo-stoichiometric type-II field is further subdivided into II,a and II,b areas by the line $z = 0.5$. The experimental data are from Kim et al. (Kim et al., 2017), Ohmichi et al. (Ohmichi et al., 1981), Beals and Handwerk (Beals and Handwerk, 1965), Wadier (Wadier, 1973). The data falling outside the quadrilateral possibly indicate the need of including of U^{+6} states into the model and/or the need of taking into account the presence of an additional phase.

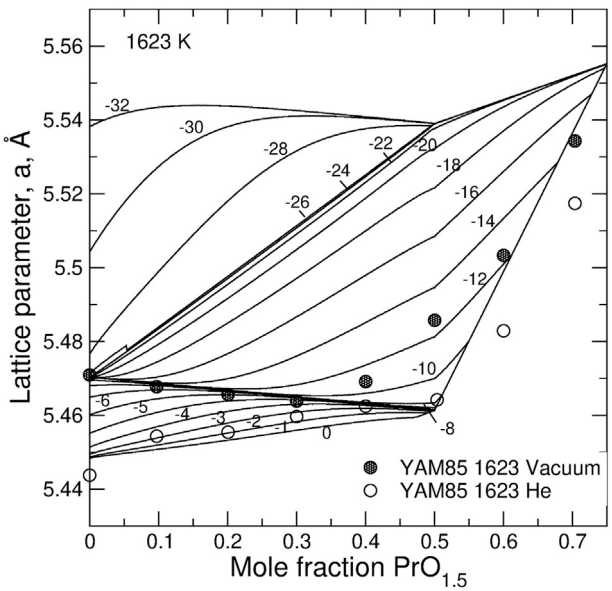

FIGURE 8 | Relationship between the lattice parameter and the degree of doping, z, and $\log(P_{O_2}/P^0)$in $PrO_{1.5}$-UO_2 system predicted from the model. The experimental data series from Yamashita et al. (Yamashita et al., 1985) are interpreted to be synthesized at $\log(P_{O_2}/P^0)$ of –2 and –12.

parameters in **Table 2** allow an estimation of their combined effect. The difference between $\Delta G^0_{UO1.5}$ and $\Delta G^0_{UO2.5}$ of 412 kJ/mol (~4.3 eV) is marginally consistent with the value of ~3.5 eV that is composed of ab initio computed defect formation energies (Nerikar et al., 2009; Cooper et al., 2018). The values in **Table 2** show also that an insertion of oxygen interstitials coupled with an oxidation of two U^{+4} cations into U^{+5} cations (the formation reaction of $UO_{2.5}$), as well as a creation of an oxygen vacancy coupled with a reduction of two U^{+4} cations into U^{+3} cations (the formation of $UO_{1.5}$), are associated with positive entropy effects. The formation of the $Ln_{0.5}U_{0.5}O_2$ endmember from UO_2 and $LnO_{1.5}$ is also associated with a positive entropy effect. The standard Gibbs free energy of the $UO_{2.5}$ endmember is predicted to be more negative than this of UO_2 consistently with the instability of UO_2 in air. The Gibbs free energies of $Ln_{0.5}U_{0.5}O_2$ endmembers are assessed to be ~60 kJ/mol more negative than the half sum of the free energies of UO_2 and $LnO_{1.5}$, consistently with the observation that the formation of hypo-stoichiometric samples along with the vacancy forming mechanism (**Eq. 14**) becomes possible only at a rather low oxygen pressure.

Figure 4 shows ΔG_{O_2} vs. non-stoichiometry plots for the Ln-doped systems. The model predicts different modes of the dependence of ΔG_{O_2} on non-stoichiometry. The transitions between the modes occur at $y = z$ and at $y = x = 0$. These boundaries correspond to states that are common to models I and II and II and III, respectively. The lowest branch of the ΔG_{O_2} curve corresponds to the oxidation of U^{+3} to U^{+4}. An important property of UO_2—$LnO_{1.5}$ systems is a two-step oxidation of U^{+4} to U^{+5}. The first oxidation step starts at $y = z$ and ends at $y = 0$. At this step the formation of U^{+5} is balanced by extra oxygen anions that fill available oxygen vacancies. Thermodynamically, this process is reflected in the gradual increase in the fraction of the stoichiometric endmember $Ln_{0.5}U_{0.5}O_2$. This process ends after all vacancies are filled in and the solution becomes stoichiometric. The second oxidation step starts at a much higher oxidation potential within a stoichiometric solid solution. The formation of U^{+5} is then balanced by oxygen anions that fill interstitial sites. This second oxidation step requires a higher oxidation potential in samples containing more $Ln_{0.5}U_{0.5}O_2$. Thus, the *Ln*-doping in this region stabilizes

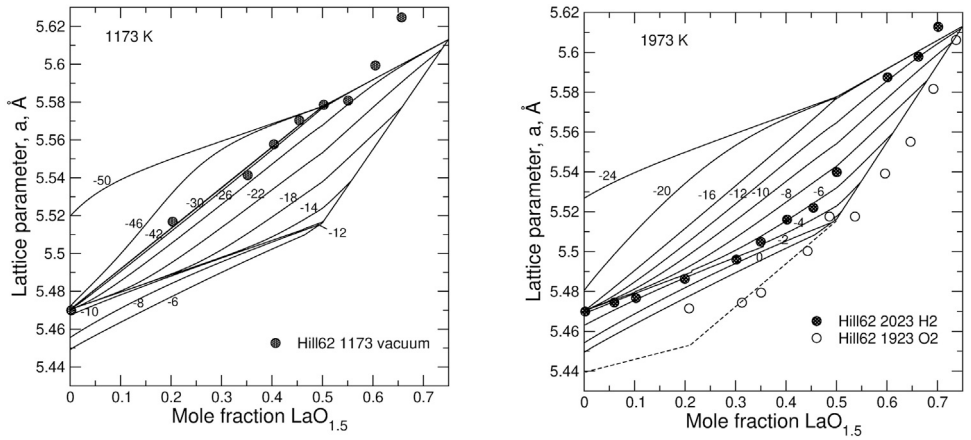

FIGURE 9 | Relationship between the lattice parameter and the degree of doping, *z*, in $LaO_{1.5}$–UO_2 system predicted from the model. The experimental data series from Hill (Hill, 1962) are interpreted to be synthesized at $-42 < \log(P_{O_2}/P^0) < -26$ **(left)** and at $\log(P_{O_2}/P^0)$ of –6 and 0 **(right)**. The data falling outside the quadrilateral possibly indicate the need of including U^{+6} states into the model.

the solid solution thermodynamically against the oxidation. This effect is particularly strong in the Gd—U system and is very weak in the system of La—U. The different behaviour correlates with the Margules interaction parameter for the $Ln_{0.5}U_{0.5}O_2$—$UO_{2.5}$ binary. The value of this parameter decreases strongly in the row of Gd > Nd > Pr > La. A possible reason for this effect is discussed further in the text.

3.2 Structural Model

Figure 5 displays the dependence of the lattice parameter in stoichiometric UO_2—$LnO_{1.5}$ systems. Linear relationships were assumed to determine (refine) values of cation radii in 8-fold coordination. Most of the values remain close to Shannon's ionic radii (Shannon, 1976). The size of the oxygen anion of 1.3736 Å was adopted from Bukaemskiy et al. (Bukaemskiy et al., 2021) as fitted to data on ZrO_2-based systems. The radii of cations in the 7-fold coordination are also from (Bukaemskiy et al., 2021). The effective size of the vacancy of 1.54 Å is slightly increased relative to the value of 1.53 ± 0.02 (Bukaemskiy et al., 2021) to give a better description of data on hypo-stoichiometric UO_2-based solids solutions (Hill, 1962; Wadier, 1973), which are discussed below.

The hyper-stoichiometric domain ($0 < x < 0.3$) is successfully described with a model in which U^{+5} cations that are needed for charge balancing the interstitials are assumed to be 9-fold coordinated with the ionic radius of 0.976 Å. This is reasonable assumption considering the lack of data. The interstitial oxygen is assumed to have no direct influence on the lattice parameter. Indeed, the size of an interstitial cannot be simply reflected within the ion-packing concept, because its structural position does not comply with a regular position of a cation or an anion. Thus, its effect is mapped onto the effective radius of $U^{5,9}$. The radii of $U^{3,7}$ and of $U^{3,8}$were assumed to vary with the same slope vs. the coordination number as the radii of $U^{4,7}$ and of $U^{4,8}$. The absolute values were increased to fit two data points from Anderson (Anderson et al., 1960) (not shown here). We note that the radii of $U^{3,7}$ and of $U^{3,8}$ adopted here have very large uncertainty, as there are almost no experimental data to be used as constraints. The set of the cation radii is given in **Table 4**.

Figure 6 shows the predicted dependence of the lattice parameter in UO_2—$PrO_{1.5}$ and UO_2—$NdO_{1.5}$ on the composition and on non-stoichiometry. An increase in the hyper-stoichiometry causes a linear decrease of the lattice parameter. Clearly, the composition dependence of the lattice parameter is significantly less pronounced in the case of Pr—U system than in the case of Nd—U system. This is because the half sum of the radii of 8-fold Pr^{+3} and U^{+5}, is almost equal to the radius of U^{+4} cation.

3.3 Structural-Thermodynamic Model

The thermodynamic relationships allow the prediction of *x* and *y*, as functions of *z*, *T*, and P_{O_2}. Consequently, the lattice parameter is also a function of *z*, *T* and P_{O_2}. This circumstance allows the computation of $\log(P_{O_2}/P^0)$ isopleths as functions of *a* and *z*. Examples of such calculations are given in **Figures 7–9**. These figures can be used to reconstruct synthesis conditions from the data on the lattice parameter variation with *z*. While an experimental description could be limited by indicating only a type of a gas used in the synthesis, the present diagrams allow a more precise characterisation of the synthesis conditions in terms of the oxygen partial pressure. The knowledge of a detailed relationship between *a*, *x*, *y*, *z*, *T*, and P_{O_2} appears to be very useful in designing experiments allowing synthesis of samples with required type and degree of non-stoichiometry. By measuring the lattice parameter and by comparing it with the predicted value, there appears a possibility of controlling the thermodynamic equilibration in synthesis experiments. This is particularly important in experiments aiming in distinguishing between various factors affecting the resistance of *Ln*-doped UO_2 to oxidation and to oxidative dissolution. The computed diagrams are particularly instructive for predicting conditions that allow the synthesis of stoichiometric samples. For example,

from **Figure 7** one can deduce that the synthesis of stoichiometric samples in $NdO_{1.5}$—UO_2 system can be performed at $T = 1123$ K and $-14 < \log(P_{O_2}/P^0) < -12$, while the developed computer program allows predicting the necessary oxygen partial pressures at any other temperature. Importantly, the slope, d*a*/d*z*, within the row of stoichiometric samples depends on the type of Ln (**Figure 5**). Zero slope is determined by the equation $R_{Ln}^{3,8} + R_{U}^{5,8} = 2R_{U}^{4,8}$ which is nearly exactly fulfilled for Pr. UO_2—$LaO_{1.5}$ is the only system characterized by a positive slope. Remarkably, on the thermodynamic level, the UO_2—$LaO_{1.5}$ system is characterized by the lowest increase in $\log(P_{O_2}/P^0)$ with the doping level (**Figure 4D**), which correlates with the low value of the Margules interaction between $La_{0.5}U_{0.5}O_2$ and $UO_{2.5}$ endmembers (**Table 2**). Recalling that a Margules parameter measures the size mismatch between two endmembers (Vinograd et al., 2013; Kowalski and Li, 2016), the low value of W^h in the case of $La_{0.5}U_{0.5}O_2$—$UO_{2.5}$ is counterintuitive. Indeed, in the case of $La_{0.5}U_{0.5}O_2$ the size mismatch between $Ln_{0.5}U_{0.5}O_2$ and $UO_{2.5}$ is maximized. The size mismatch between these endmembers occurs primarily due to the difference in the radii of $La^{3,8}$ and $U^{5,9}$. The local strain is caused due to a random formation of $La^{3,8}$-$La^{3,8}$ and $U^{5,9}$-$U^{5,9}$, pairs, which are either too large or too small to fit the common average distance along [111] (**Figure 2**). The W^h parameter of $Ln_{0.5}U_{0.5}O_2$—$UO_{2.5}$ interaction reflects this local strain effect due to the misfit between $La^{3,8}$ and $U^{5,9}$. Likewise, the W^h parameter of UO_2—$UO_{2.5}$ interaction reflects the misfit between $U^{4,8}$and $U^{5,9}$. The counterintuitive variation of the Margules $Ln_{0.5}U_{0.5}O_2$—$UO_{2.5}$ interactions can be qualitatively explained under an assumption that these parameters, besides the local strain along [111], reflect an additional strain effect, that is caused by an overlap of anion spheres along [100]. Indeed, in the case of pure stoichiometric UO_2 the condition of a close touch between anion spheres along [100] corresponds to the lattice parameter of 5.494 Å (**Figure 2**). The lattice parameter of ~5.47 Å of stoichiometric UO_2 already corresponds to a slight overlap of the anion spheres. Obviously, the lattice contraction to values significantly smaller than ~5.47 Å would cause an increasing strain along [100], as the ionic spheres would be overlapped/compressed more significantly. A normal structural reaction to such an overlap is the tendency of a cation to decrease its coordination number, as happens, for example, in monoclinic ZrO_2. Thus, the overlap is a sign of a decreased stability of the fluorite phase. Importantly, the overlap of anions is a global effect, to which all endmembers contribute, while their contributions could be of different magnitude and sign. Effectively, an addition of $La_{0.5}U_{0.5}O_2$ decreases the overlap of anion spheres (causing a negative contribution to the strain energy), while an addition of $Nd_{0.5}U_{0.5}O_2$ and $Gd_{0.5}U_{0.5}O_2$ makes the overlap stronger. The overlap also increases due to an increase in the fraction of $UO_{2.5}$ (i.e. due to the oxidation). Assuming the Margules parameters reflect both [111] and [100] strains, the low value of the $La_{0.5}U_{0.5}O_2$—$UO_{2.5}$ interaction parameter can be easily rationalized as a superposition of two effects of different signs cancelling each other to a large extent. Considering this hypothesis, an addition of La should make the oxidation of UO_2 easier, as it decreases the overlap allowing for the lattice contraction, while an addition of Gd or Nd should make it more difficult.

Our hypothesis is that the stabilizing effect of *Ln*-doping in the case of Nd, Gd (and smaller *Ln*) is primarily caused by the lattice contraction due to the doping and by the increasing strain energy cost of an additional contraction (additional overlap of oxygen anions along [100]) required by the oxidation. At the same time, an increase in the oxygen chemical potential with the extent of hyper-stoichiometry observed in both undoped and doped systems (**Figures 3**, **4**) can be equally well rationalized. As the oxidation from UO_2 to $UO_{2+0.5x}$ ($x < 0.5$) causes an unfavourable decrease in the lattice parameter, the oxidation (i.e. an increase in *x*) is a self-inhibiting process. This self-inhibition effect could be responsible for the decrease in the U^{+6} yields after repeating exposures to H_2O_2 observed recently in oxidative dissolution experiments (Maier et al., 2020).

Further development of the model would require extending it to *Ln*-dopants with the cation radii smaller than this of Gd^{+3}, to Y and to di-valent dopants. An explicit introducing of $U_{1/3}Ln_{2/3}O_2$ and UO_3 endmembers would probably cure apparent problems of the present model at $z > 0.5$.

4 CONCLUSION

The data on the dependence of the oxygen potential of doped UO_2 solid solutions on the composition, temperature and non-stoichiometry are linked to the data on the dependence of the lattice parameter on composition and non-stoichiometry within the same model frame. This brings up a possibility of relating changes in the lattice parameter to T and $\log(P_{O_2}/P^0)$. As the lattice parameter can be predicted as a function of synthesis conditions, its measuring provides a test for an attainment of the thermodynamic equilibrium in a particular experiment.

Good fit of the model to available structural data on the dependence of the lattice parameter, *a*, on *z*, *x*, and *y* shows that the model assumptions of short-range ordering, such as the vacancy-vacancy avoidance, the avoidance of di-interstitial clusters, the association of vacancies to III-valent cations and the association of U^{+5} to interstitial O^{2-} are reasonable. These assumptions have an important effect on the structural model by limiting the spectrum of cation coordination numbers and thus allowing for the application of the ion-packing concept.

The SRO also imposes a profound effect on the thermodynamic model causing a significant reduction in the configurational entropy relative to the ideal mixing model. This model feature is essential for achieving a good fit to $\log(P_{O_2}/P^0)$ vs. non-stoichiometry data.

The entropy decreases 1) due to the ordering of vacancies and interstitials, 2) due to the cation-anion association effects and 3) due to the neglect of the configurational effect from U^{+4}/U^{+3} and U^{+4}/U^{+5} mixing. The achieved consistency between the structural and thermodynamic descriptions provides an argument in favour of the validity of these assumptions. Further experimental and computational studies aiming at testing these assumptions in other similar systems would be desirable.

The developed models are thermodynamically simple and transparent. An introduction of a new chemical component, such as $LnO_{1.5}$, requires just two parameters to define the standard thermodynamic properties of a $Ln_{0.5}U_{0.5}O_2$ endmember and two

Margules parameters to model the interactions $Ln_{0.5}U_{0.5}O_2$—$UO_{2.5}$ and $LnO_{1.5}$—UO_2. This offers a great advantage over models based on the Compound Energy Formalism (Saunders and Miodownik, 1998; Hillert, 2001) that require a larger number of adjustable parameters. The present model requires the Gibbs free energy minimization with respect to just one parameter, y or x, in each model domain.

The small number of thermodynamic parameters provides a possibility of identifying main factors that are responsible for the dependence of the oxidation potential on the doping and on the extent of oxidation. In hyper-stoichiometric region these are the Margules parameters for the interactions between $Ln_{0.5}U_{0.5}O_2$ and $UO_{2.5}$ and between UO_2 and $UO_{2.5}$. As the first parameter correlates with da/dz slope, the strain associated with the lattice contraction appears to be the likely cause of the stabilization of doped samples against the oxidation.

The proposed mechanism of the resistance of *Ln*-doped UO_2 to the thermodynamically controlled oxidation may be equally applicable to more complex UO_2-based simulated spent fuel, as it is known that the lattice parameter of simulated fuel (e.g. UO_2 + Zr, Ce, Pr, Nd, and Y) decreases with the simulated burn-up (Une and Oguma, 1983b).

The thermodynamic and structural models developed here provide a possible explanation for the observed corrosion resistance of *Ln* doped UO_2 compared to pure UO_2 under conditions expected in a deep geological repository for spent nuclear fuel. However, with respect to the corrosion of SNF under disposal conditions other effects (e.g., radiation effects, He build up, effects of other non-*Ln* fission products) need to be taken into account.

DATA AVAILABILITY STATEMENT

The original contributions presented in the study are included in the article/**Supplementary Material**, further inquiries can be directed to the corresponding author.

AUTHOR CONTRIBUTIONS

The authors confirm contribution to the paper as follows: study conception and design: VV, AB, DB, GM, and GD; data collection: VV, AB; modelling: VV, AB; analysis and interpretation of results: VV, AB, DB, GM, and GD; draft manuscript preparation: VV, AB, GD, GM, and DB. All authors reviewed the results and approved the final version of the manuscript.

ACKNOWLEDGMENTS

We acknowledge discussions with Dr. D. A. Kulik (PSI) and Dr. E. Curti (PSI) which helped to develop the thermodynamic formalism.

SUPPLEMENTARY MATERIAL

The Supplementary Material for this article can be found online at: https://www.frontiersin.org/articles/10.3389/fchem.2021.705024/full#supplementary-material

REFERENCES

Anderson, J. S., Sawyer, J. O., Worner, H. W., Willis, G. M., and Bannister, M. J. (1960). Decomposition of Uranium Dioxide at its Melting Point. *Nature* 185 (4717), 915–916. doi:10.1038/185915b0

Andersson, D. A., Lezama, J., Uberuaga, B. P., Deo, C., and Conradson, S. D. (2009). Cooperativity Among Defect Sites in AO_{2+x} and A_4O_9 (A=U, Np, Pu): Density Functional Calculations. *Phys. Rev. B* 79 (2), 024110. doi:10.1103/PhysRevB.79.024110

Baena, A., Cardinaels, T., Govers, K., Pakarinen, J., Binnemans, K., and Verwerft, M. (2015). Lattice Contraction and Lattice Deformation of UO_2 and ThO_2 Doped with Gd_2 O_3. *J. Nucl. Mater.* 467, 135–143. doi:10.1016/j.jnucmat.2015.09.018

Barreiro Fidalgo, A., and Jonsson, M. (2019). Radiation Induced Dissolution of $(U,Gd)O_2$ Pellets in Aqueous Solution - A Comparison to Standard UO_2 Pellets. *J. Nucl. Mater.* 514, 216–223. doi:10.1016/j.jnucmat.2018.11.037

Beals, R. J., and Handwerk, J. H. (1965). Solid Solutions in the System Urania-Rare-Earth Oxides: I, UO_2-$GdO_{1.5}$,. *J. Am. Ceram. Soc.* 48 (5), 271–274. doi:10.1111/j.1151-2916.1965.tb14735.x

Belbeoch, M. B., Laredo, M. E., and Perio, P. (1964). Examen par rayons X, après trempe, d'oxydes d'uranium de type UO_2. *J. Nucl. Mater.* 13 (1), 100–106. doi:10.1016/0022-3115(64)90072-8

Bevan, D. J. M., Grey, I. E., and Willis, B. T. M. (1986). The crystal Structure of β-U_4O_9−y. *J. Solid State. Chem.* 61 (1), 1–7. doi:10.1016/0022-4596(86)90002-2

Bosbach, D., Brandt, F., Bukaemskiy, A., Deissmann, G., Kegler, P., Klinkenberg, M., et al. (2020). Research for the Safe Management of Nuclear Waste at Forschungszentrum Jülich: Materials Chemistry and Solid Solution Aspects. *Adv. Eng. Mater.* 22 (6), 1901417. doi:10.1002/adem.201901417

Bruno, J., and Ewing, R. C. (2006). Spent Nuclear Fuel. *Elements* 2 (6), 343–349. doi:10.2113/gselements.2.6.343

Bukaemskiy, A. A., Vinograd, V. L., and Kowalski, P. M. (2021). Ion Distribution Models for Defect Fluorite ZrO_2 - $AO_{1.5}$ (A = Ln, Y) Solid Solutions: I. Relationship between Lattice Parameter and Composition. *Acta Materialia* 202, 99–111. doi:10.1016/j.actamat.2020.10.045

Carbol, P., Wegen, D. H., Wiss, T., and Fors, P. (2012). "Spent Fuel as Waste Material," in *Comprehensive Nuclear Materials*. Editor R. Konings (Amsterdam (Netherlands): Elsevier), 389–420. doi:10.1016/b978-0-08-056033-5.00106-3

Cardinaels, T., Hertog, J., Vos, B., de Tollenaere, L., Delafoy, C., and Verwerft, M. (2012). Dopant Solubility and Lattice Contraction in Gadolinia and Gadolinia-Chromia Doped UO_2 Fuels. *J. Nucl. Mater.* 424 (1), 289–300. doi:10.1016/j.jnucmat.2012.02.014

Casella, A., Hanson, B., and Miller, W. (2016). The Effect of Fuel Chemistry on UO_2 Dissolution. *J. Nucl. Mater.* 476, 45–55. doi:10.1016/j.jnucmat.2016.04.025

Cooper, M. W. D., Murphy, S. T., and Andersson, D. A. (2018). The Defect Chemistry of $UO_{2\pm x}$ from Atomistic Simulations. *J. Nucl. Mater.* 504, 251–260. doi:10.1016/j.jnucmat.2018.02.034

Curti, E., and Kulik, D. A. (2020). Oxygen Potential Calculations for Conventional and Cr-Doped UO_2 Fuels Based on Solid Solution Thermodynamics. *J. Nucl. Mater.* 534, 152140. doi:10.1016/j.jnucmat.2020.152140

Degueldre, C., Pin, S., Poonoosamy, J., and Kulik, D. A. (2014). Redox State of Plutonium in Irradiated Mixed Oxide Fuels. *J. Phys. Chem. Sol.* 75 (3), 358–365. doi:10.1016/j.jpcs.2013.11.001

Eriksen, T. E., Shoesmith, D. W., and Jonsson, M. (2012). Radiation Induced Dissolution of UO_2 Based Nuclear Fuel - A Critical Review of Predictive Modelling Approaches. *J. Nucl. Mater.* 420 (1), 409–423. doi:10.1016/j.jnucmat.2011.10.027

Ewing, R. C. (2015). Long-term Storage of Spent Nuclear Fuel. *Nat. Mater* 14 (3), 252–257. doi:10.1038/nmat4226

Fanghänel, T., Rondinella, V. V., Glatz, J.-P., Wiss, T., Wegen, D. H., Gouder, T., et al. (2013). Reducing Uncertainties Affecting the Assessment of the Long-

Term Corrosion Behavior of Spent Nuclear Fuel. *Inorg. Chem.* 52 (7), 3491–3509. doi:10.1021/ic302012c

Ferry, C., Poinssot, C., Broudic, V., Cappelaere, C., Desgranges, L., Garcia, P., et al. (2005). *Synthesis on the Spent Fuel Long Term Evolution*. France: CEA.

Finnis, M. W., Lozovoi, A. Y., and Alavi, A. (2005). The Oxidation of NiAl: What Can We Learn from Ab Initio Calculations?. *Annu. Rev. Mater. Res.* 35 (1), 167–207. doi:10.1146/annurev.matsci.35.101503.091652

Fukushima, S., Ohmichi, T., Maeda, A., and Handa, M. (1983). Thermal Conductivity of Near-Stoichiometric (U, Nd)O_2, (U, Sm)O_2 and (U, Eu)O_2 Solid Solutions. *J. Nucl. Mater.* 114 (2), 312–325. doi:10.1016/0022-3115(83)90270-2

Fukushima, S., Ohmichi, T., Maeda, A., and Watanabe, H. (1982). The Effect of Gadolinium Content on the thermal Conductivity of Near-Stoichiometric (U,Gd)O_2 Solid Solutions. *J. Nucl. Mater.* 105 (2), 201–210. doi:10.1016/0022-3115(82)90375-0

Grønvold, F. (1955). High-temperature X-ray Study of Uranium Oxides in the UO_2·U_3O_8 Region. *J. Inorg. Nucl. Chem.* 1 (6), 357–370. doi:10.1016/0022-1902(55)80046-2

Guéneau, C., Dupin, N., Sundman, B., Martial, C., Dumas, J.-C., Gossé, S., et al. (2011). Thermodynamic Modelling of Advanced Oxide and Carbide Nuclear Fuels: Description of the U-Pu-O-C Systems. *J. Nucl. Mater.* 419 (1), 145–167. doi:10.1016/j.jnucmat.2011.07.033

Hagemark, K., and Broli, M. (1967). Equilibrium Oxygen Pressures over Solid Solutions of Urania-Yttria and Urania-Lanthana at 1100° to 14OO°C. *J. Am. Ceram. Soc.* 50 (11), 563–567. doi:10.1111/j.1151-2916.1967.tb14999.x

Hansson, N. L., Tam, P. L., Ekberg, C., and Spahiu, K. (2021). XPS Study of External α-radiolytic Oxidation of UO_2 in the Presence of Argon or Hydrogen. *J. Nucl. Mater.* 543, 152604. doi:10.1016/j.jnucmat.2020.152604

He, H., Keech, P. G., Broczkowski, M. E., Noël, J. J., and Shoesmith, D. W. (2007). Characterization of the Influence of Fission Product Doping on the Anodic Reactivity of Uranium Dioxide. *Can. J. Chem.* 85, 702–713. doi:10.1139/V07-056

Hill, D. C. (1962). Phase Relations and Crystal Chemistry in the System Uranium Oxide-Lanthanum Oxide. *J. Am. Ceram. Soc.* 45 (6), 258–263. doi:10.1111/j.1151-2916.1962.tb11140.x

Hillert, M. (2001). The Compound Energy Formalism. *J. Alloys Compd.* 320 (2), 161–176. doi:10.1016/S0925-8388(00)01481-X

Hirai, M., and Ishimoto, S. (1991). Thermal Diffusivities and Thermal Conductivities of UO_2-Gd_2O_3. *J. Nucl. Sci. Technol.* 28 (11), 995–1000. doi:10.1080/18811248.1991.9731462

Hong, S. J., and Virkar, A. V. (1995). Lattice Parameters and Densities of Rare-Earth Oxide Doped Ceria Electrolytes. *J. Am. Ceram. Soc.* 78 (2), 433–439. doi:10.1111/j.1151-2916.1995.tb08820.x

Javed, N. A. (1972). Thermodynamic Study of Hypostoichiometric Urania. *J. Nucl. Mater.* 43 (3), 219–224. doi:10.1016/0022-3115(72)90053-0

Karpov, I. K., Chudnenko, K. V., Kulik, D. A., Avchenko, O. V., and Bychinski, V. A. (2001). Minimization of Gibbs Free Energy in Geochemical Systems by Convex Programming. *Geochem. Int.* 39 (11).

Kim, J.-G., Ha, Y.-K., Park, S.-D., Jee, K.-Y., and Kim, W.-H. (2001). Effect of a Trivalent Dopant, Gd^{3+}, on the Oxidation of Uranium Dioxide. *J. Nucl. Mater.* 297 (3), 327–331. doi:10.1016/S0022-3115(01)00639-0

Kim, J., Lee, J., Youn, Y.-S., Liu, N., Kim, J.-G., Ha, Y.-K., et al. (2017). The Combined Influence of Gadolinium Doping and Non-stoichiometry on the Structural and Electrochemical Properties of Uranium Dioxide. *Electrochimica Acta* 247, 942–948. doi:10.1016/j.electacta.2017.07.023

Kleykamp, H. (1988). The Chemical State of Fission Products in Oxide Fuels at Different Stages of the Nuclear Fuel Cycle. *Nucl. Technol.* 80 (3), 412–422. doi:10.13182/NT88-A34065

Kleykamp, H. (1985). The Chemical State of the Fission Products in Oxide Fuels. *J. Nucl. Mater.* 131 (2), 221–246. doi:10.1016/0022-3115(85)90460-X

Kowalski, P. M., and Li, Y. (2016). Relationship between the Thermodynamic Excess Properties of Mixing and the Elastic Moduli in the Monazite-type Ceramics. *J. Eur. Ceram. Soc.* 36 (8), 2093–2096. doi:10.1016/j.jeurceramsoc.2016.01.051

Kulik, D. A., Wagner, T., Dmytrieva, S. V., Kosakowski, G., Hingerl, F. F., Chudnenko, K. V., et al. (2013). GEM-selektor Geochemical Modeling Package: Revised Algorithm and GEMS3K Numerical Kernel for Coupled Simulation Codes. *Comput. Geosci.* 17, 1–24. doi:10.1007/s10596-012-9310-6

Lee, S. M., Knight, T. W., McMurray, J. W., and Besmann, T. M. (2016). Measurement of the Oxygen Partial Pressure and Thermodynamic Modeling of the U-Nd-O System. *J. Nucl. Mater.* 473, 272–282. doi:10.1016/j.jnucmat.2016.02.024

Lee, S. M., Knight, T. W., Voit, S. L., and Barabash, R. I. (2016). Lattice Parameter Behavior with Different Nd and O Concentrations in ($U_{1-y}Nd_y$)$O_{2\pm X}$ Solid Solution. *Nucl. Technol.* 193 (2), 287–296. doi:10.13182/NT14-136

Lemmens, K., González-Robles, E., Kienzler, B., Curti, E., Serrano-Purroy, D., Sureda, R., et al. (2017). Instant Release of Fission Products in Leaching Experiments with High Burn-Up Nuclear Fuels in the Framework of the Euratom Project FIRST-Nuclides. *J. Nucl. Mater.* 484, 307–323. doi:10.1016/j.jnucmat.2016.10.048

Leyva, A. G., Vega, D., Trimarco, V., and Marchi, D. (2002). Homogeneity Characterisation of Sintered (U,Gd)O_2 Pellets by X-ray Diffraction. *J. Nucl. Mater.* 303 (1), 29–33. doi:10.1016/S0022-3115(02)00819-X

Lindemer, T. B., and Sutton, A. L., Jr. (1988). Study of Nonstoichiometry of $U_{1-z}Gd_zO_{2+-X>}$. *J. Am. Ceram. Soc.* 71 (7), 553–561. doi:10.1111/j.1151-2916.1988.tb05919.x

Liu, N., He, H., Noël, J. J., and Shoesmith, D. W. (2017). The Electrochemical Study of Dy_2O_3 Doped UO_2 in Slightly Alkaline Sodium Carbonate/bicarbonate and Phosphate Solutions. *Electrochimica Acta* 235, 654–663. doi:10.1016/j.electacta.2017.03.075

Lynds, L., Young, W. A., Mohl, J. S., and Libowitz, G. G. (1963). X-Ray and Density Study of Nonstoichiometry in Uranium Oxides. *Adv. Chem. Nonstoichiometric Compd.* 39, 58–65. doi:10.1021/ba-1964-0039.ch005

Maier, A. C., Kegler, P., Klinkenberg, M., Baena, A., Finkeldei, S., Brandt, F., et al. (2020). On the Change in UO_2 Redox Reactivity as a Function of H_2O_2 Exposure. *Dalton Trans.* 49, 1241–1248. doi:10.1039/c9dt04395k

Marrocchelli, D., Bishop, S. R., and Kilner, J. (2013). Chemical Expansion and its Dependence on the Host Cation Radius. *J. Mater. Chem. A.* 1 (26), 7673–7680. doi:10.1039/C3TA11020F

Marrocchelli, D., Bishop, S. R., Tuller, H. L., and Yildiz, B. (2012). Understanding Chemical Expansion in Non-stoichiometric Oxides: Ceria and Zirconia Case Studies. *Adv. Funct. Mater.* 22 (9), 1958–1965. doi:10.1002/adfm.201102648

Matsui, T., and Naito, K. (1975). Phase Relation and Defect Structures of Nonstoichiometric $U_4O_{9\pm y}$ and UO_{2+x} at High Temperatures. *J. Nucl. Mater.* 56 (3), 327–335. doi:10.1016/0022-3115(75)90050-1

McMurray, J. W., Shin, D., and Besmann, T. M. (2015). Thermodynamic Assessment of the U-La-O System. *J. Nucl. Mater.* 456, 142–150. doi:10.1016/j.jnucmat.2014.09.031

McMurray, J. W., Shin, D., Slone, B. W., and Besmann, T. M. (2013). Thermochemical Modeling of the $U_{1-y}Gd_yO_{2\pm x}$ Phase. *J. Nucl. Mater.* 443 (1), 588–595. doi:10.1016/j.jnucmat.2013.08.005

McMurray, J. W., and Silva, C. M. (2016). Experimental Oxygen Potentials for $U_{1-y}Pr_yO_{2\pm x}$ and Thermodynamic Assessment of the U-Pr-O System. *J. Nucl. Mater.* 470, 111–118. doi:10.1016/j.jnucmat.2015.11.059

Nakamura, A., and Fujino, T. (1987). Thermodynamic Study of UO_{2+x} by Solid State Emf Technique. *J. Nucl. Mater.* 149 (1), 80–100. doi:10.1016/0022-3115(87)90501-0

Nerikar, P., Watanabe, T., Tulenko, J. S., Phillpot, S. R., and Sinnott, S. B. (2009). Energetics of Intrinsic point Defects in Uranium Dioxide from Electronic-Structure Calculations. *J. Nucl. Mater.* 384 (1), 61–69. doi:10.1016/j.jnucmat.2008.10.003

Nilsson, S., and Jonsson, M. (2011). H_2O_2 and Radiation Induced Dissolution of UO_2 and SIMFUEL Pellets. *J. Nucl. Mater.* 410 (1), 89–93. doi:10.1016/j.jnucmat.2011.01.020

Ohmichi, T., Fukushima, S., Maeda, A., and Watanabe, H. (1981). On the Relation between Lattice Parameter and O/M Ratio for Uranium Dioxide-Trivalent Rare Earth Oxide Solid Solution. *J. Nucl. Mater.* 102 (1), 40–46. doi:10.1016/0022-3115(81)90544-4

Palomares, R. I., McDonnell, M. T., Yang, L., Yao, T., Szymanowski, J. E. S., Neuefeind, J., et al. (2019). Oxygen point Defect Accumulation in Single-phase UO_{2+x}. *Phys. Rev. Mater.* 3 (5), 053611. doi:10.1103/PhysRevMaterials.3.053611

Park, K., and Olander, D. R. (1992). Defect Models for the Oxygen Potentials of Gadolinium-And Europium-Doped Urania. *J. Nucl. Mater.* 187 (1), 89–96. doi:10.1016/0022-3115(92)90323-D

Prieur, D., Martel, L., Vigier, J.-F., Scheinost, A. C., Kvashnina, K. O., Somers, J., et al. (2018). Aliovalent Cation Substitution in UO_2: Electronic and Local Structures of $U_{1-y}La_yO_{2\pm x}$ Solid Solutions. *Inorg. Chem.* 57 (3), 1535–1544. doi:10.1021/acs.inorgchem.7b02839

Razdan, M., and Shoesmith, D. W. (2013). Influence of Trivalent-Dopants on the Structural and Electrochemical Properties of Uranium Dioxide (UO_2). *J. Electrochem. Soc.* 161 (3), H105–H113. doi:10.1149/2.047403jes

Saito, Y. (1974). Nonstoichiometry in Uranium Dioxide. *J. Nucl. Mater.* 51 (1), 112–125. doi:10.1016/0022-3115(74)90121-4

Saunders, N., and Miodownik, A. P. (1998). *CALPHAD (Calculation of Phase Diagrams): A Comprehensive Guide*. Oxford, New York: Pergamon.

Schaner, B. E. (1960). Metallographic Determination of the UO_2-U_4O_9 Phase Diagram. *J. Nucl. Mater.* 2 (2), 110–120. doi:10.1016/0022-3115(60)90038-6

Schreinemachers, C., Bukaemskiy, A. A., Klinkenberg, M., Neumeier, S., Modolo, G., and Bosbach, D. (2014). Characterization of Uranium Neodymium Oxide Microspheres Synthesized by Internal Gelation. *Prog. Nucl. Energ.* 72, 17–21. doi:10.1016/j.pnucene.2013.07.016

Schreinemachers, C., Leinders, G., Modolo, G., Verwerft, M., Binnemans, K., and Cardinaels, T. (2020). Fabrication of Nd- and Ce-Doped Uranium Dioxide Microspheres via Internal Gelation. *J. Nucl. Mater.* 535, 152128. doi:10.1016/j.jnucmat.2020.152128

Shannon, R. D. (1976). Revised Effective Ionic Radii and Systematic Studies of Interatomic Distances in Halides and Chalcogenides. *Acta Cryst. Sect A.* 32(5): 751–767. doi:10.1107/S0567739476001551

Shoesmith, D. W. (2000). Fuel Corrosion Processes under Waste Disposal Conditions. *J. Nucl. Mater.* 282 (1), 1–31. doi:10.1016/S0022-3115(00)00392-5

Shoesmith, D. W. (2013). "The Chemistry/electrochemistry of Spent Nuclear Fuel as a Wasteform," in *Uranium: Cradle to Grave*. Editors P. Burns and G. Simon (Canada: Mineralogical Society of Canada), 337–368.

Soldati, A. L., Gana Watkins, I., Fernández Zuvich, A., Napolitano, F., Troiani, H., Caneiro, A., et al. (2016). Synthesis and Characterization of Gd_2O_3 Doped UO_2 Nanoparticles. *J. Nucl. Mater.* 479, 436–446. doi:10.1016/j.jnucmat.2016.07.033

Solomon, J. M., Alexandrov, V., Sadigh, B., Navrotsky, A., and Asta, M. (2014). Computational Study of the Energetics and Defect Clustering Tendencies for Y- and La-Doped UO_2. *Acta Materialia* 78, 282–289. doi:10.1016/j.actamat.2014.06.052

Stadlbauer, E., Wichmann, U., Lott, U., and Keller, C. (1974). Thermodynamics and Phase Relationships of the Ternary Lanthanum-Uranium-Oxygen System. *J. Solid State. Chem.* 10 (4), 341–350. doi:10.1016/0022-4596(74)90043-7

Tetenbaum, M., and Hunt, P. D. (1968). High-Temperature Thermodynamic Properties of Oxygen-Deficient Urania. *J. Chem. Phys.* 49 (11), 4739–4744. doi:10.1063/1.1669953

Trummer, M., Dahlgren, B., and Jonsson, M. (2010). The Effect of Y_2O_3 on the Dynamics of Oxidative Dissolution of UO_2. *J. Nucl. Mater.* 407 (3), 195–199. doi:10.1016/j.jnucmat.2010.10.014

Une, K., and Oguma, M. (1983). Oxygen Potentials of $(U,Nd)O_{2\pm x}$ Solid Solutions in the Temperature Range 1000–1500°C. *J. Nucl. Mater.* 118 (2), 189–194. doi:10.1016/0022-3115(83)90224-6

Une, K., and Oguma, M. (1983). Oxygen Potentials of UO_2 Fuel Simulating High Burnup. *J. Nucl. Sci. Technol.* 20 (10), 844–851. doi:10.1080/18811248.1983.9733476

Vinograd, V. L., Brandt, F., Rozov, K., Klinkenberg, M., Refson, K., Winkler, B., et al. (2013). Solid-aqueous Equilibrium in the $BaSO_4$-$RaSO_4$-H_2O System: First-Principles Calculations and a Thermodynamic Assessment. *Geochimica et Cosmochimica Acta* 122, 398–417. doi:10.1016/j.gca.2013.08.028

Vinograd, V. L., and Bukaemskiy, A. A. (2021). Ion Distribution Models for Defect Fluorite ZrO_2 - $AO_{1.5}$ (A = Ln, Y) Solid Solutions: II. Thermodynamics of Mixing and Ordering. *Acta Materialia* 202, 55–67. doi:10.1016/j.actamat.2020.10.046

Wadier, J. F. (1973). Phase Diagrams and Thermodynamic Properties of the Uranium-Neodymium-Oxygen System. *Tech. rep. Rapport CEA-R-4507,Commisariat a l'energie atomique*.

Willis, B. T. M. (1978). The Defect Structure of Hyper-Stoichiometric Uranium Dioxide. *Acta Cryst. Sect A.* 34 (1), 88–90. doi:10.1107/S0567739478000157

Yamashita, T., Fujino, T., and Tagawa, H. (1985). Phase Relations and crystal Chemistry in the Ternary $PrO_{1.5}$-UO_2-O_2 System. *J. Nucl. Mater.* 132 (2), 192–201. doi:10.1016/0022-3115(85)90414-3

Yoshida, K., Arima, T., Inagaki, Y., Idemitsu, K., Osaka, M., and Miwa, S. (2011). Oxygen Potential of Hypo-Stoichiometric La-Doped UO_2. *J. Nucl. Mater.* 418 (1), 22–26. doi:10.1016/j.jnucmat.2011.06.045

Conflict of Interest: The authors declare that the research was conducted in the absence of any commercial or financial relationships that could be construed as a potential conflict of interest.

Publisher's Note: All claims expressed in this article are solely those of the authors and do not necessarily represent those of their affiliated organizations, or those of the publisher, the editors and the reviewers. Any product that may be evaluated in this article, or claim that may be made by its manufacturer, is not guaranteed or endorsed by the publisher.

frontiers in Chemistry

REVIEW
published: 12 November 2021
doi: 10.3389/fchem.2021.778140

Perspectives on Pyrochlores, Defect Fluorites, and Related Compounds: Building Blocks for Chemical Diversity and Functionality

Gregory R. Lumpkin and Robert D. Aughterson*

Australian Nuclear Science and Technology Organisation, Sydney, NSW, Australia

In this article we provide some perspectives on a range of pyrochlore and defect fluorite type compounds with nominal $A_2B_2O_7$, A_2BO_5, ABC_2O_7, and other stoichiometries. Typically, the phase transformations and stability fields in these systems are mapped as a function of the ionic radii of the A and B-site cations, e.g., the A/B cation radius ratio (r_A/r_B). This provides a useful guide to compatible structures and compositions for the development of advanced materials. Pyrochlore commonly transforms to a defect fluorite structure at high temperature in many systems; however, it is not uncommon to observe defect fluorite as the initial metastable phase at low temperature. The patterns of order-disorder observed in these materials are primarily due to the energetics of layer stacking, the defect formation and migration energies of cations and anions, or modulations of the parent cubic structure in $3 + n$ dimensional space. The first lead to predominantly non-cubic derivatives of the parent defect fluorite structure (e.g., zirconolite polytypes), the second control the order-disorder processes, and the latter lead to a variety of subtle additional scattering features within the cubic parent structure. Although the energetics of cation disorder and anion-vacancy disorder have become more accessible via atomistic approaches (e.g., MD and DFT), we continue to find interesting physical-chemical problems in these materials. For example, although there are significant differences in composition (Tb/Zr ratio and O content) between $Tb_2Zr_2O_7$ and Tb_2ZrO_5, both of which are defect fluorites, we note that the modulations found in these two compounds by electron scattering are virtually identical with regard to the direction and magnitude of displacement from the normal Bragg diffracted beams. This suggests that neither the A/B cation ratio nor the oxygen stoichiometry have a significant effect on the modulations. The general observations on the systems of compounds noted in this paper rest primarily in the context of industrial materials for nuclear waste disposal, potential applications in inert matrix fuel designs, and other important technological applications such as ionic conductivity, electrical conductivity, and magnetism. Scientific advances in these areas have been underpinned by recent advances in ion irradiation, synchrotron X-ray, neutron scattering, and modelling and simulation capabilities. Furthermore, there has been some renewed interest in natural samples, e.g., Th-U zirconolite and pyrochlore as analogues for potential host phases in nuclear waste forms. In particular, the natural pyrochlores have provided additional details with regard to radiation damage ingrowth, percolation

OPEN ACCESS

Edited by:
Maik Kurt Lang,
The University of Tennessee, United States

Reviewed by:
Anna Shelyug,
Institute of Solid State Chemistry, Russia
Wilson Crichton,
European Synchrotron Radiation Facility, France

***Correspondence:**
Gregory R. Lumpkin
grl@ansto.gov.au

Specialty section:
This article was submitted to Solid State Chemistry, a section of the journal Frontiers in Chemistry

Received: *16 September 2021*
Accepted: *25 October 2021*
Published: *12 November 2021*

Citation:
Lumpkin GR and Aughterson RD (2021) Perspectives on Pyrochlores, Defect Fluorites, and Related Compounds: Building Blocks for Chemical Diversity and Functionality. Front. Chem. 9:778140. doi: 10.3389/fchem.2021.778140

transitions, and the relationships between accumulated dose and physical properties including hardness, elastic modulus. Specific details of the thermal annealing of these samples have also been elucidated in considerable detail.

Keywords: defect fluorite, modulated structures, pyrochlore, weberite, zirconolite

INTRODUCTION

Compounds based on the structure of fluorite, including pyrochlore, zirconolite, and related structure types with different stoichiometries (**Table 1**) are of interest for numerous technological applications, including nuclear fuel and related materials (e.g., inert matrix fuel), nuclear waste forms, fast ion conductors, and magnetic materials, among others. Starting with the basic fluorite structure, $^{VIII}M^{IV}X_2$, where M can be a range of medium to large tetravalent cations (e.g., Zr, Hf, Th, U) or divalent cations (e.g., Ca, Sr, Ba) in eightfold coordination and X is typically O^{2-} or F^{-} in fourfold coordination, there are many variations on the theme when considering charge balancing combinations of cations and anions. A major outcome of the crystal chemical flexibility of the fluorite structure type is the ability to incorporate monovalent and trivalent cations, in particular Y and rare earth elements, presenting a wealth of compositions and potentially useful properties. These structures exist in cubic space group *Fm3m* and when there is more than one cation present, they are generally disordered over the available cation sites; however, in many compositions electron diffraction patterns reveal the structures also include one or more modulations of the parent fluorite structure (Withers et al., 1991; Tabira et al., 2001). These modulated structures indicate the presence of chemical and/or displacive disorder within the underlying crystal structure. Furthermore, oxygen vacancies may be present if additional cations having lower valence states (e.g., Y^{3+} or Ca^{2+}) are not charge balanced by higher valence cations (e.g., W^{6+} or Nb^{5+}) with the cations, anions, and vacancies being disordered over the available lattice sites. These compounds are commonly referred to as defect fluorites.

Ordered derivatives of the defect fluorite structure include compounds with the $A_2B_2O_7$ pyrochlore structure ("227" type, e.g., Subramanian et al., 1983; Chakoumakos 1984), the weberite group of layered compounds, consisting of "227" and "317" type compositions depending on valence states of the cations (Cai and Nino, 2009; Euchner et al., 2019), the A_3BO_7 defect fluorite structures ("317" type), and the A_2BO_5 ("215" type) compounds described by Lau et al. (2007); Shepelev and Petrova (2008); Lau et al. (2008); Aughterson et al., 2014; Aughterson et al., 2015; Aughterson et al., 2018b. Furthermore, the zirconolite structure types with the general formula ABC_2O_7 encompass a smaller group of layered compounds with non-cubic symmetry but based on a defect fluorite subcell. These compounds have useful properties including the ability to incorporate actinides, extreme chemical flexibility across three types of crystallographic sites, and very high resistance to dissolution. Together with pyrochlore, a range of zirconolite compositions have been developed and extensively tested as a major component of nuclear waste forms (e.g., Vance et al., 2002; Strachan et al., 2005, Strachan et al., 2008; Icenhower, et al., 2006). In these broad families there are numerous compounds that are known and possibly others yet to be synthesized in the laboratory, providing a fertile ground for continued discovery research in phase transitions and useful industrial properties. The high level of interest in these materials has been evidenced by numerous papers in the scientific literature. Many of these compounds already have important technological applications in areas including nuclear fuel, nuclear waste forms, fast ion conductors, magnetism, and other areas of materials science (Subramanian et al., 1983; van Dijk et al., 1983; Kutty et al., 1994; Wang et al., 1999; Risovany et al., 2000; Vassen et al., 2000; Wu et al., 2002; Lutique et al.,

TABLE 1 | Some general aspects of ordered structure types and their related disordered, defect fluorite structures. Table is arranged by increasing M/X ratio from top to bottom.

Nomenclature	Space Group	Ordered	Disordered	M/X	X vacancies
Ideal Fluorite	*Fm3m*	n.a.	MX_2	0.5000	0.0000
"227" Type Defect fluorite	*Fm3m*	n.a.	$MX_{1.75}$	0.5714	0.2500
Pyrochlore	*Fd3m*	$A_2B_2X_6Y$ or A_3BX_7	$MX_{1.75}$	0.5714	0.2500
Layered perovskite[a]	*P2 or Cmc2*	$A_2B_2X_7$	n.a.	0.5714	n.a.
Zirconolite 2M[b]	*C2/c* (+)	ABC_2X_7	$MX_{1.75}$	0.5714	0.2500
Weberite 2O[c]	*Imma* (+)	$A_2B_2X_7$ or A_3BX_7	$MX_{1.75}$	0.5714	0.2500
Delta Phase	*R3*	$A_4B_3X_{12}$	$MX_{1.714}$	0.5833	0.2857
"215" Type	*Fm3m*	A_2BX_5	$MX_{1.667}$	0.6000	0.3333

[a]*These compounds are not defect fluorites, but they do consist of perovskite layers alternating with A_2O_3 layers which have some topological resemblance to the fluorite structure. They are included for reference due to possible phase transitions to pyrochlore, etc.*

[b]*Plus numerous polytypes and space groups due to layer stacking variations, including 3T, 3O. 4M, and 6T. In general, layered structures may be complicated by the intergrowth of polytypes and/or stacking disorder. Incommensurate, modulated structures may be observed in the defect fluorite compounds, including 227 type, 317 type, delta phase, and 215 type compounds as a function of composition and overall stoichiometry. The X anion vacancies are given relative to the ideal fluorite structure.*

[c]*Plus numerous polytypes and space groups due to layer stacking variations, including 2O, 2M, 3T, 4M, 5M, 6M, 6T, 7M, and 8O.*

2003a; Lutique et al., 2003b; Shlyahktina et al., 2005; Bansal and Zhu, 2007; Shimamura et al., 2007; Radhakrishnan et al., 2011; Sattonnay et al., 2013; Maram et al., 2018; Euchner et al., 2019; Lyashenko et al., 2010).

STRUCTURE TYPES

Several groups of ordered fluorite-related compounds are compared in **Table 1** together with their alternative disordered formulations. The defect fluorite structure type is based upon the classical fluorite structure (*Fm3m*) with $M^{VIII}X_2^{IV}$ stoichiometry wherein the Roman number superscripts refer to the coordination numbers of the cations and anions, respectively. In general, M is typically Ca, Sr, Ba, and Pb for the compounds with X = F or Zr, Hf, Th, U, Pu, and Cm when X = O. However, in order to accommodate cations of lower or higher than the average 4 + valence state, the actual compositions may be oxygen deficient or in excess and the general formula can be written as $MX_{2 \pm x}$. For oxides, this formula is consistent with charge compensation by fewer oxygen anions if the average cation valence state is less than 4.0, leading to anion vacancies in the structure and a reduction of the cation-anion coordination number. This is the typical situation for the compounds often referred to as defect fluorites. However, if the average valence state is greater than 4.0, then excess oxygen may be present, up to some stability limit. Most nuclear fuels are based on UO_{2+x} wherein U^{4+} is the nominal starting valence state, but higher valence states (U^{5+} and/or U^{6+}) may occur in spent fuel under oxidizing conditions, leading to the condition where x > 2. In **Table 1** we list some of the structure types of interest by increasing M/X ratio from ideal fluorite (M/X = 0.5) to the "215" type compounds (M/X = 0.6). This also relates to an increasing number of X anion vacancies in the defect fluorite asymmetric unit, which may be relevant to some of the properties (e.g., ionic transport, radiation tolerance, etc.) of the different compounds.

Ordered oxide pyrochlores are described by the general formula $A_2B_2X_6Y$ (after Chakoumakos, 1984) which can be expanded to reveal the coordination environments and vacant sites in space group *Fd3m* relative to the underlying disordered MX_2 fluorite basis in space group *Fm3m*. The ordered oxide pyrochlore form can be expressed as: $^{VIII}A_2{}^{VI}B_2{}^{IV}X_6{}^{IV}Y$, where the Roman numerals represent the coordination numbers of the A and B cations, and the X and Y anions. In pyrochlore, the A and B cations are both on fixed positions located at 16*d* and 16*c*, with the X anions located on 48*f* and the Y anions located on 8*b*. We note that natural pyrochlores are common in evolved igneous systems, e.g., carbonatites and granitic pegmatites. The minerals are typically described by the end members $NaCaNb_2O_6F$ (pyrochlore), $NaCaTa_2O_6F$ (microlite), $CaUTi_2O_7$ (betafite), and other "end-member" components such as $Ln_2Ti_2O_7$ (Ln = lanthanides). Pyrochlore may be considered the quintessential "227-type" oxide compound and there are literally hundreds of compounds, both natural and synthetic, that exist in this structural configuration. Subramanian et al. (1983) provided one of the earliest comprehensive reviews of pyrochlore with extended discussion of potentially useful properties, including magnetism, electrical properties, and oxygen ion migration.

The structure of zirconolite can be thought of as a pyrochlore that is compressed normal to one set of (111) planes, resulting in a layered structure in the prototype space group *C*2/*c* which refers to a 2-layered structure. Nevertheless, this structure retains evidence of the cubic defect fluorite subcell and may transform from monoclinic to cubic symmetry under irradiation during a crystalline to amorphous phase transformation. The composition of zirconolite is generally described by the general formula ABC_2O_7 wherein A = Ca, larger actinide and lanthanide cations, B = Zr, Ti, and smaller actinide and lanthanide cations, and C = Ti, Zr, Hf, Nb, Ta, Al, Mg, and transition metals. Various polytypes of zirconolite will form due to layer stacking sequences as a function of composition, including structures based on 3, 4, and 6-layer structural configurations.

The prototype for the weberite structure is orthorhombic, in space group *Imma*, has the 227-type stoichiometry, and the name was originally given to a mineral having the composition Na_2MgAlF_7 (Knop et al., 1982). As indicated in **Table 1**, the weberite structure is also adopted by some compounds with 317-type stoichiometry. For the compounds Y_3TaO_7, Gussev et al. (2020) noted that the space group of the long-range structure is consistent with either of two space groups, Ccmm or $C222_1$, but using neutron pair distribution function (pdf) analysis, they demonstrated that the short-range structure in best represented in the latter space group. The crystal structure is derived from fluorite and is similar to the pyrochlore structure. The two structures have a similar cation sublattice with A cations in 8-fold coordination and B cations in six-fold coordination and built around (111) layers having the hexagonal tungsten bronze topology. As summarized by Cai and Nino (2009), there exists broad compositional flexibility in the weberite structure in both fluoride and oxide compounds. In oxide weberites, the A-sites are typically occupied by Na, K, Ag, Ca, Mn, Cd, Sr, Ba, Y, and lanthanides, whereas the B-sites are home to V, Sb, Te, Nb, Ta, Os, Bi, and U. In the latter two cases, the weberite compounds are $Sr_2Bi_2O_7$ and $Ba_2U_2O_7$ in which the B-site cations must be hexavalent by charge balance (Bi^{6+} and U^{6+}) unless there are oxygen vacancies in the structure.

The delta phase refers to another group of lanthanide metal oxide compounds with rhombohedral symmetry (space group *R*3) and related to defect fluorite structures when disordered. These compounds are based on the general formula $A_4B_3O_{12}$ wherein A = trivalent cations (e.g., Sc, Y and lanthanides) and B = tetravalent cations, primarily synthesized with B = Zr at this point in time. The composition of the delta phase can be reformulated to a pyrochlore type formula as: $^{VIII}A_2{}^{VI}(A_{0.286}B_{1.714})$ $^{IV}O_6{}^{IV}O_{0.857}$, and this equates to $MX_{1.714}$ if represented as a disordered, defect fluorite structure. Compounds with the delta phase structure and stoichiometry are commonly encountered as intermediate compositions in some of the A-B metal oxide systems that have been studied to date.

Considerable recent interest in the A_2BO_5 or "215" structure types has been generated from studies of the phase relations for systems with A = Y and lanthanides and B = Ti (e.g., Shepelev and

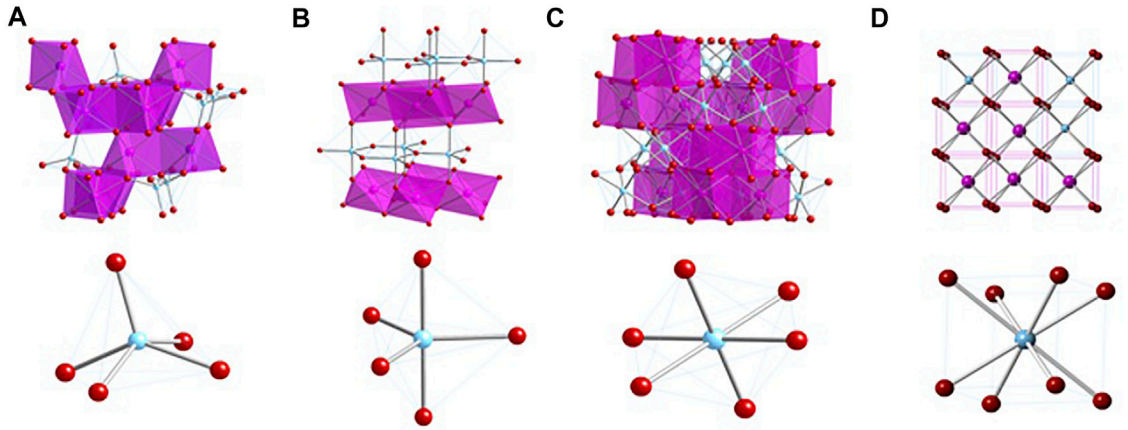

FIGURE 1 | Crystal structures of the A_2BO_5 compounds with B = Ti. **(A)** Orthorhombic structure. **(B)** Hexagonal structure. **(C)** Cubic, pyrochlore-like structure. **(D)** Cubic defect fluorite structure. Note that the cubic form of Dy_2TiO_5 may not be fully resolved as of mid-2021. The cubic form of Ho_2TiO_5 and Y_2TiO_5 consists of a pyrochlore-like structure with a 3x superstructure on (111) planes and a 7x repeat on (622) planes, as described previously (Shepelev and Petrova, 2006, Lau et al., 2007; Lau et al., 2008; Shepelev and Petrova, 2008; Aughterson et al., 2014, Aughterson et al., 2015, Aughterson et al., 2018b).

Petrova, 2006, 2008). When the A-site cation is Ho or other cations of similar radius, notably Y, or other cations from Dy to Er, a pyrochlore-like cubic structure forms with the nominal space group *Fd3m* (Lau et al., 2007, Lau et al., 2008; Aughterson et al., 2014). Although similar to the ordered structure of the $A_2B_2X_6Y$ pyrochlores, the pyrochlore-like A_2BO_5 structure is more complicated and as demonstrated using electron microscopy, the structure shows a tripling of along [111] directions and a less obvious, sevenfold repeat along the [622] directions when viewed down (110) in electron diffraction patterns. This incorporation of smaller lanthanide cations on the A-site leads to a transformation from the tripled pyrochlore structure to a disordered defect fluorite structure in these compounds.

In comparison to the "227" pyrochlores, following Newman et al. (2018) the "215" type cubic compounds can be reformulated from A_2BO_5 to give $^{VIII}A_2{}^{VI}(A_{0.667}B_{1.333})^{IV}O_6{}^{IV}O_{0.667}$, in which A and B are trivalent and tetravalent cations, respectively. This expression is particularly applicable to the A_2BO_5 compounds that are related to pyrochlore. As shown in **Figure 1**, the 215-type compounds adopt orthorhombic, hexagonal, and cubic structures from A = La to Lu and B = Ti. In samples with B = Ti and A = Y or Ho, the A//B ratio of 2/1 leads to a pyrochlore-like structure which exhibits a tripling of the lattice repeat distance on (111) planes, a feature that is not present in samples with other A-site cations or in any of the known compounds with B = Zr. The tripled lattice repeat may be due to a partial ordering of the A and B cations in the structure. We note, however, that electron diffraction patterns taken in the [110] zone axis orientation also show evidence of a 7-fold repeat on the (662) planes, as first described by Lau et al. (2007). This structure evolves to a disordered, defect fluorite with incorporation of progressively smaller cations from Er to Lu. On disordering of the cations and anions, the formula $^{VIII}M^{IV}X_{2-x}$ reflects the local coordination environments of the structure in space group *Fm3m* with the anion deficiency determined by the average valence state of the cations, giving x = 0.25 and 1.75 total oxygens in the formula for the 227 type pyrochlore (M/X = 0.5714) and x = 0.333 and 1.667 total oxygens in the formula for the 215 type (M/X = 0.6000). In the disordered defect fluorite structure, the formulae for 227 and 215 type compounds are $MX_{1.75}$ and $MX_{1.667}$, respectively.

PHASE TRANSITIONS

In setting the stage for the work to be presented here, it is important to proceed with a fundamental understanding of the pyrochlore to defect fluorite phase transformation and the underlying physical chemistry in relation to changes in stoichiometry as evidenced by intrinsic properties such as the A/B cation ionic radii and numerical ratios and overall cation/anion ratios in these materials. Extrinsic properties—time, temperature, and pressure also have an influence on the phase transformation. For example, during synthesis $Gd_2Zr_2O_7$ initially crystallizes in the defect fluorite form, possibly as a metastable phase built on a nano-domain model recently proposed by Simeone et al. (2017), but then transforms to an ordered pyrochlore at ~ 1,250–1,300°C. At higher temperatures up to ~1,500°C the structure transforms back to the disordered defect fluorite structure (see, e.g., Zhou et al., 2016 and references therein), so in many of these refractory oxide systems it is not uncommon for the thermodynamically stable lower temperature form to be kinetically inhibited during the chemical synthesis and thermal processing stage. Even at high temperature, the reaction rates in these systems may be slow, meaning that assessments of equilibrium should be approached with caution.

As a result of interest in host phases for actinides and fission products in nuclear waste forms, some of the phase transitions from the ABC_2X_7 zirconolite compounds to $A_2B_2O_7$ pyrochlore have been studied in considerable detail. However, these studies have mostly been conducted on ceramic samples as a function of composition with limited temperature variation. Vance et al.

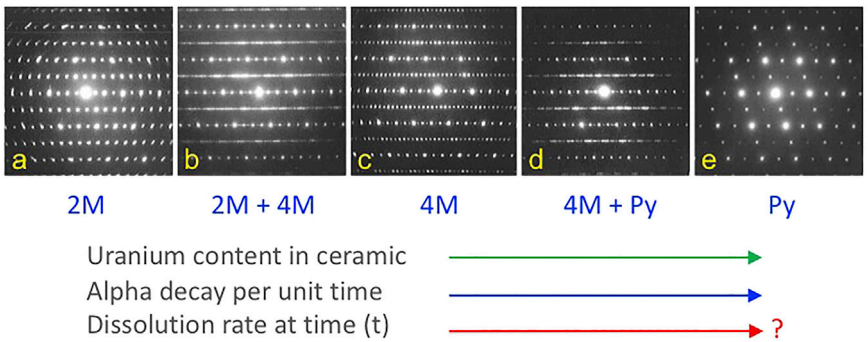

FIGURE 2 | Phase transformations in the series $CaZrTi_2O_7$-$CaUTi_2O_7$ from zirconolite to pyrochlore. From left to right, there are two main zirconolite polytypes (2 and 4M), three single-phase fields **(A, C, E)**, and two intervening two-phase fields **(B, D)** in this system. Similar materials have served as the basis for nuclear waste forms for Pu and other actinides, with reasonably high resistance to aqueous dissolution and release of radioactive components. Adapted from Vance et al. (2002).

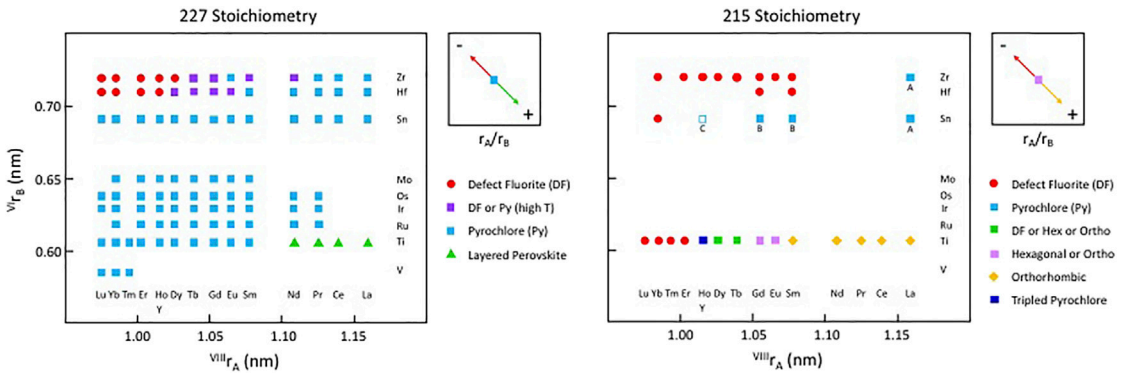

FIGURE 3 | Structure-field map for the $A_2B_2O_7$ system on the left and a partial structure-field map for some of the known A_2BO_5 compounds on the right, both with A = lanthanides and Y and B = selected transition metals at low pressure. This figure does not include the weberite type layered compounds with "227" stoichiometry. Only the series with B = Ti, Sn, Hf, or Zr have been studied fully across the range of A-site constituents and for solid-solutions between both A-site and B-site constituents. The compound Y_2SnO_5, is shown with an open square as this may be A-site deficient and multiphase, containing C-type Y_2O_3. Other compounds with A = Gd and Sm and B = Sn may contain B-type Gd_2O_3 and Sm_2O_3, whereas compounds with A = La and B = Sn and Zr may contain the A-type La_2O_3 compound as an extra phase (indicated by the letters A, B, or C below the symbols). These latter details remain to be investigated.

(2002) conducted an important study of the incorporation of uranium in zirconolite which built some of the foundations for subsequent nuclear waste form development. This work showed that substitution of U in zirconolite from $CaZrTi_2O_7$ to $CaUTi_2O_7$ resulted in the following phase fields: zirconolite 2M, zirconolite 2M + 4M, zirconolite 4M, zirconolite 4M + pyrochlore, and pyrochlore, as shown in **Figure 2**. The ability to produce ceramics in this system with fluorite superstructures, high aqueous durability, and considerable compositional flexibility led to the successful development of similar nuclear waste forms for Pu remediation (see Strachan et al., 2005; Icenhower et al., 2006; Strachan et al., 2008). In fact, this system can be tailored for the best balance of waste loading, additives (e.g., neutron absorbers), fission products, an overall aqueous durability (see Lumpkin, 2006, for further discussion and an example of a Pu-based pyrochlore-zirconolite waste form).

Figure 3 shows a version of the well-known structure map for the 227 type compounds with A = trivalent Y or La-Lu and B = tetravalent V, Ti, Ru, Ir, Os, Mo, Sn, Hf, and Zr. This structure-field map reveals that the titanates with La-Nd prefer the monoclinic layered perovskite structure (e.g., Harvey et al., 2004 and references therein) whereas the hafnates and zirconates with Lu-Y/Ho prefer the cubic, defect fluorite (DF) structure. This structure is the classical defect fluorite based on space group *Fm*3*m* with cations and anions disordered over the available sites. In between these two-phase fields, we find that most of the compounds in this system adopt the ordered pyrochlore (Py) structure and that a few of the hafnates (A = Dy-Eu) and zirconates (A = Tb-Nd, not including Eu) can be transformed to the disordered defect fluorite structure at high temperature. Within these systems, there have been numerous studies of the phase transformation from pyrochlore to defect fluorite as a function of composition using various combinations of electron diffraction, laboratory-based X-ray diffraction, synchrotron X-ray diffraction and spectroscopy, and neutron scattering (e.g., Withers et al., 1991; Whittle et al., 2009; Reid

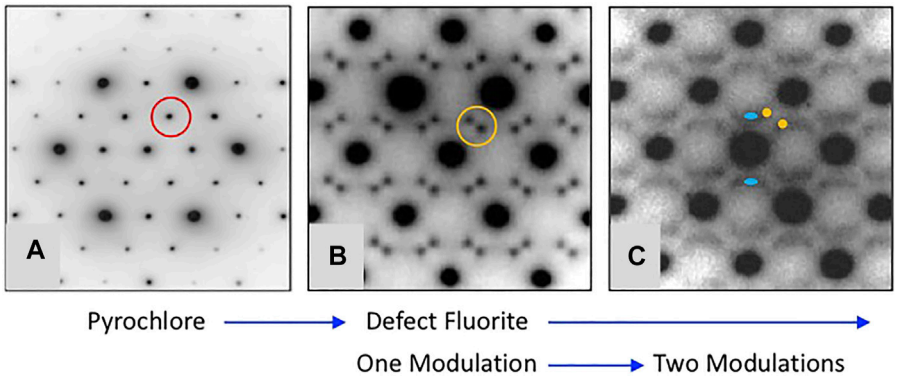

FIGURE 4 | Representative [110] zone axis electron diffraction patterns from $A_2B_2O_7$ compounds with A = Y and B = Sn and Zr showing the development of modulated structures with increasing substitution of Zr for Sn. Figure is modified from De los Reyes et al. (2013). The single modulation in **(B)** occurs at a moderate level of substitution of Zr for Sn and the characteristic split pair is defined as $G_F \pm$ ½ <111>*, e.g., compare the scattering inside the red circle in **(A)** with that inside of the orange circle in **(B)**. Upon further substitution of Zr for Sn the scattering becomes more complex as shown by diffuse streaks and the appearance of a second modulation defined as $G_F \pm$ ¼ <220>* and marked by the blue ovals in **(C)**. This sequence of diffraction patterns illustrates a common trend in the pyrochlore to defect-fluorite transformation as a function of r_A/r_B in the various chemical systems.

et al., 2012; Reynolds et al., 2013; Shamblin et al., 2016; Shamblin et al., 2018; Drey et al., 2020). The composition driven phase transformation generally proceeds as a function of the A/B cation ionic radius ratio (e.g., as r_A/r_B decreases) from Py to (Py + DF) to DF. It is well documented in the literature that the DF phase exhibits modulations of the structure as revealed by electron diffraction. An example of this effect is presented in **Figure 4** for the $Y_2Zr_xSn_{2-x}O_7$ series of compounds (De los Reyes et al., 2013). With increasing Zr content in this series, the structure transforms from pyrochlore to defect fluorite via a narrow two-phase field, initially showing one modulation ($G_F \pm$ ½ <111>*) of the DF phase which appears as a pair of sharp satellite reflections. With increasing substitution of Zr for Sn, this modulation becomes diffuse and a second modulation appears ($G_F \pm$ ¼ <220>*). This appears to be a characteristic feature of Py-DF solid solutions approaching the C-type rare earth oxide stability field. Using the same series of compounds, Zhang et al. (2013) used a combination of synchrotron X-ray diffraction, X-ray absorption spectroscopy, and *ab initio* computer simulations to show that a distinct phase transition from ordered pyrochlore to disordered defect-fluorite occurs at $x \sim 1.0$–1.2. However, X-ray absorption near-edge structure (XANES) data for the Zr L_3 and Y L_2-edges demonstrated a gradual evolution of the structure over the entire compositional range. Therefore, it is apparent that the local disorder begins long before the pyrochlore to defect-fluorite phase boundary is reached and continues to develop throughout the defect-fluorite region.

For comparison, **Figure 3** also shows a similar structure map for the 215 type compounds based on the same set of A and B-site cations. The knowledge base for compounds with this stoichiometry has been developed only for the compositions with B = Ti and, to a lesser extent B = Zr, with a few additional data points for B = Sn. Excluding the effects of cooling rate and pressure, the information presented here is reasonably complete for samples with B = Ti. The available data show that the A_2TiO_5 compounds are orthorhombic for

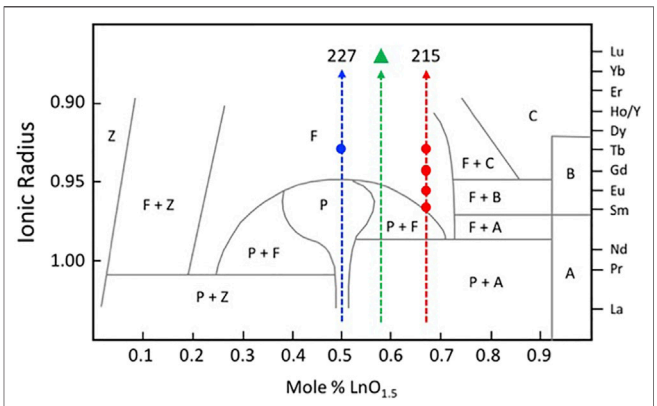

FIGURE 5 | Phase fields found in the ZrO_2—Ln_2O_3 system. This figure is adapted from Tabira et al. (2001). Z = ZrO_2, F = defect fluorite, P = pyrochlore, A = hexagonal A-type Ln_2O_3, B = monoclinic B-type Ln_2O_3, and C = C-type Ln_2O_3 (cubic bixbyite structure). The vertical dashed lines mark the stoichiometries of the 227, delta phase (green triangle), and 215 compounds in this system. The solid blue circle shows the location of the $Tb_2Zr_2O_7$ defect fluorite phase. The solid red circles show the locations of the Sm_2ZrO_5, Eu_2ZrO_5, Gd_2ZrO_5, and Tb_2ZrO_5 defect fluorite phases (see **Figures 6**, **7** for a discussion of the diffuse scattering features in these compounds resulting from modulations of the parent defect fluorite structure).

A = La-Sm; orthorhombic or hexagonal for A = Eu and Gd; orthorhombic, hexagonal, or cubic (defect fluorite) for Tb and Dy; tripled pyrochlore for Ho and Y; and defect fluorite structures for Er-Lu. For these compounds, the phase diagram of Petrova et al. (1982) is the current benchmark for the high temperature behaviour. The topology of this phase diagram is the basis for much of the recent work in providing a detailed description of phase fields as a function of composition and temperature. The phase diagram shows that the melting points of the various compounds increase from about 1,600 to 2,200°C with decreasing ionic radius from La through to Yb. The topology of the phase diagram indicates that the solid-state phase

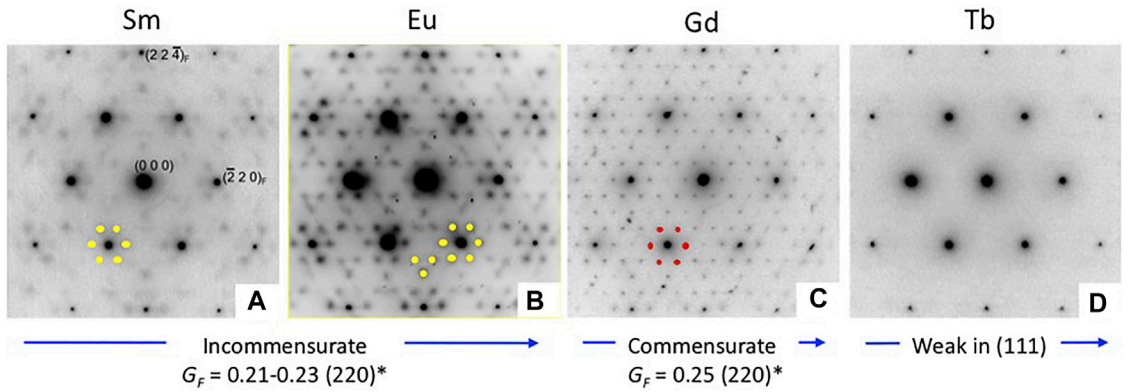

FIGURE 6 | Electron diffraction patterns taken for the [111] zone axis for Sm_2ZrO_5 **(A)**, Eu_2ZrO_5 **(B)**, Gd_2ZrO_5 **(C)**, and Tb_2ZrO_5 **(D)**, showing the gradual changes in the additional scattering features in these compounds with decreasing A-site cation radius from left to right. Modulations of the underlying defect fluorite structure are indicated by the weak beams surrounding the strong ones. Note the gradual change in the modulation of (220)* and symmetry related beams from Sm to Tb. Does the (apparently) commensurate (4x) structure in Gd_2ZrO_5 indicate ordering in the (111) plane? Note also that the extra diffraction spots are nearly absent in Tb_2ZrO_5.

transitions with increasing temperature are likely to proceed from orthorhombic to hexagonal to cubic within a narrow range of ionic radii of the trivalent lanthanide cations, e.g., approximately in the region from Sm to Er. To date, only a few other 215-type compounds have been synthesized with other B-site cations, including samples with B = Sn, Hf, and mainly Zr. The compounds shown in **Figure 3** with B = Zr and A = Sm-Yb, together with Sm_2HfO_5 and Gd_2HfO_5, are single-phase defect fluorites, whereas a production run with A = La was not stoichiometric, having led to the formation of A-type La_2O_3 as a second phase. Other samples produced with B = Sn also contained a second phase, either A-type or B-type sesquioxide depending on the particular lanthanide cation on the A-site. Microanalysis of the run product for Y_2SnO_5 indicated that it had both A-site vacancies and C-type Y_2O_3 as a second phase (see Newman et al., 2018).

A considerable amount of additional information related to the "stability" fields of defect fluorite, pyrochlore, and their component oxides is available in the phase diagram (or structure-field map) presented by Tabira et al. (2001), reproduced here in slightly modified form in **Figure 5**. This figure was developed specifically for the Ln_2O_3-ZrO_2 system of compounds and shows the various single phase and two-phase fields as a function of the $LnO_{1.5}$ content (mole %) on the *x*-axis versus the ionic radii of the Ln cations on the *y*-axis. This particular diagram provides an excellent basis for understanding the nature of the defect fluorite phase and the types of modulations that occur as a function of composition in the single-phase region and in two-phase regions next to the phase field of zirconia, on either side of the pyrochlore field, and next to the phase fields of the A, B, and C-type rare earth oxides. This work helped to underpin the concept of a Py to DF transformation driven by strain in the close-packed {111} cation layers of the DF structure by cation and oxygen vacancies. In **Figure 5**, we also plot the locations of four 215-type compounds with A = Sm, Eu, Gd, and Tb (red dots). The structural complexity of these compounds is illustrated in **Figure 6**, showing the gradual evolution of the modulations in their [111] zone axis electron diffraction patterns. With decreasing ionic radius of the A-site cation, these compositions transition away from the pyrochlore + fluorite two-phase field and presumably toward the fluorite + C-type Ln_2O_3 field. On proceeding from A = Sm through to Tb, the modulations become stronger and transition from incommensurate to (apparently) commensurate for A = Gd, but they are very weak and diffuse for A = Tb. Finally, we note also that the structural modulations for $Tb_2Zr_2O_7$ and Tb_2ZrO_5 in the [110] zone axis are virtually identical, indicating that the stoichiometry change from 227 to 215 type has not changed the modulation wave vector significantly (**Figure 7**). This is another interesting problem for the detailed interpretation of strain-driven transformations in this system as a function of the Tb/Zr ratio.

RADIATION TOLERANCE

The radiation tolerance of the large group of fluorite and related compounds has been studied extensively for the MX_2 fluorite compounds and the $A_2B_2O_7$ pyrochlore and defect fluorite compounds. Furthermore, there is a growing body of evidence in relation to the radiation tolerance and other properties of the A_2BO_5 compounds. This will be discussed briefly here for several different experimental methods. Atomistic simulations investigate the performance of the material on picosecond time scales through an analysis of the energetics of defect formation and migration (e.g., Minervini et al., 2000; Jiang et al., 2009). In the latter context, one may generally consider that radiation tolerance is promoted by high defect formation energies and low energy barriers to atomic migration in the host structure. In this situation, it is more difficult to move an atom out of its normal crystallographic site, but if enough energy is imparted to the atom to displace it, then it may easily return to either the original site or a similar one nearby. On the other

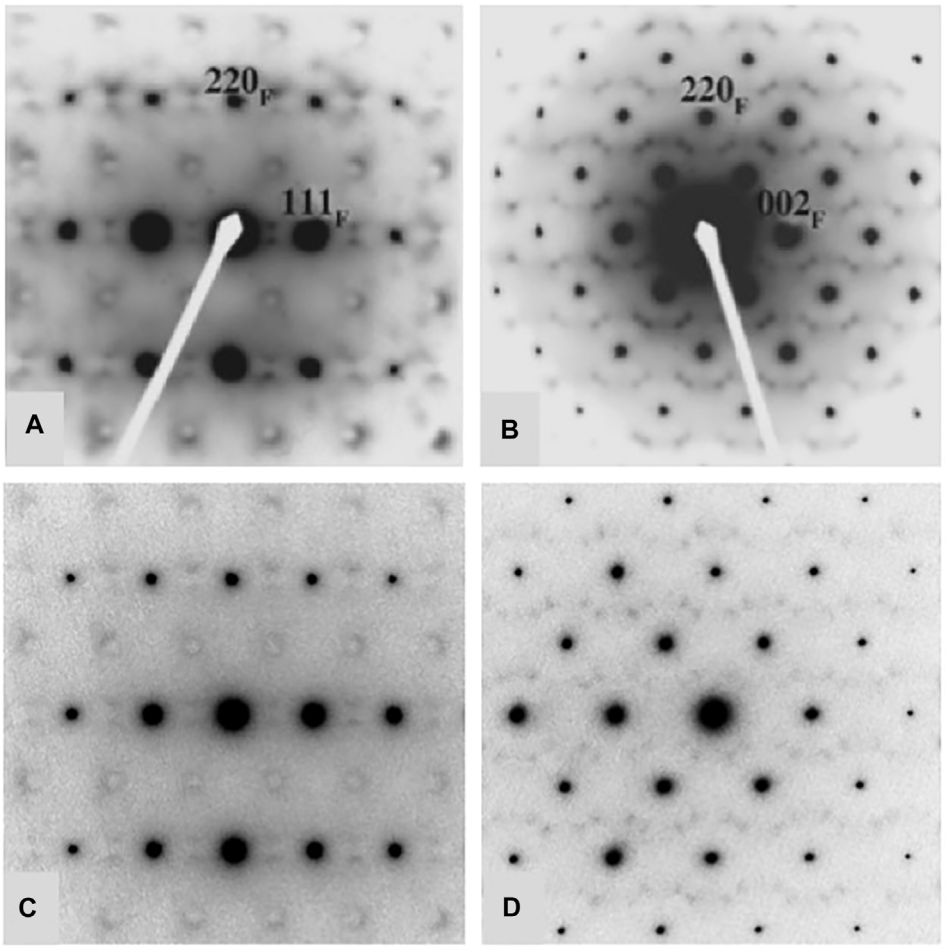

FIGURE 7 | Comparison of diffuse scattering features in $Tb_2Zr_2O_7$ **(A,B)** and Tb_2ZrO_5 **(C,D)**. Both compounds are defect fluorite structure types showing characteristic modulations the [112] zone axis in **(A,C)** and the [011] zone axis in **(B,D)**. However, in spite of the major difference in composition (A/B cation ratio and number of anion vacancies), the diffuse features and their measured wave vectors are identical within error. Figures **(A,B)** are after Tabira et al. (2001).

hand, if energy barriers to migration are high, it is more likely that radiation-induced displacements and damage will be retained under a given set of conditions (time, temperature, etc.). These principles have been demonstrated by a combination of theoretical and experimental work over the course of 30 years or more. A major outcome of the modelling work on compounds with $A_2B_2O_7$ stoichiometry is that pyrochlore and defect fluorite compounds exhibit lower cation antisite and anion Frenkel defect formation energies as a function of the A/B cation radius ratio r_A/r_B. As the value of r_A/r_B decreases, the structures may transform from pyrochlore to a defect fluorite structure as a function of temperature or possibly as a result of radiation damage.

Many ion irradiation experiments have now been completed where the experimental time is on the scale of minutes or hours (e.g., Begg et al., 2001; Aughterson et al., 2016, Aughterson et al., 2018a; Aughterson et al., 2018b; Park et al., 2018; Whittle et al., 2011). These high dose rate experiments have provided much of the fundamental physics knowledge on radiation damage in fluorite and derivative materials as a function of ion mass, energy, and temperature. Major conclusions to be drawn from these studies indicate that the $A_2B_2O_7$ pyrochlore and defect fluorite compounds are increasingly radiation tolerant (e.g., high critical amorphization dose and low critical amorphization temperature) as a function of the A/B cation radius ratio (r_A/r_B). Because the A-sites are devoted to a given set of nuclear waste elements, the B-sites are generally available to host larger cations like Hf and/or Zr, which increase the value of r_A/r_B over that of similar pyrochlores with B = Ti (and also provide the potential to improve both the chemical durability and the resistance to amorphization). As a result, a particular group of defect fluorite compounds, e.g., those with B = Zr and A = smaller lanthanides, tend to remain crystalline under irradiation. In the real world, of course, these materials must include actinides and possibly some fission products and impurity elements and maintain a similar level of radiation resistance and chemical durability for optimum performance under wasteform storage conditions. Although the A_2BO_7 compounds with B = Ti are not radiation tolerant, the orthorhombic structures do exhibit critical

amorphization temperatures that are lower than those the corresponding $A_2B_2O_7$ pyrochlore and defect-fluorite compounds. Additionally, the A_2BO_7 type compounds have the higher A/B cation radius ratio of 2:1, in theory allowing higher waste loadings. Finally, the defect-fluorite A_2BO_7 compounds with B = Zr may have the potential to provide both higher waste loadings, neutron absorbers for criticality control, and "built-in" radiation tolerance.

Unfortunately, only a few candidate materials have been doped with short-lived actinides such as ^{244}Cm ($t_{1/2}$ = 18.1 y) or ^{238}Pu ($t_{1/2}$ = 87.7 years) where the experiments generally run for less than 5 years and are highly relevant to the development of nuclear waste forms (e.g., Weber 1998; Strachan et al., 2005, 2008). This work has demonstrated that waste forms based on pyrochlore and/or zirconolite become amorphous with increasing dose with the potential for volume expansion (on the order of 5%) and cracking, thereby increasing the surface area of the waste form. Finally, there have been a few investigations of natural analogues containing long-lived ^{235}U ($t_{1/2} = 7.0 \times 10^8$ y), ^{238}U ($t_{1/2} = 4.5 \times 10^9$ y), and ^{232}Th ($t_{1/2} = 1.4 \times 10^{10}$ y), including pyrochlore, zirconolite, and other radioactive minerals. These studies demonstrate that pyrochlore and zirconolite become amorphous with increasing alpha-decay dose. However, it appears that zirconolite and, to a lesser extent, pyrochlore, are capable of actinide retention in all but the most severe conditions imposed by nature. We note here that there are no Zr-rich natural pyrochlores, as the pressure, temperature, and bulk rock compositions generally dictate that ZrO_2 (baddeleyite) is a stable phase in the mineral assemblages with low a (SiO_2), whereas zircon is stable in assemblages with high a (SiO_2).

Finally, we note here that the radiation damage effects and physical/mechanical properties of natural pyrochlores have recently been studied in some detail in relation to percolation theory, although the compositions of these samples differ significantly from the target compositions of pyrochlore-based nuclear waste forms (e.g., the natural samples may have significant amounts of Na on the A-site, Nb and Ta on the B-site, together with F and OH on the Y-site). Nevertheless, the results are significant in providing a fundamental basis for understanding the physical properties of pyrochlore based materials under irradiation. Firstly, Zeitlow et al. (2017) presented a new study of the thermal annealing behaviour and mechanical properties of natural pyrochlore samples with amorphous fractions ranging from about 8 to 100%, showing how the recovery steps of the three most damaged samples systematically increase in temperature as a function of the initial damage fraction. This work included detailed analyses of the Raman and infrared spectra of these samples. Furthermore, Reissner et al. (2020) provided additional of evolution of the hardness and elastic moduli of three of the same samples as a function of the annealing temperature and time (16 h in air, per temperature step). A further assessment of the mechanical behaviour of the pyrochlores was conducted by Beirau and Huber (2021) by using finite element-voxel models the calculate the elastic moduli and hardness values as a function of alpha-decay dose and annealing temperature. It is noteworthy that the implied, model dependent percolation points at ~16% (p1) and 84% (p2) of the amorphous fraction are reasonably consistent with previous experimental work on radiation damaged pyrochlores (Lumpkin and Ewing, 1988).

OPPORTUNITY SPACE AND QUESTIONS

Based on this brief look at defect fluorite and related compounds and systems, it is apparent that there remain considerable opportunities for ongoing research and development within the very large composition space indicated by **Table 1**. Future research opportunities include the fundamental physical chemistry of phase transitions from the various ordered structure types listed here to their disordered defect fluorite structures or from one ordered structure to another. Knowledge generated from an understanding of the basic crystal chemistry and physical chemistry across these systems opens the door to novel materials research and development, in this case, there are many potential applications in areas such as the high-technology sector and energy/nuclear materials that might benefit from further fundamental research. For these and other applications, future work might be devoted to the development of specialist materials taking advantage of the properties of structure types such as defect fluorite, pyrochlore, weberite, delta phase, and 215-type compounds in the design, production, and testing of new materials. In particular, one area of interest may be the design and testing of composite materials using various combinations of these structure types, provided that phase compatibility can be achieved via both chemical and dimensional compatibility.

In particular, **Figure 3** indicates that there are considerable opportunities for research to be conducted within the composition space for the A_2BO_5 compounds. Currently, most investigations have focused on the compounds with B = Ti, with more recent efforts devoted to the materials with B = Zr and, to a lesser extent with B = Sn and Hf. However, there have been few, if any, investigations into the systems with B = Mo, Os, Ir, Ru, and V for this particular stoichiometry. Even in the structures with B = Ti, there remain some uncertainties in the structures, e.g., as suggested by electron diffraction patterns that might lead to questions about the actual symmetry or in the details related to incommensurate, modulation effects and their origins. The fundamental physical chemistry of new materials with B = V, Ru, Rh, Ir, Os, and Mo (and possibly other elements, e.g., Sb, Nb, Ta, and Pb and Bi in their different valence states) together with new investigations of samples with B = Sn, Hf, and Zr. How do the orthorhombic, hexagonal, cubic, and other structures (e.g., Shepelev and Petrova, 2006, Shepelev and Petrova, 2008) evolve in these systems as a function of composition and what are their properties? Furthermore, there is considerable scope for new studies to be conducted on the high temperature behavior in the system with B = Ti plus variable amounts of other small cations in a substitutional role.

Another opportunity space will involve the future study of structural evolution between the $A_2B_2O_7$ compounds and their A_2BO_5 counterparts. Similar comments apply more broadly to

some of the other structure types where we may find a wealth of new information (and new functional materials?) in the study of phase transitions between the various delta phase, 215-type, 227-type, and 317-type compounds listed in **Table 1**. An interesting aspect of this problem is the wide variation in composition and stoichiometry (M/X = 0.5–0.6 and X vacancies = 0.0 to 0.5 per M cation) found in the different groups of compounds. Furthermore, the observation in this paper that $Tb_2Zr_2O_7$ and Tb_2ZrO_5 exhibit identical modulations of the underlying defect fluorite structure suggests that such modulations are not a precise function of the Tb/Zr ratio, M/X ratio, or the number of oxygen vacancies (0.250 and 0.333), respectively, relative to the disordered MX_{2-x} fluorite basis. In general terms, the origin and significance of these unusual crystallographic features presents another interesting topic for future experimental and theoretical work. For example, just what is the fraction of atoms involved in both displacive and compositional components of the modulations and how is this related to the populations of defects discussed below?

Following from the above discussion of modulations, it is of utmost importance to understand the defect chemistry of the fluorite structure and its more complex derivative compounds in greater detail in order to complement studies of physical-chemical properties and radiation damage effects. In ordered pyrochlore, for example, these defects are generally understood to be a combination of cation anti-site (CA) defects, cation Frenkel (CF) defects, and anion Frenkel (AF) defects. The transition from pyrochlore to defect fluorite is related to the energetics of the CA and AF defects and has been mapped out in some detail using atomistic simulations (e.g., Minervini et al., 2000; Jiang et al., 2009; Uberuaga et al., 2015; Archer et al., 2021) as a guide to predict order-disorder trends in these compounds as a function of the ionic radii of the A and B cations. In general, the defect formation energies of CA and AF defects decrease as the ionic radius ratio r_A/r_B decreases and this in turn corresponds to the transformation from pyrochlore to defect fluorite structures in numerous solid solutions. Together with fundamental crystal chemistry parameters, the simulations noted here were also used to develop a predictive model of radiation tolerance in pyrochlore and defect fluorite compounds (Lumpkin et al., 2007). In general terms, it would be very interesting to compare the radiation damage data for $A_2B_2O_7$ and the cubic A_2BO_5 compounds with the same A and B cations to explore the effect of anions vacancies on damage recovery, if any. Finally, we suggest that considerable improvements might be made in the study of defects in these compounds through a combined modelling and experimental approach directed toward an advanced interpretation of, for example, neutron pair distribution functions with and without specific defects. Furthermore, can the effects of incommensurate structures or layer stacking disorder be incorporated into this problem in a quantitative way? This approach would necessarily involve the calculation of the relevant scattering functions for different structure types with and without an array of defects such as interstitials, vacancies, cation anti-site arrangements, Frenkel defects, and stacking disorder within the host crystal.

AUTHOR CONTRIBUTIONS

This paper is based on a collection of data from the authors and other information from selected previous publications involving the authors, together with existing information in the literature. GL supervised some of the previous work, including the PhD research of RA, which forms the basis of part of this paper. GL also supervised some of the work of RA during a previous leadership role and provided the concept for this paper, wrote the first version of the text prior to co-author contributions and review. GL also performed some of the TEM investigations presented here. RA provided the specific scientific leadership and development of concepts and methods that underpinned our research projects, including crystal structure refinements, crystal chemical relationships, and ion irradiation experiments, and drafted **Figure 1**.

FUNDING

This work was fully funded and approved by the Australian Nuclear Science and Technology Organisation for publication.

ACKNOWLEDGMENTS

We thank the staff of the Nuclear Materials Development and Characterisation (NMDC) Platform at ANSTO for providing access to and maintenance of facilities used by the authors. We are greatly indebted to all of our colleagues with whom we have worked closely on the general topics and some of the focused research problems on pyrochlores, defect fluorites, and related compounds and materials over the course of several decades. The authors acknowledge the financial support from the Australian Government under SIA grant SHCC000002.

REFERENCES

Archer, A., Foxhall, H. R., Allan, N. L., Shearer, J. R. W., Gunn, D. S. D., Harding, J. H., et al. (2021). Multiple cascade Radiation Damage Simulations of Pyrochlore. *Mol. Simulation* 47, 273–283. doi:10.1080/08927022.2020.1805449

Aughterson, R. D., Lumpkin, G. R., de los Reyes, M., Sharma, N., Ling, C. D., Gault, B., et al. (2014). Crystal Structures of Orthorhombic, Hexagonal, and Cubic Compounds of the $Sm_{(x)}Yb_{(2-x)}TiO_5$ Series. *J. Solid State. Chem.* 213, 60–67. doi:10.1016/j.jssc.2014.02.029

Aughterson, R. D., Lumpkin, G. R., Thorogood, G. J., Zhang, Z., Gault, B., and Cairney, J. M. (2015). Crystal Chemistry of the Orthorhombic Ln_2TiO_5 Compounds with *Ln* = La, Pr, Nd, Sm, Gd, Tb and Dy. *J. Solid State. Chem.* 227, 182–192. doi:10.1016/j.jssc.2015.03.003

Aughterson, R. D., Lumpkin, G. R., de los Reyes, M., Gault, B., Baldo, P., Ryan, E., et al. (2016). The Influence of crystal Structure on Ion-Irradiation Tolerance in

the Sm(x)Yb(2-x)TiO5 Series. *J. Nucl. Mater.* 471, 17–24. doi:10.1016/j.jnucmat.2015.12.036

Aughterson, R. D., Lumpkin, G. R., Smith, K. L., Reyes, M. d. l., Davis, J., Avdeev, M., et al. (2018a). The Ion-Irradiation Tolerance of the Pyrochlore to Fluorite Ho(x)Yb(2-x)TiO5 and Er2TiO5 Compounds: A TEM Comparative Study Using Both *In-Situ* and Bulk *Ex-Situ* Irradiation Approaches. *J. Nucl. Mater.* 507, 316–326. doi:10.1016/j.jnucmat.2018.05.026

Aughterson, R. D., Lumpkin, G. R., Smith, K. L., Zhang, Z., Sharma, N., and Cairney, J. M. (2018b). The crystal Structures and Corresponding Ion-Irradiation Response for the Tb(x)Yb(2−x)TiO5 Series. *Ceramics Int.* 44 (1), 511–519. doi:10.1016/j.ceramint.2017.09.205

Bansal, N. P., and Zhu, D. (2007). Effects of Doping on thermal Conductivity of Pyrochlore Oxides for Advanced thermal Barrier Coatings. *Mater. Sci. Eng. A* 459, 192–195. doi:10.1016/j.msea.2007.01.069

Begg, B. D., Hess, N. J., McCready, D. E., Thevuthasan, S., and Weber, W. J. (2001). Heavy-ion Irradiation Effects in Gd2(Ti2−xZrx)O7 Pyrochlores. *J. Nucl. Mater.* 289, 188–193. doi:10.1016/s0022-3115(00)00696-6

Beirau, T., and Huber, N. (2021). Percolation Transitions in Pyrochlore: Radiation-Damage and Thermally Induced Structural Reorganization. *Appl. Phys. Lett.* 119, 131905. doi:10.1063/5.0068685

Cai, L., and Nino, J. C. (2009). Complex Ceramic Structures. I. Weberites. *Acta Crystallogr. Sect. B* 65, 269–290. doi:10.1107/s0108768109011355

Chakoumakos, B. C. (1984). Systematics of the Pyrochlore Structure Type, Ideal $A_2B_2X_6Y$. *J. Solid State. Chem.* 53, 120–129.

De los Reyes, M., Whittle, K. R., Zhang, Z., Ashbrook, S. E., Mitchell, M. R., Jang, L.-Y., et al. (2013). The Pyrochlore to Defect Fluorite Phase Transition in Y2Sn2−xZrxO7. *RSC Adv.* 3, 5090–5099. doi:10.1039/c3ra22704a

Drey, D. L., O'Quinn, E. C., Subramani, T., Lilova, K., Baldinozzi, G., Gussev, I. M., et al. (2020). Disorder in Ho2Ti2−xZrxO7: Pyrochlore to Defect Fluorite Solid Solution Series. *RSC Adv.* 10, 34632–34650. doi:10.1039/d0ra07118h

Euchner, H., Clemens, O., and Reddy, M. A. (2019). Unlocking the Potential of Weberite-type Metal Fluorides in Electrochemical Energy Storage. *Npj Comput. Mater.* 5, 31. doi:10.1038/s41524-019-0166-3

Gussev, I. M., O'Quinn, E. C., Baldinozzi, G., Neuefeind, J., Ewing, R. C., Zhang, F., et al. (2020). Local Order of Orthorhombic Weberite-type Y3TaO7 as Determined by Neutron Total Scattering and Density Functional Theory Calculations☆. *Acta Mater.* 196, 704–709. doi:10.1016/j.actamat.2020.07.005

Harvey, E. R., Whittle, K. R., Lumpkin, G. R., Smith, R. I., and Redfern, S. A. T. (2004). Structural Phase Transitions and Solid Solubilities of $(Nd,La)_2(Zr,Ti)_2O_7$ Phases Deduced by Neutron Diffraction. *J. Solid State. Chem.* 178, 800–810. doi:10.1016/j.jssc.2004.12.030

Icenhower, J. P., Strachan, D. M., Mcgrail, B. P., Scheele, R. D., Rodriguez, E. A., Steele, J. L., et al. (2006). Dissolution Kinetics of Pyrochlore Ceramics for the Disposition of Plutonium. *Am. Mineral.* 91, 39–53. doi:10.2138/am.2006.1709

Jiang, C., Stanek, C. R., Sickafus, K. E., and Uberuaga, B. P. (2009). First-principles Prediction of Disordering Tendencies in Pyrochlore Oxides. *Phys. Rev. B* 79, 104203. doi:10.1103/physrevb.79.104203

Knop, O., Cameron, T. S., and Jochem, K. (1982). What Is the True Space Group of Weberite? *J. Solid State. Chem.* 43, 213–221. doi:10.1016/0022-4596(82)90231-6

Kutty, K. V. G., Rajagopalan, S., Mathews, C. K., and Varadaraju, U. V. (1994). Thermal Expansion Behaviour of Some Rare Earth Oxide Pyrochlores. *Mater. Res. Bull.* 29, 759–766. doi:10.1016/0025-5408(94)90201-1

Lau, G. C., Ueland, B. G., Dahlberg, M. L., Freitas, R. S., Huang, Q., Zandbergen, H. W., et al. (2007). Structural Disorder and Properties of the Stuffed Pyrochlore Ho_2TiO_5. *Phys. Rev. B* 76, 054430. doi:10.1103/physrevb.76.054430

Lau, G. C., McQueen, T. M., Huang, Q., Zandbergen, H. W., and Cava, R. J. (2008). Long- and Short-Range Order in Stuffed Titanate Pyrochlores. *J. Solid State. Chem.* 181, 45–50. doi:10.1016/j.jssc.2007.10.025

Lumpkin, G. R., and Ewing, R. C. (1988). Alpha-decay Damage in Minerals of the Pyrochlore Group. *Phys. Chem. Mineral.* 16, 2–20. doi:10.1007/bf00201325

Lumpkin, G. R. (2006). Ceramic Waste Forms for Actinides. *Elements* 2, 365–372. doi:10.2113/gselements.2.6.365

Lumpkin, G. R., Pruneda, M., Rios, S., Smith, K. L., Trachenko, K., Whittle, K. R., et al. (2007). Nature of the Chemical Bond and Prediction of Radiation Tolerance in Pyrochlore and Defect Fluorite Compounds. *J. Solid State. Chem.* 180, 1512–1518. doi:10.1016/j.jssc.2007.01.028

Lutique, S., Konings, R. J. M., Rondinella, V. V., Somers, J., and Wiss, T. (2003a). The thermal Conductivity of Nd2Zr2O7 Pyrochlore and the thermal Behaviour of Pyrochlore-Based Inert Matrix Fuel. *J. Alloys Compd.* 352, 1–5. doi:10.1016/s0925-8388(02)01113-1

Lutique, S., Staicu, D., Konings, R. J. M., Rondinella, V. V., Somers, J., and Wiss, T. (2003b). Zirconate Pyrochlore as a Transmutation Target: thermal Behaviour and Radiation Resistance against Fission Fragment Impact. *J. Nucl. Mater.* 319, 59–64. doi:10.1016/s0022-3115(03)00134-x

Lyashenko, L. P., Shcherbakova, L. G., Belov, D. A., Knerel'man, E. I., and Dremova, N. N. (2010). Synthesis and Electrical Properties of Gd2MO5 (M = Zr, Hf). *Inorg. Mater.* 46, 1341–1347. doi:10.1134/s0020168510120137

Maram, P. S., Ushakov, S. V., Weber, R. J. K., Benmore, C. J., and Navrotsky, A. (2018). Probing Disorder in Pyrochlore Oxides Using *In Situ* Synchrotron Diffraction from Levitated Solids-A Thermodynamic Perspective. *Sci. Rep.* 8, 10658–10711. doi:10.1038/s41598-018-28877-x

Minervini, L., Grimes, R. W., and Sickafus, K. E. (2000). Disorder in Pyrochlore Oxides. *J. Am. Ceram. Soc.* 83, 1873–1878. doi:10.1111/j.1151-2916.2000.tb01484.x

Newman, R., Aughterson, R. D., and Lumpkin, G. R. (2018). Synthesis and Structure of Novel A2BO5 Compounds Containing A = Y, Yb, Gd, Sm, and La and B = Zr, Ti, and Sn. *MRS Adv.* 3, 1117–1122. doi:10.1557/adv.2018.210

Park, S., Tracy, C. L., Zhang, F., Palomares, R. I., Park, C., Trautmann, C., et al. (2018). Swift-heavy Ion Irradiation Response and Annealing Behavior of A2TiO5 (A = Nd, Gd, and Yb). *J. Solid State. Chem.* 258, 108–116. doi:10.1016/j.jssc.2017.09.028

Petrova, M. A., Novikova, A. S., and Grebenshchikov, R. G. (1982). Polymorphism of Rare Earth Titanates of the Composition Ln_2TiO_5. *Inorg. Mater.* 18, 236.

Radhakrishnan, A. N., Rao, P. P., Linsa, K. S. M., Deepa, M., and Koshy, P. (2011). Influence of Disorder-To-Order Transition on Lattice thermal Expansion and Oxide Ion Conductivity in (CaxGd1−x)2(Zr1−xMx)2O7 Pyrochlore Solid Solutions. *Dalton Trans.* 40, 3839–3848. doi:10.1039/c0dt01688h

Reid, D. P., Stennett, M. C., and Hyatt, N. C. (2012). The Fluorite Related Modulated Structures of the Gd2(Zr2−xCex)O7 Solid Solution: An Analogue for Pu Disposition. *J. Solid State. Chem.* 191, 2–9. doi:10.1016/j.jssc.2011.12.039

Reissner, C. E., Roddatis, V., Bismayer, U., Schreiber, A., Pöllmann, H., and Beirau, T. (2020). Mechanical and Structural Response of Radiation-Damaged Pyrochlore to thermal Annealing. *Materialia* 14, 100950. doi:10.1016/j.mtla.2020.100950

Reynolds, E., Blanchard, P. E. R., Kennedy, B. J., Ling, C. D., Liu, S., Avdeev, M., et al. (2013). Anion Disorder in Lanthanoid Zirconates Gd2-xTbxZr2O7. *Inorg. Chem.* 52, 8409–8415. doi:10.1021/ic4009703

Risovany, V. D., Varlashova, E. E., and Suslov, D. N. (2000). Dysprosium Titanate as an Absorber Material for Control Rods. *J. Nucl. Mater.* 281 (1), 84–89. doi:10.1016/s0022-3115(00)00129-x

Sattonnay, G., Sellami, N., Thomé, L., Legros, C., Grygiel, C., Monnet, I., et al. (2013). Structural Stability of Nd2Zr2O7 Pyrochlore Ion-Irradiated in a Broad Energy Range. *Acta Mater.* 61, 6492–6505. doi:10.1016/j.actamat.2013.07.027

Shamblin, J., Feygenson, M., Neuefeind, J., Tracy, C. L., Zhang, F., Finkeldei, S., et al. (2016). Probing Disorder in Isometric Pyrochlore and Related Complex Oxides. *Nat. Mater* 15, 507–511. doi:10.1038/nmat4581

Shamblin, J., Tracy, C. L., Palomares, R. I., O'Quinn, E. C., Ewing, R. C., Neuefeind, J., et al. (2018). Similar Local Order in Disordered Fluorite and Aperiodic Pyrochlore Structures. *Acta Mater.* 144, 60–67. doi:10.1016/j.actamat.2017.10.044

Shepelev, Y. F., and Petrova, M. A. (2008). Crystal Structures of Ln2TiO5 (Ln = Gd, Dy) Polymorphs. *Inorg. Mater.* 44, 1354–1361. doi:10.1134/s0020168508120170

Shepelev, Y. F., and Petrova, M. A. (2006). Structures of Two High-Temperature Dy2TiO5 Modifications. *Russ. J. Inorg. Chem.* 51, 1636–1640. doi:10.1134/s0036023606100196

Shimamura, K., Arima, T., Idemitsu, K., and Inagaki, Y. (2007). Thermophysical Properties of Rare-Earth-Stabilized Zirconia and Zirconate Pyrochlores as Surrogates for Actinide-Doped Zirconia. *Int. J. Thermophys.* 28, 1074–1084. doi:10.1007/s10765-007-0232-9

Shlyakhtina, A. V., Kolbanev, I. V., Knotko, A. V., Boguslavskii, M. V., Stefanovich, S. Y., Karyagina, O. K., et al. (2005). Ionic Conductivity of Ln2 + X Zr2 − X O7 − X/2 (Ln = Sm-Gd) Solid Solutions. *Inorg. Mater.* 41, 854–863. doi:10.1007/s10789-005-0226-6

Simeone, D., Thorogood, G. J., Huo, D., Luneville, L., Baldinozzi, G., Petricek, V., et al. (2017). Intricate Disorder in Defect Fluorite/pyrochlore: a concord of Chemistry and Crystallography. *Sci. Rep.* 7, 3727. doi:10.1038/s41598-017-02787-w

Strachan, D. M., Scheele, R. D., Buck, E. C., Icenhower, J. P., Kozelisky, A. E., Sell, R. L., et al. (2005). Radiation Damage Effects in Candidate Titanates for Pu Disposition: Pyrochlore. *J. Nucl. Mater.* 345, 109–135. doi:10.1016/j.jnucmat.2005.04.064

Strachan, D. M., Scheele, R. D., Buck, E. C., Kozelisky, A. E., Sell, R. L., Elovich, R. J., et al. (2008). Radiation Damage Effects in Candidate Titanates for Pu Disposition: Zirconolite. *J. Nucl. Mater.* 372, 16–31. doi:10.1016/j.jnucmat.2007.01.278

Subramanian, M. A., Aravamudan, G., and Subba Rao, G. V. (1983). Oxide Pyrochlores - A Review. *Prog. Solid State. Chem.* 15, 55–143. doi:10.1016/0079-6786(83)90001-8

Tabira, Y., Withers, R. L., Barry, J. C., and Elcoro, L. (2001). The Strain-Driven Pyrochlore to "Defect Fluorite" Phase Transition in Rare Earth Sesquioxide Stabilized Cubic Zirconias. *J. Solid State. Chem.* 159, 121–129. doi:10.1006/jssc.2001.9139

Uberuaga, B. P., Tang, M., Jiang, C., Valdez, J. A., Smith, R., Wang, Y., et al. (2015). Opposite Correlations between Cation Disordering and Amorphization Resistance in Spinels versus Pyrochlores. *Nat. Commun.* 6, 8750. doi:10.1038/ncomms9750

van Dijk, M. P., de Vries, K. J., and Burggraaf, A. J. (1983). Oxygen Ion and Mixed Conductivity in Compounds with the Fluorite and Pyrochlore Structure. *Solid State Ionics* 9-10, 913–919. doi:10.1016/0167-2738(83)90110-8

Vance, E. R., Lumpkin, G. R., Carter, M. L., Cassidy, D. J., Ball, C. J., Day, R. A., et al. (2002). Incorporation of Uranium in Zirconolite ($CaZrTi_2O_7$). *J. Am. Ceram. Soc.* 85 (7), 1853–1859. doi:10.1111/j.1151-2916.2002.tb00364.x

Vassen, R., Cao, X., Tietz, F., Basu, D., and Stöver, D. (2000). Zirconates as New Materials for thermal Barrier Coatings. *J. Am. Ceram. Soc.* 83, 2023–2028. doi:10.1111/j.1151-2916.2000.tb01506.x

Wang, S. X., Begg, B. D., Wang, L. M., Ewing, R. C., Weber, W. J., and Kutty, K. V. G. (1999). Radiation Stability of Gadolinium Zirconate: A Waste Form for Plutonium Disposition. *J. Mater. Res.* 14, 4470–4473. doi:10.1557/jmr.1999.0606

Weber, W. J. (1998). Effects of Self-Radiation Damage in Cm-Doped $Gd_2Ti_2O_7$ and $CaZrTi_2O_7$. *J. Mater. Res.* 13 (6), 1434–1484.

Whittle, K. R., Blackford, M. G., Aughterson, R. D., Lumpkin, G. R., and Zaluzec, N. J. (2011). Ion Irradiation of Novel Yttrium/ytterbium-Based Pyrochlores: The Effect of Disorder. *Acta Materialia* 59, 7530–7537. doi:10.1016/j.actamat.2011.09.021

Whittle, K. R., Cranswick, L. M. D., Redfern, S. A. T., Swainson, I. P., and Lumpkin, G. R. (2009). Lanthanum Pyrochlores and the Effect of Yttrium Addition in the Systems La2−xYxZr2O7 and La2−xYxHf2O7. *J. Solid State. Chem.* 182, 442–450. doi:10.1016/j.jssc.2008.11.008

Withers, R. L., Thompson, J. G., and Barlow, P. J. (1991). An Electron, and X-ray Powder, Diffraction Study of Cubic, Fluorite-Related Phases in Various ZrO2−Ln2O3 Systems. *J. Solid State. Chem.* 94, 89–105. doi:10.1016/0022-4596(91)90224-6

Wu, J., Wei, X., Padture, N., Klemens, P. G., Gell, M., García, E., et al. (2002). Low-thermal-conductivity Rare-earth Zirconates for Potential thermal-barrier-coating Applications. *J. Am. Ceram. Soc.* 85, 3031–3035. doi:10.1111/j.1151-2916.2002.tb00574.x

Zhang, Z., Middleburgh, S. C., de los Reyes, M., Lumpkin, G. R., Kennedy, B. J., Blanchard, P. E. R., et al. (2013). Gradual Structural Evolution from Pyrochlore to Defect-Fluorite in Y2Sn2-xZrxO7: Average vs Local Structure. *J. Phys. Chem. C* 117, 26740–26749. doi:10.1021/jp408682r

Zhou, L., Huang, Z., Qi, J., Feng, Z., Wu, D., Zhang, W., et al. (2016). Thermal-driven Fluorite-Pyrochlore-Fluorite Phase Transitions of Gd2Zr2O7 Ceramics Probed in Large Range of Sintering Temperature. *Metall. Mat Trans. A.* 47, 623–630. doi:10.1007/s11661-015-3234-4

Zietlow, P., Beirau, T., Mihailova, B., Groat, L. A., Chudy, T., Shelyug, A., et al. (2017). Thermal Annealing of Natural, Radiation-Damaged Pyrochlore. *Z. Kristallograph.* 232, 25–38. doi:10.1515/zkri-2016-1965

Conflict of Interest: The authors declare that the research was conducted in the absence of any commercial or financial relationships that could be construed as a potential conflict of interest.

Publisher's Note: All claims expressed in this article are solely those of the authors and do not necessarily represent those of their affiliated organizations, or those of the publisher, the editors and the reviewers. Any product that may be evaluated in this article, or claim that may be made by its manufacturer, is not guaranteed or endorsed by the publisher.

frontiers in Chemistry

REVIEW
published: 29 November 2021
doi: 10.3389/fchem.2021.743025

Probing Multiscale Disorder in Pyrochlore and Related Complex Oxides in the Transmission Electron Microscope: A Review

Jenna L. Wardini[1], *Hasti Vahidi*[1], *Huiming Guo*[1] *and William J. Bowman*[1,2]*

[1]*Materials Science and Engineering, University of California, Irvine, Irvine, CA, United States,* [2]*Irvine Materials Research Institute, Irvine, CA, United States*

Transmission electron microscopy (TEM), and its counterpart, scanning TEM (STEM), are powerful materials characterization tools capable of probing crystal structure, composition, charge distribution, electronic structure, and bonding down to the atomic scale. Recent (S)TEM instrumentation developments such as electron beam aberration-correction as well as faster and more efficient signal detection systems have given rise to new and more powerful experimental methods, some of which (e.g., 4D-STEM, spectrum-imaging, in situ/operando (S)TEM)) facilitate the capture of high-dimensional datasets that contain spatially-resolved structural, spectroscopic, time- and/or stimulus-dependent information across the sub-angstrom to several micrometer length scale. Thus, through the variety of analysis methods available in the modern (S)TEM and its continual development towards high-dimensional data capture, it is well-suited to the challenge of characterizing isometric mixed-metal oxides such as pyrochlores, fluorites, and other complex oxides that reside on a continuum of chemical and spatial ordering. In this review, we present a suite of imaging and diffraction (S)TEM techniques that are uniquely suited to probe the many types, length-scales, and degrees of disorder in complex oxides, with a focus on disorder common to pyrochlores, fluorites and the expansive library of intermediate structures they may adopt. The application of these techniques to various complex oxides will be reviewed to demonstrate their capabilities and limitations in resolving the continuum of structural and chemical ordering in these systems.

Keywords: disordered crystals, scanning transmission elctron microscopy, 4D-STEM, electron diffraction, order – disorder transformations: ODTs, amorphous materials, complex oxides

OPEN ACCESS

Edited by:
Maik Kurt Lang,
The University of Tennessee, United States

Reviewed by:
Yao Cheng,
Fujian Institute of Research on the Structure of Matter (CAS), China
Wei Zeng,
Northwest Normal University, China

***Correspondence:**
William J. Bowman
will.bowman@uci.edu

Specialty section:
This article was submitted to Solid State Chemistry, a section of the journal Frontiers in Chemistry

Received: *17 July 2021*
Accepted: *15 October 2021*
Published: *29 November 2021*

Citation:
Wardini JL, Vahidi H, Guo H and Bowman WJ (2021) Probing Multiscale Disorder in Pyrochlore and Related Complex Oxides in the Transmission Electron Microscope: A Review. Front. Chem. 9:743025. doi: 10.3389/fchem.2021.743025

INTRODUCTION

Crystalline materials are generally thought of as highly-ordered systems, however, this classification is not fully descriptive without a reference to the length-scale of ordering. Although crystals display long-range structural and chemical periodicity, they also commonly host various types of local imperfections which we generally categorize as 'disorder'. These local deviations from long-range order can include non-repeating variations in composition, atom displacements, bonding arrangements, molecular orientations, conformations, charge states, orbital occupancies, and/or magnetic structure (Simonov and Goodwin, 2020). Further, rather than being random in nature,

these disruptions of the long-range periodicity are more often correlated, or locally-ordered on short (sub-unit-cell) to medium (few-unit-cell) length scales. As the connection between the structure, chemistry, and properties of materials across length scales becomes clearer, it is recognized that many interesting phenomena can only be understood by embracing the role of such disorder (Chaney et al., 2021). Multi-cation, or complex oxides are an ideal class of materials to study such phenomena, since their structure-property relationships are not only related to the composition and structure, but are correlated to the extent of disorder within the cation and anion sublattices (Kreller and Uberuaga, 2021; Mullens et al., 2021).

In this review, we present a suite of high spatial resolution electron microscopy characterization techniques that are uniquely suited to probe the many types, length-scales, and degrees of disorder in complex oxides, with a focus on disorder common to isostructures of the minerals pyrochlore ($A_2B_2O_7$, Fd $\overline{3}$ m) and fluorite (BO_2, Fm $\overline{3}$ m). These isometric mixed-metal oxides represent two ends of an expansive library of intermediate structures that encompass varying degrees of disorder on their cationic and anionic sublattices (Mullens et al., 2021). Disorder is adopted during disordering transitions, often in lieu of long-range symmetry-lowering transformations away from their cubic parent phase. This makes them ideal structures to host complex types of disorder (and/or local order) that can profoundly affect their functional properties (Subramanian et al., 1983; Maram et al., 2018), which are quite diverse. Here, we focus on their high radiation tolerance (Sickafus et al., 2000) and high ionic conductivity (Jitta et al., 2015; Kim et al., 2020), two properties that make them ideal candidate materials for nuclear waste management applications (Ewing et al., 2004; Orlova and Ojovan, 2019) and as solid-oxide fuel cell components (Anantharaman and Dasari, 2021).

Pyrochlores, Fluorites and Intermediate Structures

The pyrochlore structure can accommodate various of chemical substitutions, with over 500 unique compositions synthesized to date (Subramanian et al., 1983; Chakoumakos, 1984; Lang et al., 2010). Commonly, the A-site is occupied by a larger trivalent cation and the B-site, by a smaller tetravalent cation, with other variations (e.g. A^{2+},B^{5+}) also possible (Subramanian et al., 1983). Pyrochlores can be thought of as ordered, oxygen-deficient fluorite superstructures, where the A^{3+} cations substitute half the B^{4+} fluorite cations and charge neutrality is maintained through the formation of oxygen vacancies on the 8(a) site (Chroneos et al., 2013). Both the cations and anions of pyrochlores are fully ordered on their respective sublattices, where A and B cations alternate along <110>. In addition to the fully-ordered pyrochlore and the disordered fluorite, there is a large library of partially-ordered pyrochlore and partially-disordered defect-fluorite structures (Mullens et al., 2021) (**Figure 1**) that vary in the degree of cation and/or vacancy ordering.

Disorder in these structures can be manipulated by tuning the cation ratio (r_A/r_B), which determines the stability range for different structures of the $A_2B_2O_7$ composition (Kaspar et al., 2017), the doping content (Glerup et al., 2001), or can be introduced by the application of external stimuli (e.g., irradiation, pressure (Rittman et al., 2017a), temperature, or electric field) that can be used to replicate various types of extreme environments. Sufficient cation exchange and randomization of oxygen vacancy position in pyrochlores eventually leads to a long-range transformation to the fully-disordered, anion-deficient fluorite structure in the so-called order-disorder transition (ODT). Exposure to extreme conditions can also cause reconstructive phase transformations that result in a drastic change of structural symmetry elements (Talanov and Talanov, 2021), decomposition into other phases (Garg et al., 2008), or complete amorphization (Lian et al., 2002; Turner et al., 2017), all of which can occur homogeneously by modifying the long-range order, or heterogeneously by the formation of short- or medium-range domains of order/disorder (Shamblin et al., 2016; O'Quinn et al., 2020).

Pyrochlore Disorder on Various Length Scales

Techniques that offer multi-scale structural and chemical characterization are necessary in disorder-harboring systems like pyrochlore and fluorite since their disordering processes occur over various spatial extents. The presence of multiple cations and structural oxygen vacancies endow pyrochlores with two types of intrinsic disorder, cation-antisite and anion-Frenkel defects (Minervini et al., 2000), which play a critical role in driving phase transitions (Subramanian et al., 1983; Minervini et al., 2000; Solomon et al., 2016; Maram et al., 2018) as well as controlling the energetics of ion transport. Randomization of cation species is a low-energy disordering mechanism in pyrochlores that arises via the formation of antisite defects ($A_A^x + B_B^x \rightarrow A_B^{'} + B_A^{\cdot}$) and is always accompanied by simultaneous vacancy disordering in the anion sublattice (Wuensch and Eberman, 2000) (Talanov and Talanov, 2021), which occurs by the formation of anion-Frenkel pairs ($O_O^x \rightarrow V_{O(48f)}^{\cdot\cdot} + O_{i(8a)}^{''}$).

Crystalline defects (e.g., dislocations, homo- and hetero-interfaces) and other extended structural irregularities such as strain fields are shown to control cation anti-site and anion-Frenkel defect concentrations, and can also enhance pyrochlore phase-transformation kinetics under applied pressure (Rittman et al., 2017b) and irradiation in fluorites (Schuster et al., 2009). Strain-induced structural distortions such as misfit dislocations, cation intermixing, and oxygen vacancies (Bowman et al., 2015; Bowman et al., 2017; Perriot et al., 2017; Tong et al., 2020) commonly arise at interfaces and can lead to unique chemical, transport and radiation responses (Haider et al., 1998; Gázquez et al., 2017; Lehmann et al., 2017; O'Quinn et al., 2017; Shamblin et al., 2018; Gussev et al., 2020). Heterointerface engineering of fluorites, perovskites and pyrochlores has been shown to control local oxygen diffusivity (Schweiger et al., 2017), to affect local radiation response (Spurgeon et al., 2020) and to produce novel topological phases (Gallagher et al., 2016; Li et al., 2021). Other types of extended crystalline defects, such as dislocations (Sheth

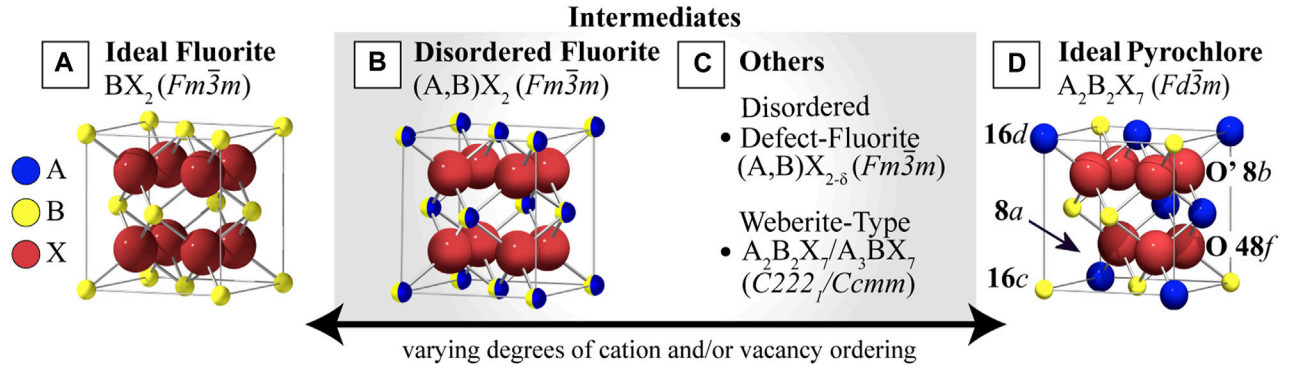

FIGURE 1 | Fluorite, Pyrochlore, and intermediate structures with varying degrees of cation and anion disorder. **(A)** The ideal fluorite structure with a single cation. **(B)** An intermediate disordered fluorite structure with two randomly distributed cation species. **(C)** Other possible intermediates, including the disordered defect-fluorite, where both cations and vacancies are disordered and the structure is anion-deficient, and the weberite-type structures with full cation and anion ordering that differs from the **(D)** ideal ordered pyrochlore structure, which has two ordered cation species and ordered structural vacancies (showing 1/8 of the unit cell). Reproduced from (Stanek, 2003; Cleave, 2006; Zhao et al., 2017).

et al., 2016; Shafieizadeh et al., 2018) and grain boundaries (Bowman et al., 2015; Bowman et al., 2017; Perriot et al., 2017; Gupta et al., 2020; Syed et al., 2020; Tong et al., 2020) have been shown to behave as fast oxygen transport pathways in some cases. Even small, localized, atomic displacements such as local changes in bonding environment (e.g., coordination), polyhedral distortions (e.g., bond length or angle), polyhedral tilting and the adoption of short-range polyhedral configurations or 'structural motifs' (Shamblin et al., 2016; Sun et al., 2016) can affect functional properties. Needless to say, characterization over all these length scales is required.

In general, complex oxides are challenging systems in which subtle changes in structure or chemistry may result in colossal changes in macroscopic physical behavior (Gázquez et al., 2017). The (S)TEM techniques that will be presented here are able to directly probe the multi-scale defects presented above as well as locally ordered/disordered domains that occur in these systems, both of which may manifest on sub-unit-cell or few-unit-cell length scales. In contrast to X-ray or neutron diffraction, two structural characterization methods that yield information averaged over large volumes (1–10 μm^3) (Lehmann et al., 2017), (S)TEM optics can be adjusted to form probes ranging from the angstrom to micrometer scale, allowing materials to be analyzed on the relevant length scales. This is critical for understanding heterogeneous disordering processes with different short- and long-range structural motifs, for example the formation of sub-nanometer domains of tetragonal symmetry in spinels (O'Quinn et al., 2017) and orthorhombic, or Weberite domains in defect-fluorites (Shamblin et al., 2018) that may be characterized by distinct space groups. Accurate structural analysis of metal oxide systems also requires sensitivity to light elements in the presence of heavy ones. For instance, the poor sensitivity of X-ray diffraction to oxygen in the presence of Y and Ta results in different space group classifications ($C222_1$ and $Ccmm$) for the same Weberite-type structure, where the only significant difference is within the local atomic arrangement of the anion sublattice (Gussev et al., 2020). While this challenge still exists in (S)TEM, electrons interact much more strongly with matter than either neutrons or X-rays and the sensitivity to light elements that can be tuned by controlling the range of electron scatter collected.

Here, we review modern and emerging transmission electron microscopy (TEM) and scanning TEM (STEM) techniques that possess adequate spatial resolution and sensitivity to analyze important types of multi-scale defects, disorder and locally-ordered domains that occurs pyrochlore, fluorite, and disordered crystalline structures in general. We hope to provide exposure to these techniques and demonstrate how they may address contemporary challenges of disordered crystal characterization, aided by examples of their application in relevant systems. We also draw attention to recently developed (S)TEM techniques that have yet to be applied to pyrochlore and fluorite systems in hopes of inspiring future research efforts.

(S)TEM AND ITS CAPABILITIES

Over the past ~20 years, sub-angstrom point-resolutions have become readily achievable in (S)TEM instruments, largely due to spherical (Haider et al., 1998) and chromatic aberration-correction (Batson et al., 2002) of electron lenses, and bolstered by improved electron sources as well as mechanical and electrical stability (Zhu and Dürr, 2015). Simultaneously, improvements in electron (MacLaren et al., 2020) and spectroscopic (Nylese and Rafaelsen, 2017; D'Alfonso et al., 2010) signal detection technologies have gradually enabled more rapid, and high signal-to-noise data collection (Hart et al., 2017). Paired with intelligent software design, multiple kinds of signals can be correlated to produce rich, multidimensional data cubes that can be flexibly analyzed. These technologies have popularized techniques that were once practically limited by the sluggish rate of signal collection, such as four-dimensional (4D)-STEM, and spectrum-imaging (SI) that are used for two-dimensional (2D) mapping of structural and chemical features, respectively.

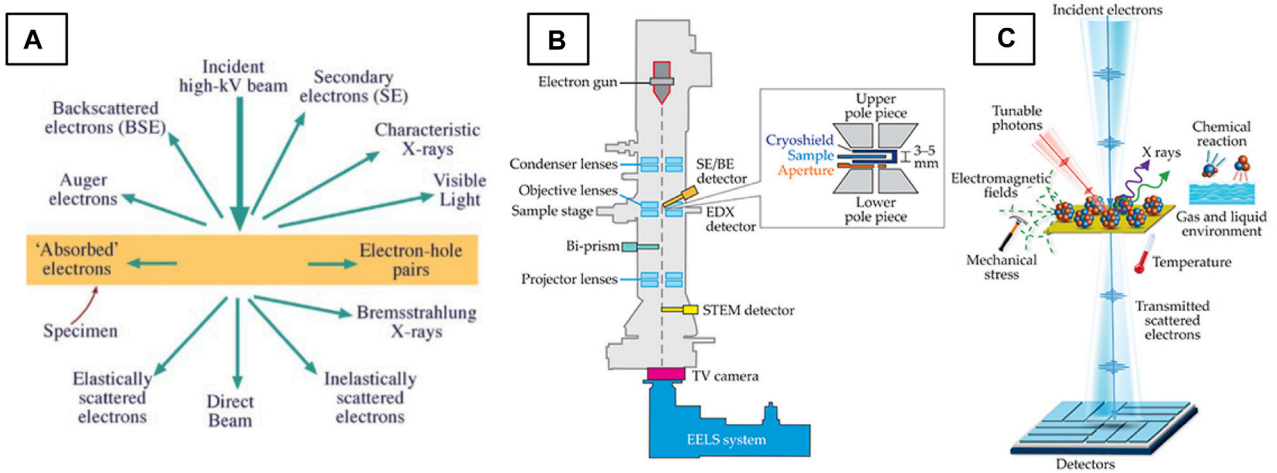

FIGURE 2 | Signals and detectors of the (S)TEM. **(A)** Schematic of signals produced through electron-matter interactions in the (S)TEM (Williams and Carter, 2009a) and **(B)** schematic of (S)TEM column hardware and detectors. **(C)** Schematic of *in situ/operando* capabilities (Zhu and Dürr, 2015).

Meanwhile, (S)TEM sample holder technology also advanced, enabling dynamic, in-column experimentation whereby various stimuli can be applied to a material while functional properties are measured (Taheri et al., 2016). These *in situ* or *in operando* experiments also benefit greatly from the development of new, fast detectors which are better equipped to observe dynamic processes. Thanks to these developments and others, many of the technical barriers have been removed (MacLaren and Ramasse, 2014) such that atomic-scale structural and chemical (S)TEM analysis of materials is broadly accessible.

Signals and Detection in the (S)TEM

High-energy electrons (typically 80–300 kV) interact strongly with matter, producing a multitude of signals (**Figure 2A**) which carry valuable information about the specimen. (S)TEM imaging utilizes elastically and inelastically scattered electrons which interact with and pass through a thinned specimen, ideally below 100 nm in thickness. Secondary signals such as Auger, backscattered and secondary electrons, characteristic and Bremsstrahlung X-rays, as well as visible, infrared and ultraviolet light are also produced (Williams and Carter, 2009a) in this interaction. With the appropriate detectors (**Figure 2B**), multiple of these signals can be collected simultaneously. Characteristic X-rays and inelastically scattered electrons can be collected to perform energy-dispersive X-ray spectroscopy (EDXS) and electron energy-loss spectroscopy (EELS), respectively, two spectroscopic techniques central to (S)TEM that are out of the scope of this review. Specialized holders can also be used to apply different stimuli to the sample (**Figure 2C**) and detect the material's functional response (see (Taheri et al., 2016) for a review of holder functionality). The diversity of these signals and the ability to detect them with high spatial resolution underpins the (S)TEM's unique and versatile characterization power.

Operational Modes

(S)TEMs are sophisticated optical instruments that allow control over the angular range of electron beam incidence (i.e., the convergence angle, α), the size of the electron beam (i.e., probed volume), and the angle of electron scatter collected (i.e., collection angle, β) post-specimen. It is this control, paired with various detector types and geometries, that gives rise to the broad range of (S)TEM techniques available. (S)TEM optics can be configured to operate in two main modes. In "TEM mode" (also called conventional TEM or CTEM) a broad, parallel electron beam with a flat wavefront of constant phase illuminates the specimen. Under parallel illumination such as this, the beam is typically broad and diffracted signals are localized to spots in the diffraction plane. In "STEM mode," the electron beam is converged to a point and scanned across the specimen while the scattered signal is collected pixelwise by detectors of various geometries (**Figure 4**, see **STEM Imaging Modes**). Under convergent illumination, the incident electron wavefront is spherical, and the beam contains electrons which illuminate the specimen over a range of incident angles, from normal incidence (0 mrad) up to the convergence angle (~15–30 mrad) (Williams and Carter, 2009b). The range of incident angles will delocalize the diffracted signal and can give access to additional crystallographic information in the diffraction plane (see **Convergent-Beam Electron Diffraction**). There are also special, quasi-parallel illumination conditions (see **Small-Beam Electron Diffraction**) that strike a balance between the typical CTEM and STEM conditions, resulting in an electron probe with near-parallel illumination and relatively small probe sizes (from several angstroms to nanometers). These optical conditions provide the basis of 4D-STEM measurements, discussed in a later section.

STRUCTURE ANALYSIS FROM REAL-SPACE IMAGING

Analysis of structure can be performed either from real-space data (images), through observation and quantification of atomic

position and signal intensity, or from reciprocal-space data (diffraction patterns), via the acquisition of electron diffraction (ED) patterns of various kinds. In this section, we discuss real-space structure analysis performed in both CTEM and STEM modes and provide examples of analysis on such images to reveal local structure and the various disorders discussed previously.

Conventional TEM

CTEM techniques utilize a broad, parallel beam to illuminate the specimen. The main real-space structure imaging approaches performed in this mode are bright-field TEM (BF-TEM), dark-field TEM (DF-TEM), weak-beam dark-field (WBDF), and high-resolution TEM (HRTEM). BF-/DF-/WBDF- TEM are primarily for morphological and defect analysis and HRTEM gives atomic-resolution images of the lattice, so it is the method of choice for analyzing atomic-scale disordering in CTEM.

High-Resolution TEM

HRTEM (Fultz and Howe, 2008) is a parallel imaging technique for atomic-resolution analysis of crystallographic structural information. The contrast of HRTEM images arises from the interference of electron waves as they are phase-shifted by their interaction with the interatomic potential of the specimen, generating 'phase contrast' (Williams and Carter, 2009c). Under the proper conditions, cation columns in a metal-oxide can be directly imaged and peak-fitting routines (see **Real-Space Structure Analysis Software Tools**) can be used extract cation positions with picometer precision (Lawrence et al., 2021).

The primary challenge of HRTEM imaging is that it is only representative of the projected crystal structure, or directly interpretable, under specific conditions so image simulations are typically required for accurate image contrast interpretation (MacLaren and Ramasse, 2014). For instance, in an uncorrected TEM, where the spherical aberration coefficient, C_s, of the objective or image-forming lens is always positive, images taken at the special 'Scherzer defocus' condition (Scherzer, 1949) will show atomic columns as dark regions (dark atom contrast). However, if the focus, specimen mass-thickness, or crystallographic tilt changes, the resulting image may display contrast reversals where atomic columns contrast may vary across the image, appearing either bright or dark depending on local sample conditions. Two common methods to bypass this issue are exit-wave reconstruction (EWR) and crystallographic image processing (CIP). To determine aperiodic atomic structure, such as in the disordered or defective regions of disordered crystalline systems, exit-wave reconstruction is preferred since CIP relies on structural periodicity (Thust et al., 1996).

Exit Wave Reconstruction

EWR can be used to reconstruct a representative image of the projected crystal structure through the acquisition of a 'focal-series,' or a stack of HRTEM images taken over a range of focus values. EWR has been used to discern the structure, orientation relationship, and matrix coherency of $Y_2Ti_2O_7$ pyrochlore nano-oxides in a nanostructured ferritic alloy (NFA) (**Figure 3A**). **Figure 3B** demonstrates the complexity of determining structure from HRTEM images, showing the difference in apparent structure in underfocused, focused, and overfocused (**Figures 3Bi–iii**) conditions. After acquisition of a focal series, the reconstructed phase image matches with a $Y_2Ti_2O_7$ pyrochlore structure simulated under compressive strain (**Figure 3C**) (Wu et al., 2016).

Negative Cs Imaging

An additional challenge of HRTEM arises due to the difference in scattering power between light and heavy elements. In the case of pyrochlores (and metal oxides in general), the phase-contrast generated from cations is typically strong due to their high nuclear charge, while oxygen generates poor phase contrast and has a relatively low scattering power (Jia et al., 2003) which can make imaging of the oxygen sublattice challenging. With the development of aberration-correctors, it is possible to precisely tune the optical parameters of the (S)TEM (MacLaren and Ramasse, 2014). When the spherical aberration coefficient (Cs) is set to a small negative value, 'negative Cs imaging,' (NCSI) (Jia et al., 2003; Jia et al., 2004) can be performed. This method delivers directly interpretable images where both heavy and light elements show strong bright-atom contrast simultaneously (Dunin-Borkowski et al., 2016). **Figures 3D–F** shows a HRTEM image of a Bi-containing pyrochlore ($Bi_{1.5}ZnNb_{1.5}O_7$, BZN) acquired under NCSI conditions, where cation columns are bright and well-defined and oxygen columns are bright, yet diffuse. 2D Gaussian peak-fitting is performed to determine precise atomic positions and displacements from ideal pyrochlore lattice positions, providing direct evidence of atomic-scale displacive disordering on the A and O′ sites (Levin et al., 2002; Jia et al., 2018). In this case, EWR and NCSI imaging **are** combined to optimize the bright atom contrast condition (Wu et al., 2016).

Although HRTEM imaging is being progressively replaced with scanning TEM (STEM) techniques due to the relative ease of image interpretation, there remains a clear advantage to using a static, broad electron beam for dynamic experiments over a scanned electron probe. Rapid specimen evolution during *in situ* experiments necessitates high temporal resolution image acquisition. In TEM mode, the acquisition rate is mainly limited by the desired signal-to-noise ratio and the frame rate of the signal detection system. However, the STEM acquisition rate is additionally limited by scan rate of the probe. For modern systems, this is on the order of a few frames per second (fps) (Ishikawa et al., 2020), where faster scan speeds can lead to significant image distortions (Sang et al., 2016). Although newly developed probe-scanning systems have demonstrated acquisitions of 25 fps (512 × 512 pixels) in STEM, approaching the necessary frame rate for many *in situ* experiments (Levin, 2021), TEM mode is still presently the choice for *in situ* experiments due the high frame rates of modern CMOS cameras (e.g., 1,600 fps at 512 × 512, K3 Gatan Inc.). *In situ* TEM experiments are routinely performed at atomic resolution, for example to track picoscale atomic surface rearrangements of CeO_2 catalytic nanoparticles imaged under low-dose NCSI imaging conditions with millisecond temporal resolution (Levin et al., 2020a).

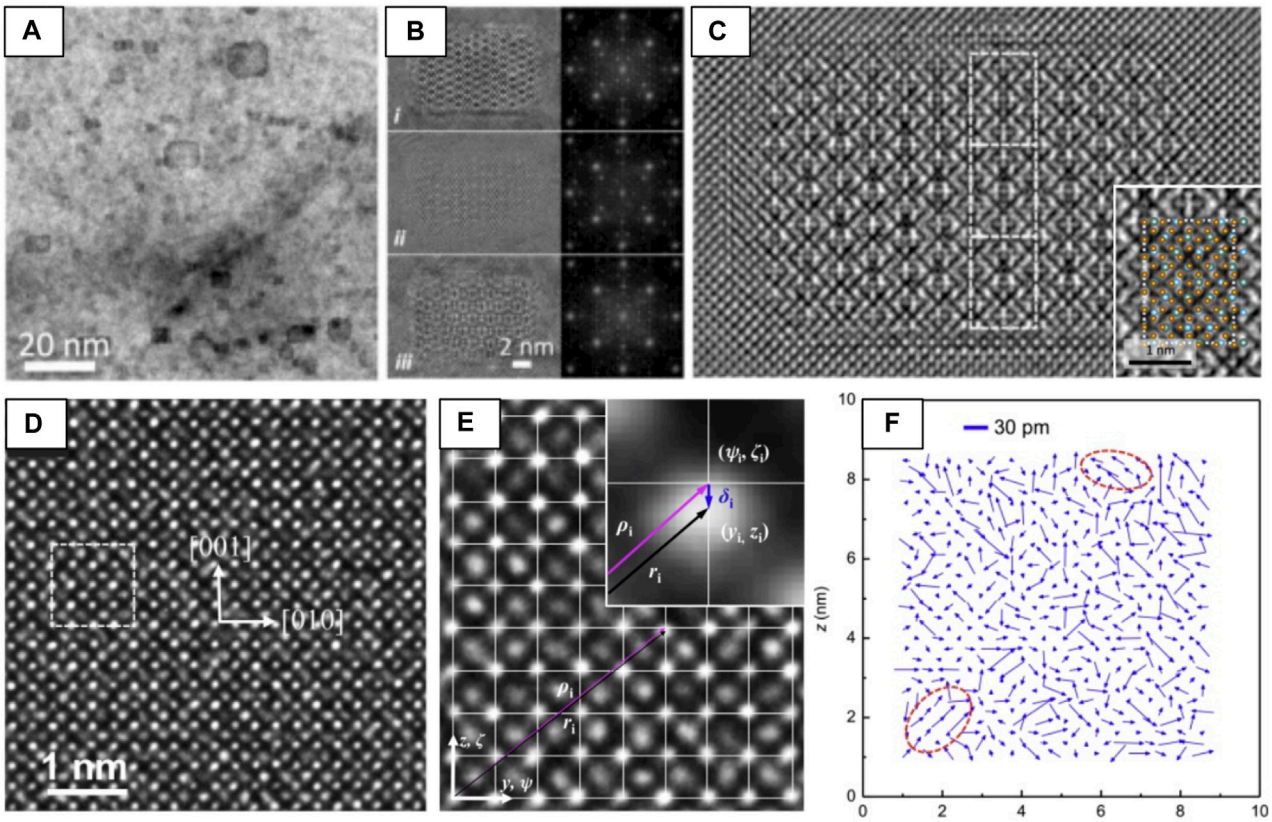

FIGURE 3 | Examples of two HRTEM imaging-based techniques, EWR **(A–C)** and NCSI **(D–F)** used to determine crystal structure and atomic displacive disorder, respectively. **(A)** BF-TEM of $Y_2Ti_2O_7$ nano-oxides in a NFA matrix. **(B)** i) underfocused, ii) focused, and iii) overfocused HRTEM images and fast-Fourier transforms (FFTs) of the nano-oxides. **(C)** Reconstructed electron wave phase obtained from EWR with white atom contrast and a simulated $Y_2Ti_2O_7$ structure overlaid on a magnified view of the EWR (inset), reproduced from (Wu et al., 2016). **(D)** HRTEM of a [$\bar{1}$00] BZN pyrochlore taken under NCSI conditions, dotted lines outline a unit cell. **(E)** Determination of the atomic displacement vector δ_i from NCSI images, white line crossings indicate the average cation positions of the ideal pyrochlore. **(F)** Map of shift vectors between the center of gravity of the A-site and the ideal A-site cation position, red circles outline the presence of nanoregions (~2 nm) of correlated A-type atomic shifts, reproduced from (Jia et al., 2018).

Scanning TEM

In "STEM mode", the electron beam is converged to form a probe and scanned across the specimen while various STEM detectors are positioned beneath the specimen that register the intensity of scatter at each probe position. The angle of electron scatter collected (β) is the basis for image interpretation, thus, considering its significance the various STEM imaging modes are named in reference to this collection angle: High-angle annular dark-field (HAADF), annular dark-field (ADF), low or medium angle dark-field (LAADF/MAADF), annular bright-field (ABF), or bright-field (BF) STEM. However, the angle of electron scatter is also affected by the probe convergence angle (α), so both α and β should be considered to acquire images in any of the modes mentioned above. These modes imply a specific scattering mechanism is dominant and provide physical meaning to the image contrast observed.

Probe convergence angles typically fall in the range of 15–30 mrad (15–20 mrad for uncorrected systems and 25–30 mrad for aberration-corrected systems since the probe can assume a (nearly) constant phase over a greater angular range). The angle of electron scatter collected by annular detectors is β_{outer} - β_{inner}, and for circular detectors just β (**Figure 4A**). **Figure 4A** also shows the angles α, and β, as well as the setup of a double-detector STEM system, whereby an annular detector and circular detector can be used to collect high-angle and low-angle scatter simultaneously. This multi-signal setup can be easily paired with EDXS, or, if the circular detector is removed then the primarily inelastic, low-angle scatter, can be directed into an EELS spectrometer so chemical analysis and imaging can be performed simultaneously. **Figures 4B,C** demonstrate that the imaging mode (and collection angle of scatter) depends not just on the type of detector used, but physical dimensions of the detectors, their positions in the TEM column and how the signal is projected onto the detector ('camera length'). All of these factors, in addition to the probe convergence will affect the collection angle so these values need to be considered on a per-microscope basis.

STEM Imaging Modes

In high-angle annular dark-field STEM (HAADF-STEM), elastic, incoherent, high-angle Rutherford scatter is collected ($\beta_{inner} > \alpha$) (MacLaren and Ramasse, 2014). Thus, the image intensity is

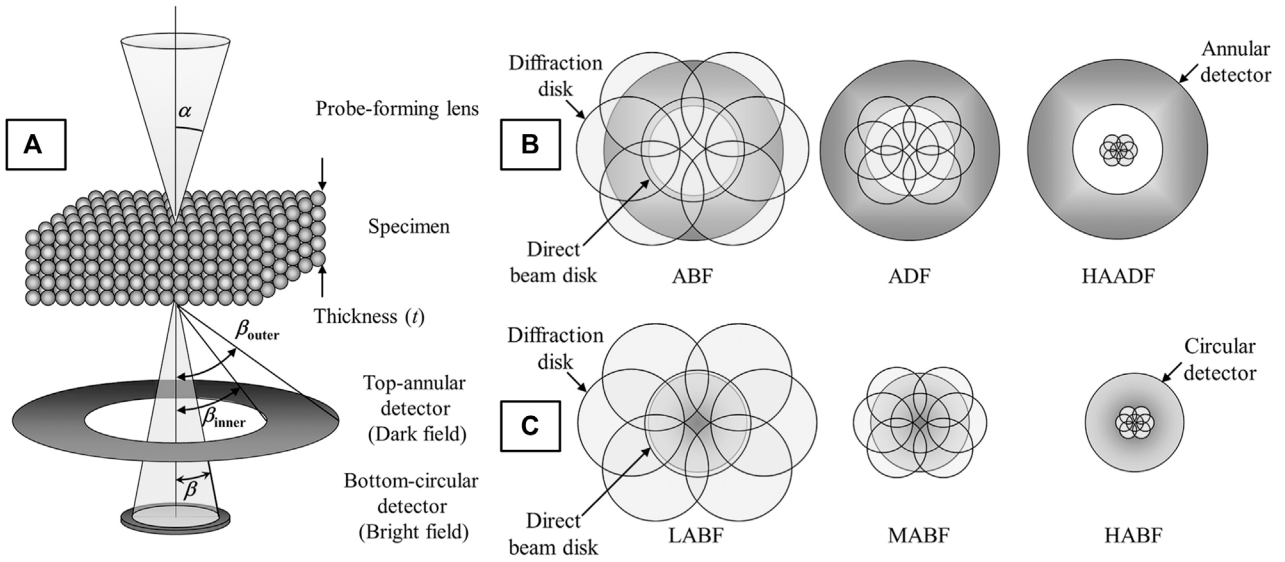

FIGURE 4 | Schematic of STEM detection configuration for **(A)** double-detector STEM imaging, **(B)** annular DF (ADF) detector under ABF, ADF, and HAADF conditions, and **(C)** a circular BF detector under low, medium, and high ABF conditions (LABF, MABF and HABF, respectively). The camera length (CL) is shortened from left to right in **(B,C)**. Reproduced from reference (Kotaka, 2012).

proportional to the mean value of Z^n; where Z is the effective atomic number, and n is a constant between 1.5 and 2 (Kirkland, 1998; Nellist et al., 2007). This technique is the most widely used because the atomic positions are clear and there are no contrast reversals (as in HRTEM). However, it is not ideal for imaging light elements since the Rutherford scattering process is inefficient for light atoms with low nuclear charge at high angles. In medium- (or low-) angle annular dark-field STEM (MAADF-/LAADF-STEM), lower angle coherent scatter is collected ($\beta_{inner} \geq \alpha$) where β_{inner} is just slightly larger than α (e.g., for α = 15–30 mrad, β_{inner} = 30–60 mrad). These images retain some of the characteristics of HAADF images (e.g., no contrast inversions, direct interpretability of atomic columns over a large focus range) but also reveal strongly diffracting features (strained areas such as dislocations or other crystalline defects, nanosized coherent or semi-coherent precipitates etc.) (MacLaren and Ramasse, 2014).

In annular bright-field STEM (ABF-STEM) the outer section of the bright-field (BF) disc is collected ($\beta_{inner} < \alpha < \beta_{outer}$) (Hammel and Rose, 1995; Findlay et al., 2010a). In contrast to images formed by the center of the BF disc which are dominated by phase contrast and are subject to contrast reversals as in HRTEM, the outer part of the BF disc produces images that are more incoherent with dark atomic contrast, including light atoms such as oxygen (Findlay et al., 2010a) or even hydrogen (Findlay et al., 2010b). Bright-field STEM (BF-STEM) is analogous to bright-field TEM images attained in TEM, especially at very low collection angles. Here the low angle scatter is small ($\beta \leq \alpha$), and the signal is coherent and dominated by phase contrast. Just as in HRTEM, the contrast is critically dependent on sample thickness and microscope defocus, and can show contrast inversions. (MacLaren and Ramasse, 2014).

Applications of HAADF-STEM

Strain-Stabilized Cation Disorder

Pyrochlores and other nuclear waste storage materials are often subjected to swift heavy ion irradiation to explore how different factors (e.g., pyrochlore composition, stopping power, irradiation temperature etc. (Lang et al., 2015)) affect local structural disordering processes and thus, their overall radiation response. HAADF-STEM images of Au irradiated $Gd_2Ti_2O_7$ shows the ion track structure consists of an amorphous core surrounded by a thin (~1 nm thick) defect-fluorite shell, apparent from the loss of cation order as compared with the pyrochlore matrix (**Figure 5A**) (Lang et al., 2015). Precise calculation of atomic column positions from HAADF-STEM images shows that the structure is increasingly strained at the ion track edge approaching the core (**Figure 5B**). The larger interatomic distances from the HAADF image suggest that the defect-fluorite structure has a larger volume than the pyrochlore structure. Although defect-fluorite is unstable with respect to pyrochlore for the volume associated with the equilibrium pyrochlore structure, density-functional theory (DFT) calculations showed that defect-fluorite eventually becomes more stable at larger volumes (**Figure 5C**). Thus, these calculations show that strain could also be used to tailor oxygen conductivity in these materials, like fluorite and perovskite materials. STEM studies are being increasingly utilized for analyzing ion track morphology (Lang et al., 2015; Sachan et al., 2017a; Sachan et al., 2017b).

β-Crystobalite Disorder

Evidence of atomic displacive disorder, commonly associated with Bi-containing pyrochlores has recently been seen in other pyrochlores (e.g., $Pr_2Zr_2O_7$ (PZO), $La_2Zr_2O_7$, and $Yb_2Ti_2O_7$) using HAADF-STEM. With rigorous treatment of scan-distortion

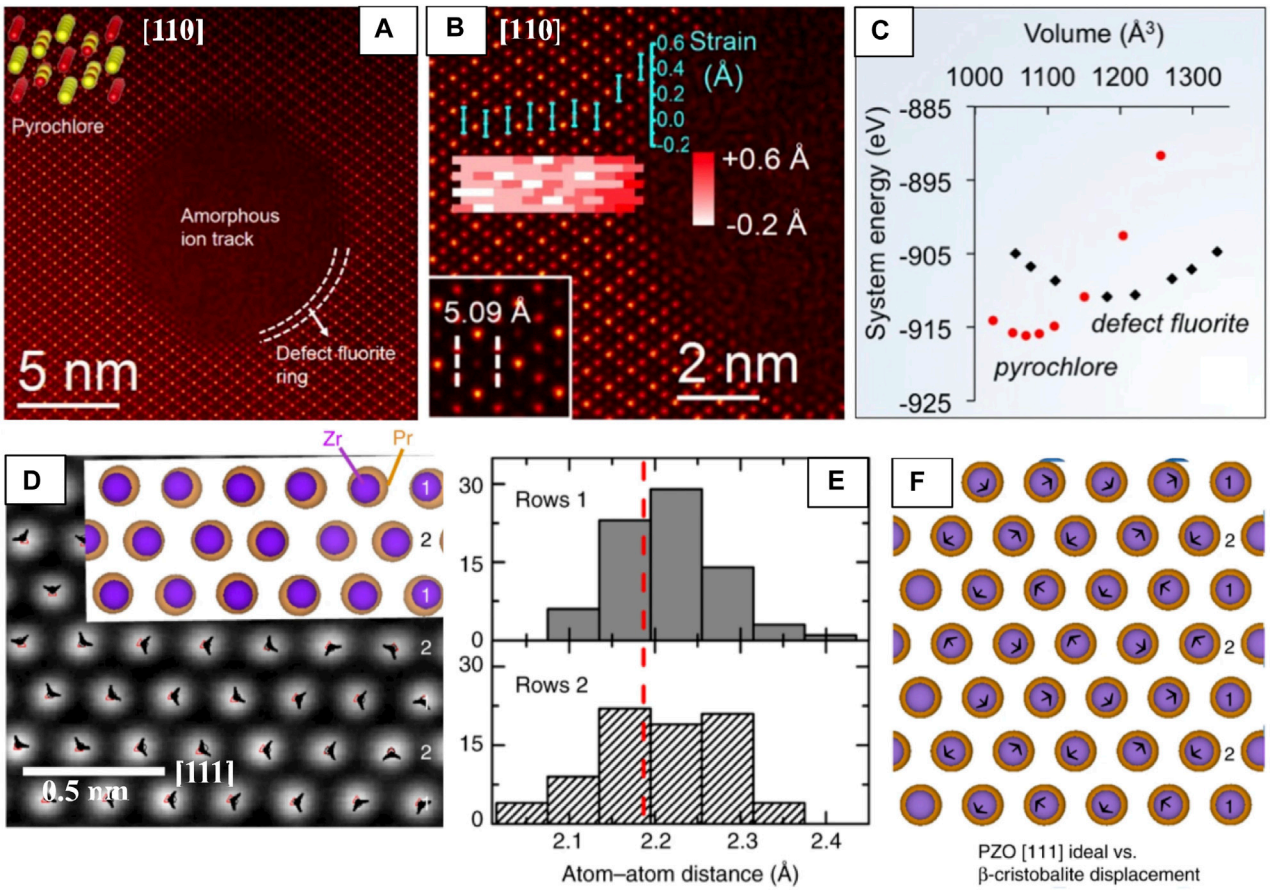

FIGURE 5 | HAADF-STEM used for high-precision determination of atomic column displacements for local strain estimate **(A–C)** and for pm-scale displacive disordering in PZO **(D–F)**. **(A)** An ion track in $Gd_2Ti_2O_7$ [110] after irradiation showing a defect-fluorite shell (dotted lines) stabilized between the amorphous core and pyrochlore matrix. An atomic model (Gd → yellow, Ti →red) (top left). **(B)** Magnified ion track edge and Gd-Ti interatomic distance of pristine $Gd_2Ti_2O_7$ (bottom left inset) with a strain map overlaid, suggesting higher strain (bright red) approaching the amorphous core/defect-fluorite shell, error bar is ±0.1 Å **(C)** DFT energy comparison of the pyrochlore and defect-fluorite structures versus volume showing defect-fluorite has a lower system energy and greater volumes, reproduced from reference (Aidhy et al., 2015). **(D)** PZO [111] with the distorted $P4_32_12$ structure overlaid. The displacement vectors (black arrowheads) of each atomic column from the ideal ($Fd\bar{3}m$) position (black circles) to experimental (red triangles) positions. **(E)** Histogram of the distance between cation columns in PZO [111] in each alternating row (1 and 2, indicated in **(D)**), red dashed line indicating the ideal ($Fd\bar{3}m$) atomic column spacing. **(F)** Comparison of ideal $Fd\bar{3}m$ structure versus a $P4_32_12$ structure with an exaggerated 0.03 nm Pr β-cristobalite displacement in the [111] direction. Black arrows demonstrate displacement vectors. Displaced Pr cations shown in blue. Pr are shown in orange and Zr in purple, with Zr cations reduced by 20% for clarity. Reproduced from reference (Trump et al., 2018).

correction, and peak-fitting procedures, the authors reveal static, β-cristobalite type (Seshadri, 2006) A and O' displacements on the order of ~0.01 nm (**Figures 5D–F**) which lower the local symmetry and surprisingly, can exist in the absence of cation disorder, non-stoichiometry, and lone-pair effects. The authors propose that such static displacements are common in pyrochlores and are driven by cation size mismatch rather than defect concentrations or electronic effects (Trump et al., 2018).

Cation Vacancy Order

HAADF-STEM has also been used to image cation vacancy ordering (**Figure 6**) in a $Bi_2Pt_2O_7$ pyrochlore (Gutiérrez–Llorente et al., 2015), a promising oxide catalyst for applications in fuel cell technology. Direct growth of $Bi_2Pt_2O_7$ films has proved challenging, so the authors implement a novel route whereby a δ-Bi_2O_3 film and Pt are co-deposited and annealed to achieve epitaxial $Bi_2Pt_2O_7$ through δ-Bi_2O_3. Since HAADF-STEM provides strong Z-contrast, the cation vacancy ordering is immediately apparent (**Figure 6A**), especially when viewed beside the ordered pyrochlore with no cation vacancies (**Figure 6C**).

Electron Beam-Induced Cation "Stuffing"

In some pyrochlores extended crystalline defects may be formed under electron irradiation (during (S)TEM observation). In $Yb_2Ti_2O_7$, two types of defects were observed; the majority of which induced no measurable strain in the crystal, while some displayed long-range strain-fields and dislocation character. The material surrounding the strain-free defect shows clear evidence of site-swapping between the cation sublattices (**Figure 6F**) where occasional Ti sites have significantly brighter contrast than their

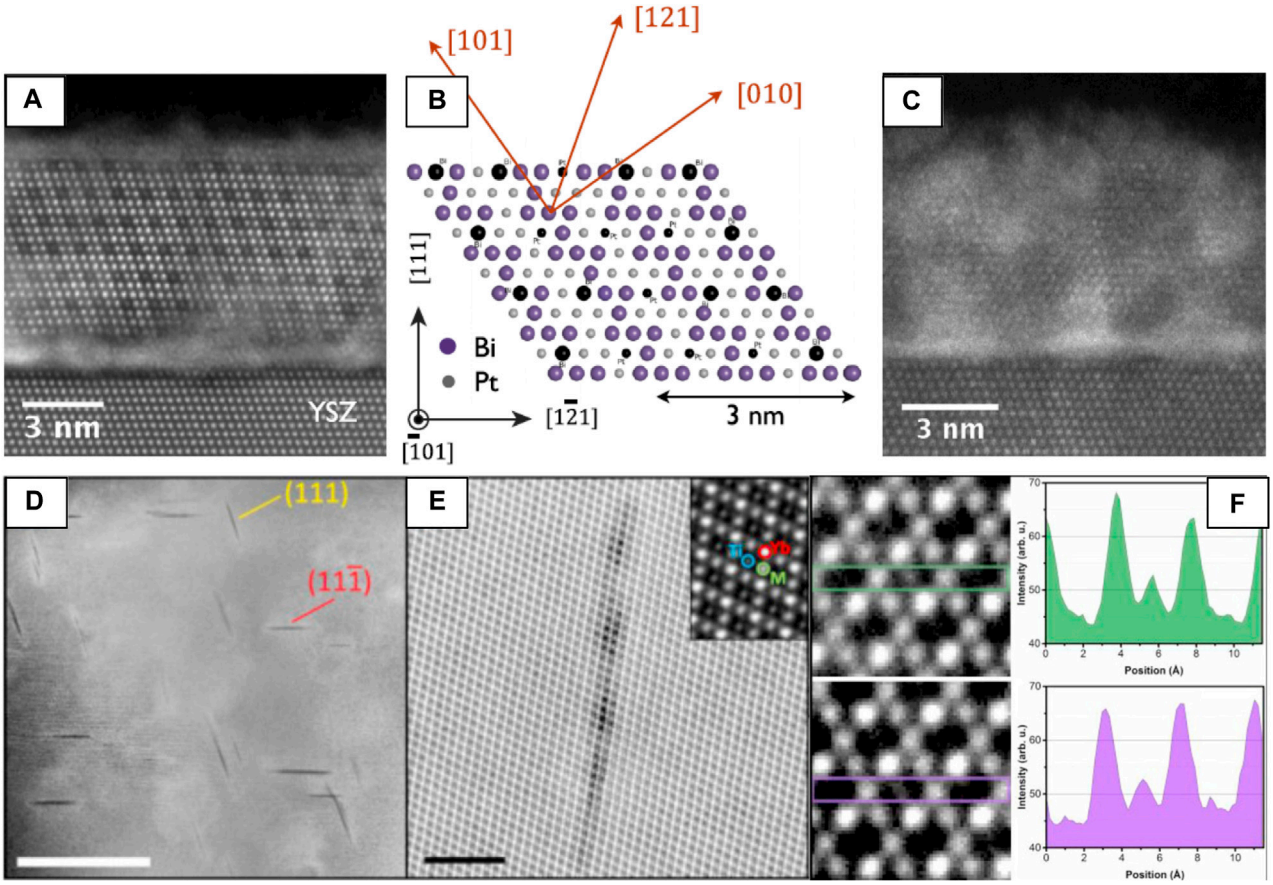

FIGURE 6 | HAADF-STEM imaging showing cation **(A–C)** vacancies and (d–f) anti-site defects. (a) HAADF-STEM image of ordered $Bi_2Pt_2O_7$ [$\bar{1}$01] epitaxial pyrochlore in the annealed bismuth-rich film. Dark, ordered atomic positions in the image indicate the presence of ordered cation vacancies. **(B)** Atomic model of the $Bi_2Pt_2O_7$ [$\bar{1}$01] pyrochlore, where black positions denote cation vacancies, as seen in the image in **(A)**. **(C)** HAADF-STEM image of $Bi_2Pt_2O_7$ [$\bar{1}$01] without cation vacancies. Reproduced from reference (Gutiérrez–Llorente et al., 2015) **(D)** ADF-STEM image of planar defects in $Yb_2Ti_{2.05}O_7$ [1$\bar{1}$0] irradiated with 200 keV electrons. **(E)** Magnified strain-free defect. **(F)** anomalously bright Ti columns on defect edges. Reproduced from reference (Mostaed et al., 2018).

neighbors, indicating the 'stuffing' of Yb on Ti sites (Mostaed et al., 2018).

Strain Analysis of Crystalline Defects, Hetero- and Homo-Interfaces

As described previously, strain-fields in pyrochlores can dramatically affect their properties, thus, analysis of strain-fields around structural defects formed in pyrochlores formed during synthesis are critical to understand (Shafieizadeh et al., 2018). Geometric phase analysis (GPA) (Hÿtch et al., 1998) and peak analysis (Bayle et al., 1994; Anthony and Granick, 2009) are two commonly used digital processing approaches that facilitate extraction of lattice parameter at high resolution, based in reciprocal- and real-space, respectively (Zhu et al., 2013). In GPA, atomic displacements are measured by calculating the 'local' Fourier components of the lattice fringes of a real-space image (Hytch, 1997), whereas peak-finding methods find atomic positions from the contrast maxima of images directly, often through center of mass calculations or by 2D Gaussian fitting which can be more precise (Anthony and Granick, 2009). In either case, contrast maxima in the image are identified as a periodic lattice so deviations of the real, local lattice with respect to an unstrained reference lattice can be calculated and mapped (Zhu et al., 2013). Although these methods are generally robust, precautions must be taken to minimize microscope and specimen effects that may produce inaccurate strains, especially from HRTEM images (Hÿtch and Plamann, 2001) where contrast interpretation is often less straightforward than in HAADF-STEM.

GPA has been used to map strain fields (**Figure 7**) around superdislocations and other extended crystalline defects in $Yb_2Ti_2O_7$ formed during synthesis (Shafieizadeh et al., 2018). HAADF-STEM reveals extended defects such as anti-phase boundaries and dissociated superdislocations with unique core structures and anomalously large Burgers vectors (**Figure 7A**) compared with other oxides (Jia et al., 2005). GPA has also been used to map strain at $La_2Zr_2O_7$(LZO)/YSZ (111) interfaces, highlighting the presence of misfit dislocations that may impact the accumulation of radiation damage at such features (Kaspar et al., 2017). This approach has also been used to

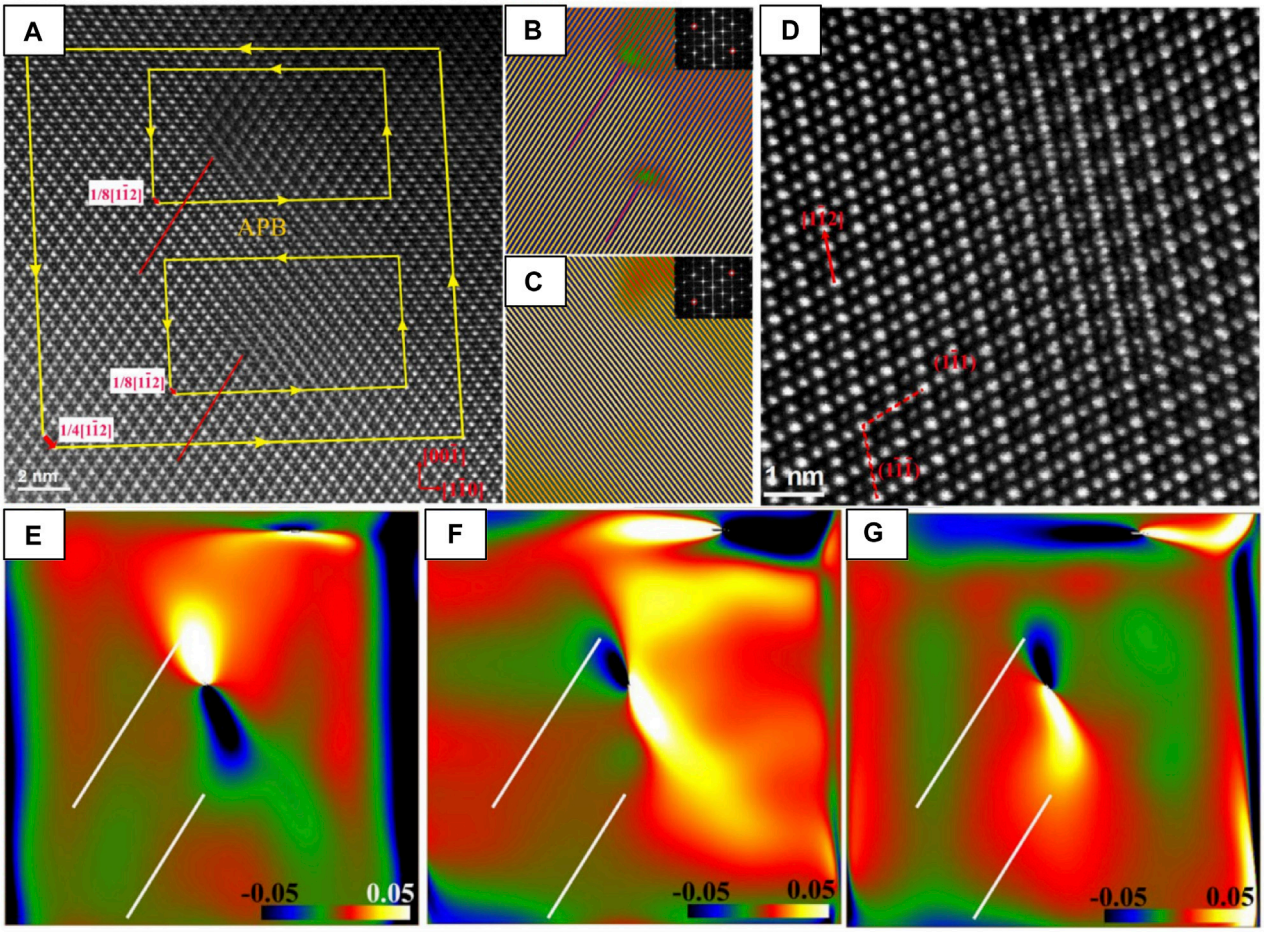

FIGURE 7 | A superdislocation with Burgers vector 1/4 [112]. **(A)** The dissociated superdislocation with two partial dislocations and an APB. Three Burgers circuits are shown as yellow frames. The projected Burgers vectors are shown by the red arrows. **(B)** Inverse FFT image using **g** = ± (222); inset: FFT diffraction with **g** circled. **(C)** Inverse FFT image using **g** = ± (222); inset: FFT diffraction with g circled. **(D)** An enlarged HAADF STEM image of a 1/8 [112] partial dislocation. **(E–G)** ε_{xx} along [110], ε_{yy} along [001], and ε_{xy} strain maps of **(A)**; the location of the two extra atomic planes of the dislocation cores indicated by lines, reproduced from (Shafieizadeh et al., 2018).

demonstrate the effect of strain at $\Sigma 3\,(11\bar{1}) < 1\bar{1}0 >$ twin boundaries in $Gd_2Ti_2O_7$, showing a local reduction of the oxygen migration barrier compared with the bulk (Gupta et al., 2020).

Applications of ABF-STEM

Layer Termination at Heterointerfaces

Because of ABF-STEM's superior sensitivity to light elements, it is the method of choice to probe the anion sublattice. In this example, it is used to map both the anion and cation positions at an $LaAlO_3$/$La_{0.5}Zr_{0.5}O_{1.75}$ (fluorite) interface. The authors simulated three candidate structural models of terminations of the interface to compare with two orientations ([001] and [110]) of the interface (**Figures 8A,B**), finding that the model matches the two ABF images best when the fluorite layer is terminated by a bulk fluorite oxide anion layer followed by a pure Zr layer (green). This example demonstrates yet another examples of complementary nature of (S) TEM data and (S)TEM simulation (O'Sullivan et al., 2016).

Anion Disorder in Ion Tracks

The ability of STEM imaging to simultaneously collect multiple angles of electron scatter can be tremendously helpful for understanding the local structure. For instance, simultaneously acquired HAADF- and ABF-STEM images of ion tracks in ceria (**Figures 8C–F**) show that 1) a decrease in atomic density occurs inside the ion track, evident from the local drop of signal intensity in that HAADF-STEM images of the Ce lattice (**Figure 8C**) and 2) the O anion lattice is preferentially disordered by the electronic excitation damage at the core of the ion track, evident from blurring/absence of O anion columns at the core region from ABF-STEM images (**Figures 8D–F**) (Takaki et al., 2014).

STEM techniques have been used to explore the structure of various pyrochlore and fluorite systems (Gallagher et al., 2016; Sachan et al., 2017b; Sachan et al., 2018; Sachan et al., 2019; Spurgeon et al., 2019; Lee et al., 2020; Spurgeon, 2020). See reference (MacLaren and Ramasse, 2014) for a review of

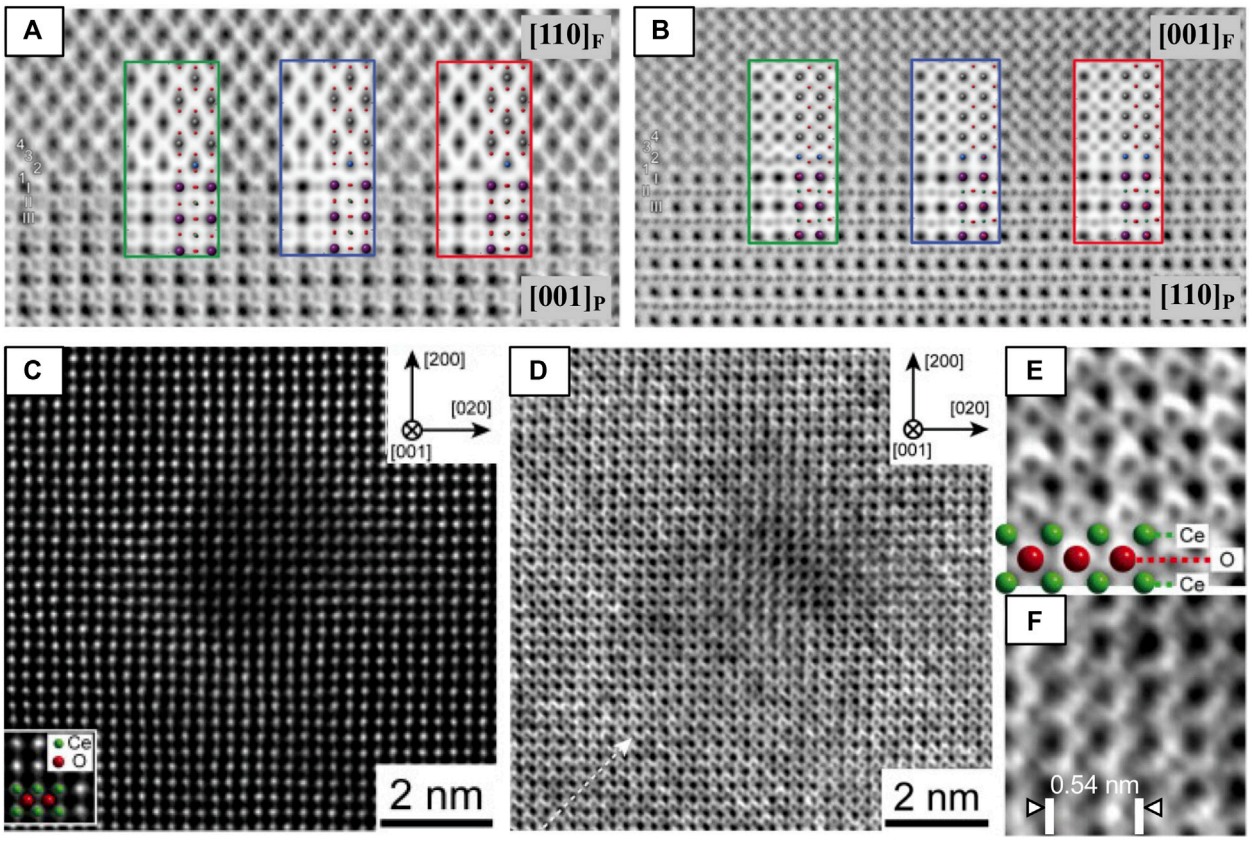

FIGURE 8 | HAADF and ABF-STEM images used to **(A,B)** clarify surface termination layer at an LAO-LZO interface and to **(C–F)** investigate the oxygen sublattice of CeO_2 after swift heavy ion irradiation. ABF-STEM images of the $LaAlO_3/La_{0.5}Zr_{0.5}O_{1.75}$ interface along the **(A)** [001]P and **(B)** [110]P zone axes. Three models of the fluorite/$LaAlO_3$ interface and their simulated ABF-STEM images were compared with experimental images to map the cation and anion positions. Comparison of images and models in both **(A,B)** shows that the O_2-terminated (green) model matches best along the two zone axes, with each cation/anion accounted for by the model. Reproduced from reference (O'Sullivan et al., 2016). **(C)** HAADF-STEM and **(D)** ABF-STEM images of an ion track in CeO_2 [001] formed by Xe ion irradiation, with magnified views of the **(E)** peripheral and **(F)** core damage regions of the ion track. Atomic models of CeO_2 are shown in the insets of **(C,E)**. Reproduced from reference (Takaki et al., 2016), original data from (Takaki et al., 2014).

STEM techniques applied to functional oxides beyond pyrochlore and fluorite systems.

Real-Space Structure Analysis Software Tools

In addition to experimental factors, such as high-quality TEM specimen preparation, and proper optical setup and image acquisition parameters, software tools can be used to correct scan distortions of STEM images and automated procedures can perform highly accurate assessment of atomic positions. There are many software programs available to do this (e.g., Ranger (Jones and Nellist, 2013), qHAADF (Galindo et al., 2007), iMtools, StatSTEM (De Backer et al., 2016), and oxygen octahedra picker [110], as well as Atomap [111], among others [112] (Jones et al., 2015)). This is still a highly active area of research, where machine learning tools are being developed to improve image quality and atom detection (Lin et al., 2021). Image simulation is useful to aid the interpretation and validation of STEM data, as conveyed through multiple examples above. The two most commonly used image simulation methods are the Bloch wave and multislice methods, see (Kirkland, 1998) for detailed descriptions. Some popular software options for STEM image simulation are Dr. Probe (Barthel, 2018) Prismatic (Ophus, 2017; Rangel DaCosta et al., 2021), and pyQSTEM (Koch, 2002), among many others.

STRUCTURE ANALYSIS FROM RECIPROCAL-SPACE (DIFFRACTION) DATA

Structural information contained in (S)TEM images is also contained in the electron diffraction (ED) pattern, represented in real-space and reciprocal-space, respectively. Electrons scattered from the specimen generate diffraction patterns that contain rich crystallographic information. From the position and symmetry of the diffraction spots, it is possible to determine the unit-cell parameters and lattice type, while the intensities of the diffraction spots are related to the arrangement of atoms within the unit cell (Jia et al., 2005). ED can also be used to assess sample crystallinity because crystalline materials produce sets of sharp

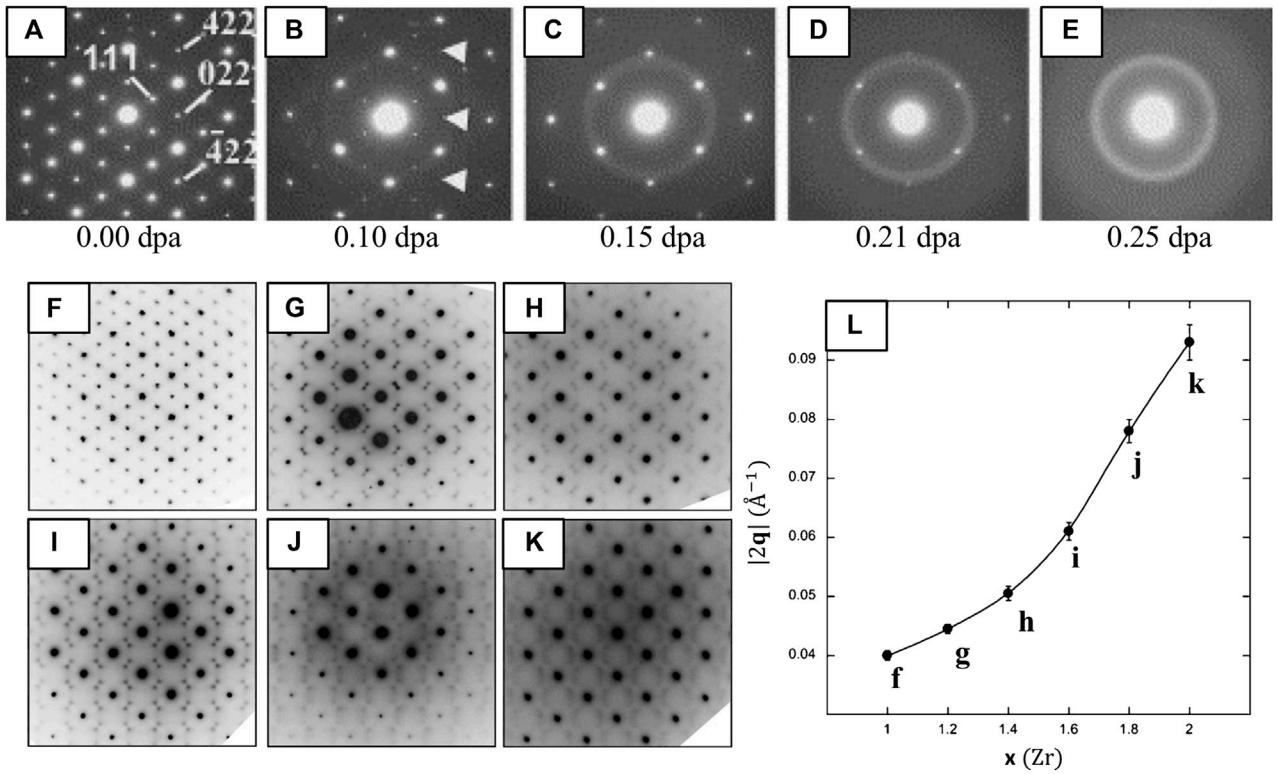

FIGURE 9 | SAED patterns illustrating ODT of ordered pyrochlores **(A–E)** due to ion-irradiation and **(F–L)** chemical doping. **(A–E)** SAED diffraction patterns of $Er_2Ti_2O_7$ [$01\bar{1}$] subjected to Kr^+ irradiation at increasing dose. The loss of diffraction maxima with indices $h + k + l = 4n$ (i.e., 022 and 422) (white arrows) suggests anion disordering occurs upon irradiation, followed by cation disordering and loss of long-range order with increasing dose, reproduced from (Lian et al., 2003). **(F–L)** SAED patterns of $Y_2Sn_{2-x}Zr_xO_7$ [110] for increasing Zr content (x) where **(F)** $x = 1.0$ ($Y_2Sn_{1.0}Zr_{1.0}O_7$) **(G)** $x = 1.2$ **(H)** $x = 1.4$ **(I)** $x = 1.6$ **(J)** $x = 1.8$ and **(K)** $x = 2.0$ ($Y_2Zr_2O_7$). **(L)** A plot of $|2\mathbf{q}|$ versus Zr content, where $|2\mathbf{q}|$ represents the characteristic spacing between pairs of satellite reflections. The real-space correlation distances for the minimum ($x = 1.0$, $|2\mathbf{q}|^{-1} = 11 \pm 0.8$ Å) and maximum ($x = 2.0$, $|2\mathbf{q}|^{-1} = 3 \pm 0.2$ Å) Zr contents. Reproduced from reference (de los Reyes et al., 2013).

and discrete Bragg reflections, whereas disordered, condensed phases such as liquids or glasses produce smooth, continuous 'halos' of scatter (**Figures 9A–E**). Selected-area electron diffraction (SAED) is the most straightforward ED method, obtained by isolating a region of the specimen for diffraction analysis with an area-limiting aperture (>0.1 μm) under parallel-illumination. However, many variations exist (see **Small-Beam ED**) where the (S)TEMs optical setup can be tuned to probe a smaller volume than with SAED while maintaining near-parallel convergence, which is necessary in some cases to acquire the desired information.

Diffraction Fine-Structure

Additional structural information is encoded in the ED 'fine structure' (e.g., extra and split peaks, satellite reflections, and structured diffuse scattering) which provide a means to analyze defects and reveal local ordering. Fine structure can indicate the presence of superstructures (Abelson et al., 2020) of various kinds (e.g., pyrochlore cation or vacancy ordering (Lian et al., 2005)), extended defects (e.g., planar interfaces and dislocations (van Landuyt et al., 1966)), and can also signify the shape of diffracting volumes in certain situations (Edington and Edington, 1975; Williams and Carter, 2009d). Diffuse electron scatter is a type of fine structure that arises from inelastic interactions such as phonon, plasmon and electron excitations or elastic interactions with crystal imperfections (Zuo et al., 2017a). Diffuse scattering may have many different origins, for example, substitutional ordering/disordering coupled to displacive disorder as atomic positions are relaxed around vacancies or substitutional atoms of different sizes, tilts of rigid polyhedra, lattice deformation, the formation of textures and others (Van Tendeloo and Amelinckx, 1998). If the diffuse scatter can be interpreted, it is a powerful signature of local ordering over the probed volume of the specimen. However, since classical crystallography provides no established protocol for its analysis, diffuse scatter is often either ignored or analysis is carried out on a case by case basis where the tools developed cannot be broadly applied across material systems (Keen and Goodwin, 2015).

Applications of Diffraction Fine-Structure and Diffuse Scatter Analysis

Often, the presence of additional scattering effects (satellite and diffuse scatter) in fluorite and pyrochlore systems are a result of local, strain-driven compositional and displacive structural modulations (Withers et al., 1991; Tabira et al., 1999; Tabira et al., 2001; Withers et al., 2004; Liu et al., 2006; Withers and

Hawkes, 2008; Welberry and Weber, 2016; Trump et al., 2018) and sometimes can be related to the formation of locally-ordered domains (García-Martín et al., 2005; Lau et al., 2008; Reid et al., 2012). For instance, the presence of local, C-type ordering in lanthanide oxides on short to intermediate length scales can give rise to ED fine structure; selective imaging of signal originating from single satellite peaks (satellite dark-field imaging) has been used to reveal the distribution of C-type ordered nanodomains on the order of ~50–100 Å in real-space (Reid et al., 2012).

Ion-Irradiation Induced Order-Disorder Transition

ED is especially useful for observing the ODT of pyrochlores to defect-fluorite since the degradation of cation and anion ordering leads to the loss of pyrochlore superstructure reflections (Lian et al., 2005; Lian et al., 2003). For instance, *in situ* ion-irradiation in the TEM with the collection of SAED patterns shed light on how the ODT advances in the temporal domain (**Figures 9A–E**) (Lian et al., 2003). These authors show that pyrochlore first becomes anion-disordered as a result of Frenkel pair accumulation and oxygen vacancy redistribution, evidenced by the loss of superstructure reflections with indices h + k + l = 4n that correspond solely to anion ordering (e.g., 220, 422). This is followed by partial cation disordering, evidenced by loss of the 111 superstructure reflections that correspond to both cation and anion ordering (**Figures 9A–E**).

Chemical Doping-Dependent Correlation Length

In addition to revealing cation and anion disordering under irradiation, ED fine structure and diffuse scatter can also reveal short to medium range ordering. de los Reyes et al. (2013) use these features to examine the ODT in $Y_2Sn_{2-x}Zr_xO_7$ ($0.0 \leq x \leq 2.0$) upon chemical doping (substitution of Zr for Sn). SAED patterns of their starting composition $Y_2Sn_{2-x}Zr_xO_7$ (**Figure 9F**) are consistent with the pyrochlore structure, where the strongest diffraction maxima correspond to the fundamental Bragg reflections of the fluorite sub-cell with weak characteristic pyrochlore superlattice reflections also present. As Zr replaces Sn ($x \geq 1.2$), the pyrochlore ordering reflections disappear and the fundamental Bragg reflections of the fluorite structure (G_F) are decorated by pairs of satellite reflections mirroring the $G_F \pm ½ <111>^*$ regions of reciprocal-space for small x ($x = 1.2–1.6$) (**Figures 9G–I**). Note that the diffuse scattering at any position in reciprocal-space can be defined by a wave-vector $\mathbf{G}_F \pm \mathbf{q}$, where $\mathbf{G}_F$ is a reciprocal lattice vector of the underlying fluorite-type cell and $\mathbf{q}$ is a modulation vector (García-Martín et al., 2005).

At higher substitutions ($x = 1.8–2.0$) the initial satellite spots weaken and the intensity transforms into a more diffuse, wavelike pattern that corresponds to a second modulation of the underlying fluorite structure at $G_F \pm ¼ <220>^*$ (**Figures 9J,K**), as observed in other pyrochlore/defect-fluorite systems (Suzuki et al., 1985; Gallardo-López et al., 2001). The inverse of the modulation wave vector magnitude ($|2q|^{-1}$) associated with the satellites gives a real-space correlation distance (or interaction length) (Whittle et al., 2009) that decreases from ~25 Å (x = 1.0) to ~11 Å (x = 2.0), equivalent to ~2 to 1 pyrochlore unit-cells, respectively. Several underlying phenomena have been proposed to explain the presence of these features, including defect-vacancy and/or interstitial ordering, ordered-cluster arrangements, micro-domain pockets, and anti-phase domain boundaries (e.g., pyrochlore order within fluorite) (Allpress and Rossell, 1979; van Dijk et al., 1986; Tabira et al., 2001). Regardless, the diffraction fine-structure can be correlated to a real-space local-ordering phenomena, where (in this case) the interaction length appears to decrease as a function of chemical doping.

3D Reconstruction of Diffuse Scatter in Reciprocal Space

Recently, the analysis of diffuse features in electron diffraction data has extended into 3D, called 3D-ED or diffraction tomography. 3D-ED data can be acquired through various specimen tilting/rotation schemes (Gemmi et al., 2019; Kolb et al., 2007) to map the Bragg and diffuse scatter from disordered materials in reciprocal-space (**Figure 10A**). Rotation ED (RED) (Zhang et al., 2010; Wan et al., 2013) is one acquisition approach, which combines electron beam tilting over many small steps with crystal rotation over a few large steps. 3D-ED has not yet been utilized to explore local structural deviations in fluorites or pyrochlores, but has been used to identify and map unique oxygen octahedral tilting systems in a 85NBT-10BKT-5BT ternary piezoceramic perovskite (Neagu and Tai, 2017), among other systems. This approach can lead to much clearer interpretation of ED fine-structure, for instance the satellite reflection pairs mirroring the $G_F \pm ½ <111>^*$ regions of reciprocal-space make up a single continuous circle of diffuse intensity in 3D reciprocal-space, however this is not immediately apparent from the 2D projections shown in **Figures 9F–K**. Further resources are available on the interpretation (Van Tendeloo and Amelinckx, 1998; Zuo et al., 2017a) and modeling (Neder and Proffen, 2009; Keen and Goodwin, 2015) of diffuse scattering and SAED fine structure from disordered crystalline systems.

Small-Beam Electron Diffraction - Microbeam, Nanobeam, Angstrom Beam and Convergent Beam Electron Diffraction

In SAED, the size of the electron beam on the specimen is typically >0.1 μm across and the area of the diffracting region is controlled by an area-limiting aperture. In μ-/N-/A-BED, the TEM optics are modified to achieve quasi-parallel illumination, much like SAED. However, the prefix micro, nano, or angstrom *roughly* indicate the size of the beam on the specimen, thereby limiting the size of the diffracting region. It is important to note that neither the terms μBED, NBED, ABED, CBED, nor the optical conditions they intend to describe are used consistently across the literature, so it is important to check beam size and convergence to understand the optical conditions used in any small-area diffraction study. We will refer to techniques where the probe size is minimized to provide localized diffraction information as 'S-BED' techniques, which is for ease of reference only and not a widely used acronym.

Applications of S-BED

Critical Dose and Temperature of Amorphization

S-BED techniques are particularly useful when the region of interest is limited in size, for instance, to assess damage at

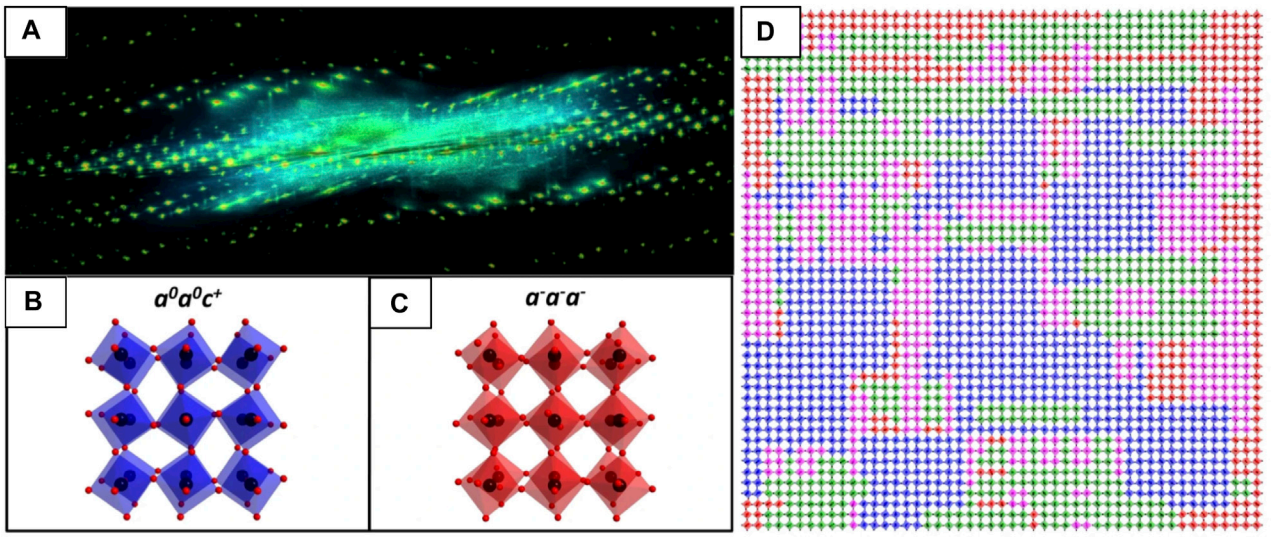

FIGURE 10 | 3D-ED mapping of Bragg and diffuse electron scatter in reciprocal-space to determine TiO_6 octahedral tilt schemes in 85NBT-10BKT-5BT $[001]_{pc}$ ceramic. **(A)** Reconstruction of the reciprocal-space volume showing intensity from both Bragg and diffuse scattering. **(B)** Schematic of the in-phase $a^0a^0c^+$ and **(C)** antiphase $a^-a^-a^-$ tilt systems. **(D)** A 2D slice cut from **(A)** showing three in-phase variants randomly distributed in the antiphase tilted matrix (red, blue, green, and magenta octahedra are tilted according to the $a^-a^-a^-$, $a^0a^0c^+$, $a^0c^+a^0$ and $c^+a^0a^0$ tilt systems, respectively. Only the TiO_6 octahedra are displayed. Reproduced from (Neagu and Tai, 2017).

various depths within an irradiated $Ho_xYb_{(2-x)}TiO_5$ pyrochlore series under *ex situ* temperature-dependent irradiation (Aughterson et al., 2018). The onset dose and depth of amorphization can be precisely determined for various temperatures with NBED, which provides the information necessary to calculate the critical dose (D_c) and temperature (T_c) for amorphization, two quantities which indicate suitability for nuclear environments. **Figures 11A,B** shows a TEM cross-section of the Se^+ irradiated Yb_2TiO_5 ($x = 0$) specimen at 300 K (**Figure 11A**) and 400 K (**Figure 11B**), respectively. NBED patterns acquired at increasing depths (**Figures 11Ai–iii**) show smooth halos of electron scatter (**Figure 11Ai**) in the near-surface region, indicating complete amorphization, sparse Bragg reflections (**Figure 11Aii**) at greater depth, indicating a mixed crystalline/amorphous state, and a fully crystalline state (**Figure 11Aiii**) furthest from the irradiated surface. The specimen irradiated at 400 K presented in **Figure 11B** provides another example of the ability to discern the state of pyrochlore ordering by the absence (**Figure 11Bi**) or presence (**Figure 11Bii**) of superstructure reflections (Aughterson et al., 2018). Determination of D_c and T_c can also be performed *in situ*, however, availability of (S)TEMs equipped with irradiation sources are limited (Hinks, 2009).

"Structure" of the Amorphized State

In the highly disordered regions near the sample surface of **Figures 11A,B** the atomic structure is either partially (**Figure 11Ai**) or fully amorphized (**Figure 11Aii**) as a result of irradiation treatment. These disordered regions likely retain some characteristic structures of their pre-irradiated parent-phase, or other defect structures that may provide clues on how the disordering process progresses. Although amorphous materials do not possess long-range order as crystals do, they often demonstrate structural correlations on the scale of a few angstroms (SRO) or nanometers (MRO) that can be teased out through various diffraction and analysis methods (Cockayne, 2007). As demonstrated by **Figure 11C**, new structure arises in the diffracted signal as the probe size is reduced to the nm- or Å-scale. When the probe is on the order of SRO/MRO, local symmetries of individual structural units appear as the probed volume approaches the structural unit size, providing many new analytical opportunities for local structural analysis of highly disordered systems. In metallic glasses, the most widely studied amorphous solids by ED methods, these speckled patterns (**Figures 11Ci–iv**) are proposed to originate from individual atomic clusters, and the assembly of those clusters (Miracle, 2004; Miracle, 2006; Sheng et al., 2006). Although the local atomic arrangements in amorphous metal oxide systems is less established, the structure is proposed to be based on metal-oxide ($M\text{-}O_x$) polyhedra, where disruptions in long-range order occur by variation in the linking of $M\text{-}O_x$ polyhedra, or by distortions of the polyhedra themselves that alter bond distances and/or bond angles (Buchholz et al., 2014; Yan et al., 2019).

Pair-distribution function (PDF) analysis (Billinge and Kanatzidis, 2004) is routinely used to extract short-range structural information from highly-disordered or amorphous materials, and is frequently used to study pyrochlore disorder. The PDF yields the probability of finding an atom at an interatomic distance, r, from another atom (Egami and Billinge, 2012), which describes the local atomic environment by providing interatomic bond-lengths

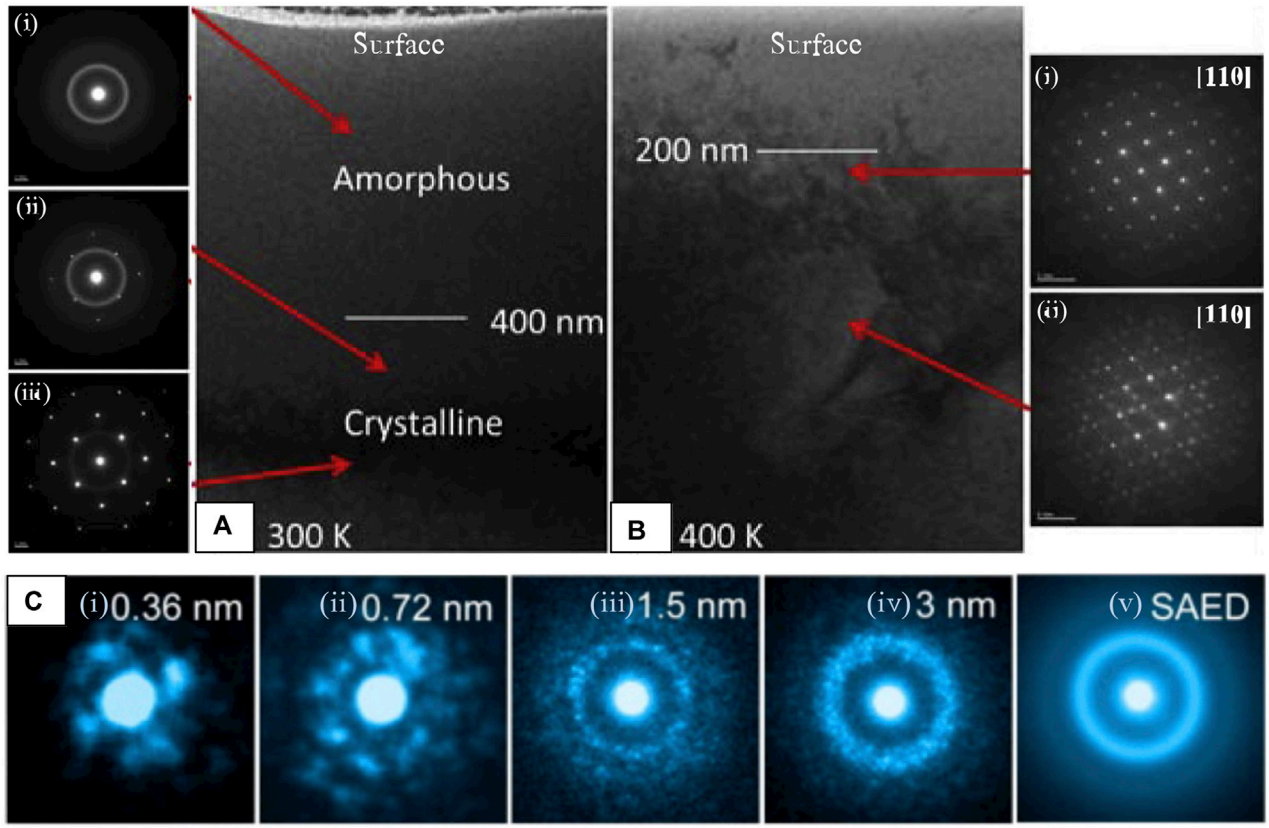

FIGURE 11 | Small (nm- or Å-scale) quasi-parallel electron probes to acquire highly localized diffraction information to **(A,B)** assess crystallinity as a function of depth and **(C)** to demonstrate the effect of probe size in detection of local atomic ordering in an amorphous solid. **(A)** BF-TEM of an ion-irradiated Yb_2TiO5 cross-section held at **(A)** 300 K, NBED showing loss of crystallinity at the **(i)** surface and **(B)** 400 K, NBED showing **(i)** absence of the (111) pyrochlore reflection which **(ii)** reappears at depth, reproduced from (Aughterson et al., 2018) **(C)** The effect of increasing probe size in a $Zr_{66.7}Ni_{33.3}$ metallic glass, where local atomic ordering emerges at the smallest (Å-scale) probe sizes, averaging out into a smooth, diffuse ring as the probe size increases. Reproduced from reference (Hirata and Chen, 2014).

and coordination numbers (CN)), averaged over the probed volume. PDF analysis is performed by taking the Fourier transform of the total scattering signal (Bragg + diffuse scatter) to generate a real-space representation, where diffuse and Bragg components of the diffraction data can reveal the local and long-range order (if present) simultaneously (Souza Junior et al., 2021). Although PDF analysis is primarily applied to X-ray and neutron diffraction data, it is also readily applicable to ED data (so-called ePDF analysis). Compared with XRD, ePDF even has an advantage when it comes to lighter atoms because of the stronger electron-matter interactions and the short electron wavelength that enables analysis of atomic-correlations out to high scattering angles (Qmax up to 20 Å−1 is feasible), corresponding to real-space bond lengths of 0.3 Å (Gorelik et al., 2019).

EPDF analysis is most commonly performed on SAED data because it offers a (relatively) large diffracting region (>0.1 μm) that yields statistically averaged information, indicated in the ED data by smooth and continuous halos of intensity (**Figure 11Cv**) as opposed to the speckled patterns acquired with smaller probes (**Figures 11Ci–iv**). However, using variable-resolution fluctuation electron microscopy (Voyles and Muller, 2002), a technique for the measurement of MRO, Hwang and Voyles (2011) showed that the diffracted signal of inorganic glasses reaches a statistically averaged representation with just an 11 nm probe. This means that the structure is almost completely homogeneous over that length scale, so ePDF measurements of the averaged amorphous structure can be made from nanometer-scale probes which are compatible with scanning diffraction experiments (4D-STEM). This section discusses scanning ePDF, that can be used to map important structural features across amorphous and highly disordered specimen.

Although X-ray and neutron diffraction-based PDF analysis is widely used in pyrochlore systems, ePDF has not yet been applied to these systems. Authors of a recent review on ePDF analysis shed light on why the technique is underutilized in general, pointing to a lack of access to a user-friendly workflow for handling ePDF processing steps (Souza Junior et al., 2021). Still, ePDF and its close-relative radial-distribution function (eRDF) analysis have been used in many systems, for instance in amorphous SiN (Cockayne, 2007), SiO_2 (McBride and Cockayne, 2003), SiC (Hirotsu et al., 2001; Ishimaru et al.,

2002; Ishimaru, 2006; Ishimaru et al., 2008)), and more software tools for ePDF analysis are being developed all the time (e.g., eRDF Analyzer (Shanmugam et al., 2017), RDFTools (Mitchell et al., 2012), PASAD (Gammer et al., 2010), SUePDF (Tran et al., 2017), ePDFsuite (Nanomegas, Belgium). Thorough overviews of ePDF analysis are given in references (Gorelik et al., 2019; Souza Junior et al., 2021).

When the electron probe is brought down to the angstrom scale (**Figure 11Ci**, information about the local atomic arrangement of clusters can be extracted. ABED has been broadly applied to metallic glasses (Hirata et al., 2011; Hirata et al., 2013; Zhu et al., 2017), and to oxides (Hirata et al., 2016), however application to amorphized mixed-metal oxides is largely absent from the literature. This is likely because metal-oxides are not ideal glass formers (Lim et al., 2015); however, their structure is still technologically important, (Yan et al., 2019), especially for understanding radiation-induced disordering processes. Recently, Raman (Tracy et al., 2016) and STEM-EELS (Sachan et al., 2017b) spectroscopies have indicated that the local atomic arrangement within amorphous pyrochlore is not fully random as previously thought, but may instead exhibit local ordering similar to that of the disordered phase (Shamblin et al., 2018). Hirata and coworkers, who have made substantial advancements in determining the local structure of amorphous materials through ABED, suggests that a combination of global (e.g., statistically averaged PDF analysis) and local (e.g., ABED) analysis is necessary to provide the overall picture of amorphous structures. PDF analysis cannot adequately reveal individual local structures, although the overall statistical information can be obtained accurately. Therefore, the higher spatial resolution of ABED compared to that of PDF is necessary to directly obtain local information (Hirata, 2021). Additionally, ABED combined with the scanning function of STEM allows the spatial extent and distribution of local structures to be understood.

Precession Electron Diffraction

In most (S)TEM techniques, data interpretation is complicated by multiple scattering which commonly occurs due to the strong interaction of electrons with the crystal potential, even in thin specimens (<100 nm). This 'dynamical' diffraction perturbs the relative intensities of Bragg reflections and diffuse scatter in ED, and leads to inaccurate measurement of CN in ePDF analysis (Ishimaru, 2006). The first line of defense to minimize multiple scattering is optimization of specimen thickness and/or electron energy (Gorelik et al., 2019), however, many other methods have been devised (Eggeman et al., 2012) specifically to avoid its effect on the relative intensities of Bragg peaks in ED patterns. PED (Ishimaru et al., 2002) is one of these methods, whereby the incident electron beam (often set to NBED conditions), is tilted and precessed to form a conical electron probe at the specimen. PED can be used to identify crystal structure, determine the local crystal orientation (Bowman et al., 2020), or to investigate crystal texture, grain rotation, and strain. Compared with a steady (unprecessed) beam, precession provides many more reflections by sampling additional layers of reciprocal-space (both the zero-order and higher-order Laue Zones, ZOLZ and HOLZ, respectively) allowing for greater sensitivity to local orientation changes as well as changes in lattice parameter. It also integrates the intensities through the Bragg condition over the precession cycle, averaging out relative intensity fluctuations due to dynamical scattering (Moeck and Rouvimov, 2010; Midgley and Eggeman, 2015).

Convergent-Beam Electron Diffraction

Until this point, the diffraction techniques discussed have utilized parallel ($\alpha \approx 0$), or quasi-parallel (small α) illumination that produce localized diffracted signals originating from a broad specimen area. CBED requires convergent illumination, where the electron beam is focused into a probe that impinges the specimen over a range of angles (Williams and Carter, 2009b) and delocalizes the diffracted signal into discs that may contain complex, and information-rich intensity distributions (Zuo et al., 2017b). Generally, the convergence angle used for CBED is several times larger than what is used in μ/N/ABED, but still significantly smaller than that used in an aberration-corrected STEM. The convergent illumination condition generates a spherical electron-wavefront capable of sampling a greater portion of reciprocal-space, thus, CBED is better suited than parallel-beam ED approaches for involved crystallographic studies because it enables unique determination of the point group from one or few zone axes, and with analysis of the systematic absences it is possible to uniquely determine most space groups. The complex intensity distributions within the Bragg discs, and 3D information in the higher-order Laue zone (HOLZ) lines (Zou et al., 2011) provide additional signatures of the underlying crystal symmetry. Positions of the HOLZ lines are sensitive to the unit cell parameters, so deviation from a standard can be used to probe any local unit cell distortions. See (Zuo et al., 2019) for an in-depth discussion of S-BED techniques and their utility.

LINKING REAL AND RECIPROCAL-SPACE INFORMATION WITH 4D-STEM

4D-STEM refers to a broad range of scanning-based diffraction techniques that generate a four-dimensional diffraction dataset, where each probe position in real-space is associated with a diffraction pattern in reciprocal-space (Zuo et al., 2019). In addition to providing a direct link between these two spaces, 4D-STEM is a powerful alternative to STEM imaging (**Figure 11A**) because it utilizes a "universal (pixelated) detector" (**Figure 11B**) such that the full angular range of electron scatter is collected simultaneously. In this 4D dataset, information can be parsed as a function of the scattering vector (k_x,k_y) in reciprocal space and probe position (x,y) on the sample (Hachtel et al., 2018) (**Figure 11C**).

Terminology, Acquisition and Challenges

The presence of the term '4D-STEM' in the literature is fairly new, largely due to a lack of agreed upon terminology. In review of 4D-STEM techniques and applications, C. Ophus (Ophus, 2019) provides early examples of work appearing under different names

despite their similar experimental setups (e.g., position-resolved diffraction, spatially-resolved diffractometry, momentum-resolved STEM, scanning electron nanodiffraction, pixelated STEM, nanobeam scanning diffraction, nanodiffraction mapping, STEM diffraction mapping, etc.). Nonetheless, variations of 4D-STEM experiments have been widely used under various aliases over the past ~20 years with increasing ease and popularity as detector technology advances.

4D-STEM is performed under small-beam diffraction conditions (described in an earlier section) since size the of the beam on the sample provides an upper limit to the achievable spatial resolution of the structural information maps in most cases. The convergence angle, determined by the probe-forming aperture and settings of the electron optics, controls the probe size on the specimen and the size of the BF and Bragg discs in the diffraction plane, where an inherent tradeoff exists between the two. Some important factors to consider in these experiments are:

1) the extent of overlap between Bragg discs which will determine what types of analyses can be performed (e.g., well-separated discs are required for phase, orientation, and strain mapping, and disc interference is needed for ptychographic reconstruction of atomic potentials).
2) the spatial sampling of the probe which in the case of undersampling, determines the spatial resolution and the field-of-view (FOV) of structure maps, and can exclude certain types of analyses (e.g., position-averaged CBED, (PACBED)) for which oversampling is required.
3) the dwell times and probe current, which will depend on how well the sample tolerates the electron beam. See (Egerton, 2019) for a review of electron beam damage and (Bustillo et al., 2021) specific to 4D-STEM experiments.
4) The number of pixels over the scanned area, and on the detector. For example, a spatial scan with 1 k × 1 k points recording data from a 512 × 512 pixel detector would occupy ~977 GB when stored in 32-bit integer format (Nord et al., 2020).

See (Nord et al., 2020; Paterson et al., 2020) for guides on 4D-STEM data acquisition and processing.

Applications of 4D-STEM

The ability to collect the full scattering range, and associate diffraction data with positions across the specimen leads to a broad range of applications. Barring some specific acquisition requirements that may complicate or exclude data analysis for certain applications, the 4D dataset contains all information needed to perform multiple types of analysis. A single 4D-STEM experiment enables a range of measurements that can be performed in post-processing. Rather than providing a comprehensive overview of possible techniques, which already exists (Ophus, 2019), we will introduce select 4D-STEM techniques that are particularly useful for the analysis of disordered crystalline systems, specifically for the types of disorders described in previous sections. These include virtual imaging, structure classification followed by crystalline/semi-crystalline orientation, phase and strain mapping, as well as analyses specific to amorphous materials such as SRO/MRO analysis with STEM-PDF/RDF, and STEM-FEM. 4D-STEM has not been widely applied to pyrochlores and fluorites, fortunately there is one detailed example of its application to a pyrochlore-structured $Gd_2Ti_2O_7$ (GTO) in the literature, used to illustrate the multimodal analysis of 4D datasets using the py4DSTEM software suite (Savitzky et al., 2021). In this example, a GTO single-crystal was amorphized through an irradiation treatment, then partially recrystallized through annealing. The sample contains a band of semi-crystalline GTO sandwiched between single-crystal and amorphous states. **Figure 12B** shows the complex, multi-phase structure of this sample, and also demonstrates the experimental setup of the 4D-STEM experiment where an SBED **Small-Beam Electron Diffraction - Microbeam, Nanobeam, Angstrom Beam and Convergent Beam Electron Diffraction** pattern is acquired for each probe position on the GTO specimen (**Figure 12B**). **Figure 12C** shows a few of types of analyses that have been performed on this GTO dataset.

Virtual Imaging

The most straightforward analysis that can be performed on a 4D-STEM dataset is to integrate the diffracted signal within a (usually circular or annular) mask generated in reciprocal-space to construct a 2D-STEM image (Levin et al., 2020b). The ability to flexibly select signals in reciprocal-space makes it possible to reconstruct images equivalent to any of the traditional STEM detectors (see **STEM Imaging Modes**), even with atomic resolution (**Figures 13C–E**) (Hachtel et al., 2018; Levin et al., 2020b). The left column of images in **Figure 12ei** (Savitzky et al., 2021) shows an example of virtual imaging with circular and annular masks at low magnification, used to generate virtual-BF (green) and virtual-DF (blue/purple) images of the irradiated GTO sample, ED patterns in the <110> projection. The second column of **Figure 12Ei** shows the unique power of virtual imaging, where specific diffraction spots, sets of spots, or other diffraction fine-structure can be selected to form images that may be otherwise impossible to generate through DF imaging techniques. Here, the virtual-DF images are constructed from sets of cation ordering reflections (Lian et al., 2003) that correspond to the pyrochlore structure (red), and from a set of reflections shared by both pyrochlore and fluorite (blue), demonstrating how local regions of cation ordering can be imaged by filtering electrons from the diffraction pattern based on their scattering vectors. Another approach to mapping cation-ordering achieved by template matching is described in the following **Structure Classification, Orientation, and Strain Mapping**. In theory, imaging of the anion-ordered regions could be achieved in a similar manner by selecting spots with indices $h + k + l = 4n$ (i.e., 022 and 422) (Lian et al., 2003) to form virtual-DF images. However, the scattering from oxygen is likely much weaker and may require methods to improve the signal-to-noise ratio.

By the same logic, virtual imaging could also be used to image locally-ordered domains (O'Quinn et al., 2020) in heterogeneously disordered pyrochlores (e.g., to reveal the

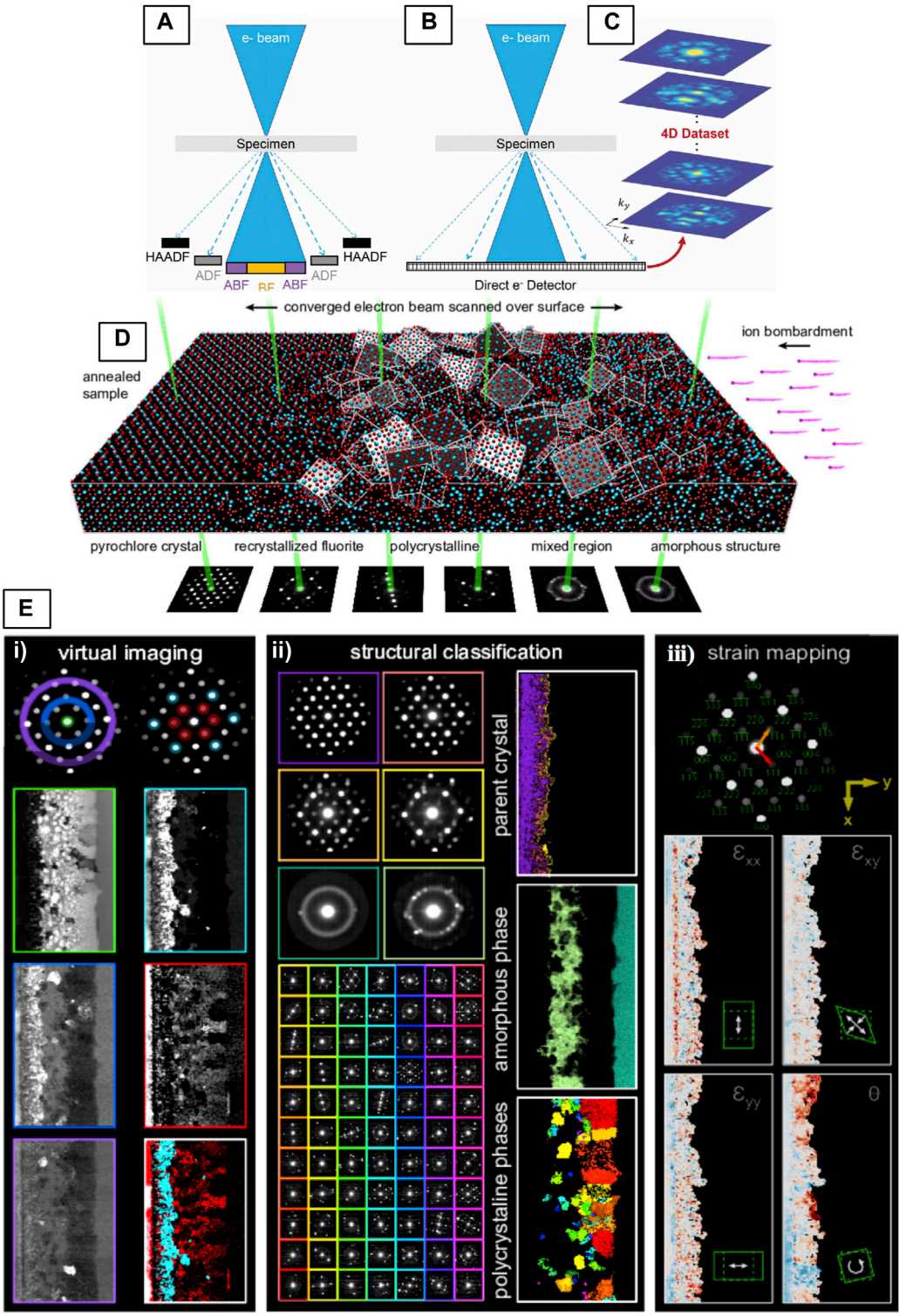

FIGURE 12 | (A–C) Illustration of conventional and 4D-STEM and **(D,E)** 4D-STEM experimental geometry, and multimodal data analysis with py4DSTEM. **(A)** In conventional STEM, signal is integrated over different angular regions of the diffraction plane. **(B)** In 4D STEM, an entire 2D CBED pattern is recorded at each probe position of a 2D-STEM raster, resulting in a **(C)** 4D dataset, Reproduced from (Levin et al., 2020b). **(D)** The experimental setup showing a pyrochlore-structured $Gd_2Ti_2O_7$ (GTO) sample that was irradiated and subsequently annealed showing gradient in structure from fully-ordered to amorphous (Savitzky et al., 2021). **(E)** Examples of various types of measurements that can be made in post-processing from the 4D-STEM dataset acquired in **(D)**. Reproduced from reference (Savitzky et al., 2021).

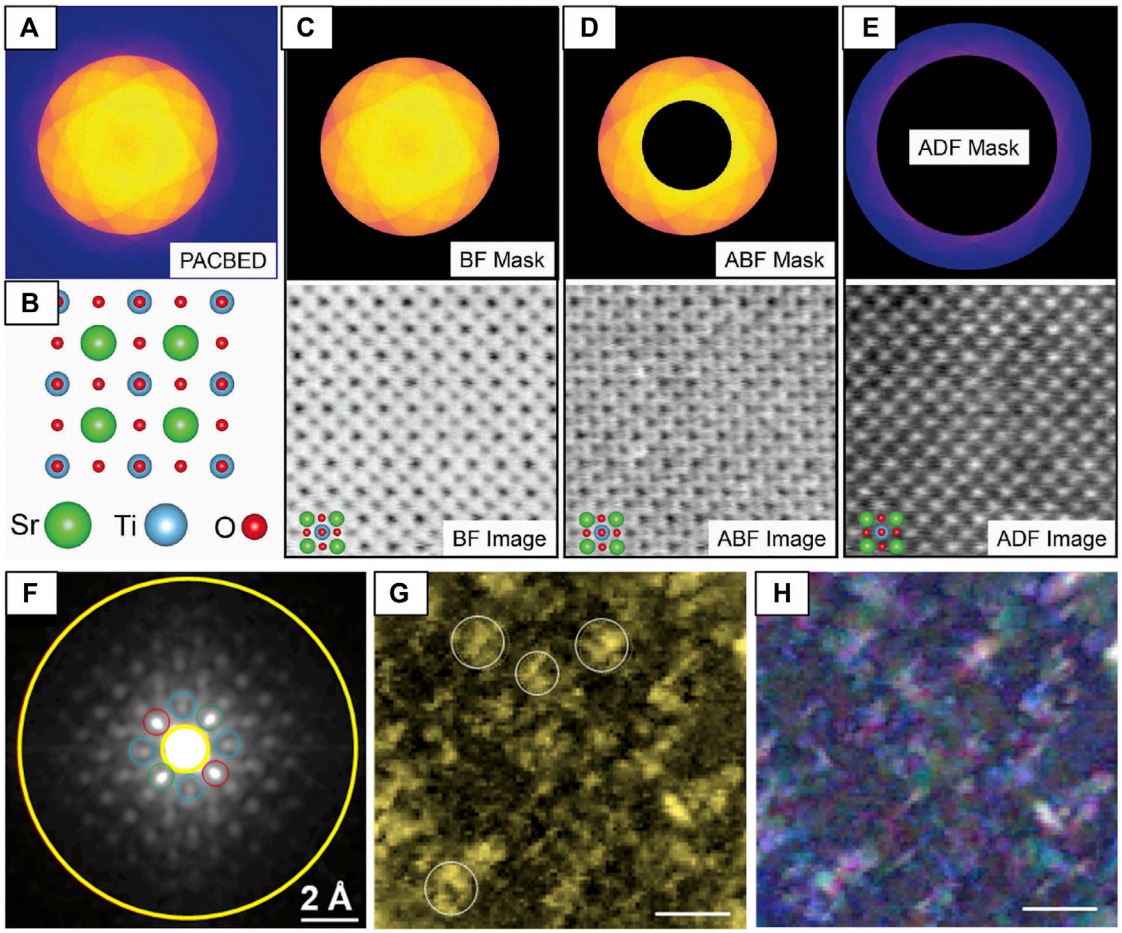

FIGURE 13 | Using 4D-STEM datasets to reconstruct virtual images **(A–E)** of SrTiO3 at atomic-resolution and **(F–H)** of severe lattice distortions in an HEA using the difference Cepstrum (dCp) transform to select only diffuse electron scatter contributions. **(A)** A 4D-STEM PACBED dataset acquired from $SrTiO_3$ [001] and the **(B)** crystal structure of $SrTiO_3$ [001]. Masks (top row) can be applied to the 4D dataset to produce **(C)** BF **(D)** ABF and **(E)** ADF images, reproduced from reference (Levin et al., 2020b). The **(F)** (dC_p) averaged across the scanned region. A **(G)** virtual-image formed from the total diffuse scattering signal integrated over yellow annulus in **(F)** and an **(H)** composite virtual-image of the blue, green, and red signals in the dC_p showing the complex structural distortions of the HEA. Scale bars in G and H are 40 nm, reproduced from (Shao et al. 2021).

formation of Weberite-type (O'Quinn et al., 2020; Shamblin et al., 2016), or bixbyite (C-type) structural units (Reid et al., 2012). It could also be used to investigate the spatial the origins of diffuse electron scatter (see **Diffraction Fine-Structure**) from the specimen, however, this presents several challenges. A more sophisticated approach is achieved by Cepstral STEM (Shao et al., 2021), which is a new 4D-STEM technique for imaging severe lattice distortions within disordered crystals using fluctuations in electron diffuse scatter that arise due to crystal disorder. Cepstral analysis is a sensitive signal processing technique for detecting weak harmonic signals by performing a Cepstral transform of the coherent NBED pattern. The Cepstrum transform has been applied previously to ED patterns for lattice strain analysis based on Bragg scatter (Padgett et al., 2020). Recently, the difference Cepstrum (dC_p) was developed, which represents the difference between the Cepstral transforms of local NBED patterns and the region-averaged NBED pattern within a 4D dataset (Shao et al., 2021). The dC_p separates electron diffuse scattering from Bragg diffraction so the diffuse signal can be analyzed to determine the distortive part of electron scattering potential. This part can then be imaged via construction of a virtual-DF image (**Figure 13**) as in the previous example, only by masking the dC_p rather than the NBED pattern directly. The sharp harmonic signals detected by Cepstral STEM make numerical quantification of lattice distortions and their mapping possible. **Figure 13** shows the dC_p of a high-entropy alloy, where the composite virtual-image from select signals in the dC_p demonstrate the complex structural distortions of and HEA. See (Ophus, 2019) for more applications of virtual imaging to various systems.

Structure Classification, Orientation, and Strain Mapping

For structure classification, phase, orientation, and strain mapping applications, precise determination of Bragg disc

positions is critical, thus, the discs must be well-separated and well-defined so automated analysis can be carried out to determine their locations. The overlap of discs can be prevented by reducing the convergence angle such that the distance between the Bragg spots is at least twice the Bragg angle ($\theta_B \approx$ few mrad) which can be achieved by ensuring $\alpha < \theta_B$. Phase and orientation mapping rely on a template matching approach, where stacks of simulated diffraction data are matched to the experimental data to determine the local phase, orientation, or strain at each probe position (Rauch et al., 2010). **Figure 12Eii** shows classification of the GTO sample into three distinct structural phases, the pyrochlore (parent) structure, the recrystallized and amorphous regions, which can then be mapped to observe their spatial distributions. 4D-STEM has been used to quantify and map the degree of cation disorder in pyrochlore materials at the nanoscale by quantifying the intensity ratio of pyrochlore superlattice reflections to the main fluorite reflections for each pattern in the scanning NBED (4D-STEM) dataset can be generated (Janish et al., 2019). Again, a template matching approach is implemented to match each experimental pattern with a dictionary of simulated diffraction patterns (Allen et al., 2015) generated for calculated structures with varying degrees of disorder (Janish et al., 2019; Janish et al., 2020).

Analysis of Amorphous Materials

In a previous section, we saw the utility of the ePDF/eRDF for analyzing the structure of amorphous materials from diffraction patterns. This approach becomes much more powerful when coupled with a scanning beam in order to map out real-space distributions of SRO (Lu and Gauntt, 2013). Most implementations of so-called "STEM-PDF" (Mu et al., 2021) or "STEM-RDF" (Mu et al., 2016a) require some type of multivariate statistical analysis (MVSA) used to mine large 4D datasets to identify relevant co-varying variables in order to map statistically significant structural components (Lu and Gauntt, 2013; Mu et al., 2019). For example, to disentangle the local atomic bonding and packing information mixed in NBED data to characterize nanoscale heterogeneous amorphous materials such as nanoglass (Mu et al., 2021). Or to reveal interfacial layers from an amorphous $ZrO_2/Zr_{0.2}Fe_{0.8}$ mutilayer system with unique atomic arrangements that could not be seen with EDX or EELS (**Figures 14A,B**) (Mu et al., 2016a). As in other 4D-STEM approaches, the size the of the beam on the sample will limit the spatial resolution of structural information maps. A small beam (down to 2 nm), can be used, but speckled regions of the pattern that appear as the beam size is reduced (recall **Figure 11C**) must be removed with masking in analysis (McBride and Cockayne, 2003). Overall, the nm-scale spatial resolution of STEM-PDF is a dramatic improvement to the 10 μm spatial resolution of x-ray synchrotron PDF mapping (Billinge, 2019).

Like ePDF, fluctuation electron microscopy (FEM) is used to characterize the structure of amorphous materials in the (S)TEM. However, in contrast to ePDF which is ideal for measuring pair-correlations out to distances of the first few shells of neighboring atoms, it is better suited for measuring MRO which extends beyond the first few shells. It has been shown that the two-body correlations are not sufficient to distinguish between competing structural models of some amorphous materials (Treacy and Borisenko, 2012), therefore access to MRO is necessary for full structural analysis. It can be performed in both TEM and STEM mode, although STEM mode facilitates easier convergence-angle adjustment to investigate different sizes of atomic clusters (Ophus, 2019; Savitzky et al., 2021) as well as to determine correlation lengths of locally-ordered regions (Voyles and Muller, 2002; Voyles et al., 2011). When these clusters deviate from a fully random distribution, they lead to "speckles" in the amorphous halo as described previously, FEM provides structural information by quantification of the degree of variability as a function of scattering angle and probe size (Treacy et al., 2005; Hilke et al., 2019). Like ePDF and ABED analyses, FEM has primarily been applied to metallic glasses however, there are some examples of its use in oxide systems. For example, to study crystal nucleation in TiO_2-SiO_2 glasses upon heat treatment (Rezikyan and Moore, 2020), and to analyze structural disordering in ion-irradiated amorphous zircons (Zhao et al., 2010). For a review of FEM theory and development see (Voyles et al., 2011).

Figure 12Eiii demonstrates crystalline strain mapping from determination of Bragg disc position. Like crystalline materials, a change of the average atomic spacing in an amorphous material will result in a change in the radius of the diffuse halo. When this halo is fit to an elliptical function local strain can be measured (Ebner et al., 2016) and mapped (Savitzky et al., 2021; Gammer et al., 2018) if acquired with a scanning beam. The py4dSTEM implementation of this analysis (Savitzky et al., 2021) on the amorphized region of the GTO sample is shown in **Figures 14C,D**, where the $1/2\,(\varepsilon_{xx} + \varepsilon_{yy})$ map shows the local dilation, which is amplified in the vicinity of amorphous-polycrystal interfacial regions. This method has also been combined with *in situ* tensile testing to reveal the accumulation of strain under mechanical deformation in a bulk metallic glass (Gammer et al., 2018).

Other Applications

Many variations of 4D-STEM exist, for example, to map electromagnetic fields (Hachtel et al., 2018). Other applications aim to increase the sensitivity to light elements (Hachtel et al., 2018; Ahmed et al., 2020) and to retrieve lost electron-wave phase information to achieve super-resolutions (Jiang et al., 2018; Chen et al., 2021). A detailed account of the various 4D-STEM methods can be found in (Ophus, 2019).

4D-STEM Resources

4D-STEM approaches are becoming increasingly accessible with the development of more suitable hardware, larger data storage capacity, more powerful computation, and the continued development of software packages for simulation and analysis that facilitates easier analysis workflows. The analysis of such large, multidimensional datasets requires powerful computers and specialized software, many of which are home-grown in various labs around the world. Some available packages are

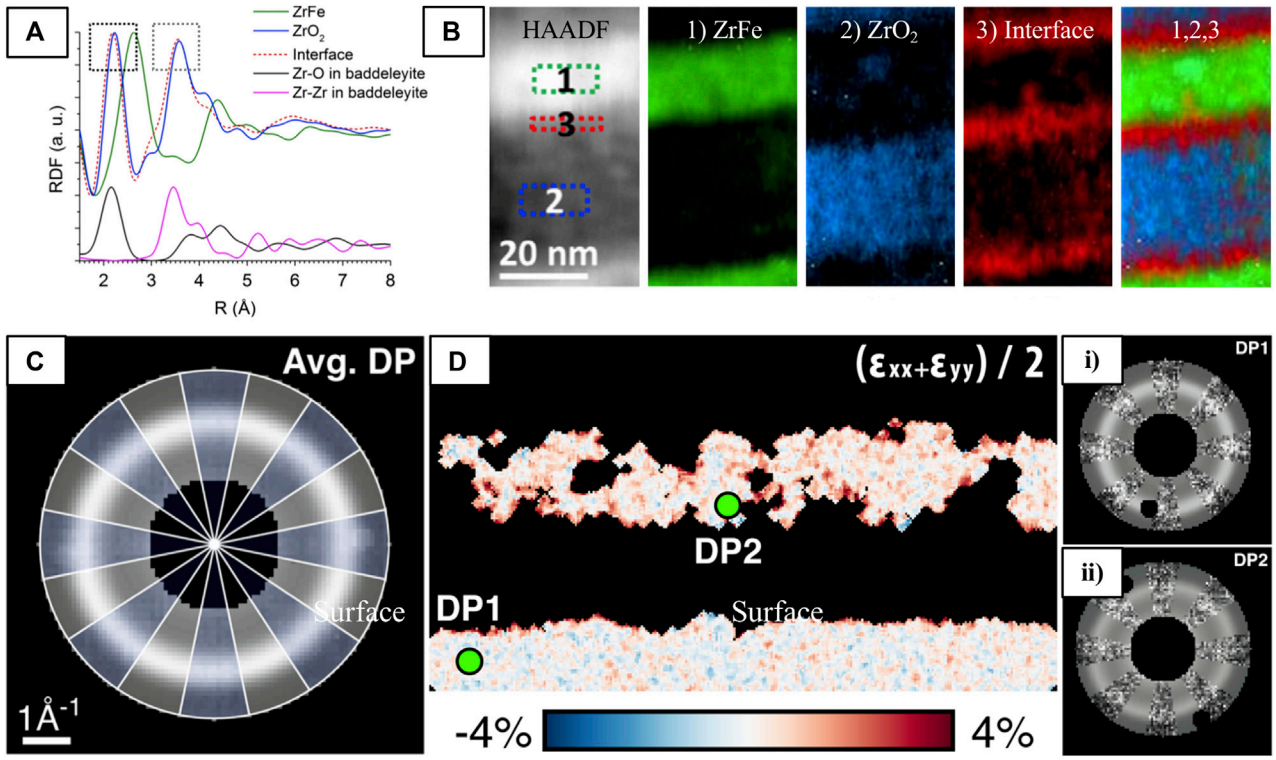

FIGURE 14 | Analysis of amorphous materials with 4D-STEM to map **(A,B)** the atomic arrangement of ZrO_2/ZrFe multilayers and **(C,D)** strain in the irradiated GTO sample. **(A)** RDFs taken from the amorphous ZrFe (green), ZrO_2 (blue), and interfacial layers (red). The interface RDF is similar to the ZrO_2 RDF with shifts in the first (0.04 Å, left) and second (0.06 Å, right) peaks indicated by black boxes. Comparison with the calculated Z-O (black) and Zr-Zr (pink) partial RDFs based on monoclinic crystalline baddeleyite ZrO_2 demonstrate that the SRO of ZrO_2 and the interfacial layer is similar to baddeleyite, and the shifts to reduced atomic distances can be explained by Fe replacing Zr in the ZrO_2 clusters at the interface. **(B)** From left to right, STEM-HAADF image of the ZrO_2/ZrFe layered structure, and maps corresponding to regions 1) ZrFe, 2) ZrO_2, 3) their interface and their composite image. **(C)** Elliptical fits (shown under grey wedges) of the averaged ED pattern (blue wedges) of the amorphous GTO from **Figure 12**. **(D)** A strain map of the amorphized regions and (i,ii) ED patterns from two distinct regions indicated in **(D)** where the fitted and raw data alternate azimuthally as in **(C)**. Reproduced from **(A,B)** (Mu et al., 2016b) and **(C,D)** (Savitzky et al., 2021).

Hyperspy, py4DSTEM, LiberTEM, Pycroscopy, pixSTEM, and the Cornell Spectrum Imager plugin for ImageJ. 4D-STEM simulation software (Pelz et al., 2021) is also critical component of analysis of 4D datasets.

SUMMARY AND OUTLOOK

In this review, we hoped to demonstrate the utility of (S)TEM for characterization of pyrochlore, fluorite, and other disorder-harboring complex oxide systems. Particularly to address the challenge of characterizing the various types of local transformations they adopt that can easily go undetected without the ability to assess the structure on a highly localized scale. In summary, the capabilities of (S)TEM to serve this end are as follows:

1) The positions of atomic columns can be extracted with picometer precision in both CTEM and STEM imaging with the assistance of image analysis software, which enables the analysis of small atomic displacements and provides the basis for at least one of the many approaches to strain mapping presented here.
2) The flexible illumination optics of (S)TEM systems offer unparalleled control over the volume (and position) of the electron probe on the specimen. This is especially useful for diffraction analysis, where the probe volume can be tuned across the sub-nanometer to tens of nanometers range to approach the length-scale of ordering/disordering in these systems (e.g., to probe short-, medium- or long-range order), revealing new signatures of local-ordering not accessible with larger probes.
3) The sensitivity of (S)TEM signals to different elemental atomic numbers can also be tuned, either through control of pre-specimen aberration-correction optics or by controlling the angular range of collected scatter post-specimen, which is key for probing the oxygen sublattice in the presence of heavy metals.
4) Small-area diffraction techniques combined with a scanning beam (4D-STEM) expand the utility of diffraction experiments by linking localized diffraction information with a real-space position on the specimen, enabling

structural features of interest to be mapped without the need for painstaking point-by-point manual acquisition.

Going forward, as 4D-STEM is increasingly used in tandem with *in situ* and *in operando* studies, the dimensionality of these already rich, multidimensional datasets will extend into the temporal domain, as well as along the axis of the applied stimuli. Additionally, these structure-function studies could be supplemented with chemical information from EDXS and EELS signals, in the latter case, yielding the BF disc to the EELS spectrometer through a physically modified, "hollow" detector (Song et al., 2018). As more data can be acquired at once to achieve *n*-dimensional datasets, software tools will advance in step to both increase user-friendliness and accessibility, as well as to provide more advanced and sophisticated analyses that can fully utilize and correlate each dimension of data. These capabilities will reveal the true value of the modern (S)TEM in providing fundamental insights into the dynamic and functional behaviors of complex systems.

AUTHOR CONTRIBUTIONS

The idea for this review was conceived by JW and WB. The review was written by JW with contributions to manuscript preparation by HG and HV. WB did critical revision.

FUNDING

JW and WB acknowledge funding under the award NSF CAREER DMR-2042638. HV and WB acknowledge partial funding by the National Science Foundation Materials Research Science and Engineering Center (MRSEC) program through the UC Irvine Center for Complex and Active Materials (NSF DMR-2011967). HG and WB acknowledge funding from the American Chemical Society's Petroleum Research Fund Doctoral New Investigator Grant. WB acknowledges funding from the UC Irvine School of Engineering new faculty set-up funding.

REFERENCES

Abelson, A., Qian, C., Salk, T., Luan, Z., Fu, K., Zheng, J.-G., et al. (2020). Collective Topo-Epitaxy in the Self-Assembly of a 3D Quantum Dot Superlattice. *Nat. Mater.* 19 (1), 49–55. doi:10.1038/s41563-019-0485-2

Ahmed, S., Bianchini, M., Pokle, A., Munde, M. S., Hartmann, P., Brezesinski, T., et al. (2020). Visualization of Light Elements Using 4D STEM: The Layered-to-Rock Salt Phase Transition in LiNiO 2 Cathode Material. *Adv. Energ. Mater.* 10 (25), 2001026. doi:10.1002/aenm.202001026

Aidhy, D. S., Sachan, R., Zarkadoula, E., Pakarinen, O., Chisholm, M. F., Zhang, Y., et al. (2015). Fast Ion Conductivity in Strained Defect-Fluorite Structure Created by Ion Tracks in Gd2Ti2O7. *Sci. Rep.* 5 (1), 16297. doi:10.1038/srep16297

Allen, L. J., D'Alfonso, A. J., and Findlay, S. D. (2015). Modelling the Inelastic Scattering of Fast Electrons. *Ultramicroscopy.* 151, 11–22. doi:10.1016/j.ultramic.2014.10.011

Allpress, J. G., and Rossell, H. J. (1979). Fluorite-Related Phases Ln3MO7, Ln = Rare Earth, Y, or Sc, M = Nb, Sb, or Ta. I. Crystal Chemistry. *J. Solid State. Chem.* 27 (1), 105–114. doi:10.1016/0022-4596(79)90149-x

Anantharaman, A. P., and Dasari, H. P. (2021). Potential of Pyrochlore Structure Materials in Solid Oxide Fuel Cell Applications. *Ceramics Int.* 47 (4), 4367–4388. doi:10.1016/j.ceramint.2020.10.012

Anthony, S. M., and Granick, S. (2009). Image Analysis With Rapid and Accurate Two-Dimensional Gaussian Fitting. *Langmuir.* 25 (14), 8152–8160. doi:10.1021/la900393v

Aughterson, R. D., Lumpkin, G. R., Smith, K. L., Reyes, M. d. l., Davis, J., Avdeev, M., et al. (2018). The Ion-Irradiation Tolerance of the Pyrochlore to Fluorite Ho(x)Yb(2-x)TiO5 and Er2TiO5 Compounds: A TEM Comparative Study Using Both *In-Situ* and Bulk *Ex-Situ* Irradiation Approaches. *J. Nucl. Mater.* 507, 316–326. doi:10.1016/j.jnucmat.2018.05.026

Barthel, J. (2018). Dr. Probe: A Software for High-Resolution STEM Image Simulation. *Ultramicroscopy.* 193, 1–11. doi:10.1016/j.ultramic.2018.06.003

Batson, P. E., Dellby, N., and Krivanek, O. L. (2002). Sub-ångstrom Resolution Using Aberration Corrected Electron Optics. *Nature.* 418 (6898), 617–620. doi:10.1038/nature00972

Bayle, P., Deutsch, T., Gilles, B., Lançon, F., Marty, A., and Thibault, J. (1994). Quantitative Analysis of the Deformation and Chemical Profiles of Strained Multilayers. *Ultramicroscopy.* 56 (1), 94–107. doi:10.1016/0304-3991(94)90149-x

Billinge, S. J. L., and Kanatzidis, M. G. (2004). Beyond Crystallography: the Study of Disorder, Nanocrystallinity and Crystallographically Challenged Materials with Pair Distribution Functions. *Chem. Commun.* 4 (7), 749–760. doi:10.1039/b309577k

Billinge, S. J. L. (2019). The Rise of the X-ray Atomic Pair Distribution Function Method: a Series of Fortunate Events. *Phil. Trans. R. Soc. A.* 377 (2147), 20180413. doi:10.1098/rsta.2018.0413

Bowman, W. J., Darbal, A., and Crozier, P. A. (2020). Linking Macroscopic and Nanoscopic Ionic Conductivity: A Semiempirical Framework for Characterizing Grain Boundary Conductivity in Polycrystalline Ceramics. *ACS Appl. Mater. Inter.* 12 (1), 507–517. doi:10.1021/acsami.9b15933

Bowman, W. J., Kelly, M. N., Rohrer, G. S., Hernandez, C. A., and Crozier, P. A. (2017). Enhanced Ionic Conductivity in Electroceramics by Nanoscale Enrichment of Grain Boundaries With High Solute Concentration. *Nanoscale.* 9 (44), 17293–17302. doi:10.1039/c7nr06941c

Bowman, W. J., Zhu, J., Sharma, R., and Crozier, P. A. (2015). Electrical Conductivity and Grain Boundary Composition of Gd-Doped and Gd/Pr Co-Doped Ceria. *Solid State Ionics.* 272, 9–17. doi:10.1016/j.ssi.2014.12.006

Buchholz, D. B., Ma, Q., Alducin, D., Ponce, A., Jose-Yacaman, M., Khanal, R., et al. (2014). The Structure and Properties of Amorphous Indium Oxide. *Chem. Mater.* 26 (18), 5401–5411. doi:10.1021/cm502689x

Bustillo, K. C., Zeltmann, S. E., Chen, M., Donohue, J., Ciston, J., Ophus, C., et al. (2021). 4D-STEM of Beam-Sensitive Materials. *Acc. Chem. Res.* 54 (11), 2543–2551. doi:10.1021/acs.accounts.1c00073

Chakoumakos, B. C. (1984). Systematics of the Pyrochlore Structure Type, Ideal A2B2X6Y. *J. Solid State. Chem.* 53 (1), 120–129. doi:10.1016/0022-4596(84)90234-2

Chaney, D., Castellano, A., Bosak, A., Bouchet, J., Bottin, F., Dorado, B., et al. (2021). Tuneable Correlated Disorder in Alloys. *Phys. Rev. Mater.* 5 (3), 035004. doi:10.1103/physrevmaterials.5.035004

Chen, Z., Jiang, Y., Shao, Y.-T., Holtz, M. E., Odstrčil, M., Guizar-Sicairos, M., et al. (2021). Electron Ptychography Achieves Atomic-Resolution Limits Set by Lattice Vibrations. *Science.* 372 (6544), 826–831. doi:10.1126/science.abg2533

Chroneos, A., Rushton, M. J. D., Jiang, C., and Tsoukalas, L. H. (2013). Nuclear Wasteform Materials: Atomistic Simulation Case Studies. *J. Nucl. Mater.* 441 (1), 29–39. doi:10.1016/j.jnucmat.2013.05.012

Cleave, A. (2006). *Atomic Scale Simulations for Waste Form Applications' Ph. D, Thesis*. London, UK: Department of Materials, Imperial College of Science, Technology and.

Cockayne, D. J. H. (2007). The Study of Nanovolumes of Amorphous Materials Using Electron Scattering. *Annu. Rev. Mater. Res.* 37 (1), 159–187. doi:10.1146/annurev.matsci.35.082803.103337

D'Alfonso, A. J., Freitag, B., Klenov, D., and Allen, L. J. (2010). Atomic-Resolution Chemical Mapping Using Energy-Dispersive X-ray Spectroscopy. *Phys. Rev. B.* 81 (10), 100101. doi:10.1103/PhysRevB.81.100101

De Backer, A., van den Bos, K. H. W., Van den Broek, W., Sijbers, J., Van Aert, S., and StatSTEM (2016). StatSTEM: An Efficient Approach for Accurate and

Precise Model-Based Quantification of Atomic Resolution Electron Microscopy Images. *Ultramicroscopy.* 171, 104–116. doi:10.1016/j.ultramic.2016.08.018

de los Reyes, M., Whittle, K. R., Zhang, Z., Ashbrook, S. E., Mitchell, M. R., Jang, L.-Y., et al. (2013). The Pyrochlore to Defect Fluorite Phase Transition in Y2Sn2−xZrxO7. *RSC Adv.* 3 (15), 5090–5099. doi:10.1039/c3ra22704a

Dunin-Borkowski, R. E., and Houben, L. (2016). "Spherical and Chromatic Aberration Correction for Atomic-Resolution Liquid Cell Electron Microscopy," in *Liquid Cell Electron Microscopy*. Editor F. M. Ross (Cambridge: Cambridge University Press), 434–455.

Ebner, C., Sarkar, R., Rajagopalan, J., and Rentenberger, C. (2016). Local, Atomic-Level Elastic Strain Measurements of Metallic Glass Thin Films by Electron Diffraction. *Ultramicroscopy.* 165, 51–58. doi:10.1016/j.ultramic.2016.04.004

Edington, J. W. (1975). "Electron Diffraction in the Electron Microscope," in *Electron Diffraction in the Electron Microscope*. Editor J. W. Edington (London: Macmillan Education UK), 1–77. doi:10.1007/978-1-349-02595-4_1

Egami, T., and Billinge, S. J. *Underneath the Bragg Peaks: Structural Analysis of Complex Materials*. Oxford, UK: Newnes2012.

Egerton, R. F. (2019). Radiation Damage to Organic and Inorganic Specimens in the TEM. *Micron* 119, 72–87. doi:10.1016/j.micron.2019.01.005

Eggeman, A. S., and Midgley, P. A. (2012). "Chapter 1 - Precession Electron Diffraction," in *Advances in Imaging and Electron Physics*. Editor P. W. Hawkes Elsevier, 1–63.

Ewing, R. C., Weber, W. J., and Lian, J. (2004). Nuclear Waste Disposal-Pyrochlore (A2B2O7): Nuclear Waste Form for the Immobilization of Plutonium and "Minor" Actinides. *J. Appl. Phys.* 95 (11), 5949–5971. doi:10.1063/1.1707213

Findlay, S. D., Shibata, N., Sawada, H., Okunishi, E., Kondo, Y., and Ikuhara, Y. (2010a). Dynamics of Annular Bright Field Imaging in Scanning Transmission Electron Microscopy. *Ultramicroscopy.* 110 (7), 903–923. doi:10.1016/j.ultramic.2010.04.004

Findlay, S. D., Saito, T., Shibata, N., Sato, Y., Matsuda, J., Asano, K., et al. (2010b). Direct Imaging of Hydrogen Within a Crystalline Environment. *Appl. Phys. Express.* 3 (11), 116603. doi:10.1143/apex.3.116603

Fultz, B., and Howe, J. M. (2008). "High-Resolution TEM Imaging," *Transmission Electron Microscopy and Diffractometry of Materials* (Berlin, Heidelberg: Springer Berlin Heidelberg), 517–582.

Galindo, P. L., Kret, S., Sanchez, A. M., Laval, J.-Y., Yáñez, A., Pizarro, J., et al. (2007). The Peak Pairs Algorithm for Strain Mapping From HRTEM Images. *Ultramicroscopy.* 107 (12), 1186–1193. doi:10.1016/j.ultramic.2007.01.019

Gallagher, J. C., Esser, B. D., Morrow, R., Dunsiger, S. R., Williams, R. E. A., Woodward, P. M., et al. (2016). Epitaxial Growth of Iridate Pyrochlore Nd2Ir2O7 Films. *Sci. Rep.* 6 (1), 22282. doi:10.1038/srep22282

Gallardo-López, A., Martínez-Fernández, J., Domínguez-Rodríguez, A., and Ernst, F. (2001). Origin of Diffuse Electron Scattering in Yttria-Cubicstabilized Zirconia Single Crystals With 24–32 Mol% Yttria. *Philosophical Mag. A.* 81 (7), 1675–1689. doi:10.1080/01418610010019053

Gammer, C., Mangler, C., Rentenberger, C., and Karnthaler, H. P. (2010). Quantitative Local Profile Analysis of Nanomaterials by Electron Diffraction. *Scripta Materialia.* 63 (3), 312–315. doi:10.1016/j.scriptamat.2010.04.019

Gammer, C., Ophus, C., Pekin, T. C., Eckert, J., and Minor, A. M. (2018). Local Nanoscale Strain Mapping of a Metallic Glass During *In Situ* Testing. *Appl. Phys. Lett.* 112 (17), 171905. doi:10.1063/1.5025686

García-Martín, S., Alario-Franco, M. A., Fagg, D. P., and Irvine, J. T. S. (2005). Evidence of Three Types of Short Range Ordered Fluorite Structure in the (1 - X) Y0.15Zr0.85O1.93-x Y0.75Nb0.25O1.75(0 ≤x≤ 1) System. *J. Mater. Chem.* 15 (19), 1903–1907. doi:10.1039/b418557a

Garg, N., Pandey, K. K., Murli, C., Shanavas, K. V., Mandal, B. P., Tyagi, A. K., et al. (2008). Decomposition of Lanthanum Hafnate at High Pressures. *Phys. Rev. B.* 77 (21), 214105. doi:10.1103/physrevb.77.214105

Gázquez, J., Sánchez-Santolino, G., Biškup, N., Roldán, M. A., Cabero, M., Pennycook, S. J., et al. (2017). Applications of STEM-EELS to Complex Oxides. *Mater. Sci. Semiconductor Process.* 65, 49–63. doi:10.1016/j.mssp.2016.06.005

Gemmi, M., Mugnaioli, E., Gorelik, T. E., Kolb, U., Palatinus, L., Boullay, P., et al. (2019). 3D Electron Diffraction: The Nanocrystallography Revolution. *ACS Cent. Sci.* 5 (8), 1315–1329. doi:10.1021/acscentsci.9b00394

Glerup, M., Nielsen, O. F., and Poulsen, F. W. (2001). The Structural Transformation From the Pyrochlore Structure, A2B2O7, to the Fluorite Structure, AO2, Studied by Raman Spectroscopy and Defect Chemistry Modeling. *J. Solid State. Chem.* 160 (1), 25–32. doi:10.1006/jssc.2000.9142

Gorelik, T. E., Neder, R., Terban, M. W., Lee, Z., Mu, X., Jung, C., et al. (2019). Towards Quantitative Treatment of Electron Pair Distribution Function. *Acta Crystallogr. Sect B.* 75 (4), 532–549. doi:10.1107/s205252061900670x

Gupta, A. K., Arora, G., Aidhy, D. S., and Sachan, R. (2020). ∑3 Twin Boundaries in Gd2Ti2O7 Pyrochlore: Pathways for Oxygen Migration. *ACS Appl. Mater. Inter.* 12 (40), 45558–45563. doi:10.1021/acsami.0c12250

Gussev, I. M., O'Quinn, E. C., Baldinozzi, G., Neuefeind, J., Ewing, R. C., Zhang, F., et al. (2020). Local Order of Orthorhombic Weberite-Type Y3TaO7 as Determined by Neutron Total Scattering and Density Functional Theory Calculations☆. *Acta Materialia.* 196, 704–709. doi:10.1016/j.actamat.2020.07.005

Gutiérrez–Llorente, A., Joress, H., Woll, A., Holtz, M. E., Ward, M. J., Sullivan, M. C., et al. (2015). Epitaxial Crystals of Bi2Pt2O7 Pyrochlore Through the Transformation of δ–Bi2O3 Fluorite. *APL Mater.* 3 (3), 036105. doi:10.1063/1.4908103

Hachtel, J. A., Idrobo, J. C., and Chi, M. (2018). Sub-Ångstrom Electric Field Measurements on a Universal Detector in a Scanning Transmission Electron Microscope. *Adv. Struct. Chem. Imag.* 4 (1), 10. doi:10.1186/s40679-018-0059-4

Haider, M., Rose, H., Uhlemann, S., Schwan, E., Kabius, B., and Urban, K. (1998). A Spherical-Aberration-Corrected 200kV Transmission Electron Microscope. *Ultramicroscopy.* 75 (1), 53–60. doi:10.1016/s0304-3991(98)00048-5

Hammel, M., and Rose, H. (1995). Optimum Rotationally Symmetric Detector Configurations for Phase-Contrast Imaging in Scanning Transmission Electron Microscopy. *Ultramicroscopy.* 58 (3), 403–415. doi:10.1016/0304-3991(95)00007-n

Hart, J. L., Lang, A. C., Leff, A. C., Longo, P., Trevor, C., Twesten, R. D., et al. (2017). Direct Detection Electron Energy-Loss Spectroscopy: A Method to Push the Limits of Resolution and Sensitivity. *Sci. Rep.* 7 (1), 8243. doi:10.1038/s41598-017-07709-4

Hilke, S., Kirschbaum, J., Hieronymus-Schmidt, V., Radek, M., Bracht, H., Wilde, G., et al. (2019). Analysis of Medium-Range Order Based on Simulated Segmented Ring Detector STEM-Images: Amorphous Si. *Ultramicroscopy.* 200, 169–179. doi:10.1016/j.ultramic.2019.02.023

Hinks, J. A. (2009). A Review of Transmission Electron Microscopes With *In Situ* Ion Irradiation. *Nucl. Instr. Methods Phys. Res. Section B: Beam Interactions Mater. Atoms.* 267 (23), 3652–3662. doi:10.1016/j.nimb.2009.09.014

Hirata, A., and Chen, M. (2014). Angstrom-beam Electron Diffraction of Amorphous Materials. *J. Non-Crystalline Sol.* 383, 52–58. doi:10.1016/j.jnoncrysol.2013.03.010

Hirata, A., Guan, P., Fujita, T., Hirotsu, Y., Inoue, A., Yavari, A. R., et al. (2011). Direct Observation of Local Atomic Order in a Metallic Glass. *Nat. Mater.* 10 (1), 28–33. doi:10.1038/nmat2897

Hirata, A., Kang, L. J., Fujita, T., Klumov, B., Matsue, K., Kotani, M., et al. (2013). Geometric Frustration of Icosahedron in Metallic Glasses. *Science.* 341 (6144), 376–379. doi:10.1126/science.1232450

Hirata, A., Kohara, S., Asada, T., Arao, M., Yogi, C., Imai, H., et al. (2016). Atomic-Scale Disproportionation in Amorphous Silicon Monoxide. *Nat. Commun.* 7 (1), 11591. doi:10.1038/ncomms11591

Hirata, A. (2021). Local Structure Analysis of Amorphous Materials by Angstrom-Beam Electron Diffraction. *Microscopy.* 70 (2), 171–177. doi:10.1093/jmicro/dfaa075

Hirotsu, Y., Ishimaru, M., Ohkubo, T., Hanada, T., and Sugiyama, M. (2001). Application of Nano-Diffraction to Local Atomic Distribution Function Analysis of Amorphous Materials. *J. Electron Microsc.* 50 (6), 435–442. doi:10.1093/jmicro/50.6.435

Houben, L. (2009). *Imtools: General Purpose Multi Platform Image Processing Tools.*

Hwang, J., and Voyles, P. M. (2011). Variable Resolution Fluctuation Electron Microscopy on Cu-Zr Metallic Glass Using a Wide Range of Coherent STEM Probe Size. *Microsc. Microanal.* 17 (1), 67–74. doi:10.1017/s1431927610094109

Hytch, M. J. (1997). Analysis of Variations in Structure From High Resolution Electron Microscope Images by Combining Real Space and Fourier Space Information. *Microsc. Microanal. Microstruct.* 8 (1), 41–57. doi:10.1051/mmm:1997105

Hÿtch, M. J., and Plamann, T. (2001). Imaging Conditions for Reliable Measurement of Displacement and Strain in High-Resolution Electron Microscopy. *Ultramicroscopy*. 87 (4), 199–212. doi:10.1016/s0304-3991(00)00099-1

Hÿtch, M. J., Snoeck, E., and Kilaas, R. (1998). Quantitative Measurement of Displacement and Strain fields From HREM Micrographs. *Ultramicroscopy*. 74 (3), 131–146. doi:10.1016/s0304-3991(98)00035-7

Ishikawa, R., Jimbo, Y., Terao, M., Nishikawa, M., Ueno, Y., Morishita, S., et al. (2020). High Spatiotemporal-Resolution Imaging in the Scanning Transmission Electron Microscope. *Microscopy*. 69 (4), 240–247. doi:10.1093/jmicro/dfaa017

Ishimaru, M., Bae, I. T., Hirotsu, Y., Matsumura, S., and Sickafus, K. E. (2002). Structural Relaxation of Amorphous Silicon Carbide. *Phys. Rev. Lett.* 89 (5), 055502. doi:10.1103/PhysRevLett.89.055502

Ishimaru, M. (2006). Electron-Beam Radial Distribution Analysis of Irradiation-Induced Amorphous SiC. *Nucl. Instr. Methods Phys. Res. Section B: Beam Interactions Mater. Atoms.* 250 (1), 309–314. doi:10.1016/j.nimb.2006.04.129

Ishimaru, M., Hirata, A., Naito, M., Bae, I.-T., Zhang, Y., and Weber, W. J. (2008). Direct Observations of Thermally Induced Structural Changes in Amorphous Silicon Carbide. *J. Appl. Phys.* 104 (3), 033503. doi:10.1063/1.2960342

Janish, M. T., Schneider, M. M., Ophus, C., Ciston, J., Valdez, J. A., McClellan, K. J., et al. (2019). Mapping Cation Disorder in Irradiated Gd2Ti2O7 Pyrochlore by 4D-STEM. *Microsc. Microanal.* 25 (S2), 1560–1561. doi:10.1017/s1431927619008535

Janish, M. T., Schneider, M. M., Valdez, J. A., McClellan, K. J., Byler, D. D., Wang, Y., et al. (2020). *In-situ* Re-Crystallization of Heavily-Irradiated Gd2Ti2O7. *Acta Materialia*. 194, 403–411. doi:10.1016/j.actamat.2020.04.026

Jia, C.-L., Jin, L., Chen, Y.-H., Urban, K. W., and Wang, H. (2018). Atomic-Scale Evidence for Displacive Disorder in Bismuth Zinc Niobate Pyrochlore. *Ultramicroscopy*. 192, 57–68. doi:10.1016/j.ultramic.2018.05.009

Jia, C. L., Lentzen, M., and Urban, K. (2004). High-Resolution Transmission Electron Microscopy Using Negative Spherical Aberration. *Microsc. Microanal.* 10 (2), 174–184. doi:10.1017/S1431927604040425

Jia, C. L., Lentzen, M., and Urban, K. (2003). Atomic-Resolution Imaging of Oxygen in Perovskite Ceramics. *Science*. 299 (5608), 870–873. doi:10.1126/science.1079121

Jia, C. L., Thust, A., and Urban, K. (2005). Atomic-Scale Analysis of the Oxygen Configuration at aSrTiO3Dislocation Core. *Phys. Rev. Lett.* 95 (22), 225506. doi:10.1103/physrevlett.95.225506

Jiang, Y., Chen, Z., Han, Y., Deb, P., Gao, H., Xie, S., et al. (2018). Electron Ptychography of 2D Materials to Deep Sub-ångström Resolution. *Nature*. 559 (7714), 343–349. doi:10.1038/s41586-018-0298-5

Jitta, R. R., Gundeboina, R., Veldurthi, N. K., Guje, R., and Muga, V. (2015). Defect Pyrochlore Oxides: as Photocatalyst Materials for Environmental and Energy Applications - a Review. *J. Chem. Technol. Biotechnol.* 90 (11), 1937–1948. doi:10.1002/jctb.4745

Jones, L., and Nellist, P. D. (2013). Identifying and Correcting Scan Noise and Drift in the Scanning Transmission Electron Microscope. *Microsc. Microanal.* 19 (4), 1050–1060. doi:10.1017/s1431927613001402

Jones, L., Yang, H., Pennycook, T. J., Marshall, M. S. J., Van Aert, S., Browning, N. D., et al. (2015). Smart Align-A New Tool for Robust Non-Rigid Registration of Scanning Microscope Data. *Adv. Struct. Chem. Imag.* 1 (1), 8. doi:10.1186/s40679-015-0008-4

Kaspar, T. C., Gigax, J. G., Shao, L., Bowden, M. E., Varga, T., Shutthanandan, V., et al. (2017). Damage Evolution of Ion Irradiated Defected-Fluorite La2Zr2O7 Epitaxial Thin Films. *Acta Materialia*. 130, 111–120. doi:10.1016/j.actamat.2017.01.012

Keen, D. A., and Goodwin, A. L. (2015). The Crystallography of Correlated Disorder. *Nature*. 521 (7552), 303–309. doi:10.1038/nature14453

Kim, M., Park, J., Kang, M., Kim, J. Y., and Lee, S. W. (2020). Toward Efficient Electrocatalytic Oxygen Evolution: Emerging Opportunities With Metallic Pyrochlore Oxides for Electrocatalysts and Conductive Supports. *ACS Cent. Sci.* 6 (6), 880–891. doi:10.1021/acscentsci.0c00479

Kirkland, E. J. (1998). *Advanced Computing in Electron Microscopy*. New York, US: Springer.

Koch, C. (2002). *Determination of Core Structure Periodicity and point Defect Density along Dislocations*. Ann Harbor: ProQuest Dissertations Publishing.

Kolb, U., Gorelik, T., Kübel, C., Otten, M. T., and Hubert, D. (2007). Towards Automated Diffraction Tomography: Part I-Ddata Acquisition. *Ultramicroscopy*. 107 (6), 507–513. doi:10.1016/j.ultramic.2006.10.007

Kotaka, Y. (2012). Direct Visualization Method of the Atomic Structure of Light and Heavy Atoms With Double-Detector Cs-Corrected Scanning Transmission Electron Microscopy. *Appl. Phys. Lett.* 101 (13), 133107. doi:10.1063/1.4756783

Kreller, C. R., and Uberuaga, B. P. (2021). The Role of Cation Ordering and Disordering on Mass Transport in Complex Oxides. *Curr. Opin. Solid State. Mater. Sci.* 25 (2), 100899. doi:10.1016/j.cossms.2021.100899

Lang, M., Devanathan, R., Toulemonde, M., and Trautmann, C. (2015). Advances in Understanding of Swift Heavy-Ion Tracks in Complex Ceramics. *Curr. Opin. Solid State. Mater. Sci.* 19 (1), 39–48. doi:10.1016/j.cossms.2014.10.002

Lang, M., Zhang, F., Zhang, J., Wang, J., Lian, J., Weber, W. J., et al. (2010). Review of A2B2O7 Pyrochlore Response to Irradiation and Pressure. *Nucl. Instr. Methods Phys. Res. Section B: Beam Interactions Mater. Atoms.* 268 (19), 2951–2959. doi:10.1016/j.nimb.2010.05.016

Lau, G. C., McQueen, T. M., Huang, Q., Zandbergen, H. W., and Cava, R. J. (2008). Long- and Short-Range Order in Stuffed Titanate Pyrochlores. *J. Solid State. Chem.* 181 (1), 45–50. doi:10.1016/j.jssc.2007.10.025

Lawrence, E. L., Levin, B. D. A., Boland, T., Chang, S. L. Y., and Crozier, P. A. (2021). Atomic Scale Characterization of Fluxional Cation Behavior on Nanoparticle Surfaces: Probing Oxygen Vacancy Creation/Annihilation at Surface Sites. *ACS Nano*. 15 (2), 2624–2634. doi:10.1021/acsnano.0c07584

Lee, D., Gao, X., Sun, L., Jee, Y., Poplawsky, J., Farmer, T. O., et al. (2020). Colossal Oxygen Vacancy Formation at a Fluorite-Bixbyite Interface. *Nat. Commun.* 11 (1), 1371. doi:10.1038/s41467-020-15153-8

Lehmann, E. H., Peetermans, S., Trtik, P., Betz, B., and Grünzweig, C. (2017). New Neutron Imaging Techniques to Close the gap to Scattering Applications. *J. Phys. Conf. Ser.* 746, 012070. doi:10.1088/1742-6596/746/1/012070

Levin, B. D. A. (2021). Direct Detectors and Their Applications in Electron Microscopy for Materials Science. *J. Phys. Mater.* 4 (4), 042005. doi:10.1088/2515-7639/ac0ff9

Levin, B. D. A., Lawrence, E. L., and Crozier, P. A. (2020a). Tracking the Picoscale Spatial Motion of Atomic Columns During Dynamic Structural Change. *Ultramicroscopy*. 213, 112978. doi:10.1016/j.ultramic.2020.112978

Levin, B. D., Zhang, C., Bammes, B., Voyles, P. M., and Bilhorn, R. B. (2020b). *4D STEM with a Direct Electron Detector*. Wiley Analytical Science.

Levin, I., Amos, T. G., Nino, J. C., Vanderah, T. A., Randall, C. A., and Lanagan, M. T. (2002). Structural Study of an Unusual Cubic Pyrochlore Bi1.5Zn0.92Nb1.5O6.92. *J. Solid State. Chem.* 168 (1), 69–75. doi:10.1006/jssc.2002.9681

Li, Y., Oh, T., Son, J., Song, J., Kim, M. K., Song, D., et al. (2021). Correlated Magnetic Weyl Semimetal State in Strained Pr2Ir2O7. *Adv. Mater.* n/a, 2008528. doi:10.1002/adma.202008528

Lian, J., Wang, L., Chen, J., Sun, K., Ewing, R. C., Matt Farmer, J., et al. (2003). The Order-Disorder Transition in Ion-Irradiated Pyrochlore. *Acta Materialia*. 51 (5), 1493–1502. doi:10.1016/s1359-6454(02)00544-x

Lian, J., Wang, L. M., Ewing, R. C., Yudintsev, S. V., and Stefanovsky, S. V. (2005). Ion-Beam-Induced Amorphization and Order-Disorder Transition in the Murataite Structure. *J. Appl. Phys.* 97 (11), 113536. doi:10.1063/1.1926394

Lian, J., Zu, X. T., Kutty, K. V. G., Chen, J., Wang, L. M., and Ewing, R. C. (2002). Ion-Irradiation-Induced Amorphization of ${\\mathrm{La}}_{2}{\\mathrm{Zr}}_{2}{\\Mathrm{O}}_{7}$ Pyrochlore. *Phys. Rev. B.* 66 (5), 054108. doi:10.1103/physrevb.66.054108

Lim, K. R., Kim, C. E., Yun, Y. S., Kim, W. T., Soon, A., and Kim, D. H. (2015). Remarkably Stable Amorphous Metal Oxide Grown on Zr-Cu-Be Metallic Glass. *Sci. Rep.* 5 (1), 18196. doi:10.1038/srep18196

Lin, R., Zhang, R., Wang, C., Yang, X.-Q., and Xin, H. L. (2021). TEMImageNet Training Library and AtomSegNet Deep-Learning Models for High-Precision Atom Segmentation, Localization, Denoising, and Deblurring of Atomic-Resolution Images. *Sci. Rep.* 11 (1), 5386. doi:10.1038/s41598-021-84499-w

Liu, Y., Withers, R. L., Welberry, T. R., Wang, H., and Du, H. (2006). Crystal Chemistry on a Lattice: The Case of BZN and BZN-Related Pyrochlores. *J. Solid State. Chem.* 179 (7), 2141–2149. doi:10.1016/j.jssc.2006.04.017

Lu, P., and Gauntt, B. D. (2013). Structural Mapping of Disordered Materials by Nanobeam Diffraction Imaging and Multivariate Statistical Analysis. *Microsc. Microanal.* 19 (2), 300–309. doi:10.1017/s1431927613000135

MacLaren, I., Macgregor, T. A., Allen, C. S., and Kirkland, A. I. (2020). Detectors-The Ongoing Revolution in Scanning Transmission Electron Microscopy and Why This Important to Material Characterization. *APL Mater.* 8 (11), 110901. doi:10.1063/5.0026992

MacLaren, I., and Ramasse, Q. M. (2014). Aberration-Corrected Scanning Transmission Electron Microscopy for Atomic-Resolution Studies of Functional Oxides. *Int. Mater. Rev.* 59 (3), 115–131. doi:10.1179/1743280413y.0000000026

Maram, P. S., Ushakov, S. V., Weber, R. J. K., Benmore, C. J., and Navrotsky, A. (2018). Probing Disorder in Pyrochlore Oxides Using *In Situ* Synchrotron Diffraction From Levitated Solids-A Thermodynamic Perspective. *Sci. Rep.* 8 (1), 10658. doi:10.1038/s41598-018-28877-x

McBride, W., and Cockayne, D. (2003). The Structure of Nanovolumes of Amorphous Materials. *J. non-crystalline Sol.* 318 (3), 233–238. doi:10.1016/s0022-3093(02)01908-7

Midgley, P. A., and Eggeman, A. S. (2015). Precession Electron Diffraction - a Topical Review. *IUCrJ.* 2 (Pt 1), 126–136. doi:10.1107/S2052252514022283

Minervini, L., Grimes, R. W., and Sickafus, K. E. (2000). Disorder in Pyrochlore Oxides. *J. Am. Ceram. Soc.* 83 (8), 1873–1878. doi:10.1111/j.1151-2916.2000.tb01484.x

Miracle, D. B. (2004). A Structural Model for Metallic Glasses. *Nat. Mater.* 3 (10), 697–702. doi:10.1038/nmat1219

Miracle, D. B. (2006). The Efficient Cluster Packing Model - an Atomic Structural Model for Metallic Glasses. *Acta Materialia.* 54 (16), 4317–4336. doi:10.1016/j.actamat.2006.06.002

Mitchell, D. R. G., Petersen, T. C., and RDFTools (2012). RDFTools: A Software Tool for Quantifying Short-Range Ordering in Amorphous Materials. *Microsc. Res. Tech.* 75 (2), 153–163. doi:10.1002/jemt.21038

Moeck, P., and Rouvimov, S. (2010). Precession Electron Diffraction and its Advantages for Structural Fingerprinting in the Transmission Electron Microscope. *Z. für Kristallographie.* 225 (2-3), 110–124. doi:10.1524/zkri.2010.1162

Mostaed, A., Balakrishnan, G., Lees, M. R., and Beanland, R. (2018). Electron-Irradiation Induced Defects in Yb2Ti2.05O7. *Acta Materialia.* 143, 291–297. doi:10.1016/j.actamat.2017.10.028

Mu, X., Chen, L., Mikut, R., Hahn, H., and Kübel, C. (2021). Unveiling Local Atomic Bonding and Packing of Amorphous Nanophases via Independent Component Analysis Facilitated Pair Distribution Function. *Acta Materialia.* 212, 116932. doi:10.1016/j.actamat.2021.116932

Mu, X., Mazilkin, A., Sprau, C., Colsmann, A., and Kübel, C. (2019). Mapping Structure and Morphology of Amorphous Organic Thin Films by 4D-STEM Pair Distribution Function Analysis. *Microscopy.* 68 (4), 301–309. doi:10.1093/jmicro/dfz015

Mu, X., Wang, D., Feng, T., and Kübel, C. (2016a). Radial Distribution Function Imaging by STEM Diffraction: Phase Mapping and Analysis of Heterogeneous Nanostructured Glasses. *Ultramicroscopy.* 168, 1–6. doi:10.1016/j.ultramic.2016.05.009

Mu, X., Wang, D., Feng, T., and Kübel, C. (2016b). Radial Distribution Function Imaging by STEM Diffraction: a Method Development in Resolving the Mysteries of Amorphous Materials. *Eur. Microsc. Congress Proc.* 168, 617–618. doi:10.1002/9783527808465.emc2016.5718

Mullens, B. G., Zhang, Z., Avdeev, M., Brand, H. E. A., Cowie, B. C. C., Saura Múzquiz, M., et al. (2021). Effect of Long- and Short-Range Disorder on the Oxygen Ionic Conductivity of Tm2(Ti2-xTmx)O7-X/2 "Stuffed" Pyrochlores. *Inorg. Chem.* 60 (7), 4517–4530. doi:10.1021/acs.inorgchem.0c03363

Neagu, A., and Tai, C.-W. (2017). Local Disorder in Na0.5Bi0.5TiO3-Piezoceramic Determined by 3D Electron Diffuse Scattering. *Sci. Rep.* 7 (1), 12519. doi:10.1038/s41598-017-12801-w

Neder, R., and Proffen, T. (2009). *Diffuse Scattering and Defect Structure Simulations: A Cook Book Using the Program DISCUS*. London, United Kingdom: Oxford University Press.

Nellist, P. D. (2007). "Scanning Transmission Electron Microscopy," in *Science of Microscopy*. Editors P. W. Hawkes and J. C. H. Spence (New York, NY: Springer New York), 65–132.

Nord, M., Vullum, P. E., MacLaren, I., Tybell, T., and Holmestad, R. (2017). Atomap: a New Software Tool for the Automated Analysis of Atomic Resolution Images Using Two-Dimensional Gaussian Fitting. *Adv. Struct. Chem. Imag.* 3 (1), 9. doi:10.1186/s40679-017-0042-5

Nord, M., Webster, R. W. H., Paton, K. A., McVitie, S., McGrouther, D., MacLaren, I., et al. (2020). Fast Pixelated Detectors in Scanning Transmission Electron Microscopy. Part I: Data Acquisition, Live Processing, and Storage. *Microsc. Microanal.* 26 (4), 653–666. doi:10.1017/s1431927620001713

Nylese, T., and Rafaelsen, J. (2017). Improvements in SDD Efficiency - From X-ray Counts to Data. *Micros. Today.* 25 (2), 46–53. doi:10.1017/s1551929517000190

O'Sullivan, M., Hadermann, J., Dyer, M. S., Turner, S., Alaria, J., Manning, T. D., et al. (2016). Interface Control by Chemical and Dimensional Matching in an Oxide Heterostructure. *Nat. Chem.* 8 (4), 347–353. doi:10.1038/nchem.2441

Ophus, C. (2017). A Fast Image Simulation Algorithm for Scanning Transmission Electron Microscopy. *Adv. Struct. Chem. Imag.* 3 (1), 13. doi:10.1186/s40679-017-0046-1

Ophus, C. (2019). Four-Dimensional Scanning Transmission Electron Microscopy (4D-STEM): From Scanning Nanodiffraction to Ptychography and Beyond. *Microsc. Microanal.* 25 (3), 563–582. doi:10.1017/s1431927619000497

O'Quinn, E. C., Shamblin, J., Perlov, B., Ewing, R. C., Neuefeind, J., Feygenson, M., et al. (2017). Inversion in Mg1–xNixAl2O4 Spinel: New Insight Into Local Structure. *J. Am. Chem. Soc.* 139 (30), 10395–10402. doi:10.1021/jacs.7b04370

O'Quinn, E. C., Sickafus, K. E., Ewing, R. C., Baldinozzi, G., Neuefeind, J. C., Tucker, M. G., et al. (2020). Predicting Short-Range Order and Correlated Phenomena in Disordered Crystalline Materials. *Sci. Adv.* 6 (35), eabc2758. doi:10.1126/sciadv.abc2758

Orlova, A. I., and Ojovan, M. I. (2019). Ceramic Mineral Waste-Forms for Nuclear Waste Immobilization. *Materials (Basel).* 12 (16), 2638. doi:10.3390/ma12162638

Padgett, E., Holtz, M. E., Cueva, P., Shao, Y.-T., Langenberg, E., Schlom, D. G., et al. (2020). The Exit-Wave Power-Cepstrum Transform for Scanning Nanobeam Electron Diffraction: Robust Strain Mapping at Subnanometer Resolution and Subpicometer Precision. *Ultramicroscopy.* 214, 112994. doi:10.1016/j.ultramic.2020.112994

Paterson, G. W., Webster, R. W. H., Ross, A., Paton, K. A., Macgregor, T. A., McGrouther, D., et al. (2020). Fast Pixelated Detectors in Scanning Transmission Electron Microscopy. Part II: Post-Acquisition Data Processing, Visualization, and Structural Characterization. *Microsc. Microanal.* 26 (5), 944–963. doi:10.1017/s1431927620024307

Pelz, P. M., Rakowski, A., DaCosta, L. R., Savitzky, B. H., Scott, M. C., and Ophus, C. (2021). A Fast Algorithm for Scanning Transmission Electron Microscopy (STEM) Imaging and 4D-STEM Diffraction Simulations *Microsc. Microanal.* 27 (4), 835–848. doi:10.1017/S1431927621012083

Perriot, R., Dholabhai, P. P., and Uberuaga, B. P. (2017). Disorder-Induced Transition From Grain Boundary to Bulk Dominated Ionic Diffusion in Pyrochlores. *Nanoscale.* 9 (20), 6826–6836. doi:10.1039/c7nr01373f

Rangel DaCosta, L., Brown, H. G., Pelz, P. M., Rakowski, A., Barber, N., O'Donovan, P., et al. (2021). Prismatic 2.0 - Simulation Software for Scanning and High Resolution Transmission Electron Microscopy (STEM and HRTEM). *Micron.* 151, 103141. doi:10.1016/j.micron.2021.103141

Rauch, E. F., Portillo, J., Nicolopoulos, S., Bultreys, D., Rouvimov, S., and Moeck, P. (2010). Automated Nanocrystal Orientation and Phase Mapping in the Transmission Electron Microscope on the Basis of Precession Electron Diffraction. *Z. für Kristallographie.* 225 (2-3), 103–109. doi:10.1524/zkri.2010.1205

Reid, D. P., Stennett, M. C., and Hyatt, N. C. (2012). The Fluorite Related Modulated Structures of the Gd2(Zr2−xCex)O7 Solid Solution: An Analogue for Pu Disposition. *J. Solid State. Chem.* 191, 2–9. doi:10.1016/j.jssc.2011.12.039

Rezikyan, A., and Moore, G. G. (2020). Fluctuation Electron Microscopy Study of crystal Nucleation in TiO2-SiO2 Glass with Heat Treatment. *J. Phys. Condens. Matter.* 32 (48), 485402. doi:10.1088/1361-648x/abae19

Rittman, D. R., Turner, K. M., Park, S., Fuentes, A. F., Yan, J., Ewing, R. C., et al. (2017a). High-Pressure Behavior of A2B2O7 Pyrochlore (A=Eu, Dy; B=Ti, Zr). *J. Appl. Phys.* 121 (4), 045902. doi:10.1063/1.4974871

Rittman, D. R., Turner, K. M., Park, S., Fuentes, A. F., Park, C., Ewing, R. C., et al. (2017b). Strain Engineered Pyrochlore at High Pressure. *Sci. Rep.* 7 (1), 2236. doi:10.1038/s41598-017-02637-9

Sachan, R., Chisholm, M. F., Ou, X., Zhang, Y., and Weber, W. J. (2019). Energetic Ion Irradiation-Induced Disordered Nanochannels for Fast Ion Conduction. *JOM.* 71 (1), 103–108. doi:10.1007/s11837-018-3171-y

Sachan, R., Zhang, Y., Ou, X., Trautmann, C., Chisholm, M. F., and Weber, W. J. (2017a). New Insights on Ion Track Morphology in Pyrochlores by Aberration Corrected Scanning Transmission Electron Microscopy. *J. Mater. Res.* 32 (5), 928–935. doi:10.1557/jmr.2016.418

Sachan, R., Cooper, V. R., Liu, B., Aidhy, D. S., Voas, B. K., Lang, M., et al. (2017b). Forging Fast Ion Conducting Nanochannels With Swift Heavy Ions: The Correlated Role of Local Electronic and Atomic Structure. *J. Phys. Chem. C.* 121 (1), 975–981. doi:10.1021/acs.jpcc.6b12522

Sachan, R., Zarkadoula, E., Ou, X., Trautmann, C., Zhang, Y., Chisholm, M. F., et al. (2018). Sculpting Nanoscale Functional Channels in Complex Oxides Using

Energetic Ions and Electrons. *ACS Appl. Mater. Inter.* 10 (19), 16731–16738. doi:10.1021/acsami.8b02326

Sang, X., Lupini, A. R., Unocic, R. R., Chi, M., Borisevich, A. Y., Kalinin, S. V., et al. (2016). Dynamic Scan Control in STEM: Spiral Scans. *Adv. Struct. Chem. Imag.* 2 (1), 6. doi:10.1186/s40679-016-0020-3

Savitzky, B. H., Zeltmann, S. E., Hughes, L. A., Brown, H. G., Zhao, S., Pelz, P. M., et al. (2021). py4DSTEM: A Software Package for Four-Dimensional Scanning Transmission Electron Microscopy Data Analysis. *Microsc. Microanalysis.* 27, 1–32. doi:10.1017/S1431927621000477

Scherzer, O. (1949). The Theoretical Resolution Limit of the Electron Microscope. *J. Appl. Phys.* 20 (1), 20–29. doi:10.1063/1.1698233

Schuster, B., Lang, M., Klein, R., Trautmann, C., Neumann, R., and Benyagoub, A. (2009). Structural Phase Transition in Induced by Swift Heavy Ion Irradiation at High-Pressure. *Nucl. Instr. Methods Phys. Res. Section B: Beam Interactions Mater. Atoms.* 267 (6), 964–968. doi:10.1016/j.nimb.2009.02.046

Schweiger, S., Pfenninger, R., Bowman, W. J., Aschauer, U., and Rupp, J. L. M. (2017). Designing Strained Interface Heterostructures for Memristive Devices. *Adv. Mater.* 29 (15), 1605049. doi:10.1002/adma.201605049

Seshadri, R. (2006). Lone Pairs in Insulating Pyrochlores: Ice Rules and High-K Behavior. *Solid State. Sci.* 8 (3), 259–266. doi:10.1016/j.solidstatesciences.2006.02.020

Shafieizadeh, Z., Xin, Y., Koohpayeh, S. M., Huang, Q., and Zhou, H. (2018). Superdislocations and Point Defects in Pyrochlore Yb2Ti2O7 Single Crystals and Implication on Magnetic Ground States. *Sci. Rep.* 8 (1), 17202. doi:10.1038/s41598-018-35283-w

Shamblin, J., Feygenson, M., Neuefeind, J., Tracy, C. L., Zhang, F., Finkeldei, S., et al. (2016). Probing Disorder in Isometric Pyrochlore and Related Complex Oxides. *Nat. Mater.* 15 (5), 507–511. doi:10.1038/nmat4581

Shamblin, J., Tracy, C. L., Palomares, R. I., O'Quinn, E. C., Ewing, R. C., Neuefeind, J., et al. (2018). Similar Local Order in Disordered Fluorite and Aperiodic Pyrochlore Structures. *Acta Materialia.* 144, 60–67. doi:10.1016/j.actamat.2017.10.044

Shanmugam, J., Borisenko, K. B., Chou, Y.-J., Kirkland, A. I., and Analyser, e. R. D. F. (2017). eRDF Analyser: An Interactive GUI for Electron Reduced Density Function Analysis. *SoftwareX.* 6, 185–192. doi:10.1016/j.softx.2017.07.001

Shao, Y.-T., Yuan, R., Hsiao, H.-W., Yang, Q., Hu, Y., and Zuo, J.-M. (2021). Cepstral Scanning Transmission Electron Microscopy Imaging of Severe Lattice Distortions. *Ultramicroscopy*, 113252. doi:10.1016/j.ultramic.2021.113252

Sheng, H. W., Luo, W. K., Alamgir, F. M., Bai, J. M., and Ma, E. (2006). Atomic Packing and Short-To-Medium-Range Order in Metallic Glasses. *Nature.* 439 (7075), 419–425. doi:10.1038/nature04421

Sheth, J., Chen, D., Kim, J. J., Bowman, W. J., Crozier, P. A., Tuller, H. L., et al. (2016). Coupling of Strain, Stress, and Oxygen Non-Stoichiometry in Thin Film Pr0.1Ce0.9O2−δ. *Nanoscale.* 8 (36), 16499–16510. doi:10.1039/c6nr04083g

Sickafus, K. E., Minervini, L., Grimes, R. W., Valdez, J. A., Ishimaru, M., Li, F., et al. (2000). Radiation Tolerance of Complex Oxides. *Science.* 289 (5480), 748–751. doi:10.1126/science.289.5480.748

Simonov, A., and Goodwin, A. L. (2020). Designing Disorder Into Crystalline Materials. *Nat. Rev. Chem.* 4 (12), 657–673. doi:10.1038/s41570-020-00228-3

Solomon, J. M., Shamblin, J., Lang, M., Navrotsky, A., and Asta, M. (2016). Chemical Ordering in Substituted Fluorite Oxides: a Computational Investigation of Ho2Zr2O7 and RE2Th2O7 (RE=Ho, Y, Gd, Nd, La). *Sci. Rep.* 6 (1), 38772. doi:10.1038/srep38772

Song, B., Ding, Z., Allen, C. S., Sawada, H., Zhang, F., Pan, X., et al. (2018). Hollow Electron Ptychographic Diffractive Imaging. *Phys. Rev. Lett.* 121 (14), 146101. doi:10.1103/physrevlett.121.146101

Souza Junior, J. B., Schleder, G. R., Bettini, J., Nogueira, I. C., Fazzio, A., and Leite, E. R. (2021). Pair Distribution Function Obtained from Electron Diffraction: An Advanced Real-Space Structural Characterization Tool. *Matter.* 4 (2), 441–460. doi:10.1016/j.matt.2020.10.025

Spurgeon, S. R., Kaspar, T. C., Shutthanandan, V., Gigax, J., Shao, L., and Sassi, M. (2020). Asymmetric Lattice Disorder Induced at Oxide Interfaces. *Adv. Mater. Inter.* 7 (8), 1901944. doi:10.1002/admi.201901944

Spurgeon, S. R. (2020). Order-Disorder Behavior at Thin Film Oxide Interfaces. *Curr. Opin. Solid State. Mater. Sci.* 24 (6), 100870. doi:10.1016/j.cossms.2020.100870

Spurgeon, S. R., Sassi, M., Ophus, C., Stubbs, J. E., Ilton, E. S., and Buck, E. C. (2019). Nanoscale Oxygen Defect Gradients in UO2+x Surfaces. *Proc. Natl. Acad. Sci. USA.* 116 (35), 17181–17186. doi:10.1073/pnas.1905056116

Stanek, C. R. (2003). *Atomic Scale Disorder in Fluorite and Fluorite Related Oxides*. London, United Kingdom: Department of Materials Imperial College of Science, Technology and Medicine, University of London, 195.

Subramanian, M. A., Aravamudan, G., and Subba Rao, G. V. (1983). Oxide Pyrochlores - A Review. *Prog. Solid State. Chem.* 15 (2), 55–143. doi:10.1016/0079-6786(83)90001-8

Sun, W., Liu, J.-Y., Gong, X.-Q., Zaman, W.-Q., Cao, L.-M., and Yang, J. (2016). OER Activity Manipulated by IrO6 Coordination Geometry: an Insight From Pyrochlore Iridates. *Sci. Rep.* 6 (1), 38429. doi:10.1038/srep38429

Suzuki, S., Tanaka, M., and Ishigame, M. (1985). Structural Studies on ZrO2-Y2O3 System by Electron Diffraction and Electron Microscopy I. *Jpn. J. Appl. Phys.* 24 (Part 1No. 4), 401–410. doi:10.1143/jjap.24.401

Syed, K., Xu, M., Ohtaki, K. K., Kok, D., Karandikar, K. K., Graeve, O. A., et al. (2020). Correlations of Grain Boundary Segregation to Sintering Techniques in a Three-Phase Ceramic. *Materialia.* 14, 100890. doi:10.1016/j.mtla.2020.100890

Tabira, Y., Withers, R. L., Barry, J. C., and Elcoro, L. (2001). The Strain-Driven Pyrochlore to "Defect Fluorite" Phase Transition in Rare Earth Sesquioxide Stabilized Cubic Zirconias. *J. Solid State. Chem.* 159 (1), 121–129. doi:10.1006/jssc.2001.9139

Tabira, Y., Withers, R., Thompson, J., and Schmid, S. (1999). Structured Diffuse Scattering as an Indicator of Inherent Cristobalite-like Displacive Flexibility in the Rare Earth Zirconate Pyrochlore LaδZr1−δO2−δ/2, 0.49. *J. Solid State. Chem.* 142 (2), 393–399. doi:10.1006/jssc.1998.8054

Taheri, M. L., Stach, E. A., Arslan, I., Crozier, P. A., Kabius, B. C., LaGrange, T., et al. (2016). Current Status and Future Directions for *In Situ* Transmission Electron Microscopy. *Ultramicroscopy.* 170, 86–95. doi:10.1016/j.ultramic.2016.08.007

Takaki, S., Yasuda, K., Yamamoto, T., Matsumura, S., and Ishikawa, N. (2014). Atomic Structure of Ion Tracks in Ceria. *Nucl. Instr. Methods Phys. Res. Section B: Beam Interactions Mater. Atoms.* 326, 140–144. doi:10.1016/j.nimb.2013.10.077

Takaki, S., Yasuda, K., Yamamoto, T., Matsumura, S., and Ishikawa, N. (2016). Structure of Ion Tracks in Ceria Irradiated With High Energy Xenon Ions. *Prog. Nucl. Energ.* 92, 306–312. doi:10.1016/j.pnucene.2016.07.013

Talanov, M. V., and Talanov, V. M. (2021). Structural Diversity of Ordered Pyrochlores. *Chem. Mater.* 33 (8), 2706–2725. doi:10.1021/acs.chemmater.0c04864

Thust, A., Coene, W. M. J., Op de Beeck, M., and Van Dyck, D. (1996). Focal-Series Reconstruction in HRTEM: Simulation Studies on Non-Periodic Objects. *Ultramicroscopy.* 64 (1), 211–230. doi:10.1016/0304-3991(96)00011-3

Tong, X., Bowman, W. J., Mejia-Giraldo, A., Crozier, P. A., and Mebane, D. S. (2020). New Data-Driven Interacting-Defect Model Describing Nanoscopic Grain Boundary Compositions in Ceramics. *J. Phys. Chem. C.* 124 (43), 23619–23625. doi:10.1021/acs.jpcc.0c05713

Tracy, C. L., Shamblin, J., Park, S., Zhang, F., Trautmann, C., Lang, M., et al. (2016). Role of Composition, Bond Covalency, and Short-Range Order in the Disordering of Stannate Pyrochlores by Swift Heavy Ion Irradiation. *Phys. Rev. B.* 94 (6), 064102. doi:10.1103/physrevb.94.064102

Tran, D. T., Svensson, G., and Tai, C.-W. (2017). SUePDF: a Program to Obtain Quantitative Pair Distribution Functions From Electron Diffraction Data. *J. Appl. Cryst.* 50 (1), 304–312. doi:10.1107/s160057671601863x

Treacy, M. M. J., and Borisenko, K. B. (2012). The Local Structure of Amorphous Silicon. *Science* 335 (6071), 950–953. doi:10.1126/science.1214780

Treacy, M. M. J., Gibson, J. M., Fan, L., Paterson, D. J., and McNulty, I. (2005). Fluctuation Microscopy: a Probe of Medium Range Order. *Rep. Prog. Phys.* 68 (12), 2899–2944. doi:10.1088/0034-4885/68/12/r06

Trump, B. A., Koohpayeh, S. M., Livi, K. J. T., Wen, J.-J., Arpino, K. E., Ramasse, Q. M., et al. (2018). Universal Geometric Frustration in Pyrochlores. *Nat. Commun.* 9 (1), 2619. doi:10.1038/s41467-018-05033-7

Turner, K. M., Rittman, D. R., Heymach, R. A., Tracy, C. L., Turner, M. L., Fuentes, A. F., et al. (2017). Pressure-Induced Structural Modifications of Rare-Earth Hafnate Pyrochlore. *J. Phys. Condens. Matter.* 29 (25), 255401. doi:10.1088/1361-648x/aa7148

van Dijk, M. P., Mijlhoff, F. C., and Burggraaf, A. J. (1986). Pyrochlore Microdomain Formation in Fluorite Oxides. *J. Solid State. Chem.* 62 (3), 377–385. doi:10.1016/0022-4596(86)90253-7

van Landuyt, J., Gevers, R., and Amelinckx, S. (1966). The fine Structure of Spots in Electron Diffraction Resulting From the Presence of Planar Interfaces and Dislocations. *Phys. Stat. Sol. (B).* 18 (1), 363–378. doi:10.1002/pssb.19660180135

Van Tendeloo, G., and Amelinckx, S. (1998). The Origin of Diffuse Intensity in Electron Diffraction Patterns. *Phase Transitions.* 67 (1), 101–135. doi:10.1080/01411599808219190

Voyles, P. M., Bogle, S., and Abelson, J. R. (2011). "Fluctuation Microscopy in the STEM," in *Scanning Transmission Electron Microscopy: Imaging and Analysis*. Editors S. J. Pennycook and P. D. Nellist (New York, NY: Springer New York), 725–756. doi:10.1007/978-1-4419-7200-2_18

Voyles, P. M., and Muller, D. A. (2002). Fluctuation Microscopy in the STEM. *Ultramicroscopy.* 93 (2), 147–159. doi:10.1016/s0304-3991(02)00155-9

Wan, W., Sun, J., Su, J., Hovmöller, S., and Zou, X. (2013). Three-Dimensional Rotation Electron Diffraction: SoftwareREDfor Automated Data Collection and Data Processing. *J. Appl. Cryst.* 46 (6), 1863–1873. doi:10.1107/s0021889813027714

Wang, Y., Salzberger, U., Sigle, W., Eren Suyolcu, Y., and van Aken, P. A. (2016). Oxygen Octahedra Picker: A Software Tool to Extract Quantitative Information From STEM Images. *Ultramicroscopy.* 168, 46–52. doi:10.1016/j.ultramic.2016.06.001

Welberry, T. R., and Weber, T. (2016). One Hundred Years of Diffuse Scattering. *Crystallogr. Rev.* 22 (1), 2–78. doi:10.1080/0889311x.2015.1046853

Whittle, K. R., Cranswick, L. M. D., Redfern, S. A. T., Swainson, I. P., and Lumpkin, G. R. (2009). Lanthanum Pyrochlores and the Effect of Yttrium Addition in the Systems La2−xYxZr2O7 and La2−xYxHf2O7. *J. Solid State. Chem.* 182 (3), 442–450. doi:10.1016/j.jssc.2008.11.008

Williams, D. B., and Carter, C. B. (2009a). "Diffraction from Small Volumes," in *Transmission Electron Microscopy: A Textbook for Materials Science*. Editors D. B. Williams and C. B. Carter (Boston, MA: Springer US), 271–282. doi:10.1007/978-0-387-76501-3_17

Williams, D. B., and Carter, C. B. (2009b). "Phase-Contrast Images," in *Transmission Electron Microscopy: A Textbook for Materials Science*. Editors D. B. Williams and C. B. Carter (Boston, MA: Springer US), 389–405. doi:10.1007/978-0-387-76501-3_23

Williams, D. B., and Carter, C. B. (2009c). "The Instrument," in *Transmission Electron Microscopy: A Textbook for Materials Science*. Editors D. B. Williams and C. B. Carter (Boston, MA: Springer US), 141–171. doi:10.1007/978-0-387-76501-3_9

Williams, D. B., and Carter, C. B. (2009d). "The Transmission Electron Microscope," in *Transmission Electron Microscopy: A Textbook for Materials Science*. Editors D. B. Williams and C. B. Carter (Boston, MA: Springer US), 3–22. doi:10.1007/978-0-387-76501-3_1

Withers, R. L. (2008). ""Disorder": Structured Diffuse Scattering and Local Crystal Chemistry,". *Advances in Imaging and Electron Physics*. Editor P. W. Hawkes (San Diego: Elsevier Academic Press Inc), 152, 303–337. doi:10.1016/s1076-5670(08)00606-x

Withers, R. L., Thompson, J. G., and Barlow, P. J. (1991). An Electron, and X-ray Powder, Diffraction Study of Cubic, Fluorite-Related Phases in Various ZrO2□Ln2O3 Systems. *J. Solid State. Chem.* 94 (1), 89–105. doi:10.1016/0022-4596(91)90224-6

Withers, R. L., Welberry, T. R., Larsson, A.-K., Liu, Y., Norén, L., Rundlöf, H., et al. (2004). Local crystal Chemistry, Induced Strain and Short Range Order in the Cubic Pyrochlore (Bi1.5−αZn0.5−β)(Zn0.5−γNb1.5−δ)O(7−1.5α−β−γ−2.5δ) (BZN). *J. Solid State. Chem.* 177 (1), 231–244. doi:10.1016/j.jssc.2003.07.005

Wu, Y., Ciston, J., Kräemer, S., Bailey, N., Odette, G. R., and Hosemann, P. (2016). The Crystal Structure, Orientation Relationships and Interfaces of the Nanoscale Oxides in Nanostructured Ferritic Alloys. *Acta Materialia.* 111, 108–115. doi:10.1016/j.actamat.2016.03.031

Wuensch, B. J., and Eberman, K. W. (2000). Order-Disorder Phenomena in A2B2O7 Pyrochlore Oxides. *JOM.* 52 (7), 19–21. doi:10.1007/s11837-000-0155-4

Yan, S., Abhilash, K. P., Tang, L., Yang, M., Ma, Y., Xia, Q., et al. (2019). Research Advances of Amorphous Metal Oxides in Electrochemical Energy Storage and Conversion. *Small.* 15 (4), e1804371. doi:10.1002/smll.201804371

Yankovich, A. B., Berkels, B., Dahmen, W., Binev, P., Sanchez, S. I., Bradley, S. A., et al. (2014). Picometre-precision Analysis of Scanning Transmission Electron Microscopy Images of Platinum Nanocatalysts. *Nat. Commun.* 5 (1), 4155. doi:10.1038/ncomms5155

Zhang, D., Oleynikov, P., Hovmöller, S., and Zou, X. (2010). Collecting 3D Electron Diffraction Data by the Rotation Method. *Z. für Kristallographie.* 225 (2-3), 94–102. doi:10.1524/zkri.2010.1202

Zhao, G., Treacy, M. M. J., and Buseck, P. R. (2010). Fluctuation Electron Microscopy of Medium-Range Order in Ion-Irradiated Zircon. *Philosophical Mag.* 90 (35-36), 4661–4677. doi:10.1080/14786431003630876

Zhao, M., Pan, W., Wan, C., Qu, Z., Li, Z., and Yang, J. (2017). Defect Engineering in Development of Low Thermal Conductivity Materials: A Review. *J. Eur. Ceram. Soc.* 37 (1), 1–13. doi:10.1016/j.jeurceramsoc.2016.07.036

Zhu, F., Hirata, A., Liu, P., Song, S., Tian, Y., Han, J., et al. (2017). Correlation Between Local Structure Order and Spatial Heterogeneity in a Metallic Glass. *Phys. Rev. Lett.* 119 (21), 215501. doi:10.1103/physrevlett.119.215501

Zhu, Y., and Dürr, H. (2015). The Future of Electron Microscopy. *Phys. Today.* 68 (4), 32–38. doi:10.1063/pt.3.2747

Zhu, Y., Ophus, C., Ciston, J., and Wang, H. (2013). Interface Lattice Displacement Measurement to 1pm by Geometric Phase Analysis on Aberration-Corrected HAADF STEM Images. *Acta Materialia.* 61 (15), 5646–5663. doi:10.1016/j.actamat.2013.06.006

Zou, X., Hovmöller, S., Oleynikov, P., and Oleynikov, P. (2011). *Electron Crystallography : Electron Microscopy and Electron Diffraction*. Incorporated, Oxford, UNITED KINGDOM: Oxford University Press.

Zuo, J.-M. (2019). "Electron Nanodiffraction," in *Springer Handbook of Microscopy*. Editors P. W. Hawkes and J. C. H. Spence (Cham: Springer International Publishing), 905–969. doi:10.1007/978-3-030-00069-1_18

Zuo, J. M., and Spence, J. C. H. (2017a). "Diffuse Scattering," in *Advanced Transmission Electron Microscopy: Imaging and Diffraction in Nanoscience*. Editors J. M. Zuo and J. C. H. Spence (New York, NY: Springer New York), 403–440. doi:10.1007/978-1-4939-6607-3_13

Zuo, J. M., and Spence, J. C. H. (2017b). "The Geometry of Electron Diffraction Patterns," in *Advanced Transmission Electron Microscopy: Imaging and Diffraction in Nanoscience*. Editors J. M. Zuo and J. C. H. Spence (New York, NY: Springer New York), 49–75. doi:10.1007/978-1-4939-6607-3_3

Conflict of Interest: The authors declare that the research was conducted in the absence of any commercial or financial relationships that could be construed as a potential conflict of interest.

Advantages of publishing in Frontiers

OPEN ACCESS
Articles are free to read for greatest visibility and readership

FAST PUBLICATION
Around 90 days from submission to decision

HIGH QUALITY PEER-REVIEW
Rigorous, collaborative, and constructive peer-review

TRANSPARENT PEER-REVIEW
Editors and reviewers acknowledged by name on published articles

Frontiers
Avenue du Tribunal-Fédéral 34
1005 Lausanne | Switzerland

Visit us: www.frontiersin.org
Contact us: frontiersin.org/about/contact

REPRODUCIBILITY OF RESEARCH
Support open data and methods to enhance research reproducibility

DIGITAL PUBLISHING
Articles designed for optimal readership across devices

FOLLOW US
@frontiersin

IMPACT METRICS
Advanced article metrics track visibility across digital media

EXTENSIVE PROMOTION
Marketing and promotion of impactful research

LOOP RESEARCH NETWORK
Our network increases your article's readership